

OKINAWA INSTITUTE OF SCIENCE AND TECHNOLOGY
GRADUATE UNIVERSITY

Thesis submitted for the degree

Doctor of Philosophy

Glioma on Chips

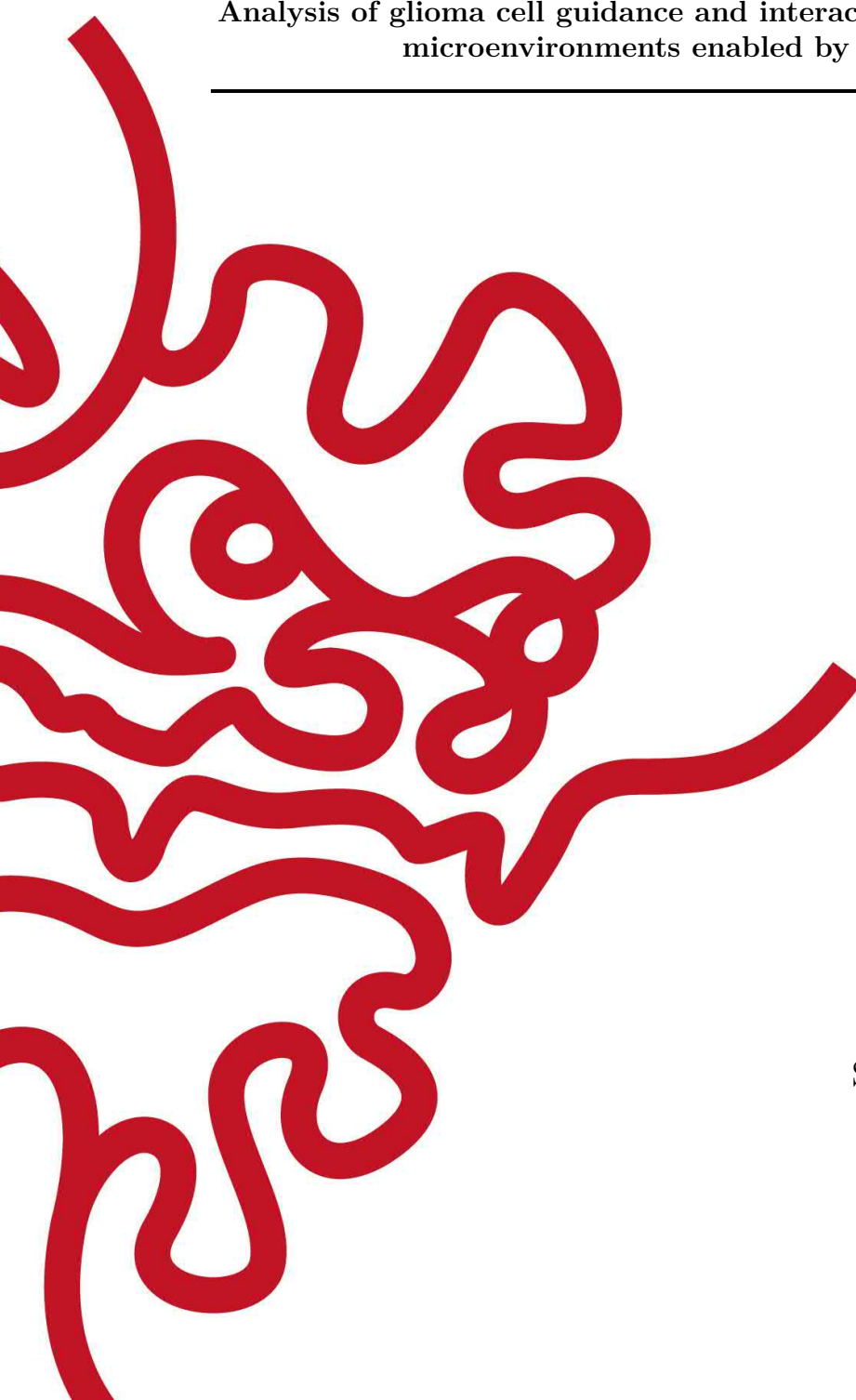
Analysis of glioma cell guidance and interaction in microfluidic-controlled
microenvironments enabled by machine learning

by

Hsieh-Fu TSAI

Supervisor: **Amy Q. SHEN**

February, 2020



Declaration of Original and Sole Authorship

I, Hsieh-Fu TSAI, declare that this thesis entitled *Glioma on Chips* and the data presented in it are original and my own work.

I confirm that:

- This work was done solely while a candidate for the research degree at the Okinawa Institute of Science and Technology Graduate University, Japan.
- No part of this work has previously been submitted for a degree at this or any other university.
- References to the work of others have been clearly attributed. Quotations from the work of others have been clearly indicated, and attributed to them.
- In cases where others have contributed to part of this work, such contribution has been clearly acknowledged and distinguished from my own work.
- None of this work has been previously published elsewhere, with the exception of the following:
 1. Hsieh-Fu Tsai *et al.*, Uniform electric field generation in circular multi-well culture plates using polymeric inserts, *Scientific Reports*, **6**:26222 (2016)
 2. EP3350310B1 3D POLYMERIC INSERT TO APPLY UNIFORM ELECTRIC FIELD IN CIRCULAR CULTUREWARE
 3. Hsieh-Fu Tsai *et al.*, Tumour-on-a-chip: microfluidic models of tumour morphology, growth, and microenvironment, *Journal of Royal Society Interface*, 20170137 (2017)
 4. Hsieh-Fu Tsai *et al.*, Usiigaci: Instance-aware cell tracking in stain-free phase contrast microscopy enabled by machine learning, *SoftwareX*, **9**, 230-237 (2019)
 5. Hsieh-Fu Tsai *et al.*, Glioblastoma adhesion in a quick-fit hybrid microdevice, *Biomedical Microdevices*, 21(**2**), 30 (2019)
 6. US Application 62/968,768 A DETACHABLE MICROFLUIDIC SYSTEM AND METHOD FOR ROBUST SPARSE CELL SEEDING WITHOUT BUBBLES

7. Hsieh-Fu Tsai *et al.*, Voltage-gated ion channels mediate the electrotaxis of glioblastoma cells in a hybrid PMMA/PDMS microdevice, Submitted (2020)

Date: February, 2020

Signature: 

Abstract

In biosystems, chemical and physical fields established by gradients guide cell migration, which is a fundamental phenomenon underlying physiological and pathophysiological processes such as development, morphogenesis, wound healing, and cancer metastasis. Cells in the supportive tissue of the brain, glia, are electrically stimulated by the local field potentials from neuronal activities. How the electric field may influence glial cells is yet fully understood. Furthermore, the cancer of glia, glioma, is not only the most common type of brain cancer, but the high-grade form of it (glioblastoma) is particularly aggressive with cells migrating into the surrounding tissues (infiltration) and contribute to poor prognosis. In this thesis, I investigate how electric fields in the microenvironment can affect the migration of glioblastoma cells using a versatile microsystem I have developed. I employ a hybrid microfluidic design to combine poly(methylmethacrylate) (PMMA) and poly(dimethylsiloxane) (PDMS), two of the most common materials for microfluidic fabrication. The advantages of the two materials can be complemented while disadvantages can be mitigated. The hybrid microfluidics have advantages such as versatile 3D layouts in PMMA, high dimensional accuracy in PDMS, and rapid prototype turnaround by facile bonding between PMMA and PDMS using a dual-energy double sided tape. To accurately analyze label-free cell migration, a machine learning software, *Usiigaci*, is developed to automatically segment, track, and analyze single cell movement and morphological changes under phase contrast microscopy. The hybrid microfluidic chip is then used to study the migration of glioblastoma cell models, T98G and U-251MG, in electric field (electrotaxis). The influence of extracellular matrix and chemical ligands on glioblastoma electrotaxis are investigated. I further test if voltage-gated calcium channels are involved in glioblastoma electrotaxis. The electrotaxes of glioblastoma cells are found to require optimal laminin extracellular matrices and depend on different types of voltage-gated calcium channels, voltage-gated potassium channels, and sodium transporters. A reversibly-sealed hybrid microfluidic chip is developed to study how electric field and laminar shear can condition confluent endothelial cells and if the biomimetic conditions affect glioma cell adhesion to them. It is found that glioma/endothelial adhesion is mediated by the Ang1/Tie2 signaling axis and adhesion of glioma is slightly increased to endothelial cells conditioned with shear flow and moderate electric field. In conclusion, robust and versatile hybrid microsystems are employed for studying glioma biology with emphasis on cell migration. The hybrid microfluidic tools can enable us to elucidate fundamental mechanisms in the field of the tumor biology and regenerative medicine.

Acknowledgment

I owe my deepest gratitude to my advisor, Amy Shen, for her support to let me take on new ideas and projects with freedom and confidence. I would like to express appreciation to members on my thesis committee, Professor Tomoyuki Takahashi and Professor Ichiro Masai for their kind advice and insightful feedback during my doctorate study. I would like to also thank Professor Shuichi Takayama and Professor Roger Kamm for their kind support as thesis examiners.

Secondly, I would like to thank the support and understanding from my family, especially Tori and Miuna, for being on this journey with me. I'd also like to thank my friends for your support, Alexandra, Hung-Ju, and Jason, especially.

Thirdly, during the six years, the members of Shen Unit, especially Kazi and Yuno, have helped me greatly on day-to-day lab operations and paperwork so that all this work is possible. I give my special thanks to Yuno who helped me greatly on dealing with paperwork and chores in research activities with JSPS grant. The postdocs in Shen Unit have taught and helped me a lot, especially Simon, Cameron, Riccardo, Sebastien, and Atsushi. I also thank Noa, Shivani, Ainash, and Santo in our unit and other PhD students in class 2014.

I am grateful for the financial support from teaching assistantship by OIST and research fellowship by Japan Society for the Promotion of Science. I would also like to acknowledge assistance received in the following areas:

- Designing the research

I particularly acknowledge suggestions and comments from Professor Shuichi Takayama and Professor Tomoyuki Takahashi for vital research directions on studying the signaling pathways in the glioma electrotaxis.

- Executing the research

In the *Usiigaci* project, several collaborators participated in the coding and architecture of the software and the tasks were funded by JSPS grant JP1700362. I would like to acknowledge the contribution from Ms. Joanna Gajda (AGH University of Science and Technology, Poland), Dr. Tyler F.W. Sloan (Quorumetrix Solutions, Canada), Dr. Andrei Rares (ImagineA, The Netherlands), Mr. Ting-Chun Chou, and Mr. Mohammad Umer Javaid. In particular, the implementation by Dr. Andrei Rares and Mr. Mohammad Umer Javaid was important for the enhancement of the software for the community. Camilo IJspeert participated in the glioblastoma ECM experiments as his intern project.

I also acknowledge the training and technical support on research instrumentation from staff in the Instrumental Analysis Section, Imaging Section, Engineer-

ing Support Section, and Scientific Computing Section of OIST. I would like to particularly thank Dr. Toshiaki Mochizuki and Dr. Toshio Sasaki for mentorship and assistance.

- Writing, proofing, or copyediting the manuscript

I acknowledge the illustration assistance from Ms. Yi-Ching Tsai (E-mail) and illustration service from Elsevier. The published papers as part of the thesis are proofread by Dr. Steven D. Aird and I'd like to acknowledge his prompt assistance for his feedback.

Abbreviations

3D	Three dimension
ABS	Acrylonitrile butadiene styrene
AI	Artificial intelligence
ANOVA	Analysis of variance
APTES	(3-Aminopropyl)triethoxysilane
ASIC	Acid-sensing ion channel
ATCC	American Type Culture Collection
BMMD	Biomedical microdevice
CAD	Computer aided design
CAM	Computer aided manufacturing
CMOS	Complementary metal-oxide semiconductor
CNC	Computer numerical control
CNN	Convolutional neural network
CNS	Central nervous system
COC	Cyclic olefin copolymers
COP	Cyclic olefin polymers
CS	Calf serum
CUDA	Compute Unified Device Architecture
CV	Coefficient of variation
dcEF	Direct current electric field
DG	Dentate gyrus
DMEM	Dulbecco's modified Eagle's medium
DMSO	Dimethylsulfoxide
D-PBS	Dulbecco's phosphate buffered saline
ds tape	Double-sided tape
de-ds tape	Dual energy double-sided tape
ECM	Extracellular matrix
EDTA	Ethylenediaminetetraacetic acid
EF	Electric field
EFS	Electric field strength
EGFR	Epidermal growth factor receptor
ENaC	Epithelial sodium channels
ESC	Embryonic stem cell
FBS	Fetal bovine serum
FDA	Food and drug administration
FDM	Fused deposition modeling

FGFR	Fibroblast growth factor receptor
FL	Fluorescence
FPGA	Field programmable gate array
FPN	Feature pyramid network
FT-IR	Fourier-transform infrared spectroscopy
GAN	Generative adversarial networks
GPCR	G-protein coupled receptor
GPTES	(3-Glycidyloxypropyl)triethoxysilane
GPU	Graphics processing unit
GUI	Graphical user interface
GWAS	Genome-wide association studies
HBSS	Hank's balanced salt solution
HEPA	High-efficiency particulate air
HGFR	Hepatocyte growth factor receptor
HPLC	High-performance liquid chromatography
ID	Identifier
iPSC	Induced pluripotent stem cell
ITO	Indium tin oxide
LFP	Local field potentials
MEM α	Minimum essential medium alpha
MEMS	Microelectromechanical systems
MMP	Matrix metalloproteinase
MIT	Massachusetts Institute of Technology
mIOU	mean Intersection over union
MOT	Multiple object tracking
MOTA	Multiple object tracking accuracy
MOTP	Multiple object tracking precision
NURBS	Non-uniform rational basis spline
PBS	Phosphate buffered saline
PC	Personal computer
PCM	Phase contrast microscopy
PDL	Poly(D-lysine)
PDMS	Poly(dimethylsiloxane)
PLA	Poly(lactic acid)
PLO	Poly(L-ornithine)
PID	Proportional-integral-derivative
PMMA	Poly(methyl methacrylate)
QPI	Quantitative phase imaging
R-CNN	Regional convolutional neural network
RH	Relative humidity
ROI	Region of interest
sCMOS	Scientific Complement Metal Oxide Semiconductor
SLS	Selective laser sintering
SVZ	Subventricular zone
TCGA	The cancer genome atlas
TCPS	Tissue-culture polystyrene

TEP	Transepithelial potential
TPU	Tensor processing unit
TTF	Tumor treating field
VEGFR	Vascular endothelial growth factor receptor
VGCC	Voltage-gated calcium channel
VGKC	Voltage-gated potassium channel
VGSC	Voltage-gated sodium channel
VUV	Vacuum ultraviolet
UV	Ultraviolet
WHO	World Health Organization

Fortuna Eruditis Favet

This thesis is dedicated to my family

Contents

Declaration of Original and Sole Authorship	iii
Abstract	v
Acknowledgment	vii
Abbreviations	ix
Contents	xv
List of Figures	xxi
List of Tables	xxvii
1 Introduction	1
1.1 Glioma: a tumor of supportive cells in the central nervous system . . .	1
1.1.1 Epidemiology, classification, and molecular pathology	2
1.1.2 Origin and metastasis of glioma	4
1.1.3 Complex microenvironment of glioma	6
1.1.4 Glioma therapy	7
1.1.5 What microenvironment governs glioma infiltration?	11
1.2 Microfluidics and bioMEMS	12
1.3 Gradients in the microenvironment as directional cues	12
1.3.1 The chemical gradient microenvironment	13
1.3.2 The voltage gradient microenvironment	18
1.3.3 Multiplex gradients in 2D microfluidic chip	28
1.4 Glioma on a chip	31
1.5 Current challenges and opportunities using microfluidics in cancer biology	35
1.6 Research aims	37
2 Hybrid microfluidic platforms for reliable <i>in vitro</i> cell studies	39
2.1 Introduction: development of 2D microfluidic cell culture platforms . .	39
2.1.1 Designing microfluidic chips	40
2.1.2 Rapid prototyping of microfluidic chips	44
2.1.3 World-to-chip interface for microfluidic chips	49

2.1.4	Bonding strategies for microfluidic chips	52
2.1.5	Culturing cells on microfluidic chips	56
2.2	PMMA thermoplastic microfluidic chip for cell culture	63
2.3	A hybrid PMMA/PDMS microfluidic chip for electrotaxis study in an on-stage incubator	65
2.3.1	Microfluidic chip design: single-layer and double-layer design	66
2.3.2	Microfluidic chip fabrication	72
2.4	A reversibly-sealed PMMA/PDMS microfluidic chip for concurrent shear and electric field stimulation	79
2.4.1	SFEFC microfluidic chip design: concurrent shear flow and electric field conditioning	80
2.4.2	Microfluidic chip fabrication	82
2.5	Summary and prospects	83
3	Usiigaci: Single cell segmentation and tracking in label-free phase contrast microscopy enabled by machine learning	85
3.1	Introduction	85
3.1.1	Computational cell migration analysis	87
3.2	Software architecture	89
3.2.1	Segmentation module	89
3.2.2	Tracking module	95
3.2.3	Data processing module	95
3.3	Performance benchmark for cell segmentation and tracking	98
3.3.1	Cell segmentation accuracy evaluation	98
3.3.2	Cell tracking accuracy evaluation	98
3.4	Results and discussion	101
3.4.1	Mask R-CNN realizes fast and highly accurate whole-cell segmentation	101
3.4.2	High performance multiple object tracking using Usiigaci tracker	107
3.4.3	Automated tracking with manual verification ensures reliable cell tracking results	108
3.4.4	Limitations of Usiigaci	111
3.5	Summary and prospects	111
4	Electrotaxis of glioma cells using hybrid PMMA/PDMS microfluidics	115
4.1	Introduction	115
4.2	Materials and methods	118
4.2.1	The hybrid PMMA/PDMS chip for high-throughput electrotaxis experiment	118
4.2.2	Cell culture and maintenance	119
4.2.3	General experimental workflow	119
4.2.4	Electrotaxis of glioma cells on different ECM coatings	121
4.2.5	Electrotaxis of T98G glioma cells under co-stimulation of different chemical ligands	123
4.2.6	Extracellular calcium dependency of glioma cell electrotaxis	123

4.2.7	Pharmaceutical inhibition of voltage-gated ion channels in electrotaxis of glioma cells	124
4.2.8	Single cell migration tracking and statistical inference	125
4.3	Results and discussion	128
4.3.1	Uniformly sparse cell seeding on chip by submerged operation	128
4.3.2	Identification of appropriate ECM coatings for glioblastoma electrotaxis	130
4.3.3	Electrotactic heterogeneity in glioblastoma cell lines	134
4.3.4	Glioma electrotaxis does not intersect with ligand-mediated chemical signaling	139
4.3.5	Glioma electrotaxis is dependent on extracellular calcium cations	140
4.3.6	Glioma electrotaxis is dependent on different types of voltage-gated ion channels	145
4.4	Summary and prospects	149
5	Study of glioma-vasculature adhesion using a quick-fit PMMA/PDMS microfluidic chip	153
5.1	Introduction	153
5.2	Materials and methods	154
5.2.1	Shear flow and electric field co-stimulation chip (SFEFC) using hybrid PMMA/PDMS microfluidic design and fabrication	154
5.2.2	Cell culture and maintenance	155
5.2.3	General experimental workflow	156
5.2.4	Endothelium conditioning by external fields in SFEFC	157
5.2.5	Glioblastoma cell adhesion on statically cultured endothelium	159
5.2.6	Glioblastoma cell adhesion on shear/EF conditioned endothelium on SFEFC	160
5.2.7	Immunofluorescence staining, microscopic imaging and statistical inference	160
5.3	Results and discussion	160
5.3.1	Reversibly sealed quick-fit microfluidic chip tolerates high flow rate	160
5.3.2	Mediation of endothelial cells alignment by shear flow and electric field	161
5.3.3	Adherence of glioblastoma cells to endothelial cells in static condition with stimulation of angiotensin signaling	163
5.3.4	Adherence of glioblastoma cells to shear flow and electric field conditioned endothelial cells	165
5.4	Summary and prospects	168
	Conclusion	171
	Appendix	173

A	Physical properties of the <i>in vitro</i> microenvironment	175
A.1	Introduction	175
A.2	Materials and methods	176
A.2.1	Preparation of cell culture media	176
A.2.2	Density measurement using densimeter	177
A.2.3	Viscosity measurement using rotational rheometry and capillary rheometry	177
A.2.4	pH and electrical conductivity measurement	180
A.2.5	Refractive index measurement using refractometry	180
A.3	Results and discussion	181
A.3.1	Density, electrical conductivity, and refractive index of different media	181
A.3.2	The geometry effect on the rotational rheometry results	183
A.3.3	Dynamic shear viscosities of selected buffer solutions and cell culture media	184
A.4	Summary and prospects	186
B	Uniform electrical cell stimulation in circular cultureware by 3D mi- crofluidics	187
B.1	Introduction	187
B.2	Theoretical design and numerical simulation	189
B.2.1	Design principle of a 3D CAD insert to create a uniform EF in different sizes of circular cultureware	189
B.2.2	Numerical simulation	194
B.3	Materials and methods	198
B.3.1	Device fabrication	198
B.3.2	Cell culture and maintenance	206
B.3.3	EF measurement setup	206
B.3.4	Microfluidic chip assembly, EF stimulation and microscopy anal- ysis	207
B.4	Results and discussion	210
B.4.1	Validation of EF uniformity in the chamber	210
B.4.2	High performance and high stimulation area percentage cell EF stimulation	211
B.4.3	Cell migration and alignment under uniform EF stimulation	212
B.5	Summary and prospects	213
C	Characterization of common thermoplastics for microfluidics	215
C.1	Introduction	215
C.2	Samples and measurement	215
C.3	Results	216
D	List of open-source models for laboratory applications	219

E List of source code of software generated in this thesis	225
Bibliography	227

List of Figures

1.1	Neuroglial cells in the CNS	2
1.2	Classification algorithm for diffuse gliomas	3
1.3	Speculative relationship of glioma cell of origin of neural progenitors . .	5
1.4	Cancer cell metastatic dissemination	5
1.5	The tumor microenvironment of glioblastoma.	6
1.6	Measurement of electric potential in mouse brain specifically along the rostral migratory stream.	8
1.7	Interactions between GSC and endothelial cells.	9
1.8	Oxygen levels regulate the phenotype of glioblastoma cells in the peri- necrotic niche.	9
1.9	Cross-talk between glioma and tumor associated macrophages (TAMs). .	9
1.10	The scheme of major signaling pathways in glioma and their targeted therapy.	10
1.11	The NovoTTF-100A non-invasive alternative electric field application system.	11
1.12	Length scale comparison between several biological and micro-fabrication structures.	12
1.13	Cells can be guided by physical as well as chemical cues.	13
1.14	Mechanisms for generating morphogen gradients.	14
1.15	Ectopic production of Shh induced a mirror image of chick wing bud. .	14
1.16	Cell polarity during chemotaxis of the calcium gradient	15
1.17	Complex signaling pathways in regulation of chemotaxis	16
1.18	Commonly used macro migration assays.	17
1.19	Classical methods of generating chemical gradients.	17
1.20	Microfluidic-based concentration gradient generator.	18
1.21	Classification of ion transporters on biological membranes.	19
1.22	Molecular basis of endogenous electric field.	20
1.23	A wound on mouse skin and measurement of the wound-associated elec- tric field.	20
1.24	Heterotaxia in zebrafish when H ⁺ -V-ATPase subunits are inhibited dur- ing early embryogenesis.	21
1.25	The polarities of transepithelial potential of mammary and prostate ducts correlate also with the direction of breast and prostate cancer cell migration relative to an EF <i>in vitro</i>	21
1.26	The anatomy of an action potential.	22
1.27	Electric field in the nervous system ultrastructure.	22

1.28	The mechanisms of cell response to EF are complex.	25
1.29	The hypothesis of electrokinetic based migration of membrane proteins as the cause for electrotaxis.	26
1.30	An abstract signaling network in EF stimulated cells.	27
1.31	The setup of a conventional device to create voltage gradients.	27
1.32	The microfluidic approach for creation of multiple voltage gradients on a single chip.	28
1.33	A microfluidic device for creating uniform voltage gradient to a large area of cell culture.	28
1.34	Complex gradients can guide cell migration.	29
1.35	A microfluidic device to create perpendicular oxygen and chemical gradients.	31
1.36	MDA-MB-231 cell migration in a combinatorial gradient generating microfluidic device	31
1.37	Microfluidic models for drug screening in glioma research.	32
1.38	Microfluidic models for study glioma cell migration.	33
1.39	Electrotaxis of glioma cells.	34
1.40	Galvanotaxis of glioblastoma cells of different transcription profile type and fetal derived neural progenitor cells (fNPC).	34
1.41	The tumor microenvironment is complex	37
2.1	Schematic illustration of soft lithography for PDMS fabrication.	46
2.2	Fabrication methodology for thermoplastic microfluidic chips.	47
2.3	Various 3D printing techniques for rapid prototyping microfluidic chips.	50
2.4	Disposable adapters for HPLC fittings.	52
2.5	Diagram of silane assisted bonding.	54
2.6	Priming method to remove bubbles in PDMS devices.	57
2.7	Effects of relative humidity on cell culture medium evaporation in the incubator	62
2.8	An enforced humidifier for Tokai Hit on-stage incubator	63
2.9	Schematics of a PMMA microfluidic chip containing two simple rectangular channels.	64
2.10	Single cell electrotaxis experimental setup.	64
2.11	The photoimage of electrotaxis setup using thermoplastic chips.	65
2.12	The concept of a small configuration hybrid PMMA/PDMS microfluidic chip.	67
2.13	The designs of single-layer and double-layer PMMA/PDMS chips.	67
2.14	The electrical equivalent circuit model of the PMMA/PDMS chip.	69
2.15	The hydraulic equivalent circuit model of single-layer (A) and double-layer (B) PMMA/PDMS chips.	70
2.16	Stable flow field in hybrid PMMA/PDMS chips.	70
2.17	4.99:2.45:1:0 ratio stepwise electric field established in the hybrid PMMA/PDMS chips.	71
2.18	Chemical transport simulated in hybrid PMMA/PDMS chips.	72
2.19	Chemical transport simulated in hybrid PMMA/PDMS chips at refined scale.	73

2.20	Chemical transport was more stable in double-layer PMMA/PDMS chip.	74
2.21	Stable chemical transport in double-layer PMMA/PDMS chip before and after 10 hours.	75
2.22	Mass fabrication of PMMA components by CO ₂ laser cutting.	77
2.23	The assembled PMMA/PDMS chip.	78
2.24	The shear flow and electric field co-stimulation microfluidic chip, SFEFC.	79
2.25	Liquid manipulation on the SFEFC.	80
2.26	Channel design in the PMMA/PDMS microchannel chip in SFEFC.	81
2.27	The electric equivalent circuit of SFEFC.	81
2.28	Numerical results of electric field strength in the shear flow and electric field co-stimulation microfluidic chip (SFEFC).	83
3.1	Workflow of Usiigaci	87
3.2	The single-cell migration parameters extracted from the electrotaxis experiments.	88
3.3	Types of cell tracking results	90
3.4	Detailed architecture of Mask R-CNN module in Usiigaci	91
3.5	An example of the training data for Usiigaci	93
3.6	Comparison of training time and sample number in Usiigaci and Deepcell	94
3.7	The GUI of the tracking modules in Usiigaci	96
3.8	Visualization examples of NIH/3T3 random cell migration generated automatically by the data analysis module.	97
3.9	Segmentation performance evaluation	98
3.10	Microscopy image of NIH/3T3 cells compared with segmentation results of Usiigaci, Fogbank, PHANTAST and Deepcell.	102
3.11	Segmentation similarity averaged among three NIH/3T3 cell images using various methods	103
3.12	Segmentation comparison between manual segmentation, fluorescence threshold, Deepcell, and Usiigaci	104
3.13	The segmentation time of one phase contrast microscopy (PCM) image acquired by various methods.	105
3.14	Higher tolerance to imaging settings during segmentation in Usiigaci	106
3.15	Visualization of valid tracks of NIH/3T3 10-hr electrotaxis in 300 V m ⁻¹ dcEF.	109
3.16	Directedness of NIH/3T3 electrotaxis after 10-hr, 300 V m ⁻¹ dcEF stimulation analyzed by different segmentation and tracking methods.	110
3.17	Segmentation results of confluent T98G glioma cells.	111
3.18	Automated AI cytoscope	114
4.1	The hypothetical mechanisms underlying electrotaxis.	117
4.2	Subfamilies of voltage-gated calcium channels.	118
4.3	The concept of a small configuration hybrid PMMA/PDMS microfluidic chip.	119
4.4	The photoimage of setup for high throughput experiments with PMMA/PDMS chips.	126

4.5	The single-cell migration parameters extracted from the electrotaxis experiments.	127
4.6	The results of U-251MG cell seeding inside microchannels by various methods.	129
4.7	Electrotaxis responses of T98G and U-251MG cells in various ECMs in PMMA chips.	130
4.8	Electrotaxis responses of T98G and U-251MG cells in various ECMs in PMMA chips.	131
4.9	Phase contrast images of T98G on PDL, Geltrex, and PLO/laminin in PMMA chips.	131
4.10	Phase contrast images of T98G & U-251MG cells on various ECMs. . .	132
4.11	The electrotaxis of T98G & U-251MG glioblastoma cells on various ECMs after 6 hours under 300 V m^{-1} EF stimulation.	133
4.12	The electrotactic responses of T98G and U-251MG are completely different and dependent on serum supplementation.	137
4.13	Time series plot of directedness in electrically stimulated glioblastoma cells.	138
4.14	Time series plot of orientation in electrically stimulated glioblastoma cells.	139
4.15	Phase contrast images of T98G and U-251MG before and after 6 hours 300 V m^{-1} stimulation.	140
4.16	The electrotactic directedness of T98G glioblastoma cells costimulated with ligands for chemical signaling.	141
4.17	The electrotactic speed of T98G glioblastoma cells costimulated with ligands for chemical signaling.	141
4.18	The effects of extracellular Ca^{2+} on glioma electrotaxis after 6 hours. .	143
4.19	The electrotaxis of T98G & U-251MG glioblastoma cells under 300 V m^{-1} dcEF after 6 hours with pharmacological inhibition on various ion channels.	144
4.20	Phase contrast images of T98G & U-251MG cells under EF stimulations in different microenvironments after 6 hours.	147
4.21	The signaling pathways of glioblastoma electrotaxis identified in this study.	148
5.1	Experimental setup of concurrent shear flow and electric field conditioning of endothelial cells in a <i>shear flow and electric field co-stimulation microfluidic chip</i> (SFEFC).	155
5.2	Liquid manipulation on the SFEFC.	156
5.3	A snapshot of the experimental setup of concurrent shear flow and electric field conditioning of endothelial cells in a “shear flow and electric field co-stimulation microfluidic chip (SFEFC)”.	158
5.4	Microscopy images of endothelial cells cultured in sections I, II, III, and V in SFEFC.	161
5.5	Immunofluorescence staining of HUVECs conditioned with shear flow (shear stress fixed at 1 Pa) and electric fields at various strengths. . . .	162
5.6	Microimages of endothelial cells and glioblastoma cells.	163

5.7	The adhesion of (A) T98G-dsRed, and (B) U251MG-dsRed, to static confluent endothelium (fluorescently labeled green).	164
5.8	The adhesion of T98G-dsRed and U251MG-dsRed to endothelium under the stimulation with Ang1 and TNF α in static condition.	165
5.9	The adherence of T98G-dsRed cells (red fluorescence) to endothelial cells (green fluorescence). Yellow fluorescence represents the intercellular transport between the two cells.	166
5.10	The adherence of U251MG-dsRed cells (red fluorescence) to endothelial cells (green fluorescence). Yellow fluorescence represents the intercellular transport between the two cells.	167
5.11	The intercellular transport events between glioblastoma and endothelial cells in static condition.	168
5.12	Adherence of glioblastoma cells to endothelium conditioned under shear flow and electric field or endothelium cultured in static flow on the SFECF.	169
A.1	Geometry used in rotational rheometry using ARES-G2 (TA Instruments).	177
A.2	Measurement setup for pH and electrical conductivity.	180
A.3	Correlation between the ionic strength and the conductivity of cell culture media.	181
A.4	The geometries effect to water viscosity measurement in rotational rheometry.	183
A.5	The geometries effect to MEM α viscosity measurement in rotational rheometry.	184
A.6	The measured viscosities at different shear rates for water and DMEM media supplemented with different sera.	186
B.1	Schematic representation of resistance difference in a circular cultureware	189
B.2	Numerical simulation of an EF stimulation device designed by Marotta <i>et al.</i>	190
B.3	Numerical simulation of a commercial C-dish EF stimulation device.	190
B.4	3D schematic of the design principle.	191
B.5	The change of relative resistance between each arbitrary current line in the insert.	195
B.6	CAD models of liquid in 3D inserts for numerical simulation.	196
B.7	Numerical simulation of EF in various designs	197
B.8	The electric potential distribution in 3D CAD inserts.	198
B.9	Numerical simulations of a scaled-up 3D CAD insert for a 100 mm TCPS petri dish.	200
B.10	Effect of chamber thickness on EF uniformity by numerical simulation.	201
B.11	Prototyping inserts by 3D printing	201
B.12	Schematics of the layered insert.	202
B.13	Photoimages of fabricated layered PMMA 3D CAD insert.	202
B.14	Schematics of a PMMA microfluidic chip containing two simple rectangular channels.	203
B.15	Fabrication of 3D insert by casting PDMS on a CNC machined mold.	203
B.16	Two-piece assembly approach	204

B.17	Two-piece assembly of metal-PMMA 3D CAD insert	205
B.18	Reversible sealing 3D CAD PMMA insert.	206
B.19	A photo snapshot of the EF measurement setup.	207
B.20	The workflow of the cell experiment by using the polymeric insert.	208
B.21	The schematic diagram of electrical stimulation setup.	209
B.22	A photo snapshot showing the setup of EF stimulation of cells on a 6-well microplate in a temperature-controlled water bath.	209
B.23	A photo snapshot showing the microscopy setup for the time lapse cell electrotaxis experiment.	210
B.24	Schematic representation of the angle to calculate cell migration direct- edness and orientation.	211
B.25	The measured EFS in a layered 3D CAD insert.	211
B.26	The phase contrast microscopy of NIH/3T3 cells after 5 hours of exper- iment with the circular 3D CAD insert.	213
B.27	Quantification of the cell electrotaxis and electro-alignment measurements.	214
C.1	Fourier-transform infrared spectra of various materials.	217
D.1	The 3D printed Nikon Ti-E custom stage with transparent heater.	219
D.2	The CNC milled PTFE casting station for PDMS soft lithography sup- porting 2-inch and 4-inch wafer.	220
D.3	The 3D printed washing stand for cover glasses.	221
D.4	The PDMS lined copper holder.	221
D.5	The CNC milled custom holder for Tokai Hit WKSM incubator.	222
D.6	A resolution testing reticle.	222
D.7	A blocking shield for resolution testing on MA/BA6 mask aligner.	223
D.8	The 3D printed washing stand for 1 cm glass wafers.	224
D.9	The 3D printed confocal holder for imaging with a transparent heater.	224

List of Tables

1.1	Key characteristics of IDH-wildtype and IDH-mutant glioblastomas . . .	3
1.2	Types of directed cell migration	15
1.3	Highlights of research activities studying multiplex gradients on cell migration using microfluidic technologies.	30
1.4	An incomplete list of reports of electrotaxis of glioma and glial cells . .	36
2.1	The analogous comparison between electrical and fluid mechanical expression of a cylindrical tube.	42
2.2	Common materials to fabricate BMMDs.	45
2.3	Summary of properties for thermoplastics	48
2.4	The dimension of fabrication in glass microfluidic chips using various methods	49
2.5	Bonding methods established in Micro/Bio/Nanofluidics Unit at OIST	52
2.6	Pumping methods for cell culturing on chips	59
2.7	Physical characteristics comparison between single-layer and double-layer PMMA/PDMS chip.	68
3.1	Step-centric and cell-centric variables for describing single-cell migration.	89
3.2	Segmentation evaluation metrics to describe the similarity between manual reference and segmentation results.	99
3.3	Multiple object tracking performance metrics to evaluate the precision and accuracy of the tracking results.	100
3.4	Segmentation performance averaged among three NIH/3T3 cell images using various methods	101
3.5	Summary of multiple object tracking of NIH3T3 electrotaxis after 10-hr under $300 \text{ V m}^{-1} \text{ dcEF}$	107
3.6	Tracking results of NIH/3T3 electrotaxis using different segmentation and different tracking methods	112
4.1	Commonly used extracellular matrix coatings for cell migration.	122
4.2	Pharmacological inhibitors to study the voltage-gated calcium channels in glioma electrotaxis.	125
4.3	Step-centric and cell-centric variables for describing single-cell migration.	127
4.4	The results of glioblastoma electrotaxis on various ECM coatings in PMMA microfluidic chips after 2 hours.	135
4.5	The results of glioblastoma electrotaxis on various ECM coatings in PMMA/PDMS microfluidic chips after 6 hours.	136

4.6	The detailed results of glioblastoma electrotaxis in the presence of antagonists against ion channels or calcium signaling after 6 hours.	150
A.1	Specification of the A05 m-VROC sensor for low viscosity fluids.	179
A.2	The ionic strength, pH, density, conductivity, and refractive index properties of culture medium used in the thesis.	182
A.3	The dynamic shear viscosities of culture media measured using rotational and capillary rheometry.	185
B.1	Numerical simulation of EF in a plain insert, smooth 3D CAD insert, and layered 3D CAD insert.	196
B.2	Specification and numerical simulation results of 3D CAD devices for different sizes of cultureware	199
B.3	Stimulation area and effective stimulation area percentage of <i>in vitro</i> EF stimulation device	212

Chapter 1

Introduction

In this chapter I will first overview glioma, a brain cancer type arising from supportive cells in the central nervous system (CNS), and the microenvironment associated with it. The guidance cues in tissue microenvironment will be further introduced and I will explain how microsystems can be useful to recapitulate microenvironments.

1.1 Glioma: a tumor of supportive cells in the central nervous system

The central nervous system (CNS) consists of the brain and the spinal cord, and it is the biological electrochemical system that integrates, interprets, and responds to information of the body and from the external environment. The nervous tissue makes up the majority of the CNS, with 80% of the tissue volume consisting cells and the rest are extracellular matrices (ECM). There are two major types of cells in the nervous tissue, neurons and neuroglia. Neurons are excitable cells for sending and receiving electrochemical signal. Neuroglia are supportive cells roughly 10 times higher in abundance than neurons and maintain homeostasis in nervous tissue by assisting nutrient delivery, waste removal, and tissue metabolism.

There are four types of neuroglial cells: astrocytes, oligodendrocytes, microglia, and ependymal cells (Figure 1.1). Astrocytes are star-shaped cells that anchor blood vessels and neurons, regulate formation of blood-brain barrier, moderate metabolism in the microenvironment, and repair damaged tissue. Oligodendrocytes wrap the neuronal axons and myelinate them to increase transduction speed of neuron transmission. Microglial cells are immune cells in the CNS. Ependymal cells maintain the cerebrospinal fluid level in the CNS.

Glioma encompass all tumors that originated from the supportive tissue of the brain, *i.e.*, any tumor formed by transformed neuroglial cells. The clinical presentation of glioma patients is often associated with CNS-related symptoms such as headaches, seizures, memory loss, and changes in behavior.

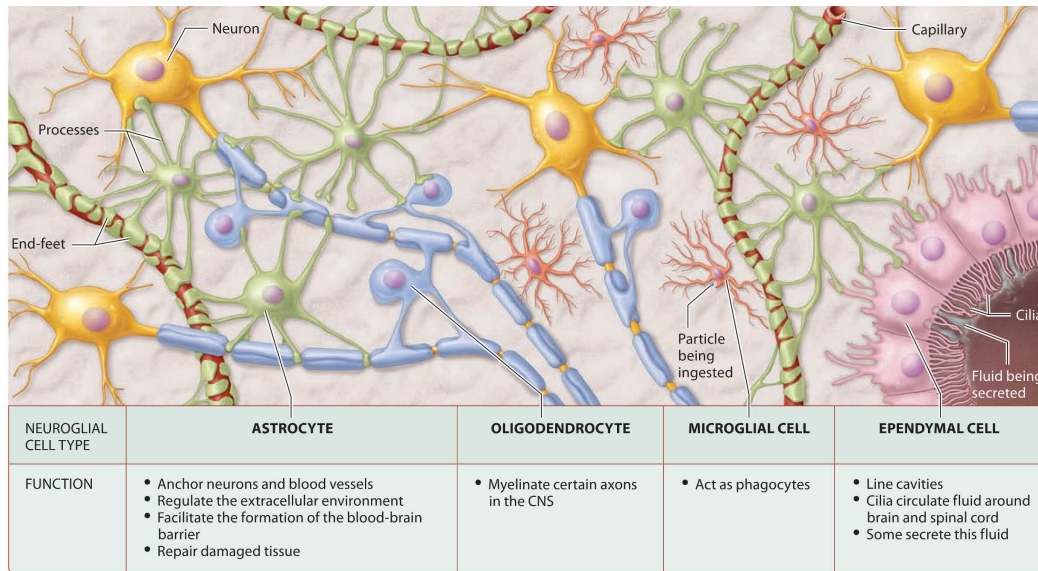


Figure 1.1: Neuroglial cells in the CNS¹. Reprinted with permission of Pearson Education, Inc., New York, New York.

1.1.1 Epidemiology, classification, and molecular pathology

Among all intracranial central nervous system tumors, gliomas are the most common type, accounting for 31% of all CNS tumors in the US and 81% of malignant CNS tumors². In Japan, analyzed by the brain tumor registry of Japan during the period from 2001 to 2004, glioma accounts for 24.9% of all primary brain tumors³.

In general, glioma can be classified based on their glial cell lineage into astrocytoma, ependymoma, oligoastrocytoma, oligodendroglioma, optic glioma and gliomatosis cerebri. The WHO updated an international classification consensus for CNS tumors in 2016⁴. The classification of CNS tumors now includes conventional clinico-pathological characteristics as well as molecular information to more precisely classify tumor subtypes that are conventionally difficult due to intermixing of differentiated cells.

In 2016 WHO classification, diffuse glioma can be classified histologically to astrocytoma, oligoastrocytoma, oligodendroglioma, and glioblastoma and further sub-typed according to genotyping of several commonly-found molecular signature among glioma, such as isocitrate dehydrogenase (IDH), 1p/19q codeletion, α -thalassemia/mental retardation syndrome X-linked protein (ARTX), and O-6-methylguanine-DNA methyltransferase (MGMT) (Figure 1.2).

Almost half of the glioma cases are glioblastoma, the most malignant form associated with poor prognosis, accounting for 10.8% of all primary brain tumors in Japan. The primary glioblastoma is the most frequent type with *de novo* development and dominates in patients over 55 years of age. The primary glioblastoma is often associated with wildtype IDH and have short life expectancy. On the other hand, secondary glioblastoma developed from previous diffuse or anaplastic astrocytoma lesions often bears mutated copies of IDH and better prognosis (Table 1.1). This shows that glioma are quite heterogeneous, complex, and possibly originate from different progenitor cells.

Physicians and pathologists now routinely perform genotyping of patient's tumor

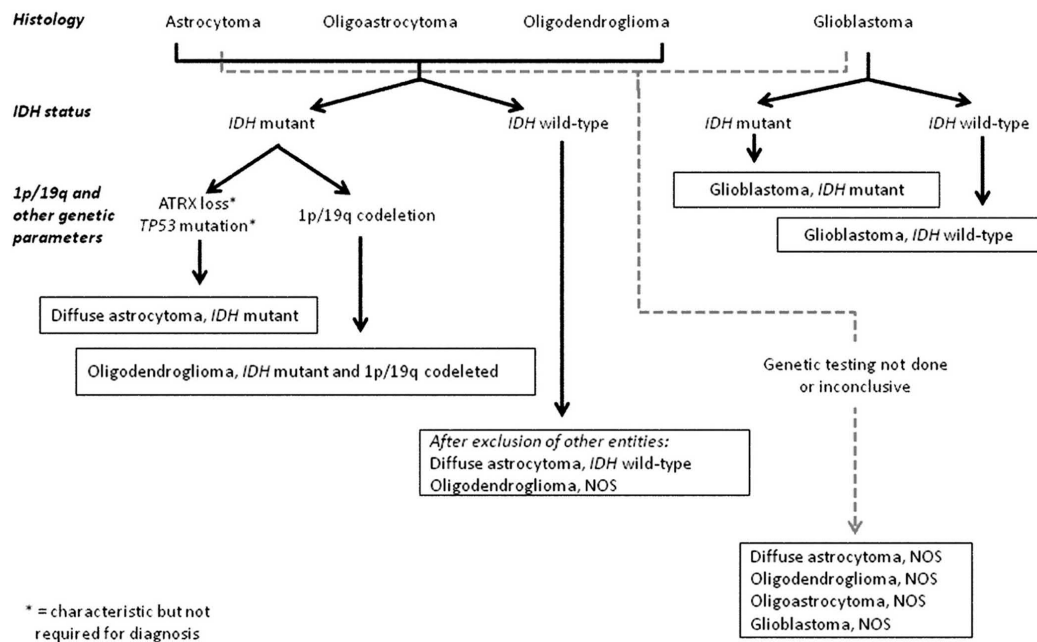


Figure 1.2: Classification algorithm for diffuse glioma based on histological and genetic features in 2016 WHO guidelines for CNS tumors⁴. Reprinted with permission of Springer Nature.

Table 1.1: Key characteristics of IDH-wildtype and IDH-mutant glioblastomas⁴. Reprinted with permission of Springer Nature.

	IDH-wildtype glioblastoma	IDH-mutant glioblastoma	References
Synonym	Primary glioblastoma, IDH-wildtype	Secondary glioblastoma, IDH-mutant	{1830}
Precursor lesion	Not identifiable; develops de novo	Diffuse astrocytoma Anaplastic astrocytoma	{1827}
Proportion of glioblastomas	~90%	~10%	{1797}
Median age at diagnosis	~62 years	~44 years	{214,1078,1797, 2103}
Male-to-female ratio	1.42:1	1.05:1	{214,1417,1797}
Mean length of clinical history	4 months	15 months	{1797}
Median overall survival			
Surgery + radiotherapy	9.9 months	24 months	{1797}
Surgery + radiotherapy + chemotherapy	15 months	31 months	{2810}
Location	Supratentorial	Preferentially frontal	{1417}
Necrosis	Extensive	Limited	{1417}
TERT promoter mutations	72%	26%	{1801,1830}
TP53 mutations	27%	81%	{1797}
ATRX mutations	Exceptional	71%	{1519}
EGFR amplification	35%	Exceptional	{1797}
PTEN mutations	24%	Exceptional	{1797}

samples to determine therapeutic strategies and prognosis. The Cancer Genome Atlas (TCGA) database started registering sequenced glioblastoma specimens in 2008 and researchers have examined profiles at genomic, transcriptomic, and epigenomic

level to conclude molecular markers for glioma subtypes with different clinical outcomes. Based on transcriptional expression profiles⁵, the gliomas can be sub-typed into proneural, neural, classical and mesenchymal glioma and have drastically different prognoses and life expectancies. In the clinics, several molecular markers can provide physicians to evaluate prognosis of the glioblastoma, including several proteins in the receptor tyrosine kinase (RTK) family, such as epidermal growth factor receptor (EGFR)^{6,7}, platelet-derived growth factor receptor (PDGFR)^{8,9}, and vascular endothelial growth factor receptor (VEGFR)^{10,11}. The phosphatidylinositol 3-kinase-Akt-mammalian target of rapamycin (PI3K/AKT/mTOR) signaling pathway is also involved in the progress of glioma. The PI3K/AKT/mTOR is a pro-survival signaling cascade that is often activated in cancer cells and it is also the common signal transduction in gliomas. The intracellular signaling of the aforementioned RTK signaling of often amplified through the PI3K/AKT signaling pathway. In glioma, there is a high mutation rate of RTK pathways and the PI3K/AKT pathway especially in primary glioblastoma (88%)¹²⁻¹⁴. The negative regulators of PI3K/AKT pathway, phosphatase and tensin homolog (PTEN), is a tumor suppressor that is inactivated in 40 to 50% of glioblastoma patients¹⁵. The comprehensive glioma genotyping together with histopathological phenotyping will help physicians to predict and correlate glioma genotypes to therapeutic responses and prognosis.

1.1.2 Origin and metastasis of glioma

The origin of glioma carcinogenesis is speculated by glioma stem cells, which are originated from transformation of neural progenitors within the brain regions that have active neurogenesis such as the subventricular zone (SVZ) and the dentate gyrus (DG) (Figure 1.3). While ionization radiation to the head and neck is a known risk factor for development of brain tumor, people suspect that the radio-frequency electromagnetic field from mobile phones could be a possible brain tumor risk factor. However, in a recent large international case-control study called INTERPHONE study, researchers failed to correlate mobile phone use with glioma prevalence^{16,17}. Some virus species have also been proposed to contribute to glioma-genesis such as cytomegalovirus^{18,19} and human simplex herpes virus²⁰. The search for risk factors for glioma is still ongoing through Genome-wide Association Studies (GWAS)⁵.

The cancer stem cell (CSC) hypothesis describes that solid and liquid tumors are composed of heterogenic groups of cells in which a small subset of cells can self-renew and contribute to regrowth and resistance of anti-tumor therapy²¹. Glioma stem cells (GSCs) have attracted much attention due to their possible involvement in the high recurrence and therapeutic resistance after surgical, chemo-, and radioactive therapy. GSCs have been isolated from clinical samples and have shown self-renewal in culture, outgrowth of a tumor in orthotopic transplant *in vivo*, and generation diversified post-mitotic progeny²²⁻²⁵. A marker for GSCs is the CD133 that is also expressed in multi-potent cells in other tissues. As little as 100 CD133-positive cells can initiate tumor formation and they are relatively resistant to radiation²⁶.

Thus investigation of the glioma cells and GSCs in the SVZ and DG microenvironments may help us identify the emergence and maintenance of the GSC phenotype, which is of great interest for therapeutic development.

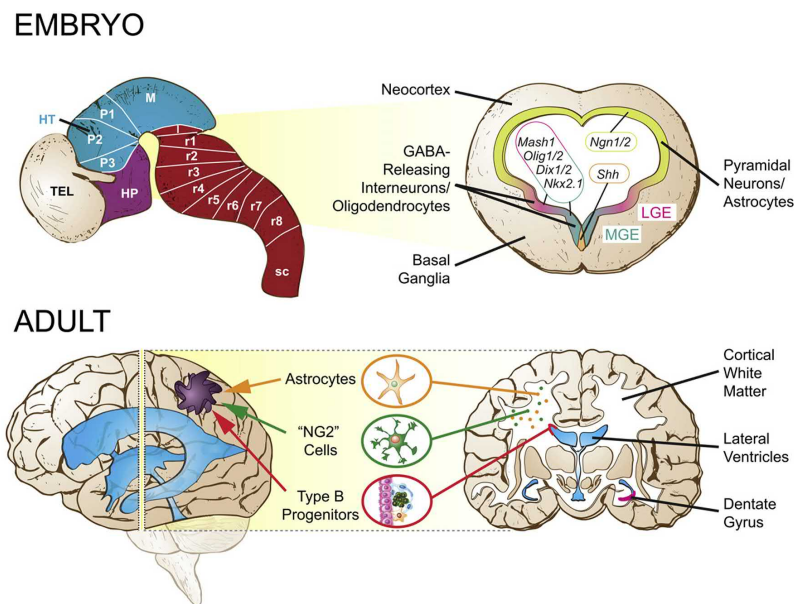


Figure 1.3: Speculative relationship of glioma cell of origin of neural progenitors²¹. Reprinted with permission of Elsevier.

Metastasis is a complex process of primary tumor cells leaving *in situ* location and disseminating to other body locations. Metastasis is the main cause of cancer-related death^{27,28}. During the dissemination, cancer cells first invade the surrounding microenvironment as single cells or as a collective group (collective cell migration). Two modes of single cell migration are used, either elongated (mesenchymal) migration or rounded (amoeboid) migration. Subsequently, cancer cells enter the circulation by migration through blood vessel walls through intravasation. After traveling through the circulatory system, the cancer cells extravasate at distant location and start to grow as new foci (Figure 1.4)²⁹. However, the metastasis of glioma is unique compared to that of other cancers.

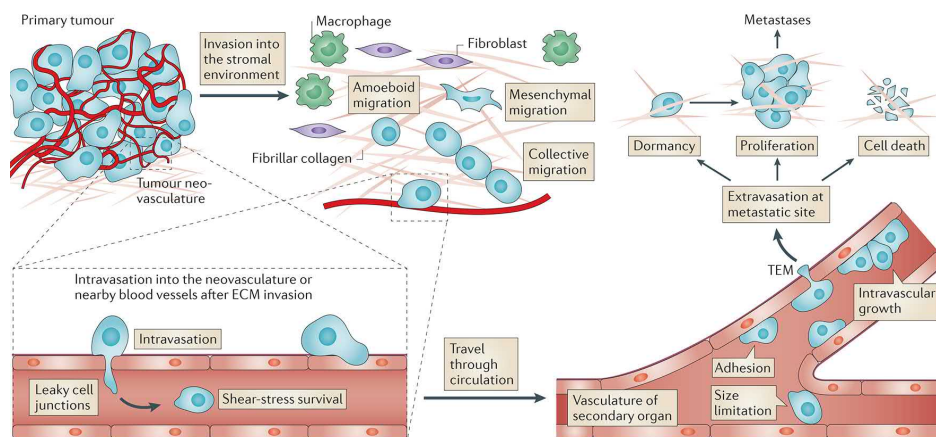


Figure 1.4: Cancer cell metastatic dissemination²⁹. Reprinted with permission of Springer Nature.

In glioma, high recurrence after surgical resection is due to the infiltrative nature of glioma cells into nearby brain tissue³⁰. Previously, due to limited cases of patients showing disseminated glioma, the medical community assumed that the metastasis of glioma to body parts outside the CNS was rare^{31–33}, but more case reports suggest that extra-neural metastasis is also possible and the previous observation could be due to the short life expectancy of patients with malignant glioma^{34,35} and also to different properties of the ECM properties in the brain microenvironment and glioma³⁶ compared to other tissue microenvironments.

1.1.3 Complex microenvironment of glioma

Glioma cells express proteolytic enzymes, serine cysteine metalloproteinases, and matrix metalloproteinases (MMPs), to aid in their digestion of ECM and crossing of brain structures^{37–40}. This also leads to local dissolution and destruction of the normal tissue. The MMPs are expressed by glioma cells and can promote the growth and invasion of the metastasis of the glioma. In high-grade glioblastoma, the cancer cells also produce ECM molecules such as glycosaminoglycans, fibronectins, tenascin-C, and vitronectin to modify the local microenvironment and promote infiltration⁴¹.

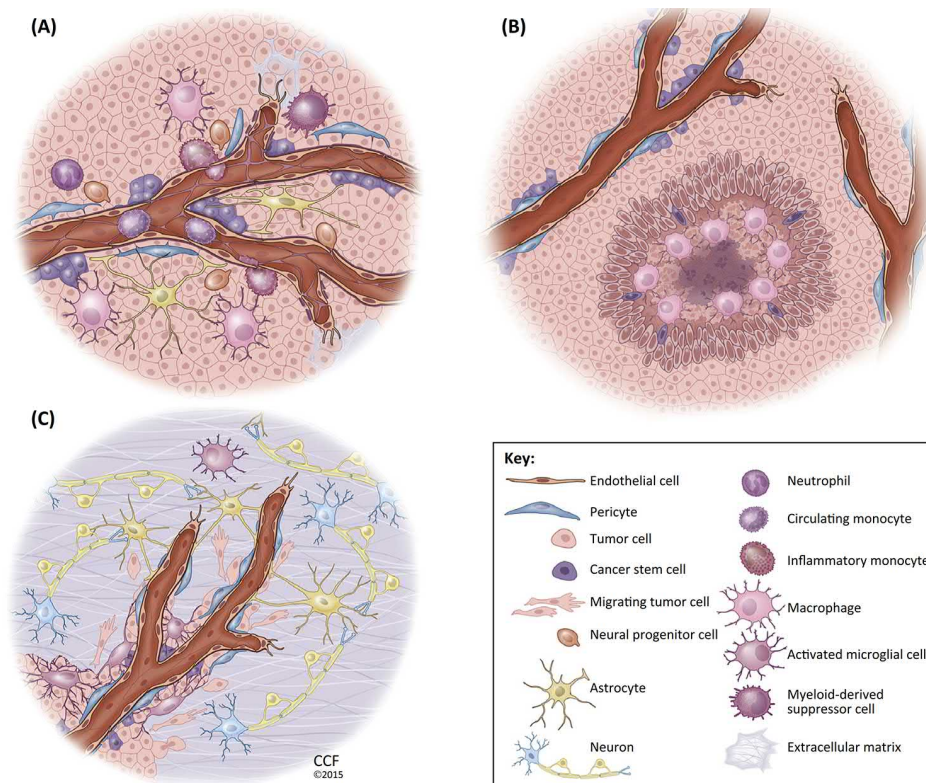


Figure 1.5: The tumor microenvironment of glioblastoma⁴². (A) The perivascular niche; (B) The peri-necrotic niche; (C) the invasive niche. Reprinted with permission of Elsevier.

Tumor cells interact with normal cells and adjacent stroma (connective tissues) within the microenvironment (tumor niche)^{43–46}. The non-malignant cells within the

tumor microenvironment often possess dynamic and tumor-promoting functions at all stages of carcinogenesis such as producing factors that stimulate CSC self-renewal. The tumor cells also interact with the non-malignant cells such as modulating immune system, stimulating stromal cells to secrete additional factors, and inducing angiogenesis to increase nutrient supply for tumor growth⁴⁷⁻⁵⁰. Glioma cells establish and remodel the microenvironment through secretion of RNAs and proteins or cross-talking with stromal cells using extracellular vesicles (exosomes)⁵¹⁻⁵³. The normal cells in the microenvironment can also secrete proteins during the natural defense process against the glioma. Thus complex chemical gradients could exist in the microenvironment. If the stoma and tissue polarity were interrupted during the glioma pathogenesis, voltage gradients and stiffness gradients could also guide the response of glioma cells.

For example, in the subventricular zone of mice brain, where the neural stem cells also reside, chemical gradients of CXCL12 coexist with a physiological electrical field that projects toward the olfactory bulb along the rostral migratory stream (RMS)⁵⁴ (Figure 1.6). While it has been suspected that the RMS only exists in small mammals such as a mice and a rat, recently the existence of RMS in the fetal as well as adult human brain have also been suggested⁵⁵. The complex microenvironment in the subventricular zone may play a pivotal role in the tumorigenesis of glioma.

To date, three types of tumor microenvironments of glioma have been proposed, the peri-vascular niche for angiogenesis^{42,56-60}, peri-necrotic niche for survival of cancer stem cells^{48,61,62}, and invasive niche for immune-privileged sanctuary⁶³⁻⁶⁶ (Figure 1.5).

In the peri-vascular niche of glioma, glioma stem cells are thought to release high levels of proangiogenic factors to drive migration and growth of endothelial cells to the tumor site and provide nutrients, while endothelial cells also provide feedback and maintain the survival of glioma stem cells (Figure 1.7)⁶².

In the perinecrotic niche, as the tumor grows in size, the level of nutrients and oxygen tension changes. A hypoxic and necrotic region in the tumor exists and regulates the phenotype of the tumor⁶⁷⁻⁷⁰ (Figure 1.8). In 2D microfluidics, manipulation of oxygen concentration can be used to study effects on single cell behavior in hypoxic condition while in 3D microfluidics with tumor spheroids, a more biomimetic whole tissue model can be studied instead^{71,72}.

In the invasive niche, cancer cells survive by avoiding the immune system. Microglia, a specialized immune macrophage cell type in the brain, is known to interact with glioma and boost glioma invasion by secreting several chemotactic and chemokinetic factors^{64-66,73,74} (Figure 1.9). In some reports, the term of tumor-associated macrophage is used^{42,66}.

1.1.4 Glioma therapy

The surgical resection is the standard therapy if the lesion can be feasibly removed. However, malignant gliomas cannot be completely removed surgically due to their infiltrative nature and the possible existence of cancer stem cells.

Conventional radiotherapy of 60 Gy of partial field external beam irradiation will be associated as part of the standard treatment. Despite the conventional effort, recurrence of malignant glioma after surgical and radiotherapy is common and often accompanied by increased drug resistance. Boron neutron capture therapy is a new

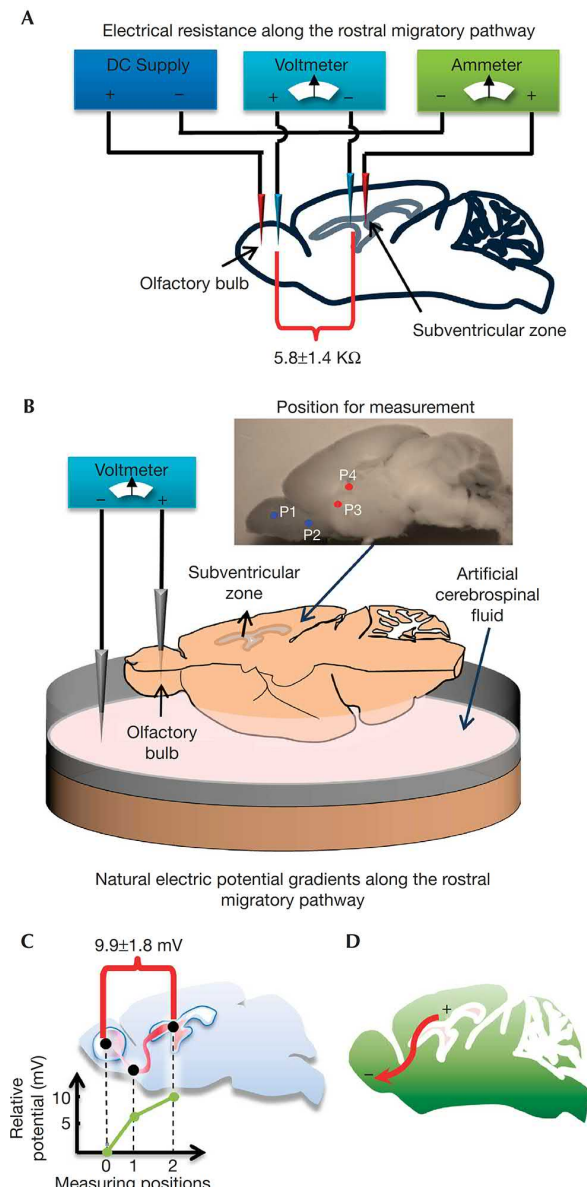


Figure 1.6: Measurement of electric potential in mouse brain specifically along the rostral migratory stream⁵⁴. An electric field is present between the subventricular zone and the olfactory bulb. Reprinted with permission of John Wiley and Sons.

modality of radiotherapy for primary brain tumors as well as head and neck cancer^{75–77}. Non-radioactive Boron-10 agents are given to the patient and boron will accumulate in cancer cells. The low energy thermal neutron from a nuclear reactor or a linear accelerated source impacts the boron and releases alpha particles that will only deliver cell killing effect around the boron, limiting the off-target killing.

In the mean time, chemotherapy has assumed an increased important role in the treatment, especially the use of temozolomide (TMZ), an oral alkylating agent with good blood-brain-barrier penetration. When glioma tissue poses hypermethylation of aforementioned MGMT promoter, the MGMT is silenced and is associated with better

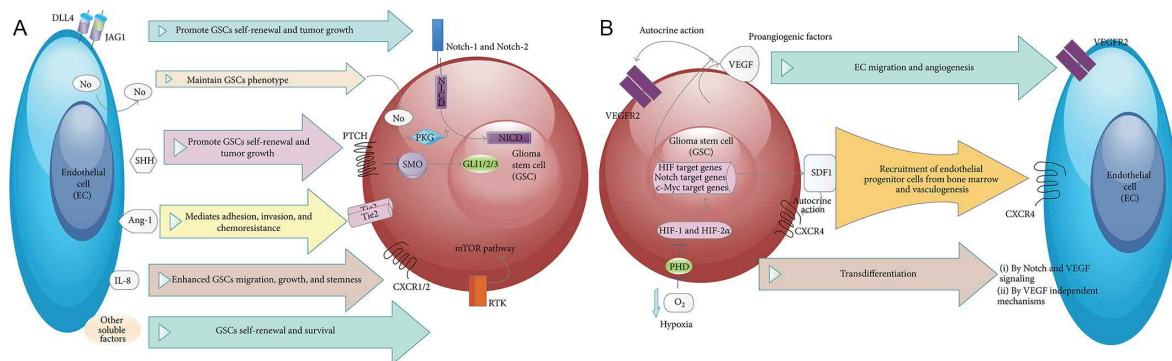


Figure 1.7: Interactions between GSC and endothelial cells⁶². (A) From endothelial cells to GSC; (B) From GSC to endothelial cells.

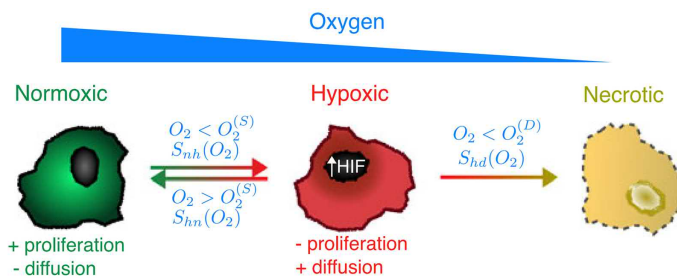


Figure 1.8: Oxygen levels regulate the phenotype of glioblastoma cells in the peri-necrotic niche⁶⁷.

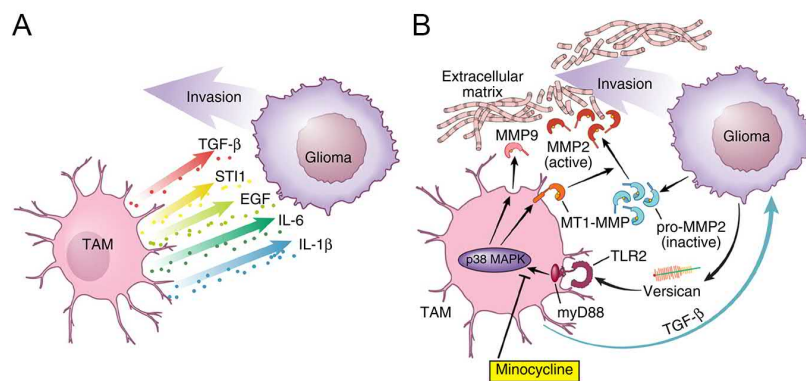


Figure 1.9: Cross-talk between glioma and tumor associated macrophages (TAMs) in the invasive niche⁶⁶. Reprinted with permission of Springer Nature.

response to TMZ treatment. Due to the identification of cellular signaling pathways in glioma molecular pathology, targeted therapeutic agents against these molecules have also been used (Figure 1.10), such as EGFR inhibitor, PI3K inhibitors, and anti-angiogenic agents such as anti-VEGF⁷⁸.

Recently, a novel therapy using alternative electric field for glioblastoma have been approved by the Food and Drug Administration in the US offered by Novocure. NovoTTF-100A applies 200 kHz alternating electric field (tumor treating field, TTF) in two perpendicular directions to the brain using a portable non-invasive device

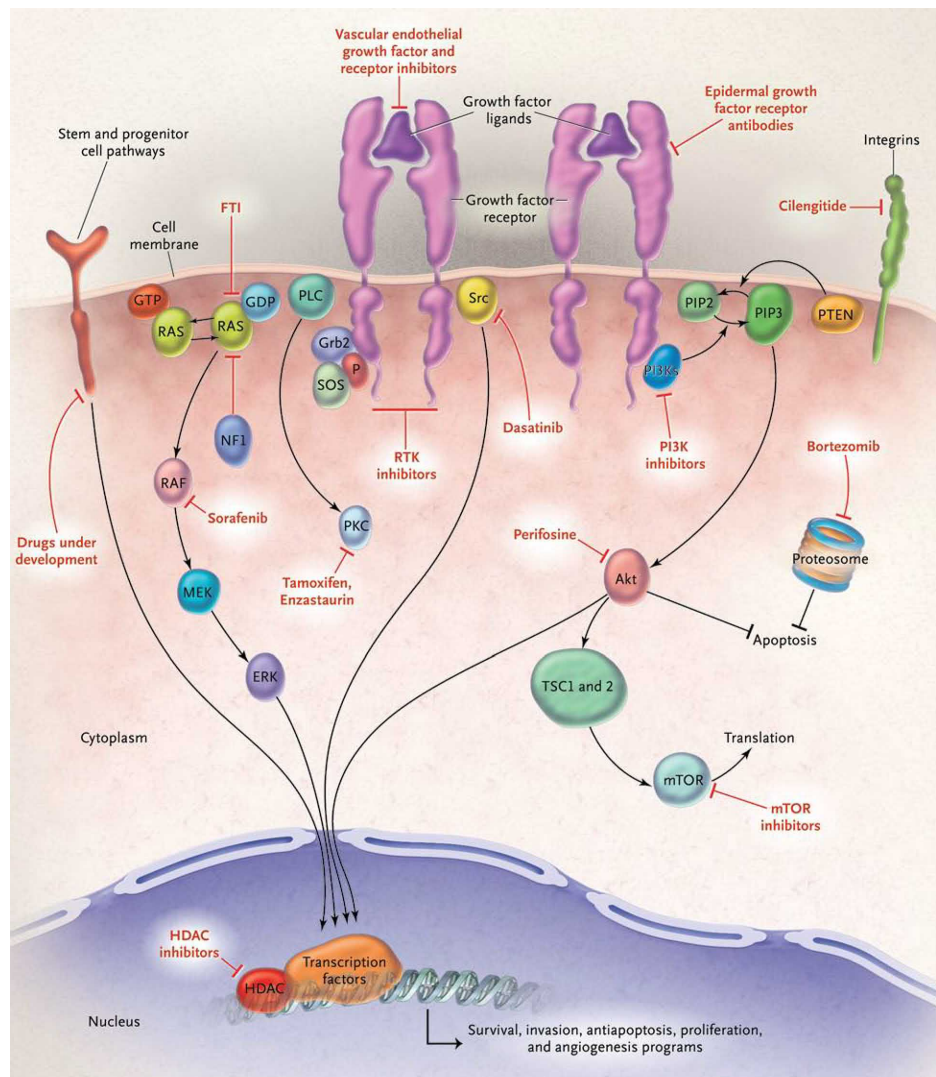


Figure 1.10: The scheme of major signaling pathways in glioma and their targeted therapy. Reproduced with permission from Wen *et al.*⁷⁸, Copyright Massachusetts Medical Society.

(Figure 1.11). The field intensity was more than 0.7 V cm^{-1} in the center of the brain. The mechanism for this treatment was based on interruption of tumor cell mitosis and proliferation by the alternative electric field presumably through the action on the mitotic spindle⁸⁰. The treatment has demonstrated improvement of life expectancy and quality of life to patients with glioblastoma^{79–82}.

Combining targeted therapies to inhibit tumor microenvironment through drugs and electrical stimulation is a potential treatment approach in the future⁸³. Investigating how cells respond to multiplex gradients is essential to create an effective treatment plan. Thus, developing an *in vitro* platform for effective evaluation of therapeutic strategy to target glioma microenvironment is urgently needed.



Figure 1.11: The NovoTTF-100A non-invasive alternative electric field application system⁷⁹.

1.1.5 What microenvironment governs glioma infiltration?

It has been known that not only the genotypic and phenotypic mutations that cancer cells adopt are important for the tumorigenesis, the microenvironment remodeling and contribution also play pivotal roles on settlement and dissemination of cancer^{84,85}. The subjects and mechanisms involved in the establishment and remodeling of microenvironment is of increasing interest to researchers as it may present new approaches to treat cancer.

In glioma, the cancer cells are extremely disseminative into the surrounding tissue. Even if surgical, radio-, and chemo-therapy were successful to remove the primary tumor, glioma often recurs presumably due to the infiltrated GSCs population in a few years. The infiltrated glioma cells will rapidly grow, interfere with normal cell populations in the CNS, and cause neural pathology. It is hoped that if the infiltration of glioma or abnormal growth of glioma can be controlled, response to standard treatment and quality of life for patients can be significantly improved as shown partly from several targeted therapy trials and Novocure tumor treating field trials^{86,87}.

In short, the ability of understanding and manipulating cancer microenvironment could provide promising insight to control and inhibit cancer growth and metastasis. However, the cancer microenvironment is inherently complex so how to establish an *in vitro* experimental platform is essential. A microfluidic chip to create multiplex chemical, voltage, or stiffness gradients can serve as an *in vitro* platform to mimic the tumor microenvironment and study how cells respond when multiple stimulations act on them simultaneously. Modeling the peri-vascular, peri-necrotic, and invasive niche of glioma and other cancers on a robust *in vitro* platform is important to elucidate fundamental processes in glioma tumor biology, formulate biological significant experimental design, and draw more clinically translational results.

1.2 Microfluidics and bioMEMS

Microfluidics refer to controlling and manipulating fluid flows with length scales smaller than milli-meter. The fundamental works in microflows started early by pioneers in fluid dynamics such as Poiseuille and Knudsen⁸⁸, who studied extensively the pressure-driven flow in small cylindrical tubes. The practical development in microelectromechanical systems (MEMS) jump started by Richard Feynman's prophetic lecture on microscale science and engineering in the 1960's.

The boom of microfluidic applications started with extensive development of high-performance liquid chromatography and on-chip capillary electrophoresis during the 1990s with rapidly technological leap in microfabrication^{89,90}.

At the reduced dimension (Figure 1.12), microfluidics bring several economical and analytical advantages over macro systems, including low sample and reagent consumption, laminar flow regime at low Reynolds number, diffusion-dominant transport, increased surface area-to-volume ratio, and portability for system integration⁸⁹⁻⁹². Thus, microfluidics has offered great potential to shed new insights in biological studies^{89,93}.

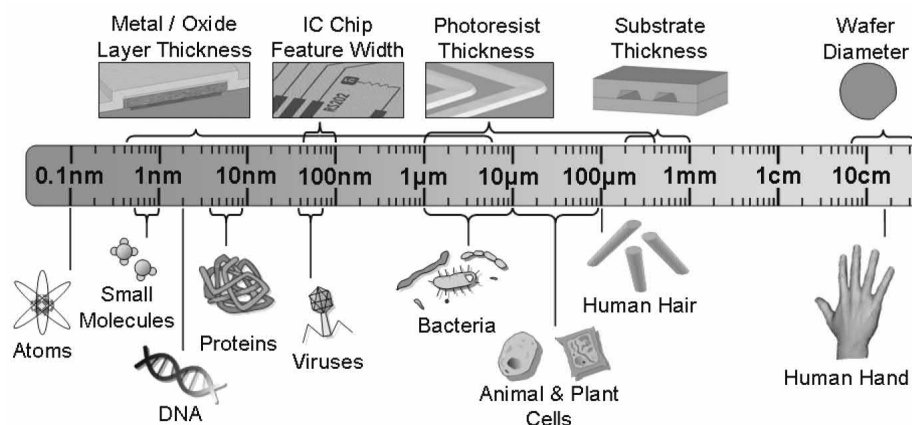


Figure 1.12: Length scale comparison between several biological and micro-fabrication structures⁹⁰. Reprinted with permission of Springer Nature.

1.3 Gradients in the microenvironment as directional cues

The nature of the extracellular environment determines the mechanical, topographical, and chemical gradients surrounding a cell (Figure 1.13)⁹⁴. In extracellular matrix (ECM), if fibrous structure exists, the topographical features may guide cells by contact guidance^{95,96}. Due to the three-dimensional tissue hierarchy, stiffness gradients may exist in the ECM and can guide cells through mechanobiology signaling. If the cell migration is guided by the stiffness of ECM, it is termed durotaxis⁹⁷⁻⁹⁹. A surface-bound chemical gradient can also exist on ECM surface and can guide cell migration in the process called haptotaxis¹⁰⁰⁻¹⁰⁴. A soluble chemical gradient and electric field existing in the medium can also guide cell migration in chemotaxis^{105,106} and electrotaxis¹⁰⁷⁻¹¹⁰.

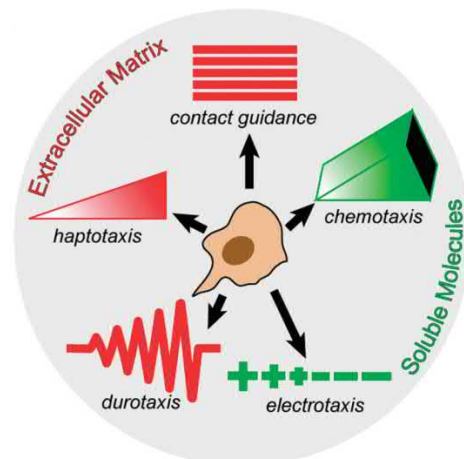


Figure 1.13: Cells can be guided by physical as well as chemical cues⁹⁴. Reprinted with permission of Oxford University Press.

1.3.1 The chemical gradient microenvironment

Chemical gradients in the physiological system

During the early development of a multicellular organism, tissue patterning and formation of polarity are pivotal. Tissue patterns are formed by cells in multicellular organisms that are potentially independent but function together to form a whole organism through different rates of cell growth and tissue regeneration^{111–113}. The observation prompted the early postulations of a formative substance gradients influencing the organism development, proposed by developmental biologists such as T.H. Morgan and C.M. Child^{114,115}.

Alan Turing proposed that chemical substances affecting the tissue form (namely morphogens), can self-organize into spatial patterns from homogenous distribution through reaction-diffusion type models¹¹⁶. The morphogen gradients then provide the spatial information to guide cell behavior in pattern formation during organism development (Figure 1.14)^{111,117}. Some examples of morphogens include members of the hedgehog (Hh) family^{118–120}, Wnt family members^{121–124}, and some members of the transforming growth factor- β (TGF- β) family^{125–128}.

For example, sonic hedgehog protein (Shh), a vertebrate protein of the hedgehog family involves in the patterning of neural tube development and limb bud development^{118,129}. A disturbed Shh concentration gradient from ectopic transplant results in malformation of neural tube or duplication of limbs (Figure 1.15)^{120,129}. The Shh protein also participates in maintenance and survival of adult neural progenitors¹³⁰.

Although critical issues such as how morphogens are moved through a tissue and how morphogen gradients are maintained are not entirely clear, it is widely understood that chemical gradients of different sorts exist in the tissues throughout the lifecycle of an organism, such gradients participate in all aspects of biological processes such as regeneration, homeostasis, inflammation, and cancer^{112,113,131–133}.

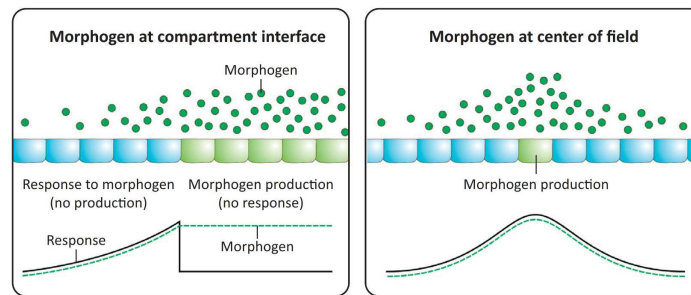


Figure 1.14: Mechanisms for generating morphogen gradients¹¹⁷. (Left) A tissue produces the morphogen at the compartment interface. (Right) A restricted group of cells release morphogens within a field of responsive cells. Reprinted with permission of Elsevier.

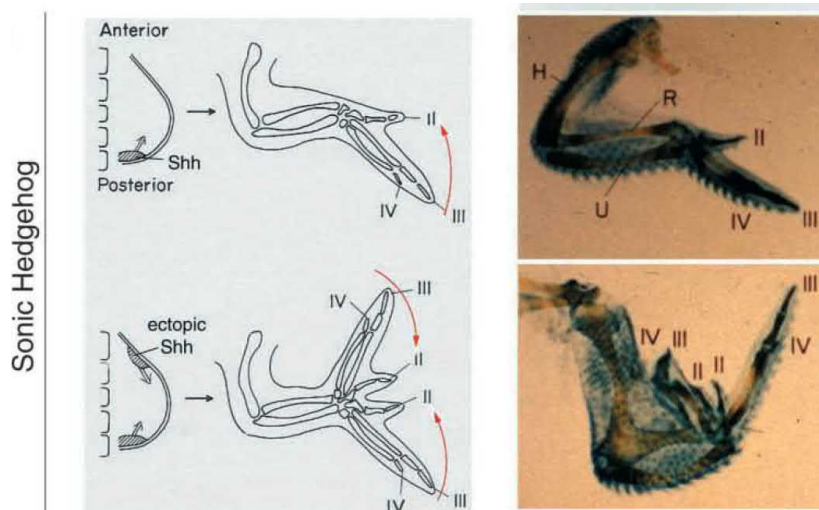


Figure 1.15: Ectopic production of Shh induced a mirror image of chick wing bud¹²⁰. Reprinted with permission of The Company of Biologists Ltd.





Cell responses to chemical gradients

Chemical gradients (chemoattractants) of proteins such as morphogens, growth factors and small molecules can guide cell migration. Cell migration is a fundamental biological process that exists in the development of the organism throughout life in physiological and pathological conditions including wound healing, inflammation, and cancers¹³⁴. The directed cell migration towards chemical gradients is called chemotaxis and can be categorized by how the cells move (Table 1.2)^{106,135–137}.

The first step of chemotaxis is the binding of chemoattractant molecule to specific receptors such as receptor tyrosine kinases, G protein coupled receptors, etc^{136,138}. The second step is the development of stable cell polarity by activation of local signaling pathways and cytoskeleton (Figure 1.16)^{105,139}. The third step involves retraction at the rear (trailing) edge of the cells leading to cell locomotion.

The signaling pathways involved in chemotaxis are complex and often have cross-talks. Elucidating the functions of molecular targets in each chemotactic signaling

Table 1.2: Types of directed cell migration¹⁰⁶. Reprinted with permission of Springer Nature.

	Single cell migration		Multicellular migration	
	Amoeboid	Mesenchymal	Collective or chain migration	Streaming
Movement type				
Cell types	<ul style="list-style-type: none"> • Dictyostelium discoideum • Leukocytes • Tumour cells 	<ul style="list-style-type: none"> • Fibroblasts • Neural crest endothelium • Tumour cells 	<ul style="list-style-type: none"> • Border cells in <i>Drosophila</i> melanogaster • Epithelial-like cells in zebrafish and <i>D. discoideum</i> • Mammalian cells involved in gastrulation, wound healing and cancer 	<ul style="list-style-type: none"> • <i>D. discoideum</i> • Tumour cells • Developing neural crest cells
Microenvironmental factors influencing migration	Chemokine and growth factor gradients	Chemokine and growth factor gradients, proteolysis	Chemokine and growth factor gradients, reorganization of extracellular matrix	Chemokine and growth factor gradients, reorganization of extracellular matrix, paracrine signalling
Extracellular matrix degradation required?	Sometimes	Yes	Yes	Probably
Can cells switch between types of migration?	Amoeboid to mesenchymal	Mesenchymal to amoeboid, mesenchymal to collective	Collective to single cell migration (amoeboid or mesenchymal)	Not determined
Cell shape during migration	Pseudopodia dominate the shape	Elongated or spindle-shaped	The leader cell is elongated, the cells in the attached sheet are cuboidal	Mixed: cells transition between pseudopod and elongated
Cell-cell junctions maintained?	No	No	Yes	No
Processes where type of migration is observed	<ul style="list-style-type: none"> • Immune response • Cancer invasion 	<ul style="list-style-type: none"> • Development • Immune response • Cancer invasion 	<ul style="list-style-type: none"> • Development and morphogenesis • Vascular sprouting • Tissue repair • Cancer invasion 	<ul style="list-style-type: none"> • Development • Cancer invasion and intravasation
Types of cancer	Breast and prostate cancers and melanoma	Breast and prostate cancers, melanoma, lung and squamous cell carcinomas	Breast, prostate, lung and colorectal cancers, melanoma and squamous cell carcinoma	Breast cancer

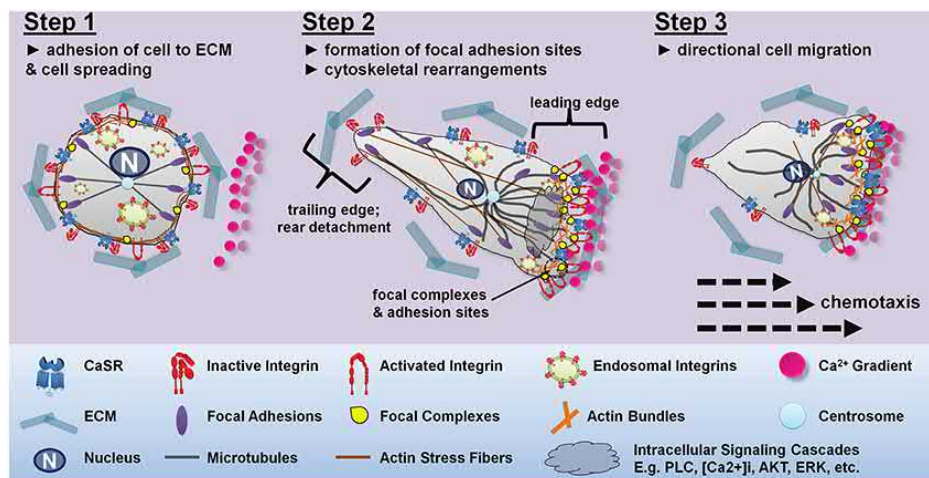


Figure 1.16: Cell polarity during chemotaxis of the calcium gradient¹³⁹.

pathway towards different chemical gradients is important for understanding fundamental biology and also for discovery of therapeutics in pathological conditions (Figure 1.17)¹⁰⁶.

Creation of chemical gradients in microfluidics

In microfluidic systems, the Reynolds numbers are low and viscous effect dominates. Thus, many microfluidic systems are used to manipulate the distribution of chemical species which is of great interest to analytical chemistry and biology^{140–142}.

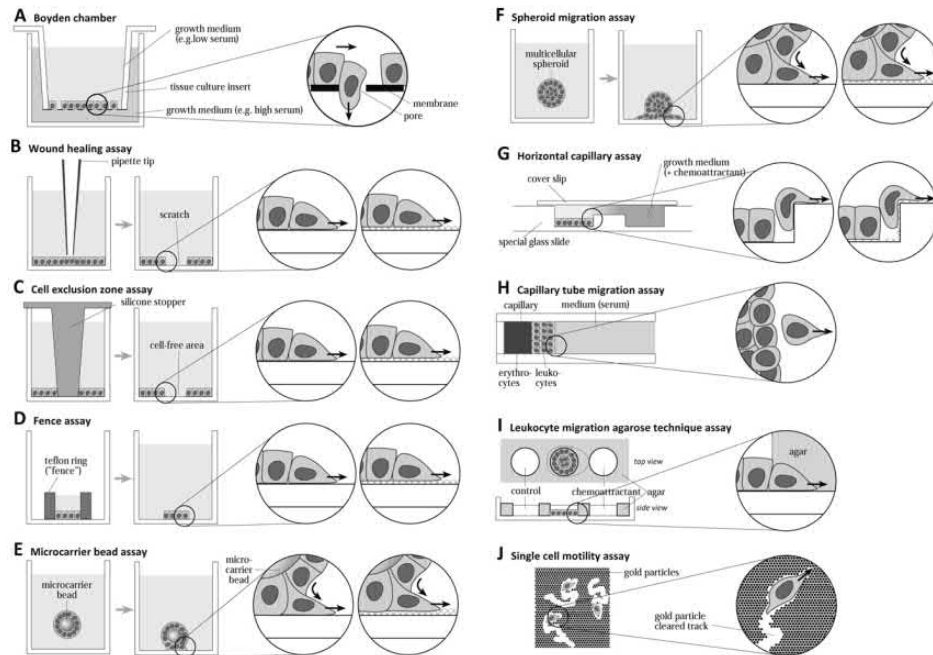


Figure 1.18: Commonly used macro migration assays¹⁴³. Reprinted with permission of Elsevier.

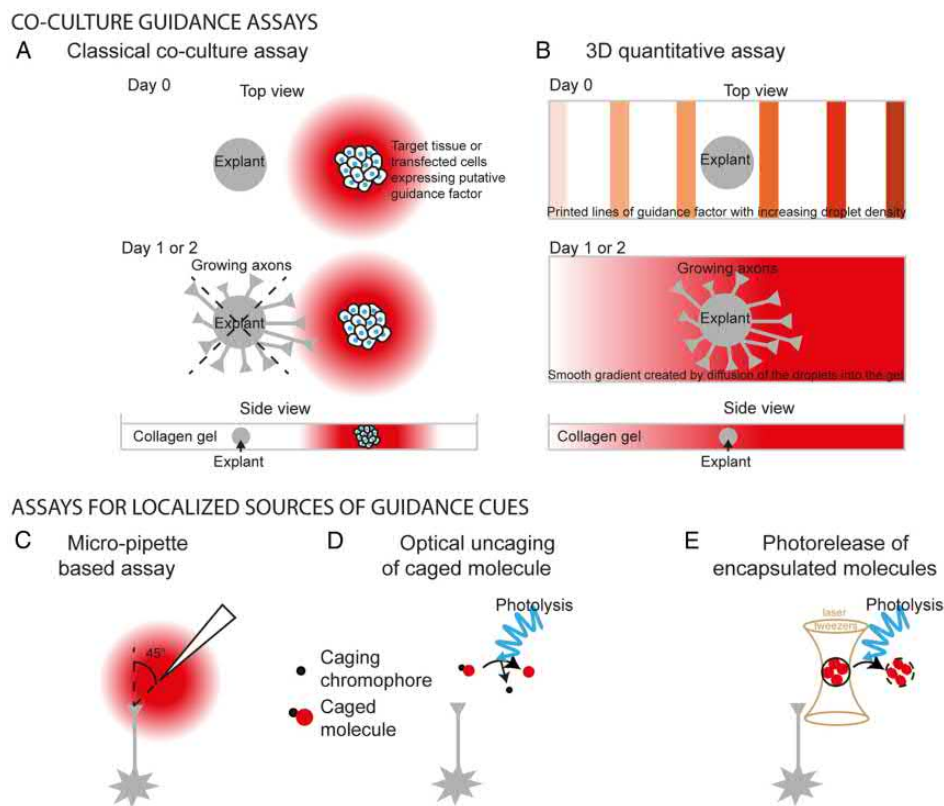


Figure 1.19: Classical methods of generating chemical gradients¹⁴⁴.

sion between two laminar flows (Figure 1.20B). Using diffusion through series of small microfluidic channels can also establish chemical gradients (Figure 1.20C). Utilizing hydrogels as the 3D cell model, chemicals can also diffuse through the hydrogel and establish chemical gradients (Figure 1.20D).

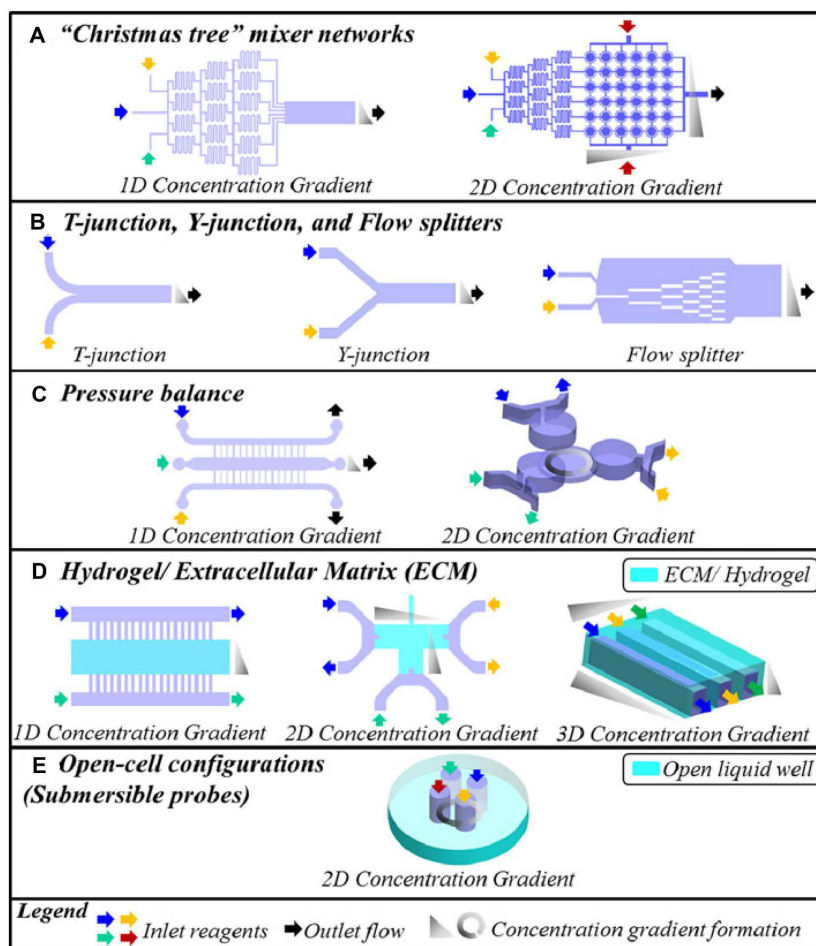


Figure 1.20: Microfluidic-based concentration gradient generator¹⁴⁵. Reprinted with permission of Springer Nature.

1.3.2 The voltage gradient microenvironment

Endogenous voltage gradients creating stable current in physiological systems

In human bodies, endogenous electric field is generated by either a voltage generator or a power source. Two main power sources exist in a living system, the epithelium surrounding the organs and body, and the lipid bilayer of biological membranes.

The resting potential arises from the differential ion transport in living cells (Figure 1.21). The resting membrane potential can be calculated based on the concentrations of major ion species, which are sodium (Na), potassium (K), and chloride (Cl)

	Passive transport				Primary active transport	
	Diffusion		Cotransport			
	PORE	CHANNEL	SYMPORT	ANTIPOINT		
Electro-neutral $v_1 z_1 = v_2 z_2$			Na ⁺ , K ⁺ - 2Cl ⁻ K ⁺ - Cl ⁻ Na ⁺ - Cl ⁻	Cl ⁻ - HCO ₃ ⁻ Cl ⁻ - Cl ⁻ Na ⁺ - H ⁺ K ⁺ - H ⁺		Na ⁺ - H ⁺ -ATPase
Rheogen $v_1 z_1 \neq v_2 z_2$	Na ⁺ , K ⁺ , Cl ⁻	Na ⁺ , K ⁺ , Cl ⁻	Na ⁺ - - Glucose	3 Na ⁺ - Ca ⁺⁺ H ⁺ - Ca ⁺⁺	H ⁺ - ATPase Ca ⁺⁺ - ATPase	3 Na ⁺ - 2 K ⁺ -ATPase

Figure 1.21: Classification of ion transporters on biological membranes¹⁴⁶. Reprinted with Permission of Springer Nature.

according to the Goldman equation:

$$\Delta\Psi = \frac{RT}{F} \ln \frac{P_{Cl}a_{Cl}^i + P_Ka_K^e + P_{Na}a_{Na}^e}{P_{Cl}a_{Cl}^e + P_Ka_K^i + P_{Na}a_{Na}^i}, \quad (1.3)$$

R is the ideal gas constant, T is the temperature in Kelvin, F is the Faraday's constant, P is the permeability of each ion, and a is the ion activity denoted i or e for intracellular or extracellular.

In the case of polarized tissue, the voltage differences across polarized membrane, also known as transepithelial potential (TEP), across the epithelium or biological membranes, originate from differential ion transportation by asymmetrically distributed transporters or ion channels (Figure 1.22)^{110,147,148}.

The endogenous electric fields play a pivotal role in wound healing^{149–153}, embryogenesis^{154–157}, morphogenesis^{157,158}, neurogenesis^{54,159,160}, and regeneration^{161,162}. The endogenous electric field has also been proposed as a possible contributing factor to cancer metastasis^{163–165}.

The physiological electric fields established by TEP differences in numerous tissues have been measured. The physiological TEP difference across a corneal epithelium is around 25 - 40 mV created by differential expression of ion transporters on apical and basolateral sides of the tissue¹⁴⁸. When a tissue polarity disruption (wound) is created on corneal epithelium, ionic fluxes of primarily chloride ions flow into the wound site, establishing an electric field. Similar endogenously generated electric field is also measured in a skin wound (Figure 1.23)¹⁶⁶.

The endogenous EF also has an important role in embryo morphogenesis. Perturbation of membrane potential and therefore the endogenous EF by molecular manipulation of ion channel expression can cause developmental defect and ectopic formation of organs. For example, manipulation of H⁺-V-ATPase affects left-right asymmetry in xenopus, zebrafish, and chick embryo development and causes heterotaxia¹⁶⁷ (Fig-

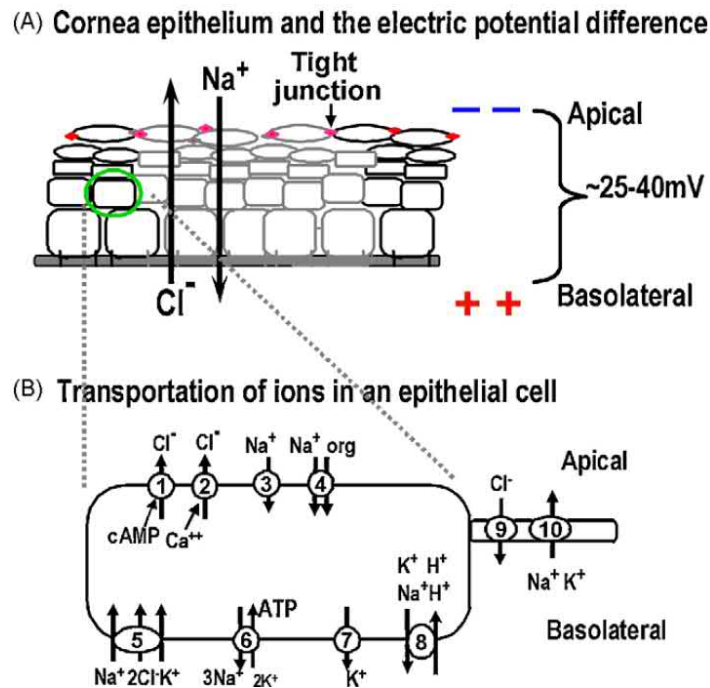


Figure 1.22: Molecular basis of endogenous electric field¹⁴⁸. After establishment of tissue polarity, asymmetrical distribution of ion channels usually can be found to contribute to biased ionic transport. The biased ionic transport maintains an electric potential difference across the epithelium (transepithelial potential). In the case of wound healing, disruption of the epithelium creates a break in the electric circuit and a net ionic flow contributes to an active endogenous electric field. Reprinted with permission of Elsevier.

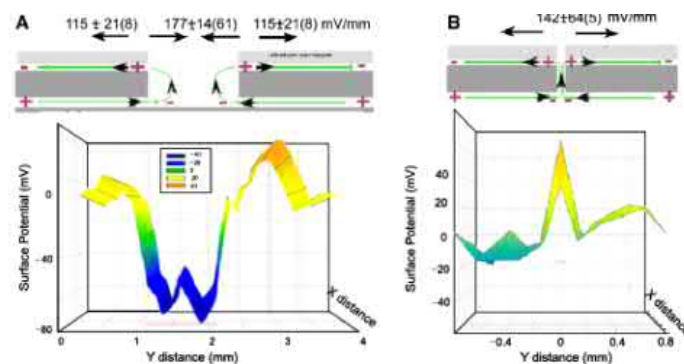


Figure 1.23: A wound on mouse skin and measurement of the wound-associated electric field¹⁶⁶. Reprinted with permission of John Wiley and Sons.

ure 1.24). Local perturbation of membrane potential can also induce ectopic eye formation in *Xenopus* species¹⁶⁸.

In the ductal structures of mammary gland and prostate, TEP differences have also been measured^{169,170}. In the breast duct, the TEP is +30 mV in the lumen whereas in the prostate duct the TEP is -10 mV, reflecting the heterogenic nature of TEP in different tissues (Figure 1.25). Interestingly, it has been found that despite the com-

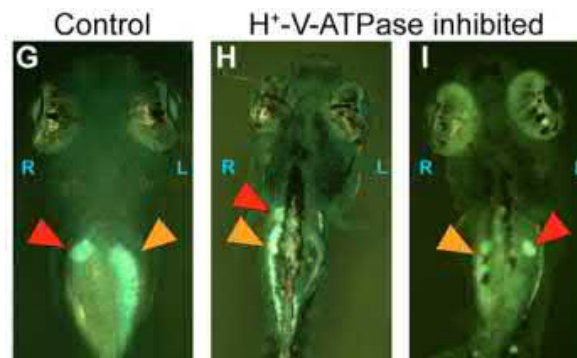


Figure 1.24: Heterotaxia in zebrafish when H^+ -V-ATPase subunits are inhibited during early embryogenesis¹⁶⁷. Reprinted with permission of the Company of Biologists Ltd.

pletely different TEP between the two tissues, under *in vitro* electric field, the tumor cells for the two tissues both migrate toward lumen direction. This correlation has been the theoretical basis of endogenous EF's contribution to cancer metastasis^{164,171}.

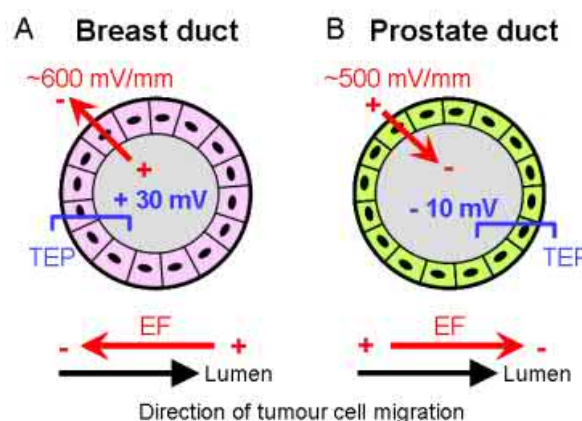


Figure 1.25: The polarities of transepithelial potential in mammary and prostate ducts correlate also with the direction of breast and prostate cancer cell migration relative to an EF *in vitro*¹¹⁰. Reprinted with permission of the Company of Biologists Ltd.

Aside from endogenous electric field generated by passive and primary active ion transporters to form the resting potential, the cells in the neuromuscular system express a set of membrane ion channels that can create ion fluxes upon stimulation by voltage (voltage-gated) or chemical (ligand-gated)¹⁷². The membranes of the cells in neuromuscular system are termed electrically excitable membranes. Upon activation, ion fluxes of excitable membranes create a rapidly propagated electrical message over membrane surfaces, called action potential¹⁷²⁻¹⁷⁵. The action potential is the fundamental unit of electrical activities in the neuromuscular system and the firing frequency and strength of it sum up to the complex electrical patterns in the central nervous system and the neuromuscular system (Figure 1.26)¹⁷³.

The pulsatile firing of action potentials by neurons propagates into tissues. The amplitude and frequency of local field potentials (LFPs) at any given position in the

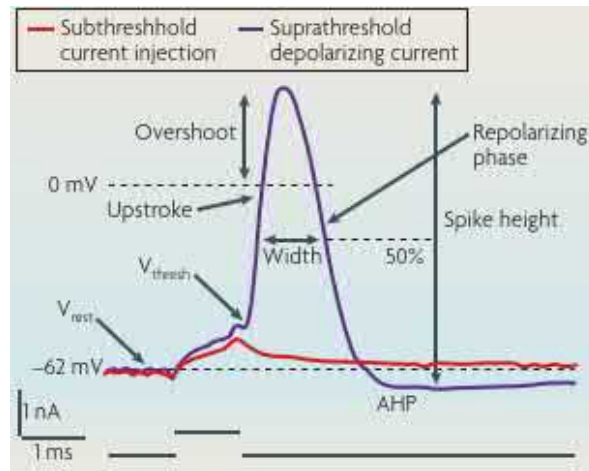


Figure 1.26: The anatomy of an action potential¹⁷³. Reprinted with permission of Springer Nature.

tissue depends on the proportional contributions of all the action potentials and tissue impedance properties (Figure 1.27). The local field potentials in the brain, heart, and muscles are the electrical activities measured by the electroencephalogram, electrocardiogram, and electromyography¹⁷⁶⁻¹⁷⁸.

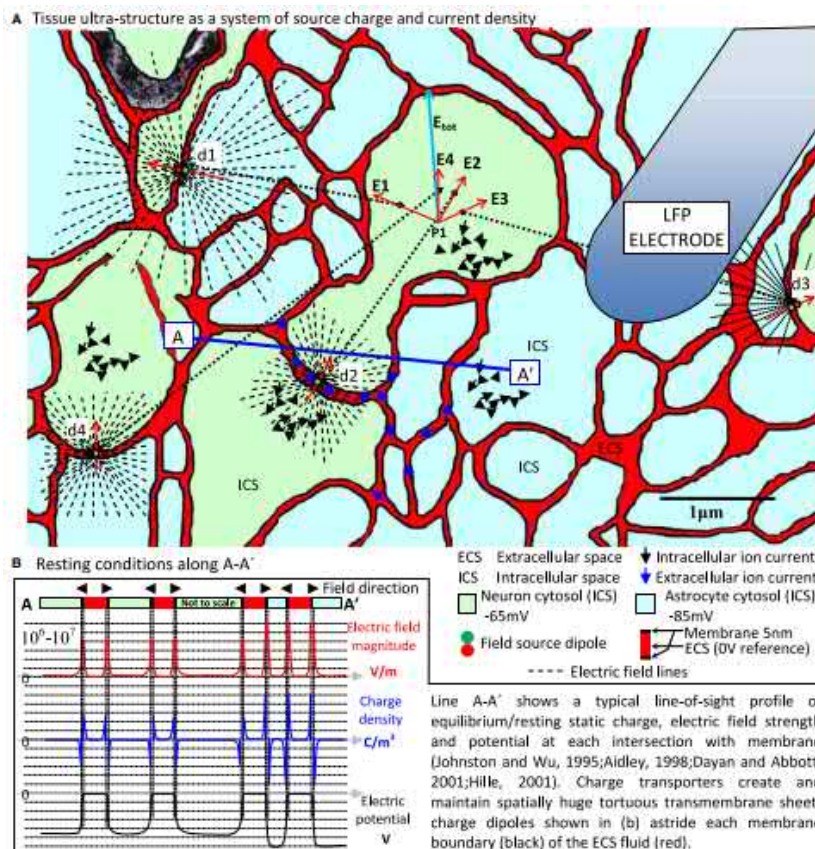


Figure 1.27: Electric field in the nervous system ultrastructure¹⁷⁸.

Therapeutics using an externally applied electric field

Historically, electrical stimulation has been used as therapeutics dated back in Roman Empire with an electric fish¹⁷⁹. While external defibrillator or electroacupuncture may be more familiar in current medical practice, electrical stimulation as part of therapeutic regime has been studied with a long history of contemporary medicine. Geddes categorized the medical applications of electricity either by static electricity or by a steady electric current (galvanism)¹⁸⁰. The static electricity is generated by placing patients in between capacitors applied with high voltage difference. Such static electricity in particular has been found to promote bone growth, by mechanisms similar to stress-generated potentials (SGP) in the bone¹⁷⁹. On the other hand, electric field can also be artificially applied by steady electric current delivered through direct-contacted or capacitively-coupled electrodes. The effect of the galvanism has been reported in researches involving wound healing, limb regeneration, spinal cord regeneration, etc, with particular focus on the effect of direct current electric field because it is believed that direct current electric field is the primary if not the only type of electric field in the physiological systems¹⁷⁹.

For the externally applied alternating current electric field (acEF), while a majority of investigations into biological effects of acEF are initiated due to concerns of radio-frequency (RF) electromagnetic field (EMF) emitting from cell phone or the extremely low frequency EMF from electricity grid, there is still yet compelling evidence to solidly suggest that acEF causes cancers. However, specifically for glioma and some other solid tumors, alternating current electric field has been shown to inhibit the mitotic spindle and to stop the proliferation of the cancer cells in the Novocure's tumor treating field technology as discussed in Section 1.1.4. The readers are referred to specialized review texts for more details^{147,179,181,182}.

Cell responses to voltage gradients

Cell response to direct current voltage gradients Under *in vitro* direct current electric field (dcEF) stimulation, cells may demonstrate directional migration toward cathode or anode, called electrotaxis or galvanotaxis^{183–188}.

In neurons under direct current electric field stimulation, the electric field can further guide or reorient the outgrowth of neurites, termed galvanotropism^{107,108,189–192}. This interesting behavior prompted on-going studies of using electric field for nerve regeneration^{193–195}.

Moreover, *in vitro*, dcEF stimulated cells often showed perpendicular alignment to the electric field vector^{196–202}. Although this behavior appeared to be associated with cytoskeleton and Golgi apparatus, it is less studied. Whether or not electro-alignment participates in pattern formation *in vivo* is not yet elucidated.

Pulsed direct current electric stimulation also have effects to promote metabolism. Note that the amplitude and frequency of the electric field used for cell stimulation usually are not as high and as strong as ones that used for nucleic acid delivery by electroporation²⁰³.

Cell responses to alternating current voltage gradients Despite the general belief that only dcEF exists in the physiological systems, the alternating current electric field can also further impose modulation and affect the endogenous EF. Under alternating current electric field stimulation, it has been reported to increase metabolism and production of antibodies in hybridoma cells²⁰⁴.

In addition, alternating current electric field has been shown to align the mitotic spindle and affects cell division^{205,206}. Palti *et al.*, discovered that an alternating electric field with intermediate frequency can affect mitotic spindle formation and cause cell deaths in glioblastoma cells^{80,206}. The discovery initiated the development of tumor-treating field technology and is now a food and drug administration (FDA)-approved therapy for recurrent glioblastoma^{207,208}.

Biophysical and biochemical signaling in electrotaxis The mechanisms underlying electrotaxis are complex. While many cells show electrotaxis to dcEF and many cellular signaling pathways have been identified, not all cells share the same signaling pathway under EF stimulation. While the electrotaxis involves biochemical signal transduction for activation of cell migratory machinery, it is believed to be initiated by a biophysical mechanism powered by the electric field¹¹⁰.

Biophysical activation of electrotaxis Biophysically, there are several hypotheses on initial steps of electrotaxis (Figure 1.28).

Firstly, through bioelectrical activation, membrane potential depolarization by dcEF could directly activate voltage-gated ion channels or voltage sensitive proteins and also influence activity of several passive ion channels. Voltage-gated ion channels such as voltage-gated sodium channels^{164,171,209–211} and voltage-gated calcium channels^{212–214} have been shown to be important to the electrotaxis of several breast cancer cell lines, prostate cancer cell lines, or human keratinocytes. Passive and active transport ion channels such as Na^+/K^+ ATPase²¹², Na^+/H^+ exchanger²¹⁵, and H^+ -V-ATPase^{167,216} have been found to be associated with the electrotaxis response of a cell. Discovery of a voltage sensitive protein with PTEN phosphatase activity (Ci-VSP) also suggests it possibly being an upstream sensor for electrotaxis, but so far there is no direct proof of its expression in all cells and its implication to electrotaxis^{217–219}.

Secondly, from early membrane protein mobility observations in embryos and cells under dcEF, researchers found polarized membrane receptors, suggest a possible activation of the receptors. Several hypotheses based on electrokinetic transport of membrane proteins are proposed so electrokinesis is widely accepted as a fundamental mechanism for electrotaxis (Figure 1.30). The membrane proteins are driven by *in situ* electrophoresis^{187,220–223}, which is the lateral movement of charged proteins on the membrane driven by dcEF, and electro-osmosis²²⁴, in which nano-scopically an electro-osmotic flow forming at the Debye layer of the cell membrane can sweep the membrane proteins. As a result, membrane proteins including many major cellular signaling proteins polarize toward either cathode or anode. Activation of asymmetrically distributed membrane components would lead to biased cellular signaling which confers the direction cue for migration. The directional migration can happen even if the ligands in the extracellular medium do not have any concentration gradient.

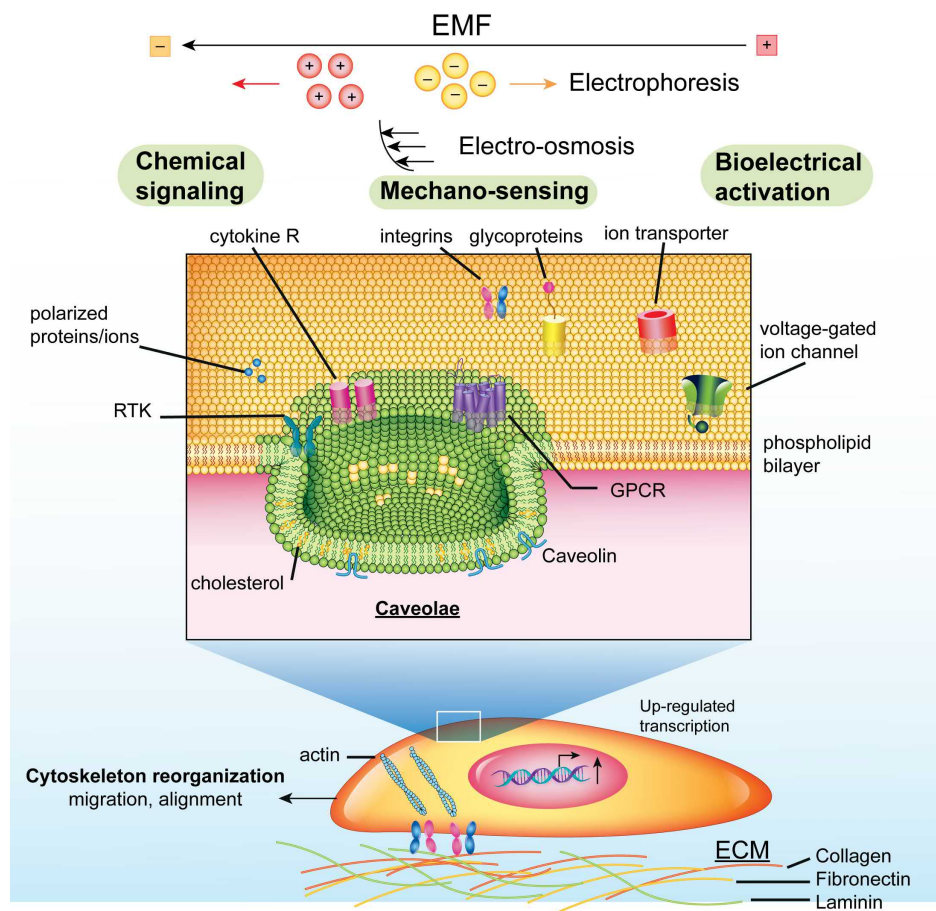


Figure 1.28: The mechanisms of cell response to EF are complex^{110,196}.

Although polarization of membrane proteins has been considered as the activation of electrotaxis, several reports suggest that the polarization of membrane proteins does not necessarily decide the directionality or activation of the signaling^{196,225,226}.

Moreover, many membrane receptors reside in cholesterol-rich or sphingolipid-rich microdomains (caveolae) on the cellular membrane (Figure 1.28). EF-induced coalescence of lipid raft or polarization of membrane receptors can lead to non-ligand mediated autoactivation²²⁷.

Thirdly, integrins are proposed to be an electromechanical transducer for the electro-osmosis flow leading to activation of cell migration^{228–230}. Recombinant expression of different integrins on Chinese hamster ovary (CHO) cells can mediate the electrotactic direction of them²³¹. Other cell junction proteins such as E-cadherin have also been found to be an essential part of electrotaxis²³².

Signaling amplification through biochemical pathways in electrotaxis

After cells sense the electric field, it is expected that the signal is amplified through a biochemical signaling. Receptor tyrosine kinase proteins have been reported to be activated in cells under dcEF stimulation by *in situ* electrophoresis, including epidermal growth factor receptor (EGFR)^{233–242}, vascular endothelial growth factor receptor (VEGFR)^{243–245}, fibroblast growth factor receptor (FGFR)¹⁸⁵, insulin receptor²⁴⁶, and

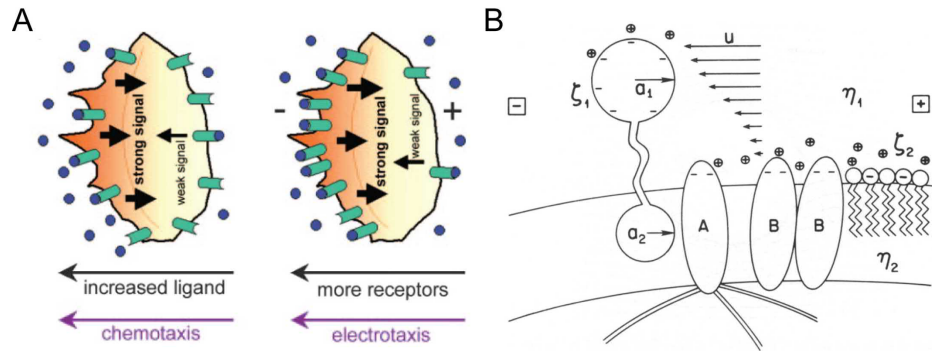


Figure 1.29: The hypothesis of electrokinetic based migration of membrane proteins as the cause for electrotaxis^{184,224}. (A) *In situ* electrophoresis of signaling receptors; (B) Electro-osmosis of integrins to contribute to electromechanical signal transduction. Reprinted with permission of Elsevier.

hepatocyte growth factor receptor (HGFR)²⁴⁷. Ligand-gated ion channels such as acetylcholine receptors are also reported as key regulators in electrotaxis of muscle cells^{223,248–251}. Although electrotaxis of *Dictyostelium* (slime mold) is found to be independent of G β protein, part of G-protein coupled receptor (GPCR) signaling²⁵², other GPCRs such as beta-2-adrenergic receptors are found to be involved in the electrotaxis of different cell lines^{253–255} accompanied by complex bimodal responses to different concentration of GPCR agonists²⁵⁴.

In the intracellular signaling of electrotaxis, PI3K/Akt signaling^{256,257} is the most common signaling pathway activated in electrically stimulated cells. Several membrane or intracellular phosphatases^{165,256,258} are also found to participate in the regulation of intracellular signaling of electrotaxis. But calcium signaling, reactive oxygen species, MAP Kinases, protein kinase C, Rho GTPases, and cyclic AMP signaling are also present and reported in the electrotaxis of different cell types^{213,254,259–264}.

Summary of current understanding of complex nature of signaling network in EF stimulated cells is shown in Figure 1.30²⁶⁵.

Creation of voltage gradients in microfluidics

Stable voltage gradients can be easily created within a microfluidic channel. The electrical resistance R of a microfluidic channel is described by the Ohm's law as $R = \rho l/A$ where ρ is electrical resistivity of the fluid, l is the length of the channel, and A is the cross-sectional area. In a microfluidic channel, the cross-sectional area is extremely small so that a strong electric field can be created by a small electric current. Conventional apparatus for creation of voltage gradients uses a rectangular microfluidic chamber flanked by two cover glasses in a petri dish (Figure 1.31)²⁶⁶. The electrical stimulation is applied through agar bridges connected into the microfluidic chamber. The agar bridges prevent the cells being contaminated to electrolysis product by isolating them from the electrodes.

Multiplexing can also be achieved by designing microchannels with different widths¹⁹⁸ or connecting networks²⁰² (Figure 1.32). The small configuration of microfluidic chips makes them suitable for real-time observation of cell migration on a microscope. For ap-

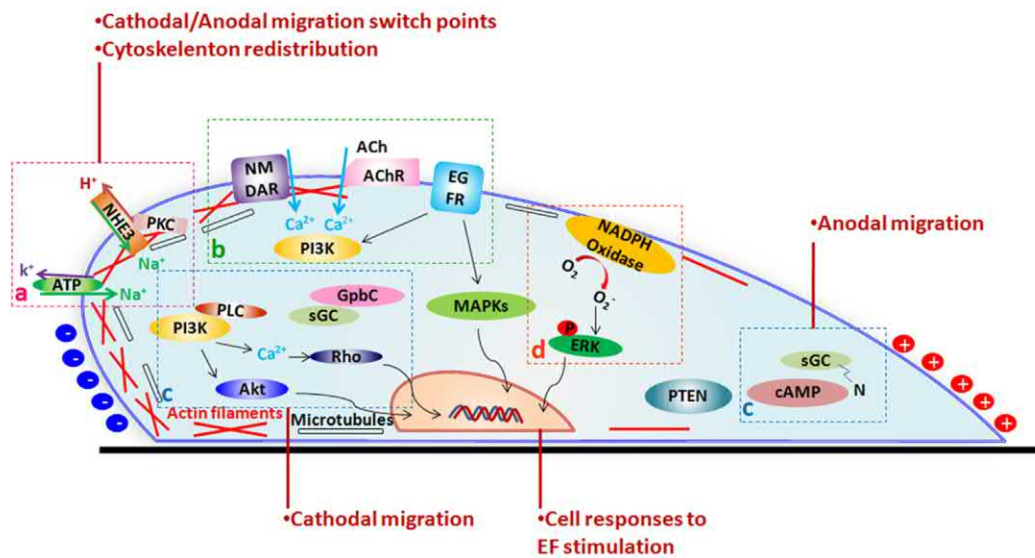


Figure 1.30: An abstract signaling network in EF stimulated cells²⁶⁵. Reprinted with permission of Elsevier.

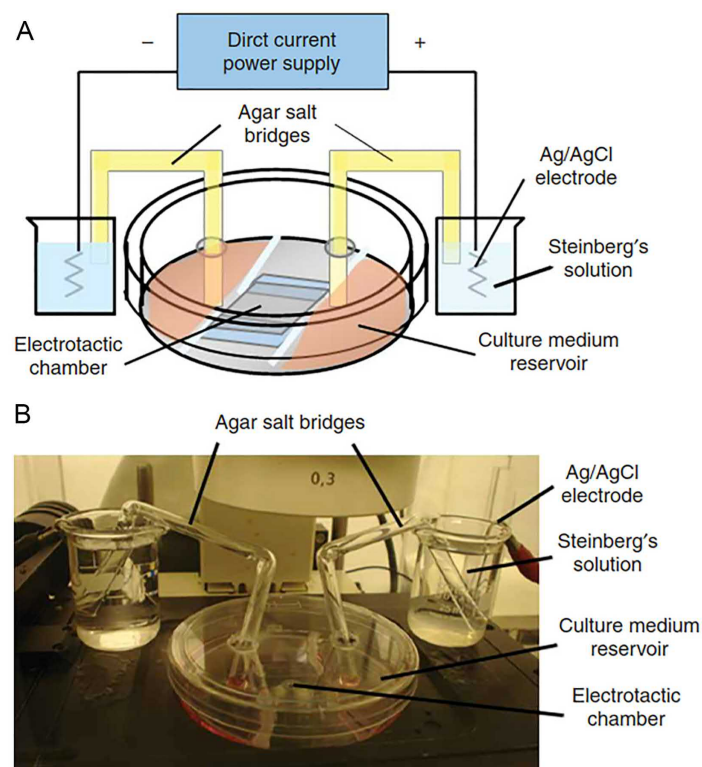


Figure 1.31: The setup of a conventional device to create voltage gradients²⁶⁶. (A) The setup diagram; (B) The photoimage of the setup. Reprinted with permission of Springer Nature.

plications that require collection of cellular products after experiment, microfluidic devices with extremely large cell culture area can be specially fabricated¹⁹⁶ (Figure 1.33).

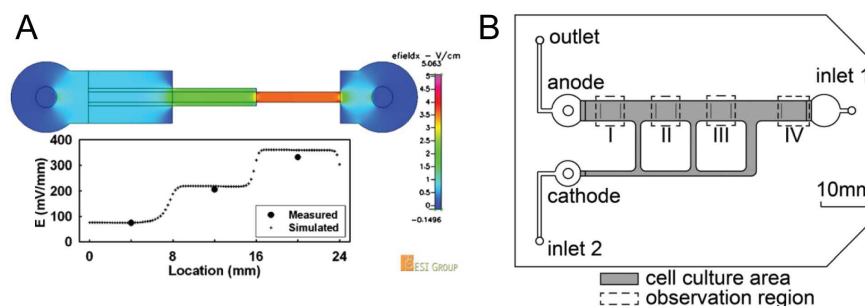


Figure 1.32: The microfluidic approach for creation of multiple voltage gradients on a single chip. (A) Multiple electric fields using varied widths¹⁹⁸; (B) Multiple electric fields using interconnected channel networks²⁰². Reprinted with permission of Elsevier and AIP Publishing.

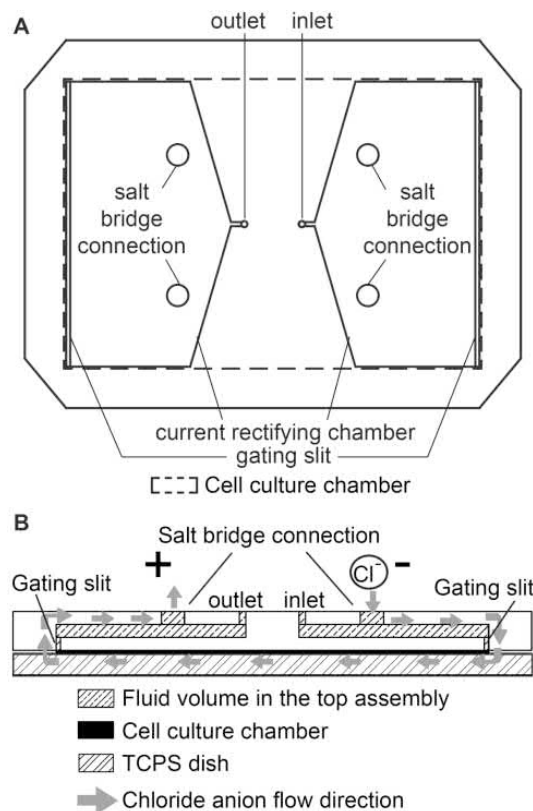


Figure 1.33: A microfluidic device for creating uniform voltage gradient to a large area of cell culture¹⁹⁶. (A) The top view of the large microfluidic device; (B) The side view of XLEFC showing the flow direction of chloride ions which are driven by the external dcEF.

1.3.3 Multiplex gradients in 2D microfluidic chip

Cell migration plays a critical role in physiological and pathological conditions. How cells respond to different gradients simultaneously and the strength of the responses are important. Recent researches in microfluidics focus on building *in vitro* systems to systematically and simultaneously control multiplex directional cues and study the

cell behavior in complex gradients (Figure 1.34)¹⁸³.

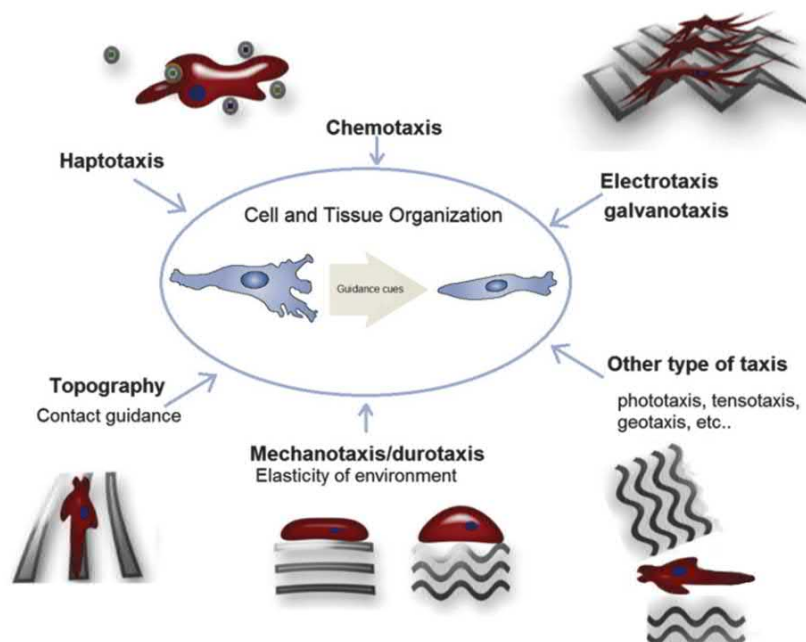


Figure 1.34: Complex gradients can guide cell migration¹⁸³. Reprinted with permission of Oxford University Press.

An intuitive approach is to place two chemical gradients in direct opposite direction, *i.e.*, in the tug-of-war configuration (Table 1.3). The cell responses under the multiplex gradients are then studied and will demonstrate effect of preference if the guidance of one gradient overpowers the other.

However, it is known that the *in vivo* microenvironment is often established with multiple gradient cues for pattern formation, which are not necessarily competitive. Several microfluidic designs specifically are restricted to generating perpendicular gradients to avoid the downfall of studying competitive effects of gradients in the tug-of-war configuration.

Chang *et al.* used the gas-permeability property of PDMS to create an oxygen gradient and a microfluidic mixer to create a chemical gradient²⁷⁶ (Figure 1.35). They demonstrated that the device can be used to screen for anticancer drug efficacy in different oxygen concentration and also for cell migration study in both chemical and oxygen gradients. A549 lung adenocarcinoma cells demonstrated chemotaxis towards SDF-1 α gradient and migration toward hypoxic region independently. When cells are exposed to both gradients, the effect of oxygen gradient overrides that of the chemical cue.

Kilinc *et al.* created a dual gradient generator microfluidic chip to create a panel of chemical combinations for drug screening and study the chemotaxis of MDA-MB-231 cells in chemical gradient of EGF and its inhibitor (Figure 1.36)²⁸⁰.

Advances in microfluidic technologies offer us the tools to create and manipulate the gradients in the microenvironment. By designing multiplex microenvironment, we can investigate how cells respond and make decisions. Elucidating the interaction between

Table 1.3: Highlights of research activities studying multiplex gradients on cell migration using microfluidic technologies.

Cue combination	Competition	Dominant cue	Cooperation	Cell model	Year	Ref
Chemo-Chemo	Yes	IL-8>LTB4	n/a	Neutrophil	2005	267
Chemo-Chemo	Yes	EGF=anti-EGF	n/a	MDA-MB-231 breast cancer	2006	268
Hapto-Chemo	Yes	BDNF>Laminin	n/a	Neuron	2008	269
Hapto-Chemo	No	CCL21+CCL19	Yes	Dendritic cells	2010	270
Chemo-Chemo	Yes	CCL19>CCL21	No	Dendritic cells	2011	271
Electro-Chemo	Yes	EF>CCL19	No	T cell	2012	272
Chemo-Chemo	No	SDF-1 α +EGF	Yes	MDA-MB-231 breast cancer	2013	273
Shear-Electro	No	EF+Shear	Yes	Human dermal fibroblasts	2013	274
Electro-Chemo	Yes	EGF=EF	n/a	CL1-5 lung adenocarcinoma cells	2014	275
Oxygen-Chemo	No	Oxygen>SDF-1 α	Yes	A549 lung adenocarcinoma cells	2014	276
Hapto-CDuro	Yes	Collagen>stiffness	n/a	Balb/c 3T3 fibroblasts	2015	277
Chemo-Chemo	No	FBS<->FBS	Yes	HT1080 fibrosarcoma cells	2015	278
Chemo-Chemo	No	Retinoic acid<->Retinoic acid	Yes	Motor neurons	2015	278
Chemo-Chemo	Yes	fMLP>LTB4	n/a	Neutrophil	2015	279
Chemo-Chemo	No	U0126 (MEK inhibitor)>BIBX(EGFR inhibitor)	n/a	A431 breast cancer cells	2016	280
Chemo-Chemo	No	Netrin-1+Slt-2	No	Mouse cortical neurons	2019	281
EF-Chemo	No	SDF-1 α +EF	Yes	Mouse retinal progenitor cells	2019	282

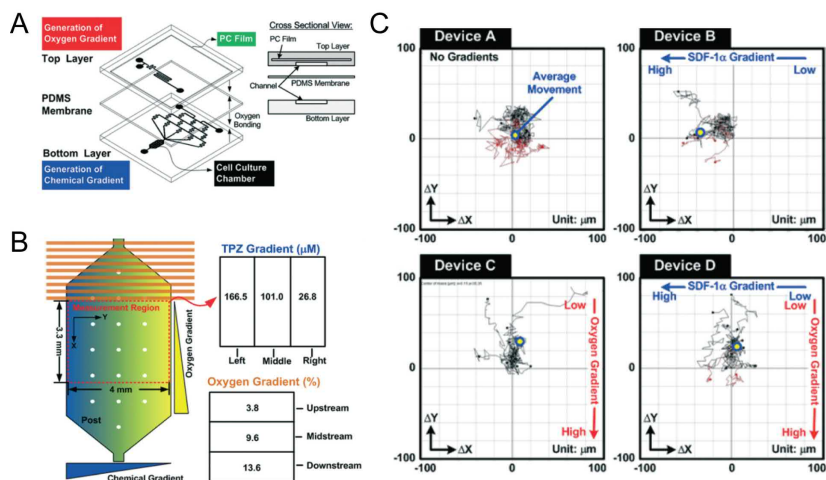


Figure 1.35: A microfluidic device to create perpendicular oxygen and chemical gradients²⁷⁶. (A) Device design; (B) The orthogonal gradients of oxygen and antitumor drug concentration gradient; (C) A540 lung adenocarcinoma cell migration is guided by SDF-1 α gradient and oxygen gradient. Reprinted with permission of Royal Society of Chemistry.

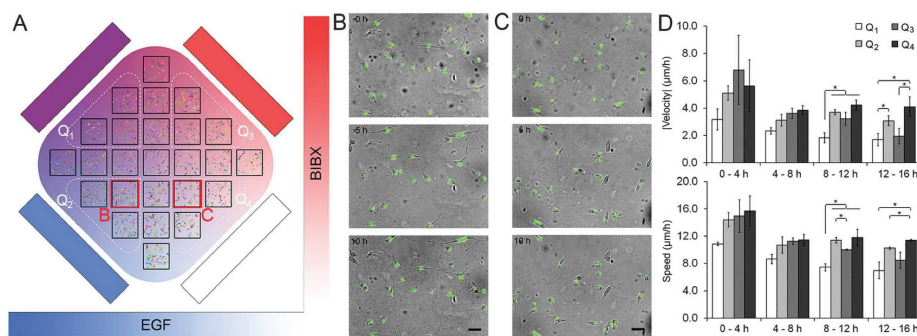


Figure 1.36: MDA-MB-231 cell migration in a combinatorial gradient generating microfluidic device²⁸⁰. (A) Experimental paradigm with orthogonal EGF and BIBX gradients; (B) Cell images taken with 5 hr intervals in region B in the chip; (C) Cell images taken with 5 hr intervals in the region C in the chip; (D) Average velocity magnitude and cell speed in each quadrant. Reprinted with permission of Oxford University Press.

the cells and the guidance cues can help us to build more biomimetic tissues or develop better *in vitro* models for drug discovery.

1.4 Glioma on a chip

Several microfluidic systems have been developed and used on glioma research focusing on drug screening, analysis of cellular signaling^{283,284}, and migration in chemical, stiffness, topography, and voltage gradients.

For drug screening, the microfluidic chips were designed with parallel chambers or

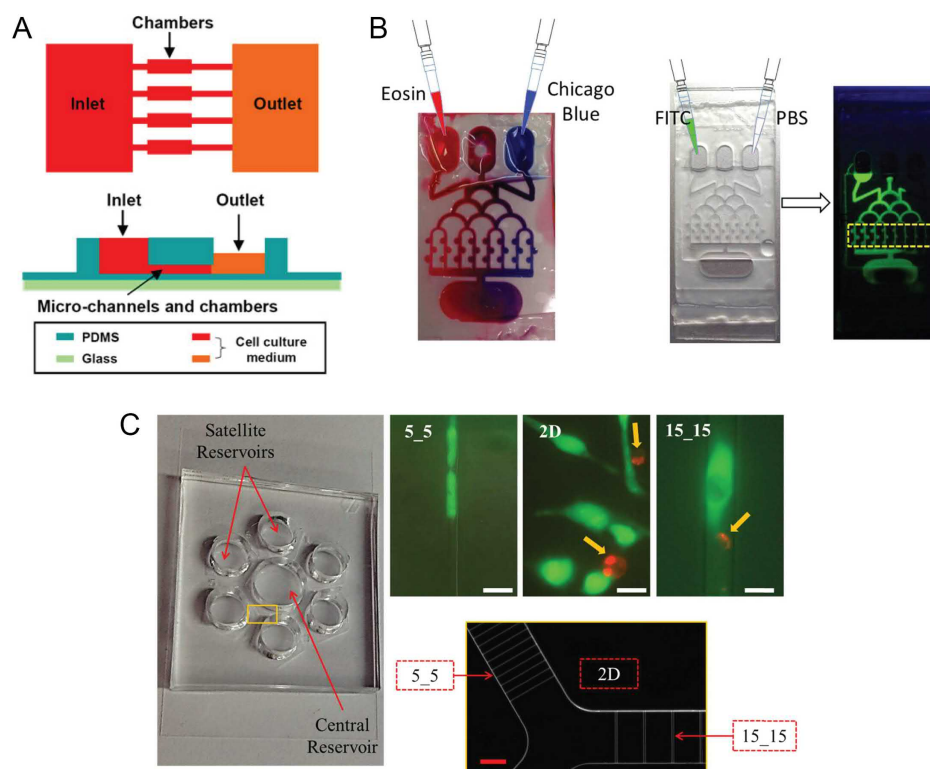


Figure 1.37: Microfluidic models for drug screening in glioma research^{285–287}. (A) Liu *et al.* used parallel chambers to perform drug screening on glioblastoma cells. Reprinted with permission of Springer Nature; (B) Fan *et al.* used a microfluidic mixers to create different drug concentrations for high throughput testing of cytotoxic drugs; (C) Bui *et al.* studied glioblastoma response to anticancer drug in different physically confined environments.

mixers to create different drug concentrations to screen for cell responses on a single chip simultaneously^{285,286}. Liu *et al.*, used a multiple chamber microfluidic chip to study the effect of an anticancer drug, colchicine, of different concentrations on a rat glioma cells (Figure 1.37A)²⁸⁵. Fan *et al.* built a christmas tree-like microfluidic mixers to create different drug concentrations and test the drug induced glioblastoma cell death on this chip (Figure 1.37B)²⁸⁶. Together with drug screening, Bui *et al.* showed that a specific Braf molecular mutation contributed to the increased resistance to a microtubule stabilizing drug toxol in glioma cells when the cells were placed in physical confinement enabled by microfluidics (Figure 1.37C)²⁸⁷.

The microfluidic chips were also used to create different gradients to study the migration of glioma cells. Gallego-Perez *et al.* used microfabricated topographical cues to study guided glioma cell migration along the topography (Figure 1.38D)²⁸⁸. Wan *et al.* used microfluidic taper channels to create EGF gradients to study the chemotaxis of glioblastoma cells (Figure 1.38A)²⁸⁹. Ayuso *et al.* used a 3D microfluidic to create chemical gradients of fetal bovine serum around glioma tumor spheroid embedded hydrogel and studied the sprouting of the spheroid (Figure 1.38B)²⁹⁰. Direct physical property of microenvironment could also guide the migration of glioma cells. Rape *et al.* used different stiffnesses of polyacrylamide substrates and varied chan-

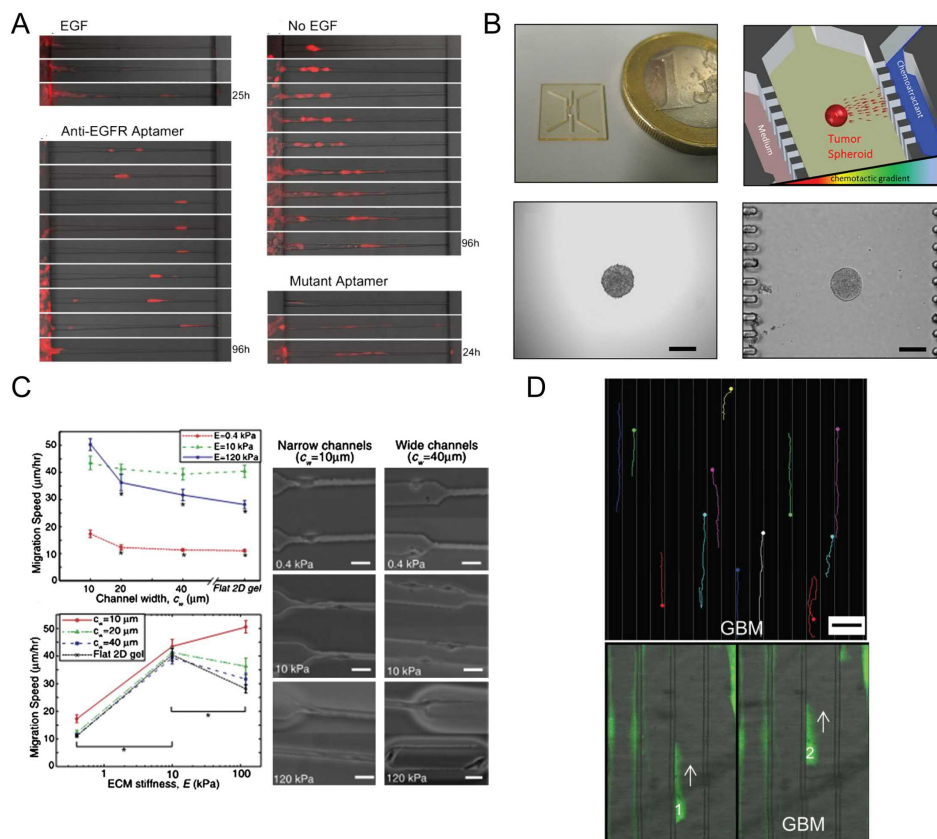


Figure 1.38: Microfluidic models for study glioma cell migration^{288–291}. (A) Study of chemotactic of glioblastoma cells towards EGF; (B) Study of U87MG spheroids chemotactic migration towards serum; (C) Study of glioblastoma cell migration on hydrogel of different stiffnesses; (D) Study of glioma migration on surfaces with micro-scale topographical features. Reprinted with permission of Royal Society of Chemistry, Springer Nature, and Elsevier.

nel widths to study the stiffness and confinement regulation of glioma cell migration (Figure 1.38C)²⁹¹.

Voltage gradients could also guide the migration of glioma cells. Direct current electric field stimulated normal astrocytes did not show electrotactic migration but several glioblastoma cell lines such as U87, C6, U251 showed cathodal migration (Figure 1.39)²⁹². The migration had been found to involve Akt and ERK signaling pathways and might be mediated by reactive oxygen species.

Interestingly, another report using brain tumor initiating cells freshly isolated from patient tumors showed anodal migration both in 2D and 3D biomimetic hydrogels (Figure 1.40)²⁹³. This could be due to the differences of substrate coating and stiffness.

Huang *et al.* further identified that heparan sulfate on cell membranes can regulate the electrotaxis of brain cancer initiating cells²⁹⁴. Lyon *et al.* reported that glioma spheroidal aggregates also demonstrated electrotaxis and U87MG glioblastoma electrotaxis involved PI3K/mTOR/AKT signaling²⁹⁵.

Not just glioma cells but the fetal neural progenitors and astrocytes also demonstrated electrotaxis. Huang *et al.* reported that human fetal neural progenitor cells

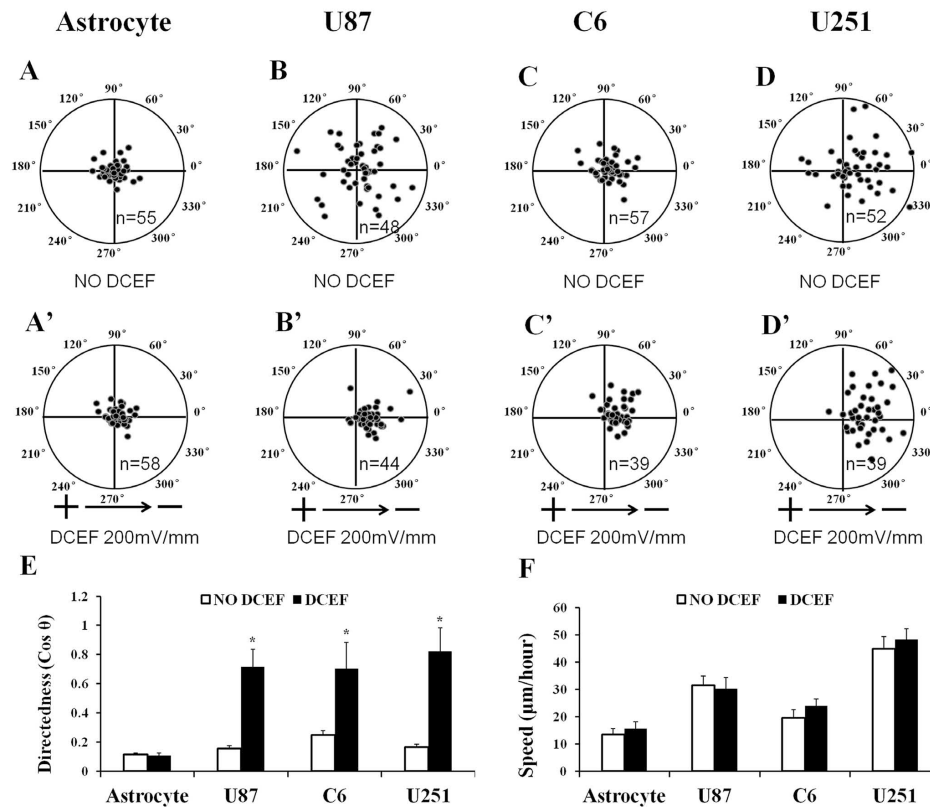


Figure 1.39: Electrotaxis of glioma cells²⁹².

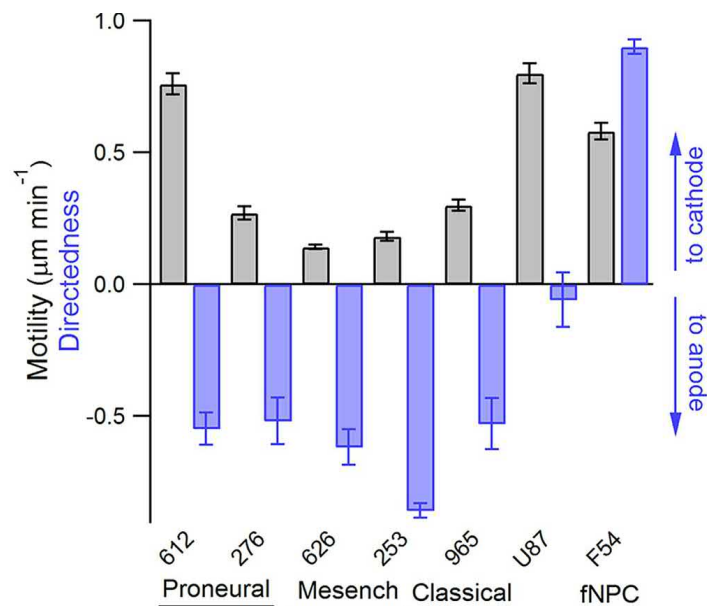


Figure 1.40: Galvanotaxis of glioblastoma cells of different transcription profile type and fetal derived neural progenitor cells (fNPC)²⁹³.

migrated toward cathode while the differentiated astrocytes from it migrated toward anode. Yang *et al.* also reported that astrocytes derived from adult human brain tissues migrated toward anode²⁹⁶.

The selected reports regarding the electrotaxis of glioma and glial cells using microfluidic systems are summarized in Table 1.4.

1.5 Current challenges and opportunities using microfluidics in cancer biology

Cancer is a complex systemic disease. Cancer cells grow without cell cycle control with high mutation frequency that contributes to heterogeneity. The cancer cells can travel to distant tissues through metastasis that leads to eventual systemic organ failure and eventual patient death³⁰¹. Contemporary cancer therapy targets cancer cells for elimination but the approach resulted in severe side effects and inevitable selective pressure on heterogeneous cancer cell population. Cancer recurrence and emergence of drug-resistant clone often occur and limit life expectancies of patients³⁰²⁻³⁰⁴.

In recent years, researches into the microenvironment surrounding the tumor revealed that the microenvironment affected the survival of cancer cells and cancer cells remodeled the surrounding microenvironment for their own gains and caused tumor progression^{84,305,306} (Figure 1.41). Understanding how and why microenvironment is modified by cancer cells and how microenvironment shapes cancer cells may shed light on new tumor treatment paradigm: stopping metastasis. If tumor cells are restricted to their *in situ* tissues, the cancer might be restricted to benign tumors and life expectancy as well as quality of life of patients could be potentially increased^{306,307}.

However, the cancer microenvironment is complex and composed of chemical and physical gradients in the ECM as well as intricate cell-cell interactions (Figure 1.41). To create a robust *in vitro* model for the tumor microenvironment is an important step toward mechanistic understanding. Some recent researches focused on using microfluidic technologies for spatiotemporal control of microenvironment to create tissue-on-a-chip devices for more biomimetic translational studies^{94,268,308,309}. However, to accurately mimic the *in vivo* microenvironment to control the cell fate and cell behavior demands a robust platform encompassing control in both extracellular chemical gradients, stiffness gradient, and voltage gradients. How to design and fabricate such platform is the first step to probe into the delicate tumor microenvironment and elucidate the fundamental tumor biology as well as discover new therapeutic targets.

In 2D microfluidic chips, cells are cultured on the substrate and the microenvironment can be manipulated by fluid flow, chemical transport, and electrical stimulation. The cell responses to gradients in the microenvironment can be easily observed through microscope at high magnification. In 3D microfluidic chips, hydrogels mimicking the extracellular matrix are used to embed singularized cells or multicellular spheroids to recapitulate cell-cell and cell-matrix interactions and realize a more biomimetic model compared to the 2D counterpart. However, in 3D microfluidic chip, special structural designs are required to hold the spheroids in place or pattern the hydrogels in the microfluidic channel with consideration of the material mechanical properties such as stiffness of the cells and yield stress of the hydrogel. Moreover, multicellular spheroids or cells in the hydrogel may not be on the sample focal plane so the microscopic observation is more difficult. A 2D microfluidic design to prove the feasibility of the concept is usually a good first step and hydrogel based platform can be subsequently incorporated

Table 1.4: An incomplete list of reports of electrotaxis of glioma and glial cells.

Lab	Year	Chamber size ($\times w \times h$) (mm)	Model	dDEF	Direction	Electrode	Primary findings	Reference
Morshhead	2011	22 \times 10 \times 0.17	CD1 mice NPCs	250	cathodal	Ag/AgCl	1. differentiated neural types do not electrotaxis 2. NPC electrotaxis dependent on EGFR	Babounis-Philippou <i>et al.</i> ²⁹⁷
Feng	2013	10 \times 2.2 \times 0.5	1. mouse astrocyte 2. rat C6 3. U87 4. U251	200	none in astrocyte cathodal in glioma	Ag/AgCl	1. N-acetyl-L-cysteine abolishes electrotaxis 2. increased ROS in glioma under electrotaxis	Li <i>et al.</i> ²⁹²
Codale	2015	10 \times 22 \times 0.17	rat cortical astrocyte	0, 4, 40, 400	anodal	Ag/AgCl	1. dDEF upregulates the speed of anodal electrotaxis 2. dDEF increases astrocyte proliferation 3. dDEF aligns astrocyte division 4. dDEF upregulates intermediate filament expression	Baer <i>et al.</i> ²⁹⁸
Yao	2015	30 \times 0.8 \times 0.15	P1-2 rat oligodendrocyte progenitor cells	0, 50, 100, 20	anodal	Ag/AgCl	dDEF induces anodal electrotaxis	Li <i>et al.</i> ²⁹⁹
Song	2016	n/a	P2 SD rat oligodendrocyte progenitor cells	0, 200, 400	cathodal	Ag/AgCl	dDEF induces cathodal electrotaxis	Zhu <i>et al.</i> ³⁰⁰
Seanson	2016	10 \times 5 \times 0.25	1. Neural progenitor cells 2. Human glioma: a. proneural (GBM612, 276) b. mesodermal (GBM626, 253) c. classical (GBM965)	100	anodal (all BTIC) cathodal (NPC) cathodal (BTIC in 3D)	Ag/AgCl	1. anodal electrotaxis depends on PLO/laninin coating 2. directionality depends on PI3K 3. inhibition of erk increases directness 4. EGFR, FGFR, PDGFR, VEGFR2 not involved in electrotaxis 5. CXCR4 and CXCR2 not involved in galvanotaxis 1. heparan sulfate localized toward anode	Huang <i>et al.</i> ²⁹³
Seanson	2017	10 \times 1 \times 0.25	1. neural progenitor F54 2. astrocytes from F54 3. GBM612	100	cathodal (NPC) anodal (astrocyte) cathodal (BTIC)	Ag/AgCl	1. heparan sulfate regulated cathodic response 2. heparan sulfate regulated cathodic response 3. shc-Robo1 mediates electrotaxis	Huang <i>et al.</i> ²⁹⁴
Feng	2019	n/a	adult human astrocytes	0, 40, 100, 300	anodal	Ag/AgCl	1. dDEF induces anodal electrotaxis and aligns perpendicularly 2. electrotaxis and alignment depends on PI3K & ERK 1. dDEF induces electrotaxis of glioblastoma and methyloblastoma cell spheroids 2. DAoy electrotaxis is enhanced by ROCK1/2 inhibition	Yang <i>et al.</i> ²⁹⁶
Lyoo	2019	19 \times 5 \times 0.2	spheroids of U87MG, DAoy, MatLyLu, MCF07 cell lines	0, 100, 250	1. MatLyLu: cathodal 2. U87MG: cathodal 3. DAoy: anodal	Platinum	3. U87MG electrotaxis is inhibited by src/abl, ATK1/2/3, mTOR, mTORC1/2 inhibition 4. U87MG cathodal electrotaxis was abolished by ErbB2 inhibition 5. Inhibition of PI3K γ but not PI3K $\alpha/\beta/\delta$ led to loss of U87MG cathodal bias	Lyoo <i>et al.</i> ²⁹⁵

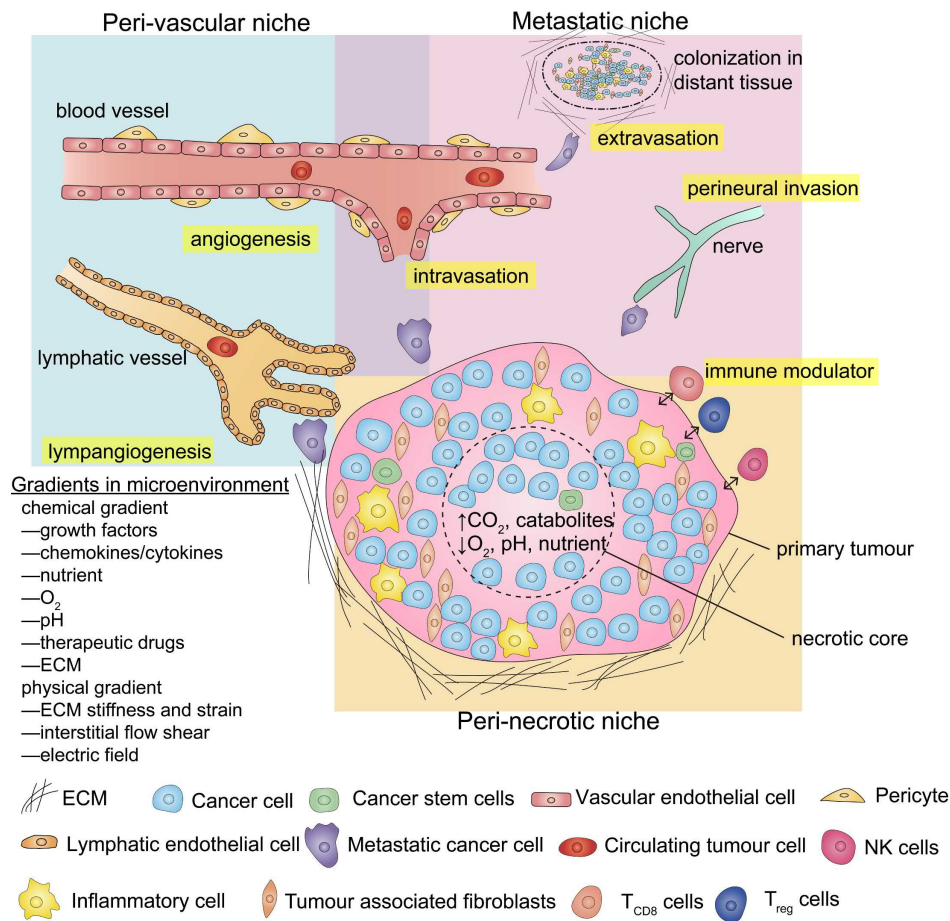


Figure 1.41: The tumor microenvironment is complex and composed of peri-vascular, metastatic (invasive), and peri-necrotic niches⁵⁰. Reprinted with permission of Royal Society.

into the design to fabricate a more biomimetic 3D organ-on-a-chip model⁵⁰.

1.6 Research aims

In this thesis, I aim to investigate the interactions between the cells and the microenvironment (niche) in glioma. I hypothesize that the physiological electric field in the brain might participate in the migration and metastasis of glioma with other coexisting gradients in the microenvironment, such as chemical ligands. The electrical fields can also have effects on stromal cells and render them more susceptible to interaction with glioma cells.

To test these hypotheses:

- First, a robust *in vitro* experiment platform must be developed. Common microfluidic prototyping materials are limited by their properties. In Chapter 2, I describe the key criteria for building 2D microfluidic chips for cell culture and the development of novel hybrid microfluidic platforms for high throughput experiments to study glioma biology.

- Secondly, an easy-to-use tool to accurately track cell migration under label-free phase contrast microscopy is still lacking. To that end, I establish a machine learning approach for segmenting and tracking of single cells in Chapter 3.
- Thirdly, I discuss the investigation of migration and the underlying mechanisms of glioma cells under electric fields, specifically involving voltage-gated calcium channels on a hybrid microfluidic system in Chapter 4.
- Lastly, I investigate the adhesion of glioma to vascular endothelial cells as a part of the infiltration process in Chapter 5.

Chapter 2

Hybrid microfluidic platforms for reliable *in vitro* cell studies

Abstract

Robust and easy-to-use microfluidic chips are vital to reliably culture cells in microenvironments. Although miniaturization offers various advantages of microscale physical phenomena, the accompanied complex integration hinders versatility and microscale interfacial phenomena become important, which can impact cell viability by microbubbles. Therefore, designing a functional microfluidic platform with microscale physics and cell viability in mind is a crucial step before probing the biological process. In this chapter, I introduce briefly the keypoints for designing and fabricating 2D microfluidic platforms for cell culture. A standard thermoplastic chip for cell culture is introduced. Next, a hybrid PMMA/PDMS microsystems is introduced for studying various topics in glioma cancer biology. A hybrid PMMA/PDMS chip design for high-throughput glioblastoma electrotaxis study is first described and later used in the work described in Chapter 4. Subsequently, a reversible hybrid PMMA/PDMS chip for glioblastoma-vascular adhesion study is introduced in detail for the work in Chapter 5. Hybrid microfluidics approach combines the advantages of thermoplastic microfluidics and PDMS microfluidics and mitigates some of their respective disadvantages. Versatile 3D microfluidic designs and world-to-chip interfaces can be implemented while maintaining high spatial dimensional accuracy on vital microfluidic channel dimensions. The hybrid microfluidic approach is suitable for rapid prototyping of complex designs to answer biomedical questions in laboratory settings.

2.1 Introduction: development of 2D microfluidic cell culture platforms

Miniaturization offers advantages such as reduced cost and precise control of microenvironment, yet it faces certain challenges. At microscale, the geometries and surface properties in microfluidic chip as well as the interface to connect reagents in macroscale to microfluidic chip, also known as “world-to-chip” interface, need to be considered carefully and tailored to the biomedical questions.

In this chapter, I discuss key aspects of designing a continuous-flow microfluidic bioMEMS system focused on cell studies. Open-surface microfluidics such as in digital microfluidics or surface acoustic wave microfluidics, two-phase microfluidics such as in

droplet microfluidics, and capillarity flow microfluidics such as in paper microfluidics, are beyond the context of this thesis. Readers are referred to specialized review articles regarding the physics and the applications in those devices^{93,310}.

2.1.1 Designing microfluidic chips

When designing microfluidic devices, the fluid mechanics and chemical transport in microsystems must be considered and respected to avoid tedious revision cycles.

Governing equations in microsystems Understanding the fundamental physical phenomena dominating at the microscale is critical. Based on the fundamental work in fluid dynamics, it is useful to employ dimensional analysis when considering microfluidic systems⁸⁹.

In continuous microfluidic systems, the fluid flow without bubbles at microscale follows the fundamental conservation laws and the fluids can be considered as incompressible. By mass conservation, the velocity and the density of the fluids are linked and can be expressed by the *continuity equation*³¹¹:

$$\rho \frac{\partial \rho}{\partial t} + \nabla \cdot (\rho \mathbf{u}) = 0, \quad (2.1)$$

where the gradient operator in the cartesian coordinate system, $\nabla = (\partial/\partial x, \partial/\partial y, \partial/\partial z)$.

For the velocity field of incompressible fluids, it satisfies:

$$\nabla \cdot \mathbf{u} = 0. \quad (2.2)$$

To further describe the motion of incompressible Newtonian fluid (assuming the liquid of consideration is Newtonian), wherein the stress is linearly related to the rate-of-strain, in microscale, the velocity vector \mathbf{u} and pressure p are related by the *Navier-Stokes* equation:

$$\rho \left(\frac{\partial \mathbf{u}}{\partial t} + \mathbf{u} \cdot \nabla \mathbf{u} \right) = -\nabla p + \mu \nabla^2 \mathbf{u} + f_b, \quad (2.3)$$

where f_b represents body forces (per unit volume) that act on the Newtonian fluid.

The Navier-Stokes equation describes the conservation of momentum. Note in Equation 2.3, the shear viscosity μ is assumed to be a constant as in Newtonian fluids, however, real-world fluids may be non-Newtonian and in some microfluidic flows, temperature variations could cause significant variation in μ , where the velocity profiles can be significantly affected.

The Navier-Stokes equation is difficult to solve analytically because it is a non-linear differential equation, but in a simple microfluidic geometry with incompressible fluid away from the inlet and the outlet, if the flow is fully developed, the non-linear term in Equation 2.3, $\mathbf{u} \cdot \nabla \mathbf{u} = 0$, can be eliminated³¹¹.

Using common microfluidic fabrication methods, we can obtain channels with rectangular or nearly rectangular cross-sectional shapes. In the simple microchannel form, where a channel is much wider in comparison to its height $h \ll w$, which is also

2.1 Introduction: development of 2D microfluidic cell culture platforms 41

known as a Hele-Shaw flow cell, the velocity profile across the channel is parabolic. And the relationship between the flow rate and the pressure can be approximated by Equation 2.4:

$$Q = \left(1 - \frac{6 \times 2^5 h}{\pi^5 w}\right) \frac{wh^3}{12\mu l} \Delta p. \quad (2.4)$$

Analogous modeling of fluidic network and electrical network The two elementary rules of electric circuits are Ohm's law and Kirchhoff's law. In Ohm's law, the electric resistance R is dependent on the system and the materials with electrical resistivity of ρ while relating the linear change between the electric potential ΔV and the current I in the following relationship:

$$R = \rho \frac{\Delta V}{I}. \quad (2.5)$$

The Kirchhoff's law describes the conservation of charge, where in steady states, for a node of a circuit where N number of currents I meet:

$$\sum_{i=1}^N I_m = 0. \quad (2.6)$$

The electrical circuits are described with algebraic relations that are also analogous to those of fluids in a channel network as far as continuity equation and single phase fluid dynamics apply. In microfluidics, the rate of mass of transported fluid, the force needed to move the fluid, and the viscosity of the fluid are analogous to the current, electrical voltage difference, and the electrical resistance in an electric circuit (Table 2.1)³¹¹.

For electrical systems, ΔV is the potential difference, I is the electrical current and R is the electrical resistance. when such analogy is translated into fluid mechanics, with single-phase laminar flow, Δp is the pressure difference, Q is the volumetric flow rate, and R_H is the hydrodynamic resistance. The electrical power is used to describe the energy/time dissipated and equals to $I^2 R$ and analogous to $Q^2 R_H$ in a fluidic circuit. The Ohm's law relates the current density \mathbf{j} to the electric field \mathbf{E} by conductivity σ of the material. The corresponding Darcy's law in flow dynamics relates the average velocity \mathbf{u}_{avg} to the pressure gradient by permeability k and viscosity μ . In a cylindrical tube of radius a , the electrical resistance R is similar although not analytically identical to the hydrodynamic resistance R_H in fluid mechanics.

The fluidic resistance of a Poiseuille flow in a rectangular microchannel is given by⁸⁹:

$$R_H = \frac{12\mu l}{wh^3} \left[1 - \frac{h}{w} \left(\frac{192}{\pi^5} \sum_{n=1,3,5}^{\infty} \frac{1}{n^5} \tanh\left(\frac{n\pi w}{2h}\right) \right) \right]^{-1}, \quad (2.7)$$

where μ is the fluid viscosity, l is the channel length, w is the channel width, and h is the channel height. If channel is much wider compared to its height $h \ll w$, the fluidic

Table 2.1: The analogous comparison between electrical and fluid mechanical expression of steady state flow in a cylindrical tube³¹¹. Reprinted with permission of Springer Nature.

Electrical relation	Fluid mechanical relation
$V = IR$	$\Delta p = QR_H$
$\sum_{i=1}^N I_i = 0$	$\sum_{i=1}^N Q_i = 0$
$Power = I\Delta V = I^2R$	$Power = Q\Delta p = Q^2R_H$
$\mathbf{j} = \sigma E$ (Ohm's law)	$\mathbf{u}_{avg} = -\frac{k}{\mu}\nabla p$ (Darcy's law)
$R = \frac{\rho l}{\pi a^2}$	$R_H = \frac{8\mu l}{\pi a^4}$

resistance can be reduced to :

$$R_H = \frac{12\mu l}{wh^3(1 - 0.53\frac{h}{w})}. \quad (2.8)$$

Consideration of hydraulic resistances of microchannels in the microfluidic circuits is especially useful and important when designing the microfluidic chip to manipulate fluid transport in order to design functional devices with relevant biological questions in mind^{312–315}. Due to the analogous relationship between the electrical expression and fluid mechanical expression, the techniques used in electrical circuit analysis can be performed similarly for hydraulic circuits⁹². We can also adapt the Ohm's law and Kirchhoff's law to calculate and analyze what the flow will behave in a microfluidic network. The analog electric circuit simulators such as Simulation Program with Integrated Circuit Emphasis (SPICE) that is part of many electronic design automation (EDA) software can also be adapted for designing microfluidic circuits³¹⁶.

Dimensionless numbers in microsystems There are several useful dimensionless numbers to consider when designing microfluidic chips for cell applications.

1. Reynolds number

The Reynolds number, Re , is a dimensionless parameter to determine if the system is in the laminar or turbulent regime. It is a measure of competition between the inertia force over the viscous force in the flow. In general, most microfluidic chips for cell studies involve Reynolds numbers much smaller than 1 and the flows in the lab-on-chip devices are observed to be laminar.

$$\begin{aligned} Re &= \frac{\rho U L_c}{\mu}, \\ &= \frac{\rho U D_h}{\mu}, \end{aligned} \quad (2.9)$$

where L_c is a characteristic length scale related to the flow field, U is the char-

characteristic velocity, ρ is the density, and μ is the dynamic viscosity of the fluid. In a microfluidic chip with small height, the characteristic length may be the hydraulic diameter of the channel D_h .

2. Poiseuille number

The Poiseuille number can be used to describe flow resistance in ducts of arbitrary cross-section and is defined as the product of a friction factor f and the Reynolds number Re ^{312,317}:

$$\begin{aligned} P_o &= \frac{fRe}{4}, \\ &= -\frac{1}{\mu} \frac{dp}{dx} \frac{D_h^2}{2U}, \end{aligned} \tag{2.10}$$

where μ is the viscosity, $\frac{dp}{dx}$ is the pressure drop per unit length, U is the velocity magnitude, and the characteristic length scale L_c used to calculate Re is D_h , the hydraulic diameter.

The inverse relationship between the friction factor and Reynolds number means that the pressure drop is linearly proportional to the flow rate³¹². Many microfluidic channels fabricated by micromachining bear a rectangular cross-section, and the fRe and the Poiseuille number of different geometries have been solved and reported³¹⁷. For example, the Poiseuille number of a round capillary has a value of 16, the Poiseuille number of a microchannel with rectangular cross-section profile can be calculated by the following equation:

$$P_{o(\text{rectangular})} = 24(1 - 1.3553\alpha + 1.9467\alpha^2 - 1.7012\alpha^3 + 0.9564\alpha^4 - 0.2537\alpha^5), \tag{2.11}$$

where α is the ratio between height and width (h/w). Using the Poiseuille number, the relative hydraulic resistance of microchannels with different cross-section areas can be estimated and compared.

3. Péclet number

Recall the mass balance equation for chemical transport (Equation 1.1), at equilibrium without reaction, the left hand side describes the passive scalar convection-diffusion in a uniform fluid:

$$\frac{\partial c}{\partial t} + \vec{u} \cdot \nabla c = \nabla \cdot (D\nabla c). \tag{2.12}$$

This equation can be nondimensionalized involving the Péclet number:

$$\frac{\partial c^*}{\partial t^*} + \vec{u}^* \cdot \nabla^* c^* = \frac{1}{P_e} \nabla^* \cdot (\nabla^* c^*). \tag{2.13}$$

The Péclet number describes the proportional relationship of chemical transport between convective fluxes and diffusive fluxes. In a system of high Péclet number, the diffusion is negligible whereas in low Péclet number system, the scalar (*i.e.*,

solute concentration) distribution governed by diffusion follows the Fick's Law⁹²:

$$P_e = \frac{UL_c}{D}, \quad (2.14)$$

where U is the characteristic velocity, L_c is the characteristic length, and D is the diffusion coefficient of the scalar.

In many microfluidic chips for cell studies, they reside in the limit of low Reynolds number (laminar) and high Péclet number (minimal diffusion) so as to allow isolation and patterning of chemical species within the microenvironment.

2.1.2 Rapid prototyping of microfluidic chips

The microfluidics thrive with the advances of the MEMS technologies but is not limited by the typical silicon materials. Due to the demands on optical transparency and sterility in many biomedical applications, prototyping microfluidic devices made significant progress with disposable materials such as thermoplastics, elastomers, and glasses^{318,319}. To manipulate and control fluids in microscale, tailor-made microfluidic chips dedicated for specific applications are common, thus microfluidics demands rapid and simple fabrication processes.

Although the materials of choice are abundant, such as SU8 epoxy³²⁰ or perfluoropolymers^{321,322} for extreme chemical resistance, in this thesis I will focus on the most common materials. Table 2.2 shows the comparison of pros and cons between different materials for microfluidic prototyping. In this section, I overview the mainstream technologies used to fabricate microfluidic chips for cell culture applications focusing on chip fabrication, world-to-chip interface, and chip assembly (bonding). The keypoints for successful cell culture on microfluidic chips will also be discussed.

Soft lithography: PDMS microfluidic chips

The standard fabrication method of microfluidic chips takes advantage of the technologies developed for microelectromechanical systems (MEMS). A specialized technique adapted from standard MEMS lithography techniques, soft lithography, is widely adapted for fabrication of poly(dimethylsiloxane) (PDMS) based microdevices^{323–326}. PDMS is a transparent and biocompatible silicone rubber suitable for fabrication of microdevices for biomedical applications.

In soft lithography, the desired microfluidic channel patterns are designed and a photomask is fabricated. A thin layer of photosensitive materials that change property when exposed to light, also known as photoresists, is coated uniformly on a substrate. Afterward the pattern is exposed by illumination (usually UV light) through the photomask or on more advanced systems, the pattern is directly written by laser scanning or projection through a structured light modulator. The photosensitized pattern is then developed and obtained as a mold for the microfluidic chip. The mixed uncured PDMS monomers with cross-linking agents are then poured onto the mold, thermally cured, and subsequently bonded to a glass or PDMS substrate (Figure 2.1). Through this process, microstructures in micrometer or nanometer scale can be replicated by the PDMS³²⁶.

Table 2.2: Common materials to fabricate BMMDs.

	Thermoplastics (PMMA, PC, COC)	Elastomer (PDMS)	Glass (Industrial)	Glass (LightFab)	Paper
Advantages	<ol style="list-style-type: none"> High spatial resolution by lithography ($1\ \mu\text{m}$) High gas permeability Versatile world-to-chip connection Easy priming to remove bubbles 	<ol style="list-style-type: none"> High spatial resolution by etching ($10\ \text{nm}$) Excellent chemical stability High transparency through UV-Vis High rigidity to sustain high flow rates 	<ol style="list-style-type: none"> 3D structures fabrication by etching Excellent chemical stability Excellent deep UV transmittance in fused silica ($<250\ \text{nm}$) 	<ol style="list-style-type: none"> Limited to 2D structures Capillary-driven flow Limited spatial resolution Limited optical detection methods Limited chemical compatibility 	
Disadvantages	<ol style="list-style-type: none"> Low spatial resolution by laser cutting ($100\ \mu\text{m}$) High μm-scale roughness by micromilling Birefringent Rigid structures only Prone to trap air bubbles Medium solvent compatibility 	<ol style="list-style-type: none"> Limited to 2.5D structures Adsorption/absorption of hydrophobic chemical species Limited bonding strategies and substrate choice due to low surface energy Limited world-to-chip interface choice Poor solvent compatibility 	<ol style="list-style-type: none"> Long etching time High surface roughness ($1\text{-}5\ \mu\text{m}$) High dimensional error in confined structure Special bonding requirement Brittle 	<ol style="list-style-type: none"> Limited to 2D structures Capillary-driven flow Limited spatial resolution Limited optical detection methods Limited chemical compatibility 	

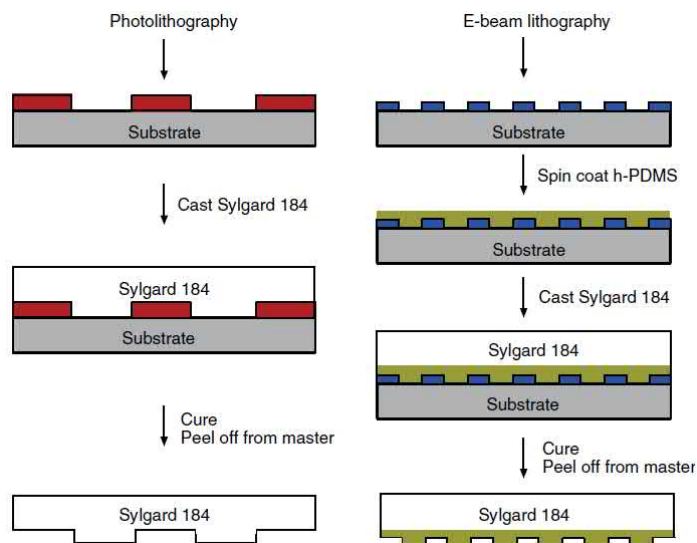


Figure 2.1: Schematic illustration of soft lithography for PDMS fabrication³²⁶. Microstructures fabricated by photolithography as well as nanostructures fabricated by E-beam lithography can be replicated by PDMS through different protocols. Reprinted with permission of Springer Nature.

The biocompatibility of PDMS and the soft lithography prototyping for highly accurate microstructures have contributed to the dominant use of the material in today's academic as well as industrial communities. Moreover, elastomeric and gas-permeable properties of PDMS have enabled its use for special lab-on-chip applications such as actively controlled microvalves^{327,328} and gaseous gradient microchip^{329–331} for studies involving automation and microenvironment manipulation. Furthermore, 3D PDMS chips can be fabricated by stacking multiple layers of designed structures very similar to the integration of multi-layer integrated circuits in the MEMS fabrication^{327,332}.

However, the low surface energy of PDMS limited the methods of bonding PDMS to versatile materials without surface activation. Furthermore, the hydrophobic and porous properties of PDMS promote adsorption and diffusion of hydrophobic compounds during experiments, making estimation of accurate chemical concentration difficult. In applications with organic solvent, depending on solubility, often PDMS will swell and deform. More advanced castable materials such as off-stoichiometry thiol-ene epoxy (OSTE) with less adsorption of hydrophobic compounds that can replace PDMS have been developed³³³.

Thermoplastic microfluidic chip

Adaption of thermoplastics and polystyrene especially for biomedical research became popular for their biocompatibility and single-use properties. The use of thermoplastics for microfluidic chip fabrication is also popular for its low cost, potential for mass production, and biocompatibility.

Thermoplastics microfluidic chip based on poly(Methyl methacrylate) (PMMA), polycarbonate, and cyclic olefin copolymer (COC) can be fabricated by laser cutting^{334,338}, micromilling^{335,339}, hot-embossing^{336,340,341} or injection molding^{337,342,343} (Fig-

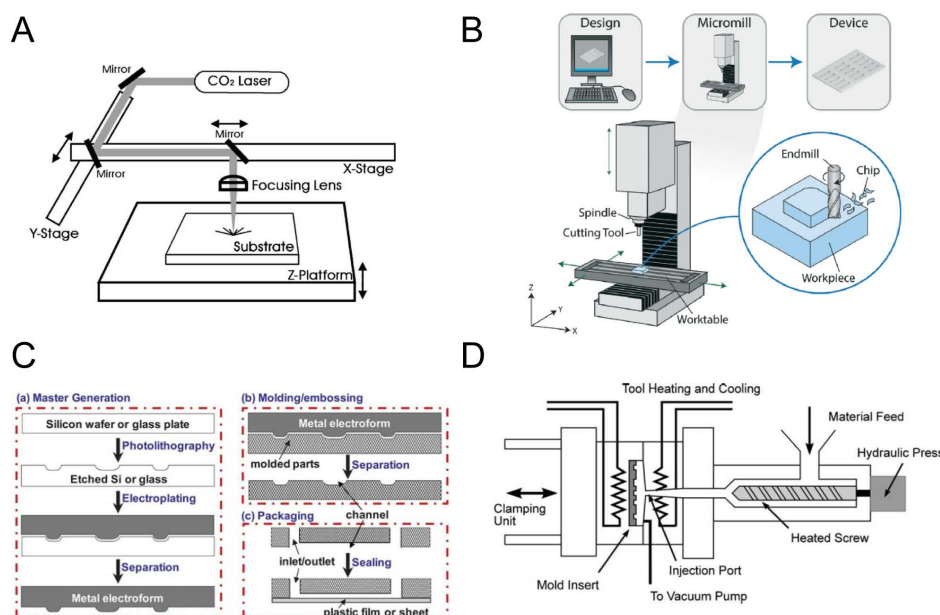


Figure 2.2: Fabrication methodology for thermoplastic microfluidic chips. (A) Direct-write laser cutting³³⁴. Reprinted with permission of Elsevier.; (B) Micromilling³³⁵; (C) Hot embossing³³⁶; (D) Injection molding³³⁷. Reprinted with permission of John Wiley and Sons.

ure 2.2). Laser cutting and micromilling is especially well adapted in laboratory settings while the same design can be fabricated in mass volume using more industrial methods such as roll-to-roll hot-embossing or injection molding³⁴⁴. PMMA can be easily processed using laser cutting or micromilling, but its chemical compatibility and moisture absorption is not excellent. COC or cyclic olefin polymers (COP) are newly invented thermoplastics that have better performance in chemical compatibility with high gas permeability but low moisture permeability (Table 2.3). Therefore, COCs and COPs have been adapted in biomedical devices and in pharmaceutical packaging.

Although, thermoplastics are favored for microfluidics for its cost-effectiveness and mass producibility^{337,346}, they have limited chemical compatibility compared to glass and usually limited spatial resolution (Table 2.2) by prototyping methods in comparison to PDMS in soft lithography. However, compared to the other two methods, complex 3D microfluidic structures and versatile world-to-chip interface can be realized easily on thermoplastics through chip stacking and surface treatment. The properties of different thermoplastics are summarized in Table 2.3³⁴⁵.

Glass microfluidic chips

The main composition of glass is silica, SiO_2 , but depending on the purity and chemical composition, glass can be categorized as fused silica, borosilicate, and soda lime. Fused silica is composed of high purity amorphous silica. Borosilicate and soda lime have additives such as boron oxide, sodium oxides, or calcium oxide to lower melting temperature for manipulability and enhancement for thermal or mechanical properties.

Conventionally, microfluidic structures can be fabricated on glass by using powder

Table 2.3: Summary of properties for thermoplastics³⁴⁵. Reprinted with permission of AIP Publishing.

Thermoplastics	Thermal expansion coefficient [m/(m K)] 10 ⁻⁶	Young's modulus (GPa)	T _g (°C)	T _m (°C)	Solubility parameter δ (MPa) ^{1/2}	Water absorption (%)	O ₂ permeability (x10 ⁻¹³ cm ³ cm cm ⁻² s ⁻¹ Pa ⁻¹)	Biocompatibility	Transparency	Auto-fluorescence
Cyclo olefin (co) polymer (COC/COP)	60–70	1.7–3.2	70–180	190–320	17.7	0.01	NA	Biocompatible	Transparent	Low
Polymethyl methacrylate (PMMA)	7077	2.4–3.4	105	250–260	20.1	0.1–0.4	0.1	Biocompatible	Transparent	Low
Polyethylene terephthalate (PET)	59.4	2–2.7	70	255	20.5	0.16	0.03	Biocompatible	Transparent	Medium
Polyethylene-low density (LDPE)	100–200	0.11–0.45	–125	105–115	17.6	0.005–0.015	2	Biocompatible	Both opaque and transparent	Medium
Polyethylene-high density (HDPE)	120	0.8	–80	120–180	18.2	0.005–0.01	0.4	Biocompatible	Both opaque and transparent	Medium
Polypropylene (PP)	72–90	1.5–2	–20	160	16.3	0.01–0.1	1.7	Biocompatible	Both opaque and transparent	Medium
Polystyrene (PS)	70	3–3.5	95	240	18.7	0.02–0.15	2	Biocompatible	Transparent	High
Polycarbonate (PC)	65–70	2.6	145	260–270	19.4	0.23	1	Biocompatible	Transparent	High
Polyvinyl chloride (PVC)	54–110	2.4–4.1	80	100–260	19.4	0.04–0.4	0.04	Biocompatible	Transparent	High
Polyamide (Nylon)	110	2.5	47–60	190–350	28	1.6–1.9	0.03	Biocompatible	Transparent	High
Polysulfone (PSU)	55–60	2.48	185	180–190	18.7	0.2–0.8	NA	Biocompatible	Translucent	High
Polylactic acid (PLA)	740	3.5	60–65	150–160	18.7	0.68	NA	Biocompatible (problematic)	Transparent	High
Polytetrafluoroethylene (PTFE)	112–135	0.4	115	326	12.6	0.005–0.01	3	Biocompatible	Translucent	High
Polyetheretherketone (PEEK)	26	4–24	143	343	21.9	0.1–0.5	0.1	Biocompatible	Opaque	NA
Acrylonitrile butadiene styrene (ABS)	72–108	1.4–3.1	105	Amorphous	18.8	0.05–1.8	0.5	Not suitable	Both opaque and transparent	High

sandblasting or ultrasonic milling³⁴⁷ (Table 2.4). Through MEMS fabrication methodology such as lithography, dry etching by reactive ion, and wet etching, precise microstructures in micrometer to nanometers can be fabricated³⁴⁸. In addition, high power lasers can be used to directly modify glass structures, photopolymerization, and induce backside wet etching. In the direct modification process, femto-second lasers can be employed to modify glass, also known as selective laser etching (SLE) (Lightfab GmbH, Germany)^{349–351}. The portion modified by lasers will have high etching selectivity compared to pristine counterparts in wet etching agents, *e.g.*, KOH. Photopolymerization of silica-containing agents using ultrafast lasers (Nanoscribe GmbH, Germany) has been shown to fabricate a full glass microdevice with comparable performance of a fused silica device after sintering^{352,353}. In addition, using organic dyes with high absorbance at diode-pumped solid-state laser wavelength, wet etching within the microchannels can be achieved through laser-induced backside wet etching (LIBWE) process^{354–356}.

The advantages for glass microfluidic chips over PDMS and thermoplastics are optical transparency, dimensional accuracy and stability, and chemical compatibility. Therefore, use of glass is especially favored in experiments where good surface property or optical quality are required, such as in electrokinetics, organic extraction, or optical absorbance in the ultraviolet region³⁵⁷.

Rapid Prototyping using 3D printing

In recent years, 3D printing techniques such as selective laser sintering (SLS), fused deposition modeling (FDM), inkjet printing, stereolithography, and two-photon polymerization or etching have been used to directly fabricate microfluidic chips or fabricate the mold for the microfluidic chip (Figure 2.3)^{359–364}.

Direct whole chip fabrication with minimum post-processing can save time and effort during the prototyping phase for microfluidic applications. Most of direct whole

Table 2.4: The dimension of fabrication in glass microfluidic chips using various methods^{351,353,354,358}. HF: hydrofluoric acid; RIE: reactive ion etching.

Method	Minimum feature size	Maximum depth	Aspect ratio	Design definition by Mask	Fabricated structures
Drilling	800 μm	>1 mm	10	No	2D
Micromilling	500 μm	>1 mm	10	No	2.5D
Ultrasonic drilling	75 μm	>1 mm	10	No	2.5D
Electrochemical discharge drilling	50 μm	>1 mm	15	No	2.5D
Photosensitive glass	50 μm	>1 mm	20	Yes	2.5D
Powder blasting	<50 μm	>1 mm	2.5	Yes	2.5D
HF etching	1 μm	>1 mm	1	Yes	2.5D
RIE etching	0.5 μm	10 μm	5	Yes	2.5D
Selective laser-induced etching	10 μm	<7 mm	700	No	3D
Two-photon photopolymerization	20 μm	>1 mm	10	No	3D
Laser induced backside wet etching	100 nm	<1 μm	10	No	2.5D

chip fabrication that is commercially available are based on the FDM method in poly(Lactic acid)³⁶⁵ or COC (Fluidic Factory, Dolomite[®]). Industrial-level mass production by using 3D printing is possible but is still inferior at current technological level and cost performance is low when compared to conventional technologies. For 3D printing to replace the mainstream industrial methods such as hot embossing and injection molding, significant industrial evolutions on both fabrication technologies and materials need to be realized. For most biomedical applications involving microscopy, optical transparency is particularly important. Many molds or devices made by 3D printing do not meet the minimum surface quality standard, hindering the deployment and application of 3D printing for microfluidics. However, several surface annealing methods or tailor made materials can realize 3D printed workpieces with higher optical quality^{366,367}. The material biocompatibility and surface quality are key issues that require revolutionary improvements for 3D-printed microfluidic chips to become mainstream devices that can be adapted by the biomedical research community.

2.1.3 World-to-chip interface for microfluidic chips

To manipulate the small fluid volume in microfluidic chips, it is necessary to connect the channels to syringe pumps, pressure source, or electrical connection for fluid actuation. A robust, versatile, and cost-effective world-to-chip interface is very important for the success of the microfluidic applications. While many world-to-chip interfaces are commercially available, it is still common for laboratories to develop custom world-to-chip interfaces due to individual experimental requirements.

In this section I will briefly discuss the common methods to build world-to-chip interface especially for microfluidic cell culture. The readers are referred to review texts for more comprehensive discussion^{368,369}.

1. Direct tubing interfacing

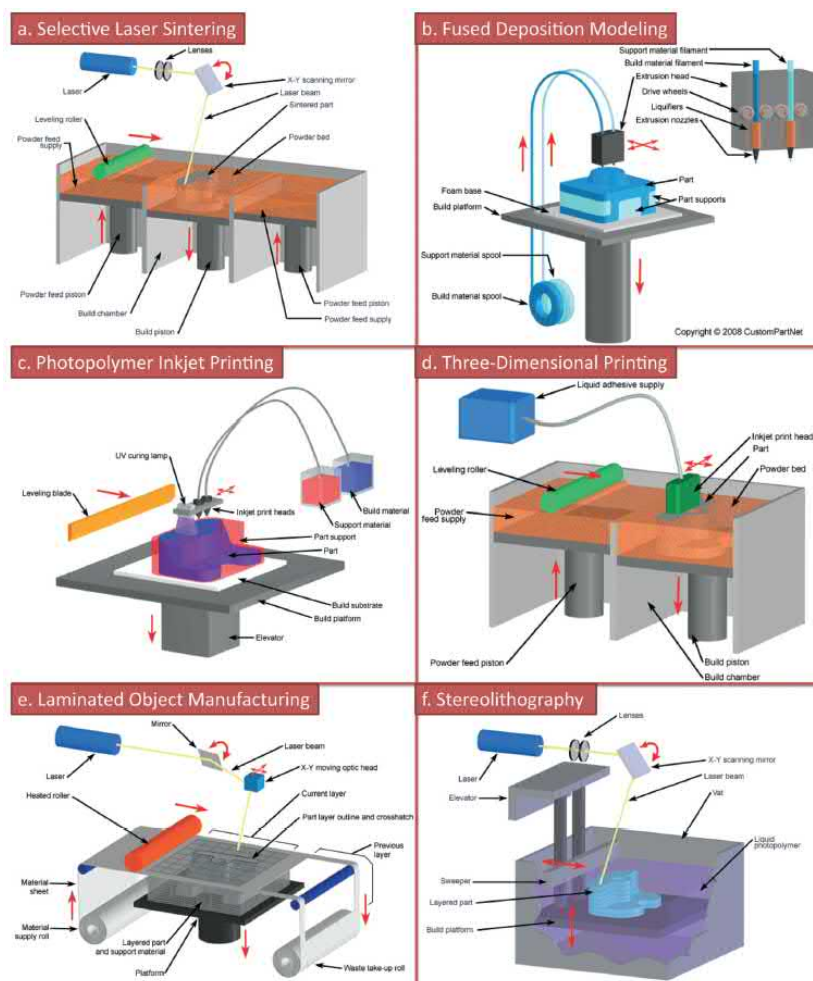


Figure 2.3: Various 3D printing techniques for rapid prototyping microfluidic chips³⁶⁰. Reprinted with permission of John Wiley and Sons.

The most straightforward method to connect tubings is by inserting into the inlet/outlets in the microfluidic chip.

- Temporary interfacing

For PDMS microfluidic chip, due to the elasticity of the PDMS rubber, a tubings with outer diameter slightly larger with the inlet/outlet diameter can securely interface with a PDMS microfluidic chip by directly inserting the tubes. However, any strains from the tubing on the PDMS may damage the inlet/outlet interface and cause leakage or introduction of bubbles.

Alternatively, small stainless steel tubes such as those from New England Small Tubes can serve as an intermediate between PDMS and tubings with higher stability. The small configuration using small stainless steel tubes also makes it popular in applications of large scale integration of high throughput PDMS devices³²⁷.

- Permanent bonding

Due to the rigidity in thermoplastics and glass, temporary interfacing of tub-

2.1 Introduction: development of 2D microfluidic cell culture platforms 51

ings on them usually are not secure. Alternatively, epoxies or cyanoacrylates can be used to permanently join the tubings with the inlet/outlet. However, there is a risk of contamination of the adhesives infiltrating into the microfluidic chips.

2. Mechanical sealing

Most commercially available world-to-chip interface for microfluidic chips employ mechanical sealing or have a fluidic interface built or affixed to the microfluidic chips, such as products from Micronit, S.E.R. Corporation, Microfluidic Chipshop, Dasfanh, Dolomite, and Corsolutions.

It is common to employ gaskets (o-rings) to seal the connect ports on the microfluidic chips by means of clamping^{370–372}, vacuum suction³⁷³, or magnetic sealing³⁷⁴ in single channel format or in multichannel manifold.

Being a reversible sealing method, it is easy to set up experiments using mechanical sealing, however, if the pumping pressure for fluid delivery exceeds the limit for the interface, leakage may bring problems such as contamination to the cells culture or microbubbles in microfluidic chips.

3. Special adapters

Special adapters can be affixed on microfluidic chips to connect the chips with tubings, offering a high pressure withstanding a permanent solution in comparison to the mechanical sealing approach. Special adapters with small dead volume, such as barb, Luer, Mini-Luer or Olive connectors, are invented to easily and securely connect to tubings but usually will require such receiving structures being fabricated on the microfluidic chips. Some other examples are D-sub-like connectors³⁷⁵ or adapters of special shapes that are fabricated by 3D printing^{376–378}.

4. HPLC fitting

Although specially designed adapters can be used to connect to chips, many microfluidic research groups choose to use fittings meant for high performance liquid chromatography (HPLC), such as provided by IDEX Corporation, Waters, or Cole-Parmer. These commercially available fittings have precise pore sizes to interface with tubings that will withstand high pumping pressure. For extremely low dead volume applications, adhesive-fixed Nanoport connectors are also used such as in on-chip electrophoresis experiments or nanofluidics.

The HPLC fittings are reusable, autoclavable, and chemically stable, making them extremely suitable for cell applications. Usually the threads of these HPLC fittings are standard such as M6 or 1/4–20. To interface with HPLC fitting to microfluidic chip, either threads must be tapped on the microfluidic chip or an adapter with threads must be affixed to the microfluidic chip (Figure 2.4)^{196,202,379}. These adapters are commercially available at a reasonable price between USD\$0.1 to 0.5 per piece.



Figure 2.4: Disposable adapters for HPLC fittings³⁷⁹. (Left) A PMMA adapter with 1/4–20 thread; (Right) A polycarbonate adapter with M6 thread.

Table 2.5: Bonding methods established in Micro/Bio/Nanofluidics Unit at OIST.

	PDMS	Quartz	Borosilicate	PMMA	COC/COP	PC	PS
PDMS	Excimer						
Quartz	Excimer O2 Plasma	KOH					
Borosilicate	Excimer O2 Plasma corona	n/a	n/a				
PMMA	Plasma+silane	n/a	n/a	Thermal Excimer			
COC/COP	Plasma+silane	n/a	n/a	n/a	Thermal Excimer		
PC	n/a	n/a	n/a	n/a	n/a	Excimer	
PS	Plasma+silane	n/a	n/a	n/a	n/a	n/a	Excimer

2.1.4 Bonding strategies for microfluidic chips

By the majority of the fabrication methods listed in Section 2.1.2, the microstructures are fabricated either by an addition or a subtraction approach. Although embedded 3D structures can be made through 3D printing or by non-linear optics as in Lightfab glass fabrication, the microfabrication technologies stemming from MEMS industry usually create microstructures affixed to one side of the substrate that require another substrate to be bonded to form a complete device.

It is also common that the microfluidic chip design is fabricated on a relative cheap and disposable device with less ideal surface properties but can bond to a more stable or less processable substrates where reaction happens such as those in PDMS microfluidic chips bonding to a piece of glass substrate.

Several bonding protocols are validated to support fabrication of microfluidic chips of different materials in our group (Table 2.5).

Bonding strategies for PDMS based microdevices

PDMS is among the most popular material to prototype microfluidic devices in both laboratory and industrial settings. However, cured PDMS has a low surface energy,

2.1 Introduction: development of 2D microfluidic cell culture platforms 53

limiting its flexibility. Here I overview the most common bonding methods of PDMS to glass, PDMS, and thermoplastics.

1. PDMS-Glass bonding

The standard method to bond a PDMS to a glass substrate utilizes silanol-silanol bonds. Due to the low surface energy of PDMS, its surface has to be activated by collision of high energy gas particles typically generated through vacuum gas plasma³⁸⁰, vacuum ultraviolet (VUV) irradiation^{381,382}, or corona discharge³⁸³.

In some reports, PDMS-glass microfluidics chips are joined reversibly using mechanical compression^{384,385} or vacuum sealing³⁸⁶⁻³⁸⁹. However, these reversible sealing approaches require utmost cleanliness and flatness of the microfluidic device to avoid deformation of the microstructures that will cause failure of the sealing.

2. PDMS-PDMS bonding

Bonding of PDMS to itself or anything other than glass is not as straightforward. For PDMS-PDMS bonding, we can use oxygen plasma, corona discharge, PDMS adhesive³⁹⁰, partial curing, and off-stoichiometry curing³⁹¹.

Typically, PDMS-PDMS direct bonding using O₂ plasma or corona discharge do not achieve high bond strength and may subject to local defects due to non-uniform surface properties of the cured PDMS. Moreover, the activated surface will bond immediately after contact, making alignment between PDMS components difficult. Alternatively, PDMS adhesives can be used to join two pieces of PDMS, however, obstruction of microstructures by the adhesives is possible.

By using partial curing^{392,393} or off-stoichiometry curing³³², very high bond strength of PDMS can be achieved. In partial curing, the PDMS will cure on the mold as in soft lithography but peel off before the PDMS is fully cured. The partially cured pieces are aligned and baked further to be completely cured. The working time window is of essence in partial curing method. In off-stoichiometry curing, the monomer-to-curing agent ratio is deliberately off-balanced for each pieces. One PDMS piece typically bears a 7.5:1 ratio while the other bears 15:1. The former will cure rapidly and still have excessive curing agent within the cured piece while the latter will be partially cured with high monomer left in the piece. After alignment and contacting both pieces, during the incubation, the excessive curing agent in the former piece will diffuse through the interface to the other and additional cross-linking creates a very strong bonding.

3. PDMS-plastic bonding

Heterogenous bonding between PDMS and thermoplastics is particularly difficult. However, with specific surface functionalization, PDMS and plastics can be joined covalently or reversibly.

- Double-sided tape

Polymeric doubled sided types could be used to join PDMS and thermoplastics by curing a thin layer of PDMS with the double-sided tape adhesive^{394–396}. However, the adhesive strength is not high and may subject to delamination by shear force.

Alternatively, a special dual energy sided tape composed of a layer of silicone type adhesive and a layer of acrylic type adhesive, can be used to join the PDMS with thermoplastics or other surface^{397,398}. Using double-sided tapes is an easy approach to assemble complex hybrid microdevices.

- Adhesives and silane-assisted functionalization

Commercial adhesive with a priming step to activate the surface can be used to join PDMS and alternative material³⁹⁹. Similar surface functionalization can be used to covalently bond PDMS and alternative materials other than glass, typically by silanes such as (3-aminopropyl)triethoxysilane (APTES)^{400–408}.

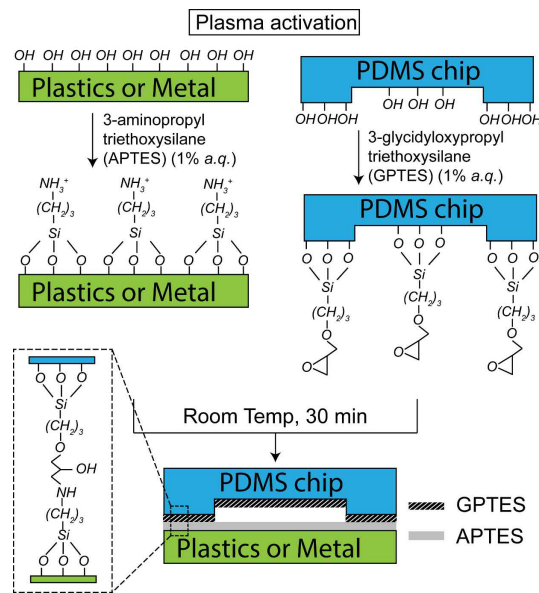


Figure 2.5: Diagram of silane assisted bonding⁴⁰⁹. Heterogenous substrates are treated with plasma and incubated with either APTES or GPTES. Afterward, the surfaces of two substrates can be bonded after contact to form stable amino-epoxy bond.

Strong and reliable chemical bonding using amino-epoxy bonds has been reported in room temperature (Figure 2.5)⁴⁰⁹. The bond strength can withstand stronger solvent such as 99.5% ethanol.

Bonding strategies in thermoplastic chips

The surface energy for thermoplastic is usually high and easy to modify further for bonding. Several bonding strategies such as thermal annealing, surface activation bonding, solvent-assisted bonding, or adhesive bonding can be used⁴¹⁰.

1. Thermal annealing

For thermoplastic substrates fabricated with microstructures through laser cutting or micro-milling, the microfluidic chips can be easily completed by assembling, compressing, and heating the assembly above glass transition temperature (T_g)^{202,334,411}.

Other energy directed methods that generate focused heating can also thermally anneal thermoplastics chips, such as ultrasound bonding⁴¹² or laser welding⁴¹³. However, special design or equipment for energy localization are typically required.

2. Surface activation bonding

The surfaces of thermoplastics are usually hydrophilic and can be easily functionalized. However, while the standard O₂ plasma can further render the surface hydrophilic, the thermoplastics such as PMMA or COC cannot be bonded simply by plasma treatment. Using higher energetic methods such as vacuum ultraviolet irradiation (VUV) at 172 nm (Ushio, Japan)^{414,415} or UV/Ozone⁴¹⁶, the thermoplastics substrates such as PMMA or COC, can be joined with their counterparts of the same material after slight compression and heating below the glass transition temperature.

3. Solvent-assisted bonding

By using organic solvent to partially melt the surface layers of thermoplastics, pieces of thermoplastics can be joined after drying of the solvent⁴¹⁷⁻⁴¹⁹. However, using this method will leave residues of solvent as well as monomers that can be toxic to cells.

4. Adhesive bonding

Using adhesive to bridge between respective plastic materials such as cyanoacrylate or UV-curable adhesives can yield very high bond strength⁴²⁰. However, if the channel dimension is very small, the adhesive can infiltrate into the microchannels and cause blockage. The adhesive can also have cytotoxic effect if in direct contact, thus this approach should be avoided for cell culture applications.

Bonding strategies in glass chips

1. Thermal bonding

Similar to thermoplastic chips, by heating glass chips above glass transition temperature, the glass microfluidic chips can be bonded to another glass piece^{421,422}. However, as the material is brittle, careful annealing process is needed to avoid cracking of the bonded chip.

2. Surface activation bonding

It has been reported by using gas plasma to activate the glass surface, the glass devices bearing nanofluidic channels can be bonded and withstand pressure of 500 kPa⁴²³⁻⁴²⁵.

By using potassium hydroxide^{426,427} or sulfuric acid^{428,429} to activate the surface, glass components withstanding extreme vacuum such as space applications can be bonded.

3. Anodic fusion bonding

For glass-silicon microfluidic chips, the anodic fusion bonding employed in the MEMS industry is commonly applied^{430–432}. Anodic fusion bonding^{433,434} allows glass to join with a metal or a silicon wafer below the glass transition temperature by using an electric potential to deplete the sodium cation at the bond interface and allow the drift of singlet oxygen ion into the depletion zone. Formation of siloxane bonds ensures the irreversible connection between the two pieces.

4. Adhesive bonding

Adhesives, such as UV-curable adhesive, epoxy, SU-8, or PDMS, can also be used to join glass microfluidic chips⁴³⁵. However, if the channel dimension is very small, the adhesive can infiltrate into the microchannels and cause blockage⁴³⁶.

2.1.5 Culturing cells on microfluidic chips

Miniaturization of microfluidics provides many advantages compared to conventional cell culture, such as sterility, low shear stress, low reagent & cell consumption, and precise microenvironmental control. However, to support good cell growth on microfluidic chips is not a simple task.

In conventional cell culture, the key parameters are sterility, pH, nutrient, and temperature. Typical cell culture media are formulated with iso-osmotic medium with carbohydrate, lipid, and proteins. To ensure acidity remaining in physiological range, one or multiple pH buffering systems are chosen. Often the CO₂/NaHCO₃ system is adapted. The modern cell culture incubators are designed with water jacket heating, CO₂ mass flow control, and high-efficiency particulate air (HEPA) filter, to provide stable temperature, gas, humidity, and sterile environment. However, when considering the cell microenvironment on microfluidic chips at low Reynolds number, the chemical transport and heat transfer processes must be taken into consideration.

To design a good microfluidic chip for cell studies is an integrative problem⁴³⁷. Here, I give a short discussion on the key issues when developing a cell culture microfluidic chip.

1. Biocompatibility of substrate and chip material

First of all, the biocompatibility and experimental compatibility of the substrate and chip materials are very important. For commonly used microfluidic materials such as PMMA and PDMS, they have good biocompatibility and usually no particular attention is needed when culturing normal cells. However, for culturing sensitive cells, such as stem cells and primary neurons, the impurity and low gas permeability in PMMA or the platinum-based curing catalyst in PDMS may have impact on cell survival on microfluidic chips.

Also, if the experiments involving strong solvents in later experiment stages, such as extraction or cell staining, the compatibility of chip materials must be

2.1 Introduction: development of 2D microfluidic cell culture platforms 57

considered to avoid dissolution or swelling. Furthermore, if high resolution cell imaging is required, use of high-precision glass coverslip as the substrate will be necessary. The bonding between microfluidic chip and the substrate will need to be optimized to avoid leakage of cell culture system which compromises the microflow and the sterility.

2. Sterilization

In thermoplastic microfluidic systems, often it is difficult to sterilize the entire microfluidic chip by steam sterilization due to significant deformation or melting of the thermoplastics at 121 °C under 1–1.2 MPa. However, in many cases, simple UV disinfection of chip surface is enough for sterile cell culture.

The PDMS and glass microfluidic chips can be easily sterilized by steam sterilization. However, the fabrication process in the clean room usually ensures good degree of sterility. In general, with use of sterilized microfluidic chips and sterilized accessories such as tubings, no antibiotic supplement in the culture medium is required.

3. Microbubbles

In microfluidic system, the surface tension effect become significant so microbubbles become difficult to eliminate and their presence will significantly impact the microflow, causing obstructed chemical transport. Furthermore, the air/liquid interfacial tension at the bubble interface can cause cell death.

Due to the dissolved CO₂ gas in the cell culture medium necessary for balancing of pH, gas bubbles over time will grow bigger (precipitation) and may be displaced by the media perfusion. The cells along the path of the displaced microbubble can easily be sheared off. To resolve the problem, several priming methods to eliminate bubbles in the system or create bubble traps to avoid transport of bubbles from the world-to-chip interface can be employed^{202,438,439} (Figure 2.6). Bubble-free environment is essential to ensure microsystems working as designed and successful long-term cell culture in them.

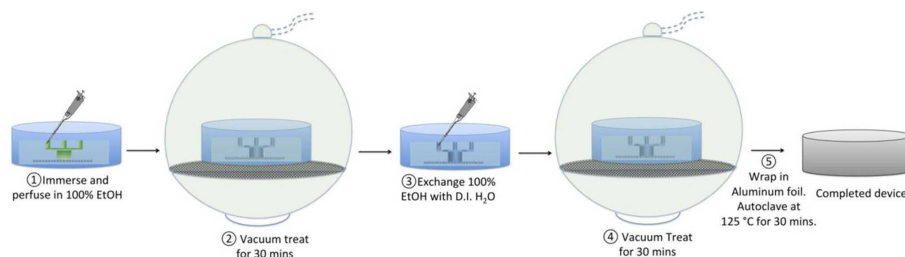


Figure 2.6: Priming method to remove bubbles in PDMS devices⁴³⁹. Reprinted with permission of Springer Nature.

4. Microflows at cell seeding

The volume in microfluidics usually range between nano-liters to tens of micro-liters. If the microfluidic cell study requires high cell density in the viewfield

under the microscope, the seeding cell density must be increased to over 1×10^6 cells mL^{-1} . In addition, the dead volume in world-to-chip interface must be considered so sufficient amount of cells can reach the microfluidic channels.

For adherent cells, after cell seeding, an adhesion period must be given to allow cells to adhere to the substrate. During this period, if there are microflows, even with velocity of just a few $\mu\text{m s}^{-1}$ potentially caused by minute pressure difference, the distribution of cells may be easily affected and may impact cell adherence, cell health, and differentiation⁴⁴⁰. Therefore, how cells are being loaded into microfluidic systems must be handled carefully.

5. Environmental control

The most important thing to consider for long-term cell culture on microfluidic chips is the environmental control. The gas, nutrient, and heat must be provided to the cells for cell survival. It is especially appropriate to couple microfluidics with live cell imaging, however, environmental control for microfluidics chip on microscopes is also non-trivial. Several companies manufacture on-stage incubators for live cell imaging, such as Tokai Hit, Okolab, Pecon, Linkam Scientific, Cherry Biotech, Bioptechs, BLAST Inc, Live cell Instruments, In Vivo Scientific, and BioSpherix.

An on-stage microscope incubator typically consists of a heating stage, a top plate with transparent heater, a humidifier, and gas mixer for appropriate gas concentration. In some cases, a bottom heater composed of a transparent heating glass can be used as a rudimentary heater to keep cells alive. Integrated solutions may have an environmental chamber surrounding the entire microscope but requires a long equilibrium time due to the large volume.

I discuss the key points in environmental control for successful cell culture in microfluidic systems:

(a) Gas permeability of chip materials

First of all, in cell culture systems, the $\text{CO}_2/\text{NaHCO}_3$ buffering is usually used. To maintain pH stability, the CO_2 level needs to equilibrate with the cell culture medium. For cell respiration, O_2 must be accessible to cells.

In PMMA microfluidic chips, usually gas permeability is low which prevents both gas equilibration as well as gas dissemination, but the $\text{CO}_2/\text{NaHCO}_3$ buffering can be ensured by using pre-equilibrated medium in the CO_2 incubator. In PDMS microfluidic chips, the gas permeability is high, thus CO_2 and O_2 can easily diffuse through the PDMS matrix if the atmosphere is provided appropriately.

(b) Nutrient and waste perfusion

Due to the low volume in microfluidic systems, the mass transport of nutrient are diffusion-dominant in low Reynolds number environment. The overall mass that cells can access is much less compared to conventional cell culture systems such as those in petri dishes.

Therefore, appropriate transport of new nutrient is necessary by perfusing the microfluidic system. Typical perfusion methods include gravity driven flow, air pressure driven pumping, peristaltic pumping, syringe pumping, and electroosmotic pumping (Table 2.6)^{441,442}. In particular, syringe pumps and air pressure driven pumps are used commonly by researchers in the microfluidics community. Syringe pumps from Cetoni GmbH, Chemyx, New Era Pumps, LabSmith, and Harvard Apparatus are particularly favored by many researchers. Fluigent, Elveflow, Corsolutions, and Dolomite also provide several variants of air pressure-driven pumps for driving microfluidic flows.

Not only the perfusion but the waste removal is also important to avoid the toxicity. Moreover, if the waste volume builds up, the hydrostatic pressure acting on the cells may be large and cause cell death.

Table 2.6: Pumping methods for cell culturing on chips⁴⁴¹.

Pumping method	Advantages	Disadvantages
Gravity-driven flow	<ol style="list-style-type: none"> 1. Simple 2. Inexpensive 3. Power-free 4. Prevents microbubbles 5. No pulsatile flow 	<ol style="list-style-type: none"> 1. No direct control 2. Flow velocity changes by time 3. Hydrostatic pressure
Air-pressure driven flow	<ol style="list-style-type: none"> 1. High stability and pulseless flow 2. Possibility to handle fluids in liters 3. Fast response time 4. Control fluids in dead-end channels 	<ol style="list-style-type: none"> 1. Require precise pressure supply and control 2. Precise flow rate control requires flow sensor 3. Potential loss of gas equilibrium 4. Works in open system
Peristaltic pump	<ol style="list-style-type: none"> 1. Works in open or close systems 2. Produces versatile push or withdraw flow 	<ol style="list-style-type: none"> 1. Pulsatile flow 2. Power requirement 3. Large footprints from mechanical parts 4. No pressure measurement 5. No direct flow rate measurement
Syringe pump	<ol style="list-style-type: none"> 1. Closed system ensures sterility 2. Fast setup and easy flow rate control 3. Produces versatile push or withdraw flow 	<ol style="list-style-type: none"> 1. Power requirement 2. Long response time 3. Limited volume 4. Minute pulsatile flow 5. No pressure measurement 6. Large footprints from mechanical parts
Electro-osmotic pump	<ol style="list-style-type: none"> 1. No mechanical parts 2. Reversible flow 3. Miniaturization integration possible 	<ol style="list-style-type: none"> 1. Power requirement 2. Electrolysis of media and cells possible 3. Difficult to ensure sterility 4. Surface properties are limited

(c) Shear flow in cell experiments

In the body, advection for nutrient and oxygen delivery through the major vessels of the circulatory system is necessary while the tissue perfusion becomes more diffusion limited. In hemodynamic flows, the Poiseuille flow exerts shear stress to the blood vessel wall lined with endothelial cells. The shear stress is part of the endothelial homeostasis^{443–445}. It is known that

confluent endothelial cell layers will respond to shear stress above 1 Pa and align in parallel to the flow vector^{443,446,447}. However, other cell types especially cells originated from the CNS, often do not like to be stimulated by shear as it can lead to cell death.

Due to small channel cross-section in microfluidics, it is very easy to create cell culture platforms with varied shear stress. A stable cell culture platform with shear stress less than 0.01 Pa for cells sensitive to shear can be easily realized by lowering the flow rate.

In a microfluidic channel, the fluidic resistance of a simple Hele-Shaw flow cell can be calculated as in Equation 2.8. The shear stress at the channel wall estimated using the parallel-plate model is:

$$\tau_w = \frac{6\mu Q}{wh^2}, \quad (2.15)$$

where Q is the volumetric flow rate, μ is the dynamic viscosity of fluids, w is the width of the microchannel, and h is the height of the microchannel.

However, when considering the shear stress acting on a cell at the bottom of the microfluidic channel, the geometry of the cell must be considered. Gaver III *et al.*, have proposed algebraic expression for the shear stress on a cell which can be considered as a semicircular bulge on a microchannel wall based on the lubrication theory⁴⁴⁸. For a cell with radius R in a microfluidic channel with height of h , dependent on various cell size-to-channel height aspect ratio, $\gamma = \frac{R}{h}$, the maximum shear stress τ_s^* can be estimated:

$$(\tau_s^*)_{max} = \frac{6\mu Q_{2-D}^*}{h^2} \left\{ \begin{array}{ll} 2.95 & \gamma < 0.25 \\ 1.158 + (1 - \gamma)^{-2} & 0.25 \leq \gamma \leq 0.85 \end{array} \right\}, \quad (2.16)$$

where μ is the fluid viscosity, Q_{2-D}^* is the flow rate per unit width, h is the channel height, respectively.

(d) Temperature

To maintain cell survival, appropriate temperature must be supplied. Typically in cell culture microfluidic systems, 37°C temperature is maintained by on-stage incubators through passive heating of chips by holders and top transparent heating lid or through close contact of the bottom of microfluidic chip to a transparent heater²⁰².

In many cases, the accuracy of the heater for microfluidic cell culture is demanding. In microfluidics, the high surface-to-volume ratio is associated with high heat exchange coefficient and low thermal inertia so very little power is consumed to keep microsystems stable at bioactive temperature. However, if the temperature is not optimal in a microfluidic system, the cell behavior will be significantly impacted.

(e) Relative humidity

Some microfluidic systems employ closed systems to ensure sterility, but closed systems require accurate balancing of inflow and outflow to avoid

hydrostatic pressure buildup that can cause cell death. Many microfluidic systems employ partially closed systems with either inlet or outlet being exposed to the ambient environment.

In microfluidic chips employing partially closed or opened systems, the adverse effect of relative humidity (RH) is often overlooked. The volume in the microfluidic system is very low in comparison to any openings on microfluidic chips for world-to-chip interface. It is practically difficult to maintain a 100% relative humid ambient environment, so the water in culture media tends to evaporate and cause significant osmotic stress to the cells.

The effect of relative humidity on media evaporation can be considered by vapor pressure using Adren Buck Equation⁴⁴⁹:

$$P_s(T) = 0.61121 \exp\left(\left(18.678 - \frac{T}{234.5}\right)\left(\frac{T}{257.14 + T}\right)\right), \quad (2.17)$$

where $P_s(T)$ is the saturation vapor pressure in kPa, T is the air temperature in degree of celsius. At 37°C the saturated vapor pressure for water is 6279.88 Pa with humidity ratio calculated as 0.0411 kg kg⁻¹.

As relative humidity is defined as the ratio of partial water vapor pressure over equilibrium vapor pressure, the partial vapor pressure at different relative humidities can be calculated. At a relative humidity of 95%, the partial vapor pressure is 5965.9 Pa with humidity ratio of 0.0389 kg kg⁻¹. At a relative humidity of 90%, the partial vapor pressure is 5651.89 Pa with humidity ratio of 0.03698 kg kg⁻¹. At a relative humidity of 75%, the partial vapor pressure is 4709.9 Pa with humidity ratio of 0.0303 kg kg⁻¹.

The evaporation rate can be further calculated using the humidity ratio:

$$g_{hr} = \Theta A(x_s - x), \quad (2.18)$$

where g_{hr} is the amount of evaporated water per hour (kg h⁻¹), Θ is the evaporation coefficient in (kg m⁻¹ h²) calculated as 25 + 19 v , v is the velocity of air above the water surface (m s⁻¹), A is the water surface area (m²), x_s is the maximum humidity ratio of saturated air at the same temperature, x is the humidity ratio air (kg kg⁻¹).

Assuming in a microfluidic chip with an inlet and outlet of 2 mm in length and height of 5 mm, and a straight channel of 8.8 mm × 1 mm × 0.1 mm. Assuming there is no draft, the total volume of the media is 126.5 μL ≈ 126.5 mg.

$$g_s(95\% RH) = 2.035 \text{ mg hr}^{-1}, \quad (2.19a)$$

$$g_s(90\% RH) = 3.811 \text{ mg hr}^{-1}, \quad (2.19b)$$

$$g_s(70\% RH) = 9.99 \text{ mg hr}^{-1}. \quad (2.19c)$$

The volume change of water in the microfluidic chip in different relative

humidities over 8 hours can be calculated by:

$$\Delta V = (126.5 - (g_s \times 8))/126.5 \times 100\%. \quad (2.20)$$

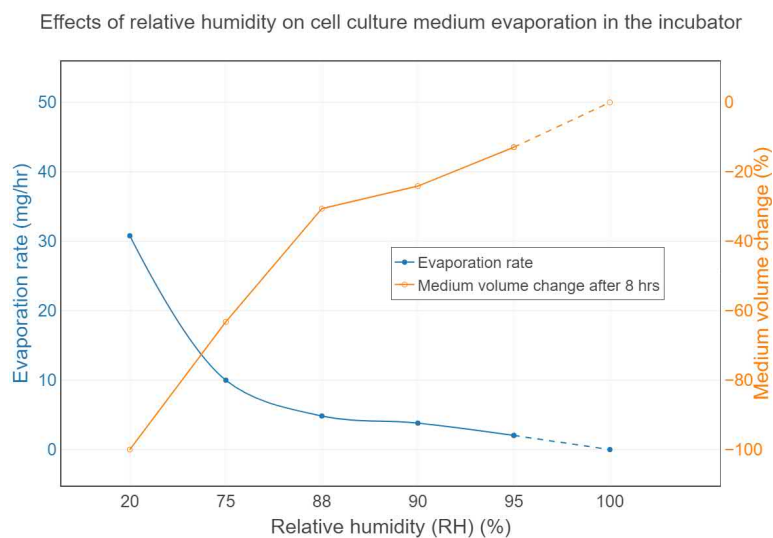


Figure 2.7: Effects of relative humidity on cell culture medium evaporation in the incubator.

Figure 2.7 shows how the evaporation rate and medium volume change depend on the relative humidity in the incubator. Because the volume in a microfluidic chip is much smaller than that in a petri dish, evaporation can cause significant volume change that affects osmolarity. Also, in conventional cell culture, petri dishes or flasks are often covered by a lid or a cap to avoid contamination or evaporation, which is difficult to implement in microfluidic chips. If the water evaporates significantly, the osmolarity stress on cells in microfluidics will be significant and hinders long-term cell culture.

To resolve this issue, typical microfluidic cell culture system employ partially or totally closed system or use of anti-evaporative oil. In combination, an enforced humidifier for on-stage incubators can be built to increase the relative humidity to the microfluidic chips (Figure 2.8).

In short, to successfully culture cell on chips for biomedical applications, the design and fabrication of the microfluidics and environmental factors must all be considered carefully. Ensuring a stable microfluidic cell culture platform is the first step before the platform can be used for any biomedical applications.

Next, I will introduce the three stable platforms I have developed for microfluidic cell culture and experiments, including a thermoplastic microfluidic chip, a small hybrid PMMA/PDMS microfluidic chip, and a reversibly-sealed hybrid PMMA/PDMS microfluidic chip.

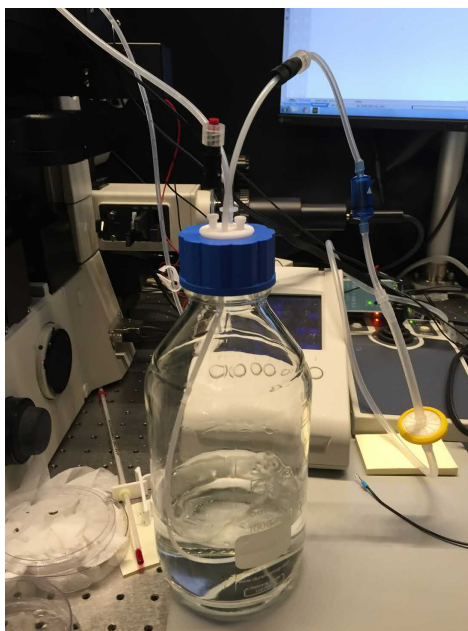


Figure 2.8: An enforced humidifier for Tokai Hit on-stage incubator.

2.2 PMMA thermoplastic microfluidic chip for cell culture

A microfluidic electrotaxis chip containing two microchannels with $l \times w \times h$ of $30 \times 3 \times 0.07$ mm was composed of a top poly(methyl methacrylate) (PMMA) chip, a piece of double-sided tape (PET8018PT, 3M, USA) cut with the microfluidic channels pattern, and a coverglass substrate (0107242, No. 1.5 high precision, Paul Marienfeld GmbH, Germany) (Figure 2.9A). The PMMA microfluidic chip was fabricated by patterning inlets, outlets, and fluidic connections on PMMA sheets (0.5 mm, CM205x, Chimei Corp, Taiwan) using a CO₂ laser scriber and bonded thermally (109.5 °C, 810 N, 30 minutes) as described previously³⁷⁹. Adapters with M6 threads (SPC-M6-C, Nabeya, Japan) were glued onto the PMMA microfluidic chip using a UV adhesive (3301, Loctite, USA). The coverglass substrate was joined with the PMMA microfluidic chip using the cut double-sided tape after UV disinfection of all surfaces.

The advantages for PMMA thermoplastic microfluidic chip include convenient creation of complex 3D structures, air-impermeant cell culture environment, and rigid microfluidic structures. A microfluidic channel can be easily created by laser cutting channel patterns on a piece of double-sided tape that is also used for joining thermoplastic chips to substrates.

By using thermoplastic microfluidic chip with CO₂-equilibrated media perfusion and a simple heater, cells could be cultured for weeks or months on chip²⁰² (Figure 2.10). The photoimage of the setup can be seen in Figure 2.11, where two thermoplastic chips are installed on a transparent heater. The cell culture temperature is regulated by an industrial proportional-integral-derivative (PID) controller and the nutrient is supplied by syringe pumps.

However, to ensure a bubble-free microenvironment in thermoplastic microfluidic

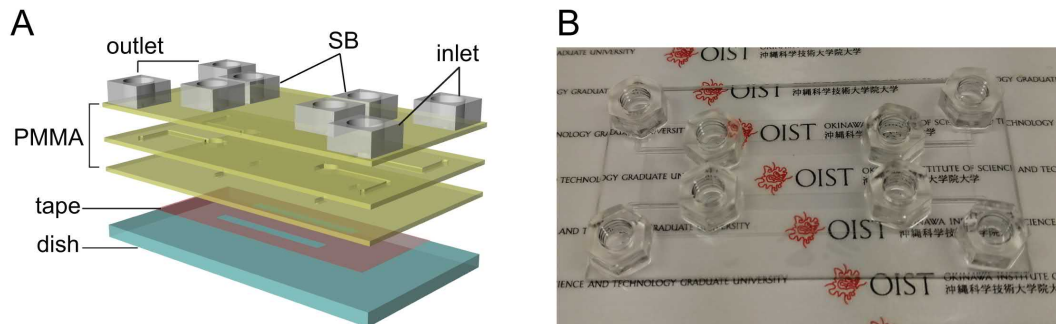


Figure 2.9: Schematics of a PMMA microfluidic chip containing two simple rectangular channels. (A) Three-layer patterned PMMA pieces are thermally bonded. The PMMA piece affixes to the dish by a double-sided tape. Adapters for inlets, outlets, and salt bridges (SB) are glued on; (B) A photoimage of the final assembled device.

chip, the fluidic fittings and tubings must be installed before seeding the cells, increasing the difficulty to adapt by non-specialists. Furthermore the dead volume in the tubings increases the amount of cells required, increasing the difficulty of using scarce and precious cells such as primary cells or stem cells.

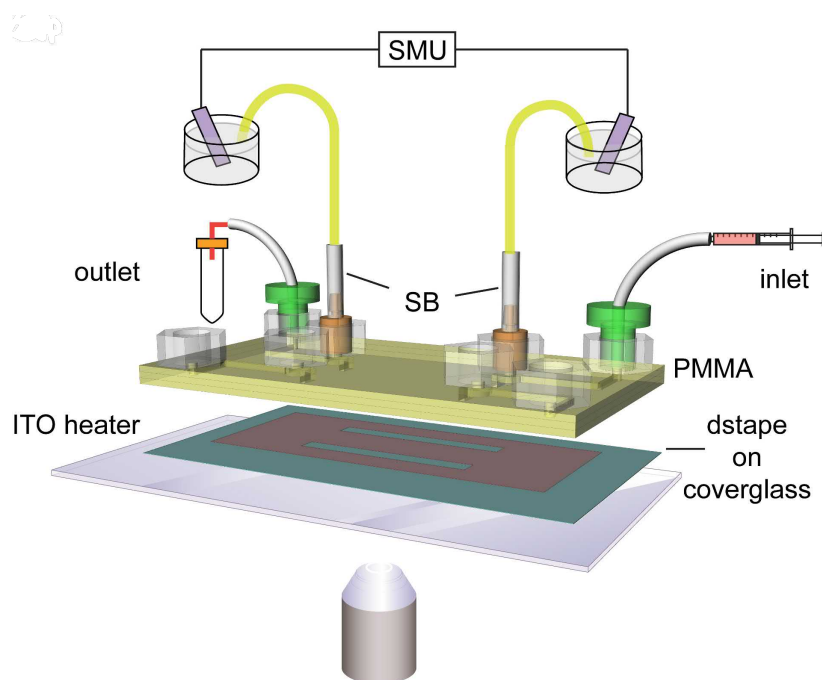


Figure 2.10: The setup diagram of an electrotaxis experiment using a microfluidic chip. SB: salt bridges; SMU: source meter unit.

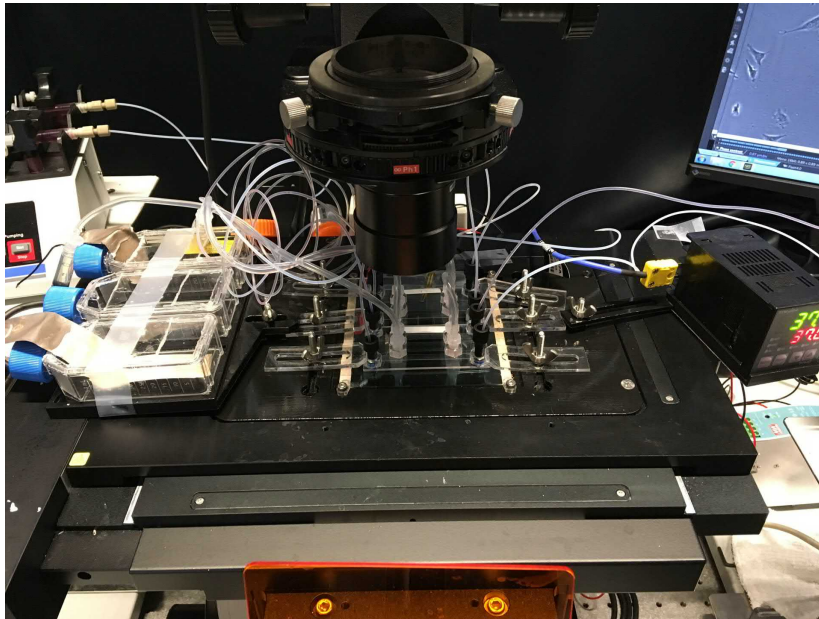


Figure 2.11: The photoimage of electrotaxis setup using thermoplastic chips.

2.3 A hybrid PMMA/PDMS microfluidic chip for electrotaxis study in an on-stage incubator

In biomedical microdevices (BMMDs), biochemical and biophysical microenvironments can be manipulated by combining device design and operation conditions to probe biochemical and biophysical properties or to investigate biological phenomena. Practical BMMD designs must consider system integration and fabrication process to reduce the production volume and cost, ensure the sterilization and user-friendly operation⁴⁵⁰. Transparent rigid thermoplastics, such as poly(methyl methacrylate) (PMMA) and cyclic olefin copolymers (COC), and transparent elastomeric silicone rubber poly(dimethyl siloxane) (PDMS) are particularly favored in BMMD production in laboratory settings^{334,451,452}.

However, each material has its distinct advantages and disadvantages (see summary in Table 2.2). By using thermoplastics, fabrication cost is low while bonding strategies and interconnect choices are more readily available for constructing the world-to-chip interface. Fabrication of complex three dimensional (3D) internal structures is also possible in thermoplastics chips, but the spatial resolution of direct-writing methods is inferior in comparison to lithographic methods³³⁴. Alternatively, micrometer-precision microstructures in PDMS substrates is possible through the soft lithography process, although the process is usually limited to quasi-planar (2.5D) microstructures³²³. PDMS is also flexible and highly gas permeable, making it suitable to fabricate BMMDs with active components such as microvalves, and to create gas concentration gradients for automated lab-on-chip applications. Although fabrication of complex 3D microstructures in PDMS BMMDs is possible, it requires complicated multi-step fabrication, alignment, and off-stoichiometry bonding³²⁷. Moreover, PDMS has very low surface

energy, which limits its bonding and world-to-chip interconnect choices.

The disadvantages of each material are not only restricted to fabrication, but also on applications. For successful and reliable cell culture in BMMDs, it is essential to ensure sterility, controlled microenvironment, and guided reagent delivery with bubble-free conditions⁴³⁷. Bubble prevention is crucial because microbubbles can impose strong interfacial tensions that shear adherent cells or cause cell damage in the microchannel. In thermoplastic BMMDs, to minimize air bubbles, the device is often pre-assembled with reagent delivery components and a world-to-chip interface prior to seeding cells into the device. As a result, the dead volume tends to be large in pre-assembled thermoplastic BMMDs, which leads to longer reagent delivery time to cells²⁰². In PDMS BMMDs, although a delicate buffer exchange procedure can be adapted to prevent air bubbles in microchannels⁴³⁹, the hydrophobic nature of PDMS often causes air bubble accumulation at world-to-chip interconnects, which can easily propagate into microchannels. Moreover, the elastic nature of PDMS is prone to leakage at interconnects⁴⁵³.

I present an approach to integrate PMMA and PDMS into a hybrid microfluidic chip to combine the advantages of the two microfluidic engineering while mitigating some of the disadvantages. High dimensional accuracy can be easily obtained in PDMS microfluidics so the main microfluidic networks where the manipulation of microenvironments and cell culture take place is in the PDMS microfluidics. Complex 3D rigid structures and versatile world-to-chip interfaces can be rapidly fabricated using PMMA microfluidics. Furthermore, double-sided adhesive tapes have been a primary method to bond heterogenous substrates in PMMA microfluidics^{334,454}. An dual energy double-sided tape that is composed of a silicone-type adhesive and an acrylic-type adhesive can easily bond between PDMS and thermoplastics^{397,398}, further increases the easiness to rapidly prototype hybrid PMMA/PDMS microfluidic chip.

In this section, I introduce the first design of the hybrid PMMA/PDMS microfluidic chip that has a small configuration which is suitable to study cell migration in on-stage CO₂ incubators. Highly accurate microfluidic channels can be designed and fabricated in the PDMS microfluidic chip. Also, bubble-free and gas-permeant microenvironments can also be easily established in PDMS microfluidics. Versatile and complex 3D world-to-chip interface such as media reservoir, electrical stimulation, and waste withdrawal outlets can be easily made in PMMA designs.

2.3.1 Microfluidic chip design: single-layer and double-layer design

The goal of this work was to design a microsystem to study cell migration under electrical stimulation (electrotaxis) in high throughput manner. Therefore, multiplexing multiple electric field strengths and suppressing unwanted chemical transport were important features in the microfluidic design. While single-layer PDMS microfluidics, *i.e.*, single-height microchannels, was the norm, multilayer PDMS microfluidics offered more delicate control of the microenvironments.

In this section, I introduce the microfluidic channel design of both single-layer and double-layer to multiplex electric field strengths and manipulate the fluid flow and

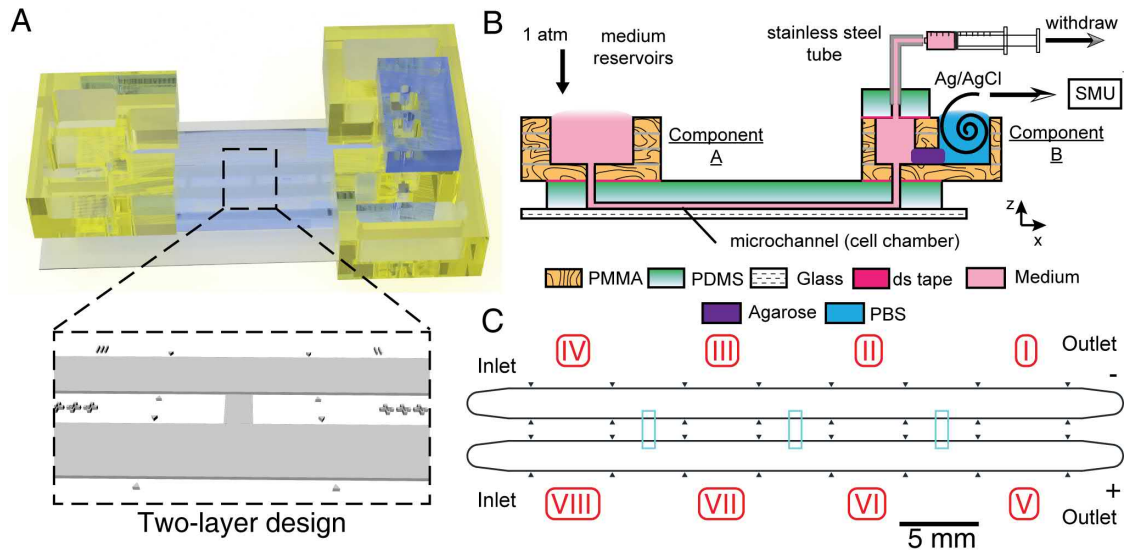


Figure 2.12: The concept of a small configuration hybrid PMMA/PDMS microfluidic chip. (A) The 3D rendered model of the final PMMA/PDMS chip. Double-layer microchannel design in the PDMS is shown; (B) The schematic diagram of using the PMMA/PDMS chip for electrotaxis experiments. Complex 3D microfluidic structures and world-to-chip interface are established in PMMA components A & B; (C) The channel design. The 10 μm -high first layer structures are shown in cyan.

chemical transport. Two 2 mm-wide main channels were designed to support study of two conditions within a single chip (Figure 2.13). Although multiplex electric field strengths could be created by changing the cross-sectional area of the microchannels, the hydraulic resistances and shear rate were modified as well¹⁹⁸. To avoid so, a R-2R resistor ladder in electric circuit design was adapted²⁰² so that interconnecting channels connect the two main channels to create parallel circuits that the electric current was split in each segment (I : VIII) in the network.

The electric field was applied from the outlets to avoid paracrine signaling from electrically stimulated cells to control cells residing in section IV and VIII. The spatial dimensions and physical properties of the main channel and the interconnecting channels in the single-layer and the double-layer design is shown in Table 2.7.

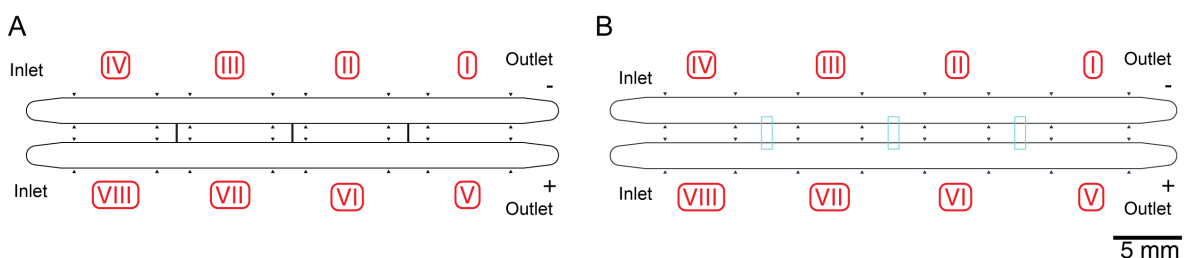


Figure 2.13: The designs of single-layer and double-layer PMMA/PDMS chips. (A) Single-layer PMMA/PDMS chip; (B) Double-layer PMMA/PDMS chip. The first layer structures are shown in cyan.

Table 2.7: Physical characteristics comparison between single-layer and double-layer PMMA/PDMS chip.

Channel type	Single-layer		Double-layer	
	Interconnection	Main	Interconnection	Main
Channel dimension (l×w×h) (mm ³)	1.5×0.083×0.1	9×2×0.1	1.5×0.838×0.01	8.95×2×0.1
Hydraulic diameter ($\frac{2wh}{w+h}$) (mm)	0.0907	0.1905	0.01976	0.1905
Relative R _Ω (mm ⁻¹)	180.72	45.18	178.99	44.75
R _H (Pa s m ⁻³) (×10 ⁹)	600	55.5	21616.4	55.2
Relative R _H	10.82	1	391.88	1
fRe	56.92	89.94	94.47	89.94
Poiseuille number (P _o)	14.23	22.49	23.62	22.49
Flow velocity simulated by PSPICE at 20 μL min ⁻¹ (m s ⁻¹)	1.44E-19	1.75E-3	2.02E-21	1.75E-3
Reynolds number (R _e)	1.30E-17	0.333	4.01E-20	0.333
Péclet number (P _e)	2.91E-13	7460	8.97E-16	7460

Electric circuit modeling The single-layer and double-layer PMMA/PDMS microfluidic chip were constructed to create multiple electric fields in a R-2R resistor ladder configuration^{202,455}. The electrical equivalent circuit of the two PMMA/PDMS microfluidic chips was the same and shown in Figure 2.14. Each segment of the microfluidic channel network was regarded as an electrical resistor in which relative electrical resistances were calculated and modeled by Ohm's law and Kirchhoff's circuit laws. In the equivalent circuit, the endpoint of R₄ and R₁₁, the adjacent segments from both inlets, were open in the electric circuit. No electric current was flowing through them so cell migration in these sections could be used to collect control cell data.

According to Ohm's law, the electrical resistance of a resistor, R , was proportional to the length and inversely proportional to the cross-sectional area:

$$R = \rho \frac{l}{A} = \frac{\rho l}{w \times h}, \quad (2.21)$$

where ρ , l , A , w , and h were the electrical resistivity of the medium, the length, the cross-sectional area, the width, and the height of the microchannel, respectively. Assuming the electrical resistance of R₁ being r , the relative electrical resistances of other segments (R₂ : R₁₁) could be calculated accordingly.

The electric current flowing through each resistor was calculated by Kirchhoff's circuit law and simulated using PSPICE in the electronic design automation software (OrCAD Lite, Cadence Design Systems, USA) by:

$$10r \times i_2 - 4r \times i_1 - 4r \times i_3 = 0, \quad (2.22a)$$

$$10r \times i_3 - 4r \times i_2 = 0. \quad (2.22b)$$

By solving the system of equations in Equation 2.22, the ratio of electric currents

between each segment, hence the ratio of electric field strengths, was derived in Equation 2.23:

$$i_1 : i_2 : i_3 = E_I : E_{II} : E_{III} : E_{IV} \quad (2.23a)$$

$$= E_V : E_{VI} : E_{VII} : E_{VIII} \quad (2.23b)$$

$$= 5.25 : 2.5 : 1 : 0 \quad (2.23c)$$

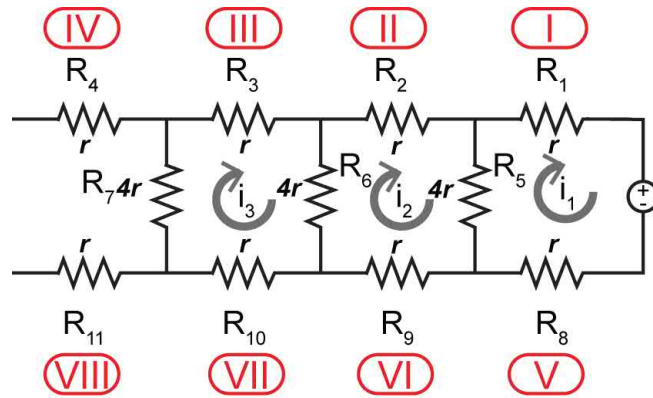


Figure 2.14: The electrical equivalent circuit model of the PMMA/PDMS chip.

Hydraulic resistance modeling The hydraulic resistance of a microfluidic channel network of PMMA/PDMS chips could be modeled and treated like its electric equivalent. Although the single-layer and double-layer PMMA/PDMS chips were designed to have the same electric equivalent circuit, due to the difference in the hydraulic diameter, the hydraulic resistances in the two chips were different. The equivalent hydraulic circuits of single-layer and double-layer PMMA/PDMS chips were shown in Figure 2.15. The hydraulic resistances of the interconnecting channels ($R_5 : R_7$) in the double-layer design were ≈ 36 times higher than those in the single-layer design due to the much smaller hydraulic diameter (Table 2.7).

The hydraulic equivalent circuits of the two designs were modeled and the flow velocity were simulated using PSPICE in the electronic design automation software (OrCAD Lite, Cadence Design Systems, USA) as shown in Table 2.7. The higher Poiseuille number and lower Péclet number in the interconnecting channels in double-layer design compared to those in single-layer suggested that it was more diffusion-dominant in the double-layer interconnecting channels and the high hydraulic resistances prevented advection-driven cross-contamination between the two main channels.

Numerical simulation and experimental validation of fluid flow, chemical transport, and electric field The 3D design models of the single-layer and double-layer chip were exported from AutoCAD and imported into COMSOL Multiphysics 5.3 (COMSOL Inc, USA). Steady-state coupled simulations using three modules, creeping flow, chemical transport of diluted species, and electric currents, were performed.

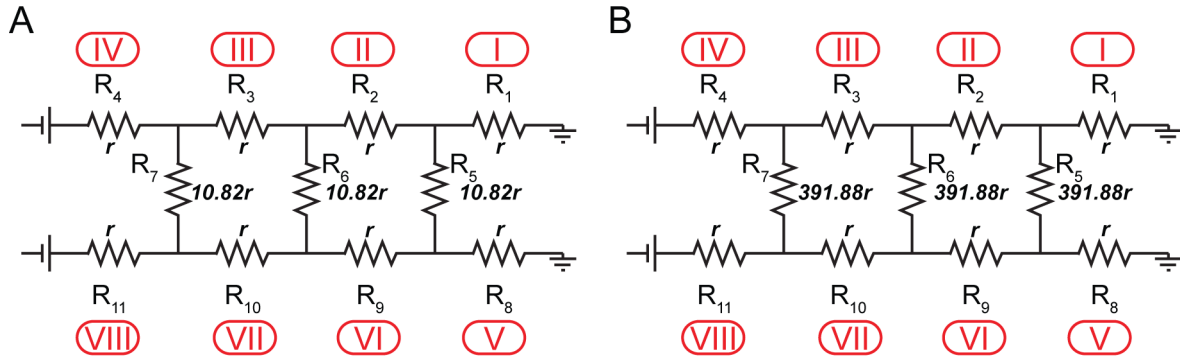


Figure 2.15: The hydraulic equivalent circuit model of single-layer (A) and double-layer (B) PMMA/PDMS chips.

To correctly simulate the system, measured material properties of the MEM α supplemented with 10% FBS medium was input (Appendix A). The materials in the 3D model was set as water with density of 1002.9 kg m^{-3} , electrical conductivity of 1.536 S m^{-1} , dynamic viscosity of 0.000946 Pa s , and relative permittivity of 80.

The boundary conditions were input accordingly for creeping flow, electric current, and chemical transport of diluted species as shown in Figure 2.13. For creeping flow, $20 \mu\text{L}/\text{min}$ flow rate was used. For chemical transport, 100 mol mm^{-3} of 40 kDa dextran was used as a baseline with diffusion coefficient of $44.7 \mu\text{m}^2 \text{ s}^{-1}$ ⁴⁵⁶. For establishment of 300 V m^{-1} electric field, $485.5 \mu\text{A m}^{-2}$ was set at the anode and electric potential of 0 V was set at the cathode.

Stable creeping flow in PMMA/PDMS microfluidic chip Due to the cross-sectional area differences between the main channels and the interconnecting channels, the majority of the fluid will flow through the main channels (Figure 2.16).

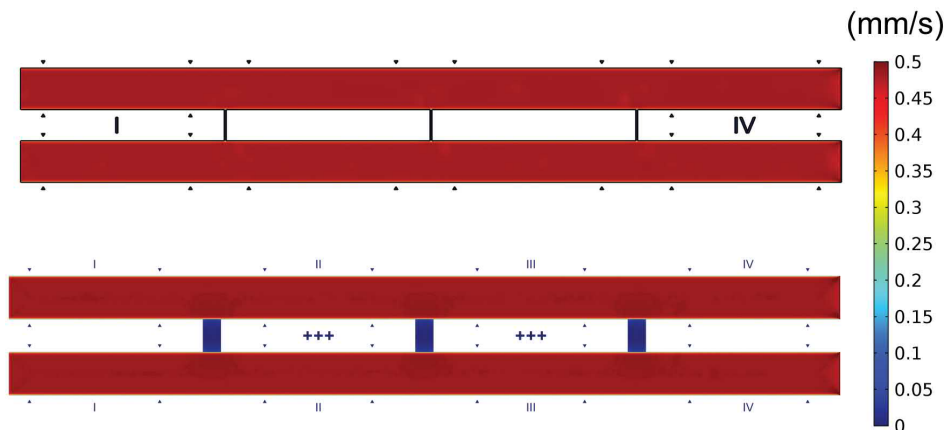


Figure 2.16: Stable flow field in hybrid PMMA/PDMS chips. Top: single-layer design; Bottom: double-layer design.

Multiplex electric fields for high throughput electrotaxis studies Multiplex electric fields were established by the R-2R resistor ladder design. By theoretical

modelling, the electric field strength (EFS) ratio between sections $E_I : E_{II} : E_{III} : E_{IV}$ was 5.25:2.5:1:0. The simulated EFS ratio between the sections agreed with the theoretical modelling as shown in Equation 2.24.

$$E_I : E_{II} : E_{III} : E_{IV} = E_V : E_{VI} : E_{VII} : E_{VIII} \quad (2.24a)$$

$$= 4.99 : 2.45 : 1 : 0. \quad (2.24b)$$

The numerical simulation results of the electric field are shown in Figure 2.17.

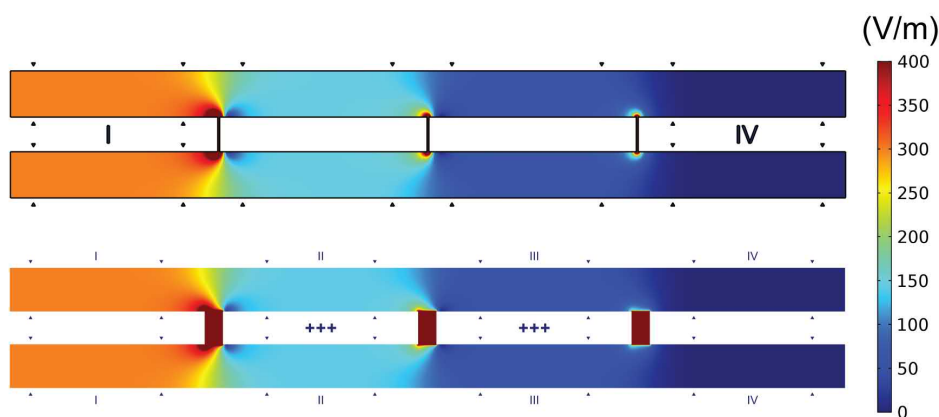


Figure 2.17: 4.99:2.45:1:0 ratio stepwise electric field established in the hybrid PMMA/PDMS chips. Top: single-layer design; Bottom: double-layer design. The triangular markers represent the limits of stable regions in each segment used in data analysis and in experiments.

Diffusion-dominant chemical transport in a double-layer PMMA/PDMS microfluidic chip The chemical transports in single-layer and double-layer PMMA/PDMS microfluidic chips were simulated and shown in Figure 2.18. The simulation showed the ideal condition where diffusion was dominant in the interconnecting channels.

By adjusting the scale of the colormap, the “cross-contamination” events where chemical leaches from one main channel to another through the interconnecting channels could be seen more clearly (Figure 2.19). In the double-layer design, it was more diffusion-dominant in comparison to the single-layer design.

Experimental validation of stable chemical transport in hybrid PMMA/PDMS chip Single-layer or double-layer PMMA/PDMS chips were fabricated and perfused as the same state as in simulation. The chemical transport in the chip was visualized using fluorescein-conjugated dextran (40 kDa, FD40, Sigma-Aldrich, USA) or tetramethylrhodamine-conjugated dextran (40 kDa, D1842, Thermo Fisher Scientific, USA) in Fluorobrite DMEM (Gibco, USA). The dyed media were loaded separately in two 2.5 mL syringes (Terumo, Japan) and the channels was primed at $20 \mu\text{L min}^{-1}$ for 10 minutes before reducing to $20 \mu\text{L h}^{-1}$ (cell culture experiment flow

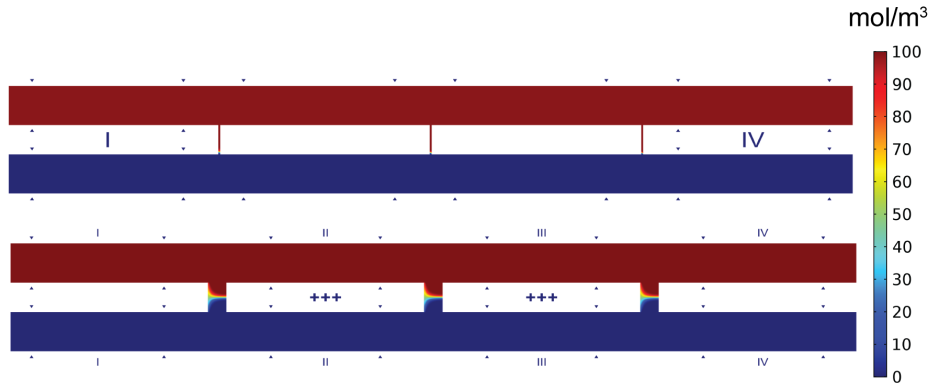


Figure 2.18: Chemical transport simulated in hybrid PMMA/PDMS chips. Top: single-layer design. Bottom: double-layer design.

rate), followed by capturing microscopy images with 10 min time lapse epifluorescence microscopy (Ti-E, Nikon, Japan).

In the single-layer channel design, the interconnecting channels had relatively low hydraulic resistances compared to those in the double-layer design. As a result, any slight disturbance in the pressure affecting microfluidic flow such as slight hydrostatic pressure difference between two media reservoirs or slight withdrawing speed difference in syringe pumps could result in advection of chemicals from one microchannel to another (Figure 2.20), causing “cross-contamination” events and limiting the experimental throughput of the PMMA/PDMS chip.

In double-layer channel design, the hydraulic resistances of the interconnecting channels were higher while the electrical equivalent circuit was the same. The laminar flows through the interconnecting channels were slower and thus limiting the chemical advection. As a result, the chemical distribution between the two main channels can be maintained stably for more than 10 hours (Figure 2.21) with only diffusion-driven contamination limited at the proximity of the interconnecting channels.

Moreover, when cells were injected in the top channel of the double-layer microfluidic chip, the cells were not able to pass through 10 μm -height interconnecting channels and were restricted to its main channel (Figure 2.21). When different cell types were seeded in separate channels, the double-layer microchannel design could further increase the experimental throughput.

2.3.2 Microfluidic chip fabrication

The fabrication of hybrid PMMA/PDMS chip can be separated into three parts: PDMS microfluidic chip, PMMA microfluidic chip, and hybrid assembly.

Fabrication of PDMS chip: soft lithography

Single-layer microfluidic chip The single-layer microfluidic chip was designed in AutoCAD software (Autodesk Inc, USA) and exported as a dxf file. The dxf file was converted to a GDS2 file using KLayout. The GDS2 files were split into microscopic

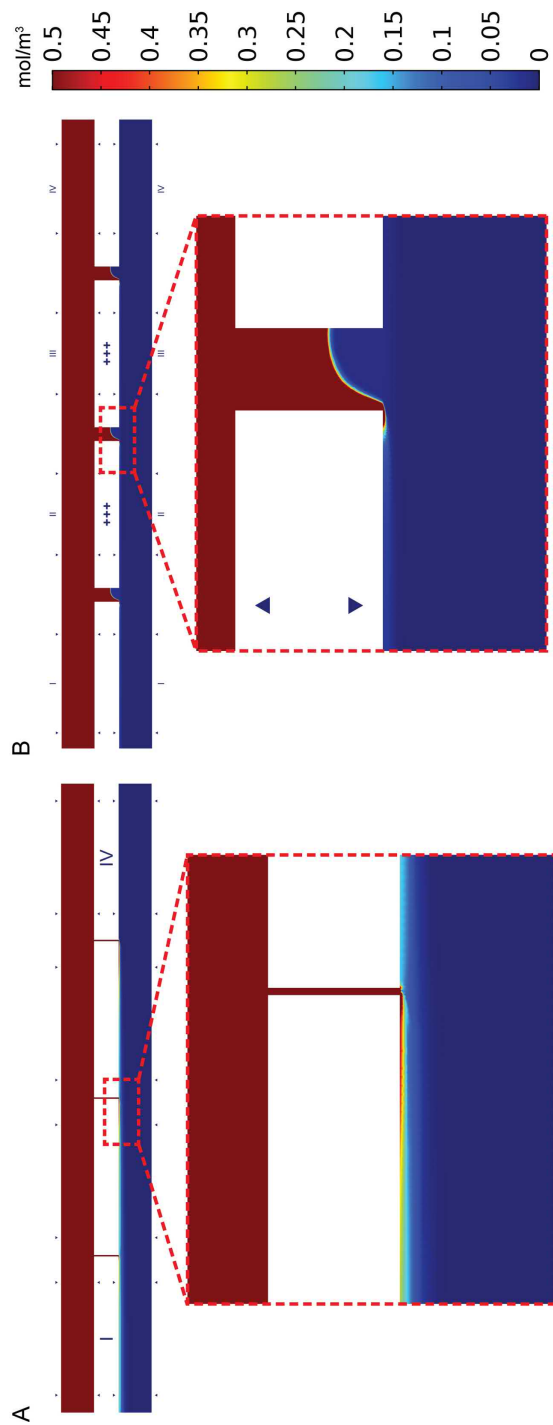


Figure 2.19: Chemical transport simulated in hybrid PMMA/PDMS chips at refined scale. (A) Single-layer design; (B) Double-layer design. The red dashed box shows the magnified regions in the channels.

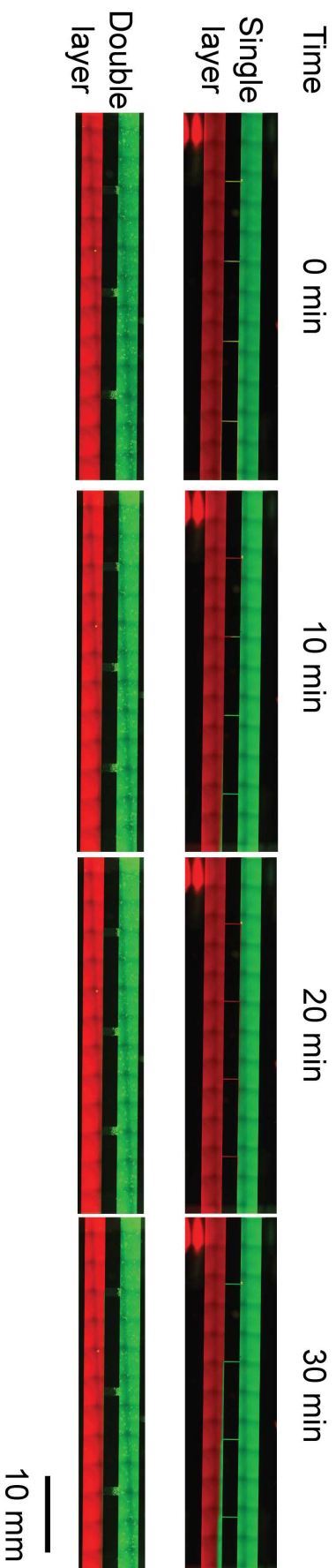


Figure 2.20: Chemical transport was more stable in double-layer PMMA/PDMS chip. Fluorescein-dextran was perfused in the top channel (Green) and tetramethylrhodamine-dextran was perfused in the bottom channel (Red). Top: The chemical transport in single-layer channel was erratic due to small disturbances in flow and changed distribution or several times during the 30 minute observation. Bottom: The chemical transport in double-layer channel was much more stable. Cells were also injected in the top channel in double-layer microfluidic chip showing that the cells were not able to pass through the interconnecting channels, further strengthen the design's capability for high throughput experiments.



Figure 2.21: Stable chemical transport in double-layer PMMA/PDMS chip before and after 10 hours. Fluorescein-dextran was perfused in the top channel (Green) and tetramethylrhodamine-dextran was perfused in the bottom channel (Red).

viewfield-based mask images and exposure recipes were created using the accessory software provided along with a maskless lithographic writer (DL-1000, Nano Systems Solutions, Japan). The mask was written on a piece of 5-inch and 540 nm-thick AZP1350 photoresist-precoated chrome mask blank (CBL5006Du-AZPFS, Clean Surface Technology, Japan) by a digital micromirror device (DMD) with 405 nm light source through a 20X objective at exposure energy of 100 mJ cm^{-2} . The exposed chrome mask was developed in 2.38% tetramethylammonium hydroxide (2.38% TMAH, NMD-3, Tokyo Ohka Kogyo, Japan) and etched with chromium etchant (651826, Sigma-Aldrich, USA).

Negative photoresist (SU-8 3050, MicroChem Corp, USA) of 100 μm -thick was spun on a piece of silicon wafer (100 mm, p-type, E&M Inc, Japan) using a spin coater (MS-A100, Mikasa Inc, Japan). After soft baking according to manufacturer's protocol, the photoresist-coated silicon wafer was exposed with the aforementioned chrome mask using a mask aligner (MA/BA6, SUSS MicroTec, Germany) with i-line UV. The pattern was developed in propylene glycol methyl ether acetate (PGMEA, Sigma-Aldrich, USA) followed by washing with isopropanol, ultrapure water, and dried by nitrogen gas. The structure height, *i.e.*, the channel height in final PDMS device, was confirmed by stylus profilometry (DektakXT, Bruker, USA). The silicon wafer with microfluidic structures was passivated with 1H, 1H, 2H, 2H-perfluorooctyltriethoxysilane (FOTS, 667420, Sigma-Aldrich, USA) inside a desiccator under vacuum for 2 hours, completing the master mold.

To fabricate the PDMS devices, PDMS was mixed and degassed at 10:1 monomer to curing agent ratio with an orbital mixer (ARE-310, Thinky corp, Japan). PDMS casting blocks made of PMMA or polytetrafluoroethylene (PTFE) were fabricated in-house by micromilling with a flat endmill (RSE230-6-50, NS Tools, Japan) on a computer numerical controlled (CNC) micromill (SLS Micro Mill/4, Minitech, USA) (Appendix D.2). The silicon wafer was placed in the casting block and mixed PDMS was poured on the wafer and degassed. After degassing, the PDMS in the casting block was flanked with a piece of 15 mm-thick PMMA block to ensure parallelism of the top surface. The PDMS was cured under 60°C for at least 2 hours. The depth of the casting block ensured the exact height of the PDMS chip (4 mm).

After curing, the PDMS substrate with the negative impression of the microstructures on master mold was delaminated and cut into single devices appropriately. Inlet/outlet ports were punched with a 1 mm-diameter biopsy punch (BPP-10F, KAI group, Japan) or by a punch station (18G, Accu-punch MP, Syneo corp, USA). The port size around 1 mm was appropriate for biologist-friendly fluid manipulation using a 200 μL pipet tip.

Each PDMS device was bonded to a piece of coverglass to complete the PDMS chip.

To ensure surface quality and optical performance, high-precision borosilicate coverglass was chosen (24×60 mm, $170 \pm 5 \mu\text{m}$ thickness, No. 1.5H, Marienfeld-Superior, Germany). The cover glasses were cleaned by ultrasonification in a washing solution (1% TFD4, Franklab, France) on a home-made washing stand (Appendix D.3) fabricated with 3D printing (Form2, Formlabs, USA). The coverslips were washed thoroughly in ultrapure water, dried, and disinfected with ultraviolet irradiation. The PDMS devices were bonded to washed coverglasses using an O₂ plasma instrument (AP-300, Nordson MARCH, USA) at 35 W for 30 s under O₂ mass flow rate of 245 sccm. The bonded devices were placed briefly on 90 °C hot plates to strengthen bonding, completing the PDMS chip fabrication.

Double-layer microfluidic chips The PDMS microfluidic chip composed of double-layer structures followed the similar processes as the single-layer microfluidic chip except on the master mold fabrication.

In double-layer chip design, the first layer was 10 μm -high and the second layer was 100 μm . The design was designed in AutoCAD and exported to KLayout. Several cross-shaped alignment markers were included in the design to assist alignment in the mold of double-layer microfluidic chip.

A 10 μm -thick layer of photoresist (DWL-5, Micro Resist Technology, Germany) was spin-coated on a 100 mm silicon wafer and soft baked. The first design layer was directly written by the maskless lithographic writer (80 mJ cm^{-2} , DL-1000, Nano Systems Solutions, Japan) and subsequently hard-baked. Next, without development, a layer of 100 μm -thick photoresist (SU-8 3050, MicroChem Corp, USA) was spin-coated on the wafer and soft baked. A chrome mask for the second layer was fabricated using the same process as explained in the previous paragraph. Using the alignment markers, the silicon wafer with the first-layer structures was aligned to the second layer structures on the chrome mask on the mask aligner (MA/BA6, SUSS MicroTec, Germany) and subsequently exposed (45 s of i-line UV irradiation). The unexposed photoresist was dissolved away in PGMEA and the wafer was washed thoroughly with isopropanol, water, and dried with nitrogen gas. After the double-layer master mold was made, the chip fabrication process followed the same steps as those in single-layer microfluidic chips. Briefly, the surface was passivated by FOTS and PDMS microdevices were fabricated through the standard soft lithography process in the casting block to ensure flat surfaces of the fabricated devices.

Fabrication of PMMA components 3D microfluidic components could be easily and rapidly fabricated using PMMA. In the PMMA/PDMS microfluidic chip, 4 PMMA components were used including the medium inlet reservoir (component A, Figure 2.12B), outlet/electrical stimulation interface (component B, Figure 2.12B), top reservoir, and salt bridge connector. The medium inlet reservoir, outlet/electrical stimulation interface, and top reservoir components are composed of four layers of 2 mm PMMA substrates.

The designs were created in AutoCAD software and the patterns were cut on a piece of 2 mm casted PMMA substrate (casted acrylic sheet K, Kanase, Japan) with a CO₂ laser cutter (VLS3.50, Universal Laser Systems, USA). For mass fabrication,

patterns for multiple devices were arranged together and bonded. Individual pieces were snapped off by hand after bonding (Figure 2.22).

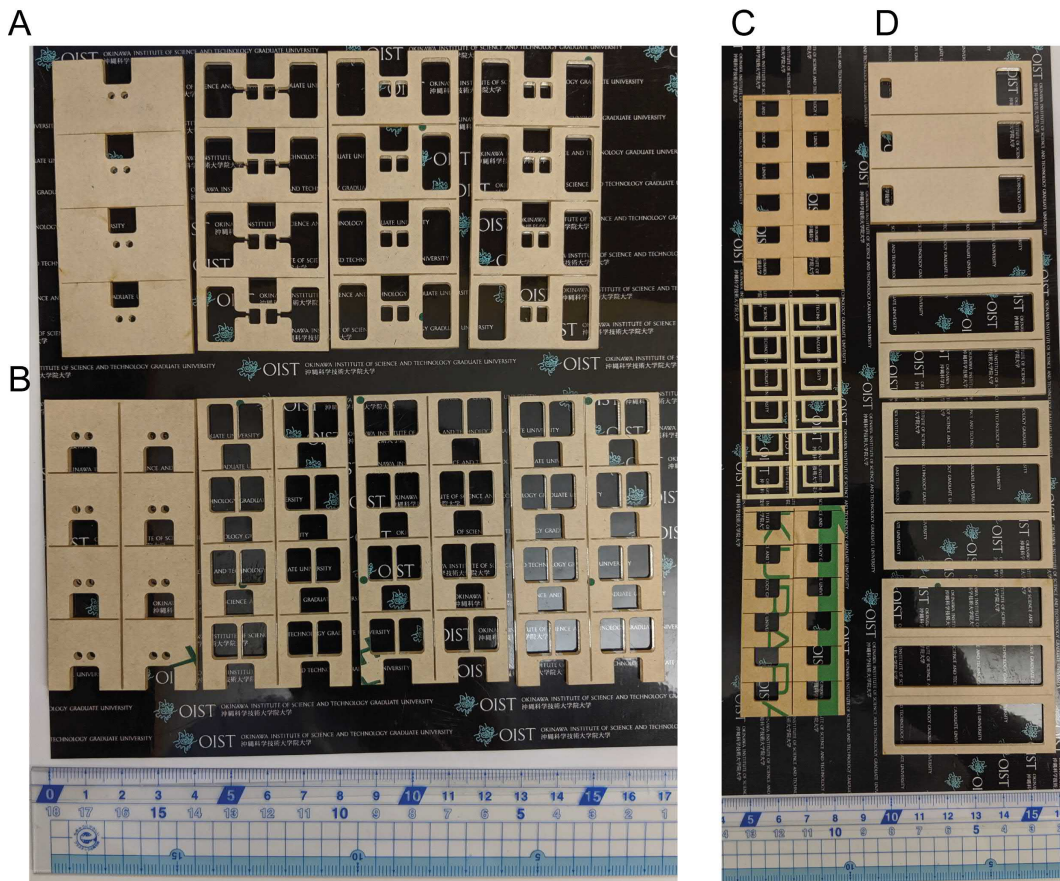


Figure 2.22: Mass fabrication of PMMA components by CO₂ laser cutting. (A) 4 layers to build the component B (outlet/electrical stimulation interface); (B) 4 layers to build the component A (medium inlet reservoir); (C) 3 layers to build the connecting salt bridges; (D) 4 layers to build the top reservoir.

3D microfluidic components can be easily fabricated by stacking the laser-cut PMMA pieces and bonding them under high temperature and pressure. The layers were aligned by hand and flanked between two pieces of 2 mm-thick, 100 mm Tempax float glass wafers (Schott AG, Germany) on a force-controlled programmable hot press (G-12RS2000, Orihara Industrial co., Ltd, Japan). The PMMA pieces were heated above its glass transition temperature with pressure to form leakage-free 3D microfluidic components (118 °C, 500 N, 30 min).

Device assembly: facile reversible bonding between PDMS and PMMA using a dual energy double-sided tape A dual energy double-sided tape (85 μm, No. 5302A, Nitto, Japan) was patterned using the CO₂ laser scribe. On No.5302A double-sided tapes, a silicone-type adhesive and an acrylic-type adhesive were overlaid on the two sides of a poly(Ethylene terephthalate) (PET) substrate. The silicone-type pressure sensitive adhesive adhered to silicone rubber, while the acrylic-type adhesive

affixed to plastic, glass, and metal surfaces. The first report of using such dual energy double-sided tape was for bonding PMMA and PDMS with sensing applications using optical waveguides³⁹⁷. I found that there was no cytotoxicity with the tape and it could be used for cell applications³⁹⁸. The double-sided tape provided an easy and facile way to bond between PDMS and PMMA, an interface typically hard to join. Thus, double-sided tape allows us to take advantage of high spatial precision of PDMS microfluidics and rapid 3D prototyping of PMMA microfluidics.

First a 2 mm-thick copper holder made of wire electrical discharge machining (wire-EDM) and backed with 0.5 mm PDMS sheet was attached reversibly to the coverglass of the PDMS microfluidic chip. The holder served as a rigid weight to hold the microfluidic chip and to prevent flexing of the thin 0.17 mm coverglass (Appendix D.4).

Second, the bonded PMMA component A and B were aligned and affixed to the PDMS microfluidic chip through two pieces of patterned dual energy double-sided tape. Third, to balance the hydrostatic pressure between the inlet and outlet to prevent Poiseuille flow due to hydrostatic pressure, a fluid reservoir was placed to connect component A and component B. The fluid reservoir was first affixed with 2 mm-thick of PDMS padding using the dual energy double-sided tape. Openings were cut by a utility knife. Afterward the PDMS part of the top reservoir was affixed to the top of the component A and B using patterned double-sided tapes, completing the assembly of the device. The zoomed-in view of the components in PMMA/PDMS microfluidic chip and the 3D render of the assembled device are shown in Figure 2.23.

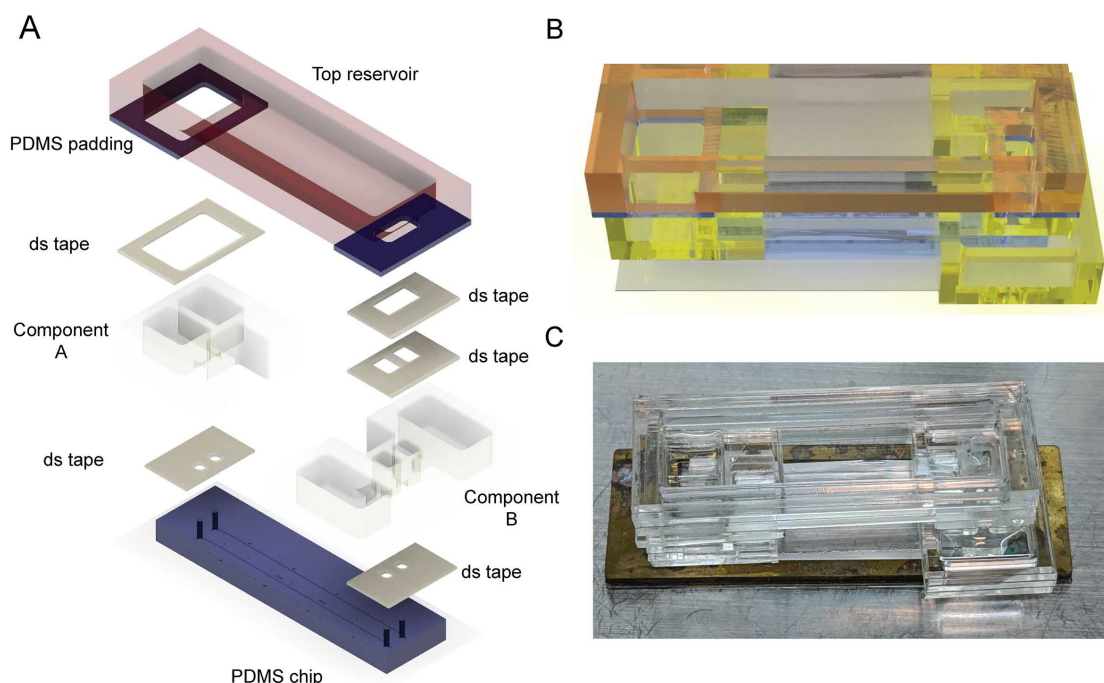


Figure 2.23: The assembled PMMA/PDMS chip. (A) The exploded view of the components for PMMA/PDMS chip; (B) The 3D rendered model of the assembled device; (C) The photoimage of the assembled device for experiment.

After cell seeding and adhesion, the top reservoir was removed and a piece of 4 mm-thick PDMS slab punched with two outlet holes (21G, Accu-punch MP, Syneo Corp,

USA) was affixed to the top of component B through the first piece of patterned double-sided tape (Figure 2.23A), creating an air-tight seal. The device was now completed and ready for media perfusion and electric field stimulation (Figure 2.12).

2.4 A reversibly-sealed PMMA/PDMS microfluidic chip for concurrent shear and electric field stimulation

The hybrid PMMA/PDMS microfluidic approach has shown promises in the previous section for constructing a microfluidic chip. The rigidity of PMMA offers versatility in engineering world-to-chip interface. In this section, I introduce a hybrid PMMA/PDMS chip that is composed of a top PMMA interface chip and a PMMA/PDMS cell culture chip (Figure 2.24). Complex fluidics routing can be designed in the top PMMA interface chip and it can reversibly seal with the PMMA/PDMS microchannel device to realize high throughput experiments. The proof-of-concept PMMA/PDMS device (shear flow and electric field co-stimulation microfluidic chip, SFEFC) will be validated with high shear rate conditioning of endothelial cells and used for study of glioblastoma-endothelium adhesion process.

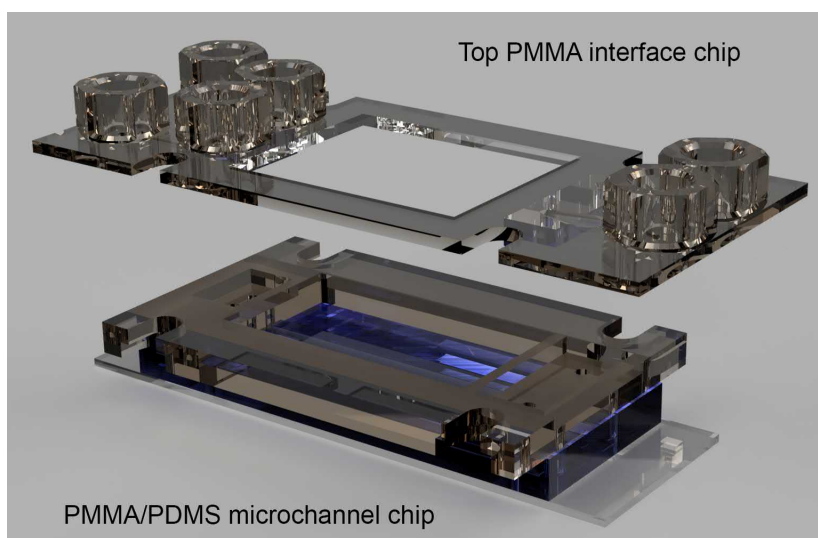


Figure 2.24: The shear flow and electric field co-stimulation microfluidic chip, SFEFC. SFEFC is composed of a top PMMA interface with fluidics and electrical stimulation interface and a bottom PMMA/PDMS microchannel chip where cells reside in.

Quick-fit reversible sealing design The shear flow and electric field co-stimulation microfluidic chip, SFEFC, was designed to maximize experimental throughput and facileness for experimentalists (Figure 2.25). On the PMMA/PDMS microchannel, PMMA component can hold certain amount of cell culture media, avoiding trapping of bubbles at the inlets/outlets in PDMS (Figure 2.25A). Common micropipette tips

familiar to biologists can be used to manipulate fluids. When starting experiments, the top PMMA interface chip with fluidic connections can be reversibly sealed to the PMMA/PDMS microchannel chip through compressive sealing by screws. After each experiment, the PMMA/PDMS microchannel chip and the cells in it could be easily recovered by removing the screws. A new PMMA/PDMS microchannel chip can be interfaced with the top interface chip and start the experiment again.

The key advantages of quick-fit SFEFC include: operator-friendly workflow, low dead volume, low reagent usage, air bubble-free operation, air-tight sealing to sustain high flow rates, and reusable top PMMA interface chip that can be assembled with different PMMA/PDMS microchannel chips.

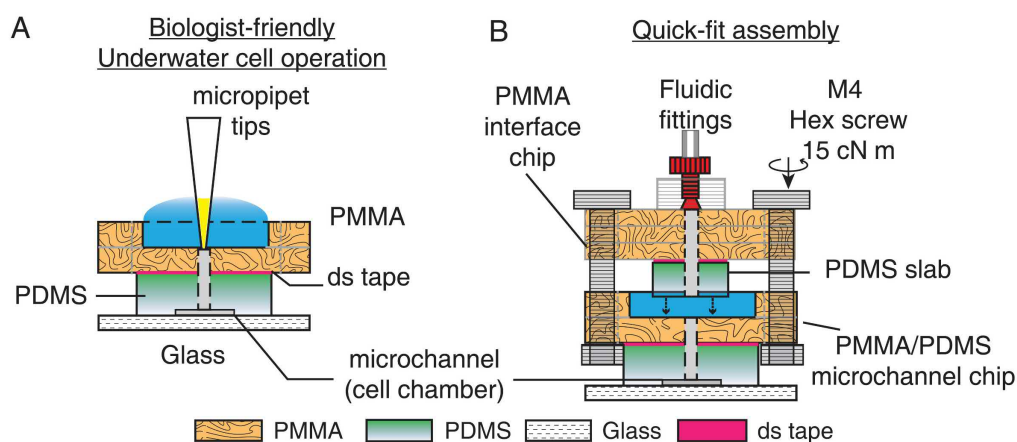


Figure 2.25: Liquid manipulation on the SFEFC. (A) Operator-friendly underwater fluid manipulation at early stage of chip preparation using the PMMA/PDMS microchannel chip. Cells are cultured in the microchannels in the PMMA/PDMS chip; (B) The complete chip can be assembled just prior to on-chip experiments. The PMMA top interface chip is shown in red dashed box. PDMS slabs on the PMMA top interface chip compress and seal the interface to the PMMA/PDMS microchannel chip (inside the black dashed box). After each experiment, the cells in the PMMA/PDMS microchannel chip can be easily recovered after disassembly.

2.4.1 SFEFC microfluidic chip design: concurrent shear flow and electric field conditioning

The microchannel design in the SFEFC was constructed to create multiple electric fields in an R-2R resistor ladder configuration^{202,455} similar to the single-layer channel design in Section 2.3. Two 2 mm-wide main microchannels with interconnected 100 μm by 1.5 mm (length \times width) channels at a spatial interval of 7.5 mm in SFEFC created 10 channel segments with various electric field strengths (EFSs) (Figure 2.26). The segments on the top side of SFEFC had electric current vector flowing against the shear flow direction, while the segments on the bottom side of SFEFC had electric current vector flowing along the shear flow direction. This multiplex configuration provided a platform for high-throughput screening of cellular responses to coexisting shear flow and electric field. Cells were observed only in the 4.5 mm-long observation

area, in the middle of each segment, 1.5 mm from the interconnection channels (where the electric fields were stable).

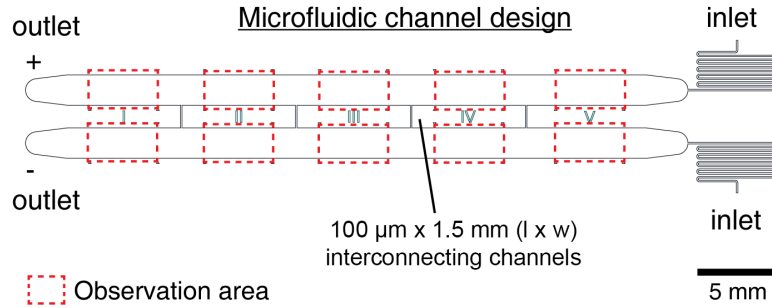


Figure 2.26: Channel design in the PMMA/PDMS microchannel chip in SFEFC.

Electric circuit modeling The electrical equivalent circuit of SFEFC is shown in Figure 2.27. Each segment of the microfluidic channel network was regarded as an electrical resistor in which relative electrical resistances were calculated and modeled by Ohm’s law and Kirchhoff’s circuit laws. In the equivalent circuit, the endpoint of R_5 and R_{14} , the adjacent segments from both inlets, were open in the electric circuit. No electric current was flowing through them. Cells in the two segments were only subjected to shear flow.

According to Ohm’s law, the electrical resistance of a resistor, R , was proportional to the length and inversely proportional to the cross-sectional area:

$$R = \rho \frac{l}{A} = \frac{\rho l}{w \times h}, \quad (2.25)$$

where ρ , l , A , w , and h were the electrical resistivity of the medium, the length, the cross-sectional area, the width, and the height of the microchannel, respectively. Assuming the electrical resistance of R_1 being r , the relative electrical resistances of other segments ($R_2 : R_{14}$) could be calculated accordingly.

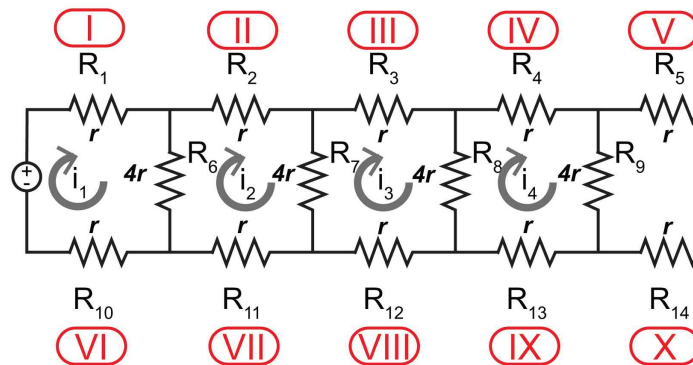


Figure 2.27: The electric equivalent circuit of SFEFC.

The electric current flowing through each resistor was calculated by Kirchhoff’s

circuit law and simulated in the electronic design automation software (OrCAD Lite, Cadence Design Systems, USA) by:

$$10r \times i_2 - 4r \times i_1 - 4r \times i_3 = 0, \quad (2.26a)$$

$$10r \times i_3 - 4r \times i_2 - 4r \times i_4 = 0, \quad (2.26b)$$

$$10r \times i_4 - 4r \times i_3 = 0. \quad (2.26c)$$

By solving the system of equations in Equation 2.26, the ratio of electric currents between each segment, hence the ratio of electric field strengths, was derived in Equation 2.27:

$$i_1 : i_2 : i_3 : i_4 = E_I : E_{II} : E_{III} : E_{IV} : E_V \quad (2.27a)$$

$$= E_{VI} : E_{VII} : E_{VIII} : E_{IX} : E_X \quad (2.27b)$$

$$= 10.5 : 5.2 : 2.5 : 1 : 0. \quad (2.27c)$$

Numerical simulation of electric field in SFEFC The 3D design model of the aforementioned microfluidic chip was exported from AutoCAD and imported into COMSOL Multiphysics 5.3 (COMSOL Inc, USA). Steady-state coupled simulation of creeping flow and direct current electric field were performed in three dimension by solving Navier-Stokes equations and Maxwell's equations. An aqueous medium with dynamic viscosity of 0.75 mPa·s, electrical conductivity of 1.44 S m⁻¹, density of 1001.7 kg m⁻³, and a relative permittivity of 80 were used to model endothelial cell growth medium used for the study (Appendix A)³⁹⁸.

In the SFEFC, 10 segments with combinations of shear flow (fixed shear stress of 1 Pa) and varying electric field strengths provided possibilities for high-throughput experiments (Figure 2.28).

The simulated EFS ratio, when an electric current of 86.4 μA was carried from one outlet of the SFEFC to the other outlet, is shown in Equation 2.28:

$$E_I : E_{II} : E_{III} : E_{IV} : E_V = E_{VI} : E_{VII} : E_{VIII} : E_{IX} : E_X \quad (2.28a)$$

$$= 9.72 : 4.97 : 2.44 : 1 : 0. \quad (2.28b)$$

2.4.2 Microfluidic chip fabrication

Fabrication of PMMA chips The PMMA interface chip (Figure 2.25) was fabricated by patterning fluidic connections, inlets/outlets, salt bridge (SB) connections, and M4 screw clamp slots on three 0.5 mm-thick PMMA sheets (CM-205x, Chi-Mei Corp, Taiwan), by using a CO₂ laser scribe (VLS3.50, Universal Laser Systems, USA). The PMMA sheets were joined by thermal bonding, as described in Section 2.3.2. Adapters with M6 threads (SPC-M6-C, Nabeya, Japan) were glued onto the PMMA chip using a UV adhesive (3301, Loctite, USA). 2 mm-thick PDMS slabs punched with

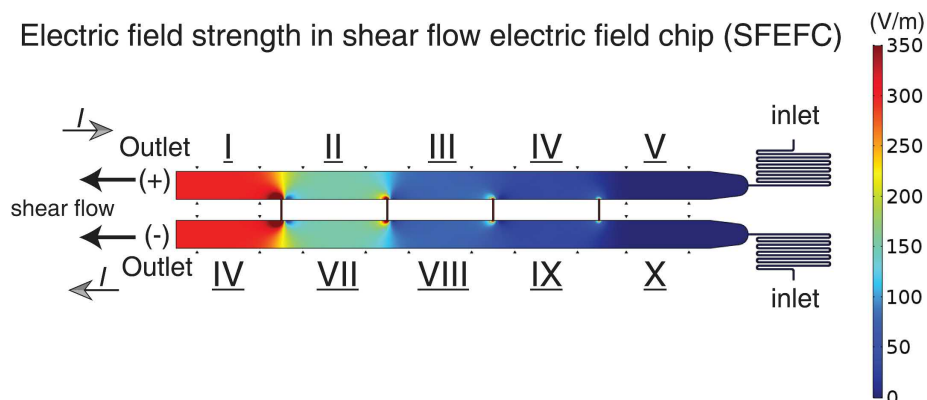


Figure 2.28: Numerical results of electric field strength in the shear flow and electric field co-stimulation microfluidic chip (SFEFC). SFEFC features 10 segments with coexistent electric field and shear flow. I denotes electric current. From sections I to IV, the shear flow flows against the electric current direction, while in sections VI to IX, the shear flow flows along the electric current vector.

inlet and outlet holes (1 mm) were affixed to the interface chip using a dual-energy silicone/acrylic double-sided tape (85 μm thick, No. 5302A, Nitto Denko, Japan).

Similar to the interface chip, the PMMA component of the PMMA/PDMS microchannel chip was fabricated by patterning liquid reservoirs, inlets, outlets, and screw clamp slots on two 2 mm-thick PMMA sheets. The PMMA pieces were again thermally bonded.

Fabrication of PDMS chip The PDMS channel chip was fabricated by the soft lithography method as described in Section 2.3.2³²³. The single-layer master mold (100 μm -thick SU-8 3025) was fabricated following steps as described in previous sections. After the master mold was treated with perfluorosilane, PDMS devices were fabricated by casting against the master mold.

The PMMA/PDMS chip was assembled by joining the bonded PMMA component and the PDMS microchannel component with the silicone/acrylic double-sided tape (No. 5302A, Nitto, Japan). The PMMA/PDMS microchannel chip was completed by bonding the joined PMMA/PDMS piece to a coverglass (60 \times 24 mm, No. 1.5H, Paul Marienfeld GmbH, Germany) after O₂ plasma treatment (AP-300, Nordson MARCH, USA). The coverglass was washed thoroughly in an industrial cleaning solution (1% TFD4, Franklab, France), ultrapure water, and dried under nitrogen gas prior to bonding.

2.5 Summary and prospects

I have developed versatile hybrid PMMA/PDMS microsystems, which offers tremendous potential for manipulation of microenvironment, reagent conservation, and live cell imaging. However, the high degree of miniaturization demands that microsystems be tailor made for specific biological applications. Establishment of robust platform is

the first step toward studying biology in quantitative terms. Specifically, I have created three different microsystems suitable for cell culture and stimulating them with different physical and chemical stimulations in thermoplastics or hybrid thermoplastics/elastomer devices. The hybrid composition approach combines the advantages of different materials and offers versatility for designing complex 3D design to manipulate microenvironment while mitigating some of the disadvantages of each material. Despite of seemingly complicated composition, the hybrid devices can be rapidly prototyped and fabricated, thus they are suitable for rapid research development in laboratory settings.

Chapter 3

Usiigaci: Single cell segmentation and tracking in label-free phase contrast microscopy enabled by machine learning

Abstract

Label-free single-cell segmentation and tracking is tantamount to the holy grail of microscopic cell migration analysis. Contrast-enhanced brightfield microscopy techniques including the phase contrast microscopy (PCM) can provide vivid stain-free cell visualization. However, these brightfield images with cells at high density are notoriously difficult to segment accurately; thus, manual segmentation remains the *de facto* standard practice. In this work, I develop Usiigaci, an all-in-one, semi-automated pipeline to segment, track, and visualize cell movement and morphological changes in PCM. Cell-labeling-free, instance-aware segmentation is accomplished using a mask regional convolutional neural network (Mask R-CNN). A TrackPy-based cell tracker with a graphical user interface is developed for cell tracking and data verification. The performance of Usiigaci is validated with electrotaxis of NIH/3T3 fibroblasts and outperforms several open-source software dedicated for PCM cell analysis. Usiigaci provides highly accurate cell movement and morphological information for quantitative cell migration analysis⁴⁵⁷.

3.1 Introduction

Cell migration is a fundamental cell behavior that underlies fundamental physiological processes, including development, tissue maintenance, immunity, and tissue regeneration, as well as pathological processes such as cancer metastasis. Many *in vitro* as well as *in vivo* platforms have been developed to investigate molecular mechanisms underlying cell migration in different microenvironments with the aid of microscopy. Using microfluidic platforms, high throughput cell migration experiments can be performed to obtain hundreds and thousands of cell microscopy images at short time intervals in a single experiment.

The movement and morphology changes of single- as well as collective-cell migration are the core characteristics of cell response to gradients in the microenvironment,

such as shear stress, surface topology, chemical gradient, and electric field^{379,458–460}. The holy grail of cell migration analysis is tantamount to quantitative analysis of detailed single-cell level behavior by segmentation and tracking of each individual cells. However, the data analysis of cell microscopy images associated with high throughput experiments remains a challenging task to both biomedical engineers and biologists due to imperfect cell segmentation and tracking⁴⁶¹, thus limiting the overall experimental throughput.

Among bright-field microscopy techniques, Zernike's phase contrast microscopy (PCM) is favored by biologists for its ability to translate phase differences from cellular components into amplitude differences, so as to make the cell membrane, the nucleus, and vacuoles more visible⁴⁶². However, PCM images are notoriously difficult to segment correctly using conventional computer vision methods, due to the low contrast between cells and their background⁴⁶³. Although advances in quantitative phase imaging (QPI) by holography, ptychography, or interferometry can provide quantitative phase information of cells instead of amplitude difference as in PCM and make segmentation easier, the QPI techniques are not widely adopted by biologist as they require delicate optical setup and alignment^{464,465}. For these reasons, many cell migration experiments still rely on fluorescent labeling of cells or manual tracking. Fluorescent labeling of cells requires transgenic expression of fluorescent proteins or cells tagged with fluorescent compounds, both of which can be toxic to cells and which require extensive validation of phenotypic changes. Although thresholding fluorescent images is relatively straightforward, cells that are in close proximity are often indistinguishable in thresholded results. On the other hand, manual tracking of cell migration is labor-intensive and prone to operator error⁴⁶⁶.

To complement high throughput microscopy experiments, the data analysis must be automated. Moreover, although many software packages have been developed for cell tracking, the majority of them handle only fluorescent images and require good thresholding results⁴⁶⁷. While some software packages tackle stain-free cell tracking, outlining each individual cell accurately to the cell boundary remains difficult and often yields suboptimal results. Without single-cell level segmentation, accurate single-cell tracking is not possible. Therefore, these packages are limited to positional tracking and cannot resolve adjacent or touching cells^{467–471}. Moreover, migrating cells in ameboid or mesenchymal mode often have thin protruding cellular structures for locomotion, such as blebs or lamellipodia⁴⁷². These structures exhibit very low contrast even in PCM, which prevents reliable segmentation, even though they are essential for cell migration. For detailed discussion of computational methods for microscopy image analysis, the reader is referred to review texts^{466,473,474}.

In recent years, accurate segmentation and classification of cells or tissue under microscopy using machine learning methods such as convolutional neural networks (CNNs) and generative adversarial networks (GANs) have been demonstrated^{475–480}. Ronneberger *et al.*, first demonstrated that using supervised training of a fully-convolutional CNN, U-net, cell outlines in PCM can be segmented accurately⁴⁷⁵. Further, Van Valen *et al.*, proposed the Deepcell CNN architecture to classify background, cell membrane, and cytoplasm in pixel-wise manner. Cells can be segmented accurately from the pixel classification even when cells are in high density and in close proximity to each other⁴⁷⁶. However, in Deepcell, fluorescent staining of cell nuclei is still needed for

optimal segmentation of PCM images. The fact that the high accuracy and flexibility of the machine learning could even surpass that of specialists has stimulated the biomedical community to adapt machine learning techniques for automated medical image analysis^{481–483}.

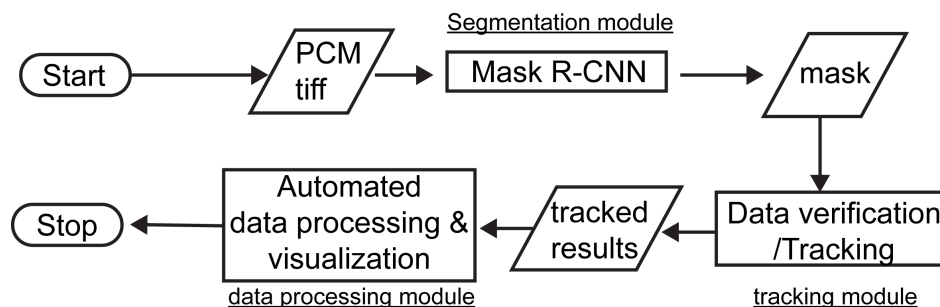


Figure 3.1: Workflow of Usiigaci. PCM images are processed in a Mask R-CNN segmentation module into instance-segmented masks. Objects in the masks are linked and tracked in a Trackpy-based tracking module. Cell migration parameters and plots are generated automatically in the data processing module.

To address the above challenges, I introduce Usiigaci, an all-in-one, semi-automated pipeline to segment, track, and visualize cell movement and morphological changes in stain-free PCM images. Usiigaci, pronounced as */ushi:gachi/* by Hepburn romanization, is a Ryukyuan word, ウシーガチ, that refers to tracing the outlines of objects (透き写し in Japanese), which is an appropriate description of the function of our software. Stain-free segmentation is appealing to biologists because cells are free of labeling damage and their analyses do not suffer from false readings. Usiigaci is composed of three independent modules: a segmentation module, a tracking module, and a data processing module (Figure 3.1). Instance-aware segmentation is first performed using a mask regional convolutional neural network (Mask R-CNN). The segmented masks are then tracked using a Trackpy-based cell tracker with a graphical user interface (GUI). Single cell migration variables and visualizations are generated automatically in the data processing module afterward. The work presented in this chapter is published in *SoftwareX*⁴⁵⁷.

I first describe the architecture and segmentation performance of Usiigaci benchmarked with existing software packages such as PHANTAST⁴⁷⁰, Fogbank⁴⁷¹, and Deep-cell⁴⁷⁶. Next, the multiple object tracking (MOT) performance of Usiigaci tracking module is evaluated using MOT metrics^{484,485}. Finally, the usability of Usiigaci for analysis of cell migration is evaluated by single cell migration variables in biological context with a dataset of NIH/3T3 fibroblasts electrotaxis.

3.1.1 Computational cell migration analysis

Cell migration is a dynamic process involving complex cellular signaling and can be categorized as single cell or collective cell migration. In single cell migration, cells migrate individually by interacting with the extracellular matrix (ECM) such as immune cells migrating in tissues and neural stem cells migrating between cortical layers. Cells

can also establish cell-cell contact and move as multicellular units in collective cell migration^{486,487}, such as the epithelial sheet migration in wound healing⁴⁸⁸.

Contemporary, *in vitro* 2D and 3D cell migration platforms are preferred over *in vivo* platforms for lower cost, easier experimental workflow, and lower biological variation. Single cell migration on *in vitro* platforms can be analyzed under high-resolution microscopes^{466,489}. Using molecular biology tools and optical techniques, cellular behavior and subcellular components can be identified for cellular phenotype, lineage, and molecular mechanisms^{474,490,491}.

Under time-lapse microscopy, cell images can be sampled and the features of the cells can be extracted reliably if the Nyquist sampling theorem is satisfied for the tracking⁴⁹². Guided by directional cues in the microenvironment, cell displaces and changes morphology to respond to the cue (Figure 3.2). Given the trajectory, the step-centric variables and cell-centric variables can be derived (Table 3.1). The step-centric variables are computed for a single cell migration between each consecutive time frames. The cell-centric variables describe a cell track by summing the step-centric data across all time frames. By analysis and categorization of cell migration patterns, phenotypes of cell migration can be identified using principle component analysis or cluster analysis^{474,491,493}.

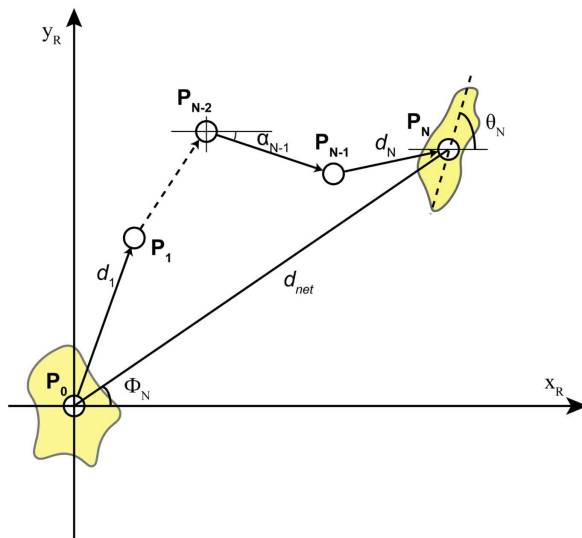


Figure 3.2: The single-cell migration parameters extracted from the electrotaxis experiments.

By analysis of microscopy images, several cell tracking data results can be obtained (Figure 3.3). Valid cell tracks that are tracked correctly are the data that is of users' interest (Figure 3.3). However, depending on the accuracy performance of the tracker, interrupted cell tracks or erroneous tracking may happen (Figure 3.3.B.G.H). Also, cells can undergo mitosis during the experiment and splits into two daughter cells, which the tracking no longer represents single cell migration (Figure 3.3.C). Moreover, in an actual microscopy experiment, there will be cells entering the view field, exiting the view field, or suddenly detaching from the substrate during the experiment (Figure 3.3.D-F).

Table 3.1: Step-centric and cell-centric variables for describing single-cell migration.

Step-centric features	
Instantaneous displacement	$d_i = \sqrt{(x_i - x_{i-1})^2 + (y_i - y_{i-1})^2}$
Instantaneous speed	$s_i = d(p_{i-1}, p_i) / \Delta t$
Turning angle	$\alpha_i = \tan^{-1} \frac{(y_i - y_{i-1})}{(x_i - x_{i-1})}$
Directional autocorrelation	$dir - aut_i = \cos(\alpha_i - \alpha_{i-1})$
Cell-centric features	
Cumulative distance	$d_{total} = \sum_{i=1}^N d(p_{i-1}, p_i)$
Net trigonometric distance (Euclidean distance)	$d_{net} = d(p_0, p_N) = \sqrt{(x_N - x_0)^2 + (y_N - y_0)^2}$
Euclidean velocity	$\bar{v}_{net} = \frac{d_{net}}{t_{elapsed}}$
End-point directionality ratio	$ep_dr = \frac{d_{net}}{d_{tot}}$
Orientation	$Index_{orientation} = \sum_{i=1}^N \frac{\cos 2\theta_i}{N}$
Directedness	$Index_{directedness} = \sum_{i=1}^N \frac{\cos \Phi_i}{N} = \sum_{i=1}^N \frac{(x_i - x_0)}{d_{net} \times n} = \frac{1}{N} \sum_{i=1}^N \frac{(x_i - x_0)}{\sqrt{(x_i - x_0)^2 + (y_i - y_0)^2}}$

A good single cell migration tracking software should yield high amount of valid cell tracks while avoiding erroneous cell tracks that may lead users to derive misleading interpretation from the data. Since the tracking algorithm may not be perfect, if the software builds in a validation function for users to check the tracked data, the potential impact of erroneous tracking can be avoided^{467,494}. How different cell tracks affect the cell tracking will be discussed in detail in section 3.3.2.

In summary, quantitative cell migration analysis provides high resolution cell information that can be used to construct *in silico* cell migration models, drug discovery, and cell phenotype profiling. Understanding single cell biology demands an analytical tool that provides high resolution and accurate single cell information.

3.2 Software architecture

I explain Usiigaci’s architecture by its three modules: segmentation, tracking, and data analysis modules.

3.2.1 Segmentation module

In the segmentation module, PCM images are segmented into instance-aware masks using a mask regional convolutional neural network (Mask R-CNN) proposed by He *et al.*⁴⁹⁵. The Mask R-CNN model is implemented in TensorFlow and Keras, as originally open-sourced by Matterport Inc. under the MIT license^{496–498}.

A detailed diagram of Mask R-CNN architecture is shown in Figure 3.4. The Mask

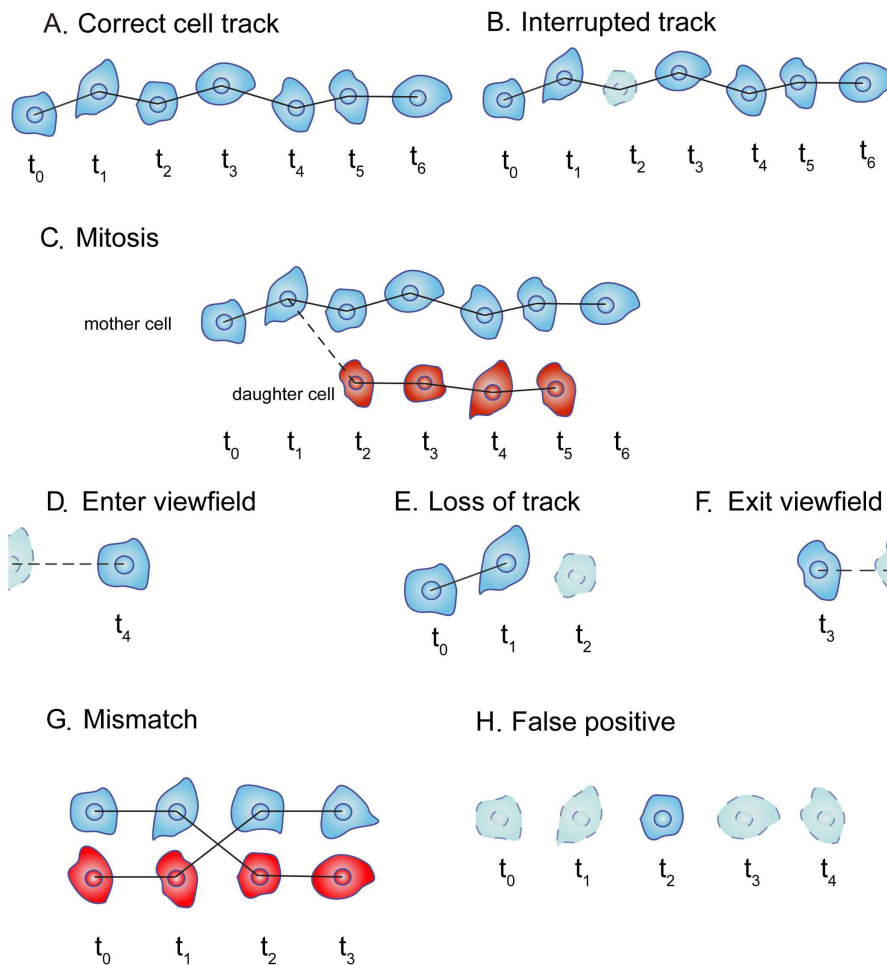


Figure 3.3: Types of cell tracking results. (A) Valid cell tracks that are identified consistently and tracked correctly in every frame throughout one time lapse experiment; (B) Interrupted cell tracks that are tracked correctly (>80% of the time) from start to end in one time lapse experiment but the data is missing in one or a few frames within the experiment; (C) Mitosis cell tracks in which cells undergo mitosis and split into daughter cells. The tracking can no longer represent true single cell migration; (D) Cell tracks entering the view field in the middle of the time lapse experiment; (E) Cell tracking fails in the middle of the time lapse experiment; (F) Cell tracks exiting the view field in the middle of the time lapse experiment; (G) Cell tracks that are linked incorrectly in tracking; (H) False positive cell tracks identified by tracker due to primarily segmentation artifacts. Tracking results in (B – F) are considered as invalid tracks.

R-CNN model is built upon the Faster R-CNN model that has achieved rapid identification of objects through searching regions of interest (ROIs) on feature maps^{495,501}. Raw images undergo multiple convolutional operations in a R-CNN backbone, which is composed of a residual function network (ResNet-101⁴⁹⁹) and a feature pyramid network (FPN⁵⁰⁰), to generate 5 feature maps (C1 to C5). ROIs are searched on feature maps using region proposal layers. An accurate instance-segmented ROI map is generated by an ROI align layer to correct for misalignment in the ROI Pooling opera-

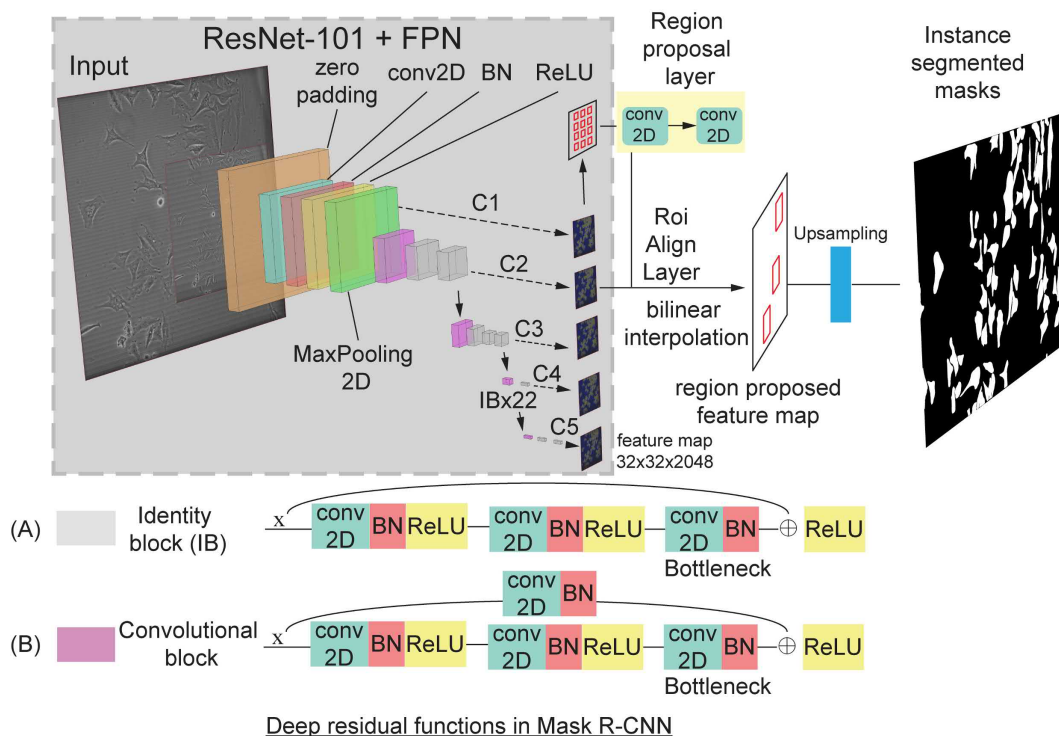


Figure 3.4: Detailed architecture of Mask R-CNN module in Usiigaci The backbone of Mask R-CNN model is a combination of 101-layer deep residual network (ResNet-101)⁴⁹⁹ and feature pyramid network (FPN)⁵⁰⁰. The ResNet-101 is a deep residual network composed by two types of deep residual functions: (A) identity block and (B) convolutional block.

tion. After upsampling, entire outlines of individual cells are segmented into polygons bearing unique identifiers (IDs) in the exported mask. As a result, highly accurate, instance-aware segmentation of stain-free PCM images is realized.

Training

Training data preparation and annotation Most of publicly accessible dataset available for benchmarking segmentation or tracking algorithms are based on fluorescent images⁵⁰². A large publicly accessible brightfield microscopy dataset is not available until recently⁵⁰³. To accurately segment cells in microscopy images, the Mask R-CNN model must be trained to be specific toward cells. Thus, I prepared training images using our microscopy setup as the dataset.

Mouse embryonic NIH/3T3 fibroblasts (CRL-1658, American Type Culture Collection, ATCC, USA) and T98G glioblastoma cells (CRL-1690, ATCC, USA) were cultured and maintained according to guidelines provided by ATCC. NIH/3T3 cells were cultured in Dulbecco's modified Eagle's medium (12800017, DMEM, Gibco, USA) supplemented with 2.2 g L^{-1} NaHCO_3 and 10% iron-fortified calf serum (CS, Sigma-Aldrich, USA). T98G cells were cultured in minimum essential medium alpha (12000022, MEM α , Gibco, USA) supplemented with 2.2 g L^{-1} NaHCO_3 and 10% fetal bovine serum (FBS, Gibco, USA). Both cell lines were cultured in a humidified 5% CO_2 at-

mosphere (MCO-18AIC, Sanyo, Japan) and subcultured whenever confluency reached 80%. Cells from passages 5 to 15 were used in the migration study. Fluorescently labeled cells were prepared by incubating 5×10^6 cells with $1 \mu\text{M}$ of CellTracker Green CMFDA dye (Thermo Fisher Scientific, USA) in 1X Dulbecco's phosphate buffered saline (D-PBS, Wako Inc., Japan) for 30 minutes at 37°C according to the protocol provided by the manufacturer. Cells were washed once in D-PBS and seeded into microfluidic chips for microscopy.

The two channel PMMA thermoplastic microfluidic chip (Chapter 2.2) was used to perform electrotaxis assay as the training data data. Briefly, prior to seeding the cells, the coverglass was coated with $100 \mu\text{g mL}^{-1}$ poly-D-lysine (P6407, Sigma-Aldrich, USA) or Geltrex (A1569601, Gibco, USA) for NIH/3T3 cells and T98G glioma cells for 2 hours at 37°C . 7.5×10^5 cells mL^{-1} were seeded into each channel and allowed to adhere at 37°C . Afterward, the tubing for infusing media and salt bridges were connected to the microfluidic chip containing adhered cells by fittings (IDEX, USA). The chips were moved onto a Nikon Ti-E microscope equipped with an in-house transparent heater made of indium-tin-oxide (ITO) glass. Media were steadily infused at $20 \mu\text{L hr}^{-1}$ using a two-channel syringe pump (YSP-202, YMC, Japan) and a stable $37 \pm 0.1^\circ\text{C}$ temperature was provided using a heater to culture the cells. A stable electrical current ($101.5 \mu\text{A}$ for 300 V m^{-1} EF) was applied with a sourcemeter unit (SMU, 2410, Keithley, USA) through salt bridges (1.5% agarose in 1X D-PBS) with a pair of silver/silver chloride electrodes in 1X D-PBS. Silver/silver chloride electrodes were fabricated by electroplating a pure silver sheet (0.1 mm-thick, Nilaco, Japan) in 1 N HCl (Sigma-Aldrich, USA) after being briefly etched in 20% nitric acid (Sigma-Aldrich, USA)¹⁹⁶.

A Nikon Ti-E microscope with Perfect Focus System and motorized XY stage was used to perform all microscopy experiments. A 10X phase contrast objective and an intermediate magnification of 1.5X were used for phase contrast and epifluorescence imaging. Images were captured with a sCMOS camera with 2×2 binning (Orca Flash 4.0, Hamamatsu, Japan) at 20-minute interval in NIS Element software (Nikon, Japan). The spatial resolution at this setting was $0.87 \mu\text{m pixel}^{-1}$. For fluorescence imaging of CellTracker Green, a FITC-channel filter set was used (FITC-3540C-NTE-ZERO, Semrock, USA) with an Intensi-light fiber mercury lamp (Nikon, Japan) as the excitation light source. The Perfect Focus System was used for all time-lapse experiments and all experiments were performed in triplicate.

After each experiment, images were exported from NIS element as tiff files and automatically organized according to the XY positions using an in-house Python script included in the Usiigaci's source code. The tiff files are then ready for segmentation.

Fifty phase contrast microimages of T98G and NIH/3T3 cells were manually segmented in Fiji ImageJ⁵⁰⁴ with the aid of a drawing tablet (Cintiq pro 16, Wacom, Japan) (Figure 3.5). Briefly, the boundary of each cell was traced manually with the freehand tool in ImageJ and saved into the ROI manager. Indexed masks were created from the manually traced ROIs by using the ROImap function in the ImageJ plugin LOCI⁵⁰⁵. A unique index for each ROI, *i.e.*, for each cell, is essential for instance-aware segmentation and downstream tracking. Phase contrast images were used in tiff format without modification. A Mask R-CNN model pretrained with the Microsoft COCO dataset⁵⁰⁶ was further trained using 50 manually annotated PCM images with

single cell outlines as a classification class. Among the fifty sets of images, forty-five sets of them were used as the training dataset and the rest as the validation dataset.

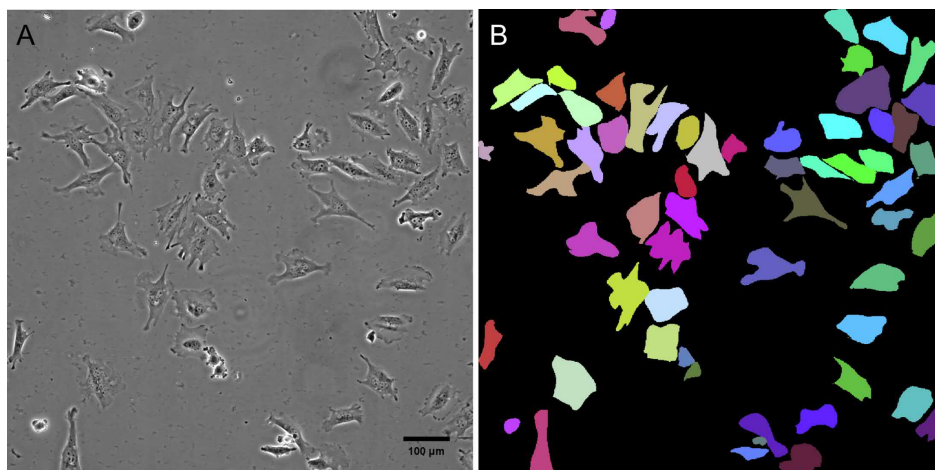


Figure 3.5: An example of the training data for Usiigaci. (A) Phase contrast image of T98G cells on Geltrex-coated substrate; (B) Cell outlines were manually segmented and saved into an 8-bit indexed mask. Each color represents a unique set of cells.

Training setup in Usiigaci and Deepcell The Mask R-CNN model (Figure 3.4) of Usiigaci was trained using our annotated training dataset on top of a pretrained Mask R-CNN model with Microsoft COCO dataset from Matterport Inc.⁵⁰⁶. Additional training of 100 epochs on the feature pyramid network (FPN) headers and 500 epochs on all ResNet-101 layers were carried out under an Ubuntu 16.04 environment with Python 3.4, TensorFlow 1.4, Keras 2.1.2, and CUDA 9.1 on an Alienware 15 laptop equipped with a GTX1070 8GB graphics processing unit (GPU) or a NVIDIA GTX1080Ti 11GB GPU (Manli, Hong Kong) mounted on an Alienware amplifier (Dell, USA).

In addition, to compare with Deepcell, a state-of-the-art machine learning based cell segmentation software, a TensorFlow implementation of Deepcell from the original authors was modified to use only the phase contrast channel for segmentation⁴⁷⁶. The modified Deepcell was trained from scratch using the aforementioned 50 sets of manually annotated training data. The sample size and training time per epoch were compared between Usiigaci’s Mask R-CNN module and Deepcell in subsample mode and fully convolutional mode (Figure 3.6). In the subsample mode of Deepcell, training data were split into small batches based on the set window size to increase arbitrary training samples, and the computation time required to complete an epoch increased. A moderate computational performance improvement was observed when using a GPU that had more CUDA cores (GTX1080Ti). Usiigaci’s Mask R-CNN model and Deepcell in fully convolutional mode used full-size images for training with simple image augmentation performed at the start of every epoch. Therefore, the time required to complete an epoch was shorter compared to Deepcell in subsample mode, but more epochs were needed to increase the accuracy of the results. Training of Mask R-CNN

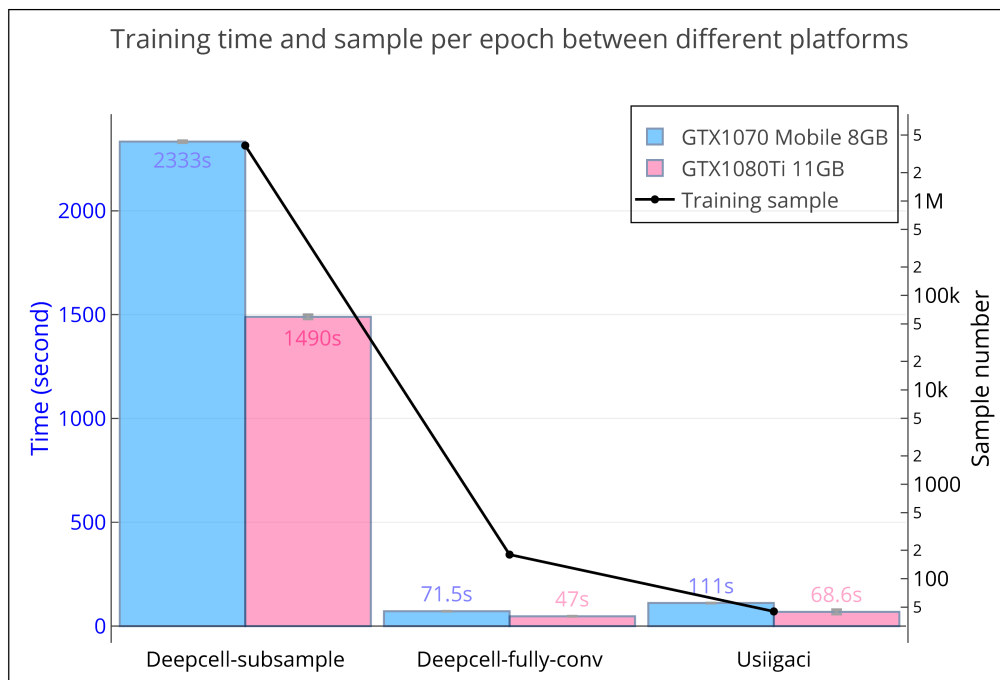


Figure 3.6: Comparison of training time and sample number per epoch using Usiigaci and Deepcell in subsample mode and in fully convolutional mode.

took only slightly more time than Deepcell despite more layers and trainable parameters in the Mask R-CNN model because the Mask R-CNN had already been trained for edge detection with the Microsoft COCO dataset (101 layers, 64.7 million parameters compared to 25 layers and 0.46 million parameters in Deepcell).

When morphologies of the cells or microscopy optical configurations change significantly, retraining the neural network may be necessary for optimal results. A training script was provided as part of the source code to allow users to train new Mask R-CNN models based on their own data for best performance after proper training data annotation as described previously. The best model was selected by observing accuracy and loss during the validation step in training. In Usiigaci’s Mask R-CNN segmentation module, it is essentially a two-class segmentation system, background and whole-cell outlines. Several hyper-parameters for training can be adjusted by users, such as neural network backbone configuration, threshold for region proposals network, and number of anchors for regional proposal networks.

Deployment

Deployment was performed under the same environment as training with GPU acceleration of either a NVIDIA GTX1070 8GB GPU or a NVIDIA GTX1080Ti 11GB GPU. The inference python script for deployment allowed users to specify a folder path with

nested folders, and Usiigaci segmented all images in each nested folder and created 8-bit indexed mask images with each cell possessing a unique identifier.

The essential blocks in convolution neural network use probability, so segmentation errors may exist between the results segmented between different model weight extracted at the end of different epochs. To obtain an average result, segmentation with multiple trained model weights and averaging among the results can be specified in the inference python script in Usiigaci if necessary.

3.2.2 Tracking module

After Mask R-CNN's instance-aware segmentation, each mask contains segmented cell outlines that bear unique IDs. The IDs are then used for linking and tracking in the tracking module built on the Trackpy library⁵⁰⁷. The features of an ID, such as location, equivalent diameter, perimeter, eccentricity, orientation, and true solidity, are used as parameters in Trackpy for tracking. IDs in each consecutive mask in a time-lapse experiment belonging to the same cell are searched by the Trackpy library using its default nearest neighbor search option, namely the k-dimension tree algorithm^{508–510}.

Linking and tracking are followed by automatic post-processing, where segmentation and tracking results are corrected in two steps. In the first step, a cell wrongly segmented as two IDs is corrected by merging the two IDs. In the second step, IDs in consecutive frames belong to the same track, but suffering from interrupted events are re-linked. A GUI based on the PyQt and PyQtGraph library for the tracking module is developed so that users can verify segmentation and tracking results^{511,512} (Figure 3.7). Manual verification is important because imperfections in segmentation can cause errors in tracking.

In addition, cells that undergo mitosis and cells that enter or exit the view field during the experiment generate tracking results that are not meaningful in single cell migration studies (Figure 3.3). In the GUI of the tracking module, by imposing a simple criterion, *select complete tracks*, the valid tracks containing IDs of ROIs exist in every frame, can be selected. Thereafter, users can manually verify whether the tracking is correct by cross-referencing against raw images. The amount of labor in the proposed workflow is less than that associated with conventional manual tracking³⁷⁹. Subsequently, centroid and morphology parameters such as angle, perimeter, and area of each ID in valid tracks can be extracted and produced using the scikit-image library⁵¹³. The results are saved into spreadsheets that can be analyzed by users using the data processing module or other statistical software.

3.2.3 Data processing module

Analysis of single-cell migration data is accomplished in the data processing module to compute migration parameters for each ID throughout the time-lapse experiment (Figure 3.2). Several data processing libraries, including the Python data analysis library (Pandas), NumPy, and SciPy, are used for processing cell migration data^{514–516}. Step-centric and cell-centric features, such as turning angle, net trigonometric distance, speed, orientation, and directedness are computed automatically in a Jupyter Notebook^{196,517} (Table 3.1). Moreover, automated visualization of cell migration in cell

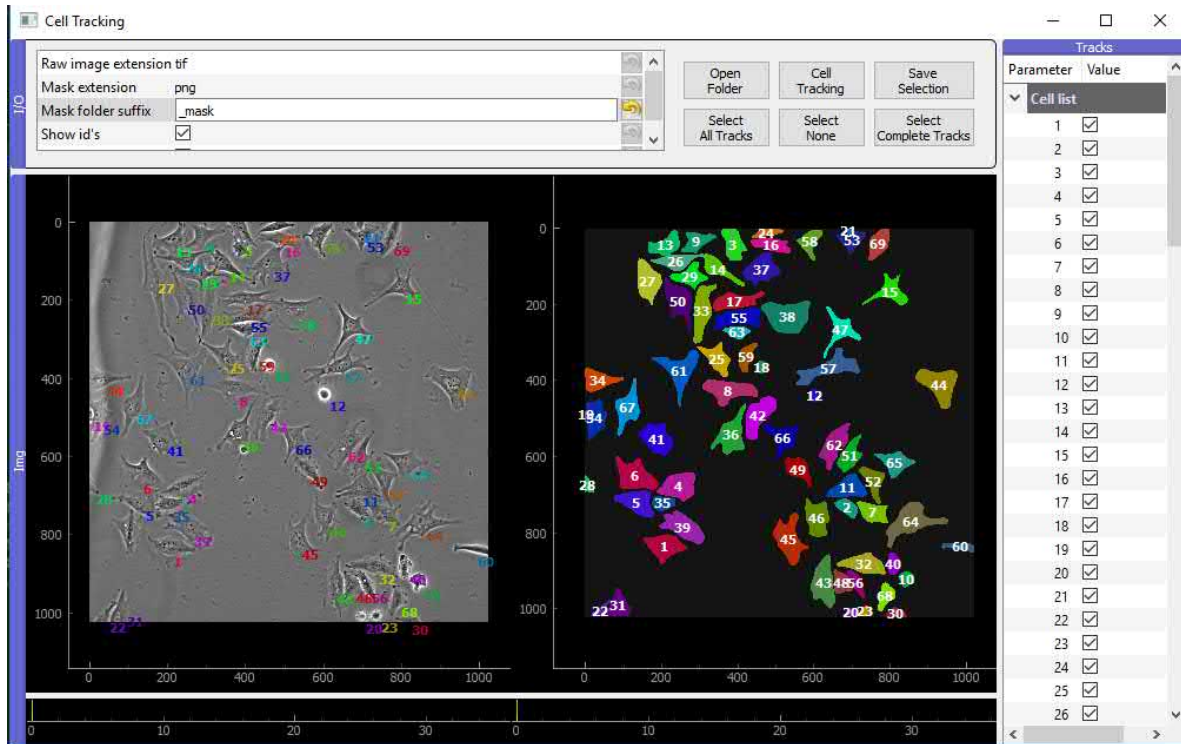


Figure 3.7: The GUI of the tracking module in Usiigaci. PCM images of a time-lapse experiment are shown in the left panel to compare with the Mask R-CNN segmented masks in the right panel. After tracking, cell tracks are listed on the right and users can verify data against PCM images and exclude bad cell tracks.

trajectory plots, box plots, and time-series plots is generated with the aid of Matplotlib and Seaborn plotting libraries (Figure 3.8)^{518,519}.

The data processing module of Usiigaci could import data output by ImageJ, Usiigaci tracker, Imaris, or Metamorph. Step-centric and cell-centric variables to quantify cell migration were computed automatically (Table 3.1). Results were exported into spreadsheets and could be reanalyzed in other statistical software. Visualizations of cell migration were also automatically generated by the data processing module (Figure 3.8). The module was written in Python syntax so that it could be easily reused if particular functionalities were needed.

Based on the three modules described above, Usiigaci provides an all-in-one, semi-automated solution for stain-free cell migration analysis in PCM, with a biologist-friendly workflow.

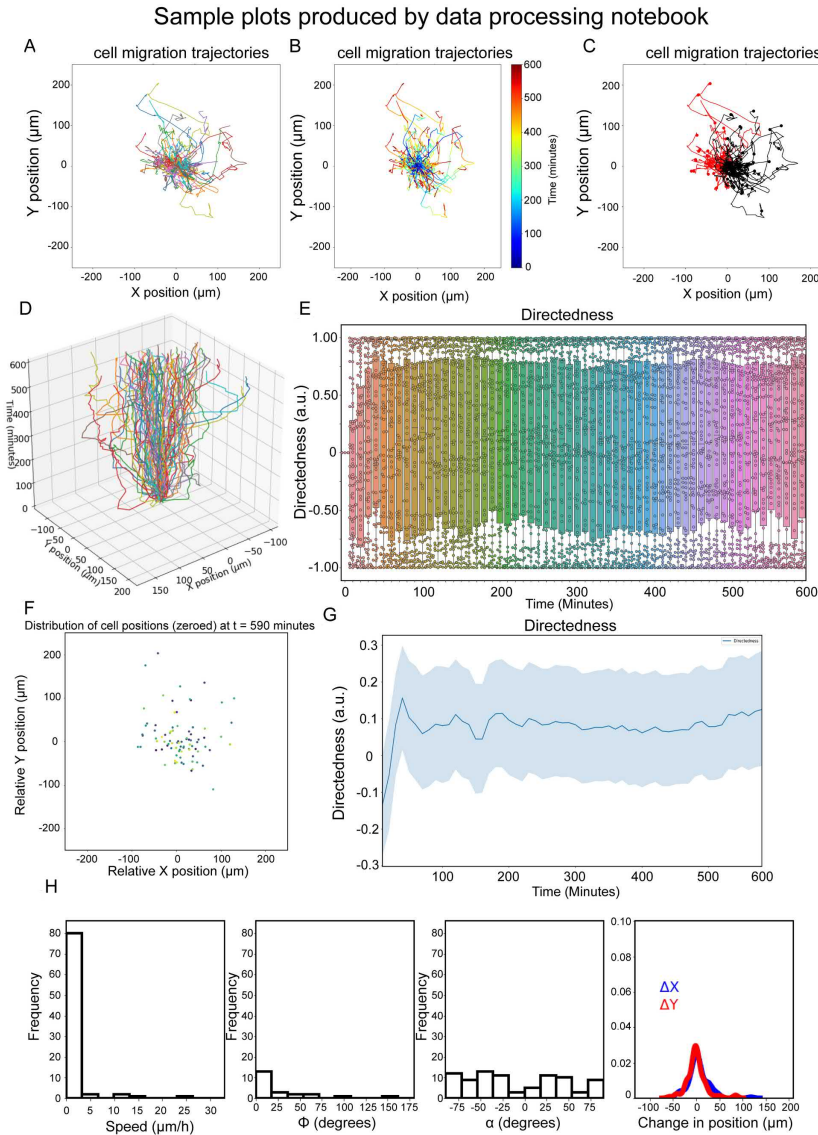


Figure 3.8: Visualization examples of NIH/3T3 random cell migration generated automatically by the data analysis module. (A) Cell migration trajectory plot with each track represented by a color; (B) Cell migration trajectory plot with cell track segments colored by time; (C) Cell migration trajectory plot with coloring depending on the displacement of cells in the x direction; (D) 3D representation of cell migration trajectory; (E) Box plots of cell migration directedness versus time; (F) Cell migration represented in a scatter plot; (G) Time series plot of directedness in a time lapse experiment; (H) Frequency histogram plots of cell migration speed, orientation, turn angle, and change in positions.

3.3 Performance benchmark for cell segmentation and tracking

3.3.1 Cell segmentation accuracy evaluation

Phase contrast microscopy images of NIH/3T3 mouse fibroblast electrotaxis under 300 V m^{-1} direct current electric field (dcEF) for 10 hr in the microfluidic chip were collected (Figure 2.10). The experiments were performed in triplicates. Segmentation similarity of Usiigaci was compared with existing state-of-the-art free software for cell segmentation, including fluorescent thresholding in ImageJ⁵⁰⁴, PHANTAST⁴⁷⁰, Fogbank⁴⁷¹, and Deepcell⁴⁷⁶. The ImageJ versions of Fogbank and PHANTAST were used for segmentation similarity evaluation. Segmentation similarity was compared against human segmentation (manual reference) by segmentation evaluation metrics (Figure 3.9 & Table 3.2). True positive (TP), true negative (TN), false positive (FP), and false negative (FN) metrics were extracted by comparing the manual reference and segmentation results. Jaccard index and F1 scores were calculated for each segmentation method.

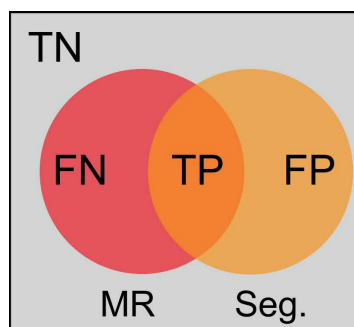


Figure 3.9: Segmentation performance evaluation. MR: Manual reference; Seg.: Segmentation results; FN: False negative; TP: True positive; FP: False positive; TN: True negative.

3.3.2 Cell tracking accuracy evaluation

In each experimental dataset, different tracking results could be identified and categorized to describe the performance of a tracker using multiple object tracking metrics (Figure 3.3 & Table 3.3)^{484,485}. In this dataset, valid single cell migration tracks were the data of interest. However, due to segmentation errors and tracking errors, the data also contained several invalid tracking results, such as interrupted tracks, mitosis tracks, loss of tracking, objects entering or exiting view field, mismatch tracks, and false positive tracks (Figure 3.3). Interrupted tracks were tracks that were tracked correctly most of the time ($>80\%$ of time) but missing partial information. Mitosis tracks contained cells that had undergone mitosis, thus could no longer represent true single cell migration. Tracks containing cells that were lost, entering, or exiting view field early in the experiment could not be analyzed either. Mismatch and false positive cell tracks must also be excluded.

Table 3.2: Segmentation evaluation metrics to describe the similarity between manual reference (MR) and segmentation (Seg.) results.

Segmentation evaluation metrics	
True positive	$TP = MR \cap Seg.$
True negative	$TN = MR \cup Seg.$
False positive	$FP = Seg. - MR$
False negative	$FN = MR - Seg.$
Jaccard index (IoU)	$Index_{Jaccard} = \frac{TP}{FN+TP+FP}$
F1 score	$F1 = \frac{2TP}{2TP+FP+FN}$
Precision	$Precision = \frac{TP}{TP+FP}$
Recall	$Recall = \frac{TP}{TP+FN}$
Specificity	$Specificity = \frac{TN}{TN+FP}$
Accuracy	$Accuracy = \frac{TP+TN}{TP+TN+FP+FN}$

Using the multiple object tracking metrics in computer vision, I used the multiple object tracking precision (MOTP) and multiple object tracking accuracy (MOTA) to benchmark Usiigaci’s tracker performance against manual tracking by a human operator (thesis author). The multiple object tracking precision (MOTP) described the total error in estimated positions for matched object-hypothesis pairs over all frames, averaged by the total number of matches recognized⁴⁸⁴. MOTP showed the ability of the tracker to estimate precise object positions. I described the MOTP by means of average pixel level precision by comparing the polygon shape of each object between the manual reference and the segmentation result (mean intersection over union). The multiple object tracking accuracy (MOTA) accounted for all object configuration errors made by the tracker, including missed events, mismatch events, and false positive events. The detailed definition is shown in Table 3.3.

In addition, I used intuitive tracking quality measures to describe the amount of valid data based on validity of cell tracks considering the uniqueness of cell migration data (Table 3.3). The Usiigaci tracker featured a GUI to allow users to manually verify tracking data. After tracking, valid cell tracks were mixed with invalid tracks, but valid cell tracks could be selected by a simple criterion, *select complete tracks*, in which only cell tracks with objects that were tracked in every frames in the experiment were selected. The valid cell tracks were then inspected by users through cross-referencing with raw image sequences to ensure the validity of the tracking result (Figure 3.7).

Furthermore, I benchmarked the overall performance of segmentation and tracking under the single cell migration analysis context (Figure 3.3 & Table 3.6). Various segmentation and tracking methods including Usiigaci’s segmentation and tracking module, Lineage Mapper⁵²⁰, ImarisTrack module of Imaris (v8.4, Bitplane Inc, UK), and the track object module of Metamorph (Molecular Devices, USA) were benchmarked

Table 3.3: Multiple object tracking performance metrics to evaluate the precision and accuracy of the tracking results.

Multiple object tracking metrics by events ^{484,485}	
Miss events	$\overline{m} = \frac{\sum_t m_t}{\sum_t g_t}$
Mismatch events	$\overline{mme} = \frac{\sum_t mme_t}{\sum_t g_t}$
False positive events	$\overline{fp} = \frac{\sum_t fp_t}{\sum_t g_t}$
Multiple object tracking accuracy (MOTA)	$MOTA = 1 - \frac{\sum_t (m_t + mme_t + fp_t)}{\sum_t g_t}$
Multiple object tracking precision (MOTP)	$MOTP = \frac{\sum_t t \cdot \overline{FN}_t^t + TP_t^t + FP_t^t}{\sum_t t \cdot c_t}$
Single cell migration tracking quality measure (this work)	
Valid single cell track (Figure 3.3.A)	A single cell is tracked correctly in every frame.
Interrupted single cell track (Figure 3.3.B)	A single cell is tracked correctly most of the time (>80%).
Mitosis cell track (Figure 3.3.C)	A single cell underwent mitosis.
Entering view field track (Figure 3.3.D)	A single cell enters view field during the experiment.
Loss of tracking track (Figure 3.3.E)	A single cell tracking is lost during the experiment.
Exiting view field track (Figure 3.3.F)	A single cell exits view field during the experiment.
Mismatch track (Figure 3.3.G)	Two cell tracks with ID switched erroneously during the experiment.
False positive track (Figure 3.3.H)	A single cell falsely tracked.
Valid track ratio	Ratio of valid single cell tracks to all tracks identified by tracker

against manual tracking in ImageJ. Segmentation results from Usiigaci, PHANTAST, Fogbank, and Deepcell as well as phase contrast raw images, or fluorescence images were input as data into each software package as needed. An ImageJ plugin (BW_Jtrack) developed by Mr. Emanuele Martini can assist ImageJ tracking and increase manual tracking speed. Cell-centric parameters of cell migration were used to validate tracking accuracy compared to manual tracking. All data were represented as the mean \pm 95% confidence interval unless otherwise noted. Statistical comparison of results from different tracking methods was done using one-way analysis of variance (ANOVA) with Tukey’s post-hoc multiple-comparison test. The significance level to reject a null hypothesis between two datasets was set at 0.05. A p-value (P, the probability for a true null hypothesis) less than 0.05 represented statistical significance with corresponding 95% confidence level.

3.4 Results and discussion

3.4.1 Mask R-CNN realizes fast and highly accurate whole-cell segmentation

Stain-free tracking of NIH/3T3 fibroblasts electrotaxis in a 300 V m^{-1} direct current electric field (dcEF) for 10 hr under PCM is used to demonstrate unique features of Usiigaci. Segmentation performance of Usiigaci is benchmarked against state-of-the-art free software such as PHANTAST⁴⁷⁰, Fogbank⁴⁷¹, Deepcell⁴⁷⁶ as well as conventional fluorescent thresholding in ImageJ. Segmentation results of Usiigaci and aforementioned software are shown in Figure 3.10 and quantitatively analyzed by segmentation evaluation metrics (Table 3.2). Segmentation similarity can be evaluated using the mean ratio of intersection over union (mIoU), which is also known as the Jaccard index (Figure 3.11).

Table 3.4: Segmentation performance averaged among three NIH/3T3 cell images using various methods. Ch: Channel; PCM: Phase contrast microscopy; FL: Fluorescence

	Ch	Jaccard index	F1 score	Precision	Recall	Specificity	Accuracy
Manual	PCM	1	1	1	1	1	1
Automatic threshold	FL	0.27 \pm 0.03	0.46 \pm 0.02	0.97 \pm 0.02	0.30 \pm 0.01	1 \pm 0	0.91 \pm 0.01
PHANTAST	PCM	0.46 \pm 0.02	0.59 \pm 0.09	0.70 \pm 0.19	0.51 \pm 0.02	0.97 \pm 0.03	0.91 \pm 0.03
Fogbank	PCM	0.63 \pm 0.02	0.77 \pm 0.02	0.65 \pm 0.02	0.93 \pm 0.02	0.94 \pm 0.01	0.94 \pm 0.01
Deepcell 3models-avg	PCM	0.36 \pm 0.04	0.56 \pm 0.06	0.39 \pm 0.06	0.96 \pm 0.01	0.92 \pm 0.01	0.92 \pm 0.01
Usiigaci 3models-avg	PCM	0.72 \pm 0.01	0.85 \pm 0.01	0.83 \pm 0.02	0.87 \pm 0.01	0.95 \pm 0.04	0.96 \pm 0.01

By fluorescence thresholding, thicker cell bodies can be segmented easily, but thinner structures, such as lamellipodia or blebs, often fail to be segmented and contribute to higher specificity and lower mIoU (Table 3.4 & Figure 3.12). In Fogbank and PHANTAST, images are thresholded by local contrast, thus segmentation is effective only if single cells are well isolated. The segmentation similarity achieved by Fogbank and

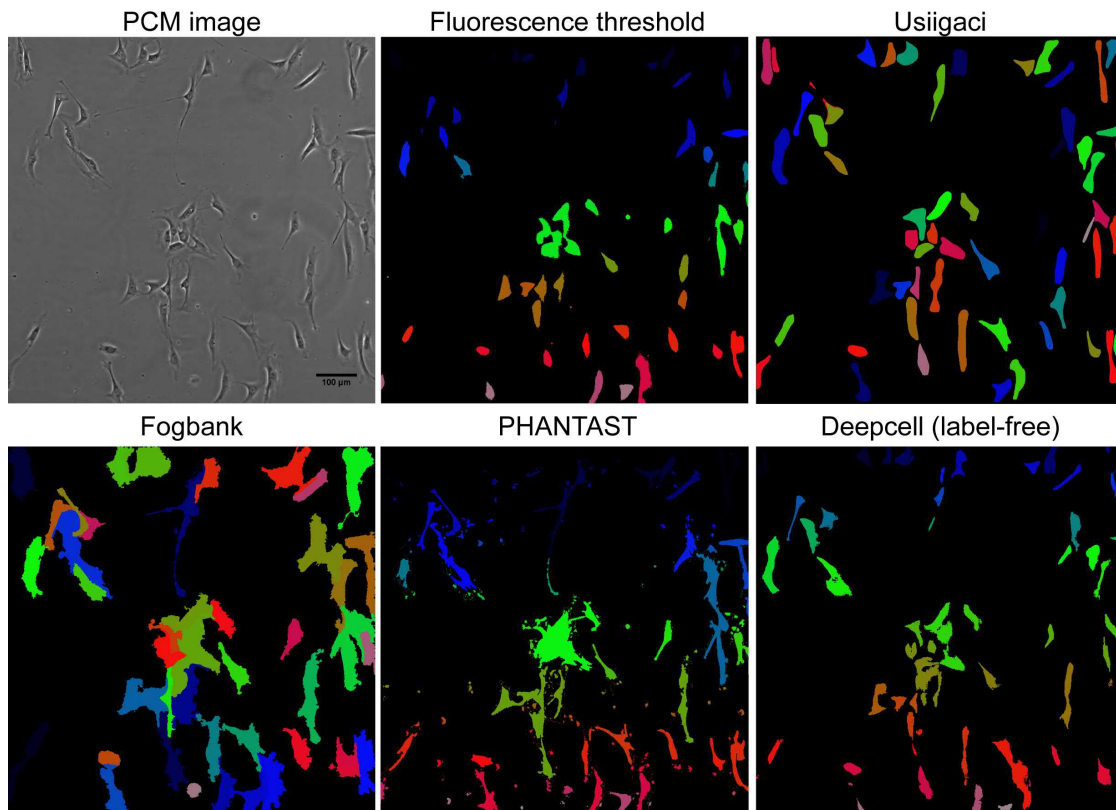


Figure 3.10: Microscopy of NIH/3T3 cells stained with CellTracker Green under PCM and fluorescence microscopy, compared with segmentation results of Usiigaci, Fogbank, PHANTAST, and Deepcell on the PCM image. Different color represents instances of each region of interest. In Usiigaci, Fogbank, and Deepcell, each cell is segmented into an instance outline with a unique ID and color. In segmented masks of fluorescence-thresholded or PHANTAST, cells are segmented into ROIs using the *analyze particle* function in ImageJ and filled with pseudocolors using the ROImap function in the LOCI plug-in. Usiigaci accurately segmented each individual cell with accuracy superior to that of other software.

PHANTAST is moderately high (mIoU 0.46 and 0.63), but single-cell tracking in images with high cell density is not effective using these two methods, because individual cells cannot be distinguished. By classifying cell membranes through machine learning methods, Deepcell segments high density cells better than conventional methods. However, due to the pixel-level classification methods in Deepcell, adjacent cells without clear boundaries are sometimes difficult to segment.

In Usiigaci, entire outlines of cells are segmented correctly in an instance-aware fashion, even if cells are densely packed. Segmentation results from Usiigaci are highly accurate. Figure 3.12 shows a segmentation comparison between the manual reference, fluorescence-thresholded results, Deepcell results, and Usiigaci results. The segmentation similarity of Usiigaci with a single trained model is 2.2 times higher than that of the fluorescence threshold method. Usiigaci’s segmentation also outperforms other benchmarked segmentation software (Table 3.4 & Figure 3.11).

In cell migration, cells in mesenchymal migration often have thin protruding cellular

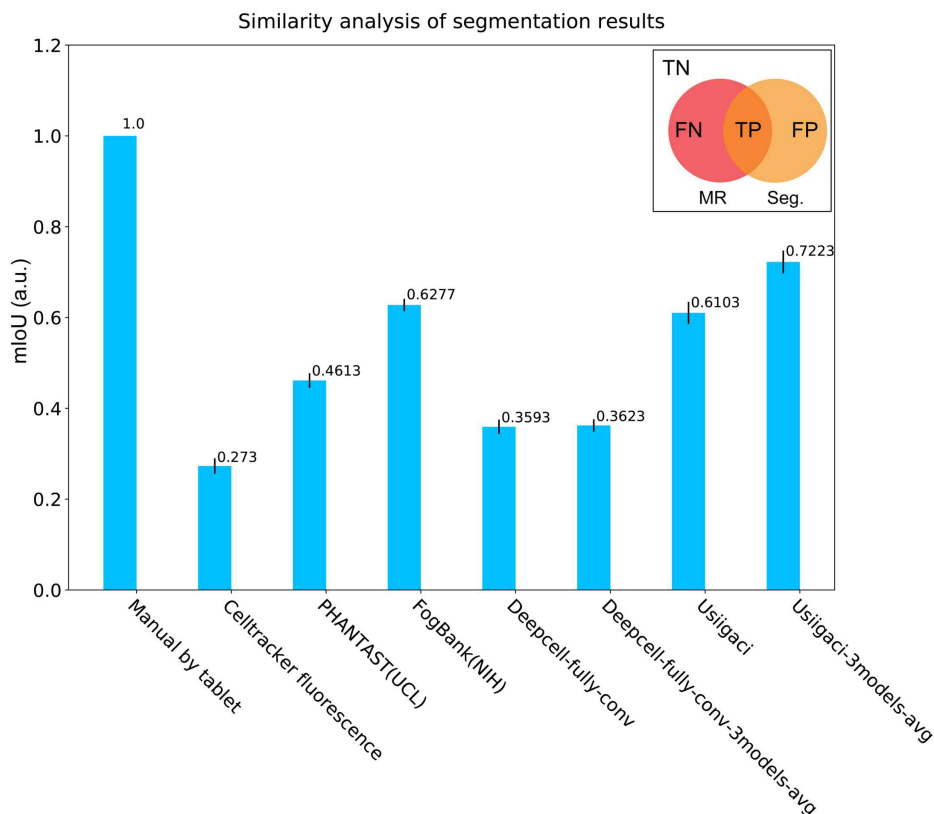


Figure 3.11: Segmentation similarity averaged among three NIH/3T3 cell images using various methods. MR: Manual reference; Seg.: Segmented results; FN: False negative; TP: True positive; FP: False positive; TN: True negative. Segmentation similarity is measured by the mean intersection over union between ground truth and segmented results ($mIoU = \frac{\sum_i TP_i}{\sum_i (FN_i + TP_i + FP_i)}$), as shown in the inset), or also known as the Jaccard index.

structures powered by the cytoskeleton to effect mechanical displacement, such as blebs or lamellipodia⁴⁷². These thin structures have very low contrast even under PCM. Segmentation results from Usiigaci closely resemble those of manual segmentation, while both fluorescence-thresholding and Deepcell have weak segmentation on weakly contrasted cell features such as lamellipodia. Correct segmentation of the entire cell outline enables researchers to not only track cell movement, but also monitor cell morphology.

One of the drawbacks of machine learning is the necessity of powerful computing resources for training as well as deployment of such tools. By taking advantage of the Mask R-CNN model, segmentation speed is comparable to that of conventional computer vision methods such as PHANTAST and Fogbank. The segmentation speed of Usiigaci is three times faster than that of Deepcell. One 1024×1022 image can be segmented into instance segmented masks in 1.5 seconds on a standard laptop equipped with a CUDA-compatible GPU (Figure 3.13). Averaging segmentation results from three different model weights can still be completed in 7 seconds per image. Usiigaci's segmentation module based on Mask R-CNN model provides speed improvement of

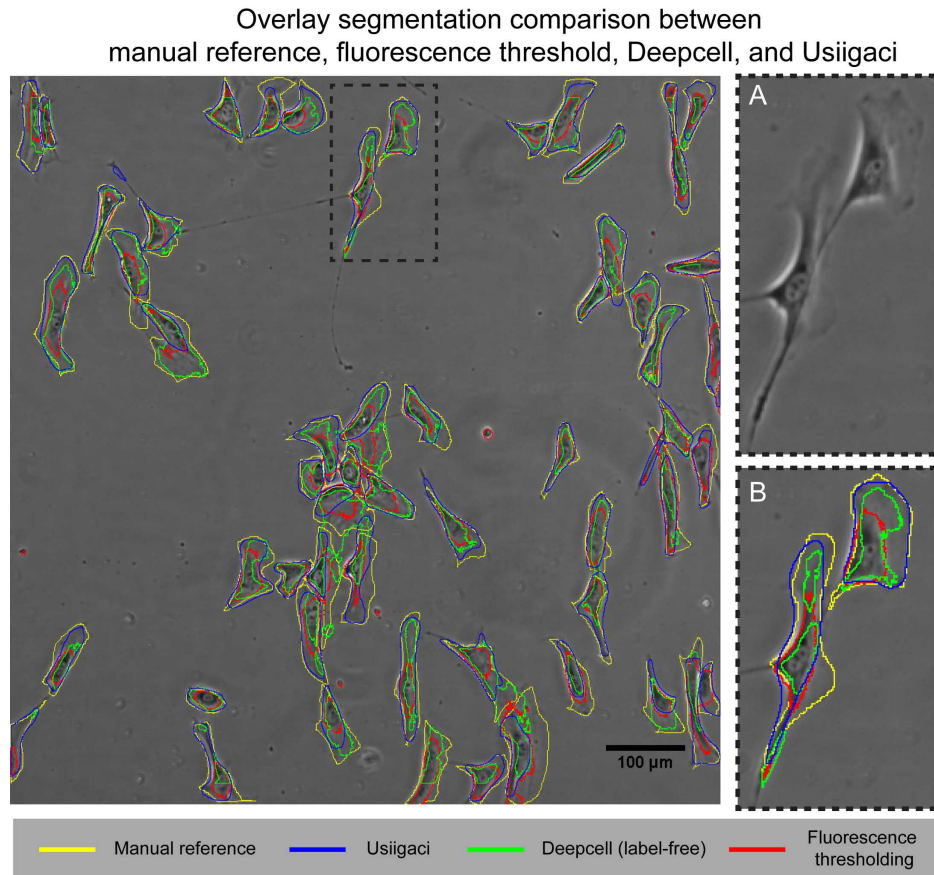


Figure 3.12: Segmentation comparison between manual segmentation as a reference (yellow), fluorescence threshold (red), Deepcell (green) and Usiigaci (blue). The magnified region of the PCM image is shown in inset A. Cells in mesenchymal migration undergo mechanical displacement using lamellipodia⁴⁷², the contrast of which under PCM is very low, making it difficult to segment the structure without labelling cell structures. Outlines of segmentation results from the three methods are overlaid in inset B. Overall segmentation accuracy on whole-cell outline by Usiigaci is more superior and resembles more closely to that of the manual segmentation reference.

orders of magnitude over manual outline segmentation. Automating the segmentation progress significantly alleviates the required workforce for cell migration analysis.

Furthermore, for establishing a useful image analysis pipeline, the software needs to be reliable even when the imaging settings such as intensity and magnification, or experimental settings such as different cells and different cell culture substrate. As shown in Figure 3.14, under low light intensity, both Deepcell and Mask R-CNN in Usiigaci perform as expected with high accuracy toward whole cell segmentation. However, as the light intensity increased, the segmentation results generated by Deepcell are of lower quality compared to Usiigaci. When the substrate is changed from glass to polystyrene which has increased surface roughness visible under the microscope, the background interference causes unacceptable cell segmentation in Deepcell but not in Usiigaci. Also, when the intermediate magnification of the microscope was decreased

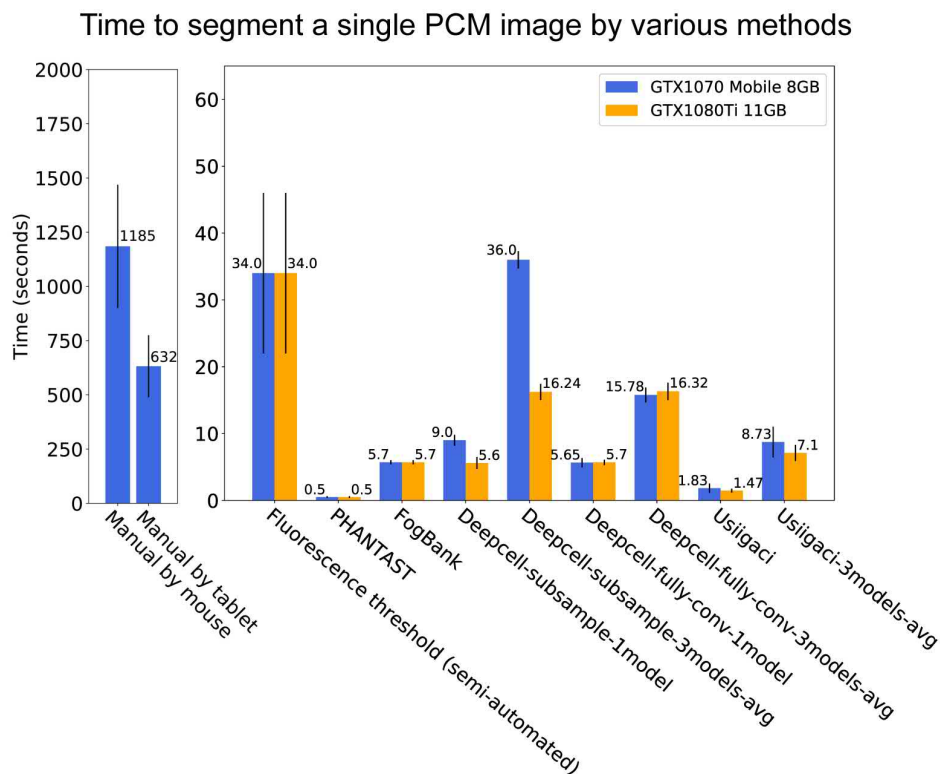


Figure 3.13: The segmentation time of one phase contrast microscopy (PCM) image acquired by various methods. Data represent the mean \pm the standard error of the mean among three experiments. Note that the time scale to manually segment cell outlines is different from other methods. Blue bars indicate data processed using an on-board GPU in the Alienware laptop and orange bars indicate data processed using a desktop GPU.

from 1.5X to 1X, Usiigaci outperforms Deepcell on the segmentation accuracy.

In general, increasing the number of training data will increase the accuracy of the CNN, but our work demonstrated that a pretrained Mask R-CNN model could be further transfer trained using a small training dataset to achieve reliable segmentation with mean intersection over union (mIoU) of 0.72 in an example dataset that the model was not exposed to during the training (Figure 3.11). The performance of Mask R-CNN surpassed several segmentation software I benchmarked. The fact that a small transfer training dataset can fulfill the need for reliable segmentation, this can be appealing to end users who do not possess extensive computational or experimental resources to generate large training datasets.

However, the segmentation accuracy may be profoundly impacted if the segmentation image is significantly different from that in the training dataset (section 3.2.1). A proper training dataset created by end users with a user-specific experimental configuration may be necessary for optimal results.

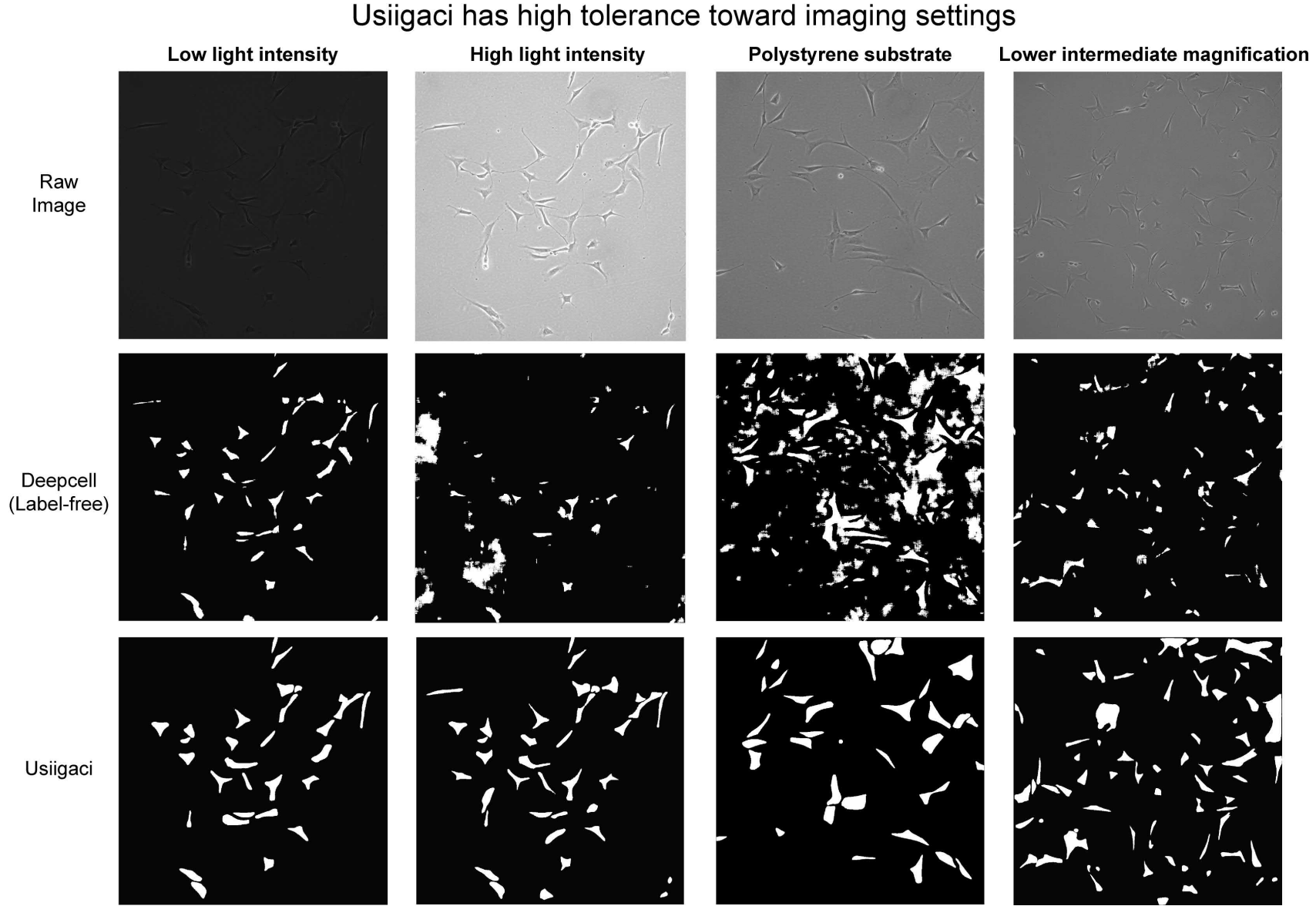


Figure 3.14: Higher tolerance to imaging settings during segmentation in Usiigaci. Usiigaci outperforms Deepcell when images are taken at lower light intensity, higher light intensity, different substrate (polystyrene over glass), and change of intermediate magnification.

3.4.2 High performance multiple object tracking using Usiigaci tracker

Mask R-CNN segments cells in an instance-aware manner such that each segmented cell possesses a unique ID (shown with pseudo-color in Figure 3.10). The IDs in consecutive images are linked and tracked in the tracking module.

The tracking performance of Usiigaci using MOT metrics and tracking quality measures are measured on a triplicate 10-hr NIH/3T3 electrotaxis dataset. MOT metrics measure the performance of trackers based on how accurately the objects in every frame are tracked. Tracking quality can be understood more intuitively by classifying individual cell tracks in tracking quality measures. The MOT performance of Usiigaci with or without manual verification is benchmarked against manual tracking as shown in Table 3.5^{484,485}.

Table 3.5: Summary of multiple object tracking of NIH/3T3 electrotaxis after 10-hr under 300 V m⁻¹dcEF (31 frames). Metrics are compared among manual tracking and Usiigaci with and without the *select complete tracks* criterion and manual verification. MOTP: Multiple object tracking precision; MOTA: Multiple object tracking accuracy.

MOT metrics	Manual	Usiigaci (unverified)	Usiigaci (select complete track)
Total events	4520 ^a	4470	1736
Miss events	0	145	0
Mismatch events	0	70	0
False positive events	0	165	0
MOTA	1	0.919 ± 0.01	n/a
MOTP (mIoU)	1	0.702 ± 0.012 ^b	0.756 ± 0.009 ^b
Tracking quality measure			
Total tracks	155 ^c	291 ^d	61
Valid single tracks	104	56	56
Interrupted single cell tracks	0	21	0
Mitosis cell tracks	5	5	5
Entering view field tracks	19	19	0
Loss of tracking tracks	0	152	0
Exiting view field tracks	27	27	0
Mismatch tracks	0	2	0
False positive tracks	0	9	0
Valid track ratio	0.67 ^e	0.19 ^f	0.92 ^g

^a Total objects identified by a human operator.

^b Mean intersection over union ratio of all matched-object pairs in mean ± standard error of mean.

^c Total cell tracks identified by a human operator.

^d Total cell tracks generated by Usiigaci's tracker.

^e Ratio of valid cell tracks to total cell tracks in the dataset identified by a human operator.

^f Ratio of valid cell tracks to total cell tracks generated by Usiigaci's tracker.

^g Ratio of valid cell tracks to total cell tracks after the *select all tracks* criterion.

In manual tracking, the multiple object tracking precision (MOTP) and multiple

object tracking accuracy (MOTA) are arbitrarily defined as 1. A total of 4520 events are identified, summed from all frames. After tracking by the Usiigaci tracker, 4470 events are identified with MOTA of 91.9%. By imposing the *select complete track* criterion, events belonging to invalid tracks (Figure 3.3.B – H) are easily removed. The MOTPs describing the total error in positions of matched object-hypothesis pairs in Usiigaci before and after manual verification are 70.2% and 75.6%, which are similar to the Jaccard index in segmentation⁴⁸⁴. The masks of tracked cells correlate well with those by manual segmentation at pixel level, which suggests that cell movements and morphology changes can be tracked and analyzed quantitatively.

Tracking quality using the Usiigaci tracker can be understood more intuitively by classifying individual cell tracks. By manual tracking, 104 valid tracks are found among 155 total tracks. Using the Usiigaci tracker, 291 tracks are generated and many of which are erroneous due to different types of cell migration tracks (Figure 3.3). The valid track ratio in Usiigaci is only 19.5% without manual verification. However, by the *select complete tracks* criterion, users can select only the tracks with the same ID in every frame. Valid cell tracks will be among those selected with the criterion. Users can also verify whether there are any erroneous tracks and exclude them if necessary. Five mitosis tracks exist in the remaining results and they are excluded manually. The valid tracks obtained from Usiigaci after manual verification correspond to 54% of valid tracks identified by a human operator. However, more viewfields can be analyzed to increase the number of valid tracks with the labor-saving workflow of Usiigaci.

3.4.3 Automated tracking with manual verification ensures reliable cell tracking results

Quantitative cellular dynamics analysis requires both accurate cell segmentation and cell tracking. The accuracy of cell segmentation and tracking are benchmarked under the context of single cell migration analysis with the dataset of NIH/3T3 electrotaxis under 300 V m^{-1} dcEF in a 10-hour time-lapse experiment.

NIH/3T3 has demonstrated classical cathodal migration and perpendicular alignment, which is visible by the increase in directedness and the decrease in orientation (Figure 3.15). Directedness is a metric to show directional cell migration. Directness is defined as the average cosine between the net trigonometric distance and electric current vector (Figure 3.2). A group of cells migrating toward the cathode has a directedness of 1, and random migrating cells possess a directedness of 0 (Table 3.1). The directedness of NIH/3T3 cells in dcEF is used to benchmark the accuracy of results tracked by various tracking methods including manual tracking in ImageJ, the track object module in Metamorph, Imaris Track, and tracking with Lineage Mapper (Figure 3.16). PCM images, fluorescence images, or segmented masks from either Usiigaci, PHANTAST, Fogbank, or Deepcell are used in each tracking software accordingly. Only valid cell tracks that contains cells being tracked in every frame are analyzed. Capture rate is defined as the ratio between valid cell tracks by a certain method and valid cell tracks identified manually. The performance of Usiigaci’s Mask R-CNN segmentation and Trackpy-based tracker benchmarked against manual tracking in ImageJ, Imaris, Metamorph, Lineage mapper are shown in detail in Table 3.6.

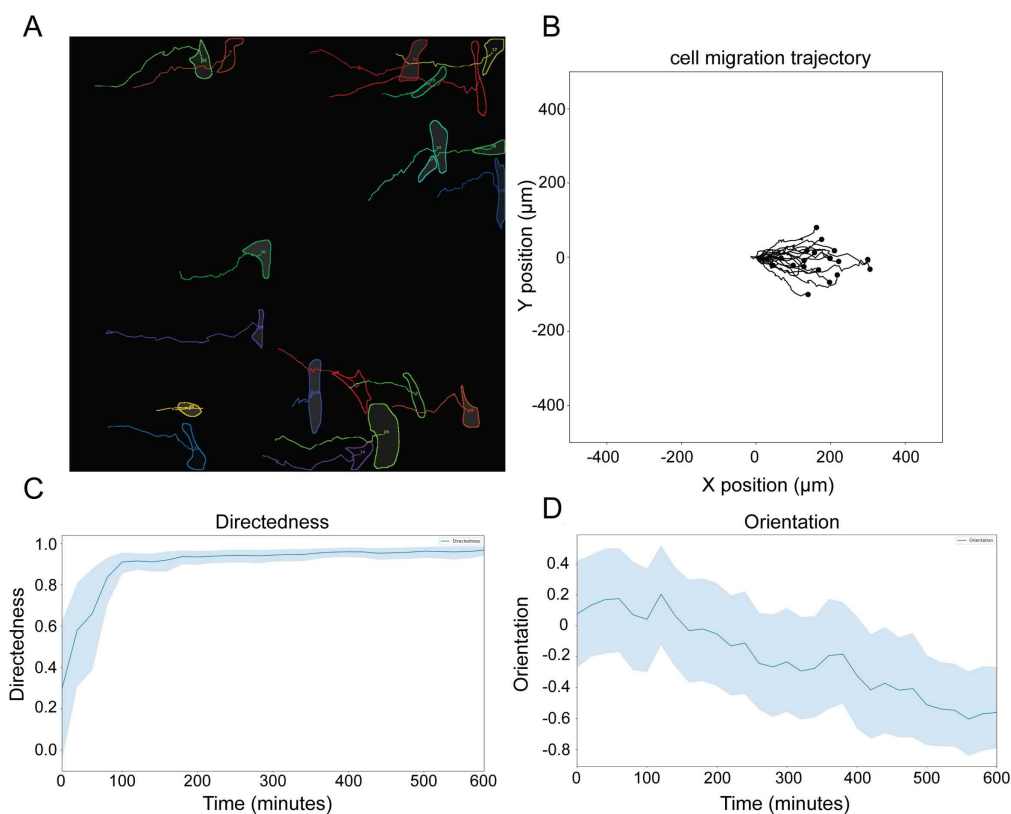


Figure 3.15: Visualization of valid tracks of NIH/3T3 10-hr electrotaxis in $300 \text{ V m}^{-1} \text{ dcEF}$. The cathode is on the right side of the view field. (A) Tracked results from Usiigaci tracker; (B) Cell migration trajectory plot; (C) Directedness of cell migration; (D) Orientation of cell migration.

While cell tracking in proprietary software such as Imaris and Metamorph yields results similar to the manual reference, both software packages only provide positional information about cells, while morphological information of cells is not available. Moreover, Imaris demands fluorescent labeling of cells to obtain good segmentation results (Table 3.6).

Even though open-source cell tracking software, such as Lineage Mapper is available⁵²⁰, segmented data may not be directly compatible with Lineage Mapper if single cells are not segmented into individual instances correctly in every frame. Because Lineage Mapper is fully automatic, a manual verification process is not available in Lineage Mapper. Imperfect segmentation results lead to erroneous tracking results and invalid tracks cannot be excluded by users. Directedness of cells segmented by Fogbank and tracked by Lineage mapper ($P < .01$, one-way ANOVA with Tukey's post-hoc) differs from the manual reference. Cells segmented by Deepcell are not tracked well with Lineage Mapper ($P < .0001$, one-way ANOVA with Tukey's post-hoc). Therefore, segmented results from PHANTAST and Deepcell on NIH/3T3 electrotaxis cannot yield good data by tracking with Lineage Mapper. While Usiigaci's segmented masks can also be tracked using Lineage Mapper, only 22% of cells are tracked compared to the manual tracking reference. The results from Lineage Mapper are also significantly different compared to a manual reference ($P < .0001$, one-way ANOVA with Tukey's

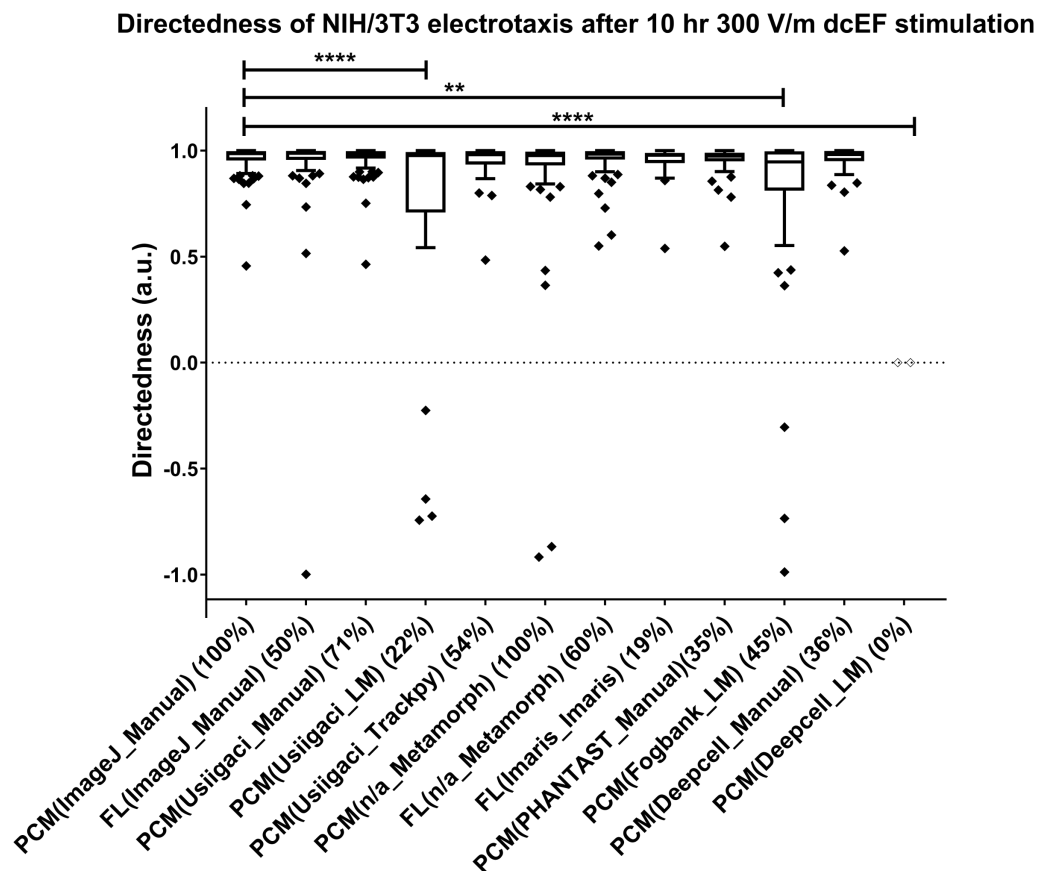


Figure 3.16: Directedness of NIH/3T3 electrotaxis after 10-hr, 300 V m⁻¹ dcEF stimulation analyzed by different segmentation and tracking methods. Data and labels are arranged based on the type of images-(segmentation method_tracking method) (capture rate). LM: Lineage Mapper; FL: Fluorescence; PCM: Phase contrast microscopy; ** denotes P<.01; **** denotes P<.0001.

post-hoc), presumably due to erroneous tracking that cannot be verified manually. Misinterpretation may be made due to bad results if users do not fully grasp the inner workings of the tracking process (Figure 3.16).

In contrast, by segmenting and tracking with Usiigaci, 54% of cells can be automatically tracked when compared to manual tracking. Moreover, directedness and migration speed of cells analyzed by Usiigaci are comparable to the manual reference and Metamorph. Migration speed can be over- or under-estimated in Imaris or Lineage Mapper. Usiigaci is the only automated cell tracking method that provides both cell movement and morphology change information among benchmarked software packages. With high segmentation and tracking accuracy, Usiigaci delivers quantitative cell migration analysis to biologists as an easy-to-use tool for cell migration phenotype analysis⁵²¹.

Usiigaci is the only all-in-one solution for automated cell tracking with manual verification functionality that provides cell movement and morphology change information. The labor-saving workflow while preserving the capacity for human intervention is es-

essential to ensure data validity in single-cell migration analysis⁵²². Quantitative analysis of cellular dynamics performed using Usiigaci offers unique advantages for quantitative biology studies.

3.4.4 Limitations of Usiigaci

I have shown that Usiigaci's instance-level segmentation can provide reliable cell outline segmentation and tracking with improved speed. However, if the cell morphology differs significantly than that in the training data, the neural network may not perform as well as expected.

A microscopy photo of confluent T98G glioma cells and its corresponding *Usiigaci* segmentation are shown in Figure 3.17. The cell boundaries of confluent cell layer may be obscured and become less sharp in comparison to those seen in single cell microscopy images. Lack of clear cell boundaries makes it difficult to be recognized by the neural network. Therefore, the Mask R-CNN neural network is limited by the training data. Preparation of proper training data may be necessary for end users to obtain optimal results if cell morphology and microscopy optical configuration are significantly different than our current setup.

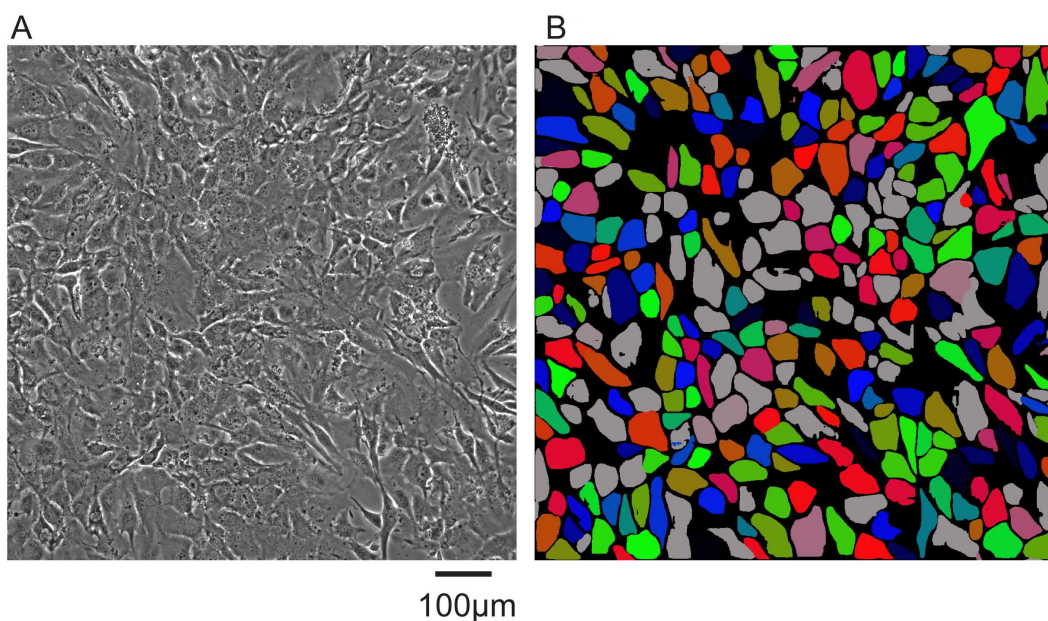


Figure 3.17: Segmentation results of confluent T98G glioma cells. (A) PCM image of confluent T98G glioma cells; (B) The corresponding segmentation result.

3.5 Summary and prospects

Usiigaci offers a reliable quantitative solution for segmentation, tracking, and analysis of cell migration in two-dimensional PCM. No label or special treatment of cells is required, so that cells can be analyzed under more natural conditions. Entire outlines of cells are automatically segmented and tracked in Usiigaci, which enables biologists

Table 3.6: Tracking results of NIH/3T3 electrotaxis using different segmentation and different tracking methods. Abbreviations: Ch: channel; PCM: phase contrast microscopy; FL: fluorescence; sem: standard error of mean.

NIH/3T3	Ch	Single cell tracks	Capture percentage	Directedness	sem	Speed ($\mu\text{m hr}^{-1}$)		Orientation		sem	
						sem	0hr	sem	10hr		
Outline tracking	PCM	104	100%	0.95	0.02	18.65	0.69	-0.08	0.08	-0.76	0.03
Outline tracking	FL	52	50%	0.92	0.04	18.51	1.19	-0.12	0.11	-0.75	0.06
Imaris	FL	20	19%	0.94	0.02	21.73	2.09	n/a	n/a	n/a	n/a
Metamorph	PCM	104	100%	0.92	0.04	18.32	0.73	n/a	n/a	n/a	n/a
Metamorph	FL	62	60%	0.95	0.01	18.15	1.03	n/a	n/a	n/a	n/a
Fogbank (Lineage Mapper)	PCM	47	45%	0.79	0.06	11.37	3.32	n/a	n/a	n/a	n/a
PHANTAST (ImageJ)	PCM	36	35%	0.95	0.01	16.65	1.35	-0.08	0.11	-0.59	0.10
Deepcell (ImageJ)	PCM	37	36%	0.95	0.01	18.68	1.19	-0.14	0.12	-0.82	0.05
Deepcell (Lineage Mapper)	PCM	0	0%	n/a	n/a	n/a	n/a	n/a	n/a	n/a	n/a
Usiigaci (ImageJ)	PCM	74	71%	0.96	0.00	18.34	0.82	-0.04	0.09	-0.74	0.05
Usiigaci (Lineage Mapper)	PCM	23	22%	0.67	0.13	4.28	0.64	n/a	n/a	n/a	n/a
Usiigaci (TrackPy)	PCM	56	54%	0.92	0.05	18.19	1.38	-0.09	0.10	-0.80	0.04

to analyze both movement and morphological changes in cellular dynamics in a quantitative manner that existing software cannot provide. The labor-saving workflow also alleviates the workload in comparison to the manual cell tracking method that is conventionally adopted. Further, the manual verification function enables users to verify the tracking data and ensure data validity. The trainable nature of the Mask R-CNN model allows Usiigaci to analyze images acquired in other bright-field microscopic techniques, and potentially for 3D cell tracking in the near future.

To benefit the biomedical research community with this tool for automated cell segmentation and tracking, Usiigaci is open-sourced in a Github repository of OIST under the Massachusetts Institute of Technology (MIT) license ([link](#)). A tutorial video of Usiigaci's usage is also available ([video link](#)).

Advances in deep learning methods for biomedical image analysis provide unique opportunities to advance biomedical discovery. Similar deep learning methods for biomedical image analysis are used to accomplish *in silico* labeling of cellular components in stain-free images and 3D segmentation of noisy medical images^{523–526}. The analytical capability of Usiigaci can also contribute to the international effort to standardize cell migration experiments⁵²⁷. In combination with advances in microsystems, an automated lab-on-chip system for quantitative biology exploration can be developed in future.

Further development for Usiigaci is envisioned such that it can be deployed on embedded systems and incorporated with a compact automated microscope which can fit inside a typical cell culture CO₂ incubator. The on-line data acquisition and analysis capabilities can be offered by future version of Usiigaci to realize the automated artificial intelligence (AI) cytoscope (Figure 3.18). A biology-centered lab can be equipped with high resolution automated cell analysis capability with such AI cytoscope.

Specifically, a control unit such as a personal computer (PC) or a smart phone for the automated microscope can be modified with a processing unit for machine learning such as a GPU, a field programmable gate array (FPGA), or a tensor processing unit (TPU). After acquisition of raw images, the images can be processed by different CNNs trained to yield *in silico* estimation results such as outlines for cell tracking (Usiigaci in its current form), nuclei, intracellular organelles, cytoskeleton, cell cycle classification, or senescence classification. These *in silico* classification results can be saved with raw images as multi-dimensional data for users to perform a broad range of cell analysis such as cell motion, cellular state, lineage, and intracellular analysis throughout a time lapse experiment. Furthermore, a feedback learning function can empower user's feedback to further train the CNNs based on users' data to yield more accurate estimation in user's experimental environment.

The specific developmental aims of Usiigaci to realize this future include:

- Increase more training data for different magnification, cell types, and different brightfield microscopy techniques to become a universal segmentation tool.
- Multi-class segmentation for Mask R-CNN to recognize different cell types for cell co-culture identification without staining.
- Include lineage tracking function that is essential in fields such as stem cell biology and neurosciences^{528,529}.

- Include cell migration phenotype classification function in the data processing module for quantitative cell migration phenotype analysis^{491,493}.

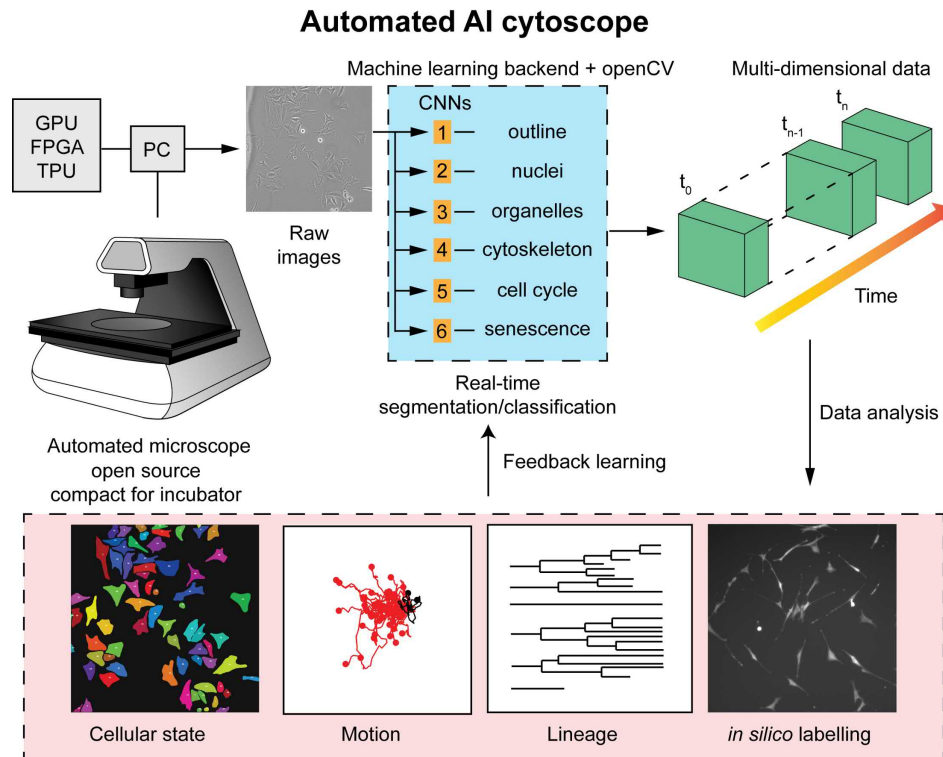


Figure 3.18: Automated AI cytoscope. A control unit on an automated microscope can be equipped with machine learning processing unit such as GPU, FPGA, or TPU. An acquired raw image can be inferred by multiple CNNs trained to recognize cell outlines, nuclei, organelles, cytoskeleton, cell cycle, or senescence. Both the raw images and inferred results by CNNs are saved into multidimensional data that can be analyzed by users after the experiment is completed. A feedback learning function can be built in to further train the CNNs *in situ* by users' data to further improve the CNNs. PC: personal computer; GPU: graphical processing unit; FPGA: Field programmable gate arrays; TPU: Tensor processing units.

Chapter 4

Electrotaxis of glioma cells using hybrid PMMA/PDMS microfluidics

Abstract

Translational research demands reliable biomedical microdevices (BMMDs) to mimic physiological conditions and answer biological questions. In this chapter, the developed hybrid PMMA/PDMS microfluidic chip is used for studying glioma electrotaxis in a high-throughput manner. Four chemical microenvironments whereas each has four electric fields further support high-throughput screening of glioblastoma cell electrotactic responses in a single experiment. Uniform cell seeding by submerged operations enables reliable single cell spatial resolution. The electrotaxis of glioblastoma cells T98G and U-251MG require optimal laminin-containing extracellular matrix coating and exhibit completely different directional and electro-alignment tendencies. Anodal T98G electrotaxis and cathodal U-251MG electrotaxis have different fetal bovine serum (FBS) dependencies but both require the presence of extracellular calcium cation. Further pharmacological investigation into the voltage-gated ion channels in T98G and U-251MG electrotaxis reveals that U-251MG electrotaxis is dependent on P/Q-type voltage-gated calcium channels (VGCCs) and T98G maybe dependent on R-type VGCCs. U-251MG and T98G electrotaxis are also mediated by A-type voltage-gated potassium channel (VGKCs) and acid-sensing sodium channels. Further elucidation of the role of voltage-gated ion channels in glioma metastasis may be important for developing new therapeutic and personalized approaches for aggressive glioma. The hybrid PMMA/PDMS approach provides a simple and flexible platform to create multiplex microenvironments, making it possible to investigate complicated biological questions in translational research.

4.1 Introduction

Glioma is the most common type of brain cancer and the aggressive form of it, glioblastoma, has poor prognosis, high morbidity, and high probability of recurrence^{530,531}, due to the infiltration nature of the disease. The high infiltrative ability of the cancer originates from the invasive/migratory ability in glioma stem cells or brain tumor initiating cells^{532,533}. However, it is now clear that not only the glioma cells are important, but also the microenvironment in the brain helps shaping the heterogeneity of the glioma⁵³⁴.

The glioma cells interact with the extracellular matrix, glial cells, and immune cells in the brain and mediate the formation of peri-vascular, peri-necrotic, and invasive tumor microenvironments^{42,50,535,536}. Understanding the molecular mechanisms of the invasiveness in glioma cells as well as the tumor microenvironment is vital for developing new therapeutic options and improving the patient outcome^{537,538}.

In the brain, glial cells are immersed in an electric field created by tissue polarity as well as the local field potentials summed from the action potentials fired by the neurons¹⁷⁸. The physiological electric fields in the brain may play an important role in mediating the glioma tumorigenesis and invasion^{293,294,398}. Under a direct current electric field, depending on the 2D or 3D microenvironment, glioblastoma cells of different origins migrate toward different electrodes through electrotaxis²⁹³⁻²⁹⁵. Huang *et al.*, identified that heparan sulfate and slit-Robo1 signaling mediates the glioma electrotaxis. In contrary, an alternating current electric field inhibits the mitotic spindle and arrests the proliferation of glioma^{79,208}. The electrical cue in tumor microenvironment in the brain has thus been explored as a therapeutic target.

Cells sense the electric field by bioelectrical activation of voltage sensitive proteins, mechanosensing due to electrokinetic phenomena, with activated chemical signaling due to electrokinetically polarized membrane receptors (Figure 4.1). The voltage gradient of the electric field creates a large voltage drop at the membrane which can directly activate voltage sensitive proteins such as voltage-gated ion channels that are often expressed on excitable membranes at neuronal synapses and neuromuscular junctions⁵³⁹. Among the voltage-gated ion channels in the brain, calcium channels are especially important as calcium influx plays a pivotal role in cellular signaling^{540,541}. Calcium signaling is also important in glioma cell proliferation, resistance to therapy, and metastasis⁵⁴²⁻⁵⁴⁶. Whether or not the calcium signaling in glioma is mediated by electric field is still an open question.

To study electric field and cell interaction, a reliable *in vitro* platform that interfaces with automated microscopy is a prerequisite. Stable electrical stimulation of cells in a high-throughput fashion is a necessity for rapid screening targets and identifying molecular mechanisms. To this end, I have developed a hybrid PMMA/PDMS microfluidic platform to reliably study single glioma cell migration under high-throughput electric field stimulations that multiple agonists/antagonists can be tested at the same time (Chapter 2.3). In combination with a machine learning-enabled software for automated cell migration analysis, the electrotaxis of glioblastoma cell line models are studied in detail (Chapter 3). The hypotheses that glioblastoma electrotaxis is mediated by extracellular matrices (ECM), chemical signaling, and voltage-gated calcium channels are tested as follows (Figure 4.1):

A. What are the appropriate extracellular matrices suitable for glioma electrotaxis?

ECM affects cell adhesion, cell migration machinery, and cell-cell junctions⁵⁴⁷. Specific cell types express different surface adhesion molecules and thus have preference toward appropriate ECMs on *in vitro* platforms. The first step is to identify the appropriate ECM coating for establishing a stable electrotaxis model of glioma (Figure 4.1A).

B. Does chemotactic signaling pathways intersect with electrotaxis of glioma?

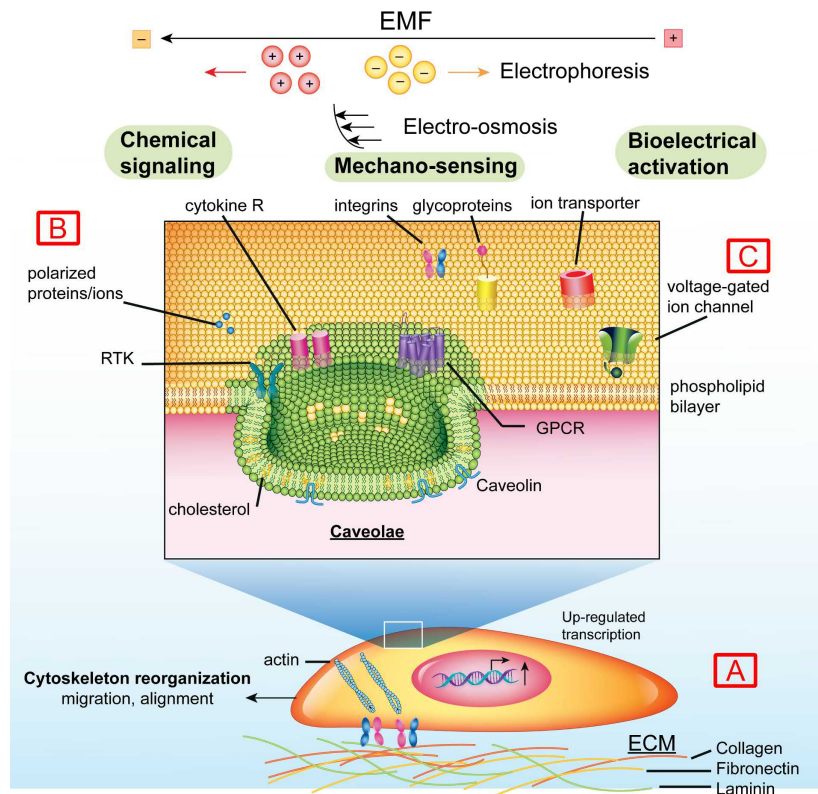


Figure 4.1: The hypothetical mechanisms underlying electrotaxis.

The cellular signaling pathways can be grossly categorized by types of receptor actions, such as enzyme-linked receptors, G-protein coupled receptors, transmembrane non-enzymatic receptors, ligand-gated ion channels, or voltage-gated ion channels⁵⁴⁸.

Many receptor tyrosine kinase receptors ligands and cytokines are overexpressed in glioma patients⁵⁴⁹. To test if the primary signaling pathways in the chemotaxis intersect with those in glioma electrotaxis, I investigate if T98G glioblastoma electrotaxis is mediated by chemical ligand stimulation from key chemotaxis pathways (Figure 4.1B). Some of the key chemotaxis pathways identified to participate in electrotaxis include epidermal growth factor (EGFR)^{233–242}, vascular endothelial growth factor receptor (VEGFR)^{243–245}, fibroblast growth factor receptor (FGFR)¹⁸⁵ in the enzyme-linked receptors category. Furthermore, G-protein coupled receptors and cytokine receptors also have been reported to be involved in electrotaxis^{550,551}, therefore the common pathways in these categories related to glioma malignancy are tested, including the CXCL12-CXCR4 axis and the tumor necrosis factor α (TNF- α) signaling.

C. Does VGCCs mediate the electrotaxis of glioma cells?

VGCCs are among a major class of membrane ion transporters regulating the calcium influx. While VGCCs abundantly express on the excitable membranes such as those on neurons and neuromuscular junctions, VGCCs also play important roles on glioma biology such as cell proliferation, apoptosis, sensitization to

ionizing radiation^{552,553}.

VGCCs can be categorized as high voltage activated (HVA) type or low voltage activated (LVA) type (Figure 4.2)^{172,554,555}. Among the HVA VGCCs, four subtypes can be identified from electrophysiological and genetic phylogeny, including L-type (long-lasting, $Ca_v1.1 - 1.4$), P/Q-type (purkinje/unknown, $Ca_v2.1$), N-type (neural, $Ca_v2.2$), and R-type (residual, $Ca_v2.3$) calcium channels. The LVA VGCCs is composed of T-type channels (transient, $Ca_v3.1 - 3.3$).

Under electric field stimulation, the VGCCs can be activated by the imposed electric field (Figure 4.1C). If and how VGCCs participate in the electrotaxis of glioblastoma may shed new insights for inhibiting glioblastoma infiltration.

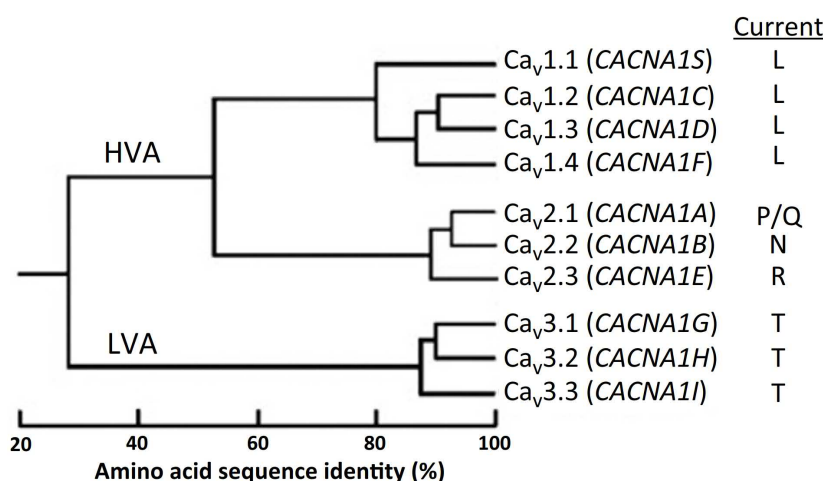


Figure 4.2: Subfamilies of voltage-gated calcium channels⁵⁵⁴.

4.2 Materials and methods

4.2.1 The hybrid PMMA/PDMS chip for high-throughput electrotaxis experiment

For electrotaxis study of glioma cells, I used thermoplastic microfluidic chips (Chapter 2.2) and hybrid PMMA/PDMS microfluidic chips (Chapter 2.3) described in detail previously.

The hybrid PMMA/PDMS chip took advantage of the double-layer microchannel design and permitted experiments of two different cell types or chemical treatments with four electric field strengths conditions in a single chip (Figure 4.3). Due to the increased hydraulic resistances of the interconnecting channels in the double-layer hybrid PMMA/PDMS chip (Figure 4.3C), the chemical transport was stable over the course of 10 hours at cell culture-relevant flow rates. Using this design, robust single cell migration experiments could be performed in high throughput fashion.

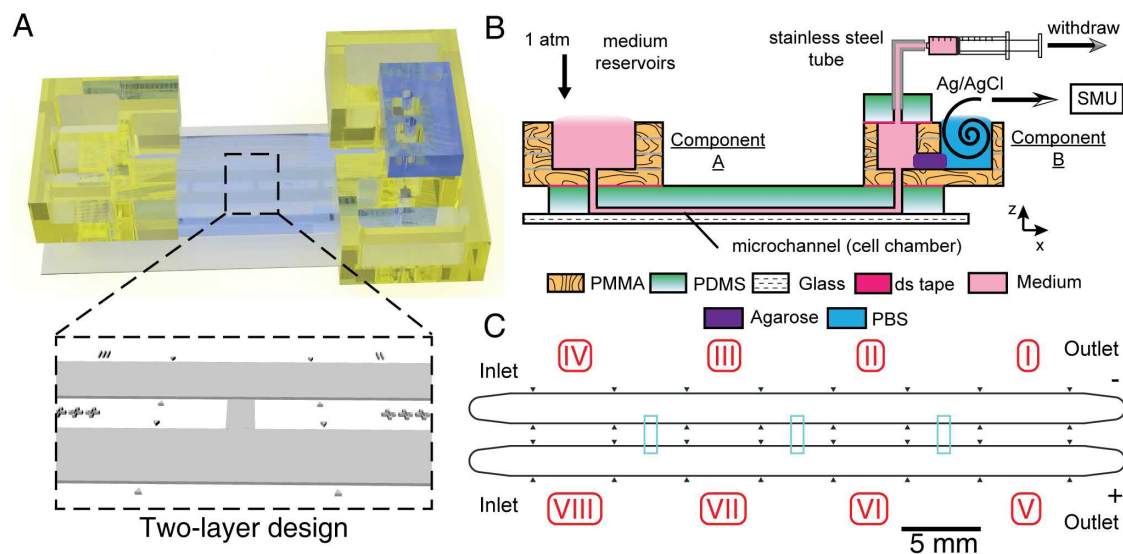


Figure 4.3: The concept of a small configuration hybrid PMMA/PDMS microfluidic chip. (A) The 3D rendered model of the final PMMA/PDMS chip. Double-layer microchannel design in the PDMS is shown; (B) The schematic diagram of using the PMMA/PDMS chip for electro taxis experiments. Complex 3D microfluidic structures and world-to-chip interface are established in PMMA components A & B; (C) The channel design. The 10 μm -high first layer structures are shown in cyan.

4.2.2 Cell culture and maintenance

Glioblastoma cell lines T98G (CRL-1690, ATCC, USA) and U-251MG (IFO50288, JCRB, Japan) were obtained from the respective tissue banks and thawed according to the received instructions. T98G and U-251MG were cultured in minimum essential media α (MEM α) supplemented with 10% FBS and 2.2 g L^{-1} under 37°C , 5% CO_2 moist atmosphere (MCO-18AIC, Sanyo, Japan). The cells were subcultured every other day or whenever cells reached 80% confluency. Mycoplasma contamination was checked every three months using a mycoplasma species-specific PCR kit (e-Myco plus, iNtRON, Korea) on a thermocycler (C1000, Bio-Rad, USA).

Frozen stocks of the cells were prepared by resuspending 1×10^6 log-phase cells in 1 mL cell banker solutions (Takara Bio, Japan) and cooled down in a freezing container (Mr. Frosty, Nunc, USA) in -80°C overnight. The frozen cells were then transferred into gaseous phase of liquid nitrogen for long term storage (Locator 6 Cryopreservation tank, Thermo Scientific, USA).

4.2.3 General experimental workflow

The cell experiment workflow included salt bridge preparation, priming of microchannels, coating substrate with extracellular matrix, seeding cells, assembly of world-to-chip interface, and electro taxis experiment.

On-chip agarose salt bridge preparation 1% agarose (Seakem LE agarose, Lonza, USA) was dissolved in 1X D-PBS and autoclaved. The agarose was injected on the

salt bridge locations of the PMMA component B and allowed to gel. The salt bridge served as a solid electroconductive separation in electrotaxis experiment between the cell culture media and D-PBS.

Priming for bubble-free microchannels 50 μL of 99.5% ethanol (Wako, Japan) loaded in 200 μL tips were used to wet the microchannels by capillary flow and gravity flow. The low surface tension of ethanol easily wetted the PDMS microchannels and avoided microbubbles. Next, reagent-grade water was put in the opposite reservoir and was introduced into the microchannels by withdrawing from the tips that loaded with ethanol in the previous step. The inlet/outlet ports were submerged under water in all steps afterward to ensure bubble-free microchannels.

Coating of substrate with extracellular matrix proteins 150 μL of extracellular matrix proteins coating, such as Geltrex, were loaded into 200 μL tips and allowed to flow into chip passively by inserting the filled tips into the inlets/outlets on the PDMS chip. The extracellular matrix was coated for 1 hour at 37 °C and washed once with 1X D-PBS.

Facile pressure-balanced underwater operation for high fidelity cell seeding The top reservoir was filled with cell culture media until the inlet and outlet were under the same liquid level, *i.e.*, balancing the inlet/outlet hydrostatic pressure. The cells were trypsinized (TrypLE, Thermo Fisher Scientific, USA), counted (Muse, Millipore, USA), centrifuged at 300 \times g for 5 min, and resuspended in culture media at 10⁶ cells mL⁻¹. Appropriate amount of cell suspension was injected into the microchannels using a P200 micropipette. Due to the small volume of a microchannel, only a minute amount of cell suspension was needed. The cells were allowed to adhere in the chip under 37 °C, 5% CO₂ atmosphere for 3 to 5 hours.

For comparison, different approaches of cell seeding were tried such as:

1. Tip loading method

The cells were loaded in 200 μL tips and cells were infused into microchannels by gravity flow without removing the tips. The cells may flocculate as it passes through the small bore of micropipet tips.

2. Tip injection method

The cells were loaded in 200 μL tips and cells were injected into microchannels by micropipette then tips were removed.

Completion of chip prior to experiment After cells attached to the bottom of microchannels, the cell culture media in the top reservoir was removed. Through the reversibility of the dual energy double-sided tape (de-ds tape), the top reservoir was removed by shearing sequentially from component B and component A. The top liner of the first ds tape on component B (Figure 2.23A) was removed and a PDMS slab punched with two holes (21G, Accupunch, Syneo, USA) was affixed to that ds tape, completing the PMMA/PDMS chip. The PMMA/PDMS chips were affixed

with double-sided tape (No.2, Nichiban, Japan) on a home-made aluminum holder (Appendix D.5, Mevii, Misumi, Japan) in a microscope on-stage 5% CO₂ incubator (WKSM, Tokai-Hit, Japan). A feedback thin-film K-type thermocouple was attached to glass bottom of the microfluidic chip (60 μm-thick, Anbesmt, Japan) and regulated the cell culture temperature at 37 °C. The reservoir on the on-stage CO₂ incubator was filled with sterilized pure water to minimize evaporation of the water in culture media which would significantly affect the cell viability (Section 2.1.5).

4.2.4 Electrotaxis of glioma cells on different ECM coatings

To investigate the extracellular matrices preferred by glioma cells, various ECM coatings in thermoplastic and PMMA/PDMS microfluidic chips were tested, such as poly(D-lysine) (PDL), poly(L-ornithine) (PLO), PLO combined with laminin, collagen, fibronectin, vitronectin and Geltrex[®]. PLO combined with laminin is a common ECM coating to support cells originated in the CNS. Geltrex is a reconstituted basement membrane purified from murine Engelbreth-Holm-Swarm (EHS) tumor containing laminin, collagen IV, entactin, and heparin sulfate proteoglycan that has been used to support human embryonic stem cells (ESCs) as well as induced pluripotent stem cells (iPSC).

The thermoplastic chip (Chapter 2.2) was prepared, vacuumed, and primed with CO₂ gas, water, and D-PBS sequentially to prevent bubbles²⁰². The ECM coatings were prepared at working concentrations accordingly (Table 4.1) and infused into 30×3×0.07 mm (length×width×height) microchannels and incubated for 1 hour at 37 °C. The channels were washed once with 1X D-PBS and cell culture media before seeding of cells. Glioblastoma cells were trypsinized and resuspended to 5 × 10⁶ cells mL⁻¹ counted by a cell counter (Muse, Millipore, USA). The cells were seeded in the channels and allowed to adhere to the bottom for 3 to 5 hours at 37 °C. Afterward, primed fluidic tubings and salt bridges were connected (Figure 2.10). A 300 V m⁻¹ electric field was applied through home-made 50×3 mm silver/silver chloride (Ag/AgCl) electrodes that the fabrication process was described previously (Nilaco, Japan)^{196,202}. A direct electric current was sourced and measured by a source measure unit (2410, Keithley, USA). The current required to establish the electric field can be calculated using Equation 4.1:

$$I = EFS \times \sigma \times w \times h, \quad (4.1)$$

where EFS , σ , w , h are the electric field strength, conductivity, width, and height of the microchannel, respectively.

The microscopic images of cells stimulated under 300 V m⁻¹ and 0 V m⁻¹ were taken by an automated phase contrast microscopy over 6 hours (Ti-E, Nikon, Japan).

The PMMA/PDMS microfluidic chips were fabricated as previously described in Section 2.3 and prepared according to the experimental workflow. Briefly, the microchannels were primed with 99.5% ethanol and washed with pure water before the working solutions of ECM coatings were infused by gravity flow in micropipette tips. The extracellular matrix coatings were incubated for 1 hour at 37 °C before washed with 1X D-PBS. The top reservoir was filled with serum-containing culture media. The glioblastoma cells were trypsinized, centrifuged by 300×g for 5 min, and resuspended in MEMα with 10% FBS to 1 × 10⁶ cells mL⁻¹ counted by a cell counter (Muse,

Table 4.1: Commonly used extracellular matrix coatings for cell migration.

ECM	Stock conc.	Working conc.	Common use
poly(D-lysine)	500 $\mu\text{g mL}^{-1}$	50 $\mu\text{g mL}^{-1}$	Positively charged synthesized amino acids for general cell adhesion.
Collagen I	3 mg mL^{-1}	50 $\mu\text{g mL}^{-1}$	General coating for cell attachment, migration and morphogenesis
Collagen IV	3 mg mL^{-1}	50 $\mu\text{g mL}^{-1}$	General coating for cell attachment, migration and morphogenesis
poly(L-ornithine)	0.01% (0.1 mg mL^{-1})	100 $\mu\text{g mL}^{-1}$	Positively charged synthesized amino acids for general cell adhesion.
poly(L-ornithine) +Laminin	n/a	100 $\mu\text{g mL}^{-1}$ + 50 $\mu\text{g mL}^{-1}$ 20 $\mu\text{g mL}^{-1}$ + 10 $\mu\text{g mL}^{-1}$	General coating for cells from central or peripheral nervous system.
Laminin	100 $\mu\text{g mL}^{-1}$	50 $\mu\text{g mL}^{-1}$ 10 $\mu\text{g mL}^{-1}$	Maintenance of ESCs; Epithelial differentiation; Neurite outgrowth
Vitronectin	0.5 mg mL^{-1}	5 $\mu\text{g mL}^{-1}$	Feeder-free maintenance of stem cells and primary neurons.
Fibronectin	1 mg mL^{-1}	10 $\mu\text{g mL}^{-1}$	Fibrillar matrices for stem cells and neural outgrowth.
iMatrix 511 (Laminin 511-E8)	0.5 mg mL^{-1}	50 $\mu\text{g mL}^{-1}$	Truncated form of laminin for enhanced iPSC feeder-free culture
Geltrex	0.12 – 0.18 mg mL^{-1} (ready-to-use)	0.12 – 0.18 mg mL^{-1} (ready-to-use)	Maintenance of ESCs; Endothelial capillary formation

Millipore, USA). Appropriate amount was seeded in the channels using micropipettes and cells were allowed to adhere to the bottom for 3 to 5 hours at 37 °C. After adhesion, the top reservoir was easily removed from the PMMA/PDMS chip by shearing and delaminating the de-ds tape. A 4 mm-thick PDMS slab punched with two 21G outlet holes (Accupunch, Syneo Corp, USA) was adhered on the component B of the PMMA/PDMS chip, completing the chip for experiment.

To start electrotaxis experiment, fresh media were supplied in the reservoir on component A of the PMMA/PDMS chip. Two sets of tubings (06419-01, Cole Parmer, USA) with stainless tubes (23RW, New England Small Tubes, USA) on one end and a double Luer gel dispensing needle on the other (23G, Musashi, Japan) were used. The tubings were steam sterilized before primed with 1X D-PBS with 2.5 mL syringes (Terumo, Japan). The stainless tube ends were inserted into the 21G holes of the PDMS slab on the PMMA/PDMS chip. The syringes were mounted on a syringe pump (YSP-202, YMC, Japan) and set in withdrawal mode to perfuse the cells on

PMMA/PDMS chips.

A 300 V m^{-1} direct current electric field strength (EFS) was established in section I (Figure 4.3) through two home-made Ag/AgCl wire electrodes^{196,202} inserted in the D-PBS reservoirs on component B by a source measure unit (2410, Keithley, USA). Time lapse phase contrast images of each condition were taken on an automated phase contrast microscope (Ti-E, Nikon, Japan).

4.2.5 Electrotaxis of T98G glioma cells under co-stimulation of different chemical ligands

To test if chemical signalings from chemical ligands mediate the electrotaxis of T98G cells, the thermoplastic chips were used. The thermoplastic chip was prepared, vacuumed, and primed with CO_2 gas, water, and D-PBS sequentially to prevent bubbles. The coverglass bottom of the chip was coated with Geltrex for 1 hour at 37°C . The microchannels were washed once with 1X D-PBS and cell culture medium before seeding of cells. The cells were trypsinized and resuspended to 5×10^6 cells mL^{-1} counted by a cell counter (Muse, Millipore, USA). The cells were seeded in the channels and allowed to adhere to the bottom for 3 to 5 hours at 37°C . Afterward, primed fluidic tubings and salt bridges were connected (Figure 2.10) and the culture media in the microchannels were exchanged to serum-free media at flow rate of $20 \mu\text{L min}^{-1}$. The cells were starved for 8 hours before exchange to ligand-containing serum-free media. The cells were stimulated with ligand-containing serum-free media for 1 hour before starting time-lapse cell imaging and electrical stimulation. The microscopy images of cells stimulated under 300 V m^{-1} and 0 V m^{-1} were taken over 6 hours.

4.2.6 Extracellular calcium dependency of glioma cell electrotaxis

To test if the electrotaxes of T98G and U-251MG cells require extracellular Ca^{2+} , calcium-free Dulbecco's minimum essential medium (Ca-free DMEM, 21068, Gibco, USA) and cation chelators such as ethylenediaminetetraacetic acid (EDTA) (15575, Thermo Fisher Scientific, USA) and ethylene glycol-bis(2-aminoethylether)-N,N,N',N'-tetraacetic acid (EGTA) (08907-84, Nacalai, Japan) were used. The PMMA/PDMS microfluidic chips were fabricated as previously described in Section 2.3 and prepared according to the experimental workflow. The microchannels were primed with 99.5% ethanol and displaced with pure water before Geltrex solutions were infused by gravity flow from micropipette tips. The Geltrex coatings were incubated for 1 hour at 37°C before being washed with 1X D-PBS. The top reservoir was filled with serum-containing culture media afterward.

The glioblastoma cells were trypsinized, centrifuged by $300\times g$ for 5 min, and resuspended in MEM α with 10% FBS to 1×10^6 cells mL^{-1} counted by a cell counter (Muse, Millipore, USA). Appropriate amount of cell suspension was seeded in the channels using micropipettes and cell were allowed to adhere to the bottom for 3 to 5 hours at 37°C . After adhesion, the top reservoir was easily removed from the PMMA/PDMS chip by shearing and delaminating the dual energy double-sided tape. A

4 mm-thick PDMS slab punched with two 21G outlet holes (Accupunch, Syneo Corp, USA) was adhered on the component B of the PMMA/PDMS chip, completing the chip for experiment.

Before the experiment, cells were incubated in Ca-free DMEM or MEM α with 10% FBS mixed with calcium chelators at indicated molar concentrations for 2 hours at 20 $\mu\text{L h}^{-1}$. Afterward a direct electric current was applied through Ag/AgCl wire electrodes in D-PBS buffer on the component B by a source measure unit (2410, Keithley, USA). Six-hour time lapse images were taken on an automated phase contrast microscope (Ti-E, Nikon, Japan).

4.2.7 Pharmaceutical inhibition of voltage-gated ion channels in electrotaxis of glioma cells

To test different inhibitors against various types of voltage-gated ion channels in high throughput fashion (Table 4.2), PMMA/PDMS microfluidic chips were used.

The PMMA/PDMS microfluidic chips were fabricated as previously described in Section 2.3 and prepared according to the experimental workflow. The microchannels were primed with 99.5% ethanol and displaced with pure water before Geltrex solutions were infused by gravity flow from micropipette tips. The Geltrex coatings were incubated for 1 hour at 37 °C before washed with 1X D-PBS. The top reservoir was filled with serum-containing culture media afterward.

The glioblastoma cells were trypsinized, centrifuged by 300 \times g for 5 min, and re-suspended in MEM α with 10% FBS to 1 \times 10⁶ cells mL⁻¹ counted by a cell counter (Muse, Millipore, USA). Appropriate amount of cell suspension was seeded in the channels using micropipettes and cell were allowed to adhere to the bottom for 3 to 5 hours at 37 °C. After adhesion, the top reservoir was easily removed from the PMMA/PDMS chip by shearing and delaminating the dual energy double-sided tape. A 4 mm-thick PDMS slab punched with two 21G outlet holes (Accupunch, Syneo Corp, USA) was adhered on the component B of the PMMA/PDMS chip, completing the chip for experiment.

For high throughput experiments, two PMMA/PDMS microfluidic chips could be set up in a single experiment (Figure 4.4), enabling screening of electrotaxis response of cells under four EFSs and four different conditions. A U-shaped PMMA salt bridge filled with 1% molten agarose in PBS was used to connect the two chips electrically by inserting into the PBS reservoirs on component B of the two PMMA/PDMS chips.

To start electrotaxis experiment with pharmaceutical inhibition, inhibitors were added to fresh MEM α media supplemented with 10% FBS at appropriate working concentrations (Table 4.2). The reagents were supplied in the reservoir on component A of the PMMA/PDMS chip. The tubings were connected as same as previously described in Section 4.2.4.

After cells were seeded and adhered well, the inhibitor-containing media were infused into the channels at 20 $\mu\text{L min}^{-1}$ for 10 minutes before changing to 20 $\mu\text{L h}^{-1}$ and incubated for 30 minutes. A direct electric current was applied through Ag/AgCl wire electrodes in D-PBS buffer on the component B by a source measure unit (2410, Keithley, USA). Six-hour time lapse images were taken on an automated phase contrast

Table 4.2: Pharmacological inhibitors to study the voltage-gated calcium channels in glioma electrotaxis.

Inhibitors	Stock conc.	Working conc.	Actions
Cadmium chloride	1 M	50 μ M	HVA VGCC inhibitor
		100 μ M	
Gadolinium chloride	1 M	50 μ M	HVA L-type VGCC inhibitor
		100 μ M	
Nickel chloride	1 M	500 μ M	LVA T-type VGCC inhibitor
		500 μ M	
EDTA	0.5 M	2 mM	Cation chelators (<i>e.g.</i> , Ca ²⁺)
EGTA	0.5 M	5 mM	Cation chelators (more selective toward Ca ²⁺)
Nicardipine	20 mM DMSO	10 μ M	L-type VGCC inhibitor
ω -Conotoxin GVIA	0.1 mM	3 μ M	N-type VGCC inhibitor
ω -Agatoxin IVA	0.1 mM	200 nM	P/Q-type VGCC inhibitor
ω -Conotoxin MVIIC	0.2 mM	500 nM	P/Q-type VGCC inhibitor
ω -Theraphotoxin-Hg1a (SNX482)	0.1 mM	500 nM	R-type VGCC inhibitor;
			A-type K ⁺ channel inhibitor
TTA-A2	0.1 M DMSO	100 μ M	T-type VGCC inhibitor
Amiloride hydrochloride	5 mM	100 μ M	T-type VGCC inhibitor;
			ENaC/ASIC/Degenerin inhibitor
Calmidazolium	10 mM DMSO	100 nM	Calmodulin antagonist
AmmTx3	0.1 mM	5 μ M	A-Type K ⁺ channel inhibitor
4-aminopyridine	50 mM	1 mM	A-Type K ⁺ channel inhibitor
		4 mM	
Benzamil hydrochloride	10 mM DMSO	5 μ M	Na ⁺ /Ca ²⁺ exchanger inhibitor;
			ASIC/ENaC inhibitor; TRPP inhibitor; TRPA1 inhibitor

microscope (Ti-E, Nikon, Japan).

4.2.8 Single cell migration tracking and statistical inference

A Nikon Ti-E automated microscope with Perfect Focus System and motorized XYZ stage was used to perform all microscopy experiments. A 10X phase contrast objective and intermediate magnification of 1.5X were used for taking 10-minute interval phase contrast images with a scientific CMOS (sCMOS) camera with 2 \times 2 binning (Orca Flash

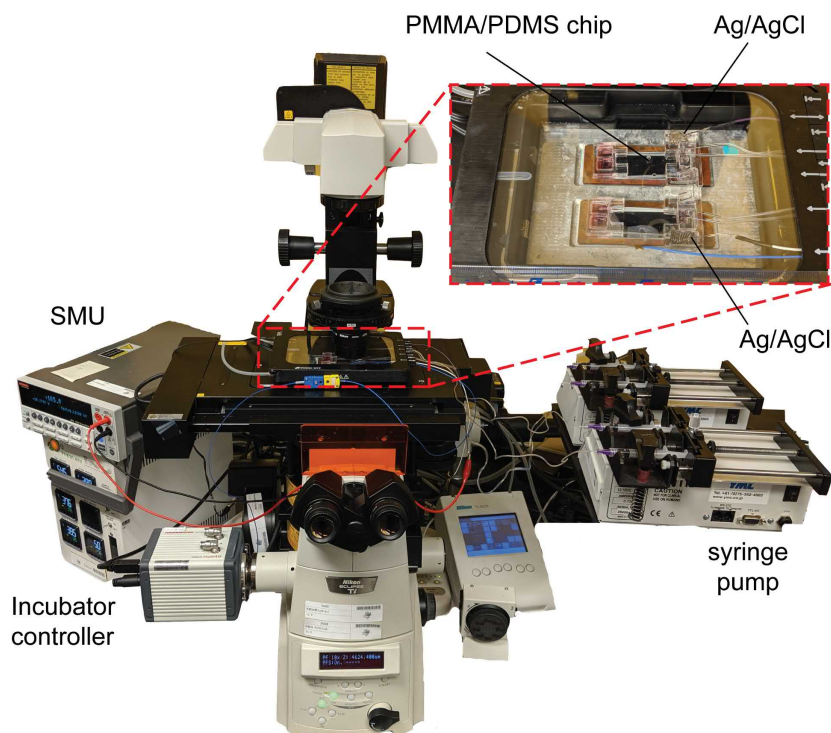


Figure 4.4: The photoimage of setup for high throughput experiments with PMMA/PDMS chips. The red dashed box indicates the magnified region with PMMA/PDMS chips in an on-stage incubator. SMU: source measure unit

4.0, Hamamatsu, Japan) in NIS Element AR software (Nikon, Japan). The spatial resolution at this setting was $\approx 0.87 \mu\text{m pixel}^{-1}$. All experiments were performed in triplicate.

After each experiment, images were exported from NIS element software as tiff files and automatically organized by XY positions into folders using an in-house developed Python script. The cells in the raw images were segmented, tracked, and automatically analyzed using the *Usiigaci* software (Chapter 3). Only cells tracked throughout all the frames in one viewfield were analyzed. At least 100 cells in every conditions were analyzed for cell-centric features such as the directedness, speed, and orientation changes before and after electric field or chemical stimulation (Table 4.3).

Briefly, the definitions of key cell-centric features used to quantify cell electrotaxis (Figure 4.5) were listed below:

- Directedness

The directedness of cell electrotaxis was defined as the average cosine of Euclidean vector and EF vector, $\sum_{i=1}^N \frac{\cos \Phi_i}{N}$, where Φ_i was the angle between the Euclidean vector of each cell migration and the vector of applied EF (from anode to cathode), and N was the total number of analyzed cells. A group of anodal moving cells held a directedness of -1; and a group of cathodal moving cells held a directedness of +1. For a group of randomly migrating cells, the directedness was zero.

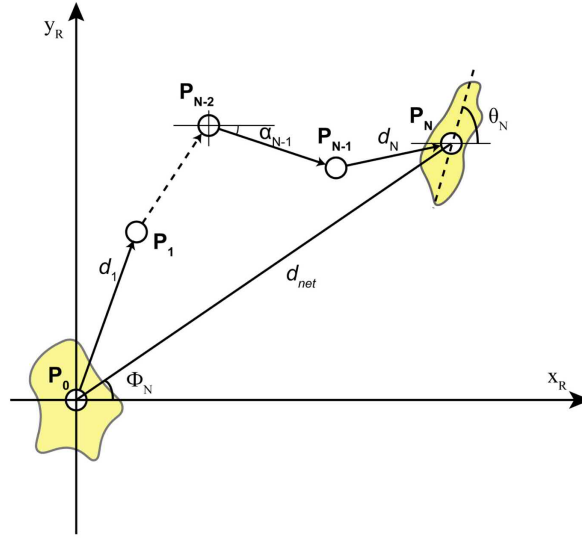


Figure 4.5: The single-cell migration parameters extracted from the electrotaxis experiments.

Table 4.3: Step-centric and cell-centric variables for describing single-cell migration.

Step-centric features	
Instantaneous displacement	$d_i = \sqrt{(x_i - x_{i-1})^2 + (y_i - y_{i-1})^2}$
Instantaneous speed	$s_i = d(p_{i-1}, p_i) / \Delta t$
Turning angle	$\alpha_i = \tan^{-1} \left(\frac{y_i - y_{i-1}}{x_i - x_{i-1}} \right)$
Directional autocorrelation	$dir - aut_i = \cos(\alpha_i - \alpha_{i-1})$
Instantaneous directedness	$Index_{directedness_{instant}} = \sum_{i=1}^N \frac{\cos \Phi_{instant_i}}{N} = \sum_{i=1}^N \frac{(x_i - x_{i-1})}{d_i \times N} = \frac{1}{N} \sum_{i=1}^N \frac{(x_i - x_{i-1})}{\sqrt{(x_i - x_{i-1})^2 + (y_i - y_{i-1})^2}}$
Cell-centric features	
Cumulative distance	$d_{total} = \sum_{i=1}^N d(p_{i-1}, p_i)$
Net trigonometric distance (Euclidean distance)	$d_{net} = d(p_0, p_N) = \sqrt{(x_N - x_0)^2 + (y_N - y_0)^2}$
Euclidean velocity	$\bar{v}_{net} = \frac{d_{net}}{t_{elapsed}}$
End-point directionality ratio	$ep_dr = \frac{d_{net}}{d_{tot}}$
Orientation	$Index_{orientation} = \sum_{i=1}^N \frac{\cos 2\theta_i}{N}$
Directedness	$Index_{directedness} = \sum_{i=1}^N \frac{\cos \Phi_i}{N} = \sum_{i=1}^N \frac{(x_i - x_0)}{d_{net} \times N} = \frac{1}{N} \sum_{i=1}^N \frac{(x_i - x_0)}{\sqrt{(x_i - x_0)^2 + (y_i - y_0)^2}}$

- Speed

The speed of cell electrotaxis was defined as the average of cell migration rate

to travel the Euclidean distance, $\sum_{i=1}^N \frac{(d_{net})_i}{t_{elapsed}}$, where the d_{net} was the Euclidean distance traveled by each cell, and $t_{elapsed}$ was the the time elapsed, and N was the total number of analyzed cells.

- Orientation

The orientation was defined as the average cosine of two times angle between the EF vector and the cell long axis, $\sum_{i=1}^N \frac{\cos 2\theta_i}{N}$, where θ_i was the angle between the applied EF vector and the long axis of a given cell; N is the total number of cells analyzed. A group of cells aligned perpendicular to the EF held an orientation of -1; and a group of cells aligned in parallel to the applied EF held an orientation of +1. For a group of randomly shaped cells, the average orientation was zero.

The cell-centric features were computed automatically and saved as Excel spreadsheets (Office365, Microsoft, USA) as part of the *Usiigaci* software analysis pipeline. The data was further statistically inferred by inputting the data in a statistical software (Prism 7, GraphPad LLC, USA). All data were presented as the mean \pm 95% confidence interval, which is 1.96 of standard error of mean, from triplicate experiments. One-way analyses of variance (ANOVA) with Tukey's multiple-comparison post-hoc tests were performed. The confidence level to reject a null hypothesis between two datasets was set at 95%. A p-value (P, the probability for a true null hypothesis) less than 0.05 represented a statistical significance at 95% confidence.

4.3 Results and discussion

4.3.1 Uniformly sparse cell seeding on chip by submerged operation

To analyze single cell migration in microchannels, cells must be seeded sparsely and allowed to adhere and culture reliably^{437,556}. However, it is known that uneven distribution of cells due to fluid flow, convection in suspension and vessel movement after seeding can cause aggregation and differentiation of cells⁴⁴⁰. Different cell loading methods affecting cell distribution in single cell migration experiments are investigated, such as tip loading method, tip injection method, and a pressure-balanced submerged cell seeding, as shown in Figure 4.6.

In tip loading method (Figure 4.6A), the cells flocculate in the small diameter of pipet tip and cannot uniformly distribute in the microchannel (Figure 4.6D, G, J). In tip injection method (Figure 4.6B), the cells are originally injected in the channels with uniform cell distribution. However, without balancing the microchannel inlet/outlet pressure, the minute hydrostatic pressure difference between inlets and outlets generate small pressure-driven flow that displaces cells and cause formation of cell aggregates (Figure 4.6E, H, K).

In tip injection method, due to the small dimension of the punched holes at inlet/outlet interfaces, bubbles are easily trapped and may be introduced into microchannels, disrupting fluid advection and chemical transport.

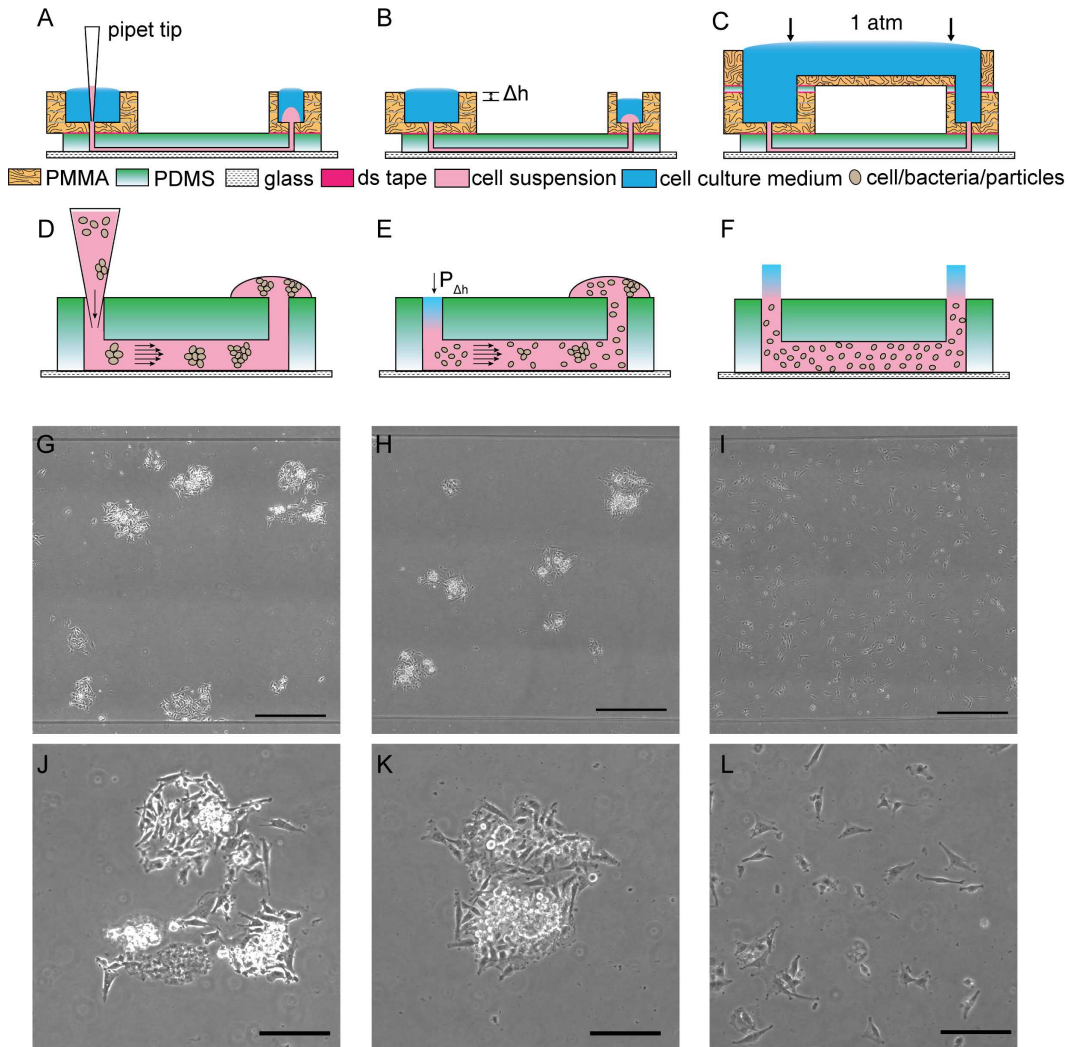


Figure 4.6: The results of U-251MG cell seeding inside microchannels by various methods. (A, D, G, J) In tip loading method, cells are introduced by using gravitational flow with micropipette tips. The cells can flocculate inside the tips and in microchannels as illustrated in (D). The microscopy image of seeded cells is shown in (G) and magnified in (J); (B, E, H, K) In tip injection method, cells are injected into the channels and tips are removed. The small hydrostatic pressure differences between the inlet/outlet (shown as Δh) will contribute to hydrodynamic flow and disturb the cell distribution, causing non-uniform cell distribution and aggregates as shown in (E). The microscopy image of seeded cells is shown in (H) and magnified in (K); (C, F, I, L) In our pressure-balanced submerged cell seeding method, the hydrostatic pressure difference is eliminated. The injected cells remain uniform throughout the channel as shown in (F). The microscopy image of seeded cells is shown in (I) and magnified in (L). The uniform and sparse cell seeding method is suitable for many different applications from single cell tracking, ensemble cell studies to cell assembly. The scale bars in (G, H, I) represent $500 \mu\text{m}$. The scale bars in (J, K, L) represent $200 \mu\text{m}$.

By submerging inlets and outlets underwater using a reversibly bonded top reservoir

and balancing the pressure between inlets and outlets (Figure 4.6C), air bubbles can be avoided and pressure-driven flow will be prevented to affect cell distribution. Moreover, using this cell seeding method, only minute amount of cells is needed (the volume of the microchannel). Uniformly distributed single cell seeding across the entire microchannel is obtained for single cell migration experiments (Figure 4.6F, I, L). The top reservoir in our submerged cell seeding method can be removed after cells are seeded and can be adapted to a wide range of microfluidic chips.

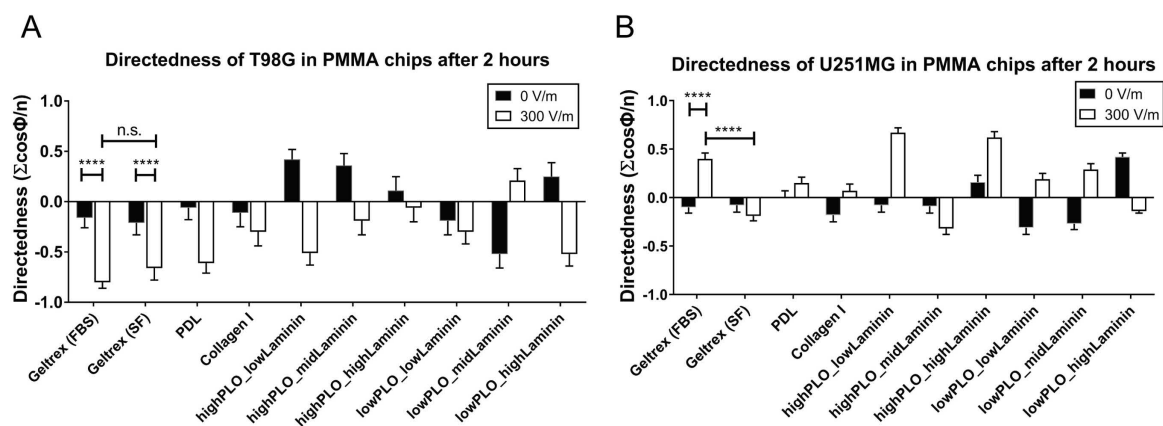


Figure 4.7: Electrotaxis responses of T98G and U-251MG cells in various ECMs in PMMA chips. (A) Directedness of T98G cells in PMMA chips; (B) Directedness of U-251MG cells in PMMA chips. High poly(L-ornithine) (PLO): $100 \mu\text{g mL}^{-1}$; low PLO: $20 \mu\text{g mL}^{-1}$; High laminin: $100 \mu\text{g mL}^{-1}$; Mid laminin: $50 \mu\text{g mL}^{-1}$; Low laminin: $10 \mu\text{g mL}^{-1}$; ****: $P < .0001$; n.s.: not significant; SF: serum free; PDL: poly(D-lysine).

4.3.2 Identification of appropriate ECM coatings for glioblastoma electrotaxis

An effective ECM coating on the substrate is essential for cell adhesion and formation of focal adhesions for cell migration^{547,557}. Glioblastoma can be molecularly classified according to The Cancer Genome Atlas (TCGA) into proneural, neural, classical, and mesenchymal types⁵⁵⁸. I investigated how different ECM coatings affected the adhesion and electrotaxis of T98G and U-251MG glioblastoma cell lines in air-impermeable thermoplastic microfluidic chip and in air-permeable hybrid PMMA/PDMS chips. Both cell lines are of caucasian male origin and classified as mesenchymal type with p53 mutant genotype^{559,560}.

Using thermoplastic chips, the electrotaxes of T98G and U-251MG glioblastoma cells in air-impermeable conditions on poly(D-lysine) (PDL), collagen I, Geltrex, and various combinations of poly(L-ornithine)(PLO) and laminin are investigated (Figure 4.7). While standard PDL and PLO/laminin coatings have been used for glioblastoma electrotaxis, the directional and speed results are not always consistent and stably reproduced (Figure 4.7 & Figure 4.8)^{292,294}. The cell morphologies of T98G cells on PDL, Geltrex, and PLO/laminin are shown in Figure 4.9. Spiky cell morphology can

be seen in T98G cells on PDL surfaces, suggesting that the cells are not well adhered on it. On Geltrex surfaces, T98G cells adhere well and demonstrate lamellipodia which is less commonly seen in T98G cells on surfaces coated with PLO/laminin.

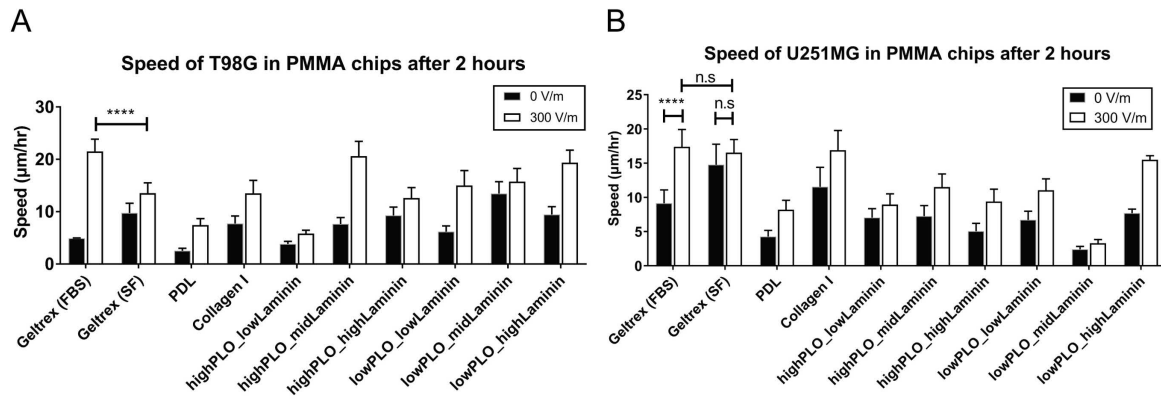


Figure 4.8: Electrotaxis responses of T98G and U-251MG cells in various ECMs in PMMA chips. (A) Speed of T98G cells in PMMA chips; (B) Speed of U-251MG cells in PMMA chips. High poly(L-ornithine) (PLO): $100 \mu\text{g mL}^{-1}$; low PLO: $20 \mu\text{g mL}^{-1}$; High laminin: $100 \mu\text{g mL}^{-1}$; Mid laminin: $50 \mu\text{g mL}^{-1}$; Low laminin: $10 \mu\text{g mL}^{-1}$; ****: $P < .0001$; n.s.: not significant; SF: serum free; PDL: poly(D-lysine).

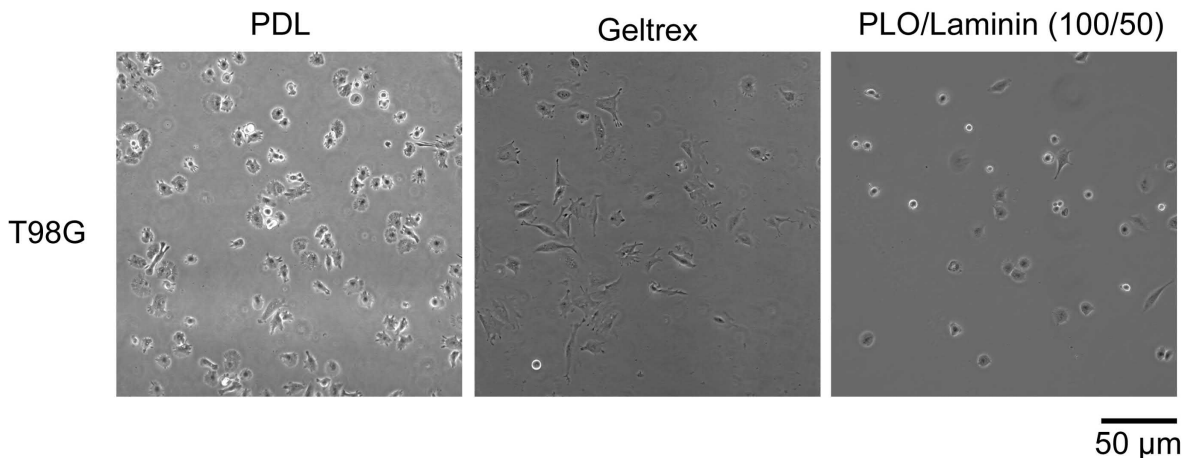


Figure 4.9: Phase contrast images of T98G on PDL, Geltrex, and PLO/laminin ($100/50 \mu\text{g mL}^{-1}$) in PMMA chips.

On Geltrex-coated substrate, both of the studied cells can adhere well on the substrate and demonstrate reproducible electrotaxis results (Table 4.4). While PLO/laminin is commonly used for cells of central nervous system (CNS) lineages, Geltrex coating is simple to apply in one shot and does not require combinatorial optimization as in cases of PLO/laminin.

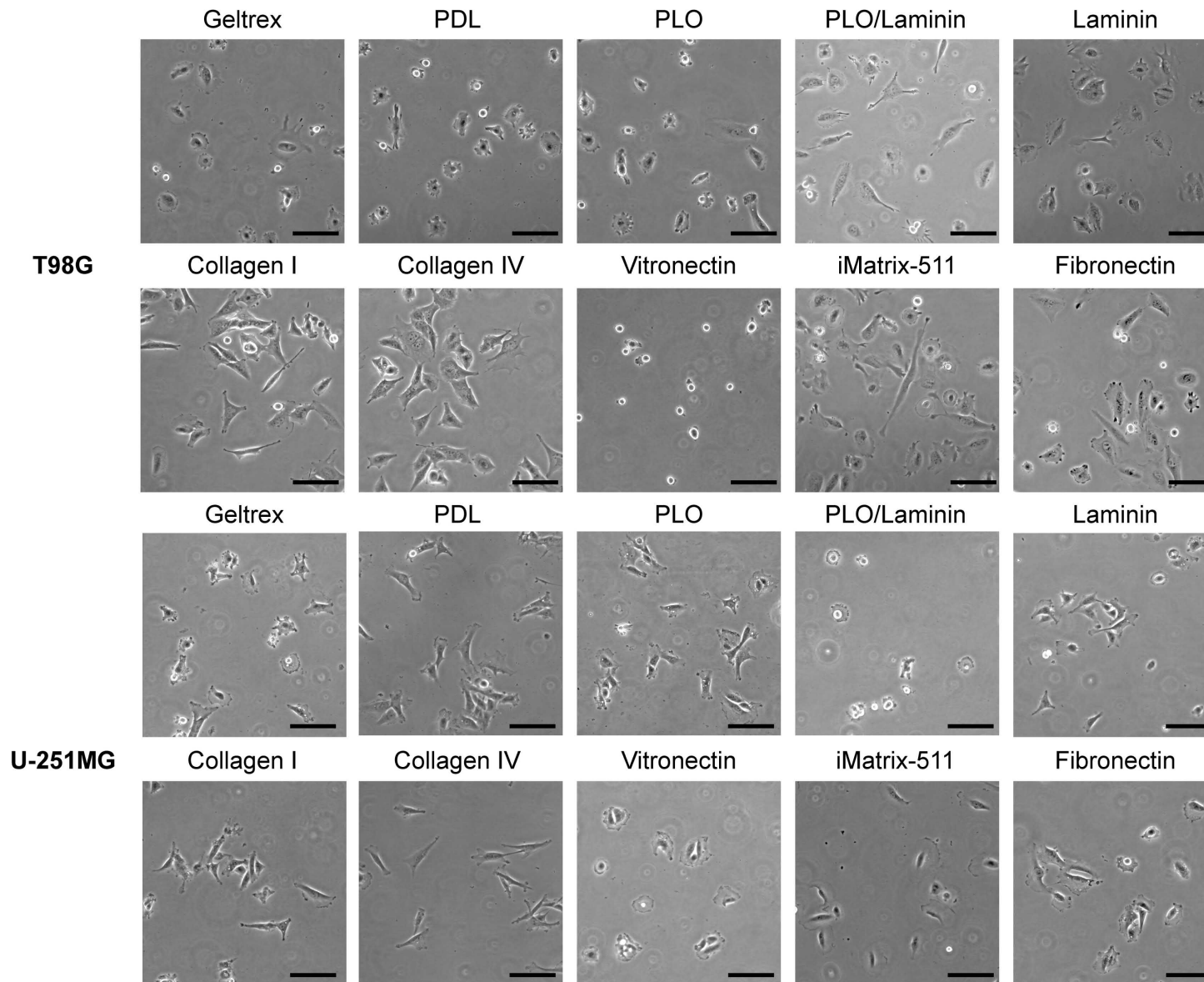


Figure 4.10: Phase contrast images of T98G & U-251MG cells on various ECMs. Scale bar: 100 μ m.

Glioma electrotaxis on various ECMs after 6 hours

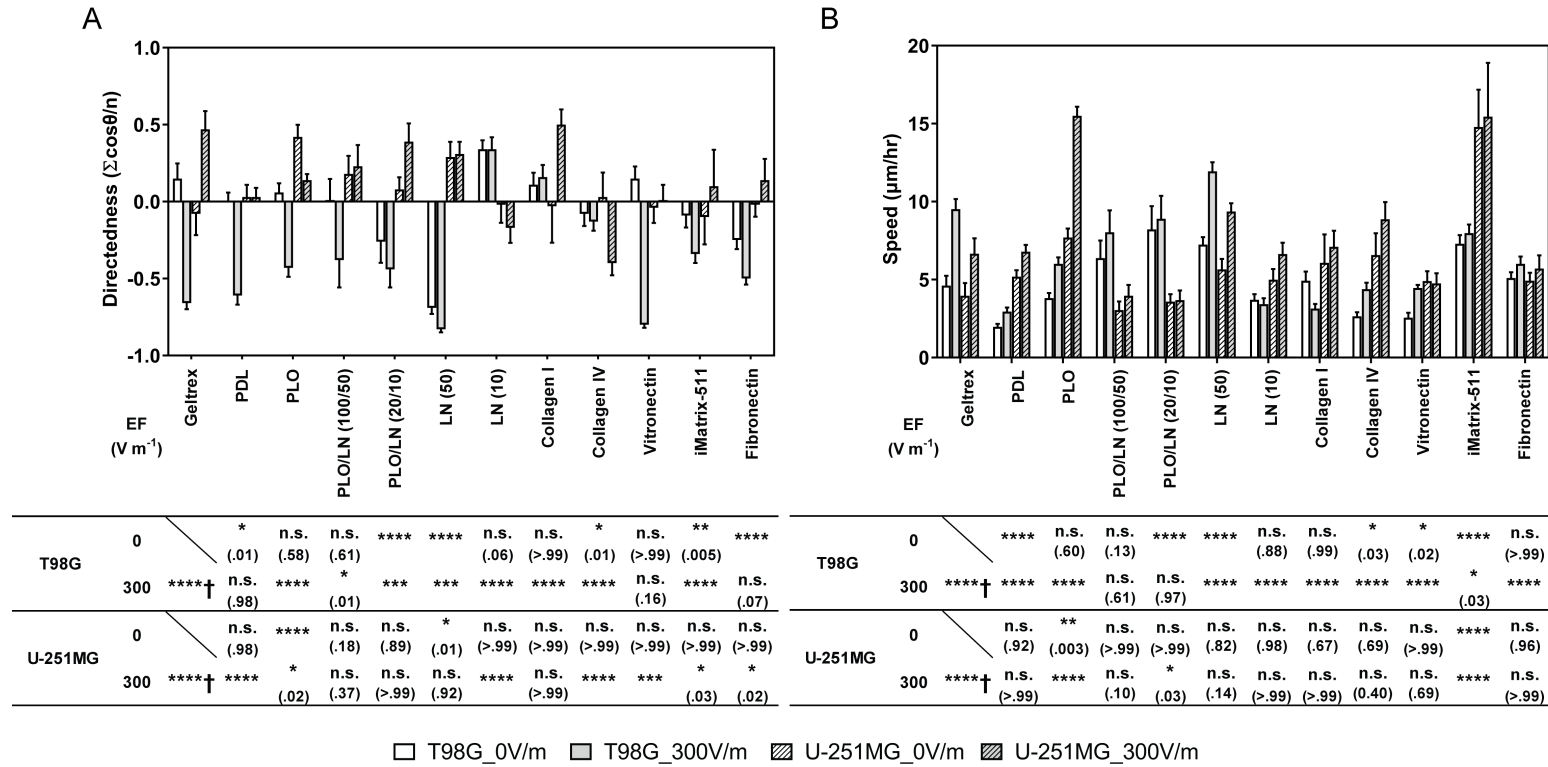


Figure 4.11: The electrotaxis of T98G & U-251MG glioblastoma cells on various ECMs after 6 hours under $300 V m^{-1}$ EF stimulation. (A) The electrotaxis directedness; (B) The electrotaxis speed; † indicate the electrotaxis groups tested against those without EF stimulation; All other groups are statistically compared to their respective controls on GeltrexTM ECM; n.s. indicates not significant; * indicates $P < .05$; ** indicate $P < .01$; *** indicate $P < .001$; **** indicate $P < .0001$; The numbers in parentheses indicate actual P-values.

The preference to Geltrex coating is also confirmed in air-permeable PMMA/PDMS chips. The morphologies of T98G and U-251MG cells on Geltrex, PDL, PLO (100 $\mu\text{g mL}^{-1}$), PLO/laminin (100/50 $\mu\text{g mL}^{-1}$), laminin (50 $\mu\text{g mL}^{-1}$), collagen I, collagen IV, vitronectin, iMatrix-511, and fibronectin in PMMA/PDMS chips are shown in Figure 4.10. The adhesion and electrotaxis of T98G and U-251MG cells are investigated on various ECMs in PMMA/PDMS chips (Figure 4.11).

While standard poly(D-lysine) (PDL) and various combinations of poly(L-ornithine) (PLO) and laminin have been used for glioblastoma electrotaxis^{294,316}, the directedness and speed results are not always consistent and stably reproduced. T98G and U-251MG electrostatic responses are also not stably reproduced on collagen I, collagen IV, vitronectin, and fibronectin coatings. Both T98G and U-251MG cells adhere well on substrates containing laminins which cells interact through various integrins including $\alpha1\beta1$, $\alpha2\beta1$, $\alpha3\beta1$, $\alpha6\beta1$, $\alpha7\beta1$ ^{561,562}. The integrins are believed to participate in the initiation of electrotaxis through mechanosensitive pathways^{224,230,231}. The cell morphologies of the two cell lines on various ECMs are shown in Supplementary FIG. S.2. T98G cells do not adhere well on PDL surfaces or vitronectin as indicated by the spiky or rounded cell morphology. On laminin containing surfaces such as GeltrexTM or pure laminin coating, cells are well adhered and demonstrate lamellipodia structures. Particularly, U-251MG cells demonstrate large lamellipodia associated with high migratory speed (15.45 $\mu\text{m hr}^{-1}$ under 300 V m^{-1} , $P < .0001$) on iMatrix-511-coated substrates but with diminished directedness (0.01, $P < .0001$). Note that iMatrix-511 is a recombinant truncated laminin with $\alpha5\beta1\gamma1$ subunits and interacts with cells through the $\alpha6\beta1$ integrin^{563,564}. This suggests that the specific molecular configuration of laminins in ECM may be vital for electrotaxis.

Particularly, T98G and U-251MG cells demonstrate high migratory speed on 50 $\mu\text{g mL}^{-1}$ laminin and Geltrex surfaces. GeltrexTM is a growth factor-reduced complex basement membrane extract purified from murine Engelbreth-Holm-Swarm tumors containing laminin, collagen IV, entactin, and heparin sulfate proteoglycan⁵⁶⁵. The electrostatic directionality and speed of both T98G and U-251MG are more prominent and reproducible on Geltrex coatings, hence all the studies in the following sections are studied with Geltrex coatings. The detailed results of T98G and U-251MG electrotaxis is shown in Table 4.5.

While it is understood that ECMs in tumor microenvironment is important⁵⁶⁶, glioblastoma cells demonstrate preference for adherence and electrotaxis on laminin-coated surfaces. Within the brain microenvironment, laminin expressions are restricted to the basement membrane of neural vasculature⁵⁶⁷ and perivascular tumor microenvironment is especially vital for glioblastoma metastasis^{537,568}. Therefore, the correlation among laminin, glioblastoma electrotaxis, and the perivascular invasion process may be important in glioblastoma cancer biology that requires further elucidation.

4.3.3 Electrotactic heterogeneity in glioblastoma cell lines

To further analyze how T98G and U-251MG cells migrate under stimulation of direct current electric fields, the electrotaxes of the two glioblastoma cells in serum-containing and serum-free media were examined.

Table 4.4: The results of glioblastoma electrotaxis on various ECM coatings in PMMA microfluidic chips after 2 hours. sem: standard error of mean.

ECM	Concentration ($\mu\text{g mL}^{-1}$)	FBS (%)	EF (V m^{-1})	T98G			U-251MG						
				N	Directedness sem	Speed ($\mu\text{m hr}^{-1}$) sem	N	Directedness sem	Speed ($\mu\text{m hr}^{-1}$) sem				
Geltrex	120 – 180 (ready to use)	10%	300	116	-0.80	0.03	21.51	1.19	123	0.40	0.06	17.39	1.28
				208	-0.16	0.05	4.91	0.04	112	-0.10	0.06	9.15	0.98
Geltrex	120 – 180 (ready to use)	0 %	300	109	-0.66	0.06	13.53	1.00	193	-0.19	0.05	16.53	0.98
				117	-0.21	0.06	9.76	0.93	111	-0.08	0.07	14.76	1.52
poly(D-lysine)	50	10%	300	102	-0.61	0.05	7.44	0.63	114	0.15	0.06	8.19	0.70
				117	-0.06	0.06	2.53	0.24	104	0.00	0.07	4.28	0.46
	100/100	10%	300	102	-0.06	0.07	12.62	1.00	102	0.62	0.06	9.40	0.91
				105	0.11	0.07	9.28	0.81	113	0.16	0.07	5.06	0.58
	100/50	10%	300	109	-0.19	0.07	20.60	1.43	102	-0.32	0.06	11.51	0.96
				107	0.36	0.06	7.67	0.61	106	-0.09	0.07	7.27	0.77
poly(L-ornithine)	100/10	10%	300	115	-0.51	0.06	5.81	0.33	104	0.67	0.05	8.95	0.79
				100	0.42	0.05	3.83	0.26	103	-0.08	0.07	7.05	0.66
+	20/100	10%	300	115	-0.52	0.06	19.36	1.21	278	-0.14	0.02	15.50	0.30
				110	0.25	0.07	9.47	0.75	189	0.42	0.04	7.70	0.29
Laminin	20/50	10%	300	127	0.21	0.06	15.74	1.28	116	0.29	0.06	3.31	0.27
				107	-0.52	0.07	13.47	1.15	130	-0.27	0.06	2.40	0.22
	20/10	10%	300	115	-0.30	0.06	15.02	1.43	120	0.19	0.06	11.04	0.85
				110	-0.19	0.07	6.19	0.55	112	-0.31	0.07	6.70	0.65
Collagen I	50	10%	300	108	-0.30	0.07	13.52	1.25	119	0.07	0.07	16.89	1.46
				107	-0.11	0.07	7.73	0.74	100	-0.18	0.07	11.55	1.43

Table 4.5: The results of glioblastoma electrotaxis on various ECM coatings in PMMA/PDMS microfluidic chips after 6 hours. sem: standard error of mean.

ECM	Concentration ($\mu\text{g mL}^{-1}$)	EF (V m^{-1})	T98G					U-251MG								
			N	Directedness	sem	Speed ($\mu\text{m hr}^{-1}$)	sem	Orientation	sem	N	Directedness	sem	Speed ($\mu\text{m hr}^{-1}$)	sem	Orientation	sem
Geltrex	120-180	300	2634	-0.66	0.02	9.52	0.33	-0.75	0.03	276	0.47	0.06	6.66	0.50	-0.07	0.07
	(ready-to-use)	0	2014	0.15	0.05	4.62	0.32	0.04	0.05	295	-0.08	0.07	3.97	0.41	0.04	0.07
Poly(D-Lysine)	50	300	1047	-0.61	0.03	2.95	0.13	-0.17	0.04	470	0.03	0.03	6.79	0.22	-0.10	0.04
	0	0	1164	0.00	0.03	1.98	0.09	-0.10	0.03	370	0.03	0.04	5.19	0.21	-0.04	0.04
Poly(L-ornithine)	100	300	960	-0.43	0.03	6.01	0.21	-0.52	0.03	278	0.14	0.02	15.50	0.30	-0.11	0.04
	0	0	1059	0.06	0.03	3.81	0.17	-0.04	0.04	189	0.42	0.04	7.70	0.29	0.03	0.06
Poly(L-ornithine) +	100/50	300	221	-0.38	0.09	8.04	0.71	-0.15	0.10	233	0.23	0.07	3.97	0.35	-0.11	0.08
	0	0	320	0.01	0.07	6.38	0.57	-0.04	0.07	265	0.18	0.06	3.05	0.28	-0.07	0.07
Laminin	20/10	300	574	-0.44	0.06	8.90	0.75	-0.22	0.07	254	0.39	0.06	3.69	0.31	-0.12	0.06
	0	0	665	-0.26	0.07	8.22	0.76	0.06	0.07	226	0.08	0.04	3.59	0.24	-0.03	0.05
Laminin	50	300	1474	-0.83	0.01	11.94	0.30	-0.69	0.02	194	0.31	0.04	9.37	0.27	-0.00	0.07
	0	0	1059	-0.69	0.02	7.25	0.24	-0.02	0.04	186	0.29	0.05	5.65	0.34	-0.02	0.08
Laminin	10	300	293	0.34	0.04	3.43	0.19	-0.28	0.04	456	-0.17	0.05	6.64	0.37	-0.10	0.05
	0	0	404	0.34	0.03	3.71	0.18	0.09	0.04	302	-0.02	0.06	4.99	0.35	0.08	0.06
Collagen I	50	300	359	0.16	0.04	3.14	0.15	-0.15	0.04	166	0.50	0.05	7.11	0.52	0.07	0.06
	0	0	891	0.11	0.04	4.93	0.30	-0.05	0.04	135	-0.03	0.12	6.08	0.92	0.04	0.13
Collagen IV	50	300	424	-0.13	0.03	4.39	0.21	-0.29	0.03	207	-0.40	0.04	8.87	0.56	-0.08	0.05
	0	0	352	-0.08	0.04	2.65	0.13	0.01	0.04	73	0.03	0.08	6.58	0.70	0.05	0.09
Vitronectin	5	300	613	0.80	0.01	4.46	0.10	-0.20	0.03	184	0.01	0.05	4.76	0.33	-0.15	0.05
	0	0	342	0.15	0.04	2.56	0.16	-0.05	0.04	200	-0.04	0.05	4.91	0.32	0.14	0.05
iMatrix-511	50	300	601	-0.34	0.03	7.98	0.28	-0.39	0.03	163	0.10	0.12	15.45	1.75	-0.31	0.13
	0	0	385	-0.09	0.04	7.30	0.28	-0.06	0.04	122	-0.10	0.09	14.79	1.21	-0.07	0.10
Fibronectin	10	300	553	-0.50	0.02	6.01	0.24	-0.55	0.03	263	0.14	0.07	5.71	0.43	-0.12	0.07
	0	0	543	-0.25	0.03	5.10	0.19	-0.11	0.03	658	-0.02	0.04	4.93	0.26	-0.02	0.04

T98G and U-251MG cells migrate toward opposite directions under electrical stimulation Figure 4.12 shows the directedness and speed of T98G and U-251MG electrotaxis. Upon 300 V m^{-1} dcEF stimulation, T98G cells migrate toward anode (positive electrode) while the U-251MG cells migrate toward cathode (negative electrode). Furthermore, the directedness in the electrotaxis of T98G cells does not depend on the presence of fetal bovine serum (FBS) ($P=.45$) but the speed is significantly decreased ($P<.0001$). The directedness of U-251MG cell electrotaxis however is highly dependent on the presence of FBS ($P<.0001$) and lack of FBS also decreases the speed of U-251MG electrotaxis ($P<.0001$) (Figure 4.12A). The serum is rich in growth factors, proteins, and ions, which can enhance the chemical signaling in electrotaxis (Figure 4.1).

Glioblastoma can be molecularly classified according to The Cancer Genome Atlas (TCGA) into proneural, neural, classical, and mesenchymal types⁵⁵⁸. Both T98G cells and U-251MG cells are categorized as mesenchymal type glioblastoma cells^{559,560}, however, their electrotactic responses are completely different. Similar results are reported in the electrotaxis of glioblastoma spheroids²⁹⁵ and lung adenocarcinoma²⁰² that although molecular and surface marker makeups are similar, the electrotaxis responses can be completely different. The opposite electrotaxis results may reflect the fundamental heterogeneity among the glioblastoma cells which has been suspected to contribute to the recurrence and therapeutic resistance after anti-tumor therapy⁵⁶⁹⁻⁵⁷³. Further elucidation of the correlation among electrotactic responses, metastatic properties of glioblastoma, and *in situ* electric field around the lesion may be beneficial to evaluate electrotaxis response as a predictive tool for glioma metastasis.

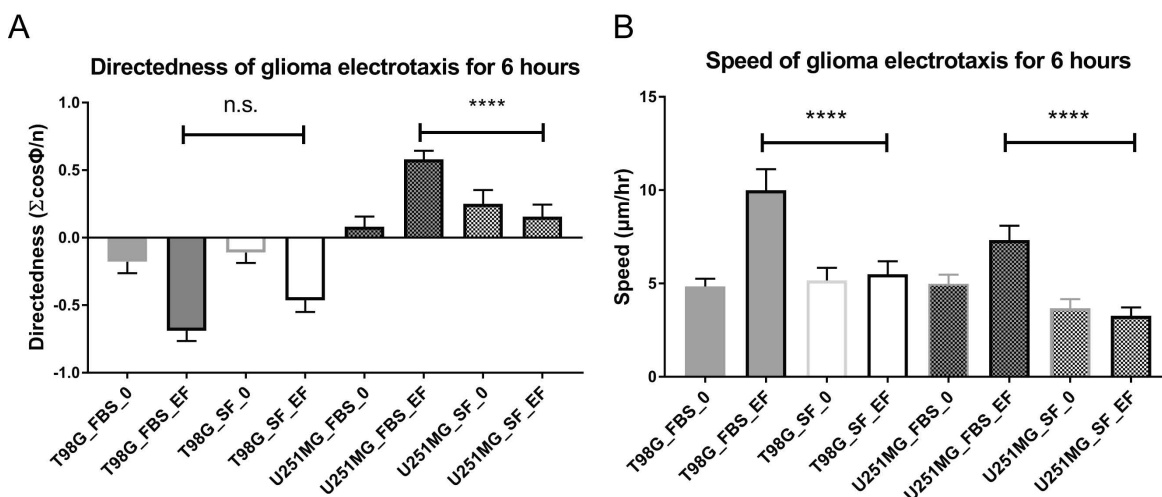


Figure 4.12: The electrotactic responses of T98G and U-251MG are completely different and dependent on serum supplementation. (A) The electrotactic directedness after 300 V m^{-1} stimulation for 6 hours; (B) The electrotactic speed after 300 V m^{-1} stimulation for 6 hours. ****: $P<.0001$.

Figure 4.13 shows the time course change of directedness in T98G and U-251MG glioblastoma cells electrotaxis. Immediately after the electrical stimulation, cells start to respond to the electric field and show directional migration. The directedness become

apparent and statistically significant ($P < .05$). This is similar to the observation found in fibroblasts, keratinocytes, and lung adenocarcinoma cells^{202,234,574,575}

T98G and U-251MG electrotactic directedness change over 6 hours

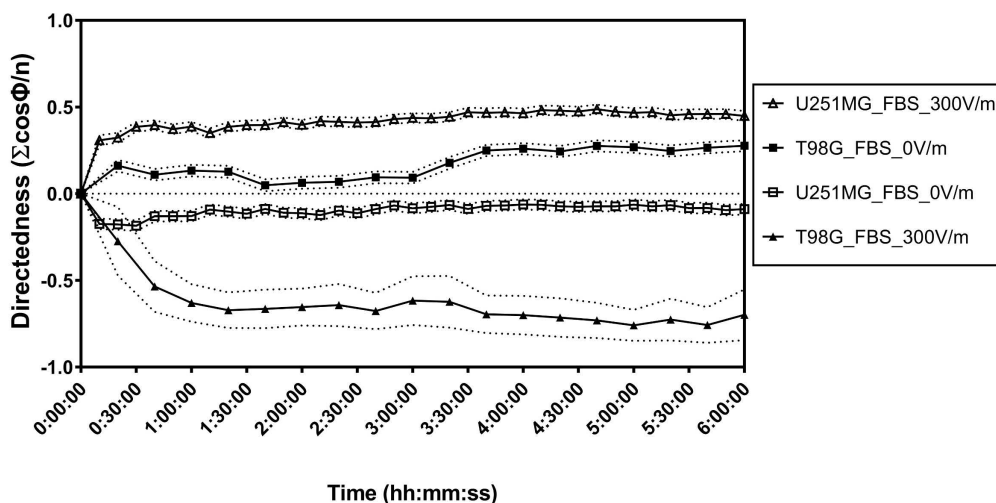


Figure 4.13: Time series plot of directedness in electrically stimulated glioblastoma cells. T98G cell results are indicated in closed symbols. U-251MG cell results are indicated in open symbol. Under the electrical stimulation, cells immediately start to respond to it. Note the directedness become apparent within the first hour of stimulation.

Only T98G cells demonstrate prominent electro-alignment behavior under electrical stimulation Aside from directional migration in the direct current electric fields, cells may also demonstrate long axial alignment in perpendicular to the electric field vector. While this phenomenon is commonly observed among many cell types^{109,202,576–578}, the mechanism and role of it are not clear. Electro-alignment may participate in the cytoskeletal restructuring in tissue morphogenesis^{579,580}, but biophysical studies show that *in vitro* microtubules align in parallel to electric field vectors rather than perpendicular^{581,582}.

Figure 4.14 shows the time course change of orientation in electrically stimulated T98G and U-251MG cells over 6 hours. The orientation index is defined as average cosine of two times the angle between the long axis of a cell and the electric field vector. For a group of perpendicularly oriented cells, the average orientation index is -1 and a group of parallelly orientated cells, the average orientation index is 1. For a group of randomly arranged cells, the average orientation index should be 0. For a group of perpendicularly oriented cells, the average orientation is -1 and a group of parallel orientated cells, the average orientation is 1. For a group of randomly arranged cells, the average orientation should be 0. Only T98G cells show prominent perpendicular alignment after electrical stimulation ($\text{Index}_{\text{orientation}}$ at 0 hr v.s. 6 hr is -0.11 v.s. 0.83, $P < .0001$, Figure 4.15). Serum deprivation slightly decreases the alignment tendency and delays the onset but does not abolish it ($\text{Index}_{\text{orientation}}$ of serum

free v.s. 10% FBS at 6 hr is -0.48 v.s. -0.83 , $P < .0001$). However, U-251MG does not show any perpendicular alignment. These results further illustrate the heterogeneity of glioblastoma cells.

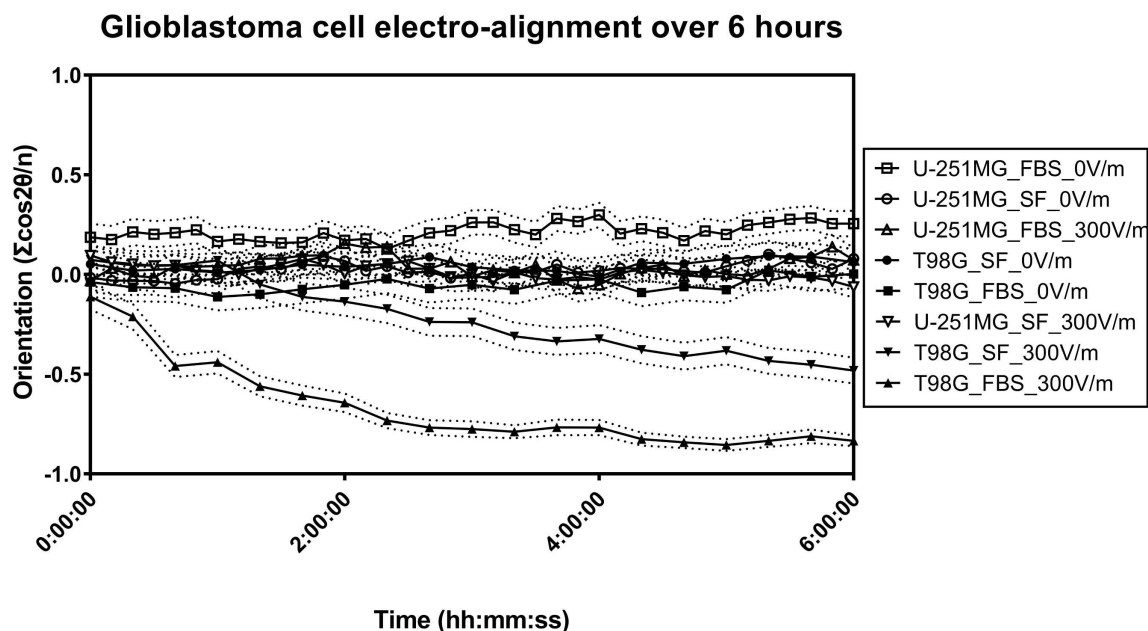


Figure 4.14: Time series plot of orientation in electrically stimulated glioblastoma cells. T98G cell results are indicated in closed symbols. U-251MG cell results are indicated in open symbol. Only T98G cells demonstrate prominent perpendicular alignment after electrical stimulation. The dashed lines indicate the 95% confidence interval for respective groups.

4.3.4 Glioma electrotaxis does not intersect with ligand-mediated chemical signaling

Several ligand-mediated chemical signaling is reported to participate in cell electrotaxis, including enzyme-linked receptors, G-protein coupled receptor, and cytokine receptors (Figure 4.1). However, currently, no consensual signaling mechanism for electrotaxis has been identified. Depending on the expression profiles of receptors, one signaling pathway participating in the electrotaxis in cell type A does not necessarily take part in cell type B as in cases of EGFR in lung cancer electrotaxis¹⁹⁶. Furthermore, under electric field stimulation, the polarized receptors by *in situ* electrophoresis can be activated in lipid microdomains without the presence of ligands²²⁷.

I investigate if the electrotaxis of T98G cells is mediated when there is also presence of ligand-mediated signaling (Figure 4.16 & Figure 4.17). If electrotaxis of T98G cells is affected by the presence of chemical ligands, it implies a particular ligand-mediated receptor signaling. However, the electrotaxis of T98G is completely unchanged even if there is presence of ligand-mediated signaling, while only the $\text{TNF}\alpha$ -stimulated cells have increased migration speed. The results suggest that the signaling of T98G cells

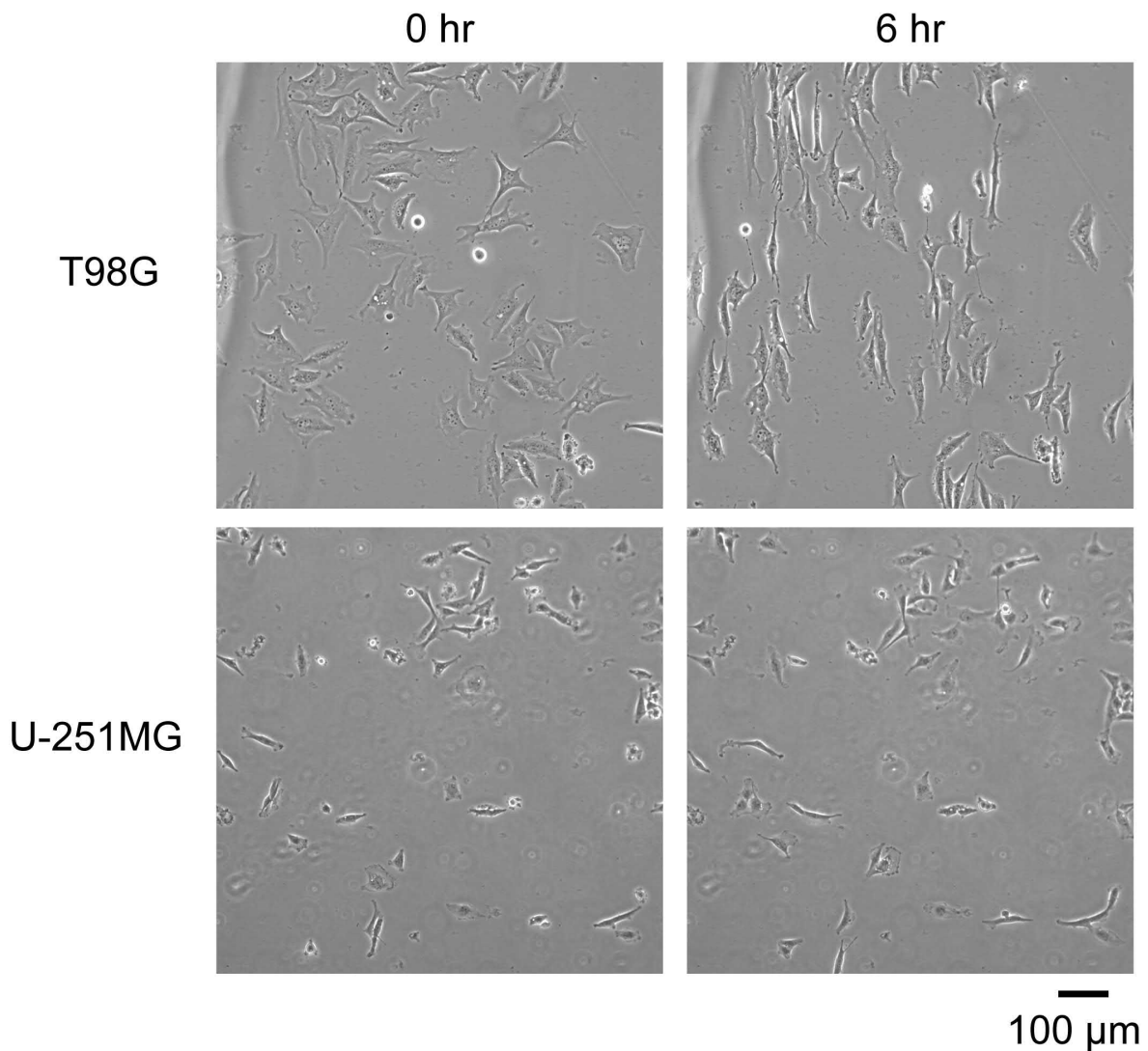


Figure 4.15: Phase contrast images of T98G and U-251MG before and after 6 hours 300 V m^{-1} stimulation. The electric field vector is from left to right. Only T98G cells demonstrate prominent perpendicular alignment after electrical stimulation.

electrotaxis does not intersect with that of ligand-mediated cellular signaling. The result is consistent with a previous report that several receptor tyrosine kinases did not involve in brain tumor initiating cells' electrotaxis such as EGFR, FGFR, PDGFR, and VEGFR2²⁹³.

4.3.5 Glioma electrotaxis is dependent on extracellular calcium cations

Calcium ion flux is known to involve in the electrotaxis signaling of multiple cell types including mouse fibroblasts, human prostate cancer cell, and neural crest cells^{214,583–586}. Deregulation of calcium influx in the cells reduces actin polymerization and affects the cell motility speed but its effect on electrotactic directedness varied depending on cell

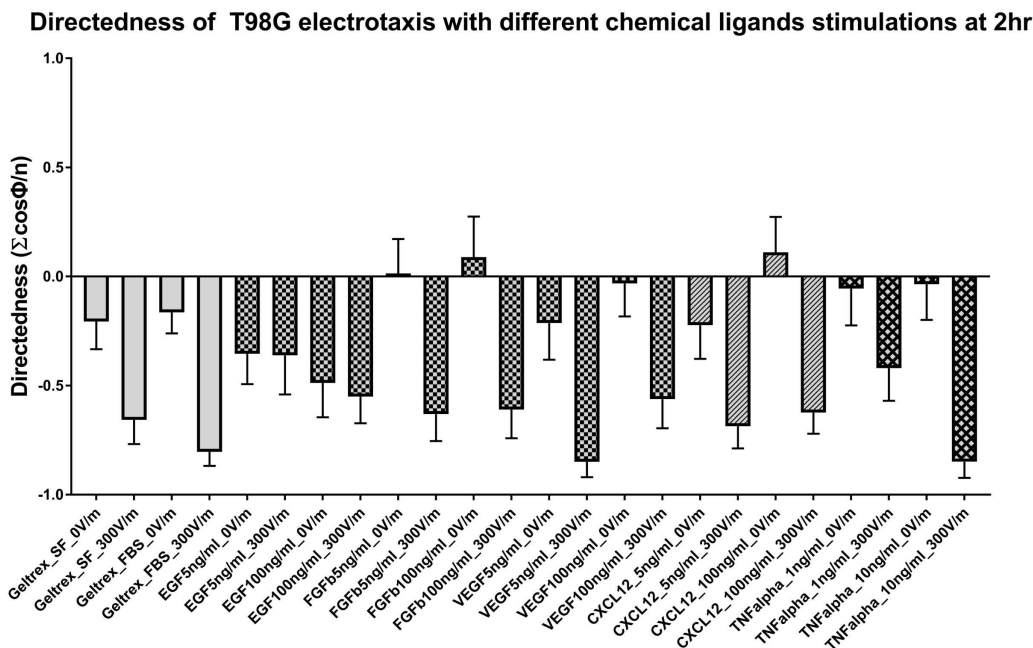


Figure 4.16: The electrotactic directedness of T98G glioblastoma cells costimulated with ligands for chemical signaling.

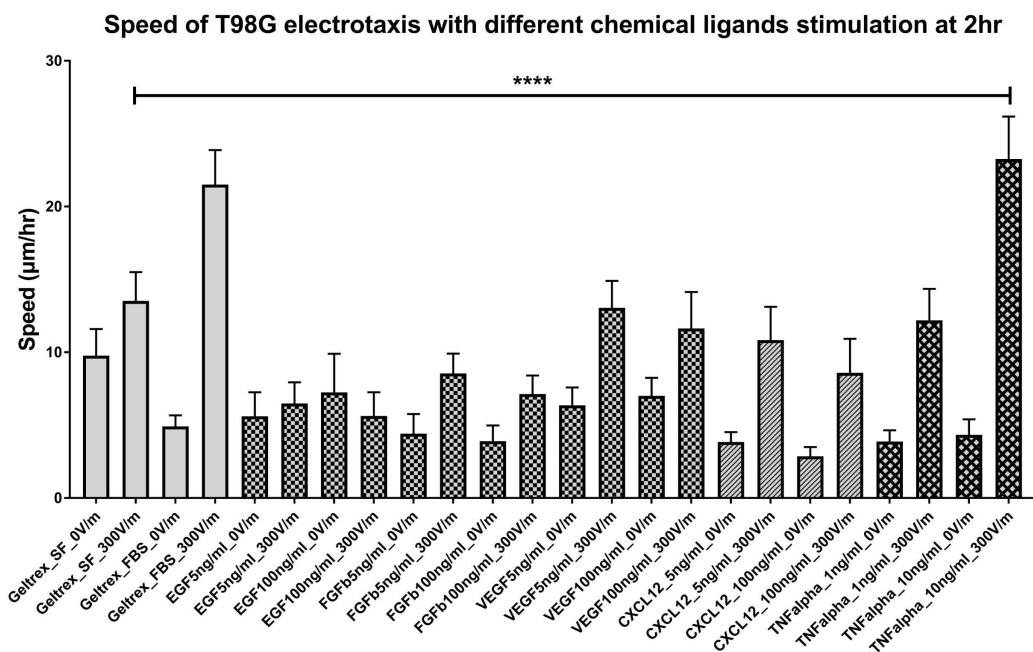


Figure 4.17: The electrotactic speed of T98G glioblastoma cells costimulated with ligands for chemical signaling.

types^{214,586}.

I further investigate if the extracellular calcium cation is important for glioblas-

toma electrotaxis (Figure 4.18). In serum-free DMEM, both T98G and U-251MG cell electrotaxes are significantly repressed in directedness ($P < .001$). Also, T98G cells lose cell viability completely in Ca-free serum-free DMEM when subjected to electrical stimulation ($N=0$). However, this loss of viability is rescued by the addition of 10% FBS which contains calcium and growth factors. The electrotaxis of U-251MG in calcium-free, serum-free media is not affected compared to those in serum-free media ($P > .99$). Interestingly, the electrotactic speed of U-251MG in calcium-free serum-free media further increases ($P < .0001$).

To identify if calcium cations are important, cation chelators EDTA and EGTA were used to chelate the free calcium in the MEM α with 10% FBS. Treatment of 2 mM EDTA significantly represses the directedness of only U-251MG cells ($P < .0001$, Figure 4.18A). To further confirm the electrotaxis inhibition is due to extracellular calcium cations, EGTA, a divalent cation chelator with increased affinity towards Ca^{2+} , is used. At 1 mM EGTA, the electrotactic directednesses of both cell lines are not affected but the electrotactic speeds of them become more dispersed ($P < .0001$). Under 2 mM EGTA treatments, the electrotactic directedness of U-251MG cells are reduced ($P < .0001$). When 5 mM EGTA is used, the electrotaxis of both cell lines are further repressed in both directedness and speed and the cells detach from the substrate. These results suggest that glioblastoma electrotaxis requires extracellular calcium cations and calcium influx may be important for electrotaxis, particularly that of U-251MG cells.

Effects of extracellular Ca²⁺ on glioblastoma electrotaxis after 6 hours

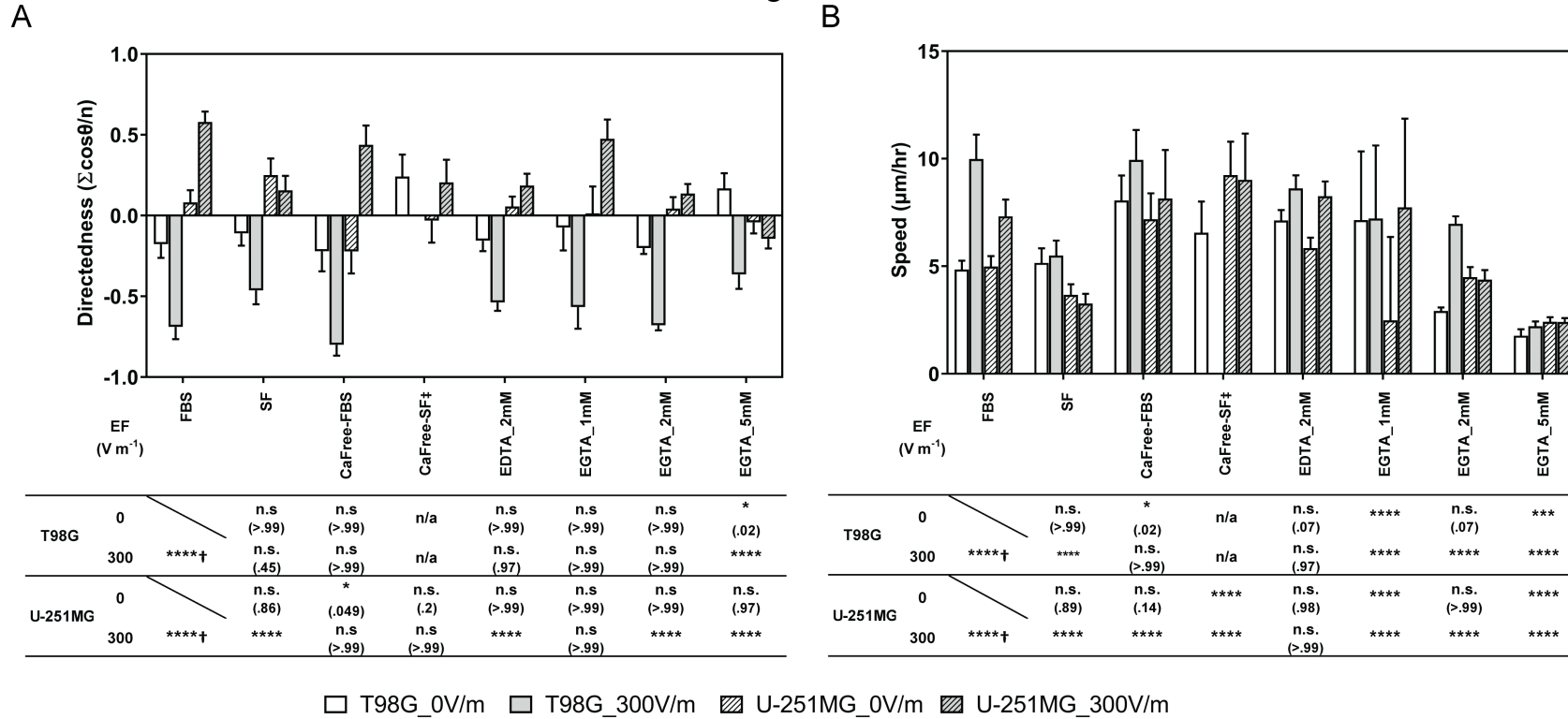


Figure 4.18: The effects of extracellular Ca²⁺ on glioma electrotaxis after 6 hours. (A) The directedness of glioma electrotaxis; (B) The speed of glioma electrotaxis; † indicate the electrotaxis groups tested against those without EF stimulation; ‡ indicate the electrotaxis group tested against those in serum-free media; All other groups are statistically compared to their respective controls in cell culture media with 10% FBS; n.s. indicates not significant; * indicates P<.05; ** indicate P<.01; *** indicate P<.001; **** indicate P<.0001; The numbers in parentheses indicate actual P-values.

Involvement of different voltage-gated calcium channels in glioma electrotaxis

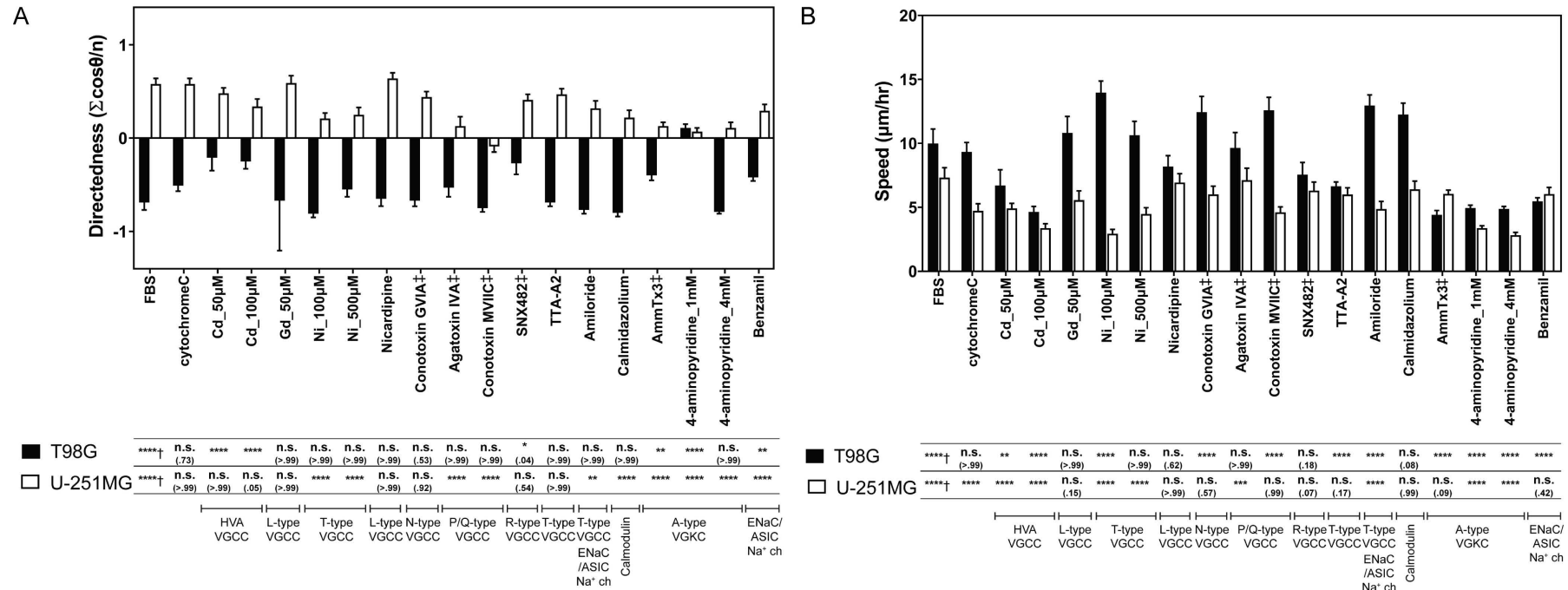


Figure 4.19: The electrotaxis of T98G & U-251MG glioblastoma cells under 300 V m^{-1} dcEF after 6 hours with pharmacological inhibition on various ion channels. (A) The directedness of glioblastoma electrotaxis; (B) The speed of glioblastoma electrotaxis. † indicates the electrotaxis tested against those without EF stimulation; ‡ indicate the electrotaxis group tested against those with cytochrome C which prevents adsorption of short peptides to experimental apparatus; All other groups are statistically compared to their respective controls in cell culture media with 10% FBS; n.s. indicates not significant; * indicates $P < .05$; ** indicate $P < .01$; *** indicate $P < .001$; **** indicate $P < .0001$; The numbers in parentheses indicate actual P-values.

4.3.6 Glioma electrotaxis is dependent on different types of voltage-gated ion channels

Ions channels expressed on glioblastoma cells including various potassium, calcium, sodium, and chloride ion channels are believed to facilitate pathogenesis of glioblastoma^{546,587-589}. Although the expression of numerous ion channels varies among clinical glioma samples⁵⁴⁴, ion channel expression profiles have been suggested to predict survival in glioma patients^{590,591}. Glioblastoma cells are immersed in the local field potentials within the brain, and extracellular calcium is required for glioblastoma electrotaxis which can influx into the cells through voltage-gated calcium channels (VGCCs), so if and how VGCCs participate in the electrotaxis of glioblastoma may shed new insights for inhibiting glioblastoma infiltration.

VGCCs are known to play important roles in glioma biology such as cell proliferation, apoptosis, and sensitization to ionizing radiation^{546,552,553}. VGCCs can be categorized as high voltage activated (HVA) or low voltage activated (LVA) types^{172,554,555}. Among the HVA VGCCs, four subtypes can be categorized by electrophysiological property and genetic phylogeny, including L-type (long-lasting, $Ca_v1.1-1.4$), P/Q-type (purkinje/unknown, $Ca_v2.1$), N-type (neural, $Ca_v2.2$), and R-type (residual, $Ca_v2.3$) VGCCs. The LVA VGCCs are composed of T-type channels (transient, $Ca_v3.1-3.3$). Although the involvement of VGCCs in the electrotaxis of glioblastoma is not yet elucidated but VGCCs' role in electrotaxis of other cell types is suggested. Trollinger *et al.*, find that a stretch-sensitive VGCC mediates the electrotaxis of human keratinocytes²¹³. Aonuma *et al.*, report that T-type VGCC mediates the electrotaxis of green paramecia⁵⁹². L-type VGCCs also regulate the chondrogenesis during early limb development which is known to be a bioelectricity process⁵⁹³.

Another class of membrane proteins that are bioelectrically activated are voltage-gated potassium channels (VGKCs), which are represented by 12 families (K_v1-K_v12). VGKCs are involved in diverse physiological and pathological processes regulating the repolarization of neuromuscular action potential, calcium homeostasis, cellular proliferation, migration, and cancer proliferation⁵⁹⁴⁻⁶⁰⁰. Voltage-gated potassium channel $K_v1.2$ ⁶⁰¹ and non voltage-gated inwardly-rectifying potassium channel $K_{ir}4.2$ ⁶⁰² have been shown to be involved in the sensing of electric field and signaling of cell electrotaxis. The potassium ion transporters confer biophysical signals that are key for regulating stem cells and tumor cells behavior in microenvironment⁶⁰³. In prostate cancer cells, VGKC expressions are linked to the increased metastatic potential⁶⁰⁴. Furthermore, inhibition of $K_v1.3$ VGKC has been shown to induce apoptosis of glioblastoma cells *in vitro*⁶⁰⁵.

I further investigate if HVA and LVA VGCCs play a role in the electrotaxis of T98G and U-251MG cells by using various inhibitors against L-type, P/Q type, R-type, and T-type VGCCs (Table 4.2). Many of these inhibitors are short peptides purified or recombinant engineered from venoms of poisonous species. When testing inhibition, cytochrome C was added to prevent non-specific adsorption of peptide inhibitors to microfluidic chips⁶⁰⁶. The detailed results of pharmacological VGCC inhibition on the electrotaxis of T98G and U-251MG cells are shown in Table 4.6.

In both glioblastoma cell lines, inhibition of L-type HVA VGCC with gadolinium⁶⁰⁷ or nifedipine⁶⁰⁸ exhibit no effect on electrotactic directedness ($P > .99$, Figure 4.19A)

as well as speed ($P > .15$, Figure 4.19B). Inhibition of N-type HVA VGCCs with ω -Conotoxin GVIA^{609,610} also has no effect on the electrotaxis of either cell type ($P > .92$).

T98G electrotaxis may depend on R-type HVA VGCC and A-type voltage-gated potassium channel The electrotaxis of T98G is repressed when treated with cadmium which is a broad spectrum HVA VGCCs inhibitor at both 50 μM and 100 μM ($P < .0001$)^{611,612}. Upon further identification, the directedness in T98G electrotaxis is repressed by use of SNX-482, a R-type VGCC inhibitor^{613,614} ($P = .0497$, Figure 4.19).

Calmodulin, a calcium binding protein, mediates many of the Ca^{2+} dependent-signaling by interacting with VGCCs and maintaining intracellular calcium homeostasis^{615,616}. However, the electrotaxis of T98G is not dependent on calmodulin by inhibition with calmidazolium ($P > 0.99$) and Ni^{2+} treatment has no inhibition on T98G cells ($P > 0.99$) which has partial inhibition on R-type VGCC^{614,617}. These results imply an alternative mechanism might be at play.

Cadmium and SNX-482 have been reported to also block a rapid inactivating (A-type) transient outward VGKC ($\text{K}_v4.3$) and experimental results using SNX-482 should be interpreted carefully⁶¹⁸⁻⁶²⁰. Using 5 μM AmmTx3, a member of the α -KTX15 family of scorpion toxins, to block A-type VGKCs ($\text{K}_v4.2$ & $\text{K}_v4.3$)⁶²¹⁻⁶²³, T98G electrotaxis directedness (FBS v.s. AmmTx3 = -0.69 v.s. -0.39, $P = .0025$) and speed (FBS v.s. AmmTx3 = 9.99 v.s. 4.42, $P < .0001$) are repressed but not completely abolished. Furthermore the inhibition on T98G directness caused by SNX-482 is stronger than AmmTx3 (SNX-482 v.s. AmmTx3 = -0.27 v.s. -0.39, $P = .039$, two-tailed t test). Another broad spectrum transient VGKC inhibitor, 4-aminopyridine (4-AP), was used to confirm the results⁶²⁴⁻⁶²⁶. Under 1 mM 4-AP, the directedness and speed in T98G electrotaxis were both repressed ($P < .0001$). Increasing of 4-AP to 4 mM, though results suggest that electrotactic directedness has not changed ($P > .99$) compared to control, but the migration speed is decreased ($P < .0001$). This is likely an artifact from part of T98G cells starting to detach from the surface rather than actual electrotaxis (Figure 4.20). These results suggest that T98G electrotaxis may be mediated by A-type VGKCs ($\text{K}_v4.3$), but the involvement of R-type VGCCs cannot be completely ruled out. Further molecular studies into the roles of VGCCs and VGKCs in glioblastoma electrotaxis are required.

Microimage of glioblastoma cells under different EF stimulations after 6 hours

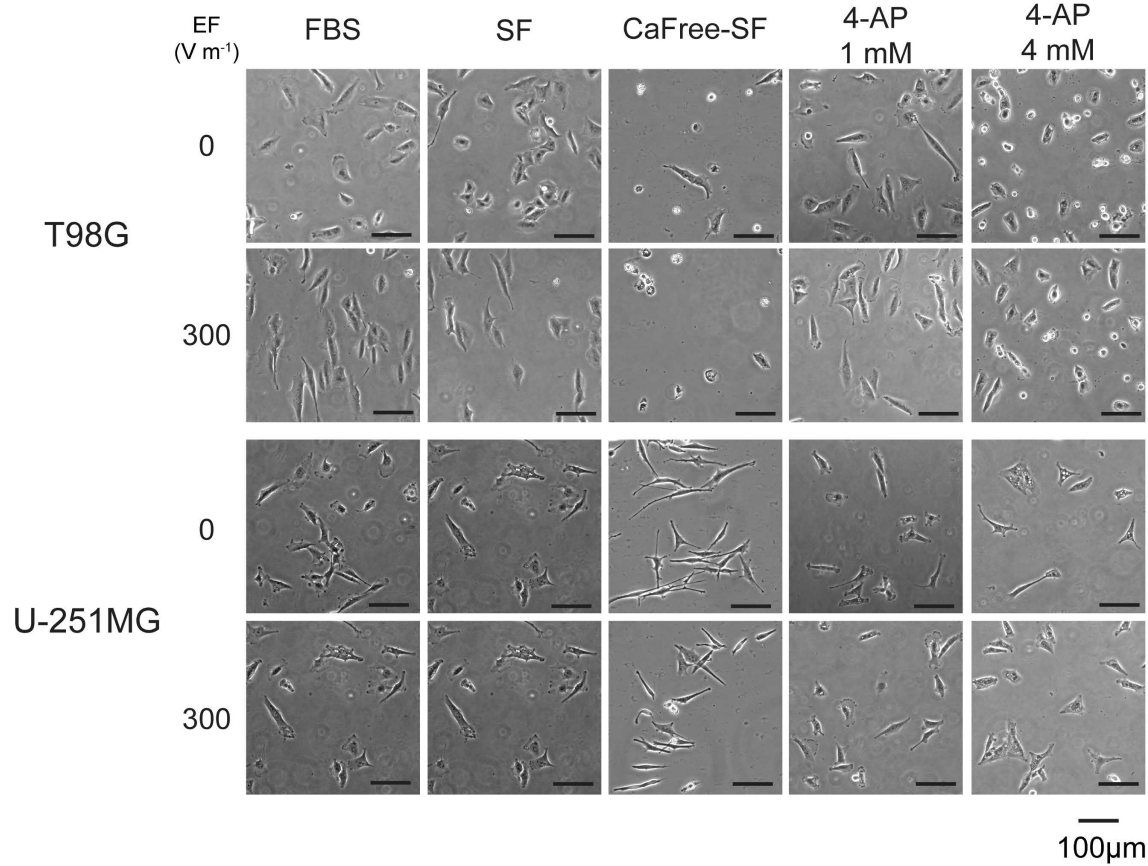


Figure 4.20: Phase contrast images of T98G & U-251MG cells under EF stimulations in different microenvironments after 6 hours.. The scale bars represent 100 μm . 4-AP: 4-aminopyridine. T98G cells demonstrate perpendicular alignment after electric field stimulation in cell culture media with or without FBS. However, without calcium and FBS in the cell culture medium, T98G cells' viability decreases. Furthermore, in cell culture medium supplemented with 4 mM 4-AP, T98G also lose viability and start to detach from the substrate. These trends were not observed in the U-251MG cells, suggesting heterogeneity between cell lines.

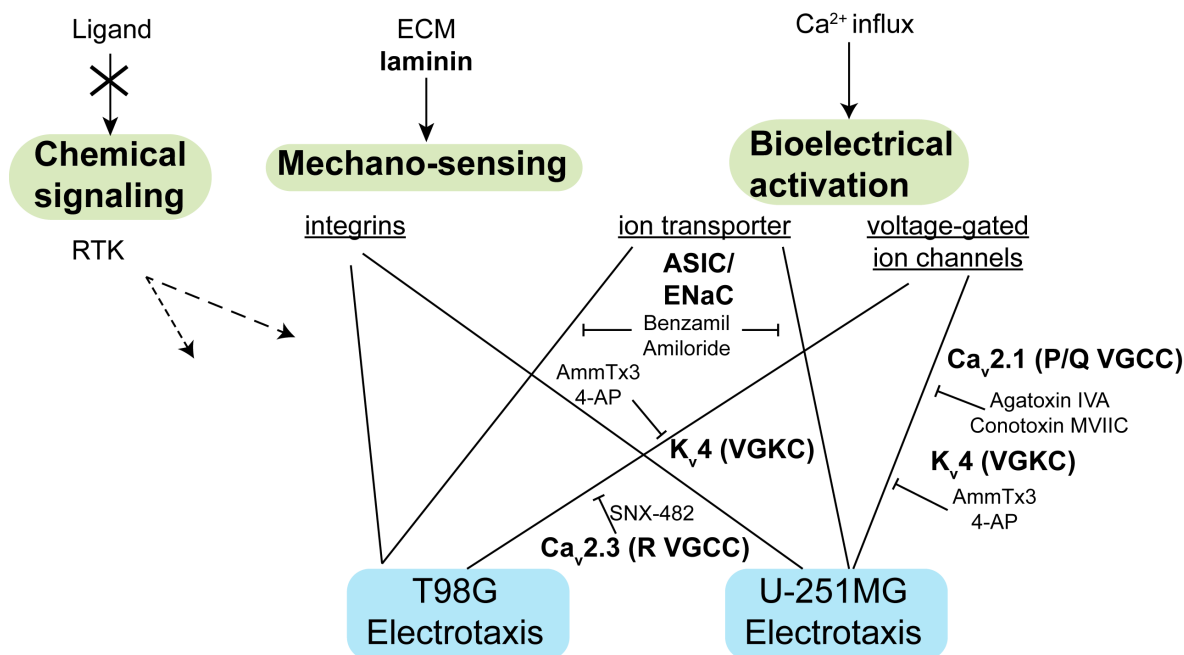


Figure 4.21: The signaling pathways of glioblastoma electrotaxis identified in this study. Laminin-based ECMs is necessary for glioblastoma electrotaxis suggesting that integrins may play a role. The voltage-gated ion channels and ion transporters also mediate glioblastoma electrotaxis that requires extracellular calcium.

U-251MG electrotaxis may depend on P/Q-type HVA VGCCs with involvement of sodium channels U-251MG electrotaxis is also dependent on high voltage activated VGCCs. Decreased directedness and speed are seen in U-251MG cells treated with 100 μM cadmium ($P=.0372$, Figure 4.19). Upon further identification, U-251MG electrotaxis is repressed when treated with P/Q-type HVA VGCC inhibitor using agatotoxin IVA and conotoxin MVIIC ($P<.0001$). However, the electrotactic speed is not affected by agatotoxin IVA ($P>0.99$) but decreased by conotoxin MVIIC ($P<.0001$). The electrotactic directedness of U-251MG is dependent on calmodulin ($P<.0001$).

Furthermore, the electrotactic directedness of U-251MG cells is repressed with nickel ($P<.0001$) and amiloride ($P<.01$) as well as the electrotactic speed ($P<.0001$). The results suggest a possible involvement of T-type VGCC⁶²⁷ in U-251MG electrotaxis. However, U-251MG electrotaxis is not affected when tested using another potent T-type VGCC inhibitor, TTA-A2^{628,629}. Nickel at high concentrations may also inhibit acid-sensing ion channel (ASIC) and epithelial sodium channel (ENaC), which are members of a superfamily of voltage-insensitive mechanosensitive sodium channels^{630,631}. Amiloride is also reported to inhibit ASIC/ENaC sodium channels, transient receptor potential polycystic 3 (TRPP3) channels, and sodium proton exchanger 1 (NHE1)⁶³²⁻⁶³⁴. Furthermore ASIC sodium channels are specifically expressed in the high-grade glioma cells but not in normal brain tissue or low grade glial cells^{635,636}. Nickel at high concentrations may also inhibit acid-sensing ion channel (ASIC) and epithelial sodium channel (ENaC), which are members of superfamily of voltage-insensitive mechanosensitive sodium channels^{630,631}. Amiloride is also re-

ported to inhibit ASIC/ENaC sodium channels, transient receptor potential polycystic 3 (TRPP3) channels, and sodium proton exchanger 1 (NHE1)^{632–634}.

To confirm the involvement of ASIC/ENaC in U-251MG electrotaxis, U-251MG cells are treated with 5 μ M benzamil hydrochloride (Alomone labs, USA)^{634,637,638}. The directedness of U-251MG electrotaxis is significantly repressed by benzamil treatment (FBS v.s. benzamil = 0.58 v.s. 0.29, $P < .0001$) but not the speed ($P = .42$). The ENaC sodium channel has been shown to mediate the electrotaxis of human keratinocytes⁵⁷⁵. Sodium ion flux may also be important in mediating electrotaxis. Voltage-gated sodium channels (VGSCs) have been suggested to direct the electrotaxis and potentially also direct the metastasis of prostate cancer cells^{164,639,640}.

Furthermore, when inhibition of A-type VGKCs are tested on U-251MG electrotaxis using AmmTx3 and 4-AP, the electrotaxis directedness is inhibited by both compounds ($P < .0001$) and the speed is repressed in only 4-AP ($P < .0001$) but not AmmTx3 ($P = .09$). These results suggest that multiple voltage-gated ion channels as well as ASIC sodium channels mediate the electrotaxis of U-251MG cells.

Various ion channels participated in the electrotaxis of glioblastoma cells of different origins

The pharmacological studies on the ion channels in T98G and U-251MG electrotaxes suggest that multiple ion channels, which may be voltage-sensitive or not, can mediate the sensing of electric field and initiate the migratory response. A-type VGKC, R-type VGCC, and ASIC sodium channels mediate the electrotaxis of T98G cells while P/Q-type VGCCs, A-type VGKC, and ASIC sodium channels mediate the electrotaxis of U-251MG cells. The mechanisms investigated in this work is shown in Figure 4.21.

Although the expression of numerous ion channels varies among clinical glioma samples⁵⁴⁴, ion channel expression profiles have been suggested to predict survival in glioma patients^{590,591}. Correlating ion channel expressions and electrotactic phenotypes of cancer cells may be beneficial to provide new insights of novel metastasis-aimed therapeutics^{641,642}. The downstream molecular signaling of VGCCs, VGKCs, and ASIC sodium channels in glioblastoma electrotaxis is an interesting future direction to investigate. Moreover, systematic screening of other potassium channels and sodium channels' ability to mediate glioblastoma electrotaxis is necessary to identify signaling pathways that may contribute to glioblastoma metastasis. The high-throughput hybrid microdevices developed here can be very useful for systematic phenotype profiling and identification of molecular mechanisms in cell electrotaxis.

4.4 Summary and prospects

The hybrid PMMA/PDMS microfluidic chip is a robust platform for high throughput electrotaxis studies. Cell migration in multiple electric fields under multiple conditions can be studied in one experiment in combination with automated microscopy. The submerged operation balances the inlet/outlet pressure guarantees a stable microenvironment that avoids microbubbles, ensures uniform cell seeding, and minimizes required number of cells. Uniformly distributed single cells can be reliably seeded in microfluidic chip that further increases the robustness for high throughput experiments.

Table 4.6: The detailed results of glioblastoma electrotaxis in the presence of antagonists against ion channels or calcium signaling after 6 hours. CytoC: Cytochrome C; sem: standard error of mean.

Condition	CytoC (1 mg mL ⁻¹)	EF (V m ⁻¹)	T98G				U-251MG					
			N	Directedness	sem	Speed ($\mu\text{m hr}^{-1}$)	sem	N	Directedness	sem	Speed ($\mu\text{m hr}^{-1}$)	sem
FBS	no	300	128	-0.69	0.04	9.99	0.57	288	0.58	0.03	7.33	0.39
		0	264	-0.18	0.04	4.85	0.21	330	0.08	0.04	4.98	0.25
Serum free	no	300	212	-0.46	0.04	5.50	0.35	250	0.16	0.05	3.27	0.23
		0	338	-0.11	0.04	5.16	0.35	186	0.26	0.05	3.67	0.25
CaFree DMEM (10% FBS)	no	300	116	-0.80	0.03	9.95	0.70	104	0.44	0.06	8.15	1.14
		0	117	-0.22	0.06	8.07	0.58	108	-0.22	0.07	7.19	0.61
CaFree DMEM (Serum free)	no	300	0	n/a	n/a	n/a	n/a	119	0.21	0.07	9.02	1.09
		0	106	0.24	0.07	6.56	0.73	123	-0.03	0.07	9.24	0.79
Cytochrome C (1 mg mL ⁻¹)	yes	300	476	-0.51	0.03	9.34	0.37	302	0.58	0.03	4.73	0.28
		0	334	-0.21	0.04	5.61	0.27	368	0.18	0.04	4.22	0.21
Cd (50 μM)	no	300	119	-0.21	0.07	6.71	0.62	314	0.48	0.03	4.92	0.20
		0	196	-0.14	0.05	4.11	0.37	276	0.02	0.03	5.12	0.21
Cd (100 μM)	no	300	339	-0.25	0.04	4.64	0.22	232	0.34	0.04	3.37	0.18
		0	294	-0.12	0.04	2.88	0.17	348	-0.21	0.04	2.21	0.11
Gd (50 μM)	no	300	118	-0.67	-0.27	10.82	0.65	188	0.59	0.04	5.56	0.37
		0	209	0.05	0.04	7.21	0.59	340	-0.11	0.05	5.47	0.23
Ni (100 μM)	no	300	359	-0.81	0.02	13.97	0.46	485	0.21	0.03	2.94	0.17
		0	400	-0.13	0.04	5.33	0.22	423	-0.09	0.03	5.50	0.29
Ni (500 μM)	no	300	226	-0.55	0.04	10.64	0.55	350	0.25	0.04	4.48	0.25
		0	264	-0.35	0.04	6.15	0.37	380	0.23	0.04	3.33	0.19
EDTA (2 mM)	no	300	461	-0.54	0.03	8.62	0.31	359	0.19	0.04	7.25	0.35
		0	473	-0.16	0.03	7.13	0.25	524	0.06	0.03	5.85	0.25
EGTA (1 mM)	no	300	141	-0.57	0.07	7.22	1.71	107	0.48	0.06	7.74	2.09
		0	153	-0.07	0.07	7.15	1.61	109	0.01	0.08	2.49	1.95
EGTA (2 mM)	no	300	1028	-0.68	0.02	6.97	0.18	587	0.14	0.03	4.38	0.23
		0	1367	-0.20	0.02	2.93	0.08	365	0.04	0.04	4.49	0.24
EGTA (5 mM)	no	300	160	-0.36	0.05	2.21	0.11	472	-0.14	0.03	2.42	0.09
		0	139	0.18	0.07	1.77	0.15	376	-0.04	0.03	2.42	0.11
Nicardipine (10 μM)	no	300	218	-0.65	0.04	8.19	0.43	315	0.64	0.03	6.94	0.35
		0	128	0.04	0.06	6.92	0.50	297	-0.03	0.04	5.43	0.31
ω -Conotoxin GVIA (3 μM)	yes	300	211	-0.67	0.03	12.43	0.63	320	0.44	0.03	6.01	0.33
		0	108	0.14	0.07	4.98	0.44	194	0.01	0.05	3.94	0.29
ω -Agatoxin IVA (200 nM)	yes	300	145	-0.53	0.05	9.64	0.61	177	0.13	0.05	7.13	0.47
		0	105	-0.08	0.07	4.77	0.47	235	-0.14	0.05	6.79	0.38
ω -Conotoxin MVIIC (500 nM)	yes	300	309	-0.75	0.02	12.59	0.51	477	-0.09	0.03	4.61	0.22
		0	362	-0.30	0.03	6.55	0.25	375	-0.24	0.03	2.77	0.15
ω -Theraphotoxin-Hg1a (500 nM)	yes	300	153	-0.27	0.06	7.56	0.48	341	0.41	0.03	6.31	0.34
		0	127	0.01	0.08	5.24	0.54	369	-0.12	0.04	4.99	0.26
TTA-A2 (200 μM)	no	300	677	-0.69	0.02	6.65	0.17	625	0.47	0.03	6.00	0.27
		0	501	-0.20	0.03	7.73	0.23	556	0.11	0.03	4.53	0.20

Continued on next page

Continued from previous page

Condition	CytoC (1 mg mL ⁻¹)	EF (V m ⁻¹)	T98G					U-251MG				
			N	Directedness	sem	Speed ($\mu\text{m hr}^{-1}$)	sem	N	Directedness	sem	Speed ($\mu\text{m hr}^{-1}$)	sem
Amiloride hydrochloride	no	300	352	-0.77	0.02	12.96	0.42	332	0.32	0.04	4.87	0.30
(100 μM)		0	524	0.06	0.03	6.02	0.23	413	-0.19	0.04	3.57	0.20
Calmidazolium	no	300	229	-0.80	0.02	12.26	0.45	346	0.22	0.04	6.42	0.32
(100 nM)		0	437	-0.18	0.03	5.75	0.24	449	-0.01	0.03	4.25	0.22
AmmTx3	yes	300	549	-0.39	0.03	4.42	0.17	816	0.13	0.02	6.06	0.15
(5 μM)		0	337	-0.10	0.04	3.63	0.20	555	-0.15	0.03	4.27	0.16
4-aminopyridine	no	300	1335	0.11	0.02	4.95	0.11	1033	0.07	0.02	3.37	0.10
(1 mM)		0	1220	0.56	0.02	4.76	0.10	570	0.08	0.03	3.66	0.16
4-aminopyridine	no	300	963	-0.79	0.01	4.89	0.09	749	0.11	0.03	2.83	0.11
(4 mM)		0	678	0.85	0.01	3.69	0.06	654	0.06	0.03	2.48	0.10
Benzamil hydrochloride	no	300	856	-0.42	0.02	5.48	0.14	428	0.29	0.03	6.05	0.26
(5 μM)		0	1108	-0.08	0.02	4.43	0.11	455	0.14	0.03	6.81	0.27

Use of *Usiigaci* software automates the single cell migration data analysis workflow for reliable quantitative data which in the past has hindered high-throughput experiments.

Geltrex coating has been identified to support reproducible electrotaxis model of T98G and U-251MG glioblastoma cells. Although no ligand-mediated chemical signaling intersects with the electrotaxis signaling in T98G cells, the importance of calcium signaling in T98G and U-251MG electrotaxis is identified. By further identification, the electrotaxis of T98G cells may depend on R-type HVA VGCCs and that of U-251MG may depend on P/Q-type HVA VGCCs. Furthermore, the electrotaxis of both cells are mediated also by A-type VGCCs and ASIC/ENaC sodium channels. Multiple ion channels, which may be voltage-sensitive or not, can mediate the sensing of electric field and initiate the electrotaxis in glioblastoma. The roles of ion channels on glioma metastasis and survival with regard to physiological electric field require further studies and *in vivo* validation.

As proof of principle, the hybrid PMMA/PDMS microfluidic design demonstrates robustness and versatility for high throughput experiments. The microfluidic chip design can be tailor-made for specific biological study. By using a robust, flexible, and high-throughput microfluidic platform together with machine learning software, the bottleneck of data analysis in high throughput experiments can be resolved, opening new opportunities for quantitatively studying cell responses in microenvironments.

Chapter 5

Study of glioma-vasculature adhesion using a quick-fit PMMA/PDMS microfluidic chip

Abstract

In this work, I introduce a reversibly sealed quick-fit hybrid biomedical microdevice that is operator-friendly and bubble-free, requires low reagent and cell consumption, enables robust and high throughput performance for biomedical experiments. Specifically, a quick-fit poly(methyl methacrylate) and poly(dimethyl siloxane) (PMMA/PDMS) prototype to illustrate its utilities by probing the adhesion of glioblastoma cells (T98G and U251MG) to primary endothelial cells. In static condition, I confirm that angiopoietin-Tie2 signaling increases the adhesion of glioblastoma cells to endothelial cells. Next, to mimic the physiological hemodynamic flow and investigate the effect of physiological electric field, the endothelial cells are pre-conditioned with concurrent shear flow (with fixed 1 Pa shear stress) and direct current electric field (dcEF) in the quick-fit PMMA/PDMS chip, namely shear flow and electric field co-stimulation microfluidic chip (SFEFC). With shear flow alone, endothelial cells exhibit classical parallel alignment; while under a concurrent dcEF, the cells align perpendicularly to the electric current when the dcEF is greater than 154 V m^{-1} . Moreover, with fixed shear stress of 1 Pa, T98G glioblastoma cells demonstrate increased adhesion to endothelial cells conditioned in dcEF of 154 V m^{-1} , while U251MG glioblastoma cells exhibit no difference. The quick-fit hybrid BMMD provides a simple and flexible platform to create multiplex systems, making it possible to investigate complicated biological conditions for translational research³⁹⁸.

5.1 Introduction

Glioblastoma, the most common primary high-grade brain tumor type in adults, can diffuse and metastasize intracranially through white matter tracts or defined perivascular structures, such as blood vessels and the subarachnoid space^{643,644}. Although intravasation and extracranial metastasis in glioblastoma seldom occur^{34,645}, endothelial cells and the associated blood-brain barrier contribute greatly to establishing and maintaining the tumor microenvironment of glioblastoma^{646,647}. An *in vitro* cell-cell interaction model of glioblastoma and endothelial cells could further our understanding

of the perivascular tumor microenvironment of glioblastoma⁵⁰. In the hemodynamic system, endothelial cells serve as inner linings of the blood vessel and regulate vasodilation and vasoconstriction to supply nutrient and gas vital to cell survival. In blood vessels, endothelial cells subject to conditioning from hemodynamic flow and the shear stress is vital to maintaining the quiescent, non-inflammatory phenotype of endothelial cells under normal physiological conditions⁶⁴⁸. Endothelial cells cultured *in vitro* can be conditioned chemically or physically through mechanical or electrical stimulation, and the cell adhesion molecules or cell morphology more mimicking to those in physiological conditions can be induced^{243,244,649–653}. To study endothelial physiology, an robust *in vitro* platform that can mimic the *in vivo* conditioning of endothelial cells is a prerequisite.

In this work³⁹⁸, I introduce a hybrid quick-fit PMMA/PDMS BMMD, combining the advantages and mitigating the disadvantages of PMMA and PDMS to create an air-tight but reversibly sealed cell culture platform with low reagent dead volumes. Reversibly sealed BMMDs are empowered by mechanical or vacuum sealing of an elastomeric PDMS slab to a rigid substrate, thus allowing the BMMD to be sealed and dismantled quickly before and after each experiment^{385,389,654–656}. This hybrid device enables further cellular treatment (*i.e.*, fixation and immuno-staining) in the BMMD. To validate this setup, the cell-cell interaction model between glioblastoma and endothelial cells is studied by applying by applying concurrent electrical and mechanical conditioning on the endothelial cells and further investigate the adherence of glioblastoma cells on the conditioned endothelium.

The design and fabrication of a shear flow and electric field co-stimulation microfluidic chip (SFEFC) with the quick-fit hybrid BMMD principle was described in Section 2.4. The adhesion of glioblastoma to endothelial cells in a static condition and in a coexisting shear flow and electric field microenvironment are discussed in this chapter with summary being provided in details in Section 5.4.

5.2 Materials and methods

5.2.1 Shear flow and electric field co-stimulation chip (SFEFC) using hybrid PMMA/PDMS microfluidic design and fabrication

The design and fabrication of the SFEFC was discussed in detail in Section 2.4.

Briefly, the SFEFC was designed to quick-fit a top PMMA interface chip with a bottom PMMA/PDMS microchannel device where cells were cultured (see schematic in Figure 5.1). The SFEFC was constructed to create multiple electric fields in an R-2R resistor ladder configuration^{202,455}. Two 2 mm-wide main microchannels with interconnected 100 μm by 1.5 mm (length \times width) channels at a spatial interval of 7.5 mm in SFEFC created 10 channel segments with various electric field strengths (EFSs) (Figure 5.1). The segments on the top side of SFEFC had electric current vector flowing against the shear flow direction, while the segments on the bottom side of SFEFC had electric current vector flowing along the shear flow direction. This multiplex configuration provided a platform for high-throughput screening of cellular responses to

coexisting shear flow and electric field. Cells were observed only in the 4.5 mm-long observation area, in the middle of each segment, 1.5 mm from the interconnection channels (where the electric fields were stable).

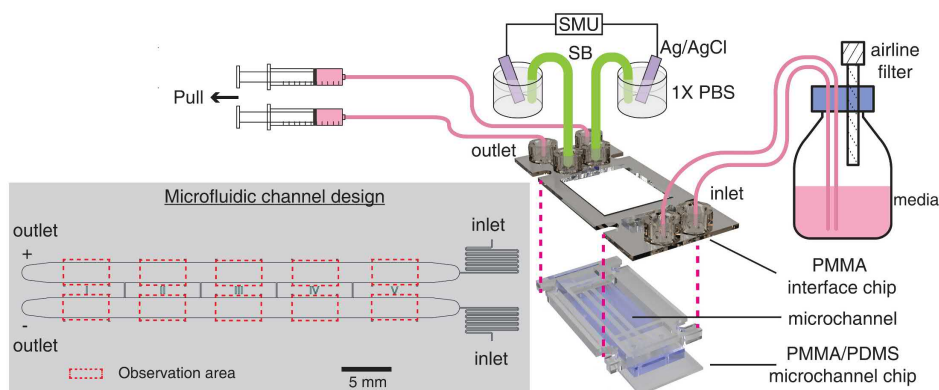


Figure 5.1: Experimental setup of concurrent shear flow and electric field conditioning of endothelial cells in a *shear flow and electric field co-stimulation microfluidic chip* (SFEC). Endothelial cells are cultured in the bottom PMMA/PDMS microchannel device in a user-friendly manner. To pre-condition the cells, the PMMA/PDMS chip is reversibly sealed with the top PMMA interface chip before applying the shear flow and electric field. After conditioning, the chip can be easily recovered. SMU: source measure unit; SB: salt bridge. Detailed configuration of PMMA top interface chip and PMMA/PDMS microchannel chip can be found in Figure 5.2.

5.2.2 Cell culture and maintenance

Primary human umbilical vein endothelial cells (HUVECs) were cultured in the endothelial cell growth medium (C12203, PromoCell GmbH, Germany). T98G (CRL-1690, ATCC, USA) and U251MG (IFO50288, JCRB, Japan) glioblastoma cells were cultured in minimum essential medium α (MEM α , 12000022, Gibco, USA) supplemented with 2.2 g L^{-1} NaHCO_3 and 10% fetal bovine serum (FBS, Invitrogen, USA). All cells were cultured in a humidified 5% CO_2 atmosphere (Forma Steri-cycle i160, ThermoFisher, USA) and passaged whenever confluency reached 80%. Cells from passages 2 to 8 were used in the adhesion study.

Red fluorescent protein-expressing clones of T98G (T98G-dsRed) and U251MG (U251MG-dsRed) cells were established by transfecting a plasmid which carries open reading frame (ORF) for translation elongation factor-1 alpha conjugated with a red fluorescent protein into the two cell lines (EF1alpha-DsRed-Express2, 631979, Takara Bio, Japan) with lipofectamine (Lipofectamine 3000, Thermo Fisher Scientific, USA). Stable fluorescent clones were selected by subculture in media containing $500 \mu\text{g mL}^{-1}$ G418 and aseptically sorted by flow cytometry (Aria II, BD, USA) using PE-Texas Red filter set with CST and AccuDrop calibration.

5.2.3 General experimental workflow

The usage of quick-fit hybrid devices consisted of two steps: user-friendly on-chip cell culture and quick-fit assembly. The step for on-chip cell culture included priming, ECM surface coating, cell seeding.

Briefly, in the first step, the cells were prepared and cultured in the microchannels on the PMMA/PDMS microchannel chip (Figure 5.2A).

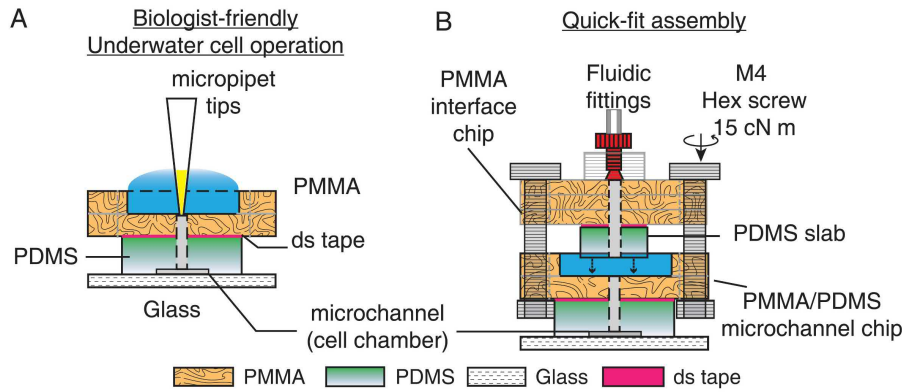


Figure 5.2: Liquid manipulation on the SFEFC. (A) Operator-friendly underwater fluid manipulation at early stage of chip preparation using the PMMA/PDMS microchannel chip. Cells are cultured in the microchannels in the PMMA/PDMS chip; (B) The complete chip can be assembled just prior to on-chip experiments. The PMMA top interface chip is shown in red dashed box. PDMS slabs on the PMMA top interface chip compress and seal the interface to the PMMA/PDMS microchannel chip (inside the black dashed box). After each experiment, the cells in the PMMA/PDMS microchannel chip can be easily recovered after disassembly.

To prepare for confluent HUVEC culture, the PMMA/PDMS chip was filled with 99.5% ethanol (Wako, Japan) to remove bubble⁴³⁹. The solution in the microchannels was then replaced by deionized water and D-PBS. The buffer held in fluid reservoirs on the PMMA part of the PMMA/PDMS chip (Figure 5.2A) ensured that no bubbles were trapped at the interface of the inlets and outlets and prevented accidental bubble injection into the microchannels that would cause disruption of microfluidic flow and cell death.

At an early stage of preparing cells, no complex tubing connections were required. Manipulation of the PMMA/PDMS chip was user-friendly because micropipet tips could be used to deliver fluids and cells by either active pressure delivery or by gravity driven flow. Furthermore, the fluid volume needed to fill the microchannels was very low (on the order of microliters), so the amount of extracellular matrix protein and the number of cells required were limited.

To start endothelium culture in the PMMA/PDMS chip, the glass bottom was coated with $10 \mu\text{g mL}^{-1}$ of human plasma fibronectin for 2 hours. HUVEC cells at concentration of $1 \times 10^7 \text{ cells mL}^{-1}$ were injected into the microchannels and allowed to adhere for 3 hours at 37°C .

To assemble the complete quick-fit microfluidic chip, the fluidic tubing and salt bridges (1.5% agarose in D-PBS) were first connected to the PMMA interface chip

and primed with cell culture media. The PMMA interface chip was then brought into contact with PMMA/PDMS microchannel chip and sealed tight with four M4 stainless hex screws and nuts. The four screw clamp slots were located on both the PMMA interface chip and PMMA/PDMS microchannel chip so that an even pressure can be applied to the PDMS slabs on the PMMA interface chip. The SFEFC was assembled after a tight seal was achieved by applying 15 cN m of torque on the four hex screws with a torque driver (RTD60CN, Tonichi, Japan) (Figure 5.2B). The pressure applied on the PDMS slabs deforms the slabs and seals the interface between the top interface chip and the microchannel chip. Moreover the reagents were primed in the channels of the PMMA interface chip, thus, after quick-fit assembly, the dead volume was reduced and the reagents could be delivered to cells with reduced delivery time. After each experiment, the cells in the PMMA/PDMS chip could be quickly recovered by removing the hex screws. In addition, the PMMA interface chip could be reused to assemble with another PMMA/PDMS chip to increase experimental throughput with low liquid dead volume.

5.2.4 Endothelium conditioning by external fields in SFEFC

Endothelium conditioned by shear flow The assembled SFEFC with a confluent HUVEC cell layer in the microchannel was set up in the incubator as shown in Figure 5.1 and Figure 5.3. I conditioned the endothelium by shear flow mimicking the physiological conditions in hemodynamic flows⁶⁵⁷. The shear stress imposed on the endothelial cells in a rectangular channel can be calculated according to the modified Hagen-Poiseuille equation in Equation 5.1⁴⁴⁸:

$$(\tau_s^*)_{max} = 2.95 \times \frac{6\mu Q}{w \times h^2}, \quad (5.1)$$

where μ , Q , w , and h are the dynamic shear viscosity, volumetric flow rate, width, and height of the rectangular microchannel, respectively.

Primary endothelial cells like HUVECs are reported to respond to shear flow and align in parallel to the flow direction when shear stress exceeds 10 dyn cm² (equivalent to 1 Pa)^{446,447}. Based on Equation 5.1, to impose 1 Pa shear stress on the endothelial cells in a 2 mm-wide and 100 μ m-high microchannel filled with a cell culture medium with dynamic viscosity of 0.756 mPa s, the flow rate should be 1.49 μ L s⁻¹ (equivalent to 5.4 mL h⁻¹).

Specifically, the flow was delivered by pulling ECGM supplemented with antibiotics cocktail (1X PSN, Invitrogen, USA) from a 250 mL serum bottle by two 50 mL syringes (Terumo, Japan) using a dual channel syringe pump (YSP-202, YMC, Japan). The syringe pump was controlled remotely with the control software (Syringepump Pro, USA). The flow rate was set starting at 0.1 mL h⁻¹ and doubled every 3 hours until the flow rate reached 5.4 mL h⁻¹.

For conditioning in shear flow, the confluent endothelial cells were conditioned in the 5.4 mL h⁻¹ flow rate for 24 hours.

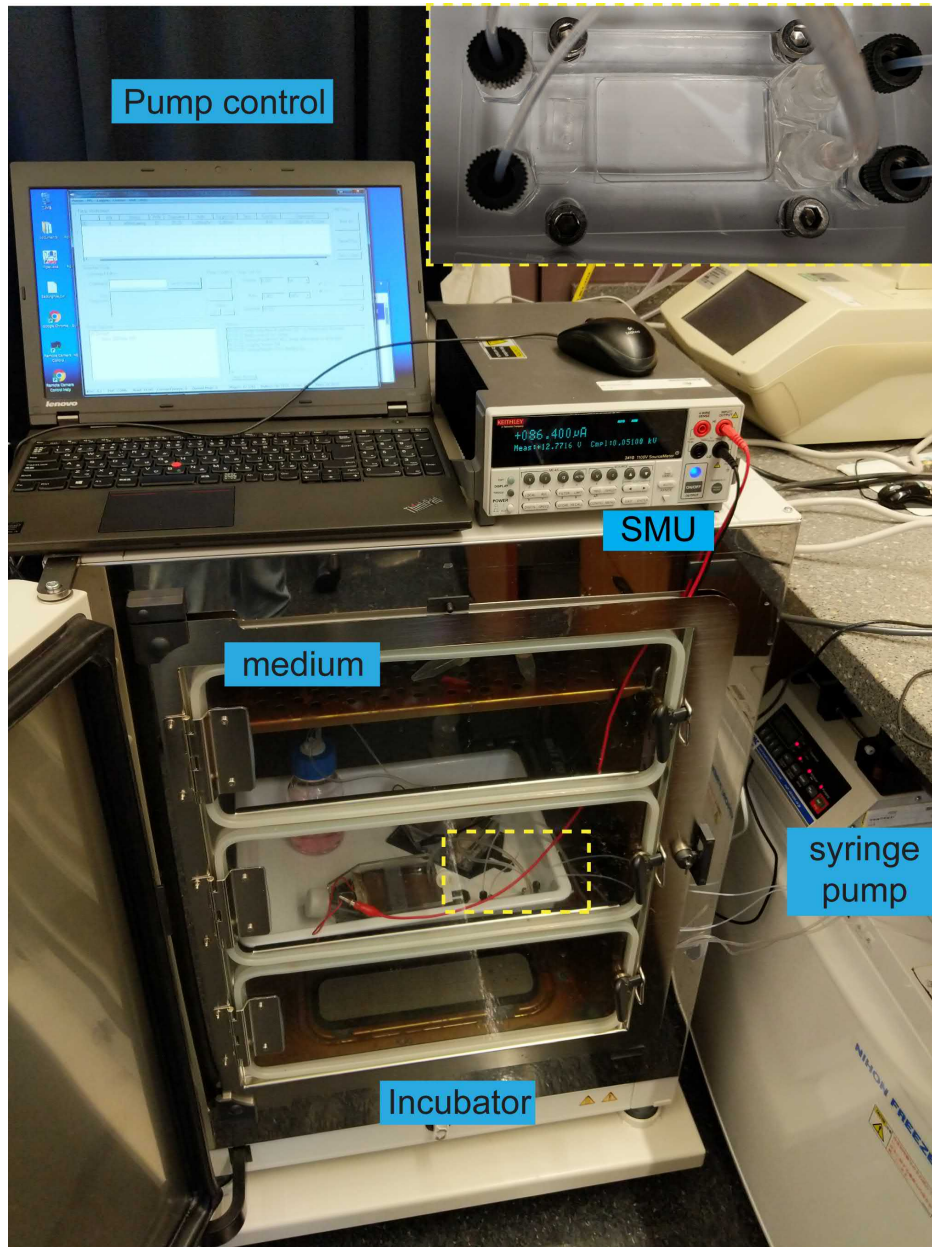


Figure 5.3: A snapshot of the experimental setup of concurrent shear flow and electric field conditioning of endothelial cells in a “shear flow and electric field co-stimulation microfluidic chip (SFEFC)”. Both the media bottle and the SFEFC chip are placed in a humidity-controlled incubator for cell culture. The shear flow is imposed by withdrawing the media using a syringe pump with programmable control software. The electric field is applied by a source measure unit (SMU). The top right image in the yellow dash-box is the zoomed-in picture of the assembled quick-fit SFEFC.

Endothelium conditioned by both shear flow and electric field For endothelium conditioned by coexisting shear flow and electric field, once the flow rate reached 5.4 mL h^{-1} (corresponding to the shear stress of 1 Pa), a direct current electric field (dcEF) was applied to HUVECs in sections I to V and VI to X at 300:153.6:75.5:30.9:0 V m^{-1} respectively based on the simulation results (described in Section 2.4). Specifically, the dcEF was applied by a source measure unit (2410, Keithley, USA) through two silver/silver chloride electrodes in D-PBS where the salt bridges were immersed (Figure 5.1). The simultaneous conditioning of the HUVECs with shear flow and electric field were carried out for 24 hours prior to glioblastoma cell adhesion experiments. Upon filling of the syringes, the content was discarded prior to restarting the syringe pump.

5.2.5 Glioblastoma cell adhesion on statically cultured endothelium

In a static adhesion experiment, glass bottoms of 8-well chambered slides (Lab-tek II, Nunc, USA) were coated with $10 \mu\text{g mL}^{-1}$ of human plasma fibronectin (Invitrogen, USA). 1×10^5 HUVEC cells were seeded in each well and allowed to adhere for 24 hours. Angiopoietin 1 (Ang1), an endothelial cell-specific tyrosine kinase receptor ligand that upregulates adhesion molecules on glioblastoma cells was purchased from Peprotech USA. Both glioblastoma cells were incubated with 100 ng mL^{-1} of Ang1 for 24 hours prior to adhesion experiments. Activated endothelial cells were prepared by incubating HUVECs with 10 ng mL^{-1} tumor necrosis factor α ($\text{TNF}\alpha$) for 24 hours (Invitrogen, USA). Prior to adhesion experiments, confluent HUVECs were labeled by incubation with $1 \mu\text{M}$ CellTracker Green CMFDA dye (C2925, Invitrogen, USA) for 15 minutes and washed twice with Dulbecco's phosphate buffered saline (D-PBS).

To commence static adhesion experiments, T98G-dsRed and U251MG-dsRed cells were trypsinized and resuspended in ECGM. The two glioblastoma cell lines were seeded at glioblastoma (2) : HUVEC (1) ratio. Glioblastoma cells were allowed to adhere to endothelial cells for 1 hour at 37°C . Unadhered cells were washed away by gentle pipetting with D-PBS. Cells were fixed with 4% paraformaldehyde in D-PBS immediately and imaged using an epifluorescence microscope with filter sets for FITC and TRITC channels. Densities of adhered glioblastoma cells were counted and averaged over four 1 mm^2 fields in the middle of each well (16 fields total). All experiments were performed in triplicates and the data were represented as the mean \pm 95% confidence interval, which is 1.96 standard errors of the mean. One-way analysis of variance with Tukey's post-hoc multiple-comparison tests were performed on collected data using Prism 7 (Graphpad, USA). The confidence level to reject a null hypothesis between two data sets was set at 95%. A p-value (P), the probability for a true null hypothesis less than 0.05 represents a statistical significance at 95% confidence.

5.2.6 Glioblastoma cell adhesion on shear/EF conditioned endothelium on SFEFC

After shear flow and dcEF conditioning, the PMMA interface chip was immediately removed by unscrewing M4 Hex screws. The confluent HUVECs were labeled by incubation with 1 μ M CellTracker Green for 15 minutes and washed twice with 1X D-PBS before the glioblastoma cell adhesion experiment. T98G-dsRed and U251MG-dsRed cells were trypsinized and suspended in ECGM. The two types of glioblastoma cells were seeded at 2×10^6 cells mL^{-1} in 200 μ L by gravity-driven flow. Glioblastoma cells were allowed to adhere for 1 hour at 37°C. Unadhered cells were washed away with 200 μ L of D-PBS by gravity flow. Cells were fixed with 4% paraformaldehyde in D-PBS and imaged with an epifluorescence microscope. Cell counting and statistical inferences in these adhesion experiments followed the same statistical measurements as those on statically cultured endothelium (Section 5.2.5).

5.2.7 Immunofluorescence staining, microscopic imaging and statistical inference

The presence of glial fibrillary acidic protein (GFAP) and Tie2 receptor in T98G-dsRed and U251MG-dsRed cells were examined by immunofluorescence staining. Both cells were fixed with 4% paraformaldehyde and permeabilized with 0.1% Triton X-100 in D-PBS. Fluorophore-conjugated species-specific secondary antibodies against the primary antibodies were used to detect the two proteins.

The expression of CD31 membrane adhesion molecule (PECAM-1) and cytoskeleton F-actin of conditioned endothelial cells was also characterized by immunofluorescence staining on chip following the same fixation and permeabilization protocol described above. The detection of CD31 and F-actin was conducted with an anti-CD31 primary antibody and a fluorophore-conjugated secondary antibody (NBP1-71663SS, Novus Biological, USA & A21467, Invitrogen, USA) as well as the fluorophore-conjugated phalloidin (A12380, Invitrogen, USA). The stained cells were scanned under a confocal laser scanning microscope with a 10X objective (A1R+, Nikon, Japan).

5.3 Results and discussion

5.3.1 Reversibly sealed quick-fit microfluidic chip tolerates high flow rate

Although the sealing of SFEFC is reversible, it can withstand high flow rates necessary in microfluidic channels to create shear stress conditions similar to that in physiological hemodynamics (0.1–0.6 Pa in normal vein and 1.0–7.0 Pa in normal artery as reported⁶⁵⁷). HUVECs cultured in SFEFC under simultaneous shear flow and electric field conditions demonstrated characteristic morphological changes (Figure 5.4).

The shear flow imposes a shear stress on adhered endothelial cells and induces an aligned morphology and a quiescent anti-inflammatory and anti-thrombotic phenotype⁶⁵¹. Electric field stimulation on endothelial cells instead induces a perpen-

dicular alignment with upregulation of a pro-angiogenic response and the release of VEGF^{243,244}.

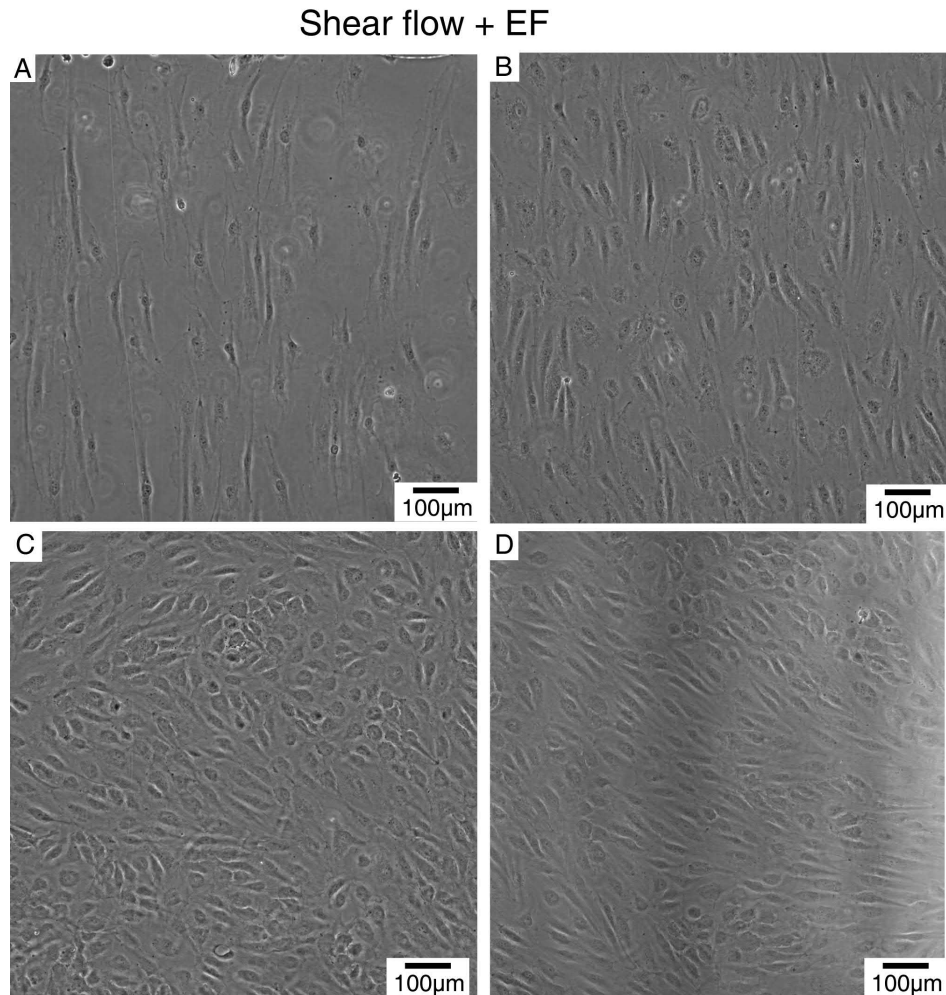


Figure 5.4: Microscopy images of endothelial cells cultured in sections I, II, III, and V in SFEFC. (A) Endothelial cells conditioned with shear flow (1 Pa) and 300 V m^{-1} ; (B) Endothelial cells conditioned with shear flow (1 Pa) and 153.6 V m^{-1} showing perpendicular alignment as a result of electrical stimulation; (C) Endothelial cells conditioned with shear flow (1 Pa) and 75.5 V m^{-1} ; (D) Endothelial cells conditioned with shear flow (1 Pa) demonstrated more parallel alignment phenotypes.

5.3.2 Mediation of endothelial cells alignment by shear flow and electric field

Under concurrent 5.4 mL hr^{-1} shear flow with 1 Pa shear stress and 300 V m^{-1} dcEF stimulation, endothelial cells aligned perpendicular to the electrical current vector and the dcEF caused some cell death that rendered the endothelial cell layer patchy as shown in Figure 5.4A. Strong perpendicular cell alignment was also evident in cells stimulated with concurrent 5.4 mL hr^{-1} shear flow and 153.6 V m^{-1} dcEF (Figure 5.4B).

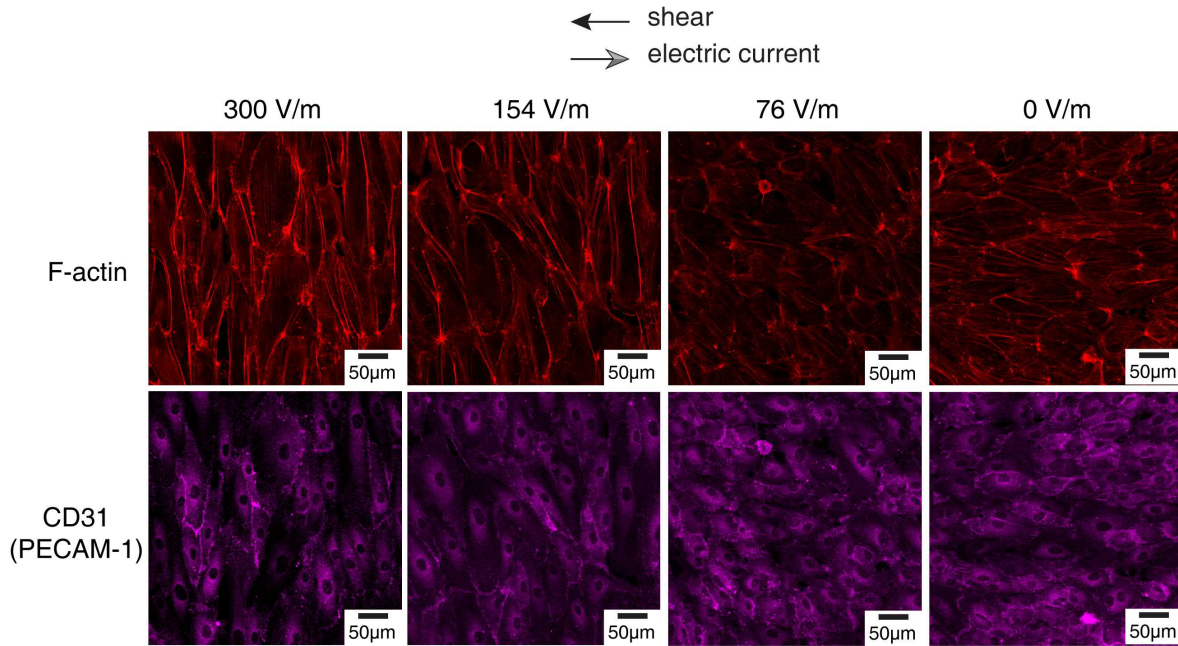


Figure 5.5: Immunofluorescence staining of HUVECs conditioned with shear flow (shear stress fixed at 1 Pa) and electric fields at various strengths. F-actin cytoskeleton staining by phalloidin shows stress fiber alignment under increasing electric field. CD31 is the platelet endothelial adhesion molecule expressed on endothelial cells. Evident perpendicular alignment of cells and the intracellular stress fibers are observed in cells stimulated with 154 V m^{-1} and 300 V m^{-1} electric field. The shear flow alone induces parallel alignment of cells and the stress fiber.

Under the fixed shear flow rate (1 Pa), perpendicular cell alignment by electrical field stimulation was not observed in cells conditioned with 75.5 V m^{-1} electric field (Figure 5.4C), suggesting that a minimum electric field stimulation on cells is required to induce the perpendicular cell alignment. Under the 5.4 mL hr^{-1} shear flow stimulation alone, the 1 Pa shear stress induced classical parallel alignment of HUVECs (Figure 5.4D), consistent with prior observations^{446,447}. Without any shear flow, the HUVECs exhibited no alignment preference (Figure 5.6A). These results imply that the SFEFC in our experimental setup can support long-term shear flow and electrical stimulation conditioning of endothelial cells on chip (Figure 5.4).

The alignment of HUVECs in SFEFC under simultaneous shear flow and electric field was further characterized by immunofluorescence staining against F-actin and CD31 (Figure 5.5). CD31 was expressed on conditioned endothelial cells. Under shear flow conditioning, endothelial cells displayed parallel alignment that was also demonstrated by the parallel orientation of actin stress fibers. When a co-existing electric field increased in strength, electrical stimulation induced cells to undertake a more perpendicular phenotype as the stress fibers became more perpendicularly oriented.

5.3.3 Adherence of glioblastoma cells to endothelial cells in static condition with stimulation of angiotensin signaling

Phenotyping endothelial cells and glioblastoma cells cultured in static condition: Prior to adhesion experiment, the phenotypes of endothelial cells and glioblastoma cells in static condition were verified. Endothelial cells cultured in static condition expressed random orientation (Figure 5.6A). The immunofluorescence staining confirmed that both T98G and U251MG glioblastoma cells exhibited both GFAP and Tie2 expressions, indicating a glial phenotype with potential angiotensin/Tie2 signaling (Figure 5.6B & Figure 5.6C).

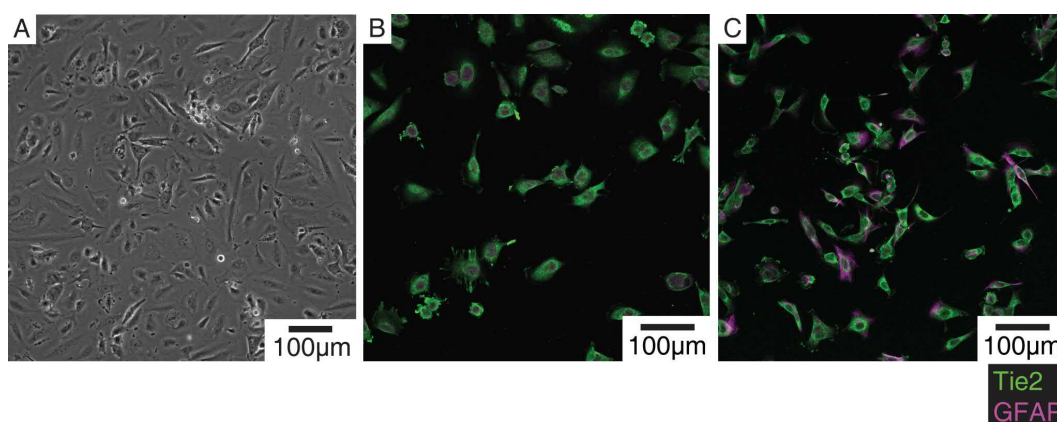


Figure 5.6: Microimages of endothelial cells and glioblastoma cells. (A) Endothelial cells cultured in static condition show random orientation; Both (B) T98G and (C) U251MG glioblastoma cells exhibit both GFAP and Tie2 expressions.

Glioblastoma cell adhesion to endothelial cells in static condition: U87MG and U251MG cells are reported to adhere to endothelial cells through Ang1/Tie2 signaling²⁸⁵. I first tested the adhesion of T98G and U251MG glioblastoma cells under similar conditions.

The adhesion of T98G-dsRed and U251MG-dsRed glioblastoma cells to confluent endothelial cells was examined (Figure 5.7). After 1 hour of adhesion, glioblastoma cells adhered to the endothelial and displaced them. The adhesion of glioblastoma cells with and without Ang1 to confluent HUVECs with and without activation with $\text{TNF}\alpha$ were quantified and statistically examined in Figure 5.8 (microscopy images are shown in Figure 5.9 & 5.10).

Without Ang1 treatment, adhesion of U251MG-dsRed to endothelium was greater than that of T98G-dsRed ($P < .0001$). Ang1 treatment increased the adhesion of both T98G-dsRed and U251MG-dsRed to endothelium ($P < .001$). This is consistent with existing reports that glioblastoma cells demonstrate enhanced interaction with endothelial cells via Ang1/Tie2 signaling²⁸⁵. $\text{TNF}\alpha$ is a cytokine known to upregulate adhesion molecules on endothelial cells^{652,658}. However, only T98G cells activated with Ang1 showed increased adhesion to $\text{TNF}\alpha$ -activated HUVECs but not U251MG cells. This result suggests that the Ang1/Tie2 signaling of glioblastoma may not directly cross-

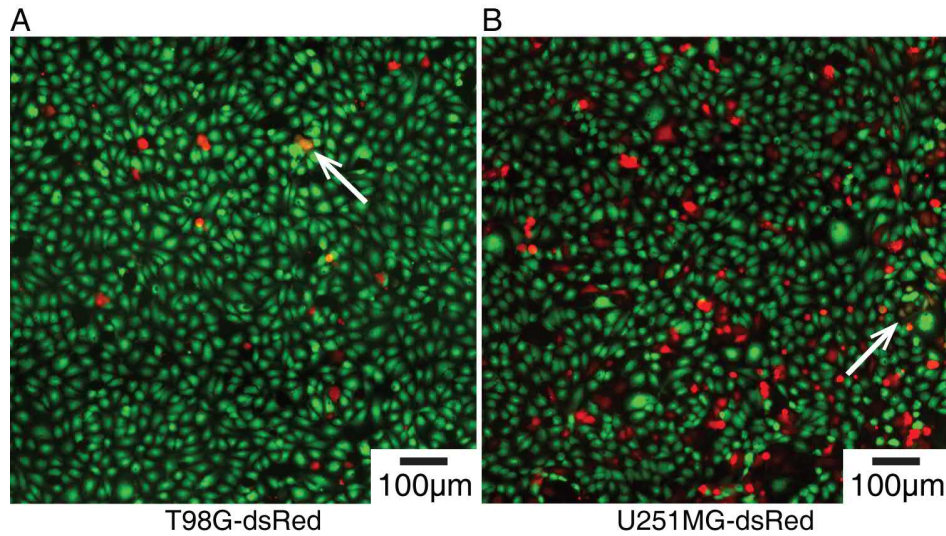


Figure 5.7: The adhesion of (A) T98G-dsRed, and (B) U251MG-dsRed, to static confluent endothelium (fluorescently labeled green). The cells with yellow color (next to the white arrows) indicate the colocalization of CellTracker Green dye in endothelial cells and dsRed fluorescent protein in glioblastoma cells. The colocalization implies cell fusion or intercellular exchange events that may be important in the perivascular microenvironment of glioblastoma.

talk with $\text{TNF}\alpha$ signaling-related adhesion molecules expressed on HUVECs. Further identification of the adhesion molecules is needed.

In addition to glioblastoma adhesion, colocalization events were observed between the dsRed fluorescence of glioblastoma and CellTracker Green fluorescence of endothelial cells *in vitro* (Figure 5.7). Colocalization events were quantified and calibrated by adhesion events as shown in Figure 5.11. The colocalization events did not increase or decrease ($P > .05$) due to Ang1 stimulation or $\text{TNF}\alpha$ activation, although Ang1-stimulation increased the adhesion in both glioblastoma cell lines. Interestingly, more colocalization events were detected in Ang1-stimulated T98G-dsRed but not in U251MG-dsRed (Figure 5.11A, $P < .0001$).

Colocalization events suggest that glioblastoma cells and endothelial cells underwent a fusion event or an intercellular transport event^{659,660}. Cell fusion may contribute to the origin of cancer stem cells and acquisition of drug resistance. Specifically, glioblastoma-endothelial cell hybrids have been proposed to play a pivotal role in the perivascular microenvironment of glioblastoma and the maintenance of glioblastoma cancer stem cells⁶⁶¹. Further identification of the molecular signaling underlying the intercellular transport and elucidation of glioblastoma-endothelial hybrid function in glioblastoma progression can further our understanding of the angiogenesis of glioblastoma. However, it has been reported that brain microvascular endothelial cells show a distinct phenotype compared to endothelial cells isolated from umbilical cord, suggesting that closer physiological models may require the use of tissue-specific endothelial cells^{662,663}.

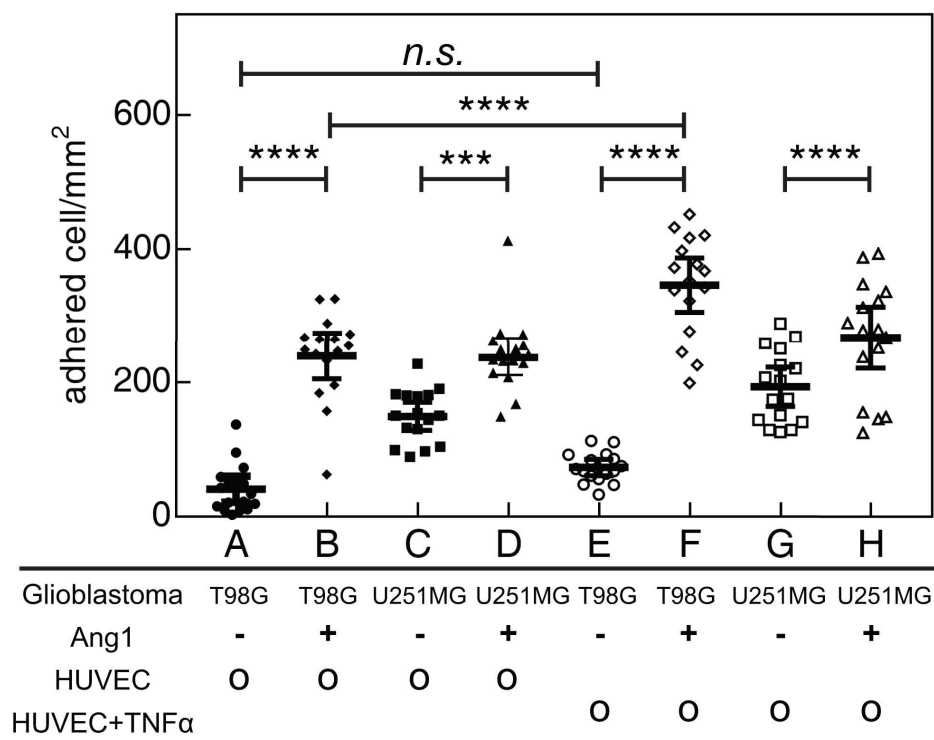


Figure 5.8: The adhesion of T98G-dsRed and U251MG-dsRed to endothelium under the stimulation with Ang1 and TNF α in static condition. *** denotes $P < .001$; **** denotes $P < .0001$; n.s. denotes no significance.

5.3.4 Adherence of glioblastoma cells to shear flow and electric field conditioned endothelial cells

I next examined how simultaneous shear flow and electric field stimulation affected the adhesion of the two glioblastoma cell lines on the endothelial cells (Figure 5.12). Only T98G-dsRed cells (not U251MG-dsRed cells, $P > .05$) showed increased adhesion to the endothelial cells preconditioned under 153.6 V m^{-1} dcEF and 1 Pa shear stress when compared to two pre-conditioned control studies: shear-flow conditioned control ($P < .01$, section V of Figure 5.12) and the static control ($P < .01$). The endothelial cells preconditioned under 300 V m^{-1} dcEF and shear flow with 1 Pa shear stress were patchy due to some cell death at this electric field strength (Figure 5.4A), which may contribute to the lower adhesion of glioblastoma cells ($P > .05$). Even though the endothelial cells conditioned in shear flow of 1 Pa and electric fields of 75.5 V m^{-1} and 30.9 V m^{-1} were confluent, the adhesion of both glioblastoma cell lines on pre-conditioned endothelial cells were similar when compared to the control groups. This suggests a dose dependent response of electric field conditioning which was observed in the adhesion of osteosarcoma to polyethylene substrate⁶⁶⁴ and migration of fibroblasts²⁷⁴. Future identification of the molecular targets that contribute to the difference of adhesion could facilitate molecular typing of glioblastoma cells and further our understanding on the cell-cell interaction between glioblastoma and the endothelial cells that may contribute to the metastasis^{665,666}.

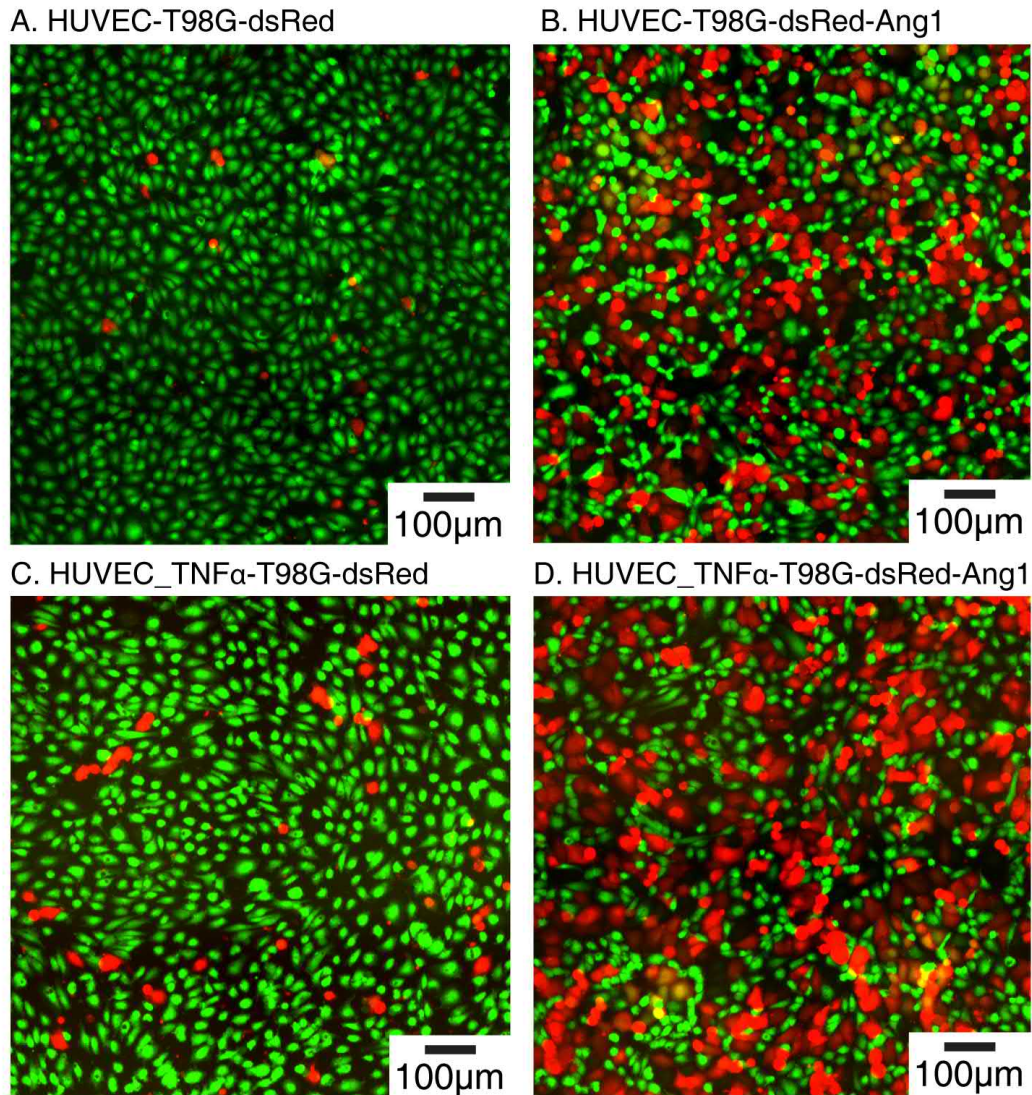


Figure 5.9: The adherence of T98G-dsRed cells (red fluorescence) to endothelial cells (green fluorescence). Yellow fluorescence represents the intercellular transport between the two cells. (A) T98G-dsRed adherence to HUVECs; (B) Increased adherence of Ang1-stimulated T98G-dsRed cells to HUVEC as evident by increased number of red fluorescent cells; (C) T98G-dsred adherence to $\text{TNF}\alpha$ -activated HUVECs; (D) Ang1-stimulated T98G-dsRed cells adherence to $\text{TNF}\alpha$ -activated HUVECs. Increased adherence is detected when the number of glioblastoma cells increases.

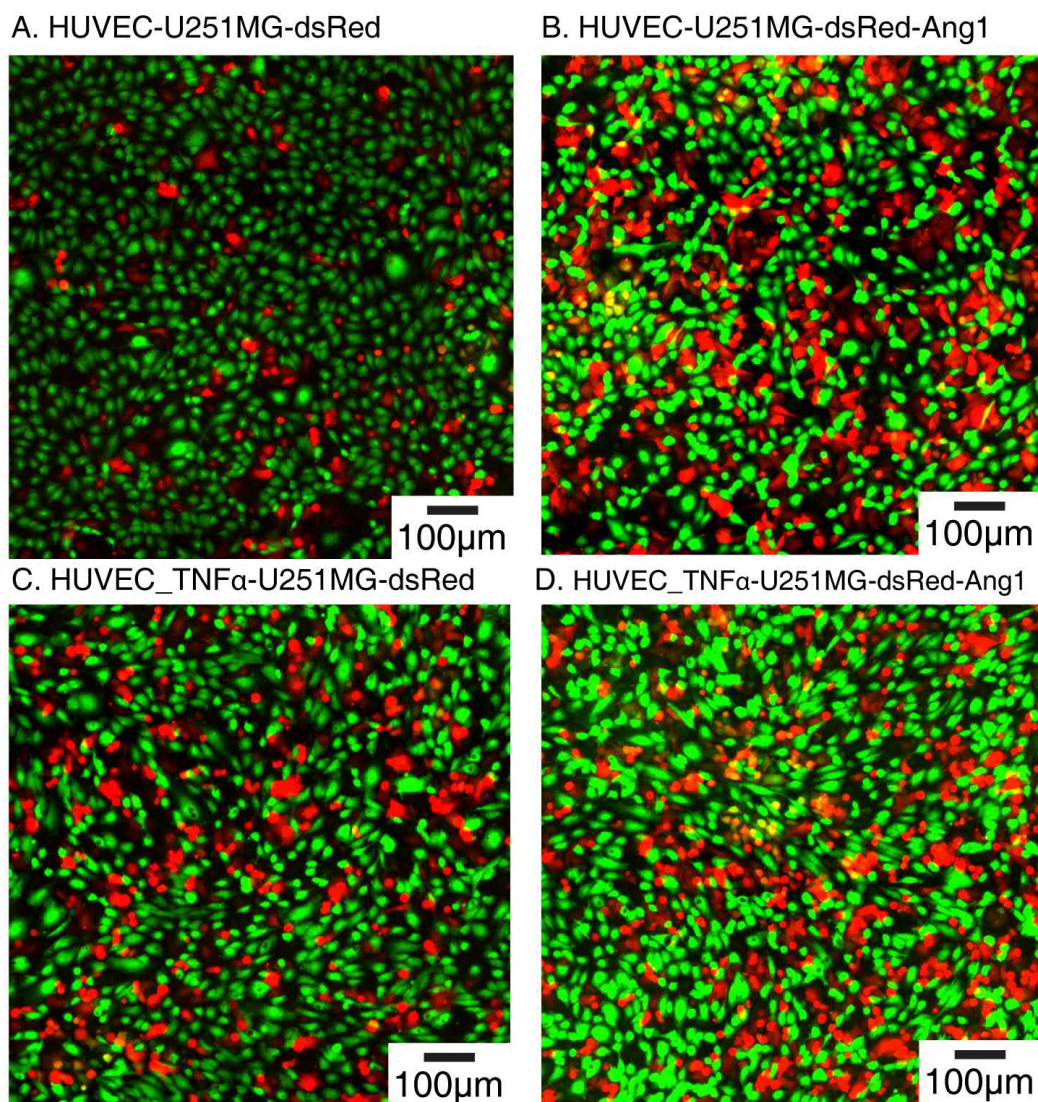


Figure 5.10: The adherence of U251MG-dsRed cells (red fluorescence) to endothelial cells (green fluorescence). Yellow fluorescence represents the intercellular transport between the two cells. (A) U251MG-dsRed adherence to HUVECs; (B) Increased adherence of Ang1-stimulated U251MG-dsRed cells to HUVEC, as evident by increased number of red fluorescent cells; (C) U251MG-dsRed adherence to $\text{TNF}\alpha$ -activated HUVECs; (D) Ang1-stimulated U251MG-dsRed cells adherence to $\text{TNF}\alpha$ -activated HUVECs. Increased adherence is detected when the number of glioblastoma cells increases.

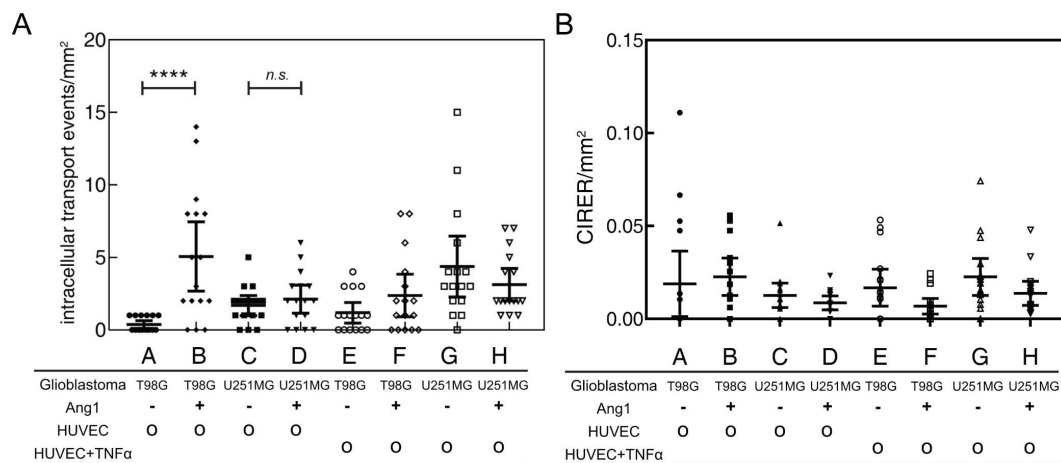


Figure 5.11: The intercellular transport events between glioblastoma and endothelial cells in static condition. (A) the intracellular transport events per unit area observed in static condition; (B) The calibrated intercellular transport event ratio (CITER) observed in static condition calibrated by adhesion count in Figure 5.8. **** denotes $P < .0001$; n.s. denotes no significance. Signs of + and - denote whether the glioblastoma cells are stimulated with angiopoietin. Circle symbol denotes if the glioblastoma adhere to HUVECs or $TNF\alpha$ -stimulated HUVECs. The intercellular transport events in T98G cells increase when T98G are stimulated with Ang1 but no increase is observed in U251MG cells. $TNF\alpha$ stimulation has no statistically significant effect on intercellular transport events.

In addition, under the static condition, the adhesion of U251MG-dsRed was higher than that of the adhesion of T98G-dsRed cells (Figure 5.8), but such difference was not observed in the on-chip static control (Figure 5.12). The shear force from the gravity flow in on-chip glioblastoma adhesion experiments could contribute to this discrepancy. It is known that hydrodynamic flow could alter the adhesion dynamics and cell-cell contact. Quantitative study of glioblastoma-endothelial adhesion dynamics under a hydrodynamic flow can elucidate the underlying biophysical mechanism in future studies⁶⁶⁷.

5.4 Summary and prospects

I demonstrated a quick-fit hybrid BMMD made of PMMA and PDMS that provided advantages over single-material counterparts, such as bubble prevention, user-friendliness, low dead volume, and air-tight sealing. The quick-fit design allows high experimental-throughput setup so that by reusing the top interface chip, multiple experiments can be performed sequentially by assembling and disassembling the quick-fit chip. The reagent waste was significantly reduced.

I verified the operation of quick-fit SFEFC by conditioning endothelial cells on-chip to concurrent shear flow and electric field. No leakage or bubbles at high volumetric flow rate was observed. The applied electrical current induced perpendicular cell alignment and shear flow instigated a parallel alignment on endothelial cells, thus cells

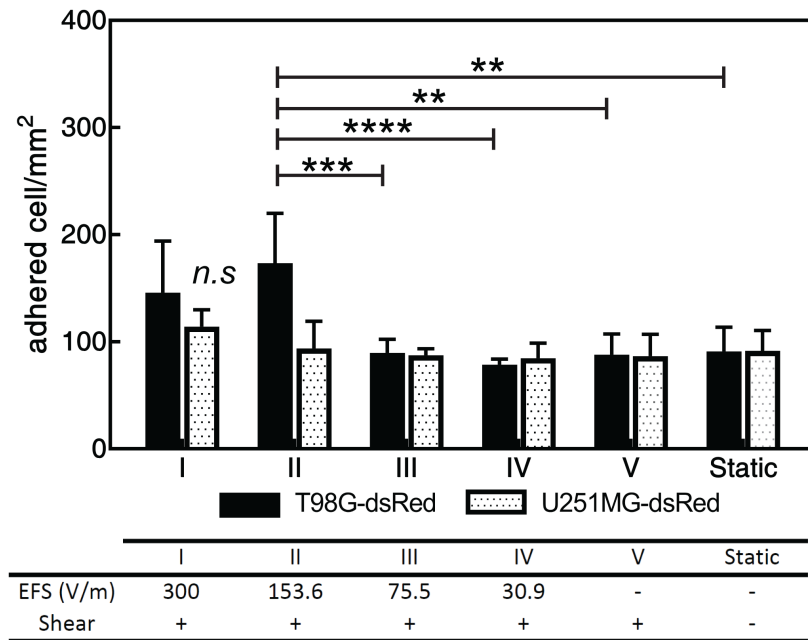


Figure 5.12: Adherence of glioblastoma cells to endothelium conditioned under shear flow and electric field or endothelium cultured in static flow on the SFEFC. ** denotes $P < .01$; *** denotes $P < .001$; **** denotes $P < .0001$.

were subjected to competing physical cues. In the future, a microfluidic design with orthogonal electric field and shear flow configuration can be useful for investigating the synergistic cell alignment effect in a complex microenvironment.

The SFEFC was validated by studying adhesion of glioblastoma cells to shear flow and electric field-conditioned endothelial cells. T98G-dsRed and U251MG-dsRed glioblastoma cell adhesion under static culture and shear flow with electric field-conditioned endothelium was examined. Angiopoietin 1 activation increased the adhesion of both glioblastoma cell lines on a statically cultured endothelial cell layer. T98G-dsRed glioblastoma cells also showed increased adhesion to an endothelial cell layer conditioned with intermediate electric field and shear flow. On the other hand, U251MG-dsRed showed no adhesion difference. Further identification and typing of adhesion molecules is expected to further our understanding of how glioblastoma interacts with endothelial cells. I envision that the quick-fit hybrid microdevice can be applied to study other cell-tissue interactions in controlled shear flow and electric field conditions. The quick-fit hybrid device can also aid in drug screening on cells conditioned under biomimetic conditions.

Conclusion

Glioblastoma, a high grade form of glioma, contributes to high mortality and high recurrence of brain cancer. To study how the physical and chemical factors in the cancer microenvironment participate in the glioma biology, a robust *in vitro* platform that can mimic the microenvironment is required. Furthermore, how to accurately and quantitatively analyze the cell behaviors on the platform in an automated fashion is essential for accelerating systematic studies.

In this thesis, I have created a new hybrid microfluidic design to create robust and flexible microfluidic platforms by combining PMMA and PDMS based substrates. The advantages of the two materials can be combined and the disadvantages can be mitigated. Using PMMA fabrication, complex microfluidic layout can be easily designed and fabricated while high spatial accuracy microchannels can be created in PDMS soft lithography fabrication. By using a dual-energy double sided tape, facile heterogeneous bonding between PMMA and PDMS further improves the design flexibility and fabrication speed. A novel submerged cell seeding operation further guarantees uniformly distributed single cells being seeded in the microchannels with advantages such as bubble-free and low cell number requirement. The hybrid microfluidic design can be tailor made to answer specific biological questions. In particular, the PMMA components in hybrid microfluidics can be quickly designed to accommodate special world-to-chip interface requirements in biomedical applications. Therefore, the potential of using hybrid microfluidics in combination of hydrogels to mimic complex microenvironments for 3D tissue engineering and stem cell biology is an appealing future direction.

Analyzing single cell migration and morphological changes have been the hallmark of single cell microscopy. However, label-free optical contrast techniques such as phase contrast microscopy or differential interference contrast microscopy, increase the contrast for transparent cells non-uniformly. As a result, the images are not easily segmented by computer vision due to image intensity gradients. Therefore, the data analysis has been a bottleneck in high-content analysis of cell migration. To that end, I have developed a machine learning software, *Usiigaci*, to segment, track, and analyze single cell migration in label-free phase contrast microscopy images. Using *Usiigaci*, the cell movement and morphological changes can be reliably analyzed in an automated fashion. The trainable nature of convolutional neural networks further suggests that small differences in cell appearance under different conditions and health states could be recognized in the future. Thus, many possibilities exist for using neural networks in image cytometry without specific labeling of cells. A machine learning-augmented microscopes in future can provide real-time prediction and quantitative measurements

to researchers and clinicians, which can vastly decrease turn around time of data interpretation.

A hybrid PMMA/PDMS microdevice and the *Usiigaci* software are used as an integrated platform to study the electrotaxis of glioblastoma cells. I find that the electrotaxis of glioblastoma cells require optimal ECM coatings, such as Geltrex. The T98G and U251MG glioblastoma cell electrotaxis are dependent on extracellular calcium and different voltage-gated ions channels are involved. For voltage-gated calcium channels, U251MG electrotaxis is dependent on the P/Q-type VGCC and T98G electrotaxis is dependent on the R-type VGCC. The electrotaxis of both cells are also mediated by A-type voltage-gated potassium channels and acid-sensing sodium channels. These results show that the electrotaxis of different glioblastoma cell lines can be mediated by different signalings, which means that if ion channels are pharmaceutical targets to inhibit the infiltration of patient's glioblastoma, a patient-specific ion channel expression profiling will be required to identify the appropriate targets and to formulate cocktails inhibiting them. Further clarification of the role of VGCCs, VGKCs, and sodium channels in glioblastoma metastasis may help to shed insight to this new therapeutic strategy. The physiological electric field is a common but often overlooked physical factor existing in the body throughout the life cycle of organisms. By further understanding of how electric fields mediate cell behavior and cellular signaling, we can explore how to use it to our advantage in tissue engineering and suppress it in pathophysiological processes.

Another hybrid PMMA/PDMS chip that can be reversibly sealed is established to condition endothelial cells with both shear flow and electric field. The adhesion of glioblastoma to conditioned and unconditioned endothelial cells were studied. Angiopoietin/Tie2 signaling increases the adhesion of glioblastoma to endothelial cells. Furthermore, the T98G glioblastoma adhesion to endothelial cells conditioned with shear flow and moderate electric field also increased. The flexibility of hybrid microfluidic platform further demonstrates its versatility to answer a broad spectrum of biological questions. Future incorporation of 3D hydrogels and more cell types to better mimic the peri-vascular glioblastoma environment and study the whole process of glioblastoma transvasational process will be interesting to characterize the fundamental mechanisms underlying the intracranial dissemination of glioblastoma through the brain vasculature.

In conclusion, the hybrid microfluidic approach provides design flexibility, cell culture robustness, and fabrication capacity to establish reliable *in vitro* microenvironments for a variety of biological studies. Furthermore, by adapting instance-aware machine learning technologies for cell classification and segmentation, single cell studies in an automated fashion can be achieved, and take us one step closer toward high-throughput quantitative understanding of biological phenomena.

Appendix

During my time at OIST, several studies were completed during the rotation or as part of experiments that do not fall within the scope of the thesis. These results are summarized and discussed in the appendix. The open-source models and software arise from the thesis are listed for interested readers to reuse them for research purposes.

Appendix A

Physical properties of the *in vitro* microenvironment

Abstract

Understanding the physical properties of the liquids in the microfluidic microenvironment is necessary for setting correct experimental conditions. Here, I characterize the densities, electrical conductivities, refractive indexes, and dynamic shear viscosities of various buffers and cell culture media at biologically relevant temperature. Although the densities, refractive index, and dynamic viscosities of the water-based buffers and cell culture media are generally similar to those of pure water, slight differences exist. Densities and refractive indexes slightly increase as the solute composition becomes more complex as in cell culture media supplemented with sera. Dynamic shear viscosities are temperature-dependent and correlate with the complexity of the solute slightly. The electrical conductivity of the solutions correlate with the ionic strengths of the solutions. The measurement results can be used as simulation parameters and for setting experimental boundary conditions in the following sections.

A.1 Introduction

The physical properties of fluids such as density, viscosity, and surface tension are important for designing and controlling the engineering process⁶⁶⁸. The physical properties have to be kept in mind when designing experiments, performing simulation, and interpreting the results. However, the biological fluids from organisms or its artificial reconstitutes are complex. In cases of cell culture media, they are composed of carbohydrates, salts, amino acids, and sometimes further supplemented with blood-derived serum. Although no large molecular weight macromolecule is added in cell culture media, in other words, they are similar to water, the dynamic viscosity measurements of these solutions may still be challenging.

Modern viscometers or shear rheometers incorporate stress-controlled transducers to precisely read the stress from the sample upon an applied shear. However, the reliable torque sensitivities, sample surface tension, secondary flow, and inertial instabilities in the measurement geometry can limit the measurement accuracy of low viscosity solutions⁶⁶⁹. On the other hand, while microfluidic-based viscometers are invented to provide viscosity measurements at very high shear rates with minute amount of sample⁶⁷⁰, the accuracies at low shear rate are still limited by detection sensitivities.

The viscosities and densities of the cell culture media are important as they are inherent properties of the fluids necessary for simulation as well as calculation for experimental conditions such as shear stress. However, the viscosities and densities of commercially available buffered solutions and cell culture media are not commonly provided by the manufacturer and not reported in detail in the literature. It is reported that Dulbecco's minimum essential medium (DMEM) has a dynamic viscosity of 0.78 mPa s at 37 °C^{671,672} and its variant supplemented with 10% fetal bovine serum (FBS) is 0.94 mPa s⁶⁷³.

The conductivities of the cell culture media are also important in cell-dcEF interaction studies²⁰² as well as in electroporation studies⁶⁷⁴. To control the electric field strength in the experimental system, the electrical conductivity of the fluids must be known. For example, it is reported that the minimum essential medium (MEM) has an electrical conductivity of 1.82 S m⁻¹ at 37 °C⁶⁷⁵.

In the following sections, I introduce the experimental approaches for collecting physical properties of relevant buffer solutions and cell culture media used in this thesis.

A.2 Materials and methods

A.2.1 Preparation of cell culture media

The ultrapure water, buffer solutions, and cell culture media were prepared in-house from commercial sources in powder or solution form. The 18.2 M Ω water was prepared from Milli-Q® Integral Water Purification System (Merck KGaA, Germany) and autoclaved (SX500, TOMY, Japan).

Two commonly used isotonic buffer solutions namely Dulbecco's phosphate buffered solution (D-PBS) and Hank's balanced salt solution (HBSS) were purchased from commercial sources (Nacalai Inc, Japan & Thermo Fisher Scientific, USA). The 1X working solutions were used directly or after dilution from 10X stock solution and autoclaved.

Several cell culture media recipes used in this work, such as Minimum essential medium α (MEM α), Dulbecco's minimum essential medium (DMEM) and Roswell Park Memorial Institute 1640 (RPMI1640), were purchased directly from the manufacturer either in powder or liquid form. The liquid form was used directly. For preparation from powder form, the displacement of the serum was considered. The powder was dissolved in appropriate amount of reagent grade water, *e.g.*, 950 mL for serum free media or 850 mL for 10% serum containing media. 50 mL of reagent grade water was used to dissolve an appropriate amount of sodium carbonate, *e.g.*, 2.2 g L⁻¹ for 1 L of DMEM and MEM in 5% CO₂ incubator. The NaHCO₃ solution was saturated with 99.9% CO₂ gas for 2 minutes before being combined with the media solution. No additional pH adjustment was done. The solutions were filtered through a filter cup (Stericup, Merck KGaA, Germany) into sterile serum bottles. Appropriate amount of sera, such as fetal bovine serum (FBS) or calf serum (CS), were added afterward. The media were stored under 4 °C and used within two weeks of preparation.

Several media varied in recipe composition were characterized, including low glucose DMEM (08456-36, Nacalai, Japan), fluorobrite DMEM (A18967-01, Thermo Fisher

Scientific, USA), high glucose with pyruvate DMEM (11995-065, Thermo Fisher Scientific, USA), neural basal medium (21103-049, Thermo Fisher Scientific, USA), calcium free DMEM (21068-028, Thermo Fisher Scientific, USA), and endothelial cell growth medium (C22210, Promocell, USA).

A.2.2 Density measurement using densimeter

The densities of the solutions at 25 °C and 37 °C were characterized using oscillating U-tube method on a handheld densimeter (DMA 35 basic, Anton Paar GmbH, Austria)^{676,677}.

In the oscillating U-tube method, the sample liquids were filled into a U-shaped glass tube and subjected to an oscillation by a piezo actuator. The internal volume was known and the eigenfrequency of the oscillation was influenced by the sample's mass. Based on the relationship between the mass and the volume, the density of the sample liquid was derived.

A.2.3 Viscosity measurement using rotational rheometry and capillary rheometry

Rotational rheometry measurement The viscosities of buffers and cell culture media were measured first on a rotational rheometer (ARES-G2, TA Instruments, USA) using either a 1° cone and flat plate geometry (402763.903 & 402619.901, Figure A.1A) or a concentric cylinder geometry (402620.901 & 402621.901, Figure A.1B).

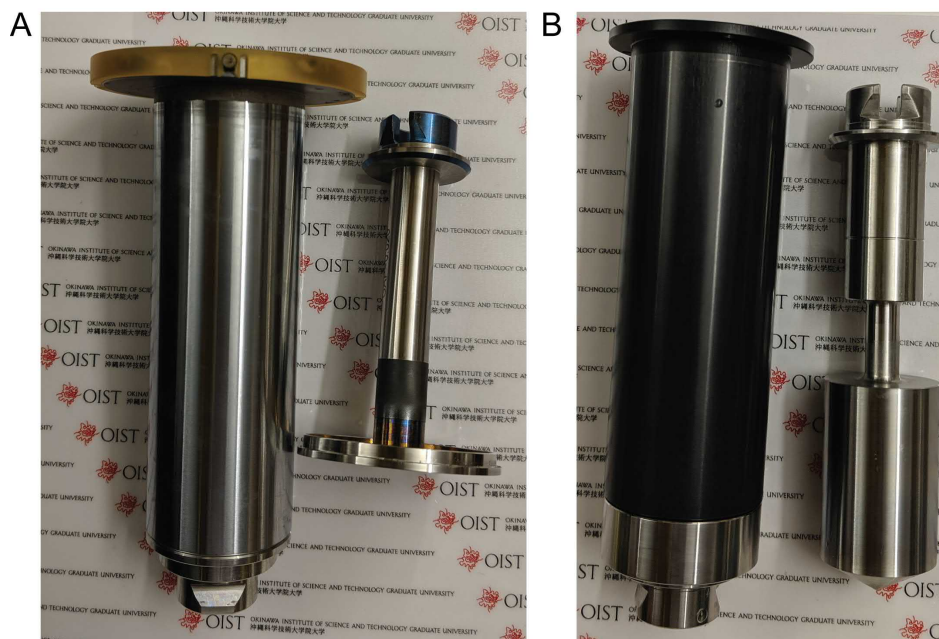


Figure A.1: Geometry used in rotational rheometry using ARES-G2 (TA Instruments). (A) A flat plate (Left) and 1° cone (Right) geometry (B) A cup (Left) and bob (Right) geometry.

Due to the low viscosities of the liquids, there was risk of sample spilling at high

shear rates, which may damage the motor and temperature controller electronics when using cone and plate geometry. In addition, the surface tension of sample liquid and drying artifacts may affect the reading in the cone plate geometry. Only water and MEM α samples were tested with the cone plate geometry for results comparison between different geometries. All other results were measured using concentric cylinders on ARES-G2. Sample fluids of 110% of the minimum required volume were loaded into the geometry and standard gap was used. Triplicate flow sweep measurements were carried out with logarithmic sweep of shear rates between 0.01 to 1000 s⁻¹ at 25 °C and 37 °C using a peltier system (Advanced Peltier System, TA Instruments, USA).

The torque measurable by the instrument is limited and thus limits the measurable shear stress. To avoid bad data, the condition for acceptable data is set so that measured torque is above some minimum limit $T > T_{min}$ ⁶⁶⁹, so the viscosity satisfies:

$$\eta > \frac{F_{\tau} T_{min}}{\dot{\gamma}}, \quad (\text{A.1})$$

where η is the minimum shear viscosity, F_{τ} is the geometry factor, T_{min} is the minimum measurable torque, $\dot{\gamma}$ is the apparent shear rate.

The geometry factors for the cone-plate geometry and the concentric cylinder are given as:

$$F_{\tau} = \frac{3}{2\pi R^3}, \quad (\text{cone-plate})$$

$$F_{\tau} = \frac{1}{2\pi R_b^2 \times H_b}, \quad (\text{concentric cylinder})$$

where, R is the radius of the cone, R_b is the radius of the bob, and H_b is the height of the bob.

In the concentric cylinder geometry, when the inner cylinder is rotating at sufficiently large velocity, secondary flow instability can generate axisymmetric vortices, also known as the Taylor-Couette flow. Since the low viscosity fluids are more prone to secondary flow, the viscosity of the testing should satisfy the following:

$$\eta > \frac{(R_o - R_i)^{\frac{5}{2}}}{1700 R_i^{\frac{1}{2}}} \rho \dot{\gamma}, \quad (\text{A.2})$$

where R_o is the outer diameter of the geometry, R_i is the inner diameter of the geometry, ρ is the density, $\dot{\gamma}$ is the shear rate.

On ARES-G2, the minimum measurable torque specified by the manufacturer was 0.1 $\mu\text{N m}$. The cup I used had an inner diameter of 29.989 mm and the bob had a diameter of 27.681 mm and a length of 41.620 mm. The compliance of upper geometry was 0.648 mrad N⁻¹ m and no value was reported for the lower geometry. The inertia for the geometry was 62.1 $\mu\text{N m s}^2$. The measured viscosities (Pa.s) at different shear

rates using a concentric cylinder geometry should satisfy the following:

$$\eta > \frac{1.996 \times 10^{-3}}{\dot{\gamma}}, \quad (\text{minimum detectable viscosity})$$

$$\eta > 2.262 \times 10^{-7} \dot{\gamma}. \quad (\text{secondary flow limit})$$

The triplicate data were averaged, and standard deviations were calculated in Excel (Microsoft, USA). Considering the sensitivity limit and the secondary flow limit, the viscosity values from rotational rheometry were reported by taking average values between shear rate of 10 to 100 s⁻¹ or fitted as Newtonian fluids in TRIOS software (TA Instruments, USA).

Capillary rheometry measurement In capillary rheometry (m-VROC, Rheosense, USA), a microfluidic channel of rectangular cross-sectional profile laden with pressure sensors along the channel is fabricated by MEMS technologies. The pressures of the Hagen-Poiseuille flow at segments along the channel are measured and pressure drops are fitted to find the apparent viscosity of the liquid⁶⁷⁸:

$$\dot{\gamma}_{app} = \frac{6Q}{wh^2}, \quad (\text{A.3})$$

$$\tau = -slope_{\Delta p} \frac{wh}{2w + 2h}, \quad (\text{A.4})$$

$$\eta_{newtonian} = \frac{\tau}{\dot{\gamma}_{app}}, \quad (\text{A.5})$$

where, Q is the flow rate, w is the channel width, h is the channel depth, τ is the wall shear stress calculated from slope of pressure drop (Δp) from m-VROC sensor by unit surface area, and $\dot{\gamma}_{app}$ is the apparent shear rate. In cases of non-Newtonian fluids, the true shear rate is calculated by Weissenberg-Rabinowitsch correction from the apparent viscosity:

$$\dot{\gamma} = \frac{\dot{\gamma}_{app}}{3} \left(2 + \frac{d \ln \dot{\gamma}_{app}}{d \ln \tau} \right). \quad (\text{A.6})$$

Using the capillary rheometry, liquid viscosities at very high shear rates can be measured with very small sample volume without artifacts from flow instabilities or interfacial effects. The dynamic viscosities of the sample liquids were measured using a capillary rheometry (m-VROC, Rheosense, USA) using a A05 sensor (Table A.1) with a 1 mL gas-tight loading syringe (VWR, USA). Triplicate measurements of viscosities with R^2 value above 0.98 were taken and averaged.

Table A.1: Specification of the A05 m-VROC sensor for low viscosity fluids.

A05 sensor, 50 μm depth	Shear rate range (s ⁻¹)		
	Low shear	Medium shear	High shear
	0.1 - 500	500 - 6000	6000+
Viscosity range (mPa s)	5 - 500	0.5 - 50	0.2 - 4

A.2.4 pH and electrical conductivity measurement

The electrical conductivities of the media were vital to calculate the amount of electrical current needed to establish appropriate electric field strength in the microchannels. Samples of buffered solutions and media were first equilibrated in the 37 °C, 5% CO₂ incubator, then before experiment incubated in a 40 °C water bath for 10 minutes. Afterward they were aliquoted to a 100 mL beaker under room temperature. The tips of a calibrated pH probe (9618S, Horiba, Japan) and a conductivity probe (3552-10D, Horiba, Japan) were submersed in the sample fluids and allow to reach to 37 °C before triplicate readings were taken (F74, Horiba, Japan). Both the conductivity probe and the pH probe were calibrated with reference solutions prior to the measurement. The setup is shown in Figure A.2.

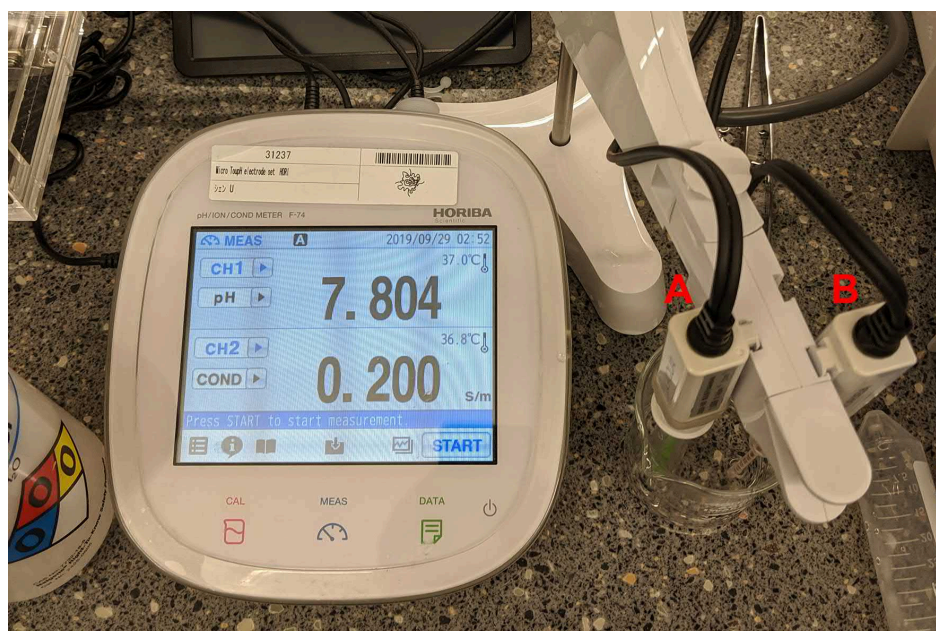


Figure A.2: Measurement setup for pH and electrical conductivity. (A) An electrical conductivity probe; (B) An internal temperature compensated pH probe.

A.2.5 Refractive index measurement using refractometry

The refractive indexes of the sample fluids were measured using a modern automatic Abbe's refractometer (Abbemat MW, Anton Paar GmbH, Austria). The automatic refractometer was based on the original Ernst Abbe's design^{679,680}. In Abbemat MW, a monochromatic light, usually the Na-D line at 589.3 nm, is generated by a white light emitting diode (LED) light source and a interferometric grating. The incident light beam passed through an Yttrium-Aluminum-Garnet (YAG) prism to the samples on the opposite side and the reflected lights at various angles were detected by a charge coupled device (CCD). The refractive index of the sample was inferred with minimum interference from color and transparency of the sample. All the measurements were done in triplicate at 37 °C maintained by the integrated temperature controller on Abbemat MW.

A.3 Results and discussion

A.3.1 Density, electrical conductivity, and refractive index of different media

The measured results of density at 25 °C and 37 °C, electrical conductivity at 37 °C, and refractive index at 589.3 nm, 37 °C are shown in Table A.2.

The densities of all solutions resemble that of water but increased slightly due to solutes and inversely correlate with the temperature.

The electrical conductivities of all the solutions are also measured at 37 °C. The electrical conductivities of cell culture media based on Eagle's or Dulbecco's original recipe yield similar electrical conductivities. Although the conductivity of MEM α is slightly smaller than reported (1.62 versus 1.82 S m⁻¹)⁶⁷⁵, it could result from the difference of the sodium bicarbonate amount. In early cell culture systems, 10% CO₂ was used instead of 5% in contemporary cell culture incubator. The amount of supplemented sodium bicarbonate is different for buffering at physiological pH, which can contribute to electrical conductivity.

Many reports have attempted to create an algebraic expression of electrical conductivity by the ionic strength of the solution, which is contributed by the dissolution and ionization of the ionic solute⁶⁸¹. The ionic strengths of the solutions are calculated based on the recipe provided by the manufacturer. From the measured data, the best curve fit shows the linear relationship between the ionic strength and the electrical conductivity (Figure A.3).

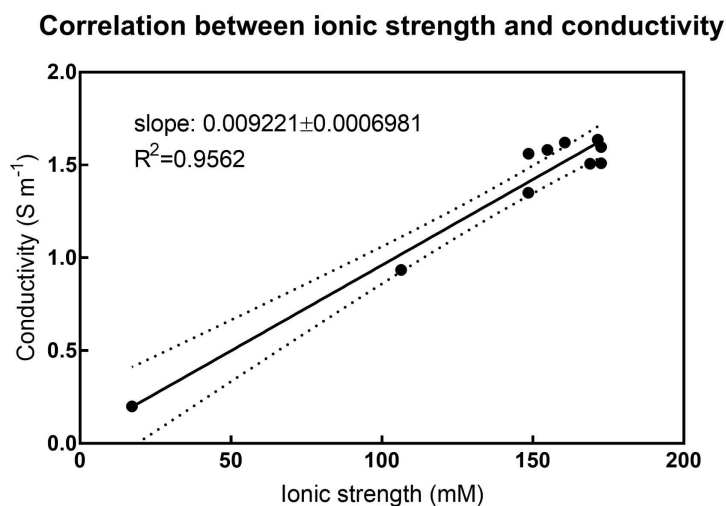


Figure A.3: Correlation between the ionic strength and the conductivity of cell culture media.

The refractive indexes of all the test solutions are very close to that of water ($n_D \approx 1.33$) (Table A.2). The effect from the solute may be only minute except in experiments demanding high optical sensitivity. However, the refractive index information maybe helpful if precise index matching is needed in high resolution microscopy.

Table A.2: The ionic strength, pH, density, conductivity, and refractive index properties of culture media used in the thesis. SD: standard deviation.

Medium	Manufacturer	Catalog number	NaHCO ₃ (g L ⁻¹)	Ionic strength (mM)	pH	Density (kg m ⁻³ , 25 °C)	Density (kg m ⁻³ , 37 °C)	Electrical conductivity (S m ⁻¹ , 37.0±0.2°C)		Refractive index (nD@589.3 nm, 37 °C)	
								mean	SD	mean	SD
18.2MΩ H ₂ O	In house	n/a	0	0	n/a	997.3	993.4	n/a	n/a	1.330972	1.0E-05
10X D-PBS(-)	Nacal	11482-15	0	1715.0	6.666	1064.2	1060.4	7.420	0.012	1.346545	2.5E-06
1X D-PBS(-)	Nacal	14249-24	0	171.5	7.436	1003.1	1002.3	1.637	0.008	1.332825	1.1E-05
0.1X D-PBS(-)	Nacal	14249-24	0	17.2	7.804	998.5	994.5	0.200	0.003	1.331132	3.5E-06
Low glucose DMEM	Nacal	08456-36	3.7	172.6	7.237	1000.2	998.3	1.597	0.014	1.332964	2.6E-06
DMEM	Gibco	12800-017	2.2	154.8	7.423	1004.1	1001.6	1.581	0.018	1.333230	2.5E-06
MEMα	Gibco	12000-022	2.2	160.6	7.156	1003.9	1001.6	1.621	0.021	1.333092	4.2E-06
Fluorobrite DMEM	Gibco	A18967-01	n/a	n/a	7.653	1006.6	1002.8	1.592	0.019	1.333460	1.0E-06
RPMI1640	Gibco	A10491-01	1.5	148.5	7.062	1004.6	1001.4	1.350	0.034	1.332864	5.8E-07
High glucose with pyruvate DMEM	Gibco	11995-065	3.7	172.6	7.315	1006.4	1003	1.509	0.028	1.333553	5.5E-06
Neural basal medium	Gibco	211103-049	2.2	106.4	7.134	1003.8	1000.4	0.935	0.008	1.333149	5.8E-07
Calcium free DMEM	Gibco	21068-028	3.7	169.0	7.663	1006.4	1002.6	1.507	0.018	1.333415	2.1E-06
HBSS	Gibco	14175-095	0.35	148.6	7.237	1003.8	999.9	1.561	0.028	1.332580	5.8E-07
Endothelial cell growth medium	Promocell	C92210	n/a	n/a	7.464	1003.3	1001.7	1.439	0.010	1.333325	1.0E-05
DMEM + 10% CS	Gibco	12800-017	2.2	n/a	7.342	1007.3	1004.7	1.614	0.018	1.334259	4.0E-06
DMEM + 10% FBS	Gibco	12800-017	2.2	n/a	7.237	1007.8	1004.2	1.602	0.032	1.334369	2.5E-06
MEMα + 10% FBS	Gibco	12000-022	2.2	n/a	7.237	1005.3	1002.9	1.536	0.027	1.333874	2.0E-06

A.3.2 The geometry effect on the rotational rheometry results

The geometry in rotational rheometry has critical effects on measurements^{670,682}. In conventional parallel-plate geometry, the results are limited by the torque sensitivity of the transducer, the surface tension of the sample, and the radial shear gradient in the parallel-plate geometry. The radial shear gradient is mitigated in the cone-plate geometry. However, the surface tension from the air/liquid interface can still create artifacts in measurement. On the other hand, in the concentric cylinder geometry, geometry is submerged in the sample fluids and the effect from the surface tension can be reduced but the inertia of the bigger geometry may introduce additional artifacts⁶⁶⁹.

Measurement of milliQ water at 25°C with cone-plate or cup-bob geometries

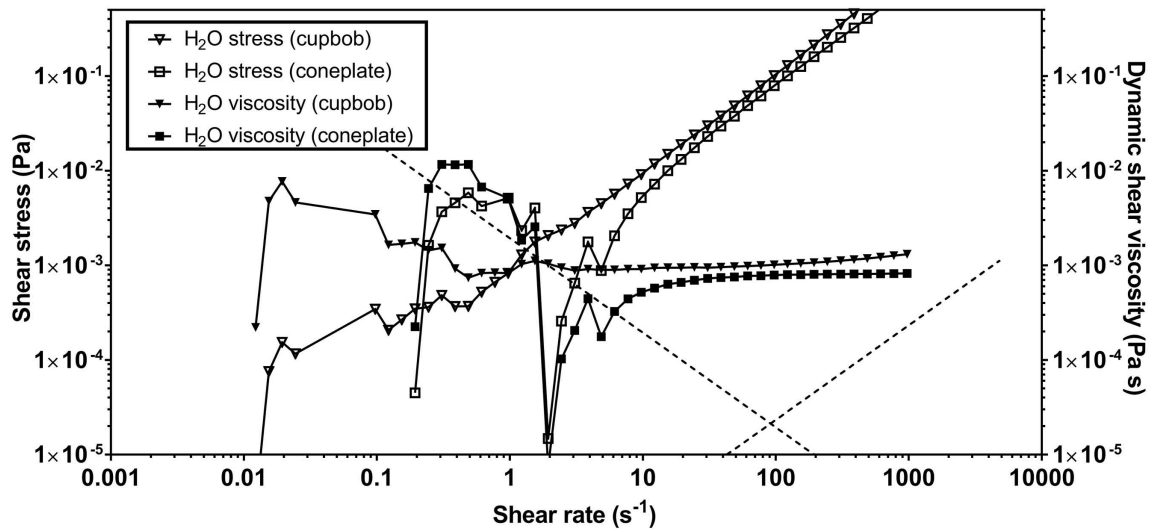


Figure A.4: The geometries effect to water viscosity measurement in rotational rheometry. The viscosity data are shown in filled symbols and shear stress data are in open symbols. The dashed lines indicate the lower torque sensitivity limit and the upper secondary flow limit. For visualization purposes, the data points were displayed but excluded during analysis as they were considered as bad data.

The flow sweep measurements of water and MEM α medium are performed at 25 °C in both cone-plate and concentric cylinder geometries. In pure water, some artifacts were detected above the torque resolution limit with the cone-plate geometry showing a false low viscosity at low shear rate, which can originate from the interfacial effect of water (Figure A.4), while the concentric cylinder (cup and bob) geometry yields better resolution at low shear rates. However, at high shear rates, although below the theoretical secondary flow limit, the viscosities measured by concentric cylinder geometry increase (but not in cone-plate geometry), which suggest potential inertial artifacts from the cup and bob geometry.

The similar results are observed in the MEM α medium. With the added complex solute in the cell culture medium, interfacial phenomena may further influence the measurement and demonstrate increased shear stress at low shear rates (Figure A.5). This suggests that different geometries subject to different disadvantages and the dynamic

viscosity measurement of low viscous fluids needs to be treated carefully.

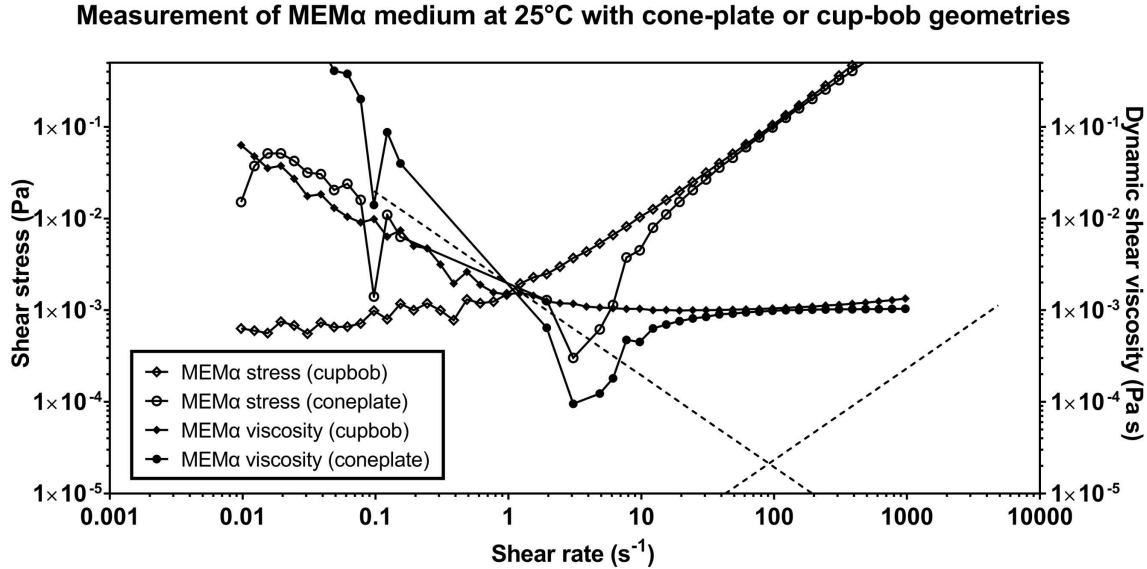


Figure A.5: The geometries effect to MEM α viscosity measurement in rotational rheometry. The viscosity data are shown in filled symbols and shear stress data are in open symbols. The dashed lines indicate the lower torque sensitivity limit and the upper secondary flow limit. For visualization purposes, the data points were displayed but excluded during analysis as they were considered as bad data.

A.3.3 Dynamic shear viscosities of selected buffer solutions and cell culture media

The dynamic viscosities of numerous buffer solutions and cell culture media are listed in Table A.3. Specifically, the dynamic viscosities of water and DMEM supplemented with or without calf serum or fetal bovine serum are measured with rotational rheometry and capillary rheometry (Figure A.6).

While qualitatively, we can see that the more complex the cell culture media is, the higher viscosity is observed. However, the data from rotational rheometry contain measurement artifacts stemming from sample surface tension, secondary flow, and instrumental inertia. The lower limit for good data point selection will need to be set considering the effect of torque sensitivity, sample surface tension, and geometrical inertia.

The viscosity measured with capillary rheometry shows that the cell culture media are Newtonian in high shear rates, but there are systematic errors between the measurement results of ARES-G2 and m-VROC, suggesting that a reference-calibration is needed if no additional interfacial effect is at play.

Table A.3: The dynamic shear viscosities of culture media measured using rotational and capillary rheometry. The cup and bob geometry (concentric cylinders) was used to measure the sample liquids in rotational rheometry. SD: standard deviation; sem: standard error of mean

Medium	Dynamic viscosity (ARES-G2, 25 °C, mPa.s)							Dynamic viscosity (ARES-G2, 37 °C, mPa.s)							Dynamic viscosity (m-VROC, A05, 37 °C, mPa.s)									
	1	SD	10	SD	100	SD	10-100 average	Newtonian fit	sem	1	SD	10	SD	100	SD	10-100 average	Newtonian fit	sem	584.1	1360.6	11281.7	26294.5		
Shear rate (s^{-1})																								
18.2 MG H ₂ O	1.2274	0.2519	0.964	0.0197	1.0166	0.003	0.972	6.26E-03	1.07	8.00E-02	1.6864	0.7351	0.8122	0.0782	0.804	0.0066	0.787	4.03E-03	0.848	0.01	0.68	0.7095	0.7335	0.728
10X D-PBS(-)	5.3400	1.7238	1.5616	0.1439	1.2535	0.0133	1.3300	0.2031	1.2620	0.0133	8.0700	0.3461	1.6334	0.0276	1.0352	0.0064	1.2000	3.20E-02	1.0430	0.004	0.883	0.884	0.879	0.874
1X D-PBS(-)	1.6831	0.6123	1.4111	0.5818	1.5072	0.6152	1.4410	0.0098	1.3605	0.1100	1.5834	0.6780	1.2445	0.5297	1.3184	0.5209	1.2600	8.09E-03	1.170	0.080	0.776	0.767	0.742	0.738
0.1X D-PBS(-)	1.1434	0.0923	0.9311	0.0107	1.0111	0.0057	0.9590	0.0085	1.0908	0.0790	1.1237	0.4090	0.7566	0.0403	0.7999	0.0028	0.7630	5.43E-03	0.775	0.008	0.689	0.720	0.732	0.722
Low glucose DMEM	2.0740	0.5130	1.2200	0.0349	1.2220	0.0115	1.1910	0.0040	1.2060	0.0160	3.3470	0.4100	1.1320	0.0348	0.9920	0.0119	0.9710	8.96E-03	1.030	0.030	0.774	0.749	0.724	0.724
DMEM	1.2200	0.1565	0.9866	0.0081	1.0568	0.0157	1.0070	0.0077	1.1403	0.0529	1.1396	0.1585	0.7776	0.0124	0.8555	0.0283	0.8030	8.17E-03	0.904	0.047	0.657	0.690	0.725	0.729
MEM α	1.4990	0.1700	1.0360	0.0131	1.0660	0.0304	0.9920	0.0044	1.0440	0.0111	1.6060	0.1720	0.8280	0.0506	0.8210	0.0019	0.7740	2.59E-03	0.806	0.001	0.738	0.732	0.731	0.729
Fluorobrite DMEM	1.2677	0.0685	0.9926	0.0433	1.0785	0.0605	1.0220	0.0090	1.0198	0.0008	1.5427	0.2640	0.8111	0.0210	0.8679	0.0547	0.8200	6.89E-03	0.811	0.005	0.736	0.731	0.727	0.726
RPMI1640	1.9470	0.5440	1.0650	0.0333	1.0780	0.0316	1.0100	0.0042	1.0609	0.0152	3.2910	0.2200	1.0120	0.0293	0.8630	0.0153	0.8430	9.35E-03	0.864	0.007	0.781	0.796	0.725	0.735
High glucose pyruvate DMEM	1.4622	0.1482	1.0349	0.0583	1.1030	0.0846	1.0473	0.0980	1.0777	0.0420	1.8974	0.0615	0.8439	0.0066	0.8408	0.0166	0.8209	0.0279	0.8312	0.007	0.730	0.742	0.748	0.750
Neural basal medium	1.9815	0.6896	1.0893	0.0302	1.1130	0.0300	1.0775	0.0040	1.0877	0.0169	3.2160	0.7563	1.0385	0.0670	0.8883	0.0256	0.9146	0.01	0.8843	0.011	0.784	0.756	0.761	0.739
Calcium free DMEM	1.1440	0.1270	0.9760	0.0167	1.0630	0.0032	1.0110	0.0063	1.0433	0.0184	1.5710	0.1910	0.8160	0.0270	0.8260	0.0030	0.8019	2.89E-03	0.812	0.001	0.753	0.756	0.745	0.739
HBSS	2.0800	0.6350	1.0670	0.0557	1.0460	0.0018	1.0310	0.0068	1.0381	0.0212	0.1690	0.1850	0.0810	0.0150	0.8510	0.0167	0.7640	9.21E-03	0.820	0.001	0.735	0.740	0.734	0.729
Endothelial cell growth medium	2.5423	1.9276	1.2474	0.2435	1.2035	0.0148	1.1910	0.0075	1.1295	0.0034	2.7291	2.1898	1.1264	0.2283	1.0027	0.0925	1.0170	1.46E-02	1.181	0.003	0.747	0.753	0.754	0.855
DMEM + 10% CS	2.5476	1.5552	1.2907	0.2588	1.2048	0.0639	1.2060	0.0114	1.2654	0.0023	2.9307	1.9749	0.9852	0.1652	0.9412	0.0349	0.9240	7.81E-03	0.967	0.013	0.812	0.803	0.786	0.774
DMEM + 10% FBS	2.3225	0.6472	1.3060	0.0338	1.2538	0.0871	1.2460	0.0081	1.2466	0.0109	3.7791	1.0734	1.1329	0.1289	1.0000	0.0781	1.0230	1.62E-02	1.028	0.00323	0.779	0.778	0.800	0.813
MEM α + 10% FBS	4.3017	4.7212	1.4356	0.5780	1.2082	0.0834	1.2600	0.0248	1.1892	0.0218	4.1587	3.2056	1.0622	0.2149	0.9383	0.0336	0.9500	1.42E-02	0.946	0.009	0.769	0.762	0.756	0.754

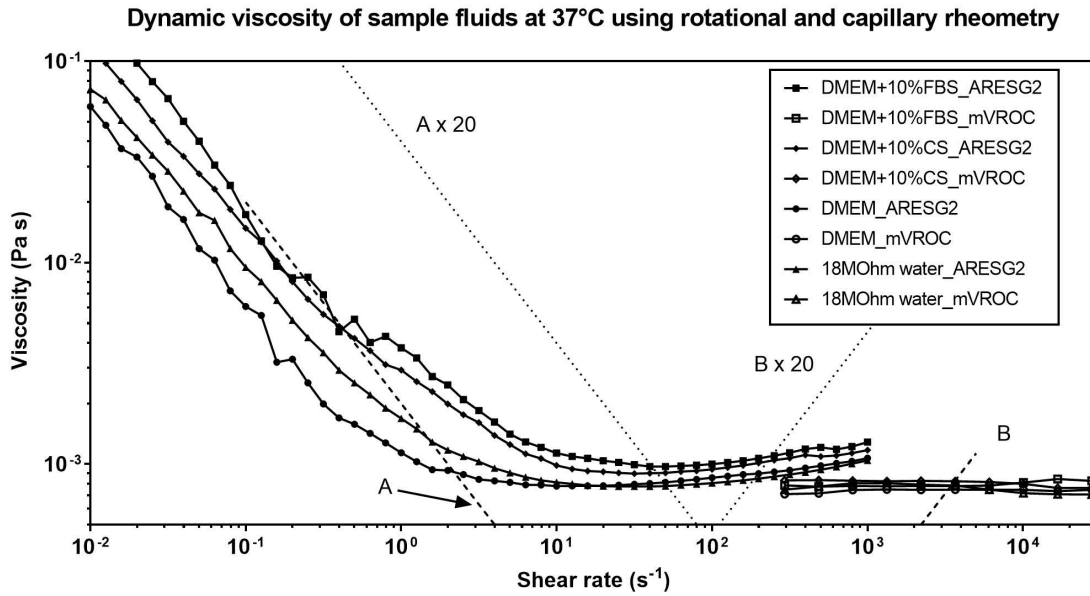


Figure A.6: The measured viscosities at different shear rates for water and DMEM media supplemented with different sera in rotational rheometry and capillary rheometry. The dashed line A shows the lower torque sensitivity limit and B shows the secondary flow limit for ARES-G2. Good data for analysis is arbitrarily taken between shear rate 10 to 100 s⁻¹.

A.4 Summary and prospects

I carried out the measurement of physical properties of several buffer solutions and cell culture media used in this thesis work using available instruments. The physical properties are used for numerical simulation and setting experimental conditions in this thesis.

It is generally accepted that cell culture media can be considered as Newtonian fluids because no long macromolecules are present. However, if macromolecules are added as part of proprietary recipe or in the supplemented sera, or if cells actively produce extracellular matrix macromolecules, the fluid might become non-Newtonian^{683–685}.

Accurate measurement of physical and biochemical parameters of the microenvironments will be important for designing successful microsystems to quantitatively manipulate them.

Appendix B

Uniform electrical cell stimulation in circular cultureware by 3D microfluidics

Abstract

Applying uniform electric field (EF) *in vitro* in the physiological range conventionally has been achieved in rectangular-shaped microchannels where the cross-sectional area is a constant. In contrast, in circular-shaped devices, it is difficult to create uniform EF from two electric potentials due to dissimilar electrical resistances originated from the length difference between the diameter and the length of any parallel chord across the bottom circular chamber in which the cells are cultured. To address this challenge, I developed a three-dimensional (3D) computer-aided designed (CAD) polymeric insert to create uniform EF in circular-shaped multi-well culture plates. A uniform EF with a coefficient of variation (CV) of 1.2% in the 6-well microplate can be generated with an effective stimulation area percentage of 70.2%. In particular, NIH/3T3 mouse embryonic fibroblasts were used to validate the performance of the 3D designed Poly(methyl methacrylate) (PMMA) insert in a circular-shaped 6-well microplate. The CAD based inserts can be easily scaled up and down (*e.g.* from 18 mm in 24-well microplate to 100 mm dishes) to further increase effective stimulation area percentages, and be implemented in commercially available cultureware for a wide variety of EF-related research such as EF-cell interaction and tissue regeneration studies.

B.1 Introduction

A weak direct-current electric field (dcEF) exists at the tissue level due to the transepithelial potential difference established by the tissue polarity¹¹⁰. Cells demonstrate directional migration (electrotaxis) or orientation-change (electro-alignment) in response to a physiological dcEF in both *in vitro* and *in vivo* settings. The electrotaxis and dcEF stimulation have played pivotal roles in physiological processes such as embryonic development, neurogenesis, morphogenesis, and wound healing^{107,110,161,162,686}. Numerous cellular signaling pathways are mediated by electric field (EF) stimulation. Various membrane receptors^{233,243,247,251,687} or ion channels^{164,212,215,688,689} have been suggested to act as EF sensors and initiate many intracellular signaling cascades in different cell types^{212,213,247,256,260,264,690,691}. Further investigations are required to clarify the func-

tional roles of EF sensory proteins and signaling networks in regulating the electrotaxis phenomena.

However, to gain a better understanding of signaling pathways demands a reliable and convenient electrical stimulation platform for microscopy imaging and cell product recovery with subsequent biochemical and molecular analysis. Even though an electrical cue can direct cell migration comparable to that of a chemical cue²⁷⁵ and synergistically promote directional migration with other physical factors such as shear stresses²⁷⁴, electrotaxis is less well studied than chemotaxis, possibly due to the lack of experimental tools for convenient EF stimulation comparable to a boyden chamber (transwell chamber) that is routinely used for chemotaxis⁶⁹². Furthermore, there is a lack of standardize electrical stimulation apparatus for cell studies.

Conventional *in vitro* electrical stimulations are performed either by direct stimulation using electrodes, or stimulation in a microfluidic chamber with salt bridges. The dcEF created through direct electrode stimulation is not uniform and cells are often exposed to toxic electrolysis products. Thus, many conventional electrotaxis studies employ a confined microfluidic chip in which cells are cultured in the bottom of the culture chamber^{196,198,258,266,574,693}. The small cross-section of the chamber limits the required voltage for the applicable electrical current and reduces the Joule heating that could be harmful to the cells. Despite the success of using microfluidic chips for electrical stimulation in recent studies, these microfluidic chips often require special fabrication procedures on cell culture dishes days prior to the actual experiment, limiting the adaptivity under common laboratory settings. Further, a simple rectangular-shaped cell culture microchamber is usually placed on a circular shaped tissue-culture polystyrene (TCPS) petri dish to generate the uniform EF. As a result, a large portion of the cell culture area on the dish is unused, leading to low cell yield and poor cell product recovery. Even though larger cell yields have been recently achieved by scaling up the rectangular shaped microchamber with increased cell culture area^{196,258}, a large fraction of the circular shaped TCPS dish is not utilized.

In a circular-shaped area in a petri dish that exists in every biomedical laboratory, a uniform EF cannot be intuitively created by two electric potentials due to dissimilar electrical resistances originated from the length difference between the diameter of the circle and the length of any parallel chord of the bottom circular chamber where cells are cultured. However, even without the uniformity, the approach is still adapted in academic and commercial settings such as those by Marotta *et al.*⁶⁹⁴ and by IonOptix⁶⁹⁵⁻⁶⁹⁸. There are also other approaches using transwell like configuration of micropatterned electrodes. Lin *et al.* used a modified transwell assay to study cell electrotaxis by applying EF through the transwell insert coupled with platinum electrodes⁶⁹⁹. Alternatively, García-Sánchez *et al.* used patterned electrodes to stimulate cells in multi-well plates⁷⁰⁰. Their systems not only require sophisticated microfabrication procedures but small EF-null gaps between electrodes also decrease the EF homogeneity. Recently, Ahirwar *et al.* used electromagnetic induction method with a boyden chamber to demonstrate non-contact induction of electrotaxis, but non-uniform EF persisted⁷⁰¹.

Computer aided design and computer aided manufacturing (CAD/CAM) use computer software to precisely design models and program manufacturing processes. Mathematically depicted 3D structures for workpieces can be easily created in CAD/CAM

software and conveniently adopted for numerical simulations. Thus time, material, and manpower are greatly reduced for prototyping effort. In recent years, additive manufacturing (3D printing)⁷⁰² takes the advantage of CAD/CAM to rapidly prototype workpieces through layer-by-layer stacking of raw materials and this technology has been used to fabricate microfluidic chips^{318,359,703,704}. In this study, I solve the non-uniform EF challenge by applying the CAD principle to modulate the electrical resistance in a polymeric insert, which is then fabricated by CAM methods and retrofitted to a common multi-well plate. Using Ohm's law, an optimized CAD structure is created to equalize the electrical resistance in the circular shaped bottom chamber to generate a uniform EF. As a result, a large area of contemporary cell culture dish can be stimulated with the uniform EF and higher cell yield is obtained.

I describe the design principle and numerical simulation of 3D CAD polymeric insert in section B.2. The microfabrication and experimental setup is described in section B.3. The validation of the polymeric insert and the discussion is followed in section B.4.

B.2 Theoretical design and numerical simulation

B.2.1 Design principle of a 3D CAD insert to create a uniform EF in different sizes of circular cultureware

In contrast to conventional *in vitro* EF stimulation systems using a rectangular chamber, to apply a uniform EF in a circular shaped chamber (*e.g.* tissue culture polystyrene petri dish, multi-well plate) is extremely difficult. The reason is due to the electrical resistance across the entire area between two opposite electrical potential sources are different. To illustrate, the electrical resistance ratio between two electric potential sources A and B through the diameter and through the circumference is $2 : \pi$ ($R_1 : R_2$, Figure B.1).

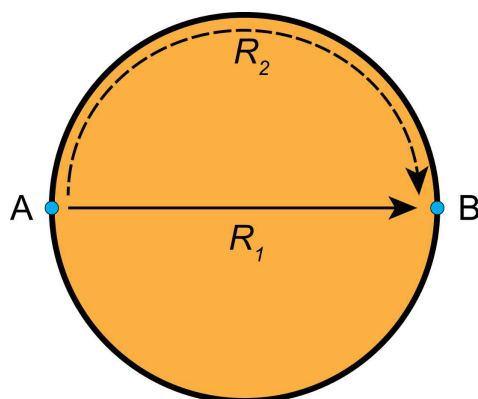


Figure B.1: Schematic representation of electric resistance difference in a circular cultureware. The electrical resistances between potential source A and B through the diameter (R_1) and through the circumferences (R_2) are different, thus the electric field is not uniform in the cultureware.

First, to apply electric field to cells, a person will intuitively insert two electrical

potentials⁶⁹⁴. If two electric potentials are applied on top of this liquid cylinder, the EF will not be uniform due to differences of electrical resistance for all current paths between both potentials through the bottom chamber (Figure B.2).

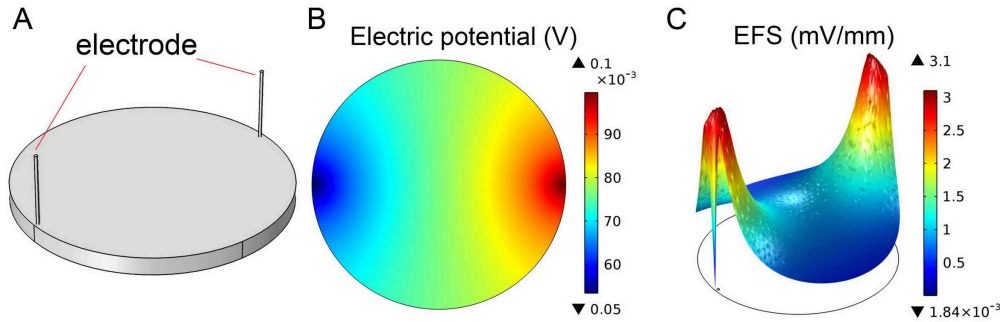


Figure B.2: Numerical simulation of an EF stimulation device designed by Marotta *et al.*⁶⁹⁴. (A) The 3D model consists of a 2 mm-deep bottom chamber in a 6-well plate and two thin platinum electrodes inserted on the opposite sides of the chamber; (B) The electric potential distribution of the EF. The non-uniform decrease of the electric potential between the electrodes creates a non-uniform EF; (C) With an electrical current with density of 500 A m^{-2} introduced from one electrode and flows to the other at ground potential, a wide distribution of the electric field strength (EFS) in the bottom chamber renders a non-uniform EF in the bottom chamber.

A similar approach but with bigger electrodes is taken in a commercial electrical stimulation system for cardiomyocyte pacing (C-Pace, Ionoptix Corp, USA). In C-Pace system, carbon plate electrodes are inserted into multi-well plates and the established EF is also not uniform (Figure B.3).

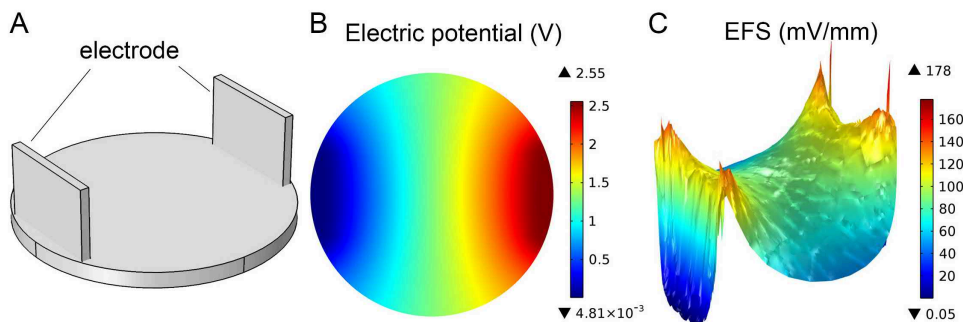


Figure B.3: Numerical simulation of a commercial C-dish EF stimulation device from Ionoptix Corp. (A) The 3D model consists of a 2 mm height bottom chamber in a 6-well plate and two carbon plate electrodes inserted on the opposite sides of the chamber; (B) The electric potential distribution of the EF. The non-uniform decrease of the electric potential between the electrodes creates a non-uniform EF; (C) The EF distribution at the bottom of the chamber is generated by an electrical current with density of 500 A m^{-2} flowing from one electrode to the other at ground potential. The non-uniformity of the EF is evident by the rough surface of the EFS distribution in the bottom chamber.

Therefore, conventional approaches to create uniform electric field often choose to sacrifice the surface area of the cultureware to ensure the electric field is uniform, *i.e.*, configure the chamber in rectangular-shaped constant cross-section area.

In this work, I created a microfluidic device to possess circular-shaped area in which a uniform EF can be generated. The cells were stimulated in a circular microfluidic chamber with a given height (red, Figure B.4). The electric field were applied through a thin layer of fluid volume surrounding the perimeter of the bottom chamber through an insert, and the fluid volume could be treated as a thin liquid column (LC , purple block in Figure B.4).

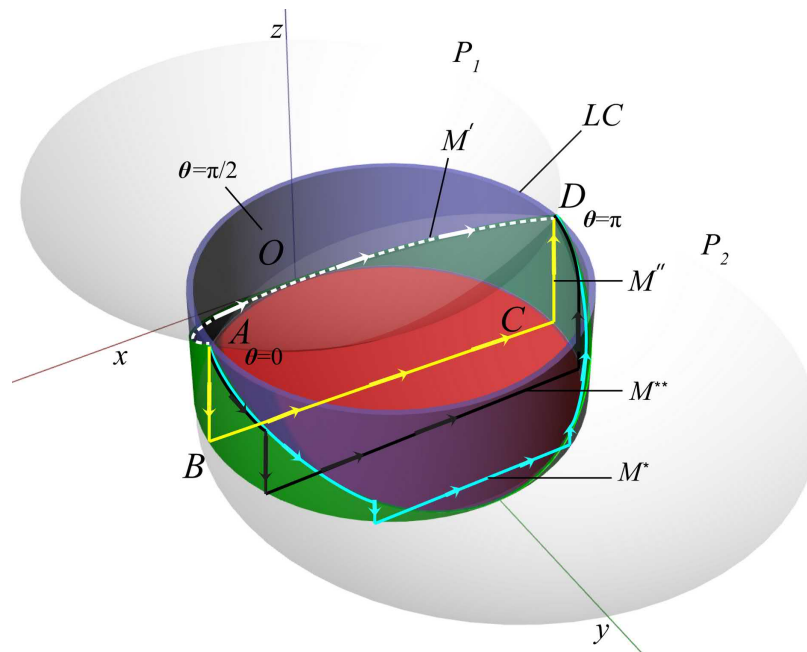


Figure B.4: 3D schematic of the design principle. Two identical axial symmetric paraboloids (P_1 & P_2) along \overline{BC} are used to equalize the electrical resistance in the bottom chamber (red region) by trimming the liquid column LC (purple region) to form our designed structure (green region).

To create a uniform EF, the electrical resistance from one electrode to the other through any cross-section in the system must be the same. To satisfy the requirement, I designed a 3D structure to equalize the electrical resistances through any arbitrary current line that passes through the bottom circular chamber. Such structure can be approximated as the liquid column (LC) intersected by two identical paraboloids whose apices are at the midpoint of the circumference of the bottom circular chamber (grey, Figure B.4) The designed 3D CAD structure (green block, Figure B.4) to equalize the electrical resistance can be created by trimming the liquid column by the two circular paraboloids using the Boolean difference tool in the non-uniform rational basis spline (NURBS)-based CAD software (Rhinoceros 5, Robert McNeel & Associates, USA). The 3D CAD model can then be used for simulation in COMSOL or to make the microfluidic chip for creating a uniform EF.

According to Ohm's law, electrical resistance R can be described as follows⁷⁰⁵:

$$R = \rho \frac{l}{A_{cross-section}} = \frac{\rho l}{wh}, \quad (B.1)$$

where ρ is the electrical resistivity, l is the length, $A_{cross-section}$ is the cross-sectional area, w is the width, and h is the height of the conductor (microchannel).

I need to identify the arc length of the curves in our system to calculate the electrical resistance. Using a polar coordinate system, the bottom chamber (red circle, Figure B.4) resides on the xy plane and the liquid column on top possesses a diameter of \overline{BC} . For paraboloid P_1 , its apex resides with the origin O in the liquid column and the yz plane. the paraboloids intersects with the liquid column at the curve $M' = \widehat{AOD}$ (white dashed line, Figure B.4). the projections of points A and D on xy plane are B and C . Consider an electrical current flowing from point A to point D . By Ohm's law, in order to have a uniform EF in the chamber bottom, the resistance of \widehat{AOD} (white dashed path, Figure B.4) must be equal to that of $\overline{AB} + \overline{BC} + \overline{CD}$ (yellow path, Figure B.4), equivalently, $R_{M'} = R_{\overline{AB}} + R_{\overline{BC}} + R_{\overline{CD}}$. If I assume the resistivity is the same across the model,

$$\frac{\widehat{AOD}}{A_{M'}} = \frac{M'}{A_{M'}} = \frac{\overline{AB}}{A_{\overline{AB}}} + \frac{\overline{BC}}{A_{\overline{BC}}} + \frac{\overline{CD}}{A_{\overline{CD}}}. \quad (B.2)$$

Equation B.2 shows that a uniform EF distribution is true when the ratio of the rectification of the curve M' over the cross-sectional area of the liquid column equals to the ratio of $\overline{AB} + \overline{CD}$ over the cross-sectional area of the liquid column, in addition to \overline{BC} over the cross-sectional area of the bottom chamber. Assuming all electrical currents pass through sufficiently thin paths.

$$\frac{M'}{column\ thickness} = \frac{2 \times \overline{AB}}{column\ thickness} + \frac{\overline{BC}}{chamber\ depth}. \quad (B.3)$$

Since \overline{AB} and \overline{BC} can be easily measured, the value of M' can be subsequently extracted by using Equation B.3. With the information of M' , I can determine the shape of the circular paraboloid P_1 and P_2 as follows.

$$\frac{x^2 + y^2}{a^2} = \frac{z}{b}, \quad (B.4)$$

where a^2/b is the constant describing the level of curvature in xz and yz planes of the paraboloid, which defines the shape of the paraboloid.

The equation for the liquid column can be considered as

$$x^2 + (y - r)^2 = r^2, \quad (B.5)$$

where r is the radius of the column (also the radius of the circular bottom chamber, *i.e.*, the culture area in the cultureware)

The coordinates of points O , A , and D can be presented in parametric form

$(r \cos \theta, r(1 - \sin \theta), \frac{2br^2}{a^2}(1 - \sin \theta))$, with

$$O : \left(r \cos \frac{\pi}{2}, r(1 - \sin \frac{\pi}{2}), \frac{2br^2}{a^2} \left(1 - \sin \frac{\pi}{2} \right) \right) = (0, 0, 0), \quad (\text{B.6a})$$

$$A : \left(r \cos 0, r(1 - \sin 0), \frac{2br^2}{a^2} (1 - \sin 0) \right) = \left(r, r, \frac{2br^2}{a^2} \right), \quad (\text{B.6b})$$

$$D : \left(r \cos \pi, r(1 - \sin \pi), \frac{2br^2}{a^2} (1 - \sin \pi) \right) = \left(-r, r, \frac{2br^2}{a^2} \right). \quad (\text{B.6c})$$

The rectification of curve M' along the paraboloid P_1 can be calculated by integrating parametric equations⁷⁰⁶,

$$M' = \int_0^{\pi} \sqrt{\left(\frac{dx}{d\theta}\right)^2 + \left(\frac{dy}{d\theta}\right)^2 + \left(\frac{dz}{d\theta}\right)^2} d\theta \quad (\text{B.7a})$$

$$= \int_0^{\pi} \sqrt{(-r \sin \theta)^2 + (-r \cos \theta)^2 + \left(-\frac{2br^2}{a^2} \times \cos \theta\right)^2} d\theta \quad (\text{B.7b})$$

$$= \int_0^{\pi} \sqrt{r^2 + \left(\frac{2br^2}{a^2}\right)^2 - \left(\frac{2br^2}{a^2}\right)^2 \sin^2 \theta} d\theta. \quad (\text{B.7c})$$

The constant of the paraboloid $\frac{a^2}{b}$ can be solved by solving Equation B.3. Equation B.3 is difficult to solve explicitly due to the elliptic integral of the second kind related to M' along the paraboloid P_1 (Equation B.7). But Equation B.3 can be evaluated using Mathematica with the following code (Listing B.1) by denoting a constant $c = \frac{2br^2}{a^2}$ (r is the radius of the circular bottom chamber) to simplify the calculation.

Listing B.1: Example code to find the descriptor for the paraboloid P_1

```
Plot [ Evaluate [ Integrate [ Sqrt [ 225 + c^2 - c^2 * Sin [ x ] ^ 2 , { x , 0 , Pi } ]
/ 0.5 - 2 * c / 0.5 - 30 / 0.26 ] , { c , - 4.715 , - 4.71 } ]
```

To design an insert for 6-well plates, denote the thickness of the liquid column to be 0.5 mm, the diameter of the bottom chamber to be 30 mm, and the thickness of the bottom chamber to be 0.26 mm, the parameter $c = \frac{2br^2}{a^2}$ (containing the constant for the paraboloid P_1) can be evaluated and used to create the 3D model (described below) in a commercial CAD software for further numerical simulation and device fabrications.

$$\frac{b}{a^2} = -0.01047. \quad (\text{B.8})$$

$$P_1 : x^2 + y^2 = -\frac{z}{0.01047}. \quad (\text{B.9})$$

With this design principle, two extreme cases can be considered: electrical current passing through the shortest chord (*i.e.*, diameter) and the longest chord (*i.e.*, circumference), which will yield the constant of the paraboloid and the height of the liquid

column required to achieve uniform EF.

The electrical resistance for all arbitrary current lines passing through each different path without the structure (only the liquid column), the following equation in Listing B.2 can be used.

Listing B.2: examples code for all M paths without structure

```
Table [ Evaluate [ 2* Sqrt [ ( 15* ( Pi/2-y ) ) ^ 2 + ( -4.713 ) ^ 2 ] / 0.5
+ 2*15* Sin [ y ] / 0.26 ] , { y , 0 , Pi/2 , Pi/180 } ]
```

To find the electrical resistance for all arbitrary current lines passing through each different paths (for example, pathline curves M'' , M^{**} , M^* , and M' , see Figure B.4) between the shortest chord ($\theta = 90^\circ$) and the diameter ($\theta = 0^\circ$), where θ is the polar coordinate azimuth, the following equation in Listing B.3 can be used.

Listing B.3: examples code for all M paths with CAD structure

```
Table [ Evaluate [ 2* Integrate [ Sqrt [ 225+4.713^2 - 4.713^2* Sin [ x ] ^ 2 ] ,
{ x , 0 , y } ] / 0.5 + 2* ( -4.713 ) * ( 1 - Sin [ y ] ) / 0.5 + 2*15* Sin [ Pi/2-y ] / 0.26 ] ,
{ y , 0 , Pi/2 , Pi/180 } ]
```

The calculated resistance range with $\theta \in (0^\circ, 90^\circ)$ is plotted in Figure B.5. The relative resistance of $\overline{AB} + \overline{BC} + \overline{CD}$ corresponds to $\theta = 0^\circ$ and that of \widehat{AOD} corresponding to $\theta = 90^\circ$. The results show that resistances of all path lines converge toward both extreme cases and our current model provides a good approximation to achieve uniform EF in a circular chamber. For future work, I plan to use quadratic surface integral to further improve our design.

B.2.2 Numerical simulation

Configuration

The CAD models were either created directly in COMSOL Multiphysics software or in Rhinoceros CAD software and imported into COMSOL for simulation. The material of all models was set as water using the measured properties of culture medium in Appendix 2. Briefly, DMEM was set as the ionic fluid and the electric potential between the salt bridges was numerically simulated by solving steady-state Maxwell's equations using the alternating current/direct current (AC/DC) module in COMSOL. The conductivity of DMEM was set as 1.515 S m^{-1} with relative permittivity set arbitrarily as 80 like water.

In experiments, an electrical current input interface was needed. Two 2 mm in diameter circular holes were designed on top of the device to connect to two electric potentials. Two shell-shaped structures then interconnected the holes to the liquid shell in the microdevice. A current density of 376.1 A m^{-2} , aiming to create a 100 V m^{-1} EF in the 30 mm in diameter and 0.26 mm-thick bottom chamber was calculated using the equation B.10.

$$I = EFS \times \sigma \times w \times h. \tag{B.10}$$

where I , EFS , σ , w , and h are the required electrical current in μA , electric field strength (EFS) in V m^{-1} , electrical conductivity in S m^{-1} , width in mm, and height in

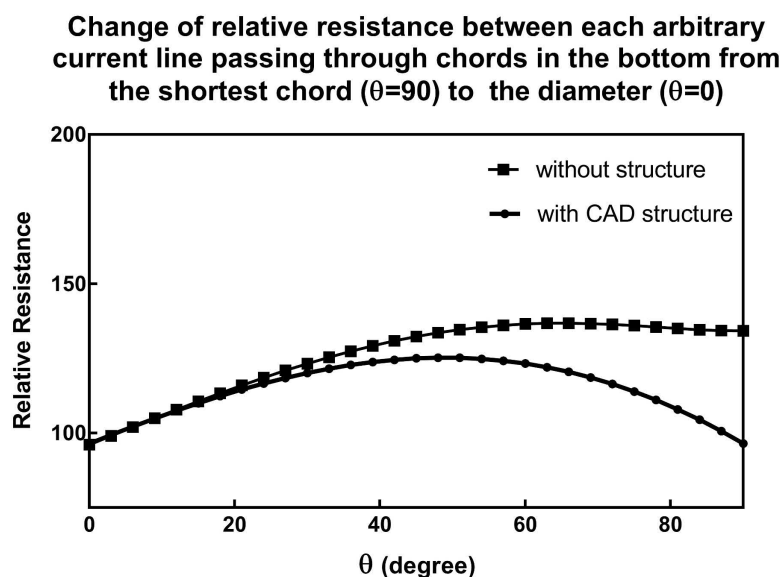


Figure B.5: The change of relative resistance between each arbitrary current line in the insert. The change of relative resistance between each arbitrary current line passing through each chord in the bottom chamber from the shortest chord to the diameter, by varying θ from 0° to 90° with or without the designed CAD structure. The CAD structure modulates the electrical resistances, so the EF becomes uniform.

mm, respectively.

The current density was set as the boundary condition at one circular hole (salt bridge connection), and a ground potential was set at the other circular hole until otherwise noted (Figure B.6). The electric field is numerically simulated for the plain polymeric insert (Figure B.6A), the smooth polymeric insert with the designed 3D structure (Figure B.6B), and the layered approximation ((Figure B.6C). The electric field strengths (EFSs) at the bottom of the cell culture chamber were analyzed to assess the EF uniformity at a height of $10\ \mu\text{m}$. The EFS data points at positions where the liquid column resides were excluded. The numerical simulation results were exported and analyzed in Prism 7 software (Graphpad, USA).

Numerical investigation of CAD structure's effect on electrical resistance modulation

I show side-by-side comparisons of simulated EF results for plain polymeric inserts, smooth 3D CAD inserts, and layered 3D CAD inserts (Figure B.7). In plain insert without the 3D designed structure, a large portion of the electrical current (red arrows) passes through the liquid column instead of through the bottom chamber where the cells are located (Figure B.7A). As a result, the EF stimulated on cells are lower ($75.03\ \text{V m}^{-1}$ and non-uniform (7.91% CV) (Figure B.7B). With the 3D designed structure, the current lines (in red arrows) are uniformly distributed in the bottom chamber (Figure B.7B), indicating that a uniform and directional EF is created ($95.1\ \text{V m}^{-1}$ with 1.22% CV) (Figure B.7E). The technical requirement to fabricate the paraboloid

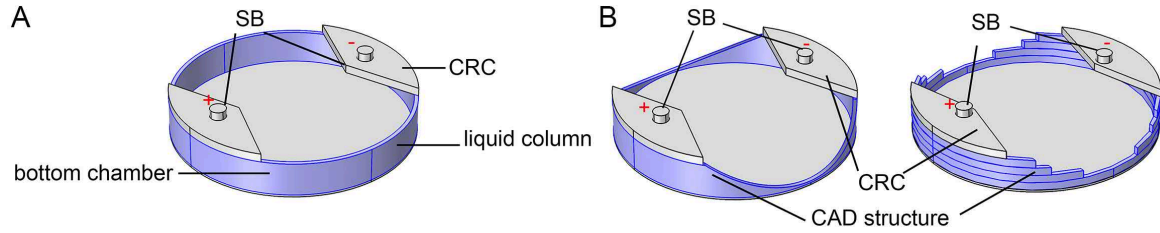


Figure B.6: CAD models of liquid in 3D inserts for numerical simulation. (A) A 3D model without any designed structure; (B) 3D models of liquid within an insert with designed CAD structure (left) and corresponding layered approximation (right). The liquid volume modified by CAD design is shown in blue. The current density was set as the boundary condition at one circular hole (salt bridge connection) and a ground potential was set at the other circular hole.

surfaces are high, however, a simple layered approximation method can be adopted to approximate the structure. By layered approximation, the established EF are slightly weaker than those created by a smooth 3D CAD insert but are reasonably uniform (89.06 V m^{-1} with 1.30% CV) (Figure B.7F). The simulated results of 3D CAD inserts designed for 0.26 mm-thick and 0.13 mm-thick bottom chambers are shown in Table B.1.

Table B.1: Numerical simulation of EF in a plain insert, smooth 3D CAD insert, and layered 3D CAD insert.

6-well	0.26 mm thick		0.13 mm thick	
	EFS	CV (%)	EFS	CV (%)
	(V m^{-1})		(V m^{-1})	
Plain	75.03 ± 5.94	7.91	74.0 ± 10.06	6.80
Smooth 3D CAD	95.10 ± 1.18	1.22	96.47 ± 1.38	1.43
Layered	89.06 ± 1.63	1.30	88.92 ± 1.69	1.90

Figure B.8 shows the uniform decrease in electric potential in the bottom chamber, suggesting a highly directional EF created by using the smooth 3D CAD insert as well as the layered 3D CAD insert. This indicates that inserts are suitable not only for cell stimulation but also for electrotaxis study where a uniform and directional electric field is required.

Numerical simulation results of devices for different sizes of cultureware

By adaption of the design principle described in section B.2, 3D CAD inserts for different sizes of cultureware can be designed. The numerical simulation results of 3D CAD devices for different sizes of cultureware are summarized in Table B.2. The coefficient of variation of the EFs in 3D CAD inserts of different sizes range from 1.22% to 1.75% demonstrates the broad applicability of this approach.

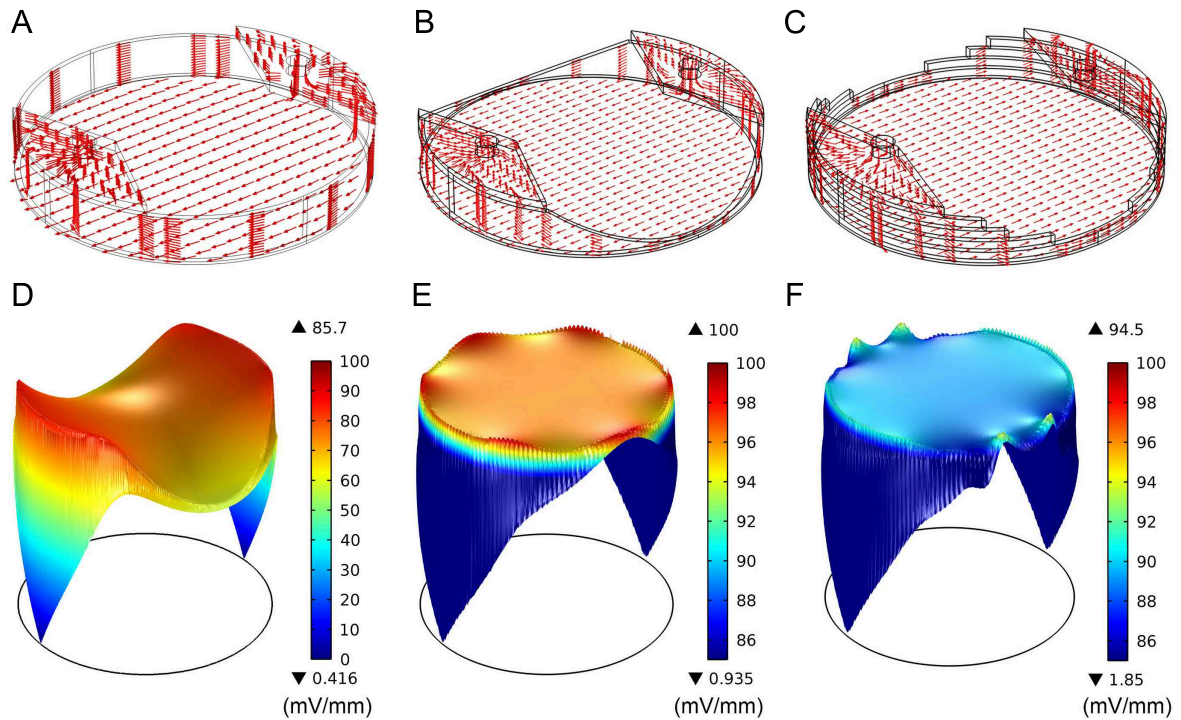


Figure B.7: Numerical simulation of EF in various designs (A) The current vector map in an insert without designed structure. A large portion of electrical current flows bypass the cells in the bottom chamber through the liquid column. The corresponding EF as shown in (D) is thus lower and non-uniform; (B) The current vector map in an insert with the designed CAD structure. The electrical resistances are modulated and passes through the cells in the bottom chamber. Thus a uniform EF is obtained as shown in (E); (C) The current vector map in the layered approximation of the designed CAD structure also shows electrical current can be delivered into the bottom chamber. The corresponding electric field is also uniform as shown in (F).

Figure B.9 shows the numerical simulation of uniform EF created in 3D CAD inserts made for 100 mm TCPS petri dish. In the smooth 3D CAD model, the mean EFS and the CV of the EFS are $97.44 \pm 1.47 \text{ V m}^{-1}$ and 1.51% in (B). The mean EFS and the CV of the EFS in the layered 3D CAD insert (D) are $94.73 \pm 1.59 \text{ V m}^{-1}$ and 1.67%. The layered insert is less ideal than the 3D CAD model due to its rough surfaces but it does not affect the uniformity of the created EF.

Effect of variation in bottom chamber thickness to EF uniformity

The double-sided tape used in this study is a pressure sensitive adhesive prone to deformation under pressure or stretching. Effect of slight deformation in the chamber thickness to the EF uniformity was examined by numerical simulations (Figure B.10). The CAD design was intended for a 0.26 mm thick chamber (the exact thickness of double-sided tape I used for fabrication). By varying the thickness of the bottom chamber thickness between 0.2 mm to 0.3 mm, the mean electric field strength (EFS) generated in the bottom chamber slightly changes, however, the EFS is still very close

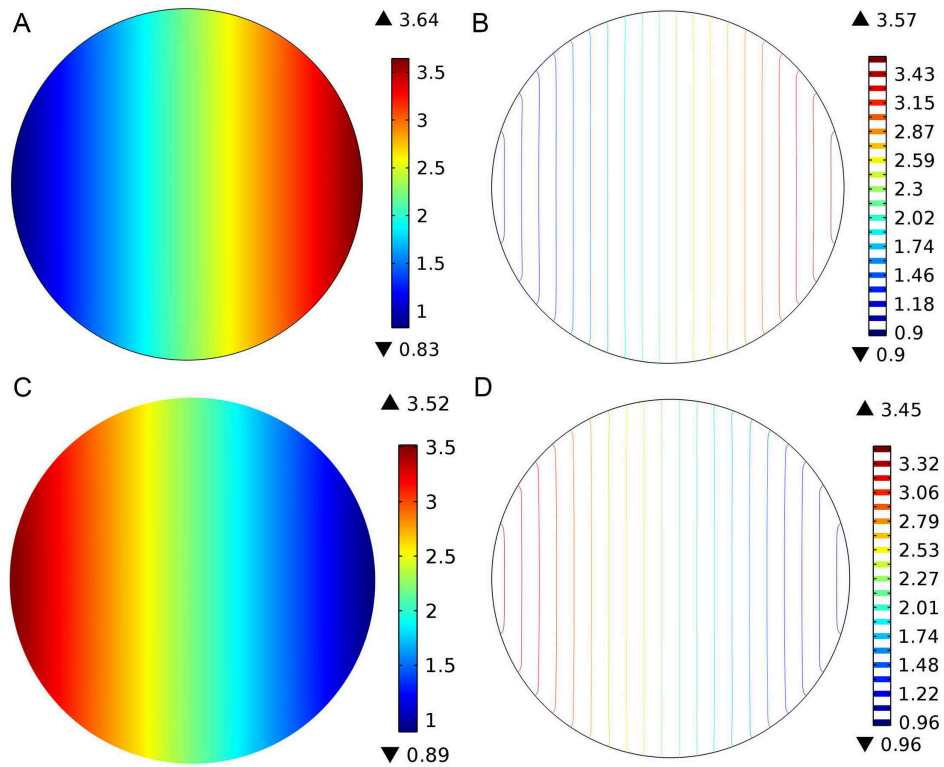


Figure B.8: The electric potential distribution in 3D CAD inserts. Electric potential distribution shown as (A) surface plot and (B) contour plot at the bottom of the insert with smooth 3D CAD structures. Electric potential distribution shown as (C) surface plot and (D) contour plot at the bottom of a 6-layered PMMA insert. Both inserts with smooth 3D CAD structures and the layered PMMA insert can create a uniform and directional EF. The directionality of the EF can be reversed by placing the high voltage to the opposite salt bridge as shown in (A) and (C). The uniform distribution of electric potential yields the uniform EF in the bottom chamber.

to the intended value of 100 V m^{-1} . The coefficient of variation of the EFS is the lowest in the intended 0.26 mm-thick chamber, but in all thicknesses examined, the CVs are below 3%. This demonstrated the robustness of the CAD design for creating a uniform EF.

B.3 Materials and methods

B.3.1 Device fabrication

Whole device fabrication by 3D printing

The designed structure contains two paraboloid surfaces so the fabrication is not easy. The first method I tried was by using fused deposition modeling (FDM) with Acrylonitrile butadiene styrene (ABS) (Dimension BST/SST 1200es, Stratasys, USA) and powder based fusion method (Zprinter 450, Z Corp, USA) (Figure B.11). However, neither method could generate a water proof device for testing and for cell culture

Table B.2: Specification and numerical simulation results of 3D CAD devices for different sizes of cultureware

Cultureware size	100 mm	6-well (35 mm)		12 well	24 well
Well diameter	86 (Corning [®]) 93.8(Eppendorf [®])	34.6 (Eppendorf [®])		21.1 (Volamo [®]) 22.4 (Eppendorf [®])	15.6 (Nunc [®]) 16.2 (Eppendorf [®])
Insert diameter	85	34	34	20	14
Culture area diameter (mm)	80	30	30	16	10
Culture area thickness (mm)	0.26	0.26	0.13	0.1	0.1
Height (mm)	8	3.9	4.5	3	2
$\frac{2br^2}{a^2}$	12.5675	4.713	4.713	3	1.875
Paraboloid X & Y	165	48	49	67.5	33
Paraboloid Z	50	13	13	50	20
Shell thickness (mm)	0.5	0.5	0.25	0.2	0.2
EF stimulation area (mm ²)	4901.7	660.5	683.5	191.1	72.4
Whole culture area (mm ²)	5674.5	940.2	940.3	391.1	208.9
EFS area percentage (%)	86.4	70.2	72.7	48.9	34.6
Mean EFS (V m ⁻¹)	97.44	96.1	96.5	95.73	94.8
Standard deviation	1.47	1.18	1.38	1.34	1.66
EFS CV (%)	1.51	1.22	1.48	1.40	1.75
Current (μ A) for 100 V m ⁻¹	3151.2	1181.7	590.85	242.4	151.5

experiments. The ABS device fabricated by FDM method appeared to be fused and water-tight, however, at high pumping pressure, solution would leak in between the fused layers. The powder-based fusion method used an adhesive to join powder layers patterned by the 3D printer. The joining of powder by the adhesive was also not strong enough to create a water-tight microdevice even after postprocessing.

PMMA 3D CAD insert fabrication and simple channel PMMA device fabrication

Due to the difficulties to fabricate the smooth 3D CAD insert (Figure B.7B) reliably, I fabricated functional prototypes using the 6-layer approximation model (Figure B.7C).

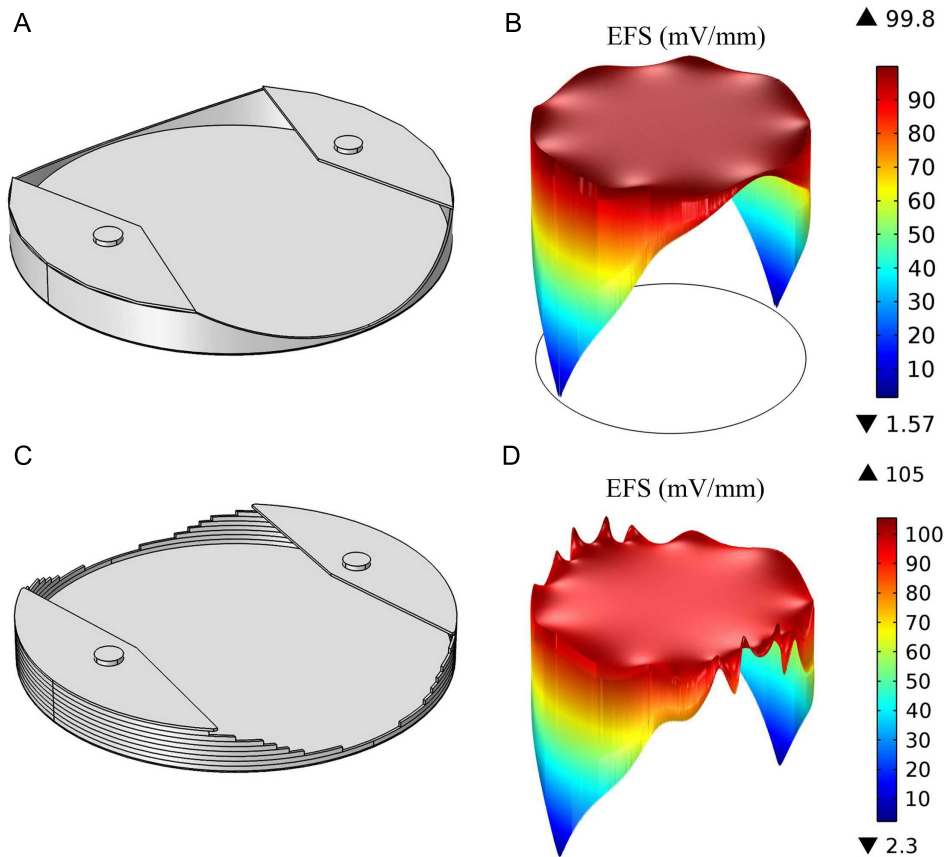


Figure B.9: Numerical simulations of a scaled-up 3D CAD insert for a 100 mm TCPS petri dish. (A) Smooth CAD model for the insert with paraboloid surfaces; (B) The uniform EF created in (A); (C) The 6-layered approximated 3D CAD insert; (D) The uniform EF created in (C).

The composition of the 3D CAD insert is shown in Figure B.12. The detailed fabrication procedure was previously reported^{334,454}.

Briefly, patterns for each layer were designed in AutoCAD software (Autodesk, USA). A 1 mm thick PMMA substrate (Comoglas, Kuraray, Japan) was cut based on the patterns by using a CO₂ laser cutter (VLS2.30, Universal Laser Systems, USA). The layers were aligned and joined by thermal bonding (Figure B.13A). Adapters for fitting connection were super-glued onto the inserts (406 Prism Instant Adhesive, Loctite, USA). The double-sided tape for the insert was then affixed to the insert bottom (0.26 mm-thick, F9473PC, 3M, USA). The assembled device is shown in Figure B.13B.

The fabrication process of the simple rectangular channel chip followed the same procedure as those for the circular insert (Figure B.14).

PDMS device by molding

With the assistance from OIST machine shop, a stainless steel mold set was fabricated using computer numerical control (CNC) milling (Figure B.15A & B). I casted and cured PDMS (10:1 ratio, Sylgard 184, Dow Corning, USA) inside the mold. Because the mold was not fine-polished, the surface roughness caused the final device being

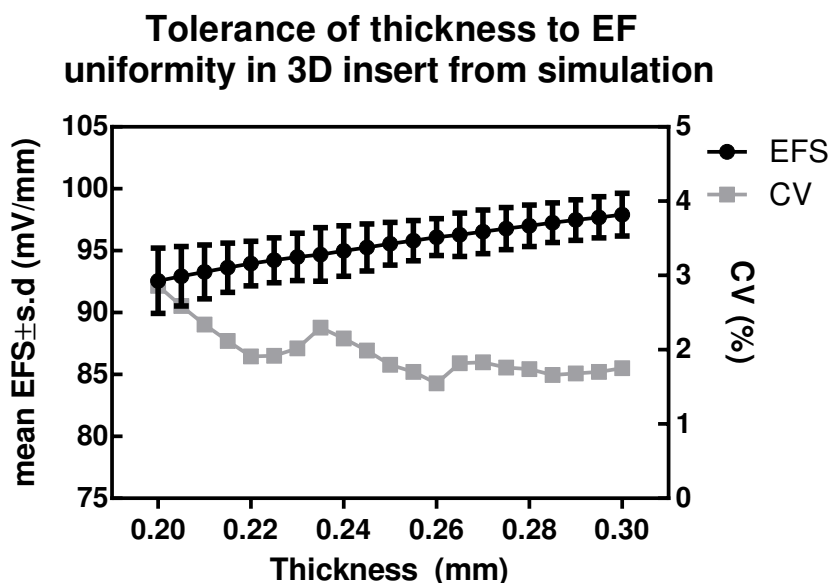


Figure B.10: Effect of chamber thickness on EF uniformity by numerical simulation. By varying the thickness of the bottom chamber thickness between 0.2 mm to 0.3 mm, the resistance decreases and the mean EFS slightly increases (dark circles). But the simulated mean EFSs in the chamber with this thickness range are very close to the intended value of 100 V m^{-1} . The coefficient of variation (CV) describing the non-uniformity in the EFS is the lowest in the intended 0.26 mm-thick chamber. Nevertheless the CVs in all thicknesses examined are below 3%, verifying the robustness of the CAD design for creating a uniform EF.



Figure B.11: Prototyping inserts by 3D printing. (Left) The ABS prototype made by FDM method; (Right) A prototype made by powder fusion method.

hazy (Figure B.15C). However, the 3D CAD structure was correctly molded in the final device visualized by food dye in water. There is a possibility that deformation of PDMS could disrupt the fluidics in the fabricated device. Based on these results, fabrication using PDMS is proven viable but a more rigid solution may still be preferred to ensure that the 3D CAD structure does not deform.

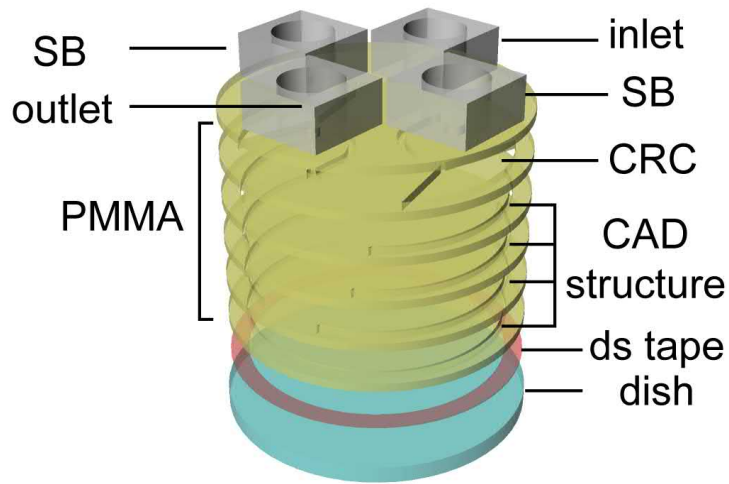


Figure B.12: Schematics of the layered insert. PMMA top assembly containing current rectifying chambers (CRC) and 3D CAD structures are affixed to the cell culture dish through a piece of double-sided tape (ds tape) to form the assembled microfluidic chip. Salt bridge is abbreviated as SB.

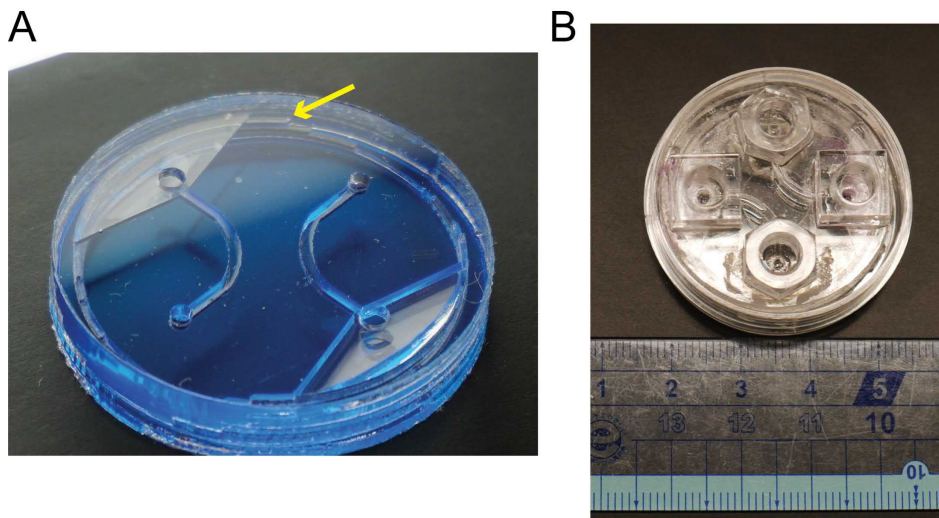


Figure B.13: Photoimages of fabricated layered PMMA 3D CAD insert. (A) A layered PMMA insert thermally bonded. Yellow arrow indicates the layered 3D structures embedded in the insert; (B) A layered PMMA insert affixed to a 35 mm dish.

Metal-PMMA composite 3D CAD insert

Besides the difficulty to fabricate the paraboloid surfaces, the structures are also small (0.5 mm or 0.25 mm-wide), thus fabrication requires extreme precision. One approach to ensure an economical manufacturing of such structure is to split the 3D CAD insert

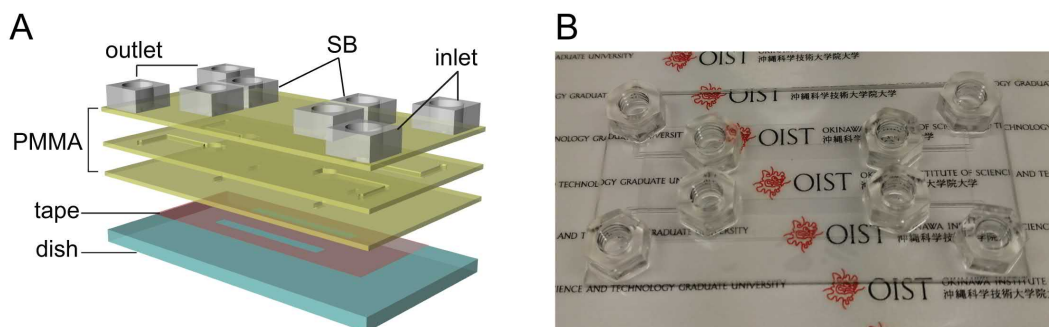


Figure B.14: Schematics of a PMMA microfluidic chip containing two simple rectangular channels. (A) Three-layer patterned PMMA pieces are thermally bonded. The PMMA piece affixes to the dish by a double-sided tape. Adapters for inlets, outlets, and salt bridges (SB) are glued on; (B) A photoimage of the final assembled device.

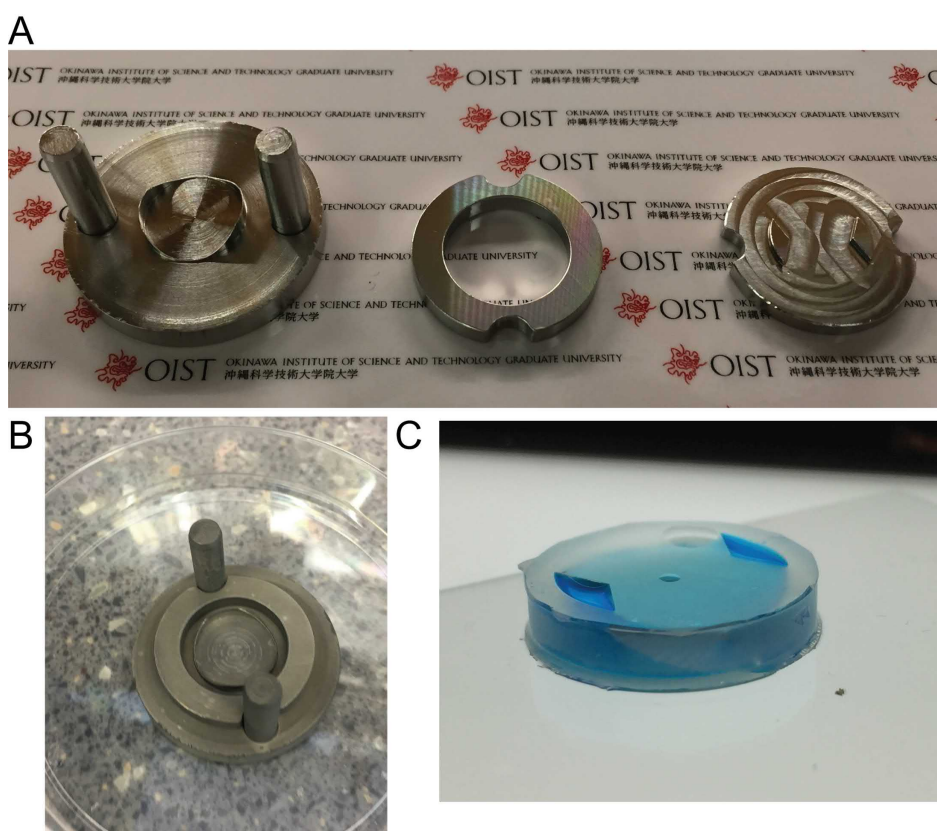


Figure B.15: Fabrication of 3D insert by casting PDMS on a CNC machined mold. (A) The CNC milled stainless steel mold on the left with spacing ring in the middle and top lid on the right with current rectifying chambers; (B) The assembled and silanized mold before casting the PDMS and closing the top lid; (C) The casted PDMS device filled with water with blue dye to visualize the CAD structure in the insert.

in two pieces with one of which containing the paraboloid structures (Figure B.16). The two structures could be manufactured with high precision using microinjection molding and joined afterwards to form a solid assembly.



Figure B.16: Two-piece assembly approach. An outer ring with paraboloid structures and an inner cylinder that can be precisely mate with the outer ring.

I used a selective laser sintering (SLS) 3D printer to fabricate a titanium-based outer ring (EOSINT M280, EOS GmbH, Germany) outsourced to DMM.Make (Japan). The technique uses ultrafast fiber laser to sinter patterns on a metal powder bed and the final workpiece is generated from sintering layers of patterns. A plain ring (left) or an outer ring with 0.5 mm-wide paraboloid structures (right) can be fabricated (Figure B.17A). A PMMA inner cylinder with paraboloid structures or a PMMA inner cylinders were fabricated by CNC micromilling from 10 mm-thick PMMA blocks (Misumi, Japan) using 1.5 mm-diameter flat endmill (RSE-230, NS Tools, Japan) on a CNC micromill (SLS Micro Mill/GX, Minitech, USA). The CAM tool path was generated in Fusion 360 software (Autodesk, USA). The metal ring and the inner PMMA piece were assembled afterwards (Figure B.17B).

By this approach, I confirmed that the two-piece assembly is feasible for economical fabrication of fine structures in 3D CAD inserts. The SLS fabricated titanium parts although were reasonable priced, they may not be practical for commercial deployment.

Reversible o-ring sealing 3D CAD insert fabricated in PMMA

An improved device was further developed using PMMA. A PMMA cylinder with paraboloid structures, outer ring with a O-ring sealing slot, and a top current rectifying chamber piece with O-ring sealing slots were fabricated on a CNC micromill (SLS Micro Mill/GX, Minitech, USA) (Figure B.18A). The CAM toolpaths were generated in Fusion 360 software (Autodesk, USA). I fabricated the inner cylinder to be slightly bigger than the outer ring by 100 μm . The device could be assembled by briefly placing the outer ring in a 60 $^{\circ}\text{C}$ oven to expand and quickly assemble with the inner piece before cooling down. The assembled device was tight and difficult to disassemble. Thereafter, the assembled device was reversibly sealed to a 10 cm-diameter glass wafer

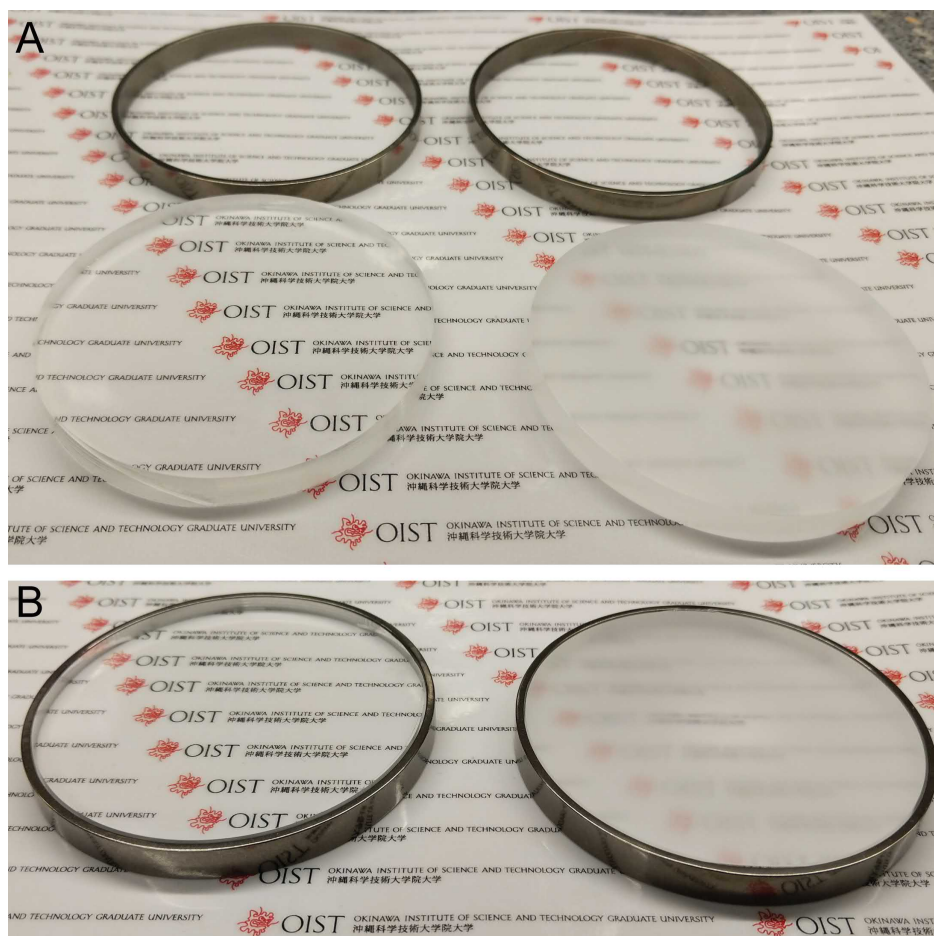


Figure B.17: Two-piece assembly of metal-PMMA 3D CAD insert (A) A plain titanium ring and its corresponding PMMA workpiece with paraboloid structure on the left; A titanium ring with paraboloid structures fabricated directly from selective laser sintering of titanium powder and a lathe-fabricated PMMA cylinder; (B) The tight assembly of the metal-PMMA 3D CAD inserts from A.

by mechanical sealing when compressive force was applied on O-rings (Figure B.18B). The approach was more operator-friendly for biologists.

Summary: microdevices for cultureware across broad range of sizes

In summary, I developed several approaches to fabricate the 3D CAD inserts with small paraboloid structures. These approaches aimed at economical fabrication of devices with the potential to transfer to the industry at high manufacturing volume instead of restricted to laboratory settings.

The design principle described in section B.2 can be used to fabricate small (16 mm-diameter) to large (100 mm-diameter) devices to accommodate a broad range of cell cultureware.

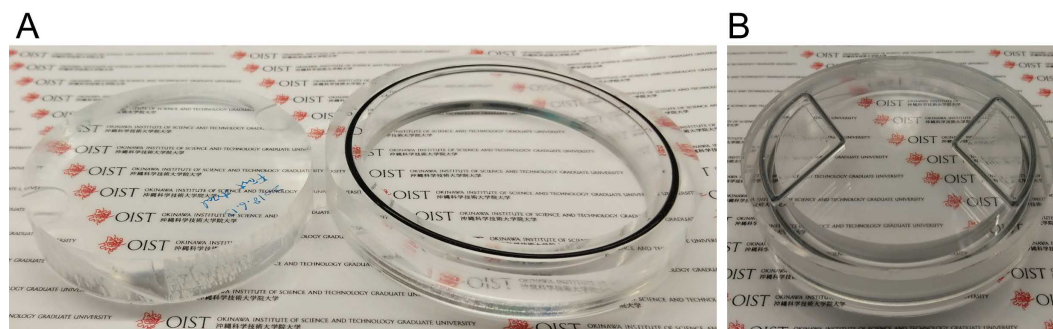


Figure B.18: Reversible sealing 3D CAD PMMA insert. (A) A PMMA cylinder with paraboloid structures (left) joins the outer ring with a o-ring slot (right); (B) The assembled device showing the 100 mm 3D CAD insert assembled to a 100 mm glass.

B.3.2 Cell culture and maintenance

A Swiss murine embryonic fibroblast cell line with 3-day transfer protocol, NIH/3T3 (American Type Culture Collection, ATCC, USA), was used in this study to demonstrate the electrical stimulation functionality with the polymeric circular insert and the rectangular microchannel. The cells were cultured on TCPS dishes in Dulbecco's minimum essential medium (DMEM, 12800017, Gibco, USA) supplemented with 10% fetal bovine serum (FBS, Sigma-Aldrich, USA) at 37 °C in a 95% relative humidity atmosphere supplemented with 5% CO₂. The cells were sub-cultured twice a week by the recommended split ratio with trypsin-EDTA (Life Technologies, USA). For long term storage, the cells supplemented with 10% dimethylsulfoxide (DMSO) were cryopreserved in liquid nitrogen.

B.3.3 EF measurement setup

To measure the EF in the bottom chamber in the insert, an array of holes in 0.3 mm diameter was drilled on a 1 mm-thick PMMA substrate^{198,574}. The spacing between each hole was 3 mm. The holes were temporarily sealed with a Kapton tape. The insert was filled with DMEM. A 46 V electric potential was applied through Ag/AgCl electrodes (25 mm × 100 mm) by a DC power supply (E3641A, Keysight technologies, USA). Preparation of Ag/AgCl electrodes was described elsewhere¹⁹⁶. To measure the voltage differences, two Ag/AgCl based electrodes (0.3 mm in diameter) were inserted into two adjacent holes after piercing the tape cover (Figure B.19)^{196,202}. The voltage differences between any two electrodes in the chamber were measured by a digital multimeter (2100, Keithley Instruments, USA) for 20 samples at every position by using the Excel add-in function provided by the manufacturer (KI-LINK, Keithley Instruments, USA). The EFSs can then be calculated by dividing the voltage differences by the distance between respective electrodes. The results of mean EFSs and standard deviations are calculated and exported using a custom MATLAB script (Mathworks, USA).

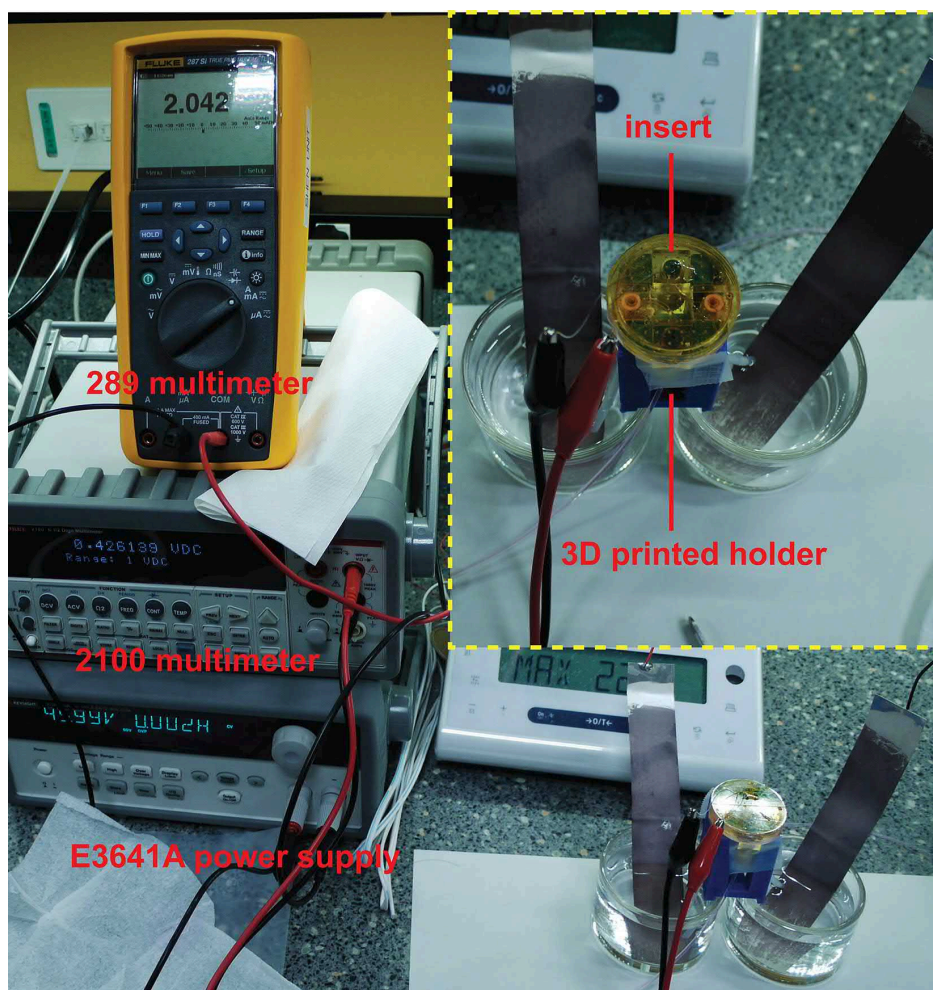


Figure B.19: A photo snapshot of the EF measurement setup. The inset shows a magnified image of a PMMA layered 3D CAD insert on a custom 3D printed holder for EF measurement.

B.3.4 Microfluidic chip assembly, EF stimulation and microscopy analysis

Each six-layered PMMA insert was disinfected and then affixed to individual wells in a 6-well TCPS plate or to a 35 mm TCPS dish (Figure B.12). Similar procedure was applied to the simple rectangular channel chip. To avoid entrapment of bubbles, which could disrupt EF uniformity and cause cell death, assembled microfluidic chips were primed by CO₂ gas, and filled with phosphate buffered saline (PBS, Life Technologies, USA) as shown in Figure B.20A. Alternatively, the inserts can be affixed to the well bottom with the presence of PBS as shown in Figure B.20B to further reduce bubble entrapment because the double-sided tape has a limited adhesiveness in protein-free buffer solution.

To start the cell experiment, PBS pre-filled chamber was first replaced by serum-containing cell culture medium, and a suspension of 5×10^5 cells was subsequently loaded into the chamber through the salt bridge ports by gravity feeding. After

overnight culture for cell adhesion and growth, fittings to supply culture medium and for salt bridges (containing 1.2% agarose (LE agarose, Lonza, USA) in PBS) were connected to the top of the inserts. A syringe pump (YSP-202, YMC, Japan) was used to exchange cell culture medium during the time lapse experiment at a flow rate of $100 \mu\text{L h}^{-1}$ for the circular insert and $20 \mu\text{L h}^{-1}$ for the rectangular channels to obtain similar shear stress acting on the cells. A DC voltage and the current was applied and measured by a high voltage source meter unit (2410, Keithley Instruments, USA) through Ag/AgCl electrodes in PBS. The required current for a 300 V m^{-1} EF in a chamber of 30 mm in diameter and 0.26 mm in thickness was 3.545 mA. The EF stimulation setup diagram and a snapshot of the 6-well plate is shown in Figure B.21 and Figure B.22.

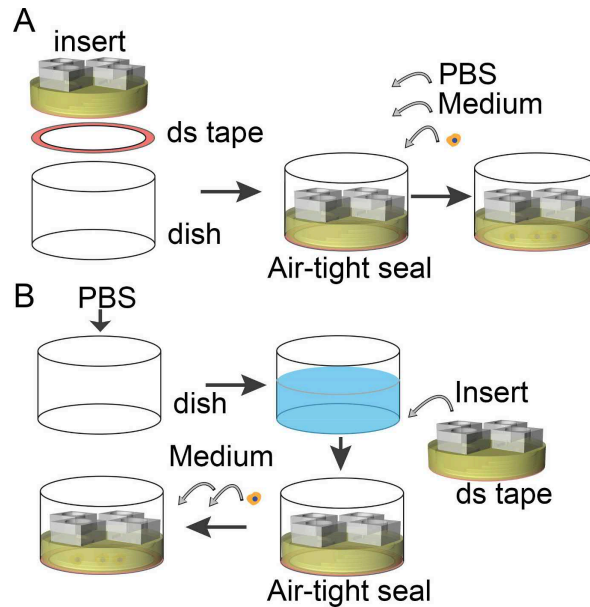


Figure B.20: The workflow of the cell experiment by using the polymeric insert. (A) The insert is affixed to the dish first, PBS, cell culture medium, and cell suspension are infused into the microfluidic chip sequentially; (B) To further avoid bubble entrapment, the insert can be affixed to the dish in PBS. Thereafter the buffer is replaced by cell culture medium and cell suspension is then seeded.

The time lapse electrotaxis experiments on simple channel chips were carried out on an automated microscope (Ti-E, Nikon, Japan) (Figure B.23). The phase contrast cell images were taken at different positions across the devices at an interval of 5 minutes. The morphology and centroid of cells were tracked manually for the duration of 5 hour time lapse using ImageJ analysis software package.

To quantify the cell migration and alignment, two parameters (directedness and orientation) are used with the following definition (Figure B.24).

- The directedness of cell electrotaxis is defined as the average of $\cos \Phi = \sum_{i=1}^N \frac{\cos \Phi_i}{N}$, where Φ_i is the angle between the Euclidean vector of each cell migration and the vector of applied EF (from anode to cathode), and N is the total number of

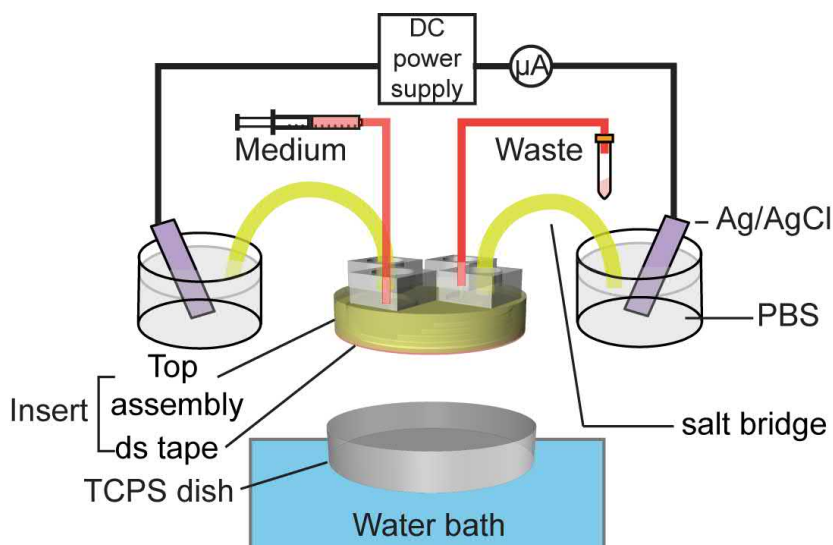


Figure B.21: The schematic diagram of electrical stimulation setup.

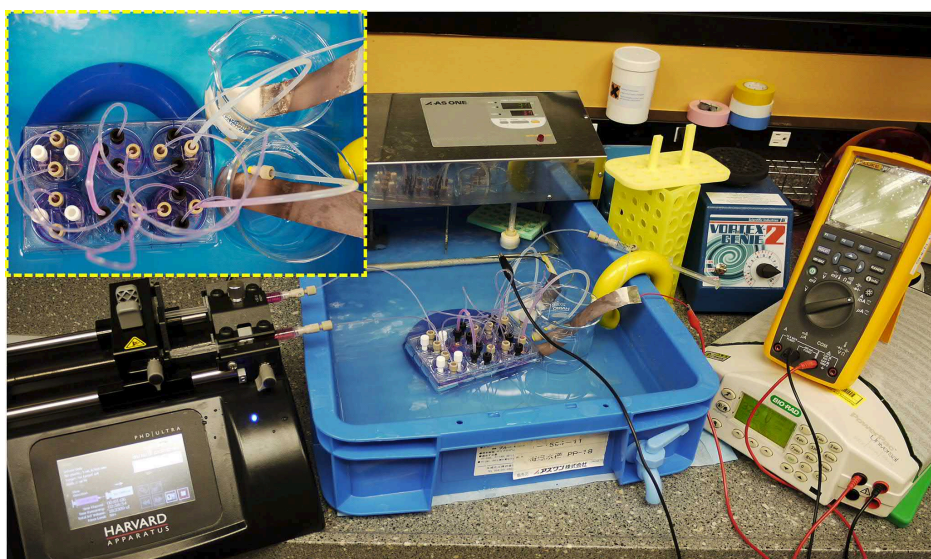


Figure B.22: A photo snapshot showing the setup of EF stimulation of cells on a 6-well microplate in a temperature-controlled water bath. Fresh cell culture medium was infused by a syringe pump. The DC electric potential bias to create an EF was applied by a BioRad DC power supply.

analyzed cells (Figure B.24). A group of anodal moving cells holds a directedness of -1; and a group of cathodal moving cells holds a directedness of +1. For a group of randomly migrating cells, the directedness is zero.

- The orientation is defined as the average of $\cos 2\theta = \frac{\sum_{i=1}^N \cos 2\theta_i}{N}$, where θ_i is the angle between the vector of applied EF and the long axis of a given cell; N is the total number of cells analyzed. A group of cells aligned perpendicular to the EF holds an orientation of -1; and a group of cells aligned in parallel to the applied

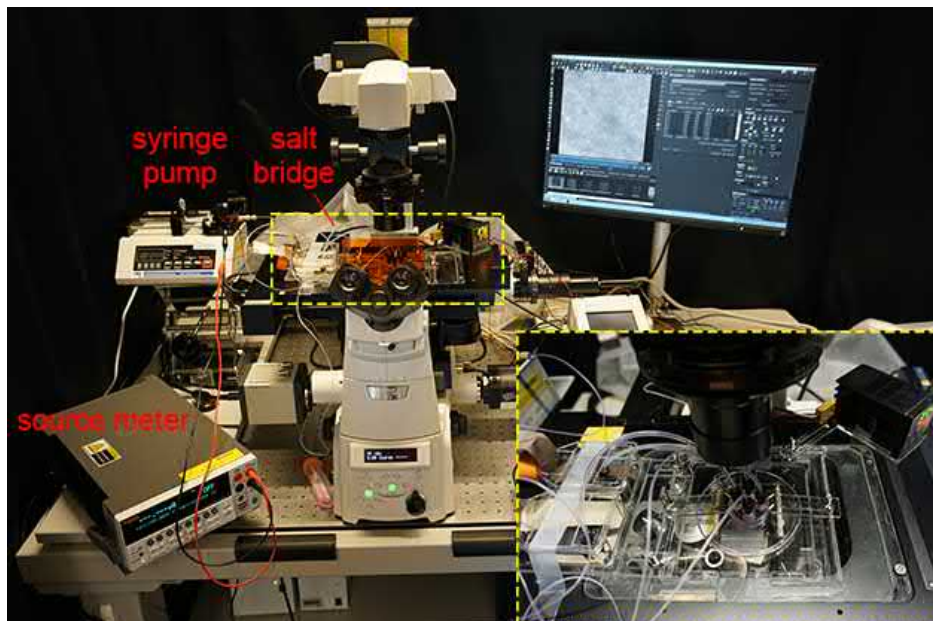


Figure B.23: A photo snapshot showing the microscopy setup for the time lapse cell electrotaxis experiment. The device was placed on top of a transparent heater on the microscope stage to provide temperature control for cell survival. Continuous culture medium was pumped through a syringe pump. The direct current for electrical stimulation was applied and monitored through a source meter. The inset shows how the devices were fixed on the microscope stage.

EF holds an orientation of $+1$. For a group of randomly shaped cells, the average orientation is zero.

All data are represented as the mean \pm 95% confidence interval, which is 1.96 of standard error of mean, from triplicate experiments. Kruskal-Wallis one-way analysis of variance on ranks tests with Dunn's multiple comparison post-hoc tests were performed when non-Gaussian distribution of sample data was indicated from Bartlett's test. The confidence level to reject a null hypothesis between two data sets was set at 95%. A p-value (the probability for a true null hypothesis) less than 0.05 represents a statistical significance at 95% confidence.

B.4 Results and discussion

B.4.1 Validation of EF uniformity in the chamber

Figure B.25 shows the experimentally measured EFS in the bottom chamber by the Ag/AgCl wire electrodes. The EFSs were measured between adjacent holes parallel to the electric current vector. The mean EFS of all measurement is $141.4 \pm 1.3 \text{ V m}^{-1}$ with a CV of 0.92%, suggesting that a highly uniform EF is created in the bottom chamber. The 46 V electric potential created an expected 150 V m^{-1} EFS in the bottom chamber. The measured mean EFS is about 94.3% of the expected value, which coincides with the measurement errors reported in previous studies^{196,258}. The CV of

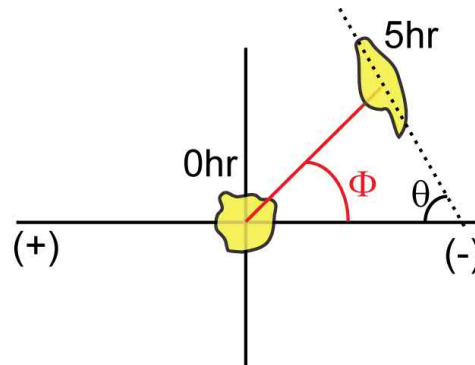


Figure B.24: Schematic representation of the angle to calculate cell migration directedness and orientation.

the measured EFSs is comparable to the 1.30% value expected from numerical simulation (see Table B.1). This value is also comparable to the 2.3% CV of measured EFS from the largest rectangular electrical stimulation device reported previously¹⁹⁶. Finally, the EFSs along the perpendicular direction to the electric current vector is measured to be $4.68 \pm 1.90 \text{ V m}^{-1}$, only 3% of that in the parallel direction, confirming that the EF is highly directional.

Measured EFS distribution in the microdevice bottom

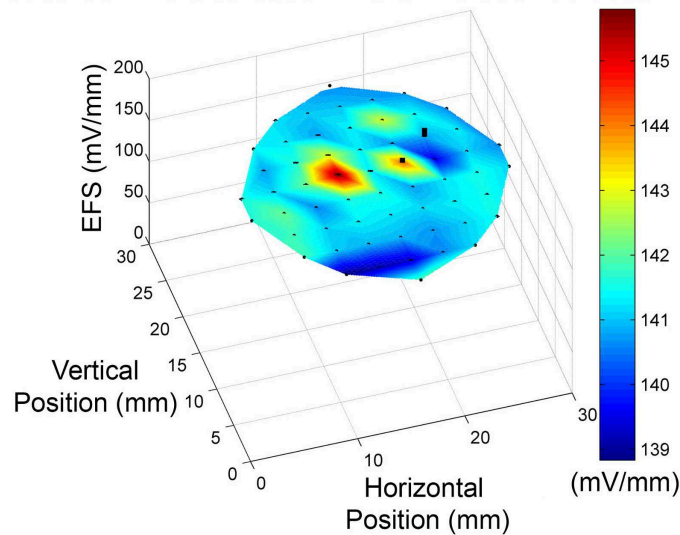


Figure B.25: The measured EFS in a layered 3D CAD insert is shown as the mesh plot and the standard deviations are shown in black error bars.

B.4.2 High performance and high stimulation area percentage cell EF stimulation

While conventional *in vitro* electrical stimulation devices either sacrifice the culture area to stimulate cells uniformly, or stimulate large areas of cells with non-uniform EF, the polymeric circular insert utilized in this study can provide uniform EF stimulation

to large area percentage of cells.

The effective stimulation area is defined as the area of the bottom chamber subtracting the area of where the liquid column resides. The effective stimulation area percentage is the ratio of the effective stimulation area over the total surface area of the TCPS dish. The effective stimulation area percentages using the polymeric insert are listed in comparison to those reported in existing literature, see Table B.3. Most existing devices cannot achieve uniform EF stimulation in more than 50% of the total cell culture area. Our polymeric inserts can provide uniform EF stimulation in more than 69% of the total area in a 6-well plate (or a 35 mm dish), and up to 87.5% in a 100 mm petri dish. Thus the cell yields are higher by using polymeric inserts for electrical stimulation. The higher cell yields will greatly benefit subsequent biochemical and molecular biology analysis.

Table B.3: Stimulation area and effective stimulation area percentage of *in vitro* EF stimulation device

Report	Substrate	Thickness (mm)	Stimulation area (cm ²)	Total area (cm ²)	Effective stimulation area percentage (%)
Song <i>et al.</i> ²⁶⁶	100 mm TCPS	0.13-0.16	2.2	55	4.0
Song <i>et al.</i> ²⁶⁶	100 mm TCPS	0.13-0.16	22	55	36.0
Tandon <i>et al.</i> ⁷⁰⁷	60 mm Glass	0.25	6.5	21	30.9
Babona-Pilipos <i>et al.</i> ²⁹⁷	60 mm TCPS	0.17	2.2	21	10.5
Huang <i>et al.</i> ²⁵⁸	150 mm TCPS	0.07	19.2	152	12.6
Tsai <i>et al.</i> ¹⁹⁶	150 mm TCPS	0.6	69	152	45.4
This work	6-well TCPS; 35 mm TCPS	0.26	6.61	9.4	70.2
	6-well TCPS; 35 mm TCPS	0.13	6.83	9.4	72.7
	100 mm TCPS	0.26	49	56.7	86.4
	100 mm TCPS	0.13	49.6	56.7	87.5

B.4.3 Cell migration and alignment under uniform EF stimulation

NIH/3T3 fibroblast cells were used to verify the performance of the inserts because they are known to align perpendicular to the EF vector after stimulation and they have shown cathodal electrotaxis^{229,708,709}. The phase contrast microscopy images of the cells under 300 V m⁻¹ EF stimulation over 5 hours were taken and analyzed in Figure B.26.

The directedness and orientation of the cells with and without EF stimulation are shown in Figure B.27. NIH/3T3 cells demonstrate strong cathodal electrotaxis under 300 V m⁻¹ EF for 5 hours in both rectangular microfluidic chips and in circular inserts

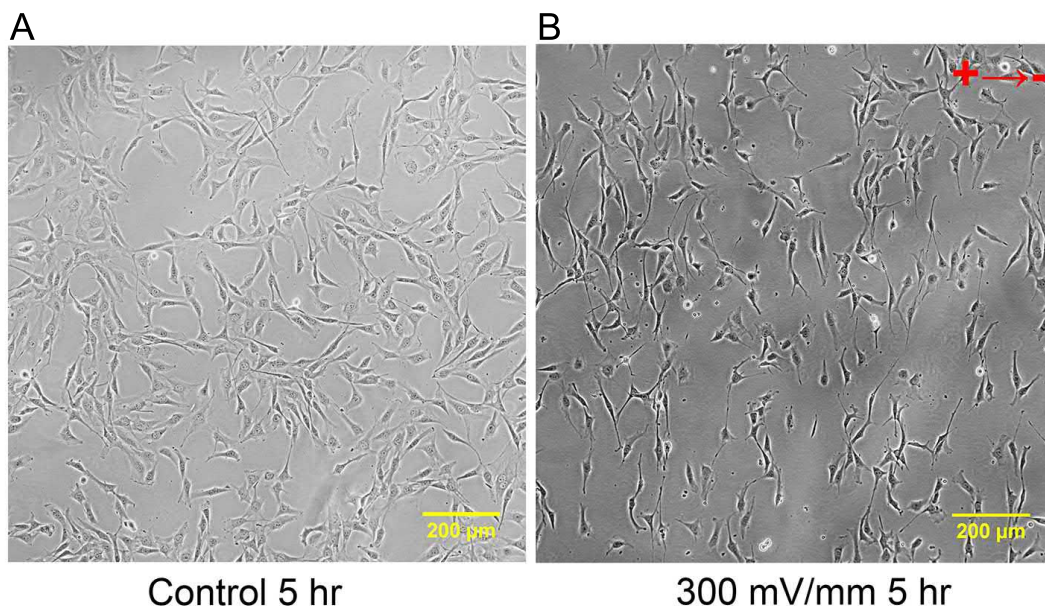


Figure B.26: The phase contrast microscopy of NIH/3T3 cells after 5 hours of experiment with the circular 3D CAD insert. (A) NIH/3T3 cells without EF stimulation; (B) NIH/3T3 cells with 300 V m^{-1} EF stimulation.

($P < 0.0001$, in comparison to their respective controls without EF stimulation) (Figure B.27A). While the directedness of NIH/3T3 cells in the polymer insert is slightly lower than that in the rectangular channels (0.78 ± 0.02 v.s. 0.87 ± 0.01), there was no statistical significance between the two ($P > 0.05$). This deviation is possibly caused by un-optimized cell culture medium flow rate. While the shear stress in the polymer insert device and the rectangular channel is of the same order, the medium replenishment takes longer for the circular insert due to its bigger cross-sectional area.

Before EF stimulation, cells in both rectangular channels and circular inserts demonstrated random orientation (0.05 to 0.09). After 300 V m^{-1} EF stimulation, the orientation of cells in rectangular channels and circular insert decreased to -0.60 ± 0.05 and -0.49 ± 0.06 , indicating perpendicular alignment (Figure B.27B). The difference of cell alignment in rectangular channels and circular inserts are significant before and after the stimulation ($P < 0.0001$). The control cells in both rectangular channels and the circular inserts do not show any alignment. These results validated the performance of the inserts for electrotaxis experiments comparable to the performance of a rectangular channel. However, the circular inserts have at least two-fold higher effective stimulation percentage in comparison to that of rectangular channels, thus more cell yield can be achieved by using circular 3D CAD inserts.

B.5 Summary and prospects

Establishment of a uniform EF in a circular-shaped microdevice is extremely difficult so the majority of existing EF stimulation devices avoided this issue by using a simple rectangular shaped chamber. The rectangular configuration requires modification to fit

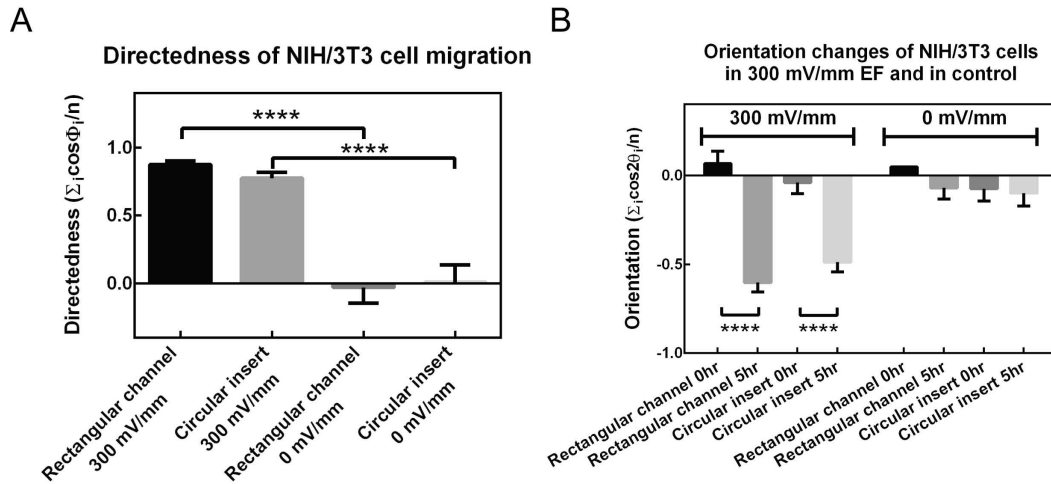


Figure B.27: Quantification of the cell electrotaxis and electro-alignment measurements. (A) Directedness of cell migration in a rectangular channel and a layered 3D CAD insert with and without EF stimulation; (B) Cell orientation in a rectangular channel and a layered 3D CAD insert with and without EF stimulation. Four asterisks indicate $P < .0001$ from Dunn’s post-hoc test.

with the commercial labware, and only a small portion of the cell culture dish is used for cell culture, thus limiting the cell yield. By using a 3D CAD insert in a circular shaped cell culture chamber, we have demonstrated that a uniform EF can be created in a circular-shaped area by modulating the electrical resistance across the device. I highlight the key contributions and outlooks below.

- The effective stimulation area percentage using the insert is at least 2 fold higher than that of existing EF stimulation devices. The yield of cells and its products can be increased for further molecular and biochemical analysis.
- The same CAD design principle can be easily scaled up or down to tailor design inserts for different sized TCPS dishes. Mass production of the polymeric insert can be achieved by CNC fabrication, injection molding, or other similar technology. The polymeric insert is useful for adapting electrical stimulation studies in a common laboratory due to the high effective stimulation area percentage and the ease of use.
- The polymeric insert is applicable for various studies. For tissue engineering, EF stimulation has been reported to induce synchronously contracting cardiac tissue^{707,710–713}. Osteoblastic differentiation from mesenchymal stem cells can be promoted under EF stimulation⁷¹⁴. Uniform EF stimulation to circular shaped area could also be useful to stimulate an entire brain slice or tissue slice.
- For future improvement, the workflow can be simplified to bring convenience of using the device to biologists.

Appendix C

Characterization of common thermoplastics for microfluidics

C.1 Introduction

Sourcing and adaptation of stable materials for microfluidic prototyping are important for quality assurance of microfluidic product both in the laboratory and in commercial application. However, the exact materials adapted in commercial products are often considered as commercial secrets and not revealed, restricting research and development of new methods to extensive trial and error processes.

New cell culture substrates products such as μ Dish[®] (Ibidi GmbH, Germany) and Lumox[®] (25 μ m TPX film, Sarstedt GmbH, Germany), have low autofluorescence, and high gas permeability that are appropriate for culturing sensitive cells such as neurons. Adaptation of the same substrate in microfluidic chip is required to generate consensus data compared to that collected on these commercial products.

Fourier-transform infrared (FTIR) spectrometry is an absorbance optical technique that can be used to fingerprint the molecular bonding of the tested material⁷¹⁵. The C-H bond stretching and bending in an organic material generates large absorbance in infrared spectra. The chemical bonds absorb infrared energy and vibrate. The absorbance spectra will also differ depending on other properties such as dipole moment, making the FTIR spectra unique for different chemicals and mixtures.

C.2 Samples and measurement

A Bruker VERTEX 80v FTIR spectrometer was used to measure the IR spectrum of several commercially available thermoplastic substrates in order to identify the high gas permeable substrate used in similar commercial products.

The samples measured include, PDMS, 0.5 mm-thick PMMA (CM205x, Chi-Mei Corp, Taiwan), μ Dish (μ Treat, Ibidi GmbH, Germany), Lumox (Sarstedt GmbH, Germany), cyclic olefin copolymers (COC) such as 5013C & 5014DP (Mitsui Chemicals Co, Japan) and 8007s (TOPAS Advanced Polymers GmbH, Germany), cyclic olefin polymers (COP) substrate (480R, ZEON, Japan), and COP films (100 μ m, ZF14 & ZF16, ZEONOR, ZEON, Japan).

The samples were cut and fixed on a holder in the optical path and measured in transmittance mode with reference of air. MIR source with KBr beam splitter and RT-DLaTGS infrared detector were used. 16 scans at resolution of 4 cm^{-1} between $400\text{--}4000\text{ cm}^{-1}$ wave number were taken and averaged. The spectra were analyzed with QPUS software (Bruker, USA).

C.3 Results

The measured FTIR spectra of each materials is shown in Figure C.1. The spectra suggested that the gas permeable materials used in μ Dish is similar to the COP films from Zeon. Use of COP film in microfluidic prototyping is suitable to build heterogenous high-gas permeability microfluidic chips for sensitive cells.

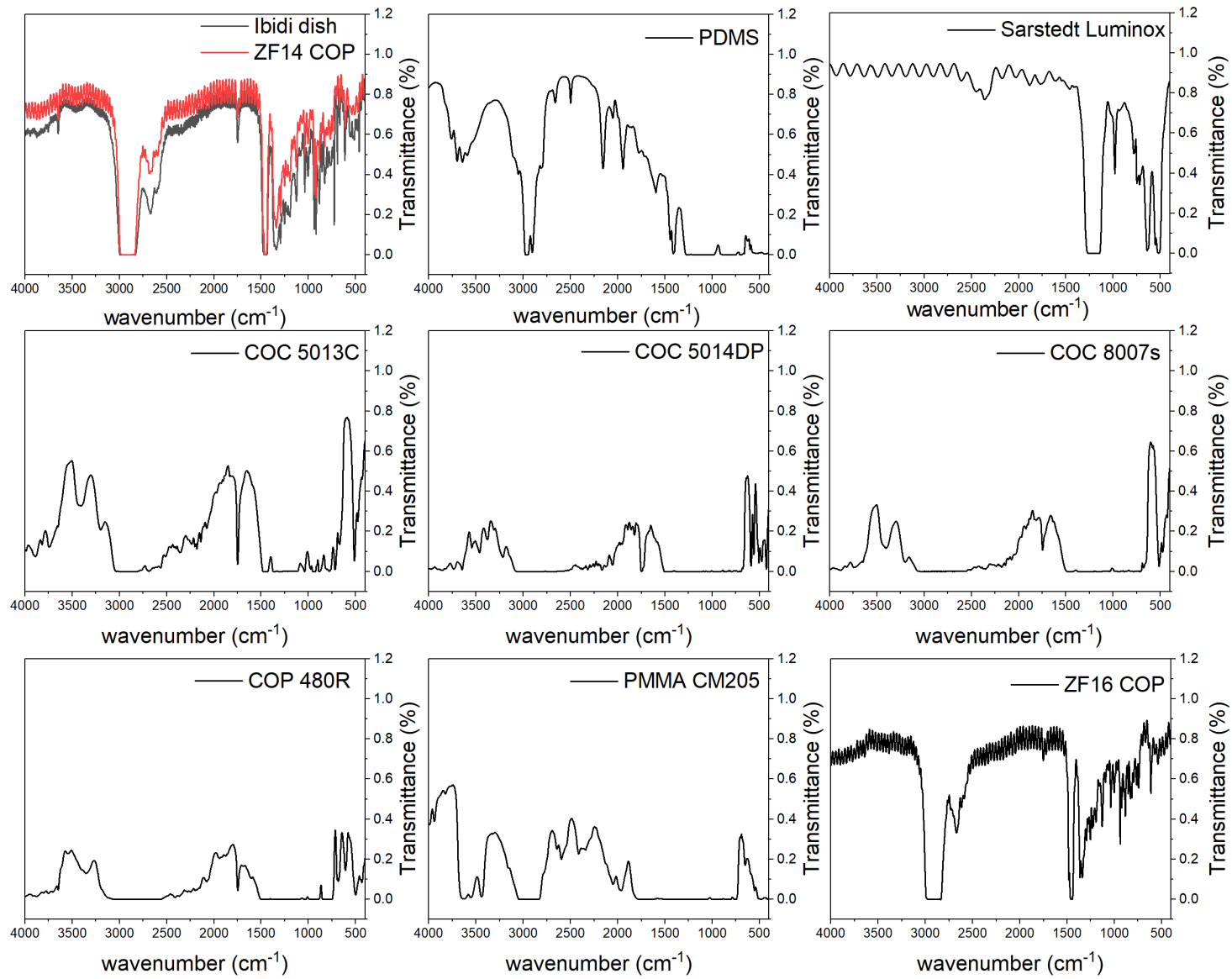


Figure C.1: Fourier-transform infrared spectra of various materials.

Appendix D

List of open-source models for laboratory applications

This chapter lists the 3D model designs that were used during the course of this thesis for various research and developments. The design schematics and 3D printable models can be find here released under

1. 3D printed Nikon Ti-E custom stage

The 3D printed custom stage can mount on a Nikon Ti-E microscope XY motorized stage with a transparent heater. The model was printed using a Connex3 Objet 500 inkjet-based 3D printer (Stratasys, USA) with Veroblack resin. For connection with ITO glass transparent heater, pogo pins were mounted on holes tapped with M2.5 threads.

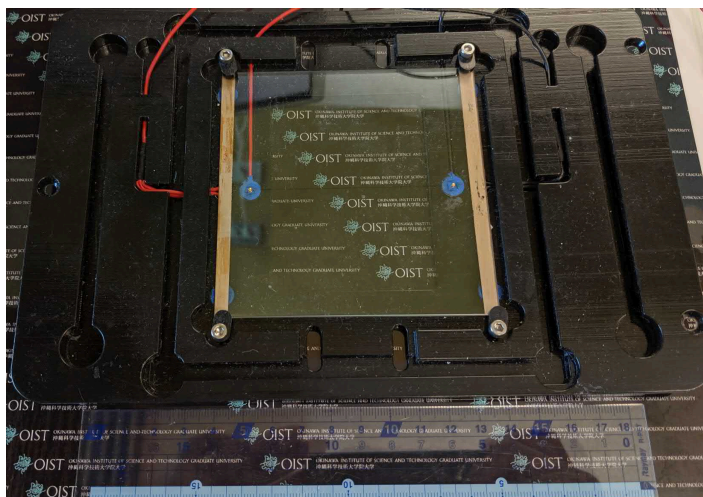


Figure D.1: The 3D printed Nikon Ti-E custom stage with transparent heater.

2. PDMS casting station for 4” and 2” wafers

A PDMS casting station for making PDMS microfluidic chips with precise thickness was milled by CNC micromill (SLS MicroMill/4, Minitech, USA) with a 6

mm-diameter flat end mill (NS Tools, Japan) on a piece of poly(tetrafluoroethylene) block.



Figure D.2: The CNC milled PTFE casting station for PDMS soft lithography supporting 2-inch and 4-inch wafer.

3. Washing stand for 24×60 mm cover glasses.

The washing stand for washing thin cover glasses (24×60 mm, Marienfeld Superior, Germany) was printed by stereolithography in Grey Pro resin on Form2 3D printer.

4. A PDMS lined copper holder for sturdy microscopy imaging of microfluidic chips bonded to No. 1.5 coverglasses.

Due to the thinness of No. 1.5 coverglasses, the microfluidic chip can flex and cause focus drift during high resolution microscopy imaging. A copper holder was made from wire electrical discharge machining (wire-EDM). A 0.5 mm-thick PDMS sheet was lined on one side of the copper holder with dual energy double sided tape (No.5302A, Nitto, Japan). The PDMS lining can help to fix the copper with the cover glass with Van der Waals force to avoid flexure.

5. Custom holder for Tokai hit incubator



Figure D.3: The 3D printed washing stand for cover glasses.

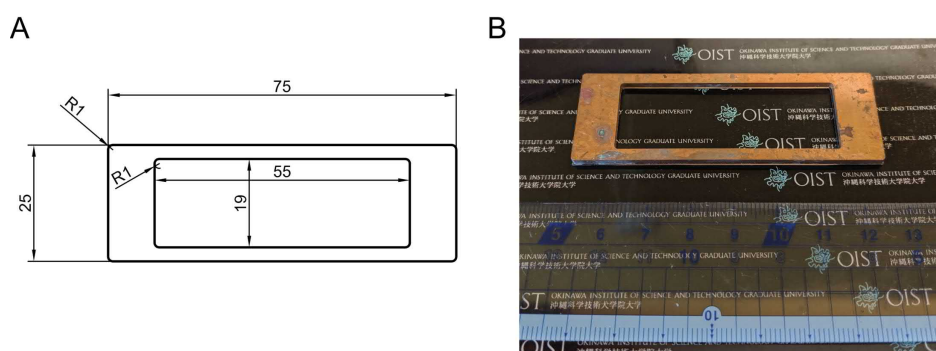


Figure D.4: The PDMS lined copper holder. (A) The design layout; (B) The fabricated copper holder.

The custom holder is made by CNC milling on A5052 aluminum alloy that can interface with Tokai Hit WKSM CO₂ incubator. Two hybrid PMMA/PDMS chips (Chapter 2.3 & 4) can be assembled on the custom holder in one experiment. The surface of the custom holder was lined with a Teflon tape (ASF-110, Chukoh, Japan) to allow easy fixing and delaminating PMMA/PDMS chips with double sided tape.

6. Resolution testing reticle design

The resolution testing reticle design is developed as a 5-inch chrome mask with high resolution patterns to test the exposure limit and lithographical param-

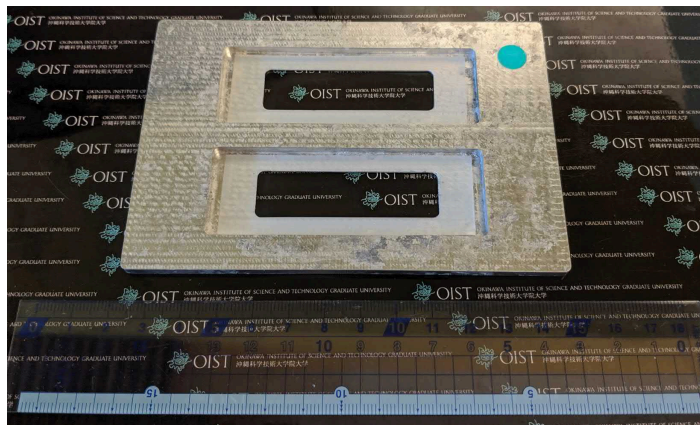


Figure D.5: The CNC milled custom holder for Tokai Hit WKSM incubator.

ters in 1:1 exposure system such as a Suss Microtech MA/BA6 mask aligner. The resolution testing reticle is licensed under a Creative Commons Attribution-ShareAlike 4.0 international license.



Figure D.6: A resolution testing reticle.

In each section, I laid out the same design containing the following patterns in both positive and negative format:

- (a) 5 mm micrometer with 50 μm div (lineweight 5 μm and 10 μm).
- (b) 1 mm micrometer with 10 μm div (lineweight 3 μm).
- (c) Siemens section star (72 sections, 5 degrees per section).
- (d) Ronchi ruling of 10, 20, 50, 100, and 200 lp mm^{-1} .
- (e) Grid of 50, 100, 150, 200 lp mm^{-1} .
- (f) Pin hole resolution dots of diameter of 5, 7.5, 10, 12.5, 15, 20, 25, 50 μm with spacing of 75, 50, 40, 30, 25, 20, 10, 7.5 μm .

- (g) A USAF 1951 target from group 1 to group 8.
 - (h) A group of different line weight, 1, 2,3, 5, 7.5, 10, 15, 20, 25, 37.5, 50, 75, 100, 125, 150, 175, 200.
 - (i) 50 μm line weight with different spacing from 1, 3, 5, 7.5, 10, 12.5, 25, 37.5, 50, 75, 100, 150, 200, 250 μm .
7. A blocking shield for resolution testing with resolution testing reticle on MA/BA6 mask aligner

A blocking shield to use in combined with resolution testing reticle was 3D printed with poly(lactic acid) resin with Ultimaker 3 (Ultimaker, USA). The blocking shield is composed of a holder and a wheel. Each section can be exposed with different parameters to rapidly optimize lithography parameters for microfabrication.

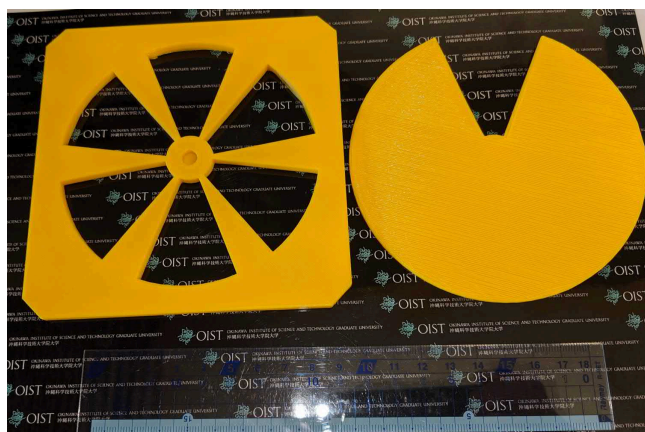


Figure D.7: A blocking shield for resolution testing on MA/BA6 mask aligner.

8. 10 cm glass wafer washing stand
- The 10 cm glass wafer washing stand is 3D printed by fused deposition modeling with autoclavable filament (Nylon680, Taulman 3D, USA).
9. A universal chip holder with transparent heater for confocal scanning
- A universal chip holder that can hold a microfluidic chip in place for confocal scanning is 3D printed with Connex3 Objet 500 (Stratasys, USA).

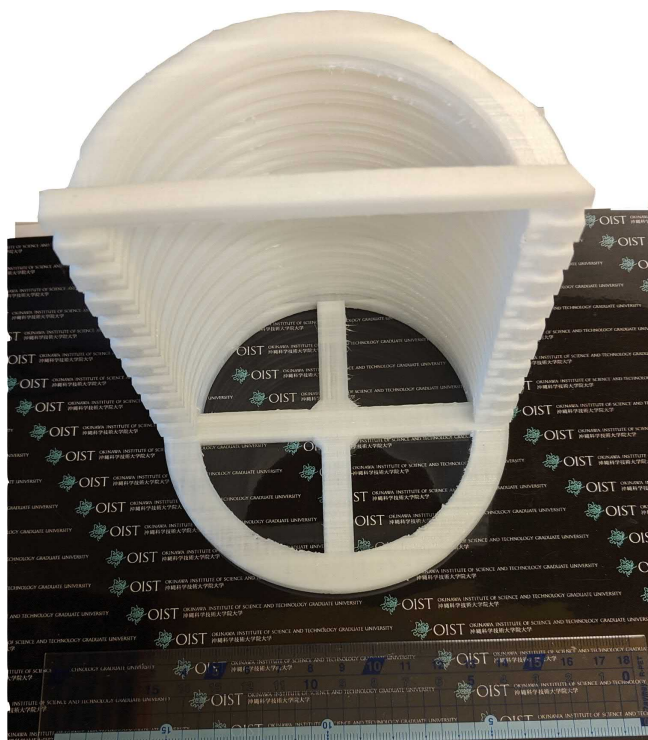


Figure D.8: The 3D printed washing stand for 1 cm glass wafers.

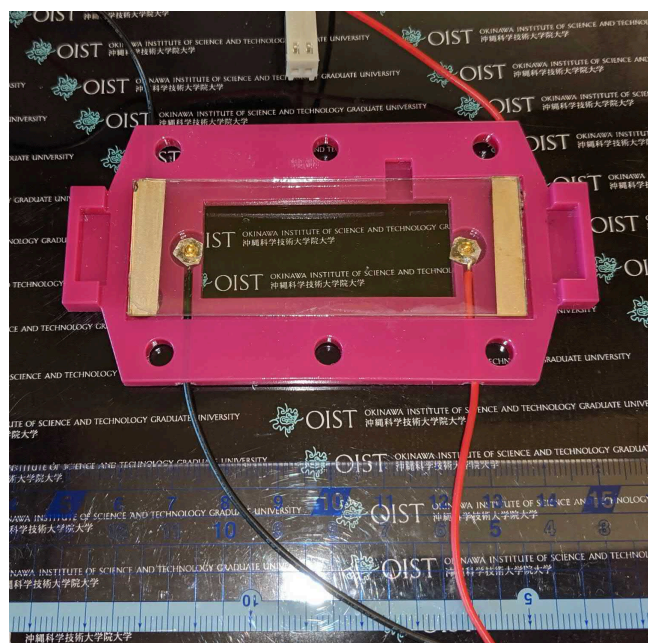


Figure D.9: The 3D printed confocal holder for imaging with a transparent heater.

Appendix E

List of source code of software generated in this thesis

The source code of software used in part of this thesis is deposited on the open-source repository on Github.

1. Usiigaci
2. Data preparation for OpenQCM
3. Cell segmentation by fully convolutional DenseNet
4. Phase contrast channel-only segmentation by Deepcell architecture
5. Automatic categorization script for images exported from NIS element
6. Python-Arduino temperature controller

Bibliography

- [1] Erin C. Amerman. *Human Anatomy & Physiology*. Pearson, 1st edition, 2015.
- [2] Quinn T Ostrom, Haley Gittleman, Gabrielle Truitt, Alexander Boscia, Carol Kruchko, and Jill S Barnholtz-Sloan. Cbtrus statistical report: Primary brain and other central nervous system tumors diagnosed in the united states in 2011-2015. *Neuro-oncology*, 20:iv1–iv86, October 2018.
- [3] Yoshitaka Narita, Soichiro Shibui, and Committee of Brain Tumor Registry of Japan Supported by the Japan Neurosurgical Society. Trends and outcomes in the treatment of gliomas based on data during 2001-2004 from the brain tumor registry of japan. *Neurologia medico-chirurgica*, 55:286–295, 2015.
- [4] David N Louis, Arie Perry, Guido Reifenberger, Andreas von Deimling, Dominique Figarella-Branger, Webster K Cavenee, Hiroko Ohgaki, Otmar D Wiestler, Paul Kleihues, and David W Ellison. The 2016 world health organization classification of tumors of the central nervous system: a summary. *Acta neuropathologica*, 131:803–820, June 2016.
- [5] Roel G W Verhaak, Katherine A Hoadley, Elizabeth Purdom, Victoria Wang, Yuan Qi, Matthew D Wilkerson, C Ryan Miller, Li Ding, Todd Golub, Jill P Mesirov, Gabriele Alexe, Michael Lawrence, Michael O’Kelly, Pablo Tamayo, Barbara A Weir, Stacey Gabriel, Wendy Winckler, Supriya Gupta, Lakshmi Jakkula, Heidi S Feiler, J Graeme Hodgson, C David James, Jann N Sarkaria, Cameron Brennan, Ari Kahn, Paul T Spellman, Richard K Wilson, Terence P Speed, Joe W Gray, Matthew Meyerson, Gad Getz, Charles M Perou, D Neil Hayes, and Cancer Genome Atlas Research Network. Integrated genomic analysis identifies clinically relevant subtypes of glioblastoma characterized by abnormalities in *pdgfra*, *idh1*, *egfr*, and *nf1*. *Cancer cell*, 17:98–110, January 2010.
- [6] Kimmo J Hatanpaa, Sandeep Burma, Dawen Zhao, and Aryn A Habib. Epidermal growth factor receptor in glioma: signal transduction, neuropathology, imaging, and radioresistance. *Neoplasia (New York, N.Y.)*, 12:675–684, September 2010.
- [7] Emily Padfield, Hayley P Ellis, and Kathreena M Kurian. Current therapeutic advances targeting *egfr* and *egfrviii* in glioblastoma. *Frontiers in oncology*, 5:5, 2015.

- [8] Nathalie A Lokker, Carol M Sullivan, Stanley J Hollenbach, Mark A Israel, and Neill A Giese. Platelet-derived growth factor (pdgf) autocrine signaling regulates survival and mitogenic pathways in glioblastoma cells: evidence that the novel pdgf-c and pdgf-d ligands may play a role in the development of brain tumors. *Cancer research*, 62:3729–3735, July 2002.
- [9] Inga Nazarenko, Sanna-Maria Hede, Xiaobing He, Anna Hedrén, James Thompson, Mikael S Lindström, and Monica Nistér. Pdgf and pdgf receptors in glioma. *Uppsala journal of medical sciences*, 117:99–112, May 2012.
- [10] Chengshi Xu, Xing Wu, and Jianhong Zhu. Vegf promotes proliferation of human glioblastoma multiforme stem-like cells through vegf receptor 2. *TheScientificWorldJournal*, 2013:417413, 2013.
- [11] Tobias Kessler, Felix Sahm, Jonas Blaes, Matthias Osswald, Petra Rübmann, David Milford, Severino Urban, Leonie Jestaedt, Sabine Heiland, Martin Bendzus, Anne Hertenstein, Philipp-Niclas Pfenning, Carmen Ruiz de Almodóvar, Antje Wick, Frank Winkler, Andreas von Deimling, Michael Platten, Wolfgang Wick, and Markus Weiler. Glioma cell vegfr-2 confers resistance to chemotherapeutic and antiangiogenic treatments in pten-deficient glioblastoma. *Oncotarget*, 6:31050–31068, October 2015.
- [12] John K Wiencke, Shichun Zheng, Nanette Jelluma, Tarik Tihan, Scott Vandenberg, Tanja Tamgüney, Rachel Baumber, Ramon Parsons, Kathleen R Lamborn, Mitchel S Berger, Margaret R Wrensch, Daphne Adele Haas-Kogan, and David Stokoe. Methylation of the pten promoter defines low-grade gliomas and secondary glioblastoma. *Neuro-oncology*, 9:271–279, July 2007.
- [13] Qi-Wen Fan and William A Weiss. Targeting the rtk-pi3k-mtor axis in malignant glioma: overcoming resistance. *Current topics in microbiology and immunology*, 347:279–296, 2010.
- [14] Kelli A McDowell, Gregory J Riggins, and Gary L Gallia. Targeting the akt pathway in glioblastoma. *Current pharmaceutical design*, 17:2411–2420, 2011.
- [15] Frank B Furnari, Tim Fenton, Robert M Bachoo, Akitake Mukasa, Jayne M Stommel, Alexander Stegh, William C Hahn, Keith L Ligon, David N Louis, Cameron Brennan, Lynda Chin, Ronald A DePinho, and Webster K Cavenee. Malignant astrocytic glioma: genetics, biology, and paths to treatment. *Genes & development*, 21:2683–2710, November 2007.
- [16] Elisabeth Cardis, Lesley Richardson, Isabelle Deltour, Bruce Armstrong, Maria Feychting, Christoffer Johansen, Monique Kilkenny, Patricia McKinney, Baruch Modan, Siegal Sadetzki, Joachim Schüz, Anthony Swerdlow, Martine Vrijheid, Anssi Auvinen, Gabriele Berg, Maria Blettner, Joseph Bowman, Julianne Brown, Angela Chetrit, Helle Collatz Christensen, Angus Cook, Sarah Hepworth, Graham Giles, Martine Hours, Ivano Iavarone, Avital Jarus-Hakak, Lars Klaeboe, Daniel Krewski, Susanna Lagorio, Stefan Lönn, Simon Mann, Mary McBride,

- Kenneth Muir, Louise Nadon, Marie-Elise Parent, Neil Pearce, Tiina Salminen, Minouk Schoemaker, Brigitte Schlehofer, Jack Siemiatycki, Masao Taki, Toru Takebayashi, Tore Tynes, Martie van Tongeren, Paolo Vecchia, Joe Wiart, Alistair Woodward, and Naohito Yamaguchi. The interphone study: design, epidemiological methods, and description of the study population. *European journal of epidemiology*, 22:647–664, 2007.
- [17] INTERPHONE Study Group. Brain tumour risk in relation to mobile telephone use: results of the interphone international case-control study. *International journal of epidemiology*, 39:675–694, June 2010.
- [18] Kristine Dziurzynski, Susan M Chang, Amy B Heimberger, Robert F Kalejta, Stuart R McGregor Dallas, Martine Smit, Liliana Soroceanu, Charles S Cobbs, HCMV, and Gliomas Symposium. Consensus on the role of human cytomegalovirus in glioblastoma. *Neuro-oncology*, 14:246–255, March 2012.
- [19] Sean E Lawler. Cytomegalovirus and glioblastoma; controversies and opportunities. *Journal of neuro-oncology*, 123:465–471, July 2015.
- [20] Yumiko Hashida, Ayuko Taniguchi, Toshio Yawata, Sena Hosokawa, Masanao Murakami, Makoto Hiroi, Tetsuya Ueba, and Masanori Daibata. Prevalence of human cytomegalovirus, polyomaviruses, and oncogenic viruses in glioblastoma among japanese subjects. *Infectious agents and cancer*, 10:3, 2015.
- [21] Charles D Stiles and David H Rowitch. Glioma stem cells: a midterm exam. *Neuron*, 58:832–846, June 2008.
- [22] Tatyana N Ignatova, Valery G Kukekov, Eric D Laywell, Oleg N Suslov, Frank D Vrionis, and Dennis A Steindler. Human cortical glial tumors contain neural stem-like cells expressing astroglial and neuronal markers in vitro. *Glia*, 39:193–206, September 2002.
- [23] Houman D Hemmati, Ichiro Nakano, Jorge A Lazareff, Michael Masterman-Smith, Daniel H Geschwind, Marianne Bronner-Fraser, and Harley I Kornblum. Cancerous stem cells can arise from pediatric brain tumors. *Proceedings of the National Academy of Sciences of the United States of America*, 100:15178–15183, December 2003.
- [24] Sheila K Singh, Ian D Clarke, Mizuhiko Terasaki, Victoria E Bonn, Cynthia Hawkins, Jeremy Squire, and Peter B Dirks. Identification of a cancer stem cell in human brain tumors. *Cancer research*, 63:5821–5828, September 2003.
- [25] Rossella Galli, Elena Binda, Ugo Orfanelli, Barbara Cipelletti, Angela Gritti, Simona De Vitis, Roberta Fiocco, Chiara Foroni, Francesco Dimeco, and Angelo Vescovi. Isolation and characterization of tumorigenic, stem-like neural precursors from human glioblastoma. *Cancer research*, 64:7011–7021, October 2004.
- [26] Shideng Bao, Qiulian Wu, Roger E McLendon, Yueling Hao, Qing Shi, Anita B Hjelmeland, Mark W Dewhirst, Darell D Bigner, and Jeremy N Rich. Glioma

- stem cells promote radioresistance by preferential activation of the dna damage response. *Nature*, 444:756–760, December 2006.
- [27] Patrick Mehlen and Alain Puisieux. Metastasis: a question of life or death. *Nature reviews. Cancer*, 6:449–458, June 2006.
- [28] Ali Mohammad Alizadeh, Sadaf Shiri, and Sadaf Farsinejad. Metastasis review: from bench to bedside. *Tumour biology : the journal of the International Society for Oncodevelopmental Biology and Medicine*, 35:8483–8523, September 2014.
- [29] Nicolas Reymond, Bárbara Borda d’Água, and Anne J Ridley. Crossing the endothelial barrier during metastasis. *Nature reviews. Cancer*, 13:858–870, December 2013.
- [30] A Giese, R Bjerkvig, M E Berens, and M Westphal. Cost of migration: invasion of malignant gliomas and implications for treatment. *Journal of clinical oncology : official journal of the American Society of Clinical Oncology*, 21:1624–1636, April 2003.
- [31] Alessandra Fabi, Antonello Vidiri, Carmine Carapella, Andrea Pace, Emanuele Occhipinti, Fabrizio Caroli, Alessandra Mirri, Paolo Carlini, and Francesco Cognetti. Bone metastasis from glioblastoma multiforme without central nervous system relapse: a case report. *Anticancer research*, 24:2563–2565, 2004.
- [32] Pierre D Mourad, Lindi Farrell, Louis D Stamps, Michael R Chicoine, and Daniel L Silbergeld. Why are systemic glioblastoma metastases rare? systemic and cerebral growth of mouse glioblastoma. *Surgical neurology*, 63:511–9; discussion 519, June 2005.
- [33] Ashwin Kumaria, Alice Teale, Girish V Kulkarni, Harshal A Ingale, Donald C Macarthur, and Iain J A Robertson. Glioblastoma multiforme metastatic to lung in the absence of intracranial recurrence: case report. *British journal of neurosurgery*, pages 1–3, November 2018.
- [34] Patrick Beauchesne. Extra-neural metastases of malignant gliomas: myth or reality? *Cancers*, 3(1):461–477, January 2011.
- [35] Jackson D Hamilton, Marion Rapp, Timo Schneiderhan, Timo Marcel Schneiderhan, Michael Sabel, Anne Hayman, Axel Scherer, Patric Kröpil, Wilfried Budach, Peter Gerber, Usha Kretschmar, Peter Arne Gerber, Sujit Prabhu, Lawrence E Ginsberg, Edwin Bölke, and Christiane Matuschek. Glioblastoma multiforme metastasis outside the cns: three case reports and possible mechanisms of escape. *Journal of clinical oncology : official journal of the American Society of Clinical Oncology*, 32:e80–e84, August 2014.
- [36] Jasti S Rao. Molecular mechanisms of glioma invasiveness: the role of proteases. *Nature reviews. Cancer*, 3:489–501, July 2003.

-
- [37] Gerard Apodaca, James T Rutka, Karyn Bouhana, Michael E Berens, Jane R Giblin, Mark L Rosenblum, James H McKerrow, and Michael J Banda. Expression of metalloproteinases and metalloproteinase inhibitors by fetal astrocytes and glioma cells. *Cancer research*, 50(8):2322–2329, 1990.
- [38] Atsuhisa Nakano, Eiichi Tani, Kaoru Miyazaki, Yoshihiro Yamamoto, and Jun-ichi Furuyama. Matrix metalloproteinases and tissue inhibitors of metalloproteinases in human gliomas. *Journal of neurosurgery*, 83(2):298–307, 1995.
- [39] Elena I Deryugina, Mario A Bourdon, Guang-Xiang Luo, Ralph A Reisfeld, and Alex Strongin. Matrix metalloproteinase-2 activation modulates glioma cell migration. *Journal of Cell Science*, 110(19):2473–2482, 1997.
- [40] Wolfgang Wick, Michael Platten, and Michael Weller. Glioma cell invasion: regulation of metalloproteinase activity by tgf-beta. *Journal of neuro-oncology*, 53:177–185, June 2001.
- [41] Rupavathana Mahesparan, Tracy-Ann Read, Morten Lund-Johansen, Kai Ove Skaftnesmo, Rolf Bjerkvig, and Olav Engebraaten. Expression of extracellular matrix components in a highly infiltrative in vivo glioma model. *Acta neuropathologica*, 105:49–57, January 2003.
- [42] Dolores Hambardzumyan and Gabriele Bergers. Glioblastoma: Defining tumor niches. *Trends in cancer*, 1:252–265, December 2015.
- [43] Johanna A Joyce and Jeffrey W Pollard. Microenvironmental regulation of metastasis. *Nature reviews. Cancer*, 9:239–252, April 2009.
- [44] Douglas Hanahan and Lisa M Coussens. Accessories to the crime: functions of cells recruited to the tumor microenvironment. *Cancer cell*, 21:309–322, March 2012.
- [45] Frances R Balkwill, Melania Capasso, and Thorsten Hagemann. The tumor microenvironment at a glance. *Journal of cell science*, 125:5591–5596, December 2012.
- [46] Giovanna Schiavoni, Lucia Gabriele, and Fabrizio Mattei. The tumor microenvironment: a pitch for multiple players. *Frontiers in oncology*, 3:90, 2013.
- [47] Harold F Dvorak, Valerie M Weaver, Thea D Tlsty, and Gabriele Bergers. Tumor microenvironment and progression. *Journal of surgical oncology*, 103:468–474, May 2011.
- [48] Thordur Oskarsson, Eduard Batlle, and Joan Massagué. Metastatic stem cells: sources, niches, and vital pathways. *Cell stem cell*, 14:306–321, March 2014.
- [49] John Termini, Josh Neman, and Rahul Jandial. Role of the neural niche in brain metastatic cancer. *Cancer research*, 74:4011–4015, August 2014.

- [50] Hsieh-Fu Tsai, Alen Trubelja, Amy Q Shen, and Gang Bao. Tumour-on-a-chip: microfluidic models of tumour morphology, growth and microenvironment. *Journal of the Royal Society, Interface*, 14(131):20170137, June 2017.
- [51] Jasmina S Redzic, Timothy H Ung, and Michael W Graner. Glioblastoma extracellular vesicles: reservoirs of potential biomarkers. *Pharmacogenomics and personalized medicine*, 7:65–77, 2014.
- [52] Crislyn D’Souza-Schorey and James W Clancy. Tumor-derived microvesicles: shedding light on novel microenvironment modulators and prospective cancer biomarkers. *Genes & development*, 26:1287–1299, June 2012.
- [53] Delphine Garnier, Nada Jabado, and Janusz Rak. Extracellular vesicles as prospective carriers of oncogenic protein signatures in adult and paediatric brain tumours. *Proteomics*, 13:1595–1607, May 2013.
- [54] Lin Cao, Dongguang Wei, Brian Reid, Siwei Zhao, Jin Pu, Tingrui Pan, Ebenezer N. Yamoah, and Min Zhao. Endogenous electric currents might guide rostral migration of neuroblasts. *EMBO reports*, 14(2):184–190, 2013.
- [55] Congmin Wang, Fang Liu, Ying-Ying Liu, Cai-Hong Zhao, Yan You, Lei Wang, Jingxiao Zhang, Bin Wei, Tong Ma, Qiangqiang Zhang, Yue Zhang, Rui Chen, Hongjun Song, and Zhengang Yang. Identification and characterization of neuroblasts in the subventricular zone and rostral migratory stream of the adult human brain. *Cell research*, 21:1534–1550, November 2011.
- [56] Nikolai N Khodarev, Jianqing Yu, Edwardine Labay, Thomas Darga, Charles K Brown, Helena J Mauceri, Reza Yassari, Nalin Gupta, and Ralph R Weichselbaum. Tumour-endothelium interactions in co-culture: coordinated changes of gene expression profiles and phenotypic properties of endothelial cells. *Journal of cell science*, 116:1013–1022, March 2003.
- [57] Christopher Calabrese, Helen Poppleton, Mehmet Kocak, Twala L Hogg, Christine Fuller, Blair Hamner, Eun Young Oh, M Waleed Gaber, David Finklestein, Meredith Allen, Adrian Frank, Ildar T Bayazitov, Stanislav S Zakharenko, Amar Gajjar, Andrew Davidoff, and Richard J Gilbertson. A perivascular niche for brain tumor stem cells. *Cancer cell*, 11:69–82, January 2007.
- [58] Richard J Gilbertson and Jeremy N Rich. Making a tumour’s bed: glioblastoma stem cells and the vascular niche. *Nature reviews. Cancer*, 7:733–736, October 2007.
- [59] Nikki Charles and Eric C Holland. The perivascular niche microenvironment in brain tumor progression. *Cell cycle (Georgetown, Tex.)*, 9:3012–3021, August 2010.
- [60] David W Infanger, YouJin Cho, Brina S Lopez, Sunish Mohanan, S Chris Liu, Demirkan Gursel, John A Boockvar, and Claudia Fischbach. Glioblastoma stem cells are regulated by interleukin-8 signaling in a tumoral perivascular niche. *Cancer research*, 73:7079–7089, December 2013.

-
- [61] Davide Schiffer, Marta Mellai, Laura Annovazzi, Valentina Caldera, Angela Piazzi, Tetyana Denysenko, and Antonio Melcarne. Stem cell niches in glioblastoma: a neuropathological view. *BioMed research international*, 2014:725921, 2014.
- [62] Elena Codrici, Ana-Maria Enciu, Ionela-Daniela Popescu, Simona Mihai, and Cristiana Tanase. Glioma stem cells and their microenvironments: Providers of challenging therapeutic targets. *Stem cells international*, 2016:5728438, 2016.
- [63] Marcin Sliwa, Darko Markovic, Konrad Gabrusiewicz, Michael Synowitz, Rainer Glass, Malgorzata Zawadzka, Aleksandra Wesolowska, Helmut Kettenmann, and Bozena Kaminska. The invasion promoting effect of microglia on glioblastoma cells is inhibited by cyclosporin a. *Brain : a journal of neurology*, 130:476–489, February 2007.
- [64] Isaac Yang, Seunggu J Han, Gurvinder Kaur, Courtney Crane, and Andrew T Parsa. The role of microglia in central nervous system immunity and glioma immunology. *Journal of clinical neuroscience : official journal of the Neurosurgical Society of Australasia*, 17:6–10, January 2010.
- [65] Salvatore J Coniglio, Eliseo Eugenin, Kostantin Dobrenis, E Richard Stanley, Brian L West, Marc H Symons, and Jeffrey E Segall. Microglial stimulation of glioblastoma invasion involves epidermal growth factor receptor (egfr) and colony stimulating factor 1 receptor (csf-1r) signaling. *Molecular medicine (Cambridge, Mass.)*, 18:519–527, May 2012.
- [66] Dolores Hambarzumyan, David H Gutmann, and Helmut Kettenmann. The role of microglia and macrophages in glioma maintenance and progression. *Nature neuroscience*, 19:20–27, January 2016.
- [67] Alicia Martínez-González, Gabriel F Calvo, Luis A Pérez Romasanta, and Víctor M Pérez-García. Hypoxic cell waves around necrotic cores in glioblastoma: a biomathematical model and its therapeutic implications. *Bulletin of mathematical biology*, 74:2875–2896, December 2012.
- [68] Sascha Seidel, Boyan K Garvalov, Valtteri Wirta, Louise von Stechow, Anne Schänzer, Konstantinos Meletis, Marietta Wolter, Daniel Sommerlad, Anne-Theres Henze, Monica Nistér, Guido Reifenberger, Joakim Lundberg, Jonas Frisé, and Till Acker. A hypoxic niche regulates glioblastoma stem cells through hypoxia inducible factor 2 alpha. *Brain : a journal of neurology*, 133:983–995, April 2010.
- [69] Davide Schiffer, Laura Annovazzi, Marta Mazzucco, and Marta Mellai. The microenvironment in gliomas: Phenotypic expressions. *Cancers*, 7:2352–2359, December 2015.
- [70] Aya Ishii, Tokuhiko Kimura, Hirokazu Sadahiro, Hiroo Kawano, Keiyo Takubo, Michiyasu Suzuki, and Eiji Ikeda. Histological characterization of the tumorigenic

- "peri-necrotic niche" harboring quiescent stem-like tumor cells in glioblastoma. *PloS one*, 11:e0147366, 2016.
- [71] Yung-Ann Chen, Andrew D King, Hsiu-Chen Shih, Chien-Chung Peng, Chueh-Yu Wu, Wei-Hao Liao, and Yi-Chung Tung. Generation of oxygen gradients in microfluidic devices for cell culture using spatially confined chemical reactions. *Lab on a chip*, 11:3626–3633, November 2011.
- [72] Jose M Ayuso, María Virumbrales-Muñoz, Alodia Lacueva, Pilar M Lanuza, Elisa Checa-Chavarria, Pablo Botella, Eduardo Fernández, Manuel Doblare, Simon J Allison, Roger M Phillips, Julián Pardo, Luis J Fernandez, and Ignacio Ochoa. Development and characterization of a microfluidic model of the tumour microenvironment. *Scientific reports*, 6:36086, October 2016.
- [73] Anna Carolina Carvalho da Fonseca and Behnam Badie. Microglia and macrophages in malignant gliomas: recent discoveries and implications for promising therapies. *Clinical & developmental immunology*, 2013:264124, 2013.
- [74] David H Gutmann. Microglia in the tumor microenvironment: taking their toll on glioma biology. *Neuro-oncology*, 17:171–173, February 2015.
- [75] Peng Wang, Haining Zhen, Xinbiao Jiang, Wei Zhang, Xin Cheng, Geng Guo, Xinggang Mao, and Xiang Zhang. Boron neutron capture therapy induces apoptosis of glioma cells through bcl-2/bax. *BMC cancer*, 10:661, December 2010.
- [76] K Nakai, T Yamamoto, H Aiyama, T Takada, F Yoshida, T Kageji, H Kumada, T Isobe, K Endo, M Matsuda, T Tsurubuchi, Y Shibata, S Takano, M Mizumoto, K Tsuboi, and A Matsumura. Boron neutron capture therapy combined with fractionated photon irradiation for glioblastoma: a recursive partitioning analysis of bnct patients. *Applied radiation and isotopes : including data, instrumentation and methods for use in agriculture, industry and medicine*, 69:1790–1792, December 2011.
- [77] Ting Sun, Zizhu Zhang, Bin Li, Guilin Chen, Xueshun Xie, Yongxin Wei, Jie Wu, Youxin Zhou, and Ziwei Du. Boron neutron capture therapy induces cell cycle arrest and cell apoptosis of glioma stem/progenitor cells in vitro. *Radiation oncology (London, England)*, 8:195, August 2013.
- [78] Patrick Y. Wen and Santosh Kesari. Malignant gliomas in adults. *New England Journal of Medicine*, 359(5):492–507, 2008.
- [79] Azeem A Rehman, Kevin B Elmore, and Tobias A Mattei. The effects of alternating electric fields in glioblastoma: current evidence on therapeutic mechanisms and clinical outcomes. *Neurosurgical focus*, 38:E14, March 2015.
- [80] Eilon D. Kirson, Vladimír Dbalý, František Továryš, Josef Vymazal, Jean F. Soustiel, Aviran Itzhaki, Daniel Mordechovich, Shirley Steinberg-Shapira, Zoya Gurvich, Rosa Schneiderman, Yoram Wasserman, Marc Salzberg, Bernhard Ryffel, Dorit Goldsher, Erez Dekel, and Yoram Palti. Alternating electric fields arrest

-
- cell proliferation in animal tumor models and human brain tumors. *Proceedings of the National Academy of Sciences*, 104(24):10152–10157, 2007.
- [81] Ekokobe Fonkem and Eric T Wong. Novotf-100a: a new treatment modality for recurrent glioblastoma. *Expert review of neurotherapeutics*, 12:895–899, August 2012.
- [82] Roger Stupp, Eric T Wong, Andrew A Kanner, David Steinberg, Herbert Engelhard, Volkmar Heidecke, Eilon D Kirson, Sophie Taillibert, Frank Liebermann, Vladimir Dbalý, Zvi Ram, J Lee Villano, Nikolai Rainov, Uri Weinberg, David Schiff, Lara Kunschner, Jeffrey Raizer, Jerome Honnorat, Andrew Sloan, Mark Malkin, Joseph C Landolfi, Franz Payer, Maximilian Mehdorn, Robert J Weil, Susan C Pannullo, Manfred Westphal, Martin Smrcka, Lawrence Chin, Herwig Kostron, Silvia Hofer, Jeffrey Bruce, Rees Cosgrove, Nina Paleologous, Yoram Palti, and Philip H Gutin. Novotf-100a versus physician’s choice chemotherapy in recurrent glioblastoma: a randomised phase iii trial of a novel treatment modality. *European journal of cancer (Oxford, England : 1990)*, 48:2192–2202, September 2012.
- [83] Steven K Carlsson, Shaun P Brothers, and Claes Wahlestedt. Emerging treatment strategies for glioblastoma multiforme. *EMBO Molecular Medicine*, 6(11):1359–1370, 2014.
- [84] Daniela F. Quail and Johanna A. Joyce. Microenvironmental regulation of tumor progression and metastasis. *Nature Medicine*, 19(11):1423–1437, 2013.
- [85] Jelle J. F. Sleenboom, Hossein Eslami Amirabadi, Poornima Nair, Cecilia M. Sahlgren, and Jaap M. J. den Toonder. Metastasis in context: modeling the tumor microenvironment with cancer-on-a-chip approaches. *Disease Models & Mechanisms*, 11(3), 2018.
- [86] Sanjib Bahadur, Arvind Kumar Sahu, Pragya Baghel, and Suman Saha. Current promising treatment strategy for glioblastoma multiform: A review. *Oncology reviews*, 13:417, July 2019.
- [87] S A Toms, C Y Kim, G Nicholas, and Z Ram. Increased compliance with tumor treating fields therapy is prognostic for improved survival in the treatment of glioblastoma: a subgroup analysis of the ef-14 phase iii trial. *Journal of neuro-oncology*, 141:467–473, January 2019.
- [88] Karniadakis G., Beskok A., and Aluru N. *Microflows and Nanoflows: Fundamentals and Simulation*, volume 29 of *Interdisciplinary Applied Mathematics*. Springer Science, 1 edition, 2005.
- [89] David J. Beebe, Glennys A. Mensing, and Glenn M. Walker. Physics and applications of microfluidics in biology. *Annual Review of Biomedical Engineering*, 4(1):261–286, 2002.
- [90] Wei-Cheng Tian and Erin Finehout. *Microfluidics for biological applications*, volume 16. Springer Science & Business Media, 2009.

- [91] Frank A Gomez. *Biological applications of microfluidics*. John Wiley & Sons, 2008.
- [92] Brian J Kirby. *Micro-and nanoscale fluid mechanics: transport in microfluidic devices*. Cambridge university press, 2010.
- [93] Howard A Stone, Abraham D Stroock, and Armand Ajdari. Engineering flows in small devices: microfluidics toward a lab-on-a-chip. *Annu. Rev. Fluid Mech.*, 36:381–411, 2004.
- [94] Laura Lara Rodriguez and Ian C. Schneider. Directed cell migration in multi-cue environments. *Integrative Biology*, 5(11):1306–1323, 2013.
- [95] Deok-Ho Kim, Paolo P. Provenzano, Chris L. Smith, and Andre Levchenko. Matrix nanotopography as a regulator of cell function. *Journal of Cell Biology*, 197(3):351–360, 2012.
- [96] Hojeong Jeon, Sangmo Koo, Willie Mae Reese, Peter Loskill, Costas P. Grigoriopoulos, and Kevin E. Healy. Directing cell migration and organization via nanocrater-patterned cell-repellent interfaces. *Nature Materials*, 14(9):918–923, 2015.
- [97] N. Wang, J. P. Butler, and D. E. Ingber. Mechanotransduction across the cell surface and through the cytoskeleton. *Science*, 260(5111):1124–1127, 1993.
- [98] Chun-Min Lo, Hong-Bei Wang, Micah Dembo, and Yu-li Wang. Cell movement is guided by the rigidity of the substrate. *Biophysical Journal*, 79(1):144–152, 2000.
- [99] Konstantinos A Lazopoulos and Dimitrije Stamenović. Durotaxis as an elastic stability phenomenon. *Journal of biomechanics*, 41:1289–1294, 2008.
- [100] S. B. Carter. Haptotaxis and the mechanism of cell motility. *Nature*, 213(5073):256–260, 1967.
- [101] S. Aznavoorian, M. L. Stracke, H. Krutzsch, E. Schiffmann, and L. A. Liotta. Signal transduction for chemotaxis and haptotaxis by matrix molecules in tumor cells. *The Journal of Cell Biology*, 110(4):1427–1438, 1990.
- [102] Terri Adams Kapur and Molly S. Shoichet. Immobilized concentration gradients of nerve growth factor guide neurite outgrowth. *Journal of Biomedical Materials Research Part A*, 68A(2):235–243, 2004.
- [103] Jason T. Smith, James T. Elkin, and W. Monty Reichert. Directed cell migration on fibronectin gradients: Effect of gradient slope. *Experimental Cell Research*, 312(13):2424–2432, 2006.
- [104] Jason Smith, Donghwan Kim, and William Reichert. Haptotactic gradients for directed cell migration: Stimulation and inhibition using soluble factors. *Combinatorial Chemistry & High Throughput Screening*, 12(6):598–603, 2009.

-
- [105] Anna Bagorda and Carole A. Parent. Eukaryotic chemotaxis at a glance. *Journal of Cell Science*, 121(16):2621–2624, 2008.
- [106] Evanthia T. Roussos, John S. Condeelis, and Antonia Patsialou. Chemotaxis in cancer. *Nature Reviews Cancer*, 11(8):573–587, 2011.
- [107] Colin D. McCaig. Electric fields, contact guidance and the direction of nerve growth. *J Embryol Exp Morphol*, 94(1):245–255, June 1986.
- [108] Colin D McCaig. On the mechanism of nerve galvanotropism. *The Biological Bulletin*, 176(2):136–139, 1989.
- [109] M Zhao, J V Forrester, and C D McCaig. A small, physiological electric field orients cell division. *Proceedings of the National Academy of Sciences of the United States of America*, 96(9):4942–4946, 1999.
- [110] Colin D. McCaig, Bing Song, and Ann M. Rajnicek. Electrical dimensions in cell science. *Journal of Cell Science*, 122(23):4267–4276, December 2009.
- [111] Ortrud Wartlick, Anna Kicheva, and Marcos González-Gaitán. Morphogen gradient formation. *Cold Spring Harbor Perspectives in Biology*, 1(3):a001255, 2009.
- [112] Teresa Adell, Francesc Cebrià, and Emili Saló. Gradients in planarian regeneration and homeostasis. *Cold Spring Harbor Perspectives in Biology*, 2(1):a000505, 2010.
- [113] Gerald Schwank and Konrad Basler. Regulation of organ growth by morphogen gradients. *Cold Spring Harbor Perspectives in Biology*, 2(1):a001669, 2010.
- [114] Thomas Hunt Morgan. *Regeneration*. Macmillan, 1901.
- [115] Mary Evelyn Sunderland. Regeneration: Thomas hunt morgan’s window into development. *Journal of the History of Biology*, 43(2):325–361, 2009.
- [116] A. M. Turing. The chemical basis of morphogenesis. *Philosophical Transactions of the Royal Society of London B: Biological Sciences*, 237(641):37–72, 1952.
- [117] Ben-Zion Shilo, Michal Haskel-Ittah, Danny Ben-Zvi, Eyal D Schejter, and Naama Barkai. Creating gradients by morphogen shuttling. *Trends in Genetics*, 29(6):339–347, 2013.
- [118] Yann Echelard, Douglas J. Epstein, Benoit St-Jacques, Liya Shen, Jym Mohler, Jill A. McMahon, and Andrew P. McMahon. Sonic hedgehog, a member of a family of putative signaling molecules, is implicated in the regulation of CNS polarity. *Cell*, 75(7):1417–1430, 1993.
- [119] David A. Bumcrot and Andrew P. McMahon. Sonic hedgehog: making the gradient. *Chemistry & Biology*, 3(1):13–16, 1996.
- [120] Tetsuya Tabata and Yuki Takei. Morphogens, their identification and regulation. *Development*, 131(4):703–712, 2004.

- [121] Ken M. Cadigan and Roel Nusse. Wnt signaling: a common theme in animal development. *Genes & Development*, 11(24):3286–3305, 1997.
- [122] Clemens Kiecker and Christof Niehrs. A morphogen gradient of wnt/ β -catenin signalling regulates anteroposterior neural patterning in xenopus. *Development*, 128(21):4189–4201, 2001.
- [123] R. Nusse, C. Fuerer, W. Ching, K. Harnish, C. Logan, A. Zeng, D. ten Berge, and Y. Kalani. Wnt signaling and stem cell control. *Cold Spring Harbor Symposia on Quantitative Biology*, 73:59–66, 2008.
- [124] Sung-Eun Kim, He Huang, Ming Zhao, Xinjun Zhang, Aili Zhang, Mikhail V. Semonov, Bryan T. MacDonald, Xiaowu Zhang, Jose Garcia Abreu, Leilei Peng, and Xi He. Wnt stabilization of β -catenin reveals principles for morphogen receptor-scaffold assemblies. *Science*, 340(6134):867–870, 2013.
- [125] S. M. Jackson, H. Nakato, M. Sugiura, A. Jannuzi, R. Oakes, V. Kaluza, C. Golden, and S. B. Selleck. dally, a drosophila glypican, controls cellular responses to the TGF-beta-related morphogen, dpp. *Development*, 124(20):4113–4120, 1997.
- [126] K. Miyazono. Positive and negative regulation of TGF-beta signaling. *Journal of Cell Science*, 113(7):1101–1109, 2000.
- [127] Yu Chen and Alexander F. Schier. The zebrafish nodal signal squint functions as a morphogen. *Nature*, 411(6837):607–610, 2001.
- [128] S. Y. Lin, Morrison, D. J. Phillips, and DM de Kretser. Regulation of ovarian function by the TGF-beta superfamily and follistatin. *Reproduction*, 126(2):133–148, 2003.
- [129] Robert D. Riddle, Randy L. Johnson, Ed Laufer, and Cliff Tabin. Sonic hedgehog mediates the polarizing activity of the ZPA. *Cell*, 75(7):1401–1416, 1993.
- [130] Karen Lai, Brian K. Kaspar, Fred H. Gage, and David V. Schaffer. Sonic hedgehog regulates adult neural progenitor proliferation in vitro and in vivo. *Nature Neuroscience*, 6(1):21–27, 2003.
- [131] Katherine W. Rogers and Alexander F. Schier. Morphogen gradients: From generation to interpretation. *Annual Review of Cell and Developmental Biology*, 27(1):377–407, 2011.
- [132] J. B. Gurdon and P.-Y. Bourillot. Morphogen gradient interpretation. *Nature*, 413(6858):797–803, 2001.
- [133] Arthur D. Lander. Morpheus unbound: Reimagining the morphogen gradient. *Cell*, 128(2):245–256, 2007.
- [134] Timothy C. Williams. *Chemotaxis: Types, Clinical Significance, and Mathematical Models*. Nova Science Publishers, 1 edition edition, 2011.

-
- [135] Robert R. Kay, Paul Langridge, David Traynor, and Oliver Hoeller. Changing directions in the study of chemotaxis. *Nature Reviews Molecular Cell Biology*, 9(6):455–463, 2008.
- [136] Victor Sourjik and Ned S Wingreen. Responding to chemical gradients: bacterial chemotaxis. *Current Opinion in Cell Biology*, 24(2):262–268, 2012.
- [137] Kristen F. Swaney, Chuan-Hsiang Huang, and Peter N. Devreotes. Eukaryotic chemotaxis: A network of signaling pathways controls motility, directional sensing, and polarity. *Annual Review of Biophysics*, 39(1):265–289, 2010.
- [138] Chang Y Chung, Satoru Funamoto, and Richard A Firtel. Signaling pathways controlling cell polarity and chemotaxis. *Trends in Biochemical Sciences*, 26(9):557–566, 2001.
- [139] Sujeenthar Tharmalingam and David R. Hampson. The calcium-sensing receptor and integrins in cellular differentiation and migration. *Integrative Physiology*, page 190, 2016.
- [140] Thomas M. Keenan and Albert Folch. Biomolecular gradients in cell culture systems. *Lab on a Chip*, 8(1):34–57, 2007.
- [141] Bong Geun Chung and Jaebum Choo. Microfluidic gradient platforms for controlling cellular behavior. *Electrophoresis*, 31(18):3014–3027, 2010.
- [142] Sudong Kim, Hyung Joon Kim, and Noo Li Jeon. Biological applications of microfluidic gradient devices. *Integrative Biology*, 2(11):584–603, 2010.
- [143] Nina Kramer, Angelika Walzl, Christine Unger, Margit Rosner, Georg Krupitza, Markus Hengstschläger, and Helmut Dolznig. In vitro cell migration and invasion assays. *Mutation Research/Reviews in Mutation Research*, 752(1):10–24, 2013.
- [144] Isabelle Dupin, Maxime Dahan, and Vincent Studer. Investigating axonal guidance with microdevice-based approaches. *The Journal of Neuroscience*, 33(45):17647–17655, 2013.
- [145] Alicia G. G. Toh, Z. P. Wang, Chun Yang, and Nam-Trung Nguyen. Engineering microfluidic concentration gradient generators for biological applications. *Microfluidics and Nanofluidics*, 16(1):1–18, 2013.
- [146] Roland Glaser. *Biophysics*. Springer, 2001.
- [147] Frank S Barnes and Ben Greenebaum. *Handbook of Biological Effects of Electromagnetic Fields-Two Volume Set*. CRC press, 2018.
- [148] Min Zhao. Electrical fields in wound healing—an overriding signal that directs cell migration. *Seminars in Cell & Developmental Biology*, 20(6):674–682, 2009.
- [149] Richard Nuccitelli. A role for endogenous electric fields in wound healing. *Current Topics in Developmental Biology*, 58:1–26, 2003.

- [150] Robert Goldman and Solomon Pollack. Electric fields and proliferation in a chronic wound model. *Bioelectromagnetics*, 17(6):450–457, 1996.
- [151] D. S. Weiss, R. Kirsner, and W. H. Eaglstein. Electrical stimulation and wound healing. *Archives of Dermatology*, 126(2):222–225, 1990.
- [152] Bart Vanhaesebroeck. Charging the batteries to heal wounds through PI3k. *Nature Chemical Biology*, 2(9):453–455, 2006.
- [153] En-tong Wang and Min Zhao. Regulation of tissue repair and regeneration by electric fields. *Chinese Journal of Traumatology*, 13(1):55–61, 2010.
- [154] R B Borgens, J W Vanable, and L F Jaffe. Bioelectricity and regeneration: large currents leave the stumps of regenerating newt limbs. *Proceedings of the National Academy of Sciences of the United States of America*, 74(10):4528–4532, 1977.
- [155] RB Borgens, E Roederer, and MJ Cohen. Enhanced spinal cord regeneration in lamprey by applied electric fields. *Science*, 213(4508):611–617, 1981.
- [156] Richard Nuccitelli. *Ionic Currents in Development*. Wiley-Liss, 1986. bibtex: nuccitelli_ionic_1986.
- [157] M. E. Mourey Metcalf and Richard B Borgens. Weak applied voltages interfere with amphibian morphogenesis and pattern. *Journal of Experimental Zoology*, 268(4):323–338, 1994.
- [158] Michael Levin. Bioelectromagnetics in morphogenesis. *Bioelectromagnetics*, 24(5):295–315, 2003.
- [159] Li Yao, Lynne Shanley, Colin McCaig, and Min Zhao. Small applied electric fields guide migration of hippocampal neurons. *Journal of Cellular Physiology*, 216(2):527–535, 2008.
- [160] Li Yao, Abhay Pandit, Sheng Yao, and Colin D. McCaig. Electric field-guided neuron migration: A novel approach in neurogenesis. *Tissue Engineering Part B: Reviews*, 17(3):143–153, 2011.
- [161] Mark A. Messerli and David M. Graham. Extracellular Electrical Fields Direct Wound Healing and Regeneration. *The Biological Bulletin*, 221(1):79–92, August 2011.
- [162] Michael Levin. Morphogenetic fields in embryogenesis, regeneration, and cancer: Non-local control of complex patterning. *Biosystems*, 109(3):243–261, September 2012.
- [163] Przemyslaw Borys, Monika Krasowska, Zbigniew J Grzywna, Mustafa B A Djamgoz, and Maria E Mycielska. Lacunarity as a novel measure of cancer cells behavior. *Bio Systems*, 94(3):276–281, 2008.

-
- [164] Mustafa B. A. Djamgoz, Maria Mycielska, Zbigniew Madeja, Scott P. Fraser, and Wlodzimierz Korohoda. Directional movement of rat prostate cancer cells in direct-current electric field involvement of voltage-gated Na⁺ channel activity. *Journal of Cell Science*, 114(14):2697–2705, July 2001.
- [165] Cristina Martin-Granados, Alan R. Prescott, Nele Van Dessel, Aleyde Van Eynde, Miguel Arocena, Izabela P. Klaska, Janina Görnemann, Monique Beullens, Mathieu Bollen, John V. Forrester, and Colin D. McCaig. A role for PP1/NIPP1 in steering migration of human cancer cells. *PLoS ONE*, 7(7):e40769, 2012.
- [166] Richard Nuccitelli, Pamela Nuccitelli, Samdeo Ramlatchan, Richard Sanger, and Peter J.S. Smith. Imaging the electric field associated with mouse and human skin wounds. *Wound Repair and Regeneration*, 16(3):432–441, 2008.
- [167] Dany S. Adams, Kenneth R. Robinson, Takahiro Fukumoto, Shipeng Yuan, R. Craig Albertson, Pamela Yelick, Lindsay Kuo, Megan McSweeney, and Michael Levin. Early, h⁺-v-ATPase-dependent proton flux is necessary for consistent left-right patterning of non-mammalian vertebrates. *Development*, 133(9):1657–1671, 2006.
- [168] Vaibhav P. Pai, Sherry Aw, Tal Shomrat, Joan M. Lemire, and Michael Levin. Transmembrane voltage potential controls embryonic eye patterning in *Xenopus laevis*. *Development*, 139(3):623, 2012.
- [169] M Szatkowski, M Mycielska, R Knowles, A L Kho, and M B Djamgoz. Electrophysiological recordings from the rat prostate gland in vitro: identified single-cell and transepithelial (lumen) potentials. *BJU International*, 86(9):1068–1075, 2000.
- [170] Mark Faupel, Daniel Vanel, Volker Barth, Richard Davies, Ian S. Fentiman, Roland Holland, Jean Louis Lamarque, Virgilio Sacchini, and Ingrid Schreer. Electropotential evaluation as a new technique for diagnosing breast lesions. *European Journal of Radiology*, 24(1):33–38, 1997.
- [171] Scott P Fraser, James K J Diss, Athina-Myrto Chioni, Maria E Mycielska, Huiyan Pan, Rezan F Yamaci, Filippo Pani, Zuzanna Siwy, Monika Krasowska, Zbigniew Grzywna, William J Brackenbury, Dimis Theodorou, Meral Koyutürk, Handan Kaya, Esra Battaloglu, Manuela Tamburo De Bella, Martin J Slade, Robert Tolhurst, Carlo Palmieri, Jie Jiang, David S Latchman, R Charles Coombes, and Mustafa B A Djamgoz. Voltage-gated sodium channel expression and potentiation of human breast cancer metastasis. *Clinical Cancer Research*, 11(15):5381–5389, 2005.
- [172] Bertil Hille. *Ion Channels of Excitable Membranes, Third Edition*. Sinauer Associates, 3rd edition edition edition, 2011.
- [173] Bruce P. Bean. The action potential in mammalian central neurons. *Nature Reviews Neuroscience*, 8(6):451–465, 2007.

- [174] James Julian Bennett Jack, Denis Noble, and Richard W. Tsien. *Electric current flow in excitable cells*. Clarendon Press Oxford, 1975.
- [175] Harry Grundfest. Heterogeneity of excitable membrane: Electrophysiological and pharmacological evidence and some consequences*. *Annals of the New York Academy of Sciences*, 137(2):901–949, 1966.
- [176] Michael W. Reimann, Costas A. Anastassiou, Rodrigo Perin, Sean L. Hill, Henry Markram, and Christof Koch. A biophysically detailed model of neocortical local field potentials predicts the critical role of active membrane currents. *Neuron*, 79(2):375–390, 2013.
- [177] György Buzsáki, Costas A. Anastassiou, and Christof Koch. The origin of extracellular fields and currents —EEG, ECoG, LFP and spikes. *Nature Reviews Neuroscience*, 13(6):407–420, 2012.
- [178] Colin G. Hales and Susan Pockett. The relationship between local field potentials (LFPs) and the electromagnetic fields that give rise to them. *Frontiers in Systems Neuroscience*, 8:233, 2014.
- [179] Richard B Borgens. *Electric fields in vertebrate repair: natural and applied voltages in vertebrate regeneration and healing*. Wiley-Liss, 1989.
- [180] Leslie Alexander Geddes. A short history of the electrical stimulation of excitable tissue. including electrotherapeutic applications. *The Physiologist*, 27(1 Suppl):S1–47, 1984.
- [181] Christine E Pullar. *The physiology of bioelectricity in development, tissue regeneration and cancer*. CRC Press, 2016.
- [182] Orjan G Martinsen and Sverre Grimnes. *Bioimpedance and bioelectricity basics*. Academic press, 2011.
- [183] Barbara Cortese, Ilaria Elena Palamà, Stefania D’Amone, and Giuseppe Gigli. Influence of electrotaxis on cell behaviour. *Integrative Biology*, 9(6):817, 2014.
- [184] Colin D. McCaig, Ann M. Rajnicek, Bing Song, and Min Zhao. Controlling cell behavior electrically: current views and future potential. *Physiol. Rev.*, 85(3):943–978, 2005.
- [185] Entong Wang, Min Zhao, John V. Forrester, and Colin D. McCaig. Bi-directional migration of lens epithelial cells in a physiological electrical field. *Experimental Eye Research*, 76(1):29–37, 2003.
- [186] Min Zhao, Jin Pu, John V Forrester, and Colin D McCaig. Membrane lipids, EGF receptors, and intracellular signals colocalize and are polarized in epithelial cells moving directionally in a physiological electric field. *The FASEB Journal*, 2002.

-
- [187] M Poo. In situ electrophoresis of membrane components. *Annual Review of Biophysics and Bioengineering*, 10:245–276, 1981.
- [188] R Nuccitelli and C A Erickson. Embryonic cell motility can be guided by physiological electric fields. *Experimental Cell Research*, 147(1):195–201, 1983.
- [189] Lionel F Jaffe and Mu-Ming Poo. Neurites grow faster towards the cathode than the anode in a steady field. *Journal of Experimental Zoology*, 209(1):115–127, 1979.
- [190] N. Patel and M. M. Poo. Orientation of neurite growth by extracellular electric fields. *The Journal of Neuroscience*, 2(4):483–496, 1982.
- [191] NB Patel and MM Poo. Perturbation of the direction of neurite growth by pulsed and focal electric fields. *The Journal of Neuroscience*, 4(12):2939–2947, 1984.
- [192] C.D. McCaig, D.W. Allan, L. Erskine, A.M. Rajniecek, and R. Stewart. Growing nerves in an electric field. *Neuroprotocols*, 4(2):134–141, 1994.
- [193] Youngnam Cho and Richard Ben Borgens. Polymer and nano-technology applications for repair and reconstruction of the central nervous system. *Experimental Neurology*, 233(1):126–144, 2012.
- [194] Linjie Pan and Richard Ben Borgens. Strict perpendicular orientation of neural crest-derived neurons in vitro is dependent on an extracellular gradient of voltage. *Journal of Neuroscience Research*, 90(7):1335–1346, 2012.
- [195] Andrew O. Koob, Julia M. Colby, and Richard B. Borgens. Behavioral recovery from traumatic brain injury after membrane reconstruction using polyethylene glycol. *Journal of Biological Engineering*, 2(1):9, 2008.
- [196] Hsieh-Fu Tsai, Ching-Wen Huang, Hui-Fang Chang, Jeremy JW Chen, Chau-Hwang Lee, and Ji-Yen Cheng. Evaluation of egfr and rtk signaling in the electro-taxis of lung adenocarcinoma cells under direct-current electric field stimulation. *PLoS One*, 8(8):e73418, 2013.
- [197] Am Rajniecek, Na Gow, and Cd McCaig. Electric field-induced orientation of rat hippocampal neurones in vitro. *Experimental Physiology*, 77(1):229–232, 1992.
- [198] Ching-Wen Huang, Ji-Yen Cheng, Meng-Hua Yen, and Tai-Horng Young. Electrotaxis of lung cancer cells in a multiple-electric-field chip. *Biosensors and Bioelectronics*, 24(12):3510–3516, August 2009.
- [199] Juana Magdalena, Thomas H Millard, and Laura M Machesky. Microtubule involvement in NIH 3t3 golgi and MTOC polarity establishment. *Journal of Cell Science*, 116:743–756, 2003.
- [200] Jin Pu and Min Zhao. Golgi polarization in a strong electric field. *Journal of Cell Science*, 118(6):1117–1128, 2005.

- [201] Li Yao, Colin D McCaig, and Min Zhao. Electrical signals polarize neuronal organelles, direct neuron migration, and orient cell division. *Hippocampus*, 19(9):855–868, 2009.
- [202] Hsieh-Fu Tsai, Shih-Wei Peng, Chun-Ying Wu, Hui-Fang Chang, and Ji-Yen Cheng. Electrotaxis of oral squamous cell carcinoma cells in a multiple-electric-field chip with uniform flow field. *Biomicrofluidics*, 6(3):34116, 2012.
- [203] Hong Ye, Lin-Ling Huang, Shu-De Chen, and Jian-Jiang Zhong. Pulsed electric field stimulates plant secondary metabolism in suspension cultures of *taxus chinensis*. *Biotechnology and bioengineering*, 88(6):788–795, 2004.
- [204] Masayasu Suzuki, Eiichi Tamiya, Hideaki Matsuoka, Masahito Sugi, and Isao Karube. Electrical stimulation of hybridoma cells producing monoclonal antibody to camp. *Biochimica et Biophysica Acta (BBA)-Molecular Cell Research*, 889(2):149–155, 1986.
- [205] Robert J. Fitzsimmons, Donna D. Strong, Subburaman Mohan, and David J. Baylink. Low-amplitude, low-frequency electric field-stimulated bone cell proliferation may in part be mediated by increased IGF-II release. *Journal of Cellular Physiology*, 150(1):84–89, 1992.
- [206] Eilon D Kirson, Zoya Gurvich, Rosa Schneiderman, Erez Dekel, Aviran Itzhaki, Yoram Wasserman, Rachel Schatzberger, and Yoram Palti. Disruption of cancer cell replication by alternating electric fields. *Cancer research*, 64(9):3288–3295, 2004.
- [207] Kenneth D Swanson, Edwin Lok, and Eric T Wong. An overview of alternating electric fields therapy (novotf therapy) for the treatment of malignant glioma. *Current neurology and neuroscience reports*, 16(1):8, 2016.
- [208] Elijah J Mun, Hani M Babiker, Uri Weinberg, Eilon D Kirson, and Daniel D Von Hoff. Tumor-treating fields: a fourth modality in cancer treatment. *Clinical Cancer Research*, 24(2):266–275, 2018.
- [209] William J Brackenbury and Mustafa B A Djamgoz. Activity-dependent regulation of voltage-gated na⁺ channel expression in mat-LyLu rat prostate cancer cell line. *The Journal of Physiology*, 573:343–356, 2006.
- [210] William J Brackenbury, Mustafa B A Djamgoz, and Lori L Isom. An emerging role for voltage-gated na⁺ channels in cellular migration: regulation of central nervous system development and potentiation of invasive cancers. *The Neuroscientist*, 14(6):571–583, 2008.
- [211] Rustem Onkal and Mustafa B A Djamgoz. Molecular pharmacology of voltage-gated sodium channel expression in metastatic disease: clinical potential of neonatal nav1.5 in breast cancer. *European Journal of Pharmacology*, 625(1):206–219, 2009.

-
- [212] Nurdan Özkucur, Thomas K. Monsees, Srikanth Perike, Hoa Quynh Do, and Richard H. W. Funk. Local Calcium Elevation and Cell Elongation Initiate Guided Motility in Electrically Stimulated Osteoblast-Like Cells. *PLoS ONE*, 4(7):e6131, July 2009.
- [213] Donna R. Trollinger, R. Rivkah Isseroff, and Richard Nuccitelli. Calcium channel blockers inhibit galvanotaxis in human keratinocytes. *J. Cell. Physiol.*, 193(1):1–9, October 2002.
- [214] Richard Nuccitelli and Tanya Smart. Extracellular calcium levels strongly influence neural crest cell galvanotaxis. *The Biological Bulletin*, 176(2):130–135, 1989.
- [215] Srikanth Perike, Nurdan Özkucur, Priyanka Sharma, Wolfgang Staroske, Robert Bläsche, Kathrin Barth, and Richard HW Funk. Phospho-NHE3 forms membrane patches and interacts with beta-actin to sense and maintain constant direction during cell migration. *Experimental Cell Research*, 324(1):13–29, May 2014.
- [216] Dany S. Adams, Alessio Masi, and Michael Levin. H⁺ pump-dependent changes in membrane voltage are an early mechanism necessary and sufficient to induce xenopus tail regeneration. *Development*, 134(7):1323–1335, 2007.
- [217] Souhei Sakata, Md. Israil Hossain, and Yasushi Okamura. Coupling of the phosphatase activity of ci-VSP to its voltage sensor activity over the entire range of voltage sensitivity. *The Journal of Physiology*, 589(11):2687–2705, 2011.
- [218] Hirohide Iwasaki, Yoshimichi Murata, Youngjun Kim, Md. Israil Hossain, Carolyn A. Worby, Jack E. Dixon, Thomas McCormack, Takehiko Sasaki, and Yasushi Okamura. A voltage-sensing phosphatase, ci-VSP, which shares sequence identity with PTEN, dephosphorylates phosphatidylinositol 4,5-bisphosphate. *Proceedings of the National Academy of Sciences*, 105(23):7970–7975, 2008.
- [219] Yoshimichi Murata, Hirohide Iwasaki, Mari Sasaki, Kazuo Inaba, and Yasushi Okamura. Phosphoinositide phosphatase activity coupled to an intrinsic voltage sensor. *Nature*, 435(7046):1239–1243, 2005.
- [220] Lionel F. Jaffe. Electrophoresis along cell membranes. *Nature*, 265(5595):600–602, 1977.
- [221] M Poo and K R Robinson. Electrophoresis of concanavalin a receptors along embryonic muscle cell membrane. *Nature*, 265(5595):602–605, 1977.
- [222] M. Poo, J.W. Lam, N. Orida, and A.W. Chao. Electrophoresis and diffusion in the plane of the cell membrane. *Biophysical Journal*, 26(1):1–21, 1979.
- [223] N Orida and M M Poo. Electrophoretic movement and localisation of acetylcholine receptors in the embryonic muscle cell membrane. *Nature*, 275(5675):31–35, 1978.

- [224] S McLaughlin and M M Poo. The role of electro-osmosis in the electric-field-induced movement of charged macromolecules on the surfaces of cells. *Biophysical Journal*, 34(1):85–93, 1981.
- [225] Erik I Finkelstein, Pen-hsiu Grace Chao, Clark T Hung, and Jeannette Chloë Bulinski. Electric field-induced polarization of charged cell surface proteins does not determine the direction of galvanotaxis. *Cell Motility and the Cytoskeleton*, 64(11):833–846, 2007.
- [226] Chun-Chieh Wang, Yu-Chiu Kao, Pei-Yin Chi, Ching-Wen Huang, Jiunn-Yuan Lin, Chia-Fu Chou, Ji-Yen Cheng, and Chau-Hwang Lee. Asymmetric cancer-cell filopodium growth induced by electric-fields in a microfluidic culture chip. *Lab on a Chip*, 11(4):695, 2011.
- [227] Bo-jian Lin, Shun-hao Tsao, Alex Chen, Shu-Kai Hu, Ling Chao, and Pen-hsiu Grace Chao. Lipid rafts sense and direct electric field-induced migration. *Proceedings of the National Academy of Sciences*, 114(32):8568–8573, 2017.
- [228] Michael R. Cho, Hemant S. Thatte, Raphael C. Lee, and David E. Golan. Integrin-dependent human macrophage migration induced by oscillatory electrical stimulation. *Annals of Biomedical Engineering*, 28(3):234–243, 2000.
- [229] M. J. Brown and L. M. Loew. Electric field-directed fibroblast locomotion involves cell surface molecular reorganization and is calcium independent. *Journal of Cell Biology*, 127(1):117–128, October 1994.
- [230] Francis X Hart. Integrins may serve as mechanical transducers for low-frequency electric fields. *Bioelectromagnetics*, 27(6):505–508, 2006.
- [231] Kan Zhu, Yoko Takada, Kenichi Nakajima, Yaohui Sun, Jianxin Jiang, Yan Zhang, Qunli Zeng, Yoshikazu Takada, and Min Zhao. Expression of integrins to control migration direction of electrotaxis. *The FASEB Journal*, pages fj–201802657R, 2019.
- [232] Li Li, Robert Hartley, Bjoern Reiss, Yaohui Sun, Jin Pu, Dan Wu, Francis Lin, Trung Hoang, Soichiro Yamada, Jianxin Jiang, and Min Zhao. E-cadherin plays an essential role in collective directional migration of large epithelial sheets. *Cellular and molecular life sciences*, 69(16):2779–2789, 2012.
- [233] T. D. Giugni, D. L. Braslau, and H. T. Haigler. Electric field-induced redistribution and postfield relaxation of epidermal growth factor receptors on A431 cells. *Journal of Cell Biology*, 104(5):1291–1297, May 1987.
- [234] Kathy S Fang, Behnom Farboud, Richard Nuccitelli, and R Rivkah Isseroff. Migration of human keratinocytes in electric fields requires growth factors and extracellular calcium. *Journal of Investigate Dermatology*, 111(5):751–756, 1998.

-
- [235] KS Fang, E Ionides, G Oster, R Nuccitelli, and RR Isseroff. Epidermal growth factor receptor relocalization and kinase activity are necessary for directional migration of keratinocytes in DC electric fields. *Journal of Cell Science*, 112(12):1967–1978, 1999.
- [236] Min Zhao, Andrew Dick, John V. Forrester, and Colin D. McCaig. Electric field-directed cell motility involves up-regulated expression and asymmetric redistribution of the epidermal growth factor receptors and is enhanced by fibronectin and laminin. *Molecular Biology of the Cell*, 10(4):1259–1276, 1999.
- [237] Christine E. Pullar, Brian S. Baier, Yoshinobu Kariya, Alan J. Russell, Basil A.J. Horst, M. Peter Marinkovich, and R. Rivkah Isseroff. beta4 integrin and epidermal growth factor coordinately regulate electric field-mediated directional migration via rac1. *Molecular Biology of the Cell*, 17(11):4925–4935, 2006.
- [238] Pinar Uysal-Onganer and Mustafa Ba Djamgoz. Epidermal growth factor potentiates in vitro metastatic behaviour of human prostate cancer PC-3m cells: involvement of voltage-gated sodium channel. *Molecular Cancer*, 6:76, 2007.
- [239] Jin Pu, Colin D. McCaig, Lin Cao, Zhiqiang Zhao, Jeffrey E. Segall, and Min Zhao. EGF receptor signalling is essential for electric-field-directed migration of breast cancer cells. *Journal of Cell Science*, 120(19):3395–3403, 2007.
- [240] Yanning Ding, William J Brackenbury, Pinar U Onganer, Ximena Montano, Louise M Porter, Lucy F Bates, and Mustafa B. A Djamgoz. Epidermal growth factor upregulates motility of mat-LyLu rat prostate cancer cells partially via voltage-gated na⁺ channel activity. *Journal of Cellular Physiology*, 215(1):77–81, 2008.
- [241] Xiaolong Yan, Jing Han, Zhipei Zhang, Jian Wang, Qingshu Cheng, Kunxiang Gao, Yunfeng Ni, and Yunjie Wang. Lung cancer a549 cells migrate directionally in DC electric fields with polarized and activated EGFRs. *Bioelectromagnetics*, 30(1):29–35, 2009.
- [242] Dan Wu, Xiuli Ma, and Francis Lin. DC electric fields direct breast cancer cell migration, induce EGFR polarization, and increase the intracellular level of calcium ions. *Cell Biochemistry and Biophysics*, 67(3):1115–1125, 2013.
- [243] Min Zhao, Huai Bai, Entong Wang, John V. Forrester, and Colin D. McCaig. Electrical stimulation directly induces pre-angiogenic responses in vascular endothelial cells by signaling through VEGF receptors. *Journal of Cell Science*, 117(3):397–405, January 2004.
- [244] Huai Bai, John V Forrester, and Min Zhao. DC electric stimulation upregulates angiogenic factors in endothelial cells through activation of VEGF receptors. *Cytokine*, 55(1):110–115, 2011.
- [245] Zhiqiang Zhao, Lu Qin, Brian Reid, Jin Pu, Takahiko Hara, and Min Zhao. Directing migration of endothelial progenitor cells with applied DC electric fields. *Stem Cell Research*, 8(1):38–48, 2012.

- [246] Lynne J Shanley, Colin D McCaig, John V Forrester, and Min Zhao. Insulin, not leptin, promotes in vitro cell migration to heal monolayer wounds in human corneal epithelium. *Investigative Ophthalmology & Visual Science*, 45(4):1088–1094, 2004.
- [247] Vikki A. McBain, John V. Forrester, and Colin D. McCaig. HGF, MAPK, and a Small Physiological Electric Field Interact during Corneal Epithelial Cell Migration. *Investigative Ophthalmology & Visual Science*, 44(2):540, February 2003.
- [248] P. W. Luther and H. B. Peng. Membrane-related specializations associated with acetylcholine receptor aggregates induced by electric fields. *The Journal of Cell Biology*, 100(1):235–244, 1985.
- [249] M. William Rochlin and H. Benjamin Peng. The influence of AChR clustering stimuli on the formation and maintenance of AChR clusters induced by polycation-coated beads in xenopus muscle cells. *Developmental Biology*, 140(1):27–40, 1990.
- [250] H. B. Peng, L. P. Baker, and Z. Dai. A role of tyrosine phosphorylation in the formation of acetylcholine receptor clusters induced by electric fields in cultured xenopus muscle cells. *The Journal of Cell Biology*, 120(1):197–204, 1993.
- [251] Hailong Luke Zhang and H. Benjamin Peng. Mechanism of Acetylcholine Receptor Cluster Formation Induced by DC Electric Field. *PLoS ONE*, 6(10):e26805, October 2011.
- [252] Min Zhao, Tian Jin, Colin D McCaig, John V Forrester, and Peter N Devreotes. Genetic analysis of the role of g protein-coupled receptor signaling in electrotaxis. *The Journal of Cell Biology*, 157(6):921–928, 2002.
- [253] Deniz Saltukoglu, Julian Gr̄unewald, Nico Strohmeyer, Robert Bensch, Maximilian H. Ulbrich, Olaf Ronneberger, and Matias Simons. Spontaneous and electric field-controlled front-rear polarization of human keratinocytes. *Molecular Biology of the Cell*, 26(24):4373–4386, 2015.
- [254] Christine E Pullar and R Rivkah Isseroff. Cyclic AMP mediates keratinocyte directional migration in an electric field. *Journal of Cell Science*, 118:2023–2034, 2005.
- [255] Christine E. Pullar, Min Zhao, Bing Song, Jin Pu, Brian Reid, Shahed Ghoghawala, Colin McCaig, and R. Rivkah Isseroff. β -adrenergic receptor agonists delay while antagonists accelerate epithelial wound healing: Evidence of an endogenous adrenergic network within the corneal epithelium. *Journal of Cellular Physiology*, 211(1):261–272, 2007.
- [256] Min Zhao, Bing Song, Jin Pu, Teiji Wada, Brian Reid, Guangping Tai, Fei Wang, Aihua Guo, Petr Walczysko, Yu Gu, Takehiko Sasaki, Akira Suzuki, John V. Forrester, Henry R. Bourne, Peter N. Devreotes, Colin D. McCaig, and Josef M. Penninger. Electrical signals control wound healing through phosphatidylinositol-3-OH kinase-gamma and PTEN. *Nature*, 442(7101):457–460, July 2006.

-
- [257] Xiaoting Meng, Miguel Arocena, Josef Penninger, Fred H. Gage, Min Zhao, and Bing Song. PI3k mediated electrotaxis of embryonic and adult neural progenitor cells in the presence of growth factors. *Experimental Neurology*, 227(1):210–217, 2011.
- [258] Ching-Wen Huang, Huai-Yi Chen, Meng-Hua Yen, Jeremy J. W. Chen, Tai-Horng Young, and Ji-Yen Cheng. Gene Expression of Human Lung Cancer Cell Line CL1–5 in Response to a Direct Current Electric Field. *PLoS ONE*, 6(10):e25928, October 2011.
- [259] Heinrich Sauer, Ramona Stanelle, Jürgen Hescheler, and Maria Wartenberg. The DC electrical-field-induced ca^{2+} response and growth stimulation of multicellular tumor spheroids are mediated by ATP release and purinergic receptor stimulation. *Journal of Cell Science*, 115(16):3265–3273, 200.
- [260] Maria Wartenberg, Nina Wirtz, Alexander Grob, Wilhelm Niedermeier, Jürgen Hescheler, Saskia C. Peters, and Heinrich Sauer. Direct current electrical fields induce apoptosis in oral mucosa cancer cells by NADPH oxidase-derived reactive oxygen species. *Bioelectromagnetics*, 29(1):47–54, January 2008.
- [261] Ling Huang, Peter Cormie, Mark A. Messerli, and Kenneth R. Robinson. The involvement of ca^{2+} and integrins in directional responses of zebrafish keratocytes to electric fields. *Journal of Cellular Physiology*, 219(1):162–172, 2009.
- [262] Amy M Palmer, Mark A Messerli, and Kenneth R Robinson. Neuronal galvanotropism is independent of external ca^{2+} entry or internal ca^{2+} gradients. *Journal of Neurobiology*, 45(1):30–38, 2000.
- [263] C E Pullar, R R Isseroff, and R Nuccitelli. Cyclic AMP-dependent protein kinase a plays a role in the directed migration of human keratinocytes in a DC electric field. *Cell Motility and the Cytoskeleton*, 50(4):207–217, 2001.
- [264] C. D. McCaig and P. J. Dover. Raised Cyclic-AMP and a Small Applied Electric Field Influence Differentiation, Shape, and Orientation of Single Myoblasts. *Developmental Biology*, 158(1):172–182, July 1993.
- [265] Qian Liu and Bing Song. Electric field regulated signaling pathways. *The International Journal of Biochemistry & Cell Biology*, 55:264–268, 2014.
- [266] Bing Song, Yu Gu, Jin Pu, Brian Reid, Zhiqiang Zhao, and Min Zhao. Application of direct current electric fields to cells and tissues in vitro and modulation of wound electric field in vivo. *Nature Protocols*, 2(6):1479–1489, June 2007.
- [267] Francis Lin, Connie Minh-Canh Nguyen, Shur-Jen Wang, Wajeeh Saadi, Steven P Gross, and Noo Li Jeon. Neutrophil migration in opposing chemoattractant gradients using microfluidic chemotaxis devices. *Annals of biomedical engineering*, 33(4):475–482, 2005.

- [268] Wajeeh Saadi, Shur-Jen Wang, Francis Lin, and Noo Li Jeon. A parallel-gradient microfluidic chamber for quantitative analysis of breast cancer cell chemotaxis. *Biomedical Microdevices*, 8(2):109–118, 2006.
- [269] C Joanne Wang, Xiong Li, Benjamin Lin, Sangwoo Shim, Guo-li Ming, and Andre Levchenko. A microfluidics-based turning assay reveals complex growth cone responses to integrated gradients of substrate-bound ecm molecules and diffusible guidance cues. *Lab on a Chip*, 8(2):227–237, 2008.
- [270] Kathrin Schumann, Tim Lämmermann, Markus Bruckner, Daniel F Legler, Julien Polleux, Joachim P Spatz, Gerold Schuler, Reinhold Förster, Manfred B Lutz, Lydia Sorokin, et al. Immobilized chemokine fields and soluble chemokine gradients cooperatively shape migration patterns of dendritic cells. *Immunity*, 32(5):703–713, 2010.
- [271] Brendon G Ricart, Beena John, Dooyoung Lee, Christopher A Hunter, and Daniel A Hammer. Dendritic cells distinguish individual chemokine signals through *ccr7* and *cxcr4*. *The Journal of Immunology*, 186(1):53–61, 2011.
- [272] Jing Li, Ling Zhu, Michael Zhang, and Francis Lin. Microfluidic device for studying cell migration in single or co-existing chemical gradients and electric fields. *Biomicrofluidics*, 6(2):024121, 2012.
- [273] Beum Jun Kim, Pimkhuan Hannanta-Anan, Michelle Chau, Yoon Soo Kim, Melody A Swartz, and Mingming Wu. Cooperative roles of *sdf-1 α* and *egf* gradients on tumor cell migration revealed by a robust 3d microfluidic model. *PLoS one*, 8(7):e68422, 2013.
- [274] Sukhyun Song, Hana Han, Ung Hyun Ko, Jaemin Kim, and Jennifer H. Shin. Collaborative effects of electric field and fluid shear stress on fibroblast migration. *Lab on a Chip*, 13(8):1602–1611, March 2013.
- [275] Yu-Chiu Kao, Meng-Hua Hsieh, Chung-Chun Liu, Huei-Jyuan Pan, Wei-Yu Liao, Ji-Yen Cheng, Po-Ling Kuo, and Chau-Hwang Lee. Modulating chemotaxis of lung cancer cells by using electric fields in a microfluidic device. *Biomicrofluidics*, 8(2):024107, March 2014.
- [276] Chia-Wen Chang, Yung-Ju Cheng, Melissa Tu, Ying-Hua Chen, Chien-Chung Peng, Wei-Hao Liao, and Yi-Chung Tung. A polydimethylsiloxane–polycarbonate hybrid microfluidic device capable of generating perpendicular chemical and oxygen gradients for cell culture studies. *Lab on a Chip*, 14(19):3762–3772, 2014.
- [277] Gaurav Jain, Andrew J Ford, and Padmavathy Rajagopalan. Opposing rigidity-protein gradients reverse fibroblast durotaxis. *ACS Biomaterials Science & Engineering*, 1(8):621–631, 2015.
- [278] Sebastien GM Uzel, Ovid C Amadi, Taylor M Pearl, Richard T Lee, Peter TC So, and Roger D Kamm. Simultaneous or sequential orthogonal gradient formation in a 3d cell culture microfluidic platform. *Small*, 12(5):612–622, 2016.

-
- [279] SF Moussavi-Harami, HM Pezzi, A Huttenlocher, and DJ Beebe. Simple microfluidic device for studying chemotaxis in response to dual gradients. *Biomedical microdevices*, 17(3):51, 2015.
- [280] Devrim Kilinc, Jefrem Schwab, Stefano Rampini, Oshoke W. Ikpekha, Ashwin Thampi, Agata Blasiak, Peng Li, Robert Schwamborn, Walter Kolch, David Matallanas, and Gil U. Lee. A microfluidic dual gradient generator for conducting cell-based drug combination assays. *Integrative Biology*, 8(1):39–49, 2016.
- [281] Wenming Liu, Kai Han, Meilin Sun, Zhongchao Huang, and Jinyi Wang. A microfluidic model with hydrogel barriers for the construction of shear-free attractive and repulsive cue gradients. *Advanced Materials Technologies*, 4(2):1800434, 2019.
- [282] Shawn Mishra, Juan S Peña, Stephen Redenti, and Maribel Vazquez. A novel electro-chemotactic approach to impact the directional migration of transplantable retinal progenitor cells. *Experimental eye research*, 2019.
- [283] Jing Sun, Michael D Masterman-Smith, Nicholas A Graham, Jing Jiao, Jack Mottahedeh, Dan R Laks, Minori Ohashi, Jason DeJesus, Ken-ichiro Kamei, Ki-Bum Lee, Hao Wang, Zeta T F Yu, Yi-Tsung Lu, Shuang Hou, Keyu Li, Max Liu, Nangang Zhang, Shutao Wang, Brigitte Angenieux, Eduard Panosyan, Eric R Samuels, Jun Park, Dirk Williams, Vera Konkankit, David Nathanson, R Michael van Dam, Michael E Phelps, Hong Wu, Linda M Liau, Paul S Mischel, Jorge A Lazareff, Harley I Kornblum, William H Yong, Thomas G Graeber, and Hsian-Rong Tseng. A microfluidic platform for systems pathology: multiparameter single-cell signaling measurements of clinical brain tumor specimens. *Cancer research*, 70:6128–6138, August 2010.
- [284] Huilin Shao, Jaehoon Chung, Leonora Balaj, Alain Charest, Darell D Bigner, Bob S Carter, Fred H Hochberg, Xandra O Breakefield, Ralph Weissleder, and Hakho Lee. Protein typing of circulating microvesicles allows real-time monitoring of glioblastoma therapy. *Nature medicine*, 18:1835–1840, December 2012.
- [285] Wenming Liu, Peng Sun, Linyan Yang, Jinfeng Wang, Li Li, and Jinyi Wang. Assay of glioma cell responses to an anticancer drug in a cell-based microfluidic device. *Microfluidics and Nanofluidics*, 9(4):717–725, 2010.
- [286] Yantao Fan, Duong Thanh Nguyen, Yasemin Akay, Feng Xu, and Metin Akay. Engineering a brain cancer chip for high-throughput drug screening. *Scientific Reports*, 6:25062, 2016.
- [287] Loan Bui, Alissa Hendricks, Jamie Wright, Cheng-Jen Chuong, Digant Davé, Robert Bachoo, and Young-Tae Kim. Brain tumor genetic modification yields increased resistance to paclitaxel in physical confinement. *Scientific reports*, 6:26134, May 2016.
- [288] Daniel Gallego-Perez, Natalia Higuera-Castro, Lisa Denning, Jessica DeJesus, Kirstin Dahl, Atom Sarkar, and Derek J. Hansford. Microfabricated mimics of

- in vivo structural cues for the study of guided tumor cell migration. *Lab Chip*, 12:4424–4432, 2012.
- [289] Yuan Wan, Deepika Tamuly, Peter B Allen, Young-Tae Kim, Robert Bachoo, Andrew D Ellington, and Samir M Iqbal. Proliferation and migration of tumor cells in tapered channels. *Biomedical microdevices*, 15:635–643, August 2013.
- [290] Jose M. Ayuso, Haneen A. Basheer, Rosa Monge, Pablo Sánchez-Álvarez, Manuel Doblaré, Steven D. Shnyder, Victoria Vinader, Kamyar Afarinkia, Luis J. Fernández, and Ignacio Ochoa. Study of the chemotactic response of multicellular spheroids in a microfluidic device. *PLOS ONE*, 10(10):1–16, 2015.
- [291] Andrew Rape, Badriprasad Ananthanarayanan, and Sanjay Kumar. Engineering strategies to mimic the glioblastoma microenvironment. *Advanced drug delivery reviews*, 79-80:172–183, December 2014.
- [292] Fei Li, Tunan Chen, Shengli Hu, Jiangkai Lin, Rong Hu, and Hua Feng. Superoxide Mediates Direct Current Electric Field-Induced Directional Migration of Glioma Cells through the Activation of AKT and ERK. *PLOS ONE*, 8(4):e61195, April 2013.
- [293] Yu-Ja Huang, Gwendolyn Hoffmann, Benjamin Wheeler, Paula Schiapparelli, Alfredo Quinones-Hinojosa, and Peter Searson. Cellular microenvironment modulates the galvanotaxis of brain tumor initiating cells. *Scientific Reports*, 6:21583, February 2016.
- [294] Yu-Ja Huang, Paula Schiapparelli, Kristen Kozielski, Jordan Green, Emily Lavell, Hugo Guerrero-Cazares, Alfredo Quinones-Hinojosa, and Peter Searson. Electrophoresis of cell membrane heparan sulfate regulates galvanotaxis in glial cells. *Journal of Cell Science*, page jcs.203752, January 2017.
- [295] Johnathan G Lyon, Sheridan L Carroll, Nassir Mokarram, and Ravi V Belamkonda. electrotaxis of glioblastoma and medulloblastoma spheroidal aggregates. *Scientific Reports*, 9(1):5309, 2019.
- [296] Chun Yang, Lei Wang, Weiji Weng, Shen Wang, Yuxiao Ma, Qing Mao, Guoyi Gao, Rui Chen, and Junfeng Feng. Steered migration and changed morphology of human astrocytes by an applied electric field. *Experimental Cell Research*, 374(2):282–289, January 2019.
- [297] Robart Babona-Pilipos, Ilia A. Droujinine, Milos R. Popovic, and Cindi M. Moreshead. Adult Subependymal Neural Precursors, but Not Differentiated Cells, Undergo Rapid Cathodal Migration in the Presence of Direct Current Electric Fields. *PLoS ONE*, 6(8):e23808, August 2011.
- [298] Matthew L. Baer, Scott C. Henderson, and Raymond J. Colello. Elucidating the Role of Injury-Induced Electric Fields (EFs) in Regulating the Astrocytic Response to Injury in the Mammalian Central Nervous System. *PLoS ONE*, 10(11):e0142740, November 2015.

-
- [299] Yongchao Li, Xinkun Wang, and Li Yao. Directional migration and transcriptional analysis of oligodendrocyte precursors subjected to stimulation of electrical signal. *American Journal of Physiology-Cell Physiology*, 309(8):C532–C540, 2015.
- [300] Bangfu Zhu, Matthew Nicholls, Yu Gu, Gaofeng Zhang, Chao Zhao, Robin Franklin, and Bing Song. Electric signals regulate the directional migration of oligodendrocyte progenitor cells (opcs) via $\beta 1$ integrin. *International journal of molecular sciences*, 17(11):1948, 2016.
- [301] Mina J. Bissell and Derek Radisky. Putting tumours in context. *Nature Reviews Cancer*, 1(1):46–54, October 2001.
- [302] Caitriona Holohan, Sandra Van Schaeybroeck, Daniel B. Longley, and Patrick G. Johnston. Cancer drug resistance: an evolving paradigm. *Nature Reviews Cancer*, 13:714, September 2013.
- [303] Michael M. Gottesman. Mechanisms of cancer drug resistance. *Annual Review of Medicine*, 53(1):615–627, 2002.
- [304] Hiba Zahreddine and Katherine Borden. Mechanisms and insights into drug resistance in cancer. *Frontiers in Pharmacology*, 4:28, 2013.
- [305] Fei Chen, Xueqian Zhuang, Liangyu Lin, Pengfei Yu, Ying Wang, Yufang Shi, Guohong Hu, and Yu Sun. New horizons in tumor microenvironment biology: challenges and opportunities. *BMC Medicine*, 13:45, 2015.
- [306] Nor Eddine Sounni and Agnès Noel. Targeting the tumor microenvironment for cancer therapy. *Clinical Chemistry*, 59(1):85–93, 2013.
- [307] Madeleine J Oudin and Valerie M Weaver. Physical and chemical gradients in the tumor microenvironment regulate tumor cell invasion, migration, and metastasis. In *Cold Spring Harbor symposia on quantitative biology*, volume 81, pages 189–205. Cold Spring Harbor Laboratory Press, 2016.
- [308] Andrea Pavesi, Giulia Adriani, Andy Tay, Majid Ebrahimi Warkiani, Wei Hseun Yeap, Siew Cheng Wong, and Roger D. Kamm. Engineering a 3d microfluidic culture platform for tumor-treating field application. *Scientific Reports*, 6:26584, 2016.
- [309] Michael Mak, Fabian Spill, Roger D. Kamm, and Muhammad H. Zaman. Single-cell migration in complex microenvironments: Mechanics and signaling dynamics. *Journal of Biomechanical Engineering*, 138(2):021004–021004, 2016.
- [310] M S Ferry, I A Razinkov, and J Hasty. Microfluidics for synthetic biology: from design to execution. *Methods in enzymology*, 497:295–372, 2011.
- [311] Howard A. Stone. *Introduction to Fluid Dynamics for Microfluidic Flows*, chapter 1, pages 5–30. Springer US, Boston, MA, 2007.

- [312] Kendra Sharp, Ronald Adrian, Juan Santiago, and Joshua Molho. Liquid flows in microchannels. In Mohamed Gad-el Hak, editor, *The MEMS Handbook*, volume 20013566. CRC Press, 2001.
- [313] Sungyoung Choi, Myung Gwon Lee, and Je-Kyun Park. Microfluidic parallel circuit for measurement of hydraulic resistance. *Biomicrofluidics*, 4(3), 2010.
- [314] Kwang W. Oh, Kangsun Lee, Byungwook Ahn, and Edward P. Furlani. Design of pressure-driven microfluidic networks using electric circuit analogy. *Lab on a Chip*, 12(3):515–545, 2012.
- [315] Bruce Gale, Alexander Jafek, Christopher Lambert, Brady Goenner, Hossein Moghimifam, Ugochukwu Nze, and Suraj Kamarapu. A review of current methods in microfluidic device fabrication and future commercialization prospects. *Inventions*, 3(3):60, 2018.
- [316] Sheng-Shian Li and Chao-Min Cheng. Analogy among microfluidics, micromechanics, and microelectronics. *Lab on a chip*, 13:3782–3788, October 2013.
- [317] Ramesh K Shah and Alexander Louis London. *Laminar flow forced convection in ducts: a source book for compact heat exchanger analytical data*. Academic press, 1978.
- [318] Ansgar Waldbaur, Holger Rapp, Kerstin Lange, and Bastian E. Rapp. Let there be chip—towards rapid prototyping of microfluidic devices: one-step manufacturing processes. *Analytical Methods*, 3(12):2681–2716, 2011.
- [319] Kangning Ren, Jianhua Zhou, and Hongkai Wu. Materials for microfluidic chip fabrication. *Accounts of chemical research*, 46(11):2396–2406, November 2013.
- [320] Santeri Tuomikoski and Sami Franssila. Free-standing su-8 microfluidic chips by adhesive bonding and release etching. *Sensors and Actuators A: Physical*, 120(2):408–415, 2005.
- [321] William H Grover, Marcio G von Muhlen, and Scott R Manalis. Teflon films for chemically-inert microfluidic valves and pumps. *Lab on a Chip*, 8(6):913–918, 2008.
- [322] Kangning Ren, Wen Dai, Jianhua Zhou, Jing Su, and Hongkai Wu. Whole-teflon microfluidic chips. *Proceedings of the National Academy of Sciences*, 108(20):8162–8166, 2011.
- [323] Younan Xia and George M. Whitesides. Soft lithography. *Angewandte Chemie International Edition*, 37(5):550–575, 1998.
- [324] Marc A Unger, Hou-Pu Chou, Todd Thorsen, Axel Scherer, and Stephen R Quake. Monolithic microfabricated valves and pumps by multilayer soft lithography. *Science*, 288(5463):113–116, 2000.

-
- [325] George M Whitesides, Emanuele Ostuni, Shuichi Takayama, Xingyu Jiang, and Donald E Ingber. Soft lithography in biology and biochemistry. *Annual review of biomedical engineering*, 3(1):335–373, 2001.
- [326] Dong Qin, Younan Xia, and George M Whitesides. Soft lithography for micro-and nanoscale patterning. *Nature protocols*, 5(3):491, 2010.
- [327] Todd Thorsen, Sebastian J Maerkl, and Stephen R Quake. Microfluidic large-scale integration. *Science*, 298(5593):580–584, 2002.
- [328] Kwang W. Oh and Chong H. Ahn. A review of microvalves. *Journal of Micromechanics and Microengineering*, 16(5):R13, 2006.
- [329] Geeta Mehta, Khamir Mehta, Dhruv Sud, Jonathan W. Song, Tommaso Bersano-Begey, Nobuyuki Futai, Yun Seok Heo, Mary-Ann Mycek, Jennifer J. Linderman, and Shuichi Takayama. Quantitative measurement and control of oxygen levels in microfluidic poly(dimethylsiloxane) bioreactors during cell culture. *Biomedical Microdevices*, 9(2):123–134, Apr 2007.
- [330] Micha Adler, Mark Polinkovsky, Edgar Gutierrez, and Alex Groisman. Generation of oxygen gradients with arbitrary shapes in a microfluidic device. *Lab on a Chip*, 10:388–391, 2010.
- [331] Joe F. Lo, Elly Sinkala, and David T. Eddington. Oxygen gradients for open well cellular cultures via microfluidic substrates. *Lab on a Chip*, 10(18):2394–2401, 2010.
- [332] Sebastian J Maerkl and Stephen R Quake. A systems approach to measuring the binding energy landscapes of transcription factors. *Science*, 315(5809):233–237, 2007.
- [333] Carl Fredrik Carlborg, Tommy Haraldsson, Kim Öberg, Michael Malkoch, and Wouter van der Wijngaart. Beyond pdms: off-stoichiometry thiol-ene (oste) based soft lithography for rapid prototyping of microfluidic devices. *Lab on a Chip*, 11(18):3136–3147, 2011.
- [334] Ji-Yen Cheng, Cheng-Wey Wei, Kai-Hsiung Hsu, and Tai-Horng Young. Direct-write laser micromachining and universal surface modification of pmma for device development. *Sensors and Actuators B: Chemical*, 99(1):186–196, 2004.
- [335] David J. Guckenberger, Theodorus E. de Groot, Alwin M. D. Wan, David J. Beebe, and Edmond W. K. Young. Micromilling: a method for ultra-rapid prototyping of plastic microfluidic devices. *Lab on a Chip*, 15(11):2364–2378, 2015.
- [336] Ke Liu and Z. Hugh Fan. Thermoplastic microfluidic devices and their applications in protein and DNA analysis. *Analyst*, 136(7):1288–1297, 2011.
- [337] Holger Becker and Claudia Gärtner. Polymer microfabrication methods for microfluidic analytical applications. *Electrophoresis*, 21(1):12–26, 2000.

- [338] Ting-Fu Hong, Wei-Jhong Ju, Ming-Chang Wu, Chang-Hsien Tai, Chien-Hsiung Tsai, and Lung-Ming Fu. Rapid prototyping of pmma microfluidic chips utilizing a co2 laser. *Microfluidics and Nanofluidics*, 9:1125–1133, 2010.
- [339] Justin S. Mecomber, Douglas Hurd, and Patrick A. Limbach. Enhanced machining of micron-scale features in microchip molding masters by CNC milling. *International Journal of Machine Tools and Manufacture*, 45(12):1542–1550, 2005.
- [340] Jagannathan Narasimhan and Ian Papautsky. Polymer embossing tools for rapid prototyping of plastic microfluidic devices. *Journal of Micromechanics and Microengineering*, 14:96–103, 2004.
- [341] Jessie S. Jeon, Seok Chung, Roger D. Kamm, and Joseph L. Charest. Hot embossing for fabrication of a microfluidic 3d cell culture platform. *Biomedical Microdevices*, 13(2):325–333, 2010.
- [342] Usama M. Attia, Silvia Marson, and Jeffrey R. Alcock. Micro-injection moulding of polymer microfluidic devices. *Microfluidics and Nanofluidics*, 7(1):1, 2009.
- [343] Ulri N. Lee, Xiaojing Su, David J. Guckenberger, Ashley M. Dostie, Tianzi Zhang, Erwin Berthier, and Ashleigh B. Theberge. Fundamentals of rapid injection molding for microfluidic cell-based assays. *Lab on a Chip*, 18(3):496–504, 2018.
- [344] Linfa Peng, Yujun Deng, Peiyun Yi, and Xinmin Lai. Micro hot embossing of thermoplastic polymers: a review. *Journal of Micromechanics and Microengineering*, 24(1):013001, 2013.
- [345] Elif Gencturk, Senol Mutlu, and Kutlu O. Ulgen. Advances in microfluidic devices made from thermoplastics used in cell biology and analyses. *Biomicrofluidics*, 11(5):051502, 2017.
- [346] Holger Becker and Claudia Gärtner. Polymer microfabrication technologies for microfluidic systems. *Analytical and bioanalytical chemistry*, 390(1):89–111, 2008.
- [347] Muhammad Pervej Jahan, Asma Perveen, and Ann M Rumsey. A review on the conventional, non-conventional, and hybrid micromachining of glass. *Machining Science and Technology*, 23(2):264–338, 2019.
- [348] Tao Wang, Jing Chen, Tianfeng Zhou, and Lu Song. Fabricating microstructures on glass for microfluidic chips by glass molding process. *Micromachines*, 9(6):269, 2018.
- [349] Jens Gottmann, Martin Hermans, Nikolai Repiev, and Jürgen Ortmann. Selective laser-induced etching of 3d precision quartz glass components for microfluidic applications—up-scaling of complexity and speed. *Micromachines*, 8(4):110, 2017.
- [350] Dirk Wortmann, Jens Gottmann, Nelli Brandt, and Herbert Horn-Solle. Micro- and nanostructures inside sapphire by fs-laser irradiation and selective etching. *Optics Express*, 16(3):1517–1522, 2008.

-
- [351] Noa Burshtein, San To Chan, Kazumi Toda-Peters, Amy Q Shen, and Simon J Haward. 3d-printed glass microfluidics for fluid dynamics and rheology. *Current opinion in colloid & interface science*, 2019.
- [352] Frederik Kotz, Norbert Schneider, Andreas Striegel, Andre Wolfschläger, Nico Keller, Matthias Worgull, Werner Bauer, Dieter Schild, Marcel Milich, Christian Greiner, et al. Glassomer—processing fused silica glass like a polymer. *Advanced Materials*, 30(22):1707100, 2018.
- [353] Frederik Kotz, Patrick Risch, Karl Arnold, Semih Sevim, Josep Puigmartí-Luis, Alexander Quick, Michael Thiel, Andrei Hrynevich, Paul D Dalton, Dorothea Helmer, et al. Fabrication of arbitrary three-dimensional suspended hollow microstructures in transparent fused silica glass. *Nature communications*, 10(1):1439, 2019.
- [354] K Zimmer and R Böhme. Laser-induced backside wet etching of transparent materials with organic and metallic absorbers. *Laser Chemistry*, 2008, 2008.
- [355] Hiroyuki Niino. Progress in laser-induced backside wet etching. In *Optical Fabrication and Testing*, page OWC1. Optical Society of America, 2008.
- [356] Ji-Yen Cheng, Mansoureh Z Mousavi, Chun-Ying Wu, and Hsieh-Fu Tsai. Blue light plasma emission during libwe using 532 nm q-switched nanosecond laser. *Journal of Laser Micro Nanoengineering*, 7(1):87, 2012.
- [357] Ciprian Iliescu, Hayden Taylor, Marioara Avram, Jianmin Miao, and Sami Franssila. A practical guide for the fabrication of microfluidic devices using glass and silicon. *Biomicrofluidics*, 6(1):016505, 2012.
- [358] Henk Wensink, Johan W Berenschot, Henri V Jansen, and Miko C Elwenspoek. High resolution powder blast micromachining. In *Proceedings IEEE Thirteenth Annual International Conference on Micro Electro Mechanical Systems (Cat. No. 00CH36308)*, pages 769–774. IEEE, 2000.
- [359] Chee Meng Benjamin Ho, Sum Huan Ng, King Ho Holden Li, and Yong-Jin Yoon. 3d printed microfluidics for biological applications. *Lab on a Chip*, 15(18):3627–3637, 2015.
- [360] Anthony K. Au, Wilson Huynh, Lisa F. Horowitz, and Albert Folch. 3d-printed microfluidics. *Angew. Chem. Int. Ed.*, 55(12):3862–3881, 2016.
- [361] Reza Amin, Stephanie Knowlton, Alexander Hart, Bekir Yenilmez, Fariba Ghaderinezhad, Sara Katebifar, Michael Messina, Ali Khademhosseini, and Savas Tasoglu. 3d-printed microfluidic devices. *Biofabrication*, 8(2):022001, 2016.
- [362] Sidra Waheed, Joan M. Cabot, Niall P. Macdonald, Trevor Lewis, Rosanne M. Guijt, Brett Paull, and Michael C. Breadmore. 3d printed microfluidic devices: enablers and barriers. *Lab on a Chip*, 16:1993–2013, 2016.

- [363] Chengpeng Chen, Benjamin T Mehl, Akash S Munshi, Alexandra D Townsend, Dana M Spence, and R Scott Martin. 3d-printed microfluidic devices: fabrication, advantages and limitations—a mini review. *Analytical Methods*, 8(31):6005–6012, 2016.
- [364] Ryan D. Sochol, Eric Sweet, Casey C. Glick, Sung-Yueh Wu, Chen Yang, Michael Restaino, and Liwei Lin. 3d printed microfluidics and microelectronics. *Microelectronic Engineering*, 189:52 – 68, 2018.
- [365] Valentin Romanov, Raheel Samuel, Marzieh Chaharlang, Alexander R Jafek, Adam Frost, and Bruce K Gale. Fdm 3d printing of high-pressure, heat-resistant, transparent microfluidic devices. *Analytical chemistry*, 90(17):10450–10456, 2018.
- [366] Tobias Dahlberg, Tim Stangner, Hanqing Zhang, Krister Wiklund, Petter Lundberg, Ludvig Edman, and Magnus Andersson. 3d printed water-soluble scaffolds for rapid production of pdms micro-fluidic flow chambers. *Scientific reports*, 8(1):3372, 2018.
- [367] Nirveek Bhattacharjee, Cesar Parra-Cabrera, Yong Tae Kim, Alexandra P Kuo, and Albert Folch. Desktop-stereolithography 3d-printing of a poly (dimethylsiloxane)-based material with sylgard-184 properties. *Advanced Materials*, 30(22):1800001, 2018.
- [368] Carl K Fredrickson and Z Hugh Fan. Macro-to-micro interfaces for microfluidic devices. *Lab on a Chip*, 4(6):526–533, 2004.
- [369] Yuksel Temiz, Robert D Lovchik, Govind V Kaigala, and Emmanuel Delamarche. Lab-on-a-chip devices: How to close and plug the lab? *Microelectronic Engineering*, 132:156–175, 2015.
- [370] Zhen Yang and Ryutaro Maeda. A world-to-chip socket for microfluidic prototype development. *Electrophoresis*, 23(20):3474–3478, 2002.
- [371] Kwang W Oh, Chinsung Park, Kak Namkoong, Jintae Kim, Kyeong-Sik Ock, Suhyeon Kim, Young-A Kim, Yoon-Kyoung Cho, and Christopher Ko. World-to-chip microfluidic interface with built-in valves for multichamber chip-based pcr assays. *Lab on a Chip*, 5(8):845–850, 2005.
- [372] Elisabeth Wilhelm, Christiane Neumann, Thomas Dутtenhofer, Leonardo Pires, and Bastian E Rapp. Connecting microfluidic chips using a chemically inert, reversible, multichannel chip-to-world-interface. *Lab on a Chip*, 13(22):4343–4351, 2013.
- [373] Gregory A Cooksey, Anne L Plant, and Javier Atencia. A vacuum manifold for rapid world-to-chip connectivity of complex pdms microdevices. *Lab on a Chip*, 9(9):1298–1300, 2009.
- [374] Javier Atencia, Gregory A Cooksey, Andreas Jahn, Justin M Zook, Wyatt N Vreeland, and Laurie E Locascio. Magnetic connectors for microfluidic applications. *Lab on a Chip*, 10(2):246–249, 2010.

-
- [375] Adina Scott, Anthony K Au, Elise Vinckenbosch, and Albert Folch. A microfluidic d-subminiature connector. *Lab on a chip*, 13(11):2036–2039, 2013.
- [376] OH Paydar, CN Paredes, Y Hwang, J Paz, NB Shah, and RN Candler. Characterization of 3d-printed microfluidic chip interconnects with integrated o-rings. *Sensors and Actuators A: Physical*, 205:199–203, 2014.
- [377] Michael B Dentry, James R Friend, and Leslie Y Yeo. Continuous flow actuation between external reservoirs in small-scale devices driven by surface acoustic waves. *Lab on a Chip*, 14(4):750–758, 2014.
- [378] Sander van den Driesche, Frieder Lucklum, Frank Bunge, and Michael Vellekoop. 3d printing solutions for microfluidic chip-to-world connections. *Micromachines*, 9(2):71, 2018.
- [379] Hsieh-Fu Tsai, Ji-Yen Cheng, Hui-Fang Chang, Tadashi Yamamoto, and Amy Q Shen. Uniform electric field generation in circular multi-well culture plates using polymeric inserts. *Scientific reports*, 6:26222, May 2016.
- [380] Shantanu Bhattacharya, Arindom Datta, Jordan M Berg, and Shubhra Gangopadhyay. Studies on surface wettability of poly (dimethyl) siloxane (pdms) and glass under oxygen-plasma treatment and correlation with bond strength. *Journal of microelectromechanical systems*, 14(3):590–597, 2005.
- [381] Takatoki Yamamoto. Study on 172-nm vacuum ultraviolet light surface modifications of polydimethylsiloxane for micro/nanofluidic applications. *Surface and Interface Analysis*, 43(9):1271–1276, 2011.
- [382] Takatoki Yamamoto. Solid-state bonding of silicone elastomer to glass by vacuum oxygen plasma, atmospheric plasma, and vacuum ultraviolet light treatment. *Surface and Interface Analysis*, 45(4):817–822, 2013.
- [383] Kathryn Haubert, Tracy Drier, and David Beebe. Pdms bonding by means of a portable, low-cost corona system. *Lab on a Chip*, 6(12):1548–1549, 2006.
- [384] Peder Skafte-Pedersen, Christopher G Sip, Albert Folch, and Martin Dufva. Modular microfluidic systems using reversibly attached pdms fluid control modules. *Journal of Micromechanics and Microengineering*, 23(5):055011, 2013.
- [385] Vinay V Abhyankar, Meiye Wu, Chung-Yan Koh, and Anson V Hatch. A reversibly sealed, easy access, modular (seam) microfluidic architecture to establish in vitro tissue interfaces. *PloS one*, 11(5):e0156341, 2016.
- [386] Ulrich Y Schaff, Malcolm MQ Xing, Kathleen K Lin, Ning Pan, Noo Li Jeon, and Scott I Simon. Vascular mimetics based on microfluidics for imaging the leukocyte–endothelial inflammatory response. *Lab on a chip*, 7(4):448–456, 2007.
- [387] Javier Atencia, Jayne Morrow, and Laurie E Locascio. The microfluidic palette: a diffusive gradient generator with spatio-temporal control. *Lab on a Chip*, 9(18):2707–2714, 2009.

- [388] Irmeli Barkefors, Sara Thorslund, Fredrik Nikolajeff, and Johan Kreuger. A fluidic device to study directional angiogenesis in complex tissue and organ culture models. *Lab on a Chip*, 9(4):529–535, 2009.
- [389] Sebastien GM Uzel, Randall J Platt, Vidya Subramanian, Taylor M Pearl, Christopher J Rowlands, Vincent Chan, Laurie A Boyer, Peter TC So, and Roger D Kamm. Microfluidic device for the formation of optically excitable, three-dimensional, compartmentalized motor units. *Science advances*, 2(8):e1501429, August 2016.
- [390] Hongkai Wu, Bo Huang, and Richard N Zare. Construction of microfluidic chips using polydimethylsiloxane for adhesive bonding. *Lab on a Chip*, 5(12):1393–1398, 2005.
- [391] Mark A Eddings, Michael A Johnson, and Bruce K Gale. Determining the optimal pdms–pdms bonding technique for microfluidic devices. *Journal of Micromechanics and Microengineering*, 18(6):067001, 2008.
- [392] Ok Chan Jeong, Sin Wook Park, Sang Sik Yang, and James Jungho Pak. Fabrication of a peristaltic pdms micropump. *Sensors and Actuators A: Physical*, 123:453–458, 2005.
- [393] Andre Lai, Nicolas Altemose, Jonathan A White, and Aaron M Streets. On-ratio pdms bonding for multilayer microfluidic device fabrication. *Journal of Micromechanics and Microengineering*, 29(10):107001, 2019.
- [394] Jungkyu Kim, Rajesh Surapaneni, and Bruce K Gale. Rapid prototyping of microfluidic systems using a pdms/polymer tape composite. *Lab on a Chip*, 9(9):1290–1293, 2009.
- [395] C Shea Thompson and Adam R Abate. Adhesive-based bonding technique for pdms microfluidic devices. *Lab on a Chip*, 13(4):632–635, 2013.
- [396] José Antonio Jofre-Reche, Jérôme Pulpytel, Farzaneh Arefi-Khonsari, and José Miguel Martín-Martínez. Increased adhesion of polydimethylsiloxane (pdms) to acrylic adhesive tape for medical use by surface treatment with an atmospheric pressure rotating plasma jet. *Journal of Physics D: Applied Physics*, 49(33):334001, 2016.
- [397] Carl Fredrik Carlborg, Kristinn Björgvin Gylfason, Andrzej Kaźmierczak, Fabian Dortu, MJ Bañuls Polo, A Maquieira Catala, Gerhard M Kresbach, Hans Sohlström, Thomas Moh, Laurent Vivien, et al. A packaged optical slot-waveguide ring resonator sensor array for multiplex label-free assays in labs-on-chips. *Lab on a Chip*, 10(3):281–290, 2010.
- [398] Hsieh-Fu Tsai, Kazumi Toda-Peters, and Amy Q Shen. Glioblastoma adhesion in a quick-fit hybrid microdevice. *Biomedical microdevices*, 21(2):30, 2019.

-
- [399] J. Waynelovich, Da'Kandryia Peters, P. Salamon, A.M. Segall, and Nicholas Sam-soon. Facile and plasma-free bonding of pdms. Technical report, San Diego State University, 2012.
- [400] ME Vlachopoulou, A Tserepi, P Pavli, P Argitis, M Sanopoulou, and K Misiakos. A low temperature surface modification assisted method for bonding plastic substrates. *Journal of Micromechanics and Microengineering*, 19(1):015007, 2008.
- [401] Kevin S Lee and Rajeev J Ram. Plastic-pdms bonding for high pressure hydrolytically stable active microfluidics. *Lab on a Chip*, 9(11):1618–1624, 2009.
- [402] Kangil Kim, Sin Wook Park, and Sang Sik Yang. The optimization of pdms-pmma bonding process using silane primer. *BioChip Journal*, 4(2):148–154, Jun 2010.
- [403] Hsih Yin Tan, Weng Keong Loke, and Nam-Trung Nguyen. A reliable method for bonding polydimethylsiloxane (pdms) to polymethylmethacrylate (pmma) and its application in micropumps. *Sensors and Actuators B: Chemical*, 151(1):133 – 139, 2010.
- [404] Pan Gu, Ke Liu, Hong Chen, Toshikazu Nishida, and Z. Hugh Fan. Chemical-assisted bonding of thermoplastics/elastomer for fabricating microfluidic valves. *Anal. Chem.*, 83(1):446–452, January 2011.
- [405] Vijaya Sunkara, Dong-Kyu Park, Hyundoo Hwang, Rattikan Chantiwas, Steven A Soper, and Yoon-Kyoung Cho. Simple room temperature bonding of thermoplastics and poly(dimethylsiloxane). *Lab on a chip*, 11:962–965, March 2011.
- [406] Bi-Yi Xu, Xiao-Na Yan, Jing-Juan Xu, and Hong-Yuan Chen. One step high quality poly(dimethylsiloxane)-hydrocarbon plastics bonding. *Biomicrofluidics*, 6:16507–165078, March 2012.
- [407] S Y Ahn and N Y Lee. Solvent-free thermoplastic-poly(dimethylsiloxane) bonding mediated by UV irradiation followed by gas-phase chemical deposition of an adhesion linker. *Journal of Micromechanics and Microengineering*, 25(7):075007, jun 2015.
- [408] Wenming Wu, Jing Wu, Jae-Heon Kim, and Nae Yoon Lee. Instantaneous room temperature bonding of a wide range of non-silicon substrates with poly(dimethylsiloxane) (pdms) elastomer mediated by a mercaptosilane. *Lab on a chip*, 15:2819–2825, July 2015.
- [409] Linzhi Tang and Nae Yoon Lee. A facile route for irreversible bonding of plastic-pdms hybrid microdevices at room temperature. *Lab on a chip*, 10:1274–1280, May 2010.
- [410] Chia-Wen Tsao and Don L. DeVoe. Bonding of thermoplastic polymer microfluidics. *Microfluidics and Nanofluidics*, 6(1):1–16, Jan 2009.

- [411] Seyed Ali Mousavi Shaegh, Adel Pourmand, Mahboubeh Nabavinia, Huseyin Avci, Ali Tamayol, Pooria Mostafalu, Habib Badri Ghavifekr, Esmaeil Najafi Aghdam, Mehmet Remzi Dokmeci, Ali Khademhosseini, and Yu Shrike Zhang. Rapid prototyping of whole-thermoplastic microfluidics with built-in microvalves using laser ablation and thermal fusion bonding. *Sensors and Actuators B: Chemical*, 255:100 – 109, 2018.
- [412] Marco Matteucci, Arto Heiskanen, Kinga Zór, Jenny Emnéus, and Rafael Taborski. Comparison of ultrasonic welding and thermal bonding for the integration of thin film metal electrodes in injection molded polymeric lab-on-chip systems for electrochemistry. *Sensors (Basel, Switzerland)*, 16, October 2016.
- [413] H. Potente, J. Korte, and F. Becker. Laser transmission welding of thermoplastics: Analysis of the heating phase. *Journal of Reinforced Plastics and Composites*, 18(10):914–920, 1999.
- [414] Takahiko Yamaguchi, Shuichi Asakura, and Akio Fuwa. Evaluation of changes in chemical structures of poly (methyl-methacrylate) using 172nm vacuum ultraviolet light. *Journal of Materials Life Society*, 17(4):140–145, 2005.
- [415] Chenxi Wang, Xiaoyun Qi, Yuan Wang, Bin Wu, and Yanhong Tian. Room-temperature direct heterogeneous bonding of glass and polystyrene substrates. *Journal of The Electrochemical Society*, 165(8):B3091–B3097, 2018.
- [416] C W Tsao, L Hromada, J Liu, P Kumar, and D L DeVoe. Low temperature bonding of pmma and coc microfluidic substrates using uv/ozone surface treatment. *Lab on a chip*, 7:499–505, April 2007.
- [417] Yi-Chu Hsu and Tang-Yuan Chen. Applying taguchi methods for solvent-assisted pmma bonding technique for static and dynamic μ -tas devices. *Biomedical microdevices*, 9(4):513–522, 2007.
- [418] Dieudonne A Mair, Marco Rolandi, Marian Snauko, Richard Noroski, Frantisek Svec, and Jean MJ Fréchet. Room-temperature bonding for plastic high-pressure microfluidic chips. *Analytical chemistry*, 79(13):5097–5102, 2007.
- [419] Alwin MD Wan, Amir Sadri, and Edmond WK Young. Liquid phase solvent bonding of plastic microfluidic devices assisted by retention grooves. *Lab on a Chip*, 15(18):3785–3792, 2015.
- [420] Lutz Riegger, Oliver Strohmeier, Bernd Faltin, Roland Zengerle, and Peter Koltay. Adhesive bonding of microfluidic chips: influence of process parameters. *Journal of Micromechanics and Microengineering*, 20(8):087003, 2010.
- [421] Che-Hsin Lin, Gwo-Bin Lee, Yen-Heng Lin, and Guan-Liang Chang. A fast prototyping process for fabrication of microfluidic systems on soda-lime glass. *Journal of Micromechanics and Microengineering*, 11(6):726, 2001.

-
- [422] Björn Renberg, Kae Sato, Takehiko Tsukahara, Kazuma Mawatari, and Takehiko Kitamori. Hands on: thermal bonding of nano-and microfluidic chips. *Microchimica Acta*, 166(1-2):177–181, 2009.
- [423] Yan Xu, Chenxi Wang, Yiyang Dong, Lixiao Li, Kihoon Jang, Kazuma Mawatari, Tadatomu Suga, and Takehiko Kitamori. Low-temperature direct bonding of glass nanofluidic chips using a two-step plasma surface activation process. *Analytical and bioanalytical chemistry*, 402(3):1011–1018, 2012.
- [424] Yan Xu, Chenxi Wang, Lixiao Li, Nobuhiro Matsumoto, Kihoon Jang, Yiyang Dong, Kazuma Mawatari, Tadatomu Suga, and Takehiko Kitamori. Bonding of glass nanofluidic chips at room temperature by a one-step surface activation using an o₂/cf₄ plasma treatment. *Lab on a Chip*, 13(6):1048–1052, 2013.
- [425] Chenxi Wang, Yuan Wang, Yanhong Tian, Chunqing Wang, and Tadatomu Suga. Room-temperature direct bonding of silicon and quartz glass wafers. *Applied Physics Letters*, 110(22):221602, 2017.
- [426] S. Rowan, S.M. Twyford, J. Hough, D.-H. Gwo, and R. Route. Mechanical losses associated with the technique of hydroxide-catalysis bonding of fused silica. *Physics Letters A*, 246(6):471 – 478, 1998.
- [427] E J Elliffe, J Bogenstahl, A Deshpande, J Hough, C Killow, S Reid, D Robertson, S Rowan, H Ward, and G Cagnoli. Hydroxide-catalysis bonding for stable optical systems for space. *Classical and Quantum Gravity*, 22(10):S257–S267, apr 2005.
- [428] Zhi-Jian Jia, Qun Fang, and Zhao-Lun Fang. Bonding of glass microfluidic chips at room temperatures. *Analytical chemistry*, 76:5597–5602, September 2004.
- [429] Lingxin Chen, Guoan Luo, Kehui Liu, Jiping Ma, Bo Yao, Yongchen Yan, and Yiming Wang. Bonding of glass-based microfluidic chips at low- or room-temperature in routine laboratory. *Sensors and Actuators B: Chemical*, 119(1):335 – 344, 2006.
- [430] A Berthold, L Nicola, PM Sarro, and MJ Vellekoop. Glass-to-glass anodic bonding with standard ic technology thin films as intermediate layers. *Sensors and Actuators A: Physical*, 82(1-3):224–228, 2000.
- [431] Pan Mao and Jongyoon Han. Fabrication and characterization of 20 nm planar nanofluidic channels by glass–glass and glass–silicon bonding. *Lab on a Chip*, 5(8):837–844, 2005.
- [432] Ville Saarela, Markus Haapala, Risto Kostianen, Tapio Kotiaho, and Sami Franssila. Glass microfabricated nebulizer chip for mass spectrometry. *Lab on a Chip*, 7(5):644–646, 2007.
- [433] George Wallis and Daniel I Pomerantz. Field assisted glass-metal sealing. *Journal of applied physics*, 40(10):3946–3949, 1969.

- [434] George Wallis. Field assisted glass sealing. *Active and Passive Electronic Components*, 2(1):45–53, 1975.
- [435] Yu-Jen Pan and Ruey-Jen Yang. A glass microfluidic chip adhesive bonding method at room temperature. *Journal of Micromechanics and Microengineering*, 16(12):2666, 2006.
- [436] Pin-Chuan Chen, Yu-Min Liu, and Huang-Chieh Chou. An adhesive bonding method with microfabricating micro pillars to prevent clogging in a microchannel. *Journal of Micromechanics and Microengineering*, 26(4):045003, 2016.
- [437] Lily Kim, Yi-Chin Toh, Joel Voldman, and Henry Yu. A practical guide to microfluidic perfusion culture of adherent mammalian cells. *Lab on a chip*, 7(6):681–694, June 2007.
- [438] Jong Hwan Sung and Michael L Shuler. Prevention of air bubble formation in a microfluidic perfusion cell culture system using a microscale bubble trap. *Biomedical microdevices*, 11:731–738, August 2009.
- [439] Yong Wang, Dongyoung Lee, Lisa Zhang, Hyojin Jeon, Joshua E Mendoza-Elias, Tricia A Harvat, Sarah Z Hassan, Amanda Zhou, David T Eddington, and José Oberholzer. Systematic prevention of bubble formation and accumulation for long-term culture of pancreatic islet cells in microfluidic device. *Biomedical microdevices*, 14(2):419–426, April 2012.
- [440] Paul M Reynolds, Camilla Holzmann Rasmussen, Mattias Hansson, Martin Dufva, Mathis O Riehle, and Nikolaj Gadegaard. Controlling fluid flow to improve cell seeding uniformity. *PloS one*, 13(11):e0207211, 2018.
- [441] Margaret Elizabeth Prendergast, Gabriel Montoya, Taciana Pereira, Jakub Lewicki, Ricky Solorzano, and Anthony Atala. Microphysiological systems: automated fabrication via extrusion bioprinting. *Microphysiological Systems*, 2(3), 2018.
- [442] Chang Kyu Byun, Kameel Abi-Samra, Yoon-Kyoung Cho, and Shuichi Takayama. Pumps for microfluidic cell culture. *Electrophoresis*, 35:245–257, February 2014.
- [443] M Masuda and Keigi Fujiwara. Morphological responses of single endothelial cells exposed to physiological levels of fluid shear stress. *Frontiers of medical and biological engineering: the international journal of the Japan Society of Medical Electronics and Biological Engineering*, 5(2):79–87, 1993.
- [444] E VanBavel. Effects of shear stress on endothelial cells: possible relevance for ultrasound applications. *Progress in biophysics and molecular biology*, 93(1-3):374–383, 2007.
- [445] Dimitry A Chistiakov, Alexander N Orekhov, and Yuri V Bobryshev. Effects of shear stress on endothelial cells: go with the flow. *Acta Physiologica*, 219(2):382–408, 2017.

-
- [446] Cara F Buchanan, Scott S Verbridge, Pavlos P Vlachos, and Marissa Nichole Rylander. Flow shear stress regulates endothelial barrier function and expression of angiogenic factors in a 3d microfluidic tumor vascular model. *Cell adhesion & migration*, 8(5):517–524, 2014.
- [447] Hasan Erbil Abaci, Yu-I Shen, Scott Tan, and Sharon Gerecht. Recapitulating physiological and pathological shear stress and oxygen to model vasculature in health and disease. *Scientific reports*, 4:4951, 2014.
- [448] Donald P Gaver III and Stephanie M Kute. A theoretical model study of the influence of fluid stresses on a cell adhering to a microchannel wall. *Biophysical journal*, 75(2):721–733, 1998.
- [449] Arden L. Buck. New equations for computing vapor pressure and enhancement factor. *Journal of Applied Meteorology*, 20:1527–1532, 1981.
- [450] Michael P McRae, Glennon Simmons, and John T McDevitt. Challenges and opportunities for translating medical microdevices: insights from the programmable bio-nano-chip. *Bioanalysis*, 8:905–919, May 2016.
- [451] Ales Prokop, Zdenka Prokop, David Schaffer, Eugene Kozlov, John Wikswo, David Cliffler, and Franz Baudenbacher. Nanoliterbioreactor: long-term mammalian cell culture at nanofabricated scale. *Biomedical microdevices*, 6:325–339, December 2004.
- [452] J Steigert, S Haeberle, T Brenner, C Müller, CP Steinert, P Koltay, N Gottschlich, H Reinecke, J Rühle, R Zengerle, et al. Rapid prototyping of microfluidic chips in coc. *Journal of Micromechanics and Microengineering*, 17(2):333, 2007.
- [453] Andrew M Christensen, David A Chang-Yen, and Bruce K Gale. Characterization of interconnects used in pdms microfluidic systems. *Journal of Micromechanics and Microengineering*, 15(5):928, 2005.
- [454] Ji-Yen Cheng, Meng-Hua Yen, Ching-Te Kuo, and Tai-Horng Young. A transparent cell-culture microchamber with a variably controlled concentration gradient generator and flow field rectifier. *Biomicrofluidics*, 2(2):24105, 2008.
- [455] Siwei Zhao, Kan Zhu, Yan Zhang, Zijie Zhu, Zhengping Xu, Min Zhao, and Tingrui Pan. Electrotaxis-on-a-chip (etc): an integrated quantitative high-throughput screening platform for electrical field-directed cell migration. *Lab on a Chip*, 14(22):4398–4405, 2014.
- [456] Takanori Kihara, Junri Ito, and Jun Miyake. Measurement of biomolecular diffusion in extracellular matrix condensed by fibroblasts using fluorescence correlation spectroscopy. *PLoS One*, 8(11):e82382, 2013.
- [457] Hsieh-Fu Tsai, Joanna Gajda, Tyler FW Sloan, Andrei Rares, and Amy Q Shen. Usiigaci: Instance-aware cell tracking in stain-free phase contrast microscopy enabled by machine learning. *SoftwareX*, 9:230–237, 2019.

- [458] J E Moore, E Bürki, A Suciu, S Zhao, M Burnier, H R Brunner, and J J Meister. A device for subjecting vascular endothelial cells to both fluid shear stress and circumferential cyclic stretch. *Annals of biomedical engineering*, 22:416–422, 1994.
- [459] Christopher J Bettinger, Robert Langer, and Jeffrey T Borenstein. Engineering substrate topography at the micro- and nanoscale to control cell function. *Angewandte Chemie (International ed. in English)*, 48:5406–5415, 2009.
- [460] Robert Steward, Dhananjay Tambe, C Corey Hardin, Ramaswamy Krishnan, and Jeffrey J Fredberg. Fluid shear, intercellular stress, and endothelial cell alignment. *American journal of physiology. Cell physiology*, 308:C657–C664, April 2015.
- [461] Roy Wollman and Nico Stuurman. High throughput microscopy: from raw images to discoveries. *Journal of cell science*, 120:3715–3722, November 2007.
- [462] F. Zernike. Phase contrast, a new method for the microscopic observation of transparent objects. *Physica*, 9(7):686 – 698, 1942.
- [463] N Jaccard, N Szita, and L D Griffin. Segmentation of phase contrast microscopy images based on multi-scale local basic image features histograms. *Computer methods in biomechanics and biomedical engineering. Imaging & visualization*, 5:359–367, September 2017.
- [464] Richard Kasprowicz, Rakesh Suman, and Peter O’Toole. Characterising live cell behaviour: Traditional label-free and quantitative phase imaging approaches. *The International Journal of Biochemistry & Cell Biology*, 84:89–95, March 2017.
- [465] YongKeun Park, Christian Depeursinge, and Gabriel Popescu. Quantitative phase imaging in biomedicine. *Nature Photonics*, 12(10):578–589, October 2018.
- [466] Paola Masuzzo, Marleen Van Troys, Christophe Ampe, and Lennart Martens. Taking aim at moving targets in computational cell migration. *Trends in cell biology*, 26(2):88–110, 2016.
- [467] Erik Meijering, Oleh Dzyubachyk, and Ihor Smal. Methods for cell and particle tracking. In *Methods in enzymology*, volume 504, pages 183–200. Elsevier, 2012.
- [468] M E Ambühl, C Brepsant, J-J Meister, A B Verkhovsky, and I F Sbalzarini. High-resolution cell outline segmentation and tracking from phase-contrast microscopy images. *Journal of microscopy*, 245:161–170, February 2012.
- [469] Fabrice P Cordelières, Valérie Petit, Mayuko Kumasaka, Olivier Debeir, Véronique Letort, Stuart J Gallagher, and Lionel Larue. Automated cell tracking and analysis in phase-contrast videos (itrack4u): development of java software based on combined mean-shift processes. *PLoS ONE*, 8(11):e81266, 2013.
- [470] Nicolas Jaccard, Lewis D Griffin, Ana Keser, Rhys J Macown, Alexandre Super, Farlan S Veraitch, and Nicolas Szita. Automated method for the rapid and precise estimation of adherent cell culture characteristics from phase contrast microscopy images. *Biotechnology and bioengineering*, 111:504–517, March 2014.

-
- [471] Joe Chalfoun, Michael Majurski, Alden Dima, Christina Stuelten, Adele Peskin, and Mary Brady. Fogbank: a single cell segmentation across multiple cell lines and image modalities. *Bmc Bioinformatics*, 15(1):431, 2014.
- [472] Claudia Tanja Mierke. The fundamental role of mechanical properties in the progression of cancer disease and inflammation. *Reports on Progress in Physics*, 77(7):076602, 2014.
- [473] V. Wiesmann, D. Franz, C. Held, C. Munzenmayer, R. Palmisano, and T. Wittenberg. Review of free software tools for image analysis of fluorescence cell micrographs. *Journal of Microscopy*, 257(1):39–53, 2015.
- [474] Kevin Smith, Filippo Piccinini, Tamas Balassa, Krisztian Koos, Tivadar Danka, Hossein Azizpour, and Peter Horvath. Phenotypic Image Analysis Software Tools for Exploring and Understanding Big Image Data from Cell-Based Assays. *Cell Systems*, 6(6):636–653, June 2018.
- [475] Olaf Ronneberger, Philipp Fischer, and Thomas Brox. U-net: Convolutional networks for biomedical image segmentation. In *International Conference on Medical image computing and computer-assisted intervention*, pages 234–241. Springer, 2015.
- [476] David A Van Valen, Takamasa Kudo, Keara M Lane, Derek N Macklin, Nicolas T Quach, Mialy M DeFelice, Inbal Maayan, Yu Tanouchi, Euan A Ashley, and Markus W Covert. Deep learning automates the quantitative analysis of individual cells in live-cell imaging experiments. *PLoS computational biology*, 12(11):e1005177, 2016.
- [477] Hirohiko Niioka, Satoshi Asatani, Aina Yoshimura, Hironori Ohigashi, Seiichi Tagawa, and Jun Miyake. Classification of c2c12 cells at differentiation by convolutional neural network of deep learning using phase contrast images. *Human cell*, 31:87–93, January 2018.
- [478] A. Arbelle and T. R. Raviv. Microscopy cell segmentation via adversarial neural networks. In *2018 IEEE 15th International Symposium on Biomedical Imaging (ISBI 2018)*, pages 645–648, April 2018.
- [479] Matthias Haering, Joerg Grosshans, Fred Wolf, and Stephan Eule. Automated Segmentation of Epithelial Tissue Using Cycle-Consistent Generative Adversarial Networks. *bioRxiv*, page 311373, April 2018.
- [480] L. Han, R. F. Murphy, and D. Ramanan. Learning Generative Models of Tissue Organization with Supervised GANs. In *2018 IEEE Winter Conference on Applications of Computer Vision (WACV)*, pages 682–690, March 2018.
- [481] Dinggang Shen, Guorong Wu, and Heung-Il Suk. Deep learning in medical image analysis. *Annual Review of Biomedical Engineering*, 19(1):221–248, 2017.

- [482] Travers Ching, Daniel S Himmelstein, Brett K Beaulieu-Jones, Alexandr A Kalinin, Brian T Do, Gregory P Way, Enrico Ferrero, Paul-Michael Agapow, Michael Zietz, Michael M Hoffman, et al. Opportunities and obstacles for deep learning in biology and medicine. *Journal of The Royal Society Interface*, 15(141):20170387, 2018.
- [483] F. Xing, Y. Xie, H. Su, F. Liu, and L. Yang. Deep Learning in Microscopy Image Analysis: A Survey. *IEEE Transactions on Neural Networks and Learning Systems*, 29(10):4550–4568, October 2018.
- [484] Keni Bernardin and Rainer Stiefelwagen. Evaluating multiple object tracking performance: the clear mot metrics. *Journal on Image and Video Processing*, 2008:1, 2008.
- [485] Anton Milan, Laura Leal-Taixé, Ian Reid, Stefan Roth, and Konrad Schindler. Mot16: A benchmark for multi-object tracking. *arXiv preprint arXiv:1603.00831*, 2016.
- [486] Elena Scarpa and Roberto Mayor. Collective cell migration in development. *J Cell Biology*, 212(2):143–155, January 2016.
- [487] Damian Stichel, Alistair M. Middleton, Benedikt F. Muller, Sofia Depner, Ursula Klingmuller, Kai Breuhahn, and Franziska Matthaus. An individual-based model for collective cancer cell migration explains speed dynamics and phenotype variability in response to growth factors. *npj Systems Biology and Applications*, 3(1):5, March 2017.
- [488] Veronika te Boekhorst, Luigi Preziosi, and Peter Friedl. Plasticity of Cell Migration In Vivo and In Silico. *Annual Review of Cell and Developmental Biology*, 32(1):491–526, 2016.
- [489] Carl-Magnus Svensson, Anna Medyukhina, Ivan Belyaev, Naim Al-Zaben, and Marc Thilo Figge. Untangling cell tracks: Quantifying cell migration by time lapse image data analysis. *Cytometry Part A*, 93(3):357–370, 2018.
- [490] Sachiko Sato, Ann Rancourt, Yukiko Sato, and Masahiko S. Satoh. Single-cell lineage tracking analysis reveals that an established cell line comprises putative cancer stem cells and their heterogeneous progeny. *Scientific Reports*, 6:23328, March 2016.
- [491] Jacob C. Kimmel, Amy Y. Chang, Andrew S. Brack, and Wallace F. Marshall. Inferring cell state by quantitative motility analysis reveals a dynamic state system and broken detailed balance. *PLOS Computational Biology*, 14(1):e1005927, January 2018.
- [492] Elena Holden, Attila Tarnok, and Gabriel Popescu. Quantitative phase imaging for label-free cytometry. *Cytometry Part A*, 91(5):407–411, 2017.

-
- [493] Jacob Kimmel, Andrew Brack, and Wallace F. Marshall. Deep convolutional and recurrent neural networks for cell motility discrimination and prediction. *bioRxiv*, 2018.
- [494] Versari Cristian, Stoma Szymon, Batmanov Kirill, Llamosi Artémis, Mroz Filip, Kaczmarek Adam, Deyell Matt, Lhoussaine Cédric, Hersen Pascal, and Batt Gregory. Long-term tracking of budding yeast cells in brightfield microscopy: Cellstar and the evaluation platform. *Journal of The Royal Society Interface*, 14(127):20160705, February 2019.
- [495] K. He, G. Gkioxari, P. Dollár, and R. Girshick. Mask r-CNN. In *Proc. IEEE Int. Conf. Computer Vision (ICCV)*, pages 2980–2988, October 2017.
- [496] Martín Abadi, Paul Barham, Jianmin Chen, Zhifeng Chen, Andy Davis, Jeffrey Dean, Matthieu Devin, Sanjay Ghemawat, Geoffrey Irving, Michael Isard, Manjunath Kudlur, Josh Levenberg, Rajat Monga, Sherry Moore, Derek G. Murray, Benoit Steiner, Paul Tucker, Vijay Vasudevan, Pete Warden, Martin Wicke, Yuan Yu, and Xiaoqiang Zheng. Tensorflow: A system for large-scale machine learning. In *Proceedings of the 12th USENIX Conference on Operating Systems Design and Implementation, OSDI'16*, pages 265–283, Berkeley, CA, USA, 2016. USENIX Association.
- [497] François Chollet et al. Keras. <https://keras.io>, 2015.
- [498] Waleed Abdulla. Mask r-cnn for object detection and instance segmentation on keras and tensorflow. https://github.com/matterport/Mask_RCNN, 2017.
- [499] Kaiming He, Xiangyu Zhang, Shaoqing Ren, and Jian Sun. Deep residual learning for image recognition. In *Proceedings of the IEEE conference on computer vision and pattern recognition*, pages 770–778, 2016.
- [500] T. Lin, P. Dollár, R. Girshick, K. He, B. Hariharan, and S. Belongie. Feature pyramid networks for object detection. In *Proc. IEEE Conf. Computer Vision and Pattern Recognition (CVPR)*, pages 936–944, July 2017.
- [501] S. Ren, K. He, R. Girshick, and J. Sun. Faster r-CNN: Towards real-time object detection with region proposal networks. *IEEE Transactions on Pattern Analysis and Machine Intelligence*, 39(6):1137–1149, June 2017.
- [502] Ainhoa Urbiola, Arrate Muñoz-Barrutia, Carlos Ortiz-de Solorzano, Craig Carthel, Cristina Ederra, Daniel Jimenez-Carretero, David Pastor-Escuredo, David Svoboda, Deepak M.W. Balak, Erik Meijering, Guy M. Hagen, Helen M. Blau, Joakim Jaldén, Karl Rohr, Klas E. G. Magnusson, Maria J. Ledesma-Carbayo, Markéta Štreitová, Martin Maška, Michal Kozubek, Nathalie Harder, Oleh Dzyubachyk, Pavel Karas, Pavel Křížek, Pavel Matula, Petr Matula, Stefano Coraluppi, Subramanian Venkatesan, Tereza Bolcková, Tomás España, and Vladimír Ulman. A benchmark for comparison of cell tracking algorithms. *Bioinformatics*, 30(11):1609–1617, 02 2014.

- [503] Dai Fei Elmer Ker, Sungeun Eom, Sho Sanami, Ryoma Bise, Corinne Pascale, Zhaozheng Yin, Seung-il Huh, Elvira Osuna-Highley, Silvina N. Junkers, Casey J. Helfrich, Peter Yongwen Liang, Jiyan Pan, Soojin Jeong, Steven S. Kang, Jinyu Liu, Ritchie Nicholson, Michael F. Sandbothe, Phu T. Van, Anan Liu, Mei Chen, Takeo Kanade, Lee E. Weiss, and Phil G. Campbell. Phase contrast time-lapse microscopy datasets with automated and manual cell tracking annotations. *Scientific Data*, 5:180237, November 2018.
- [504] Johannes Schindelin, Ignacio Arganda-Carreras, Erwin Frise, Verena Kaynig, Mark Longair, Tobias Pietzsch, Stephan Preibisch, Curtis Rueden, Stephan Saalfeld, Benjamin Schmid, Jean-Yves Tinevez, Daniel James White, Volker Hartenstein, Kevin Eliceiri, Pavel Tomancak, and Albert Cardona. Fiji: an open-source platform for biological-image analysis. *Nature methods*, 9:676–682, June 2012.
- [505] Kevin Eliceiri. Loci:imagej plugin, 2018.
- [506] Tsung-Yi Lin, Michael Maire, Serge Belongie, James Hays, Pietro Perona, Deva Ramanan, Piotr Dollár, and C. Lawrence Zitnick. Microsoft coco: Common objects in context. In David Fleet, Tomas Pajdla, Bernt Schiele, and Tinne Tuytelaars, editors, *Computer Vision – ECCV 2014*, pages 740–755, Cham, 2014. Springer International Publishing.
- [507] Daniel B. Allan, Thomas Caswell, Nathan C. Keim, and Casper M. van der Wel. trackpy: Trackpy v0.4.1, April 2018.
- [508] Jon Louis Bentley. Multidimensional binary search trees used for associative searching. *Commun. ACM*, 18(9):509–517, September 1975.
- [509] John C Crocker and David G Grier. Methods of digital video microscopy for colloidal studies. *Journal of colloid and interface science*, 179(1):298–310, 1996.
- [510] Songrit Maneewongvatana and David M Mount. On the efficiency of nearest neighbor searching with data clustered in lower dimensions. In *International Conference on Computational Science*, pages 842–851. Springer, 2001.
- [511] Riverbank Computing. PyQt. *PyQt is available online at <http://www.riverbankcomputing.co.uk/>, visited on June, 13, 2013.*
- [512] Luke Campagnola. Pyqtgraph-scientific graphics and gui library for python, 2016.
- [513] Stéfan van der Walt, Johannes L Schönberger, Juan Nunez-Iglesias, François Boulogne, Joshua D Warner, Neil Yager, Emmanuelle Gouillart, Tony Yu, and scikit-image contributors. scikit-image: image processing in python. *PeerJ*, 2:e453, 2014.
- [514] Wes McKinney et al. Data structures for statistical computing in python. In *Proceedings of the 9th Python in Science Conference*, volume 445, pages 51–56. Austin, TX, 2010.

-
- [515] Travis E Oliphant. *A guide to NumPy*, volume 1. Trelgol Publishing USA, 2006.
- [516] Travis E Oliphant. Scipy: Open source scientific tools for python. *Computing in Science and Engineering*, 9:10–20, 2007.
- [517] Thomas Kluyver, Benjamin Ragan-Kelley, Fernando Pérez, Brian E Granger, Matthias Bussonnier, Jonathan Frederic, Kyle Kelley, Jessica B Hamrick, Jason Grout, Sylvain Corlay, et al. Jupyter notebooks—a publishing format for reproducible computational workflows. In *ELPUB*, pages 87–90, 2016.
- [518] John D Hunter. Matplotlib: A 2d graphics environment. *Computing in science & engineering*, 9(3):90–95, 2007.
- [519] Michael Waskom, Olga Botvinnik, Drew O’Kane, Paul Hobson, Saulius Lukauskas, David C Gemperline, Tom Augspurger, Yaroslav Halchenko, John B. Cole, Jordi Warmenhoven, Julian de Ruiter, Cameron Pye, Stephan Hoyer, Jake Vanderplas, Santi Villalba, Gero Kunter, Eric Quintero, Pete Bachant, Marcel Martin, Kyle Meyer, Alistair Miles, Yoav Ram, Tal Yarkoni, Mike Lee Williams, Constantine Evans, Clark Fitzgerald, Brian, Chris Fonnesbeck, Antony Lee, and Adel Qalieh. mwaskom/seaborn: v0.8.1 (september 2017), September 2017.
- [520] Joe Chalfoun, Michael Majurski, Alden Dima, Michael Halter, Kiran Bhadriraju, and Mary Brady. Lineage mapper: A versatile cell and particle tracker. *Scientific Reports*, 6:36984, November 2016.
- [521] Ioana Niculescu, Johannes Textor, and Rob J De Boer. Crawling and gliding: a computational model for shape-driven cell migration. *PLoS computational biology*, 11(10):e1004280, 2015.
- [522] Paola Masuzzo, Lynn Huyck, Aleksandra Simiczyjew, Christophe Ampe, Lennart Martens, and Marleen Van Troys. An end-to-end software solution for the analysis of high-throughput single-cell migration data. *Scientific reports*, 7:42383, February 2017.
- [523] Özgün Çiçek, Ahmed Abdulkadir, Soeren S Lienkamp, Thomas Brox, and Olaf Ronneberger. 3d u-net: learning dense volumetric segmentation from sparse annotation. In *International Conference on Medical Image Computing and Computer-Assisted Intervention*, pages 424–432. Springer, 2016.
- [524] Mengjia Xu, Dimitrios P Papageorgiou, Sabia Z Abidi, Ming Dao, Hong Zhao, and George Em Karniadakis. A deep convolutional neural network for classification of red blood cells in sickle cell anemia. *PLoS computational biology*, 13(10):e1005746, 2017.
- [525] Eric M Christiansen, Samuel J Yang, D Michael Ando, Ashkan Javaherian, Gaia Skibinski, Scott Lipnick, Elliot Mount, Alison O’Neil, Kevan Shah, Alicia K Lee, et al. In silico labeling: Predicting fluorescent labels in unlabeled images. *Cell*, 173(3):792–803, 2018.

- [526] Chawin Ounkomol, Sharmishta Seshamani, Mary M. Maleckar, Forrest Collman, and Gregory R. Johnson. Label-free prediction of three-dimensional fluorescence images from transmitted-light microscopy. *Nature Methods*, 15(11):917–920, November 2018.
- [527] Paola Masuzzo, Lennart Martens, et al. An open data ecosystem for cell migration research. *Trends in cell biology*, 25(2):55–58, 2015.
- [528] Mike J. Downey, Danuta M. Jeziorska, Sascha Ott, T. Katherine Tamai, Georgy Koentges, Keith W. Vance, and Till Bretschneider. Extracting Fluorescent Reporter Time Courses of Cell Lineages from High-Throughput Microscopy at Low Temporal Resolution. *PLOS ONE*, 6(12):e27886, December 2011.
- [529] Katja M. Piltti, Brian J. Cummings, Krystal Carta, Ayla Manughian-Peter, Colleen L. Worne, Kulbir Singh, Danier Ong, Yuriy Maksymyuk, Michelle Khine, and Aileen J. Anderson. Live-cell time-lapse imaging and single-cell tracking of in vitro cultured neural stem cells –Tools for analyzing dynamics of cell cycle, migration, and lineage selection. *Methods*, 133:81–90, January 2018.
- [530] O Gallego. Nonsurgical treatment of recurrent glioblastoma. *Current oncology*, 22(4):e273, 2015.
- [531] Supriya Mallick, Rony Benson, Abdul Hakim, and Goura K Rath. Management of glioblastoma after recurrence: A changing paradigm. *Journal of the Egyptian National Cancer Institute*, 28(4):199–210, 2016.
- [532] Akira Hara, Tomohiro Kanayama, Kei Noguchi, Ayumi Niwa, Masafumi Miyai, Masaya Kawaguchi, Kazuhisa Ishida, Yuichiro Hatano, Masayuki Niwa, and Hiroyuki Tomita. Treatment strategies based on histological targets against invasive and resistant glioblastoma. *Journal of Oncology*, 2019, 2019.
- [533] Maria Alieva, Verena Leidgens, Markus J Riemenschneider, Christoph A Klein, Peter Hau, and Jacco van Rheenen. Intravital imaging of glioma border morphology reveals distinctive cellular dynamics and contribution to tumor cell invasion. *Scientific reports*, 9(1):2054, 2019.
- [534] Anne Dirkse, Anna Golebiewska, Thomas Buder, Petr V Nazarov, Arnaud Muller, Suresh Poovathingal, Nicolaas HC Brons, Sonia Leite, Nicolas Sauvageot, Dzjemma Sarkisjan, et al. Stem cell-associated heterogeneity in glioblastoma results from intrinsic tumor plasticity shaped by the microenvironment. *Nature communications*, 10(1):1787, 2019.
- [535] Ivana Manini, Federica Caponnetto, Anna Bartolini, Tamara Ius, Laura Mariuzzi, Carla Di Loreto, Antonio Paolo Beltrami, and Daniela Cesselli. Role of microenvironment in glioma invasion: what we learned from in vitro models. *International journal of molecular sciences*, 19(1):147, 2018.
- [536] William Tomaszewski, Luis Sanchez-Perez, Thomas F Gajewski, and John H Sampson. Brain tumor microenvironment and host state: Implications for immunotherapy. *Clinical Cancer Research*, 25(14):4202–4210, 2019.

-
- [537] Mohammed Diksin, Stuart J Smith, and Ruman Rahman. The molecular and phenotypic basis of the glioma invasive perivascular niche. *International journal of molecular sciences*, 18(11):2342, 2017.
- [538] Adam Hatoum, Raihan Mohammed, and Omar Zakieh. The unique invasiveness of glioblastoma and possible drug targets on extracellular matrix. *Cancer Management and Research*, 11:1843, 2019.
- [539] Barbara E Goodman. Channels active in the excitability of nerves and skeletal muscles across the neuromuscular junction: basic function and pathophysiology. *Advances in physiology education*, 32(2):127–135, 2008.
- [540] WC Taft and RJ DeLorenzo. Regulation of calcium channels in brain: implications for the clinical neurosciences. *The Yale journal of biology and medicine*, 60(2):99, 1987.
- [541] Elisa Mitikp Kawamoto, Carmen Vivar, and Simonetta Camandola. Physiology and pathology of calcium signaling in the brain. *Frontiers in pharmacology*, 3:61, 2012.
- [542] Noemie Robil, Fabien Petel, Marie-Claude Kilhoffer, and Jacques Haiech. Glioblastoma and calcium signaling-analysis of calcium toolbox expression. *Int. J. Dev. Biol*, 59:407–415, 2015.
- [543] Fernanda B Morrone, Marina P Gehring, and Natália F Nicoletti. Calcium channels and associated receptors in malignant brain tumor therapy. *Molecular pharmacology*, 90:403–409, September 2016.
- [544] Julia Pollak, Karan G Rai, Cory C Funk, Sonali Arora, Eunjee Lee, Jun Zhu, Nathan D Price, Patrick J Paddison, Jan-Marino Ramirez, and Robert C Rostomily. Ion channel expression patterns in glioblastoma stem cells with functional and therapeutic implications for malignancy. *PloS one*, 12:e0172884, 2017.
- [545] Nam Nhut Phan, Chih-Yang Wang, Chien-Fu Chen, Zhengda Sun, Ming-Derg Lai, and Yen-Chang Lin. Voltage-gated calcium channels: Novel targets for cancer therapy. *Oncology letters*, 14:2059–2074, August 2017.
- [546] Ahmed Maklad, Anjana Sharma, and Iman Azimi. Calcium signaling in brain cancers: Roles and therapeutic targeting. *Cancers*, 11, January 2019.
- [547] J Thomas Parsons, Alan Rick Horwitz, and Martin A Schwartz. Cell adhesion: integrating cytoskeletal dynamics and cellular tension. *Nature reviews Molecular cell biology*, 11(9):633, 2010.
- [548] Arathi Nair, Prashant Chauhan, Bhaskar Saha, and Katharina F Kubatzky. Conceptual evolution of cell signaling. *International journal of molecular sciences*, 20(13):3292, 2019.

- [549] Radu Albuлесcu, Elena Codrici, Ionela Daniela Popescu, Simona Mihai, Laura Georgiana Necula, Daniel Petrescu, Mihaela Teodoru, and Cristiana Pistol Tanase. Cytokine patterns in brain tumour progression. *Mediators of inflammation*, 2013:979748, 2013.
- [550] Sherman M Cheng, Bing Xing, James C B Li, Benny K W Cheung, and Allan S Y Lau. Interferon-gamma regulation of tnfalpha-induced matrix metalloproteinase 3 expression and migration of human glioma t98g cells. *International journal of cancer*, 121:1190–1196, September 2007.
- [551] Russell L Blaylock. Immunoexcitatory mechanisms in glioma proliferation, invasion and occasional metastasis. *Surgical neurology international*, 4:15, 2013.
- [552] Nicholas C K Valerie, Barbara Dziegielewska, Amol S Hosing, Ewa Augustin, Lloyd S Gray, David L Brautigan, James M Larner, and Jaroslaw Dziegielewski. Inhibition of t-type calcium channels disrupts akt signaling and promotes apoptosis in glioblastoma cells. *Biochemical pharmacology*, 85:888–897, April 2013.
- [553] Ying Zhang, Nichola Cruickshanks, Fang Yuan, Baomin Wang, Mary Patuski, Julia Wulfkuhle, Isela Gallagher, Alexander F Koeppel, Sarah Hatef, Christopher Papanicolas, Jeongwu Lee, Eli E Bar, David Schiff, Stephen D Turner, Emanuel F Petricoin, Lloyd S Gray, and Roger Abounader. Targetable t-type calcium channels drive glioblastoma. *Cancer research*, 77:3479–3490, July 2017.
- [554] Gareth R Tibbs, David J Posson, and Peter A Goldstein. Voltage-gated ion channels in the pns: Novel therapies for neuropathic pain? *Trends in pharmacological sciences*, 37:522–542, July 2016.
- [555] Marie Strickland, Bisma Yacoubi-Loueslati, Balkiss Bouhaouala-Zahar, Sylvia L F Pender, and Anis Larbi. Relationships between ion channels, mitochondrial functions and inflammation in human aging. *Frontiers in physiology*, 10:158, 2019.
- [556] Gustavo A Villalona, Brooks Udelsman, Daniel R Duncan, Edward McGillicuddy, Rajendra F Sawh-Martinez, Narutoshi Hibino, Christopher Painter, Tamar Mirensky, Benjamin Erickson, Toshiharu Shinoka, et al. Cell-seeding techniques in vascular tissue engineering. *Tissue Engineering Part B: Reviews*, 16(3):341–350, 2010.
- [557] Chiara De Pascalis and Sandrine Etienne-Manneville. Single and collective cell migration: the mechanics of adhesions. *Molecular biology of the cell*, 28(14):1833–1846, 2017.
- [558] Cameron W Brennan, Roel G W Verhaak, Aaron McKenna, Benito Campos, Houtan Noushmehr, Sofie R Salama, Siyuan Zheng, Debyani Chakravarty, J Zachary Sanborn, Samuel H Berman, Rameen Beroukhim, Brady Bernard, Chang-Jiun Wu, Giannicola Genovese, Ilya Shmulevich, Jill Barnholtz-Sloan, Lihua Zou, Rahulsimham Vegesna, Sachet A Shukla, Giovanni Ciriello, W K Yung, Wei Zhang, Carrie Sougnez, Tom Mikkelsen, Kenneth Aldape, Darell D

- Bigner, Erwin G Van Meir, Michael Prados, Andrew Sloan, Keith L Black, Jennifer Eschbacher, Gaetano Finocchiaro, William Friedman, David W Andrews, Abhijit Guha, Mary Iacocca, Brian P O'Neill, Greg Foltz, Jerome Myers, Daniel J Weisenberger, Robert Penny, Raju Kucherlapati, Charles M Perou, D Neil Hayes, Richard Gibbs, Marco Marra, Gordon B Mills, Eric Lander, Paul Spellman, Richard Wilson, Chris Sander, John Weinstein, Matthew Meyerson, Stacey Gabriel, Peter W Laird, David Haussler, Gad Getz, Lynda Chin, and TCGA Research Network. The somatic genomic landscape of glioblastoma. *Cell*, 155:462–477, October 2013.
- [559] L. N. Kiseleva, A. V. Kartashev, N. L. Vartanyan, A. A. Pinevich, and M. P. Samoilovich. A172 and t98g cell lines characteristics. *Cell and Tissue Biology*, 10(5):341–348, Sep 2016.
- [560] Brett W Stringer, Jens Bunt, Bryan W Day, Guy Barry, Paul R Jamieson, Kathleen S Ensbey, Zara C Bruce, Kate Goasdoué, H el ene Vidal, Sara Charmaz, Fiona M Smith, Leanne T Cooper, Michael Piper, Andrew W Boyd, and Linda J Richards. Nuclear factor one b (nfib) encodes a subtype-specific tumour suppressor in glioblastoma. *Oncotarget*, 7:29306–29320, May 2016.
- [561] R O Hynes. Integrins: versatility, modulation, and signaling in cell adhesion. *Cell*, 69:11–25, April 1992.
- [562] M S Diamond and T A Springer. The dynamic regulation of integrin adhesiveness. *Current biology : CB*, 4:506–517, June 1994.
- [563] Yukimasa Taniguchi, Hiroyuki Ido, Noriko Sanzen, Maria Hayashi, Ryoko Sato-Nishiuchi, Sugiko Futaki, and Kiyotoshi Sekiguchi. The c-terminal region of laminin beta chains modulates the integrin binding affinities of laminins. *The Journal of biological chemistry*, 284:7820–7831, March 2009.
- [564] Takamichi Miyazaki, Sugiko Futaki, Hirofumi Suemori, Yukimasa Taniguchi, Masashi Yamada, Miwa Kawasaki, Maria Hayashi, Hideaki Kumagai, Norio Nakatsuji, Kiyotoshi Sekiguchi, and Eihachiro Kawase. Laminin e8 fragments support efficient adhesion and expansion of dissociated human pluripotent stem cells. *Nature communications*, 3:1236, 2012.
- [565] R Fridman, M C Kibbey, L S Royce, M Zain, M Sweeney, D L Jicha, J R Yannelli, G R Martin, and H K Kleinman. Enhanced tumor growth of both primary and established human and murine tumor cells in athymic mice after coinjection with matrigel. *Journal of the National Cancer Institute*, 83:769–774, June 1991.
- [566] Junghwa Cha and Pilnam Kim. Biomimetic strategies for the glioblastoma microenvironment. *Frontiers in Materials*, 4:45, 2017.
- [567] Lorraine W Lau, Rowena Cua, Michael B Keough, Sarah Haylock-Jacobs, and V Wee Yong. Pathophysiology of the brain extracellular matrix: a new target for remyelination. *Nature Reviews Neuroscience*, 14(10):722–729, 2013.

- [568] Gregory J Baker, Viveka Nand Yadav, Sebastien Motsch, Carl Koschmann, Anda-Alexandra Calinescu, Yohei Mineharu, Sandra Ines Camelo-Piragua, Daniel Orringer, Serguei Bannykh, Wesley S Nichols, et al. Mechanisms of glioma formation: iterative perivascular glioma growth and invasion leads to tumor progression, vegf-independent vascularization, and resistance to antiangiogenic therapy. *Neoplasia*, 16(7):543–561, 2014.
- [569] Akio Soeda, Akira Hara, Takahiro Kunisada, Shin-ichi Yoshimura, Toru Iwama, and Deric M Park. The evidence of glioblastoma heterogeneity. *Scientific reports*, 5:7979, January 2015.
- [570] Z Zakaria, A Tivnan, L Flanagan, D W Murray, M Salvucci, B W Stringer, B W Day, A W Boyd, D Kögel, M Rehm, D F O’Brien, A T Byrne, and J H M Prehn. Patient-derived glioblastoma cells show significant heterogeneity in treatment responses to the inhibitor-of-apoptosis-protein antagonist birinapant. *British journal of cancer*, 114:188–198, January 2016.
- [571] Si Chen, Thien Le, Brendan A C Harley, and P I Imoukhuede. Characterizing glioblastoma heterogeneity via single-cell receptor quantification. *Frontiers in bioengineering and biotechnology*, 6:92, 2018.
- [572] Sally L Perrin, Michael S Samuel, Barbara Koszyca, Michael P Brown, Lisa M Ebert, Mariana Oksdath, and Guillermo A Gomez. Glioblastoma heterogeneity and the tumour microenvironment: implications for preclinical research and development of new treatments. *Biochemical Society transactions*, 47:625–638, April 2019.
- [573] Niklas Schäfer, Gerrit H Gielen, Laurèl Rauschenbach, Sied Kebir, Andreas Till, Roman Reinartz, Matthias Simon, Pitt Niehusmann, Christoph Kleinschnitz, Ulrich Herrlinger, Torsten Pietsch, Björn Scheffler, and Martin Glas. Longitudinal heterogeneity in glioblastoma: moving targets in recurrent versus primary tumors. *Journal of translational medicine*, 17:96, March 2019.
- [574] C. A. Erickson and R. Nuccitelli. Embryonic fibroblast motility and orientation can be influenced by physiological electric fields. *Journal of Cell Biology*, 98(1):296–307, January 1984.
- [575] Hsin-Ya Yang, Roch-Philippe Charles, Edith Hummler, Deborah L Baines, and R Rivkah Isseroff. The epithelial sodium channel mediates the directionality of galvanotaxis in human keratinocytes. *Journal of cell science*, 126:1942–1951, May 2013.
- [576] E K Onuma and S W Hui. A calcium requirement for electric field-induced cell shape changes and preferential orientation. *Cell calcium*, 6:281–292, June 1985.
- [577] L Tung, N Sliz, and M R Mulligan. Influence of electrical axis of stimulation on excitation of cardiac muscle cells. *Circulation research*, 69:722–730, September 1991.

-
- [578] T A Banks, P S B Luckman, J E Frith, and J J Cooper-White. Effects of electric fields on human mesenchymal stem cell behaviour and morphology using a novel multichannel device. *Integrative biology : quantitative biosciences from nano to macro*, 7:693–712, June 2015.
- [579] Gerard H Markx. The use of electric fields in tissue engineering: A review. *Organogenesis*, 4:11–17, January 2008.
- [580] Lucília P da Silva, Subhas C Kundu, Rui L Reis, and Vitor M Correlo. Electric phenomenon: A disregarded tool in tissue engineering and regenerative medicine. *Trends in biotechnology*, October 2019.
- [581] Itsushi Minoura and Etsuko Muto. Dielectric measurement of individual microtubules using the electroorientation method. *Biophysical journal*, 90:3739–3748, May 2006.
- [582] Taesung Kim, Ming-Tse Kao, Ernest F Hasselbrink, and Edgar Meyhöfer. Active alignment of microtubules with electric fields. *Nano letters*, 7:211–217, January 2007.
- [583] Lynne J Shanley, Petr Walczysko, Mary Bain, David J MacEwan, and Min Zhao. Influx of extracellular ca^{2+} is necessary for electrotaxis in dictyostelium. *J Cell Sci*, 119(22):4741–4748, 2006.
- [584] Przemysław Borys. The role of passive calcium influx through the cell membrane in galvanotaxis. *Cellular & molecular biology letters*, 18(2):187, 2013.
- [585] Liang Guo, Chunyan Xu, Dong Li, Xiulan Zheng, Jiebing Tang, Jingyi Bu, Hui Sun, Zhengkai Yang, Wenjing Sun, and Xiaoguang Yu. Calcium ion flow permeates cells through socs to promote cathode-directed galvanotaxis. *PloS one*, 10(10):e0139865, 2015.
- [586] R Babona-Pilipos, N Liu, A Pritchard-Oh, A Mok, D Badawi, MR Popovic, and CM Morshead. Calcium influx differentially regulates migration velocity and directedness in response to electric field application. *Experimental cell research*, 368(2):202–214, 2018.
- [587] Michael B Mcferrin and Harald Sontheimer. A role for ion channels in glioma cell invasion. *Neuron glia biology*, 2(1):39–49, 2006.
- [588] Harald Sontheimer. An unexpected role for ion channels in brain tumor metastasis. *Experimental biology and medicine*, 233(7):779–791, 2008.
- [589] Remco J Molenaar. Ion channels in glioblastoma. *ISRN neurology*, 2011, 2011.
- [590] Rong Wang, Christopher I Gurguis, Wanjun Gu, Eun A Ko, Inja Lim, Hyoweon Bang, Tong Zhou, and Jae-Hong Ko. Ion channel gene expression predicts survival in glioma patients. *Scientific reports*, 5:11593, August 2015.

- [591] Hao-Yuan Wang, Ji-Ye Li, Xiu Liu, Xiao-Yan Yan, Wen Wang, Fan Wu, Ting-Yu Liang, Fan Yang, Hui-Min Hu, Heng-Xu Mao, Yan-Wei Liu, and Shi-Zhong Zhang. A three ion channel genes-based signature predicts prognosis of primary glioblastoma patients and reveals a chemotherapy sensitive subtype. *Oncotarget*, 7:74895–74903, November 2016.
- [592] Miki Aonuma, Takashi Kadono, and Tomonori Kawano. Inhibition of anodic galvanotaxis of green paramecia by t-type calcium channel inhibitors. *Zeitschrift fur Naturforschung. C, Journal of biosciences*, 62:93–102, 2007.
- [593] Yuji Atsuta, Reiko R Tomizawa, Michael Levin, and Clifford J Tabin. L-type voltage-gated ca²⁺ channel cav1.2 regulates chondrogenesis during limb development. *Proceedings of the National Academy of Sciences of the United States of America*, 116:21592–21601, October 2019.
- [594] Luis A Pardo, Constanza Contreras-Jurado, M Zientkowska, Frauke Alves, and Walter Stühmer. Role of voltage-gated potassium channels in cancer. *The Journal of membrane biology*, 205(3):115–124, 2005.
- [595] Heike Wulff, Neil A Castle, and Luis A Pardo. Voltage-gated potassium channels as therapeutic targets. *Nature reviews Drug discovery*, 8(12):982, 2009.
- [596] Lily Yeh Jan and Yuh Nung Jan. Voltage-gated potassium channels and the diversity of electrical signalling. *The Journal of physiology*, 590(11):2591–2599, 2012.
- [597] Xi Huang and Lily Yeh Jan. Targeting potassium channels in cancer. *J Cell Biol*, 206(2):151–162, 2014.
- [598] AV Grizel, GS Glukhov, and OS Sokolova. Mechanisms of activation of voltage-gated potassium channels. *Acta Naturae*, 6(4 (23)), 2014.
- [599] Nuria Comes, Antonio Serrano-Albarras, Jesusa Capera, Clara Serrano-Novillo, Enric Condom, Santiago Ramón y Cajal, Joan Carles Ferreres, and Antonio Felipe. Involvement of potassium channels in the progression of cancer to a more malignant phenotype. *Biochimica et Biophysica Acta (BBA)-Biomembranes*, 1848(10):2477–2492, 2015.
- [600] Dorothy M Kim and Crina M Nimigea. Voltage-gated potassium channels: a structural examination of selectivity and gating. *Cold Spring Harbor perspectives in biology*, 8(5):a029231, 2016.
- [601] Gaofeng Zhang, Mathew Edmundson, Vsevolod Telezhkin, Yu Gu, Xiaoqing Wei, Paul J Kemp, and Bing Song. The role of kv1.2 channel in electrotaxis cell migration. *Journal of cellular physiology*, 231:1375–1384, June 2016.
- [602] Ken-Ichi Nakajima, Kan Zhu, Yao-Hui Sun, Bence Hegyi, Qunli Zeng, Christopher J Murphy, J Victor Small, Ye Chen-Izu, Yoshihiro Izumiya, Josef M Penninger, and Min Zhao. Kcnj15/kir4.2 couples with polyamines to sense weak

- extracellular electric fields in galvanotaxis. *Nature communications*, 6:8532, October 2015.
- [603] Junji Morokuma, Douglas Blackiston, Dany S Adams, Guiscard Seeböhm, Barry Trimmer, and Michael Levin. Modulation of potassium channel function confers a hyperproliferative invasive phenotype on embryonic stem cells. *Proceedings of the National Academy of Sciences of the United States of America*, 105:16608–16613, October 2008.
- [604] Marc E Laniado, Scott P Fraser, and Mustafa BA Djamgoz. Voltage-gated k⁺ channel activity in human prostate cancer cell lines of markedly different metastatic potential: Distinguishing characteristics of pc-3 and lncap cells. *The Prostate*, 46(4):262–274, 2001.
- [605] Elisa Venturini, Luigi Leanza, Michele Azzolini, Stephanie Kadow, Andrea Mattarei, Michael Weller, Ghazaleh Tabatabai, Michael J Edwards, Mario Zoratti, Cristina Paradisi, et al. Targeting the potassium channel kv1. 3 kills glioblastoma cells. *Neurosignals*, 25(1):26–38, 2017.
- [606] Stefan I McDonough, Linda M Boland, Isabelle M Mintz, and Bruce P Bean. Interactions among toxins that inhibit n-type and p-type calcium channels. *The Journal of general physiology*, 119:313–328, April 2002.
- [607] A Lacampagne, F Gannier, J Argibay, D Garnier, and J Y Le Guennec. The stretch-activated ion channel blocker gadolinium also blocks l-type calcium channels in isolated ventricular myocytes of the guinea-pig. *Biochimica et biophysica acta*, 1191:205–208, April 1994.
- [608] P Turlapaty, R Vary, and J A Kaplan. Nicardipine, a new intravenous calcium antagonist: a review of its pharmacology, pharmacokinetics, and perioperative applications. *Journal of cardiothoracic anesthesia*, 3:344–355, June 1989.
- [609] J M McIntosh, B M Olivera, L J Cruz, and W R Gray. Gamma-carboxyglutamate in a neuroactive toxin. *The Journal of biological chemistry*, 259:14343–14346, December 1984.
- [610] B M Olivera, G P Miljanich, J Ramachandran, and M E Adams. Calcium channel diversity and neurotransmitter release: the omega-conotoxins and omega-agatoxins. *Annual review of biochemistry*, 63:823–867, 1994.
- [611] P M Hinkle, P A Kinsella, and K C Osterhoudt. Cadmium uptake and toxicity via voltage-sensitive calcium channels. *The Journal of biological chemistry*, 262:16333–16337, December 1987.
- [612] Baoshan Xu, Sujuan Chen, Yan Luo, Zi Chen, Lei Liu, Hongyu Zhou, Wenxing Chen, Tao Shen, Xiuzhen Han, Long Chen, and Shile Huang. Calcium signaling is involved in cadmium-induced neuronal apoptosis via induction of reactive oxygen species and activation of mapk/mtor network. *PloS one*, 6:e19052, April 2011.

- [613] R C Foehring, P G Mermelstein, W J Song, S Ulrich, and D J Surmeier. Unique properties of r-type calcium currents in neocortical and neostriatal neurons. *Journal of neurophysiology*, 84:2225–2236, November 2000.
- [614] Carola Wormuth, Andreas Lundt, Christina Henseler, Ralf Müller, Karl Broich, Anna Papazoglou, and Marco Weiergräber. Review: Cav2.3 r-type voltage-gated ca²⁺ channels - functional implications in convulsive and non-convulsive seizure activity. *The open neurology journal*, 10:99–126, 2016.
- [615] Nasrin Nejatbakhsh and Zhong-ping Feng. Calcium binding protein-mediated regulation of voltage-gated calcium channels linked to human diseases. *Acta pharmacologica Sinica*, 32:741–748, June 2011.
- [616] Manu Ben-Johny and David T Yue. Calmodulin regulation (calmodulation) of voltage-gated calcium channels. *The Journal of general physiology*, 143(6):679–692, 2014.
- [617] Brett A Simms and Gerald W Zamponi. Neuronal voltage-gated calcium channels: structure, function, and dysfunction. *Neuron*, 82(1):24–45, 2014.
- [618] J F Faivre, T P Calmels, S Rouanet, J L Javré, B Cheval, and A Bril. Characterisation of kv4.3 in hek293 cells: comparison with the rat ventricular transient outward potassium current. *Cardiovascular research*, 41:188–199, January 1999.
- [619] Noriyuki Hatano, Susumu Ohya, Katsuhiko Muraki, Wayne Giles, and Yuji Imaizumi. Dihydropyridine ca²⁺ channel antagonists and agonists block kv4.2, kv4.3 and kv1.4 k⁺ channels expressed in hek293 cells. *British journal of pharmacology*, 139:533–544, June 2003.
- [620] Tilia Kimm and Bruce P Bean. Inhibition of a-type potassium current by the peptide toxin snx-482. *The Journal of neuroscience : the official journal of the Society for Neuroscience*, 34:9182–9189, July 2014.
- [621] Hélène Vacher, Meriem Alami, Marcel Crest, Lourival D Possani, Pierre E Bougis, and Marie-France Martin-Eauclaire. Expanding the scorpion toxin alpha-ktx 15 family with ammtx3 from androctonus mauretanicus. *European journal of biochemistry*, 269:6037–6041, December 2002.
- [622] Jon K Maffie, Elena Dvoretzkova, Pierre Edouard Bougis, Marie-France Martin-Eauclaire, and Bernardo Rudy. Dipeptidyl-peptidase-like-proteins confer high sensitivity to the scorpion toxin ammtx3 to kv4-mediated a-type k⁺ channels. *The Journal of physiology*, 591:2419–2427, May 2013.
- [623] Pierre Edouard Bougis and Marie-France Martin-Eauclaire. Shal-type (kv4.x) potassium channel pore blockers from scorpion venoms. *Sheng li xue bao : [Acta physiologica Sinica]*, 67:248–254, June 2015.
- [624] S Thompson. Aminopyridine block of transient potassium current. *The Journal of general physiology*, 80:1–18, July 1982.

-
- [625] T Takahashi. Inward rectification in neonatal rat spinal motoneurons. *The Journal of physiology*, 423:47–62, April 1990.
- [626] Taro Ishikawa, Yukihiro Nakamura, Naoto Saitoh, Wen-Bin Li, Shinichi Iwasaki, and Tomoyuki Takahashi. Distinct roles of kv1 and kv3 potassium channels at the calyx of held presynaptic terminal. *The Journal of neuroscience : the official journal of the Society for Neuroscience*, 23:10445–10453, November 2003.
- [627] Cha-Min Tang, Fernando Presser, and Martin Morad. Amiloride selectively blocks the low threshold (t) calcium channel. *Science*, 240(4849):213–215, 1988.
- [628] Richard L Kraus, Yuxing Li, Yun Gregan, Anthony L Gotter, Victor N Uebele, Steven V Fox, Scott M Doran, James C Barrow, Zhi-Qiang Yang, Thomas S Reger, Kenneth S Koblan, and John J Renger. In vitro characterization of t-type calcium channel antagonist tta-a2 and in vivo effects on arousal in mice. *The Journal of pharmacology and experimental therapeutics*, 335:409–417, November 2010.
- [629] Eduardo Chavez-Colorado, Zazil Herrera-Carrillo, and Juan C Gomora. Blocking of t-type calcium channels by tta-a2 reveals a conservative binding site for state-dependent antagonists. *Biophysical Journal*, 110(3):439a–440a, 2016.
- [630] Stefan Gründer and Xuanmao Chen. Structure, function, and pharmacology of acid-sensing ion channels (asics): focus on asic1a. *International journal of physiology, pathophysiology and pharmacology*, 2(2):73, 2010.
- [631] Israel Hanukoglu. Asic and enac type sodium channels: conformational states and the structures of the ion selectivity filters. *The FEBS journal*, 284:525–545, February 2017.
- [632] Thomas R Kleyman and Edward J Cragoe. Amiloride and its analogs as tools in the study of ion transport. *Journal of Membrane Biology*, 105(1):1–21, 1988.
- [633] Xiang-Ping Chu, Jennifer Miesch, Martha Johnson, Leslie Root, Xiao-Man Zhu, Dexi Chen, Roger P Simon, and Zhi-Gang Xiong. Proton-gated channels in pc12 cells. *Journal of neurophysiology*, 87(5):2555–2561, 2002.
- [634] Xiao-Qing Dai, Alkarim Ramji, Yan Liu, Qiang Li, Edward Karpinski, and Xing-Zhen Chen. Inhibition of trpp3 channel by amiloride and analogs. *Molecular pharmacology*, 72(6):1576–1585, 2007.
- [635] Bakhrom K Berdiev, Jiazeng Xia, Lee Anne McLean, James M Markert, G Yancey Gillespie, Timothy B Mapstone, Anjaparavanda P Naren, Biljana Jovov, James K Bubien, Hong-Long Ji, Catherine M Fuller, Kevin L Kirk, and Dale J Benos. Acid-sensing ion channels in malignant gliomas. *The Journal of biological chemistry*, 278:15023–15034, April 2003.
- [636] Yuemin Tian, Pia Bresenitz, Anna Reska, Laila El Moussaoui, Christoph Patrick Beier, and Stefan Gründer. Glioblastoma cancer stem cell lines express functional

- acid sensing ion channels *asic1a* and *asic3*. *Scientific reports*, 7:13674, October 2017.
- [637] Karl-Georg Fischer, Nils Jonas, Florian Poschenrieder, Clemens Cohen, Matthias Kretzler, Stefan Greiber, and Hermann Pavenstädt. Characterization of a $\text{na}(+)\text{-ca}(2+)$ exchanger in podocytes. *Nephrology, dialysis, transplantation : official publication of the European Dialysis and Transplant Association - European Renal Association*, 17:1742–1750, October 2002.
- [638] Seongtae Jeong, Seong Heon Lee, Yeo Ok Kim, and Myung Ha Yoon. Antinociceptive effects of amiloride and benzamil in neuropathic pain model rats. *Journal of Korean medical science*, 28:1238–1243, August 2013.
- [639] Mustafa B A Djamgoz and Rustem Onkal. Persistent current blockers of voltage-gated sodium channels: a clinical opportunity for controlling metastatic disease. *Recent patents on anti-cancer drug discovery*, 8:66–84, January 2013.
- [640] Mustafa B A Djamgoz, Scott P Fraser, and William J Brackenbury. In vivo evidence for voltage-gated sodium channel expression in carcinomas and potentiation of metastasis. *Cancers*, 11, October 2019.
- [641] Alisa Litan and Sigrid A Langhans. Cancer as a channelopathy: ion channels and pumps in tumor development and progression. *Frontiers in cellular neuroscience*, 9:86, 2015.
- [642] Luigi Leanza, Antonella Manago, Mario Zoratti, Erich Gulbins, and Ildiko Szabo. Pharmacological targeting of ion channels for cancer therapy: in vivo evidences. *Biochimica et Biophysica Acta (BBA)-Molecular Cell Research*, 1863(6):1385–1397, 2016.
- [643] Eric C Holland. Glioblastoma multiforme: the terminator. *Proceedings of the National Academy of Sciences*, 97(12):6242–6244, 2000.
- [644] Marta Segarra, Bettina C Kirchmaier, and Amparo Acker-Palmer. A vascular perspective on neuronal migration. *Mechanisms of development*, 138:17–25, 2015.
- [645] Jerald J Bernstein and Christopher A Woodard. Glioblastoma cells do not intravasate into blood vessels. *Neurosurgery*, 36(1):124–132, 1995.
- [646] Vishnu Anand Cuddapah, Stefanie Robel, Stacey Watkins, and Harald Sontheimer. A neurocentric perspective on glioma invasion. *Nature Reviews Neuroscience*, 15(7):455–465, 2014.
- [647] Stacey Watkins, Stefanie Robel, Ian F Kimbrough, Stephanie M Robert, Graham Ellis-Davies, and Harald Sontheimer. Disruption of astrocyte–vascular coupling and the blood–brain barrier by invading glioma cells. *Nature communications*, 5:4196, 2014.

-
- [648] Ton J Rabelink and Thomas F Luscher. Endothelial nitric oxide synthase: host defense enzyme of the endothelium? *Arteriosclerosis, thrombosis, and vascular biology*, 26:267–271, February 2006.
- [649] Sajila Sheikh, G Ed Rainger, Zoe Gale, Mahbub Rahman, and Gerard B Nash. Exposure to fluid shear stress modulates the ability of endothelial cells to recruit neutrophils in response to tumor necrosis factor- α : a basis for local variations in vascular sensitivity to inflammation. *Blood*, 102(8):2828–2834, 2003.
- [650] Omar F Khan and Michael V Sefton. Endothelial cell behaviour within a microfluidic mimic of the flow channels of a modular tissue engineered construct. *Biomedical microdevices*, 13(1):69–87, 2011.
- [651] Joseph S Uzarski, Edward W Scott, and Peter S McFetridge. Adaptation of endothelial cells to physiologically-modeled, variable shear stress. *PloS one*, 8(2):e57004, 2013.
- [652] Justyna Jaczewska, Midhat H Abdulreda, Chi Y Yau, Martin M Schmitt, Irene Schubert, Per-Olof Berggren, Christian Weber, Rory R Koenen, Vincent T Moy, and Ewa P Wojcikiewicz. Tnf- α and ifn- γ promote lymphocyte adhesion to endothelial junctional regions facilitating transendothelial migration. *Journal of leukocyte biology*, 95(2):265–274, 2014.
- [653] Caleb A Davis, Steve Zambrano, Pratima Anumolu, Alicia CB Allen, Leonardo Sonoqui, and Michael R Moreno. Device-based in vitro techniques for mechanical stimulation of vascular cells: a review. *Journal of biomechanical engineering*, 137(4):040801, 2015.
- [654] Ali Khademhosseini, Judy Yeh, George Eng, Jeffrey Karp, Hirokazu Kaji, Jeffrey Borenstein, Omid C Farokhzad, and Robert Langer. Cell docking inside microwells within reversibly sealed microfluidic channels for fabricating multiphenotype cell arrays. *Lab on a chip*, 5:1380–1386, December 2005.
- [655] Hyunwoo Bang, Won Gu Lee, Junha Park, Hoyoung Yun, Joonmo Lee, Seok Chung, Keunchang Cho, Chanil Chung, Dong-Chul Han, and Jun Keun Chang. Active sealing for soft polymer microchips: method and practical applications. *Journal of Micromechanics and Microengineering*, 16(4):708, 2006.
- [656] Peder Skafte-Pedersen, Mette Hemmingsen, David Sabourin, Felician Stefan Blaga, Henrik Bruus, and Martin Dufva. A self-contained, programmable microfluidic cell culture system with real-time microscopy access. *Biomedical Microdevices*, 14(2):385, April 2012.
- [657] Adel M Malek, Seth L Alper, and Seigo Izumo. Hemodynamic shear stress and its role in atherosclerosis. *Jama*, 282(21):2035–2042, 1999.
- [658] F Mackay, H Loetscher, D Stueber, G Gehr, and W Lesslauer. Tumor necrosis factor alpha (tnf-alpha)-induced cell adhesion to human endothelial cells is under dominant control of one tnf receptor type, tnf-r55. *The Journal of experimental medicine*, 177:1277–1286, May 1993.

- [659] Xin Lu and Yibin Kang. Cell fusion as a hidden force in tumor progression. *Cancer research*, 69:8536–8539, November 2009.
- [660] Jennifer Pasquier, Bella S Guerrouahen, Hamda Al Thawadi, Pegah Ghiabi, Mahtab Maleki, Nadine Abu-Kaoud, Arthur Jacob, Massoud Mirshahi, Ludovic Galas, Shahin Rafii, Frank Le Foll, and Arash Rafii. Preferential transfer of mitochondria from endothelial to cancer cells through tunneling nanotubes modulates chemoresistance. *Journal of translational medicine*, 11:94, April 2013.
- [661] Soufiane El Hallani, Carole Colin, Younas El Houfi, Ahmed Idbaih, Blandine Boisselier, Yannick Marie, Philippe Ravassard, Marianne Labussière, Karima Mokhtari, Jean-Léon Thomas, et al. Tumor and endothelial cell hybrids participate in glioblastoma vasculature. *BioMed research international*, 2014, 2014.
- [662] Mao Ye, Henry M Sanchez, Margot Hultz, Zhen Yang, Max Bogorad, Andrew D Wong, and Peter C Searson. Brain microvascular endothelial cells resist elongation due to curvature and shear stress. *Scientific reports*, 4:4681, April 2014.
- [663] Adam Reinitz, Jackson DeStefano, Mao Ye, Andrew D Wong, and Peter C Searson. Human brain microvascular endothelial cells resist elongation due to shear stress. *Microvascular research*, 99:8–18, May 2015.
- [664] RJ Naegele, J Lipari, D Chakkalakal, B Strates, and M McGuire. Electric field stimulation of human osteosarcoma-derived cells: a dose-response study. *Cancer biochemistry biophysics*, 12(2):95–101, 1991.
- [665] Rong Wang, Kalyani Chadalavada, Jennifer Wilshire, Urszula Kowalik, Koos E Hovinga, Adam Geber, Boris Fligelman, Margaret Leversha, Cameron Brennan, and Viviane Tabar. Glioblastoma stem-like cells give rise to tumour endothelium. *Nature*, 468(7325):829, 2010.
- [666] Arnaud Lombard, Nicolas Goffart, and Bernard Rogister. Glioblastoma circulating cells: reality, trap or illusion? *Stem cells international*, 2015, 2015.
- [667] C Korn and US Schwarz. Efficiency of initiating cell adhesion in hydrodynamic flow. *Physical review letters*, 97(13):138103, 2006.
- [668] James O. Wilkes. *Fluid mechanics for chemical engineers: with microfluidics, CFD, and COMSOL Multiphysics 5*. Prentice Hall, 3rd edition, 2017.
- [669] Saverio E Spagnolie. Complex fluids in biological systems. *Biological and Medical Physics, Biomedical Engineering*, 2015.
- [670] Siddhartha Gupta, William S Wang, and Siva A Vanapalli. Microfluidic viscometers for shear rheology of complex fluids and biofluids. *Biomicrofluidics*, 10(4):043402, 2016.
- [671] Rommel G Bacabac, Theo H Smit, Stephen C Cowin, Jack J W A Van Loon, Frans T M Nieuwstadt, Rob Heethaar, and Jenneke Klein-Nulend. Dynamic shear stress in parallel-plate flow chambers. *Journal of biomechanics*, 38:159–167, January 2005.

-
- [672] Andrew K Wong, Pierre Llanos, Nickolas Boroda, Seth R Rosenberg, and Sina Y Rabbany. A parallel-plate flow chamber for mechanical characterization of endothelial cells exposed to laminar shear stress. *Cellular and molecular bioengineering*, 9:127–138, March 2016.
- [673] Eleonore Fröhlich, Gudrun Bonstingl, Anita Höfler, Claudia Meindl, Gerd Leitinger, Thomas R Pieber, and Eva Roblegg. Comparison of two in vitro systems to assess cellular effects of nanoparticles-containing aerosols. *Toxicology in vitro : an international journal published in association with BIBRA*, 27:409–417, February 2013.
- [674] Aude Silve, Isabelle Leray, Clair Poignard, and Lluís M Mir. Impact of external medium conductivity on cell membrane electropermeabilization by microsecond and nanosecond electric pulses. *Scientific reports*, 6:19957, February 2016.
- [675] A P Mazzoleni, B F Siskin, and R L Kahler. Conductivity values of tissue culture medium from 20 degrees c to 40 degrees c. *Bioelectromagnetics*, 7:95–99, 1986.
- [676] Otto Kratky, Hans Leopold, and Hans Stabinger. Device for density determination, August 11 1970. US Patent 3,523,446.
- [677] RF Chang and MR Moldover. High-temperature high-pressure oscillating tube densimeter. *Review of scientific instruments*, 67(1):251–256, 1996.
- [678] Kenneth Walters. *Rheometry*. London : Chapman and Hall ; New York : Wiley, 1975.
- [679] Laurence Ellsworth Dodd. Calibration of abbe refractometer with compensating prisms, to measure refractive index for any wave length. *Review of Scientific Instruments*, 2(8):466–501, 1931.
- [680] Richard A. Paselk. The evolution of abbe refractometer. *Bulletin of the Scientific Instrument Society*, 62:19–22, September 1999.
- [681] R Blaine McCleskey, D Kirk Nordstrom, and Joseph N Ryan. Comparison of electrical conductivity calculation methods for natural waters. *Limnology and Oceanography: Methods*, 10(11):952–967, 2012.
- [682] Thomas G Mezger. *The rheology handbook: for users of rotational and oscillatory rheometers*. Vincentz Network GmbH & Co KG, 2006.
- [683] James Michaels, Ameet K Mallik, Jason E Nowak, Darsh T Wasan, and ET Pappasakis. Dynamic interfacial tension and rheological properties of cell culture medium with shear protectant additives. In *Animal Cell Technology*, pages 389–391. Elsevier, 1994.
- [684] Chantal N van den Broek, Rolf AA Pullens, Ole Frøbert, Marcel Rutten, Wilfred F den Hartog, and Frans N van de Vosse. Medium with blood-analog mechanical properties for cardiovascular tissue culturing. *Biorheology*, 45(6):651–661, 2008.

- [685] Sungmin Nam, Joanna Lee, Doug G Brownfield, and Ovijit Chaudhuri. Viscoplasticity enables mechanical remodeling of matrix by cells. *Biophysical journal*, 111(10):2296–2308, 2016.
- [686] Alexander Golberg, Saiqa Khan, Vasily Belov, Kyle P. Quinn, Hassan Albadawi, G. Felix Broelsch, Michael T. Watkins, Irene Georgakoudi, Mikhail Papisov, Martin C. Mihm Jr., William G. Austen Jr., and Martin L. Yarmush. Skin Rejuvenation with Non-Invasive Pulsed Electric Fields. *Scientific Reports*, 5:10187, May 2015.
- [687] M. W. Rochlin and H. B. Peng. Localization of intracellular proteins at acetylcholine receptor clusters induced by electric fields in *Xenopus* muscle cells. *J Cell Sci*, 94(1):73–83, September 1989.
- [688] Lei Li, Youssef H. El-Hayek, Baosong Liu, Yonghong Chen, Everlyne Gomez, Xiaohua Wu, Ke Ning, Lijun Li, Ning Chang, Liang Zhang, Zhengguo Wang, Xiang Hu, and Qi Wan. Direct-Current Electrical Field Guides Neuronal Stem/Progenitor Cell Migration. *STEM CELLS*, 26(8):2193–2200, August 2008.
- [689] Nurdan Özkucur, Srikanth Perike, Priyanka Sharma, and Richard HW Funk. Persistent directional cell migration requires ion transport proteins as direction sensors and membrane potential differences in order to maintain directedness. *BMC Cell Biology*, 12(1):4, January 2011.
- [690] Fei Li, Hui Wang, Li Li, Chuanshu Huang, Jiangkai Lin, Gang Zhu, Zhi Chen, Nan Wu, and Hua Feng. Superoxide plays critical roles in electrotaxis of fibrosarcoma cells via activation of ERK and reorganization of the cytoskeleton. *Free Radical Biology and Medicine*, 52(9):1888–1896, May 2012.
- [691] Xiaowei Guo, Xupin Jiang, Xi Ren, Huanbo Sun, Dongxia Zhang, Qiong Zhang, Jiaping Zhang, and Yuesheng Huang. The Galvanotactic Migration of Keratinocytes is Enhanced by Hypoxic Preconditioning. *Scientific Reports*, 5:10289, May 2015.
- [692] Stephen Boyden. The Chemotactic Effect of Mixtures of Antibody and Antigen on Polymorphonuclear Leucocytes. *J Exp Med*, 115(3):453–466, March 1962.
- [693] M. Zhao, A. Agius-Fernandez, J. V. Forrester, and C. D. McCaig. Orientation and directed migration of cultured corneal epithelial cells in small electric fields are serum dependent. *Journal of Cell Science*, 109(6):1405–1414, June 1996.
- [694] Mario Marotta, Ramón Bragós, and Anna M Gómez-Foix. Design and performance of an electrical stimulator for long-term contraction of cultured muscle cells. *BioTechniques*, 36:68–73, 2004.
- [695] Jorge A. Genovese, Cristiano Spadaccio, Jason Langer, Jaclyn Habe, Johnna Jackson, and Amit N. Patel. Electrostimulation induces cardiomyocyte predifferentiation of fibroblasts. *Biochemical and Biophysical Research Communications*, 370(3):450–455, June 2008.

-
- [696] Saeko Okutsu, Hiroyasu Hatakeyama, Makoto Kanazaki, Hiroshi Tsubokawa, and Ryoichi Nagatomi. Electric Pulse Stimulation Induces NMDA Glutamate Receptor mRNA in NIH3t3 Mouse Fibroblasts. *The Tohoku Journal of Experimental Medicine*, 215(2):181–187, 2008.
- [697] Ken-ichi Yamasaki, Hiroyuki Hayashi, Keiko Nishiyama, Hiroyuki Kobayashi, Sadahito Uto, Hideo Kondo, Shigehiro Hashimoto, and Toshia Fujisato. Control of myotube contraction using electrical pulse stimulation for bio-actuator. *Journal of Artificial Organs*, 12(2):131–137, June 2009.
- [698] Nathalie Burch, Anne-Sophie Arnold, Flurin Item, Serge Summermatter, Gesa Brochmann Santana Santos, Martine Christe, Urs Boutellier, Marco Toigo, and Christoph Handschin. Electric Pulse Stimulation of Cultured Murine Muscle Cells Reproduces Gene Expression Changes of Trained Mouse Muscle. *PLoS ONE*, 5(6):e10970, June 2010.
- [699] Francis Lin, Fabio Baldessari, Christina Crenguta Gyenge, Tohru Sato, Robert D. Chambers, Juan G. Santiago, and Eugene C. Butcher. Lymphocyte Electrotaxis In Vitro and In Vivo. *Journal Immunology*, 181(4):2465–2471, August 2008.
- [700] Tomás García-Sánchez, Beatriz Sánchez-Ortiz, Ingrid Vila, Maria Guitart, Javier Rosell, Anna M. Gómez-Foix, and Ramón Bragós. Design and Implementation of a Microelectrode Assembly for Use on Noncontact In Situ Electroporation of Adherent Cells. *J Membrane Biol*, 245(10):617–624, July 2012.
- [701] Dinesh K. Ahirwar, Mohd W. Nasser, Travis H. Jones, Emily K. Sequin, Joseph D. West, Timothy L. Henthorne, Joshua Javor, Aniruddha M. Kaushik, Ramesh K. Ganju, and Vish V. Subramaniam. Non-contact method for directing electrotaxis. *Scientific Reports*, 5:11005, June 2015.
- [702] E. Sachs, M. Cima, P. Williams, D. Brancazio, and J. Cornie. Three Dimensional Printing: Rapid Tooling and Prototypes Directly from a CAD Model. *J. Eng. Ind*, 114(4):481–488, November 1992.
- [703] Ansgar Waldbaur, Bernardo Carneiro, Paul Hettich, Elisabeth Wilhelm, and Bastian E. Rapp. Computer-aided microfluidics (CAMF): from digital 3d-CAD models to physical structures within a day. *Microfluid Nanofluid*, 15(5):625–635, April 2013.
- [704] Aliaa I. Shallan, Petr Smejkal, Monika Corban, Rosanne M. Guijt, and Michael C. Breadmore. Cost-Effective Three-Dimensional Printing of Visibly Transparent Microchips within Minutes. *Analytical Chemistry*, 86(6):3124–3130, March 2014.
- [705] Russell K. Hobbie and Bradley J. Roth. *Intermediate Physics for Medicine and Biology*. Springer-Verlag, New York, 4 edition, 2007.
- [706] R. Larson and B.H. Edwards. *Calculus*. Cengage Learning, 2009.

- [707] Nina Tandon, Christopher Cannizzaro, Pen-Hsiu Grace Chao, Robert Maidhof, Anna Marsano, Hoi Ting Heidi Au, Milica Radisic, and Gordana Vunjak-Novakovic. Electrical stimulation systems for cardiac tissue engineering. *Nature Protocols*, 4(2):155–173, January 2009.
- [708] Erik Finkelstein, Winston Chang, P.-H. Grace Chao, Dorota Gruber, Audrey Minden, Clark T. Hung, and J. Chloë Bulinski. Roles of microtubules, cell polarity and adhesion in electric-field-mediated motility of 3t3 fibroblasts. *Journal of Cell Science*, 117(8):1533–1545, March 2004.
- [709] Yu-Ja Huang, Justin Samorajski, Rachel Kreimer, and Peter C. Searson. The Influence of Electric Field and Confinement on Cell Motility. *PLoS ONE*, 8(3):e59447, March 2013.
- [710] P. M. McDonough and C. C. Glembofski. Induction of atrial natriuretic factor and myosin light chain-2 gene expression in cultured ventricular myocytes by electrical stimulation of contraction. *J. Biol. Chem.*, 267(17):11665–11668, June 1992.
- [711] Milica Radisic, Hyounghsin Park, Helen Shing, Thomas Consi, Frederick J. Schoen, Robert Langer, Lisa E. Freed, and Gordana Vunjak-Novakovic. Functional assembly of engineered myocardium by electrical stimulation of cardiac myocytes cultured on scaffolds. *Proc. Natl. Acad. Sci. U.S.A.*, 101(52):18129–18134, December 2004.
- [712] Elena Serena, Elisa Figallo, Nina Tandon, Christopher Cannizzaro, Sharon Gerecht, Nicola Elvassore, and Gordana Vunjak-Novakovic. Electrical stimulation of human embryonic stem cells: Cardiac differentiation and the generation of reactive oxygen species. *Experimental Cell Research*, 315(20):3611–3619, December 2009.
- [713] Yiftach Barash, Tal Dvir, Pini Tandeitnik, Emil Ruvinov, Hugo Guterman, and Smadar Cohen. Electric Field Stimulation Integrated into Perfusion Bioreactor for Cardiac Tissue Engineering. *Tissue Engineering Part C: Methods*, 16(6):1417–1426, April 2010.
- [714] Marie Hronik-Tupaj, William L. Rice, Mark Cronin-Golomb, David L. Kaplan, and Irene Georgakoudi. Osteoblastic differentiation and stress response of human mesenchymal stem cells exposed to alternating current electric fields. *BioMedical Engineering OnLine*, 10(1):9, January 2011.
- [715] Peter Larkin. *Infrared and Raman spectroscopy: principles and spectral interpretation*. Elsevier, 2017.